ACKNOWLEDGMENT

The authors gratefully acknowledge the US Department of Energy, Office of Fusion Energy for supporting this work, along with sincere acknowledgment to Idaho National Engineering and Environmental Laboratory, Fusion Safety Program for their support.

Great appreciation and recognition goes to Mr. John Phillip Sharpe, the PhD graduate student who worked on the project, carefully did all of the experimentation and data analysis, and worked hard on editing the three main ITER EDF files attached to this report.

Indeed, a great deal of appreciation goes to graduate and undergraduate students in the department of nuclear engineering who helped on the experiment during the course of this research, namely, Mr. Huu Ngo who helped in preparation of collection substrates and pre and post shot weight balance, Mr. K.S. Murali who worked on spectral measurements and analysis in support of the experiment, and Mr. Brian Bures and Mr. Ryan Davis who helped in experimentation preparations.

The authors deeply appreciate and highly acknowledge the help they received from Dr. David Petti and Dr. Kathy McCarthy of INEEL for valuable discussions and support during the course of this research, without their valuable help this work could not have been completed. Further acknowledgment goes to Mr. William J. Carmack of INEEL for his great help assisting in the techniques necessary for particulate counting and evaluation.

TABLE OF CONTENTS

ATTACHMENTS:

SAFETY OF PLASMA-FACING COMPONENTS AND AEROSOL TRANSPORT DURING HARD DISRUPTIONS AND ACCIDENTAL ENERGY RELEASE IN FUSION REACTORS

Final Technical Report

by

Mohamed A. Bourham and John G. Gilligan
North Carolina State University, Department of Nuclear Engineering
Raleigh, N. C. 27695-7909

Prepared for

The US Department of Energy
Office of Fusion Energy Research
Contract DE-FG02-96ER54363

North Carolina State University
Department of Nuclear Engineering
Raleigh, NC 27695-7909

August 1999

ABSTRACT

Safety considerations in large future fusion reactors like ITER are important before licensing the reactor. Several scenarios are considered hazardous, which include safety of plasma-facing components during hard disruptions, high heat fluxes and thermal stresses during normal operation, accidental energy release, and aerosol formation and transport. Disruption events, in large tokamaks like ITER, are expected to produce local heat fluxes on plasma-facing components, which may exceed 100 GW/m^2 over a period of about 0.1 ms. As a result, the surface temperature dramatically increases, which results in surface melting and vaporization, and produces thermal stresses and surface erosion. Plasma-facing components safety issues extends to cover a wide range of possible scenarios, including disruption severity and the impact of plasma-facing components on disruption parameters, accidental energy release and short/long term LOCA's, and formation of airborne particles by convective current transport during a LOVA (water/air ingress disruption) accident scenario. Study, and evaluation of, disruption-induced aerosol generation and mobilization is essential to characterize database on particulate formation and distribution for large future fusion tokamak reactor like ITER. In order to provide database relevant to ITER, the SIRENS electrothermal plasma facility at NCSU has been modified to closely simulate heat fluxes expected in ITER.

This report is composed of three parts, each is an ITER EDA file, namely, EDF No. ITER/US/97/TE/SA-14, June 1997, which describes scoping the SIRENS facility for generating wall material vapors; EDF No. ITER/US/97/TE/SA-21, November 1997, which details the results obtained on characterization of ITER disruption-induced particulate for metals; and EDF No. ITER/US/98/TE/SA-11, June 1998, which details the results for carbon-based materials and mixed materials.

The SIRENS high heat flux facility at N.C. State University has been modified to closely simulate disruption conditions expected in tokamak reactors, and to provide an experimental study on disruption-induced aerosol mobilization for fusion accident analysis. SIRENS source forms a hot vapor plasma by an ablation-controlled arc and expansion cooled into a glass chamber, where particle condensation and growth occurs. The particles are collected and analyzed for relevant transport properties (e.g. size distribution and shape), as described in detail in Part 1: EDF No. ITER/US/97/TE/SA-14, June 1997. Results on metals (copper, stainless steel 316, tungsten, and aluminum) have shown particulate size range of 0.075 - 25 μm in a simulated disruption heat load of 2.8 MJ/m^2 over a 50 μs heat pulse. Particle size distributions have been determined and are presented in Part 2: EDF No. ITER/US/97/TE/SA-21, November 1997. The response of carbon-based material and carbon/metal mixtures (Lexan polycarbonate, graphite grades UTR-22 and ATJ, and combinations of Lexan with each copper, stainless steel 316, tungsten, and aluminum.) to disruption simulation in SIRENS has been studied and the resulting particle size data are presented in Part 3: EDF No. ITER/US/98/TE/SA-11, June 1998.

DISCLAIMER

DISCLAIMER

Portions of this document may be illegible in electronic image products. Images are produced from the best available original document.

I. INTRODUCTION

Safe operation of future large tokamaks like ITER necessitates a resolution for each safety issue that may develop regarding the licensing of the reactor. Various hazard scenarios are related to plasma-facing components, and varies from surface erosion and material concerns during normal operation and abnormal events to worst case scenarios of hard disruptions, LOCA's and LOVA's. Disruption severity and the impact of plasma-facing components on disruption parameters is an important issue, which requires thorough research on various candidate materials as plasma-facing components (divertors, limiters, and first wall). Erosion of plasma-facing components during hard disruptions is a limiting factor in the design of large tokamaks like ITER. During a disruption event, much of the stored thermal energy of the plasma will be dumped to the limiter or divertor plates, resulting in local heat fluxes, which may exceed 100 GW/m^2 over a period of about 0.1 ms. As a result, the surface temperature dramatically increases, which produces thermal stresses and surface erosion. Surface erosion must be minimized for a longer lifetime of the plasma-facing components. Materials and components must withstand thermal shock for first wall and divertors under normal and disruption conditions.

It is difficult to simulate disruption damage conditions on current tokamaks. Erosion studies of plasma-facing components can be obtained from small devices suitable to simulate disruption conditions. Plasma guns (light gas and electrothermal guns), and some electron beam facilities, can produce disruption-like conditions to simulate disruption events. The heat flux from a low temperature electrothermal plasma gun is produced, primarily, from the black-body spectrum photons. The energy in a tokamak disruption, on the other hand, may be carried by higher energy (10 keV and above) electrons and ions emanating from the core plasma. However, no direct measurements of the actual spectrum have been done. Calculations have shown that the scale length for slowing down of electrons and ions with energies less than 20 keV is much less than the scale thickness of the vapor shield itself. Hence, the vapor is opaque to the incoming particles and once the energy could be deposited in the vapor shield then low energy photon transport becomes the dominant mechanism by which energy is transferred to the material surface, as shown by results of several computational models. The developed pressures in the vapor shield (>100 MPa) are large enough to expand against incoming plasma flux or magnetic field as in tokamak, so much of the stored internal energy of the vapor will be propagated away from the surface. The vapor shield can reduce surface energy flux by greater than 90%. Energetic ions and electrons may penetrate through the vapor shield layer, and under such conditions the energy transmission factor through the vapor shield will increase, thus producing increased surface damage. Such penetrating suprathermal electrons can reduce this percentage to less than 50%. High pressures (> kbar) can also be generated at the PFC surfaces, which can lead to cracking and material failure. Calculations can demonstrate the effectiveness of the vapor shield and estimate vapor shield pressures and forces, but the calculations are highly dependent on the characteristics of the outflux disruption plasma. Thus in order to do meaningful calculations, the heat flux, species, flow velocities, temperatures, pressures, and magnetic field must be known at the divertor plate.

Safety considerations of plasma-facing components extend over a wide range of possible scenarios other than erosion problems. Disruption severity and the impact of plasma-facing components on disruption parameters depends on the performance of selected candidate materials, and possible improvement of disruption resistance. High heat fluxes and thermal stresses during normal operation and abnormal events (disruptions) are related, again, to the performance of selected materials and their ability to withstand thermal shocks. Additional safety issues include accidental energy release, LOCA's and LOVA's, where both short and long terms must be considered. Accidental ingress of air (LOVA) or water (in-vessel LOCA) may cause chemical reactions and thus release energy. The formation of airborne particles by convective current transport during a LOVA accident scenario (water/air ingress disruption) may result in a release of activated products. Mobilization and transport of activated materials may also take place by ingress of some gas, air, or steam, which could be developed during in-vessel accident scenarios.

II. The Experimental Device SIRENS and Modifications for Aerosol Transport and Accident Scenarios

Complete and detailed description of SIRENS facility, scoping for disruption-induced mobilization and wall material vaporization is attached in Part 1: "Scoping of SIRENS for Wall material Vaporization Studies", J.P. Sharpe and M.A. Bourham, EDF No. ITER/US/97/TE/SA-14, June 1997.

II.1 Disruption Simulation with SIRENS

In order to simulate aerosol mobilization from tokamak disruption events, a suitable facility must be devised that simulates the extreme environment present in a disrupting tokamak reactor. The most difficult parameter to satisfy is the high heat flux incident on the divertor targets. Disruption energies of the order of 20-100 MJ/m^2 are expected in ITER, and no existing tokamak can achieve this loading. One demonstrated technique to achieve disruption heat loading over a relatively small surface area utilizes an electrothermal (ET) plasma. Typically in SIRENS, ET plasmas are produced by high current arc discharge through a capillary lined with a polycarbonate ablator. Evolved mass from the liner is heated and ionized by the discharge current. This hot plasma (1-3 eV) is essentially a black body radiation source, which provides high heat flux to any exposed surface. To study disruption-induced aerosol mobilization, however, requires some modification to the plasma source section of SIRENS. In place of the polycarbonate liner, which generates a 'dirty' plasma composed of ionized carbon, oxygen, and hydrogen that is un-representative of tokamak conditions, a liner of some material of interest is inserted into the capillary. Figure 1 displays the general arrangement of the modified source section to produce a vapor plasma of the desired material via wall ablation. The source section has, additionally, been modified to include a setup to measure the plasma pressure at the source exit, as shown in Fig. 2. When mixed materials are used, sections of such materials are then be arranged inside of the source to produce mixed vapor plasma, as shown in Fig. 3.

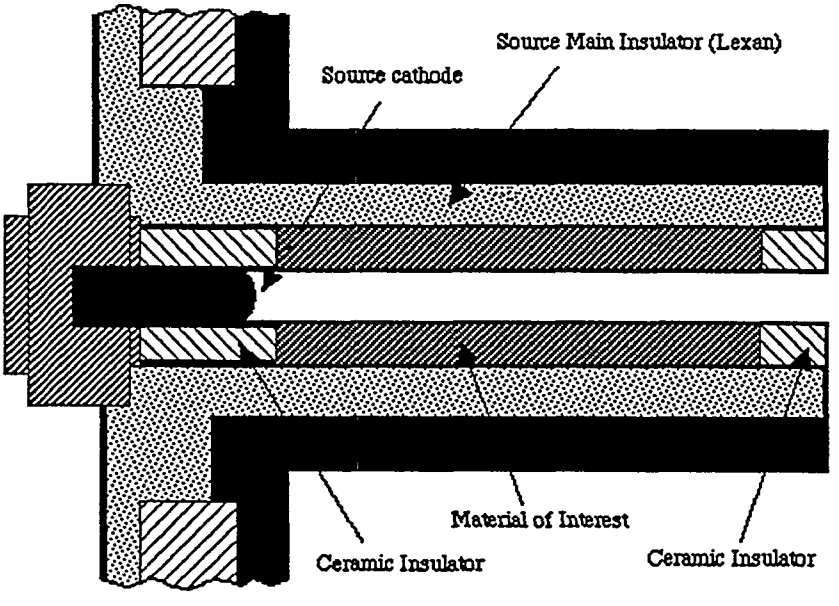

Fig. 1 Single-material modified source showing location of material sleeve and end-on insulators.

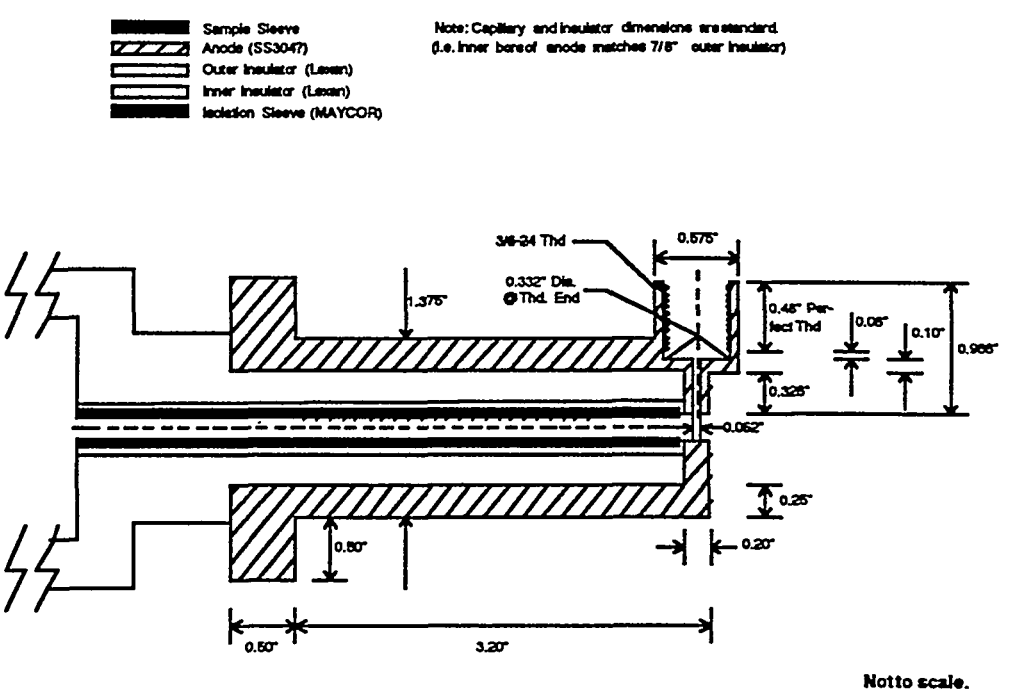

Fig. 2 Modified source showing location of pressure transducer, and location of tube-shaped test material, either a single-sleeve material or sectioned-sleeve to form a mixed materials source. The mixed plasma is formed inside the source and is allowed to expand into the collection cell.

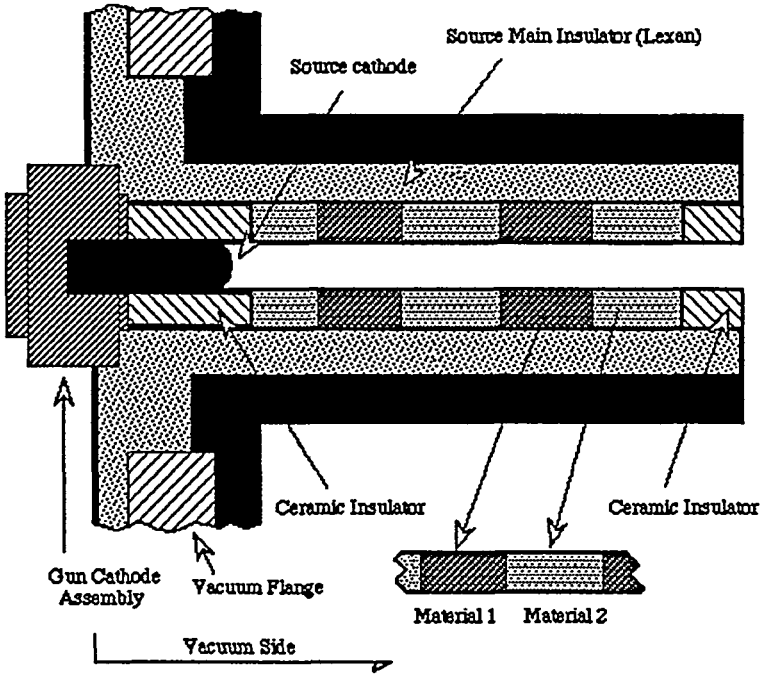

Fig. 3 Mixed materials modified source showing short sections of materials arranged inside of the central section of the source between the two insulating rings.

The above mentioned modifications to the ET plasma source allows it to act as a disruption simulator in the following manner. As the discharge arc travels through the capillary, a radiative heat flux is incident upon the inner surface of the source liner (the material of interest). The resulting temperature increase causes the surface material to directly ablate, forming a plasma vapor representative of that generated from a PFM surface during a disruption event. An important assumption regarding the application of this source to tokamak disruptions is that the dominant disruption energy transport mechanism causing surface erosion is radiation (i.e. melt-layer splashing is not considered). This assumption is justified in that the developed vapor shield at the surface of the PFM will absorb incident plasma particle energy, thereby exciting and ionizing the vapor cloud. Line and continuum radiation are generated in the vapor cloud and continue to heat the PFM surface by black body radiation.

II.2 Formation and Expansion of Aerosol Particulates

In a tokamak disruption. the vapor cloud develops high pressure in a short time due to the continual mass evolution from surface erosion. This pressure allows the vapor to expand against the transient disruption plasma into the vacuum vessel. Adiabatic expansion cooling then supersaturates the vapor; condensation occurs by plating of interior vacuum vessel structure and by formation of small particles (aerosols). Similarly in SIRENS, the pressure of the vapor increases as ablation continues, thus forcing the vapor out of the capillary and into an expansion chamber. Again, expansion cooling is responsible for vapor condensation and aerosol formation. Figure 4 shows how the source section and expansion chamber are arranged in SIRENS.

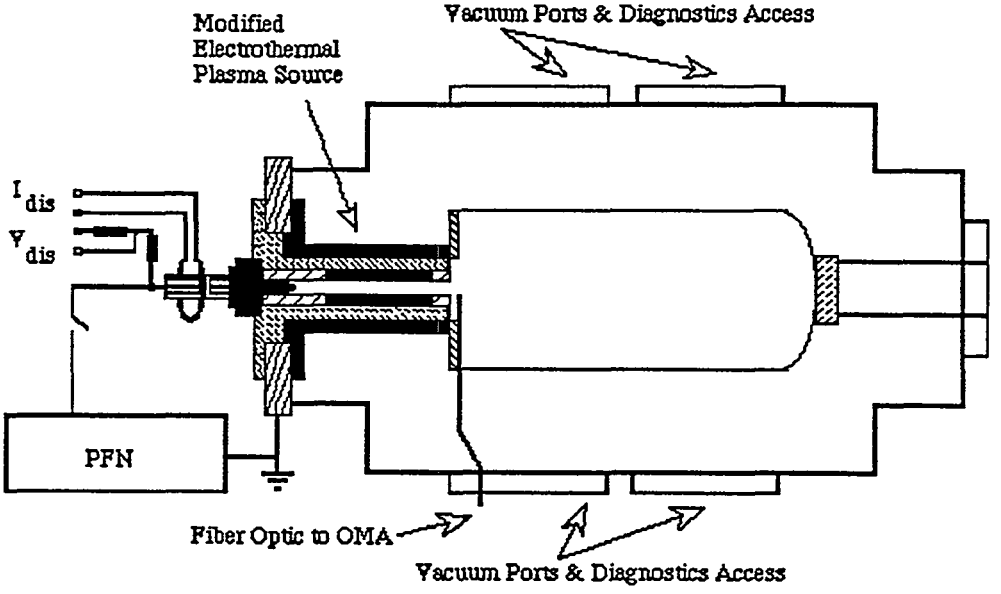

Fig. 4 Schematic of the modified SIRENS facility showing the modified source section and the collection cell. A fiber optic cable is located at the source exit, and is interfaced to an optical multichannel analyzer for optical emission spectroscopy measurements.

Chamber size is determined by comparing available expansion volume for a given amount of ablated mass to the expansion volume available in a tokamak. Due to geometrical limitations, the present chamber on SIRENS is cylindrical with a diameter of 10 cm and length of 40.6 cm, giving an expansion volume of 0.0032 m^3. In ITER, the expansion volume is approximately 2600 m^3. If 10 μm of a given surface material is eroded in a given disruption simulation (with appropriate heat

flux), the effective volume of eroded material in SIRENS is 3.75×10^{-9} m^3. The same erosion depth on 200 m^2 of divertor targets for an ITER disruption yields an effective volume of about 0.002 m^3. The volumetric expansion ratio is therefore 1.17×10^{-6} ($3.75 \times 10^{-9}/0.0032$) for SIRENS and 7.7×10^{-7} (0.002/2600) for ITER. Volume expansion scaling for SIRENS to ITER is then roughly 1.5: 1 in this configuration. This volume comparison alone is not sufficient to assure scaling of particle formation, however the consistency is important in aerosol nucleation physics.

II.3 Aerosol Characterization

Following generation of aerosol particles from the source section of SIRENS, and expansion into the collection chamber, particles are collected on collection buttons and measured. Several collection schemes are possible, however only three have presently been considered: collection buttons distributed on the expansion chamber surface, a filtering system placed at the end of the chamber, and a high temperature pressure cascade impactor installed at the end of the chamber. Particle shape and size may be determined by examining the collection substrate (buttons, filter, or impactor plates) using scanning electron microscopy (SEM) and image analysis software. The general concept of using collection buttons in the expansion chamber is shown in Fig. 5. As the vapor condenses, particles are formed and transported to the wall of the expansion chamber, where some are captured on the surfaces of collection buttons. A plate at the end of the chamber will also collect particles. Axial particle transport can be characterized by different levels of deposition on the distributed buttons.

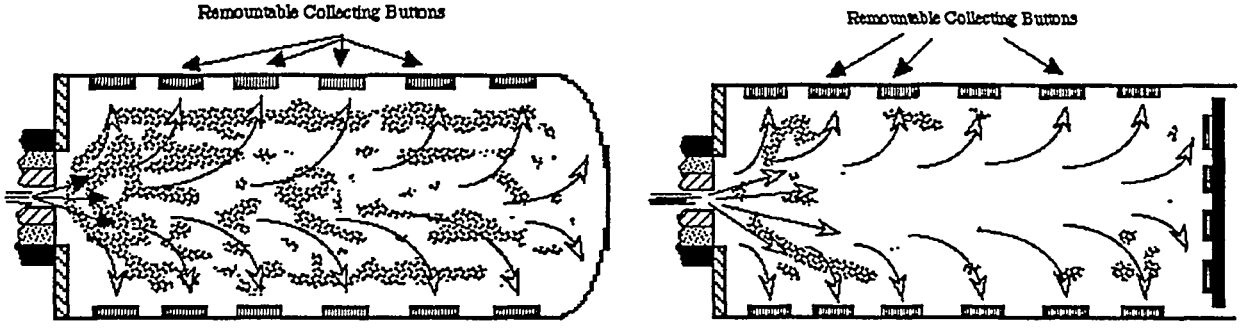

Fig. 5 Schematic of the expansion chamber showing concept of remountable collecting buttons. Chamber is either closed-end (a) or open-end (b).

Filter or cascade impactor placement at the end of the chamber is useful because particle size pre-selection is performed, making size analysis more accurate than collecting all particles on a single plate. Filters and impactors are designed to allow passage of particles of known size; measuring deposition (i.e. weight gain) of the collection substrate will give the particle size distribution. This characterization method is independent of SEM analysis, thus size distribution confirmation is performed. With an appropriately designed chamber (i.e. sufficient expansion geometry), particle formation should be complete before the vapor transports to the end of the chamber. Particles collected on the filter or impactor plates then represent the final particle distribution that would be expected from PFM mobilized during a disruption. This data would be used with the collection button data to understand initial aerosol formation and transport following a disruption event.

II.4 Proof-of-Principle Tests

Proof-of-principle tests have been performed on the modified SIRENS disruption simulation facility for aerosol production. Each test utilized a copper source section liner as the test material, and collection buttons were distributed in the expansion chamber. For the second test, a porous membrane filter (cellulose nitride) was attached to the end of the chamber. A cascade impactor has not been tested due to complications in impactor design for a high pressure environment. The discharge energy densities for these tests were 4.49 MJ/m^2 and 4.70 MJ/m^2 (both over 75μs), with total mass loss of copper source section of 0.49 g and 0.35 g, respectively. Reduced mass loss on the second test is possibly due to insulator cracking. A faint copper-colored haze appeared to coat the inside wall of the expansion chamber for both tests, indicating either vapor deposition or particle collection. SEM analysis of wall-mounted buttons has shown that spherical particles were deposited on the wall, as well as vapor condensation and particle deposition on the end plate. This seems to indicate incomplete vapor nucleation. Particle size distribution for each test was obtained by using image analysis software with particle counting. Several SEM micrographs of the collection buttons were made and analyzed to obtain particle size and number. The mean particle size (count mean diameter) was found to be 2.11 μm for test 1 and 7.75 μm for test 2. Axial particle deposition along the length of the chamber wall was also characterized during these tests. Four buttons placed circumferentially at 4 axial locations were measured for weight gain. The results from test I and 2 are displayed in Fig. 6. Test 1 displays decreasing deposition because the buttons were arranged in such a fashion as to shadow buttons farther down the channel. A different arrangement was used for test 2. Increasing deposition down the channel length for test 2 indicates the relative amount of condensed vapor at each axial location due to radial particle transport. The small relative weight gains measured (compared to the overall source liner mass loss and mass gain of the end-plates) also display incomplete vapor condensation in the expansion chamber geometry, which necessitates changing the chamber length to an appropriate value based on vapor expansion calculations and compared to the ITER volume expansion scale.

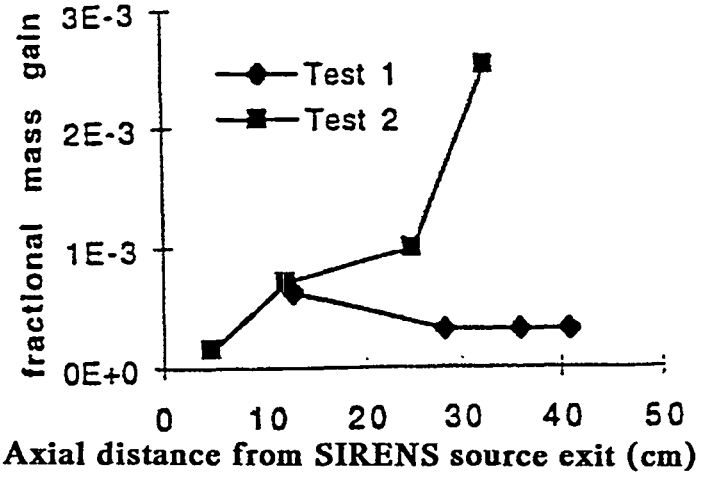

Fig. 6 Mass gain on collecting buttons along the length of the expansion chamber

III. Experiments on Metals Relevant to ITER (Copper, Stainless Steel 316, Tungsten and Aluminum)

Complete and detailed description of experiments conducted on metals relevant to ITER is attached in Part 2: "Characterization of Disruption-Induced Particulate from ITER Relevant Metals", J.P. Sharpe and M.A. Bourham, EDF No. ITER/US/97/TE/SA-21, November 1997.

A series of experiments have been performed with SIRENS to simulate the erosion and mobilization effects on ITER-relevant materials exposed to hard disruption conditions. Specifically, size distributions have been produced for various particulate generated from condensation or deposition of vaporized surface material. This section presents a description of experiments conducted on metals, and the particle size distributions. Test material was fabricated into a cylindrical sleeve of 0.4 cm ID, 0.7 cm OD, and 6 cm length, and placed into a Lexan inner insulator of 0.7 cm ID and 12 cm length. A ceramic (Maycor) insulator was used to isolate the electrically conducting test sleeves, thus forcing the arc discharge through the inside of the test sleeve (capillary) and exposing the inner surface of the test material to radiative heating from the plasma. Energy deposited on the surface from the intense arc mobilizes material from the test sleeve by vaporization or ablation; this mobilized mass flows from the capillary into a large glass expansion chamber (18 cm ID, 76 cm length) designed to scale to the expansion volume available in the ITER divertor. During the expansion process, the vaporized mass cools well into super-saturation and hence condenses, forming the particulate of interest. This particulate is transported to the wall of the expansion cell and is intercepted by circular collection substrates (buttons) distributed along the chamber wall and on the end-plate. A detailed description of button locations and test results on metals is available in Part 2 of this report: "Characterization of Disruption-Induced Particulate from ITER Relevant Metals", J.P. Sharpe and M.A. Bourham, EDF No. ITER/US/97/TE/SA-21, November 1997. Following the test, buttons are removed, weighed for relative mass gain, and viewed in a Scanning Electron Microscope (SEM). Photographic images of a button's surface are obtained, and the captured particles are sized and counted, generating the particulate size frequencies for that button. These measured frequencies are then fitted to the log-normal distribution.

III.1 Copper Test Results

Tests were performed in SIRENS using copper as the test material. A sample of test matrix is given in the following table, which displays test energy, sample mass loss, and particulate size distribution parameters from two copper tests. Sample mass loss was consistent for shots of nearly equivalent discharge energies. Analysis for particle size distribution was performed using buttons 1, 6, 7, 9, 12, and 14. These buttons were chosen because they best represent different locations for collection available in the expansion chamber. Differences observed in particulate size distributions, especially on end-plate buttons, are a direct result of differences in SEM image quality. Images obtained from buttons used in Cu Test 1 were not optimized and displayed significant levels of noise due to improper operational parameters of the SEM. Incorrect contrast and brightness levels allowed clear imaging of the substrate grain boundaries. Presence of such distinct background features interfered with the ability of the size analysis computer software to recognize individual particles. This problem was corrected for other tests by simply reducing the background brightness until the grain boundaries disappear from the image. Corresponding brightness reduction of imaged particles is countered by increasing the contrast level, enhancing only the particles since they are of different composition than the substrate. Images from buttons used in Cu Test 2 were fully optimized by applying these techniques. Fig. 7 shows the particle size distribution for button 7 from Cu Test 2, which is a log-probability plot, showing the general linear

trend observed in all the particle size data collect from the copper tests. Data points for the smaller sized particles (< 2 μm), however, do not fit this linear trend, possibly indicating a different underlying distribution for these particles. Unfortunately, these particles approach the size resolution limit of this characterization technique, and improvements have been implemented in further tests.

TEST MATRIX FROM TWO COPPER TESTS.

	Cu Test 1 (Shot S734)			Cu Test 2 (Shot S737)		
Energy (kJ)	4.260			4.458		
Δm (mg)	436.67			451.13		
	CMD (μm)	GSD	R^2	CMD (μm)	GSD	R^2
Button 1	0.66	1.77	0.966	0.58	2.17	0.988
Button 6	0.78	2.13	0.986	0.63	2.43	0.989
Button 7	0.55	2.38	0.962	0.505	2.57	0.983
Button 9	0.77	2.07	0.984	0.426	2.63	0.991
Button 12	0.97	2.04	0.988	0.366	3.06	0.989
Button 14	0.84	2.27	0.970	0.381	2.70	0.981

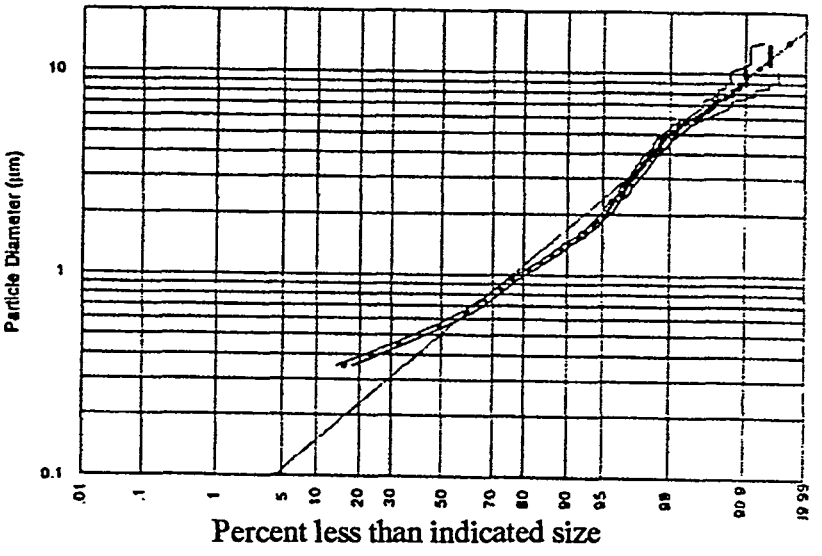

Fig. 7 Particle size distribution for copper in Cu Test 2 button 7, SIRENS Shot S737

III.2 Stainless Steel (316) Test Results

Stainless steel 316 (SS316) has also been tested. A sample of test matrix is given in the table below. Particulate size distributions for buttons at the same location for the both tests are generally consistent having CMD equal to, or less than, 1.3 μm. Several interesting features were observed on the images. Buttons on the end plate generally showed large numbers of distinct particles. Many larger particles had smaller particles attached (5-20% diameter of the large particle; for example, one particular particle 6 μm in diameter on button 14 had two satellites attached, one of 0.6 μm diameter and another of 1μm diameter). The counting process does not distinguish different particles among these agglomerates. Another feature of interest includes buttons located on the side wall containing several 'streakers' with tails all pointing in the same general direction. The tail

lengths where approximately 2.5 - 5 times the particle diameter. This suggests that the incident particle had a molten surface layer that froze as it was deposited rolling along the surface. This feature was also observed with the copper tests, but was not as prevalent.

TEST MATRIX FROM TWO STAINLESS STEEL TESTS

	SS316 Test 1 (Shot S735)			SS316 Test 2 (Shot S738)		
Energy (kJ)	4.259			4.260		
Δm (mg)	349.93			367.61		
	CMD (μm)	GSD	R^2	CMD (μm)	GSD	R^2
Button 1	0.45	1.78	0.955	0.45	1.94	0.986
Button 6	1.31	1.69	0.996	0.75	2.21	0.991
Button 7	0.84	2.14	0.992	1.46	2.10	0.994
Button 9	0.92	1.78	0.984	0.618	2.27	0.993
Button 12	0.54	2.33	0.980	0.75	2.37	0.995
Button 14	0.73	1.87	0.989	0.62	2.29	0.974

III.3 Tungsten Test Results

Tungsten has also been tested. A sample of test matrix is given in the table below. The sample sleeves from both tests shattered due to the brittle nature of tungsten, and the reported sample mass losses are best estimates from weighing all debris collected from the shattered sleeves. The amount of mass deposited on each button was very small, in some instances being less than the resolution of the balance used to weigh them.

TEST MATRIX FROM TWO TUNGSTEN TESTS

	Tungsten Test 1 (Shot S736)			Tungsten Test 2 (Shot S739)		
Energy (kJ)	4.260			4.259		
Δm (mg)	154.85			241.93		
	CMD (μm)	GSD	R^2	CMD (μm)	GSD	R^2
Button 1	0.30	1.97	0.997	0.38	1.99	0.974
Button 6	0.50	1.76	0.996	0.30	2.11	0.986
Button 7	0.70	1.65	0.980	0.36	2.15	0.992
Button 9	1.05	2.59	0.965	N/A	N/A	N/A
Button 12	0.66	2.49	0.974	N/A	N/A	N/A
Button 14	0.80	2.49	0.968	N/A	N/A	N/A

A feature that interfered with the particle counting technique was cratering or pitting that resulted from impact of tungsten particles on the copper button substrate. Edges of the craters are significantly distinct, and in the particle characterization procedure they are counted as particles. This skews the resulting distribution. Crater diameters are, however, on the order of the particle sizes. They were examined on the SEM to prove that the substrate surface was deformed. Two images taken at different angles were used to generate a relief image that showed the craters to be indentations into the surface and particles to be bodies on the surface. Also, EDXA was used to analyze crater edges for material other than that of the substrate, where no other material was

found. Cratering was not severe in W Test #1, but was so abundant in W Test #2 such that end-plate buttons could not be analyzed.

III.4 Aluminum Test Results

Aluminum has been chosen as a replacement for beryllium due to the fact that aluminum has thermo-physical properties very similar to those of beryllium, thus avoiding handling beryllium in the SIRENS facility and avoiding toxicity. Also, aluminum is often used to simulate beryllium in the context of thermal response. With the assumption that beryllium will respond to disruptions in a fashion similar to aluminum, tests were performed with aluminum sleeves. The following table provides a test matrix that has been conducted on aluminum.

TEST MATRIX FROM TWO ALUMINUM TESTS

	Aluminum Test 1 (Shot S744)			Aluminum Test 2 (Shot S745)		
Energy (kJ)	4.226			4.260		
Δm (mg)	526.41			493.40		
	CMD (μm)	GSD	R^2	CMD (μm)	GSD	R^2
Button 3	1.90	2.15	0.989	2.29	2.01	0.972
Button 7	3.01	2.04	0.978	1.60	2.19	0.991
Button 9	0.85	2.48	0.991	1.27	2.29	0.984

Particulate size distributions were generated for selected buttons (3, 7 and 9). Fewer buttons were analyzed in the aluminum tests due difficulties in handling because of the tendency of the Al coating to flake from the substrate surface. Particles deposited on side wall and end-plate buttons for this test were generally larger than particles observed from the tests of other materials. Lower magnifications were suitable to characterize the observed particle size range, and no particles smaller than ~ 0.5 μm were observed at high magnifications (1000x). Figure 8 displays a representative particle size distribution from aluminum Al Test 1.

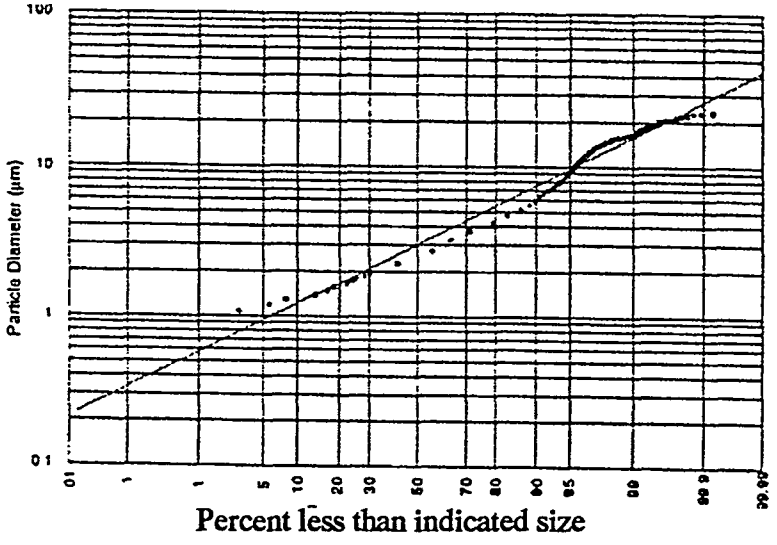

Fig. 8 Particle size distribution for aluminum in Al Test 1 button 7, SIRENS Shot S744

A notable feature of this distribution and others of this test is that the data for large particles strays from the linear shape typically observed with the other materials. This deviation suggests the underlying distribution for each button is possibly bimodal. A physical interpretation of this observation comes about when the low melting temperature of aluminum is considered. It is possible that the normally small amount of transmitted heat flux into the test sleeve is sufficient to increase the temperature of a surface layer of Al beyond the melting point. The pressure associated with the mass vaporization in the sleeve could then eject molten aluminum from the surface, entraining relatively large molten particles in the flow of vaporized mass. These particles are not generated by vapor condensation and growth, and could possibly be larger than those that are generated by condensation and growth. The resulting size distributions then have at least two particle types generated by different mechanisms, thus skewing the log-normal approximation of the overall distribution. This effect was not observed in tests with other materials possibly because of their higher melting temperatures.

IV. Experiments on Carbon Materials and Mixed Carbon/Copper, Carbon/Stainless Steel, Carbon/Tungsten and Carbon/Aluminum

Complete and detailed description of experiments conducted on carbon-based materials relevant to ITER and mixed carbon/metals is attached in Part 3: "Characterization of Carbon-Based Particulate from Disruption Simulations", J.P. Sharpe and M.A. Bourham, EDF No. ITER/US/98/TE/SA-11, June 1998.

The response of carbon-based material and carbon/metal mixtures to disruption simulation in the SIRENS facility has been studied and the resulting particle size data have been obtained. Specific materials investigated include Lexan polycarbonate, graphite grades UTR-22 and ATJ, and combinations of Lexan with each copper, stainless steel 316, tungsten, and aluminum. When conducting mixed materials experiments, the source section was arranged in segments as previously shown in Fig. 3. The reason for using Lexan polycarbonate is because it is a carbon-based material that ablates more evenly and can be used as a good simulator for carbon. Carbon particulate (dust) generated from vaporization during a disruption is a concern because of tritium retention within the dust. If a release pathway is present, the tritiated dust will contribute to the radiological source term of the accident scenario. Another concern with the presence of carbon dust is the effects of chemical reactivity, specifically hydrogen production in a steam ingress accident. In order to quantify each of these concerns in a defensible safety analysis, physical properties of the generated carbon particulate must be well known.

A series of experiments have been performed with SIRENS to simulate the erosion and mobilization effects of carbon-based materials exposed to hard disruption conditions. Specifically, size distributions have been produced for particulate generated by exposing carbon and carbon/metal surfaces to heat fluxes on the order of 6 MJ/m^2 for 80 μS. Successful generation of carbon particulate required utilizing various configurations in the placement, or "stacking order", of test material within the inner insulator. Tests with Lexan-only sleeves were performed with the entire exposed length (8.8 cm) consisting of Lexan. For graphite, a series of tests was performed with different, configurations to find a stacking order that generated a sufficient amount of particulate. Difficulties encountered in the graphite tests will be discussed. These difficulties influenced the selection of Lexan for carbon/metal mixture tests. Using Lexan as the carbon-based material in these tests is justifiable given that sufficient heat flux is available to completely dissociate the polycarbonate into its elemental constituents. Atomic and molecular hydrogen, oxygen (H, H_2, O and O_2), and potentially molecular methane (CH_4) are non-condensable that have little impact on particle formation of the dominant condensable species, i.e. carbon. Water

vapor is unlikely to form into an appreciable amount because of the stoichiometic balance of hydrogen and oxygen.

Two primary configurations were used in the carbon/metal mixture tests: a "short" configuration test to characterize the particles formed when the condensing species is predominately carbon, and a "segmented" configuration test to characterize particles formed from roughly equivalent surface areas of carbon and metal exposed to a high heat flux. The short configuration consists of a 1 cm length of metal surrounded by two Lexan sleeves 3 cm and 3.5 cm in length. The segmented configuration is made of three sets of Lexan/metal pairs with each component 1.0 cm in length, giving a total exposed length of 6.0 cm. These configurations are illustrated in Fig. 9 bellow. The segmented configuration has repeated identical sections of Lexan-metal segments.

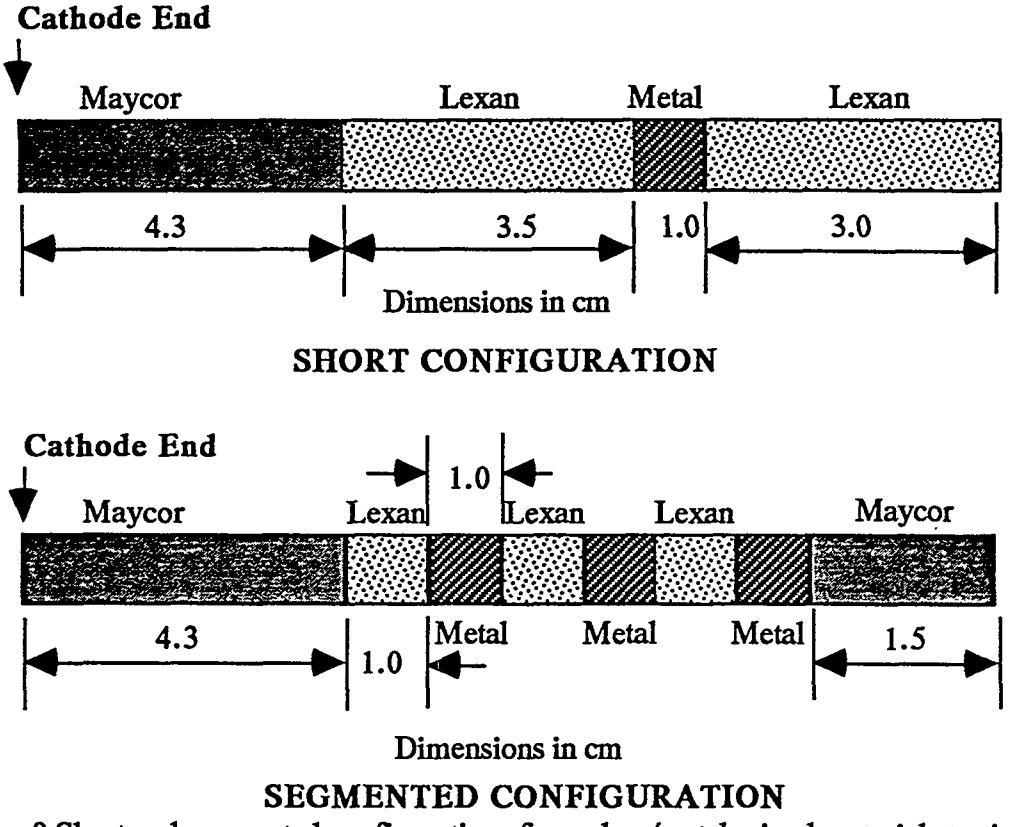

Fig. 9 Short and segmented configurations for carbon/metal mixed materials testing.

IV.1 Carbon Test Results

Lexan polycarbonate and graphitic carbon. Lexan is often employed as the ablative surface in ET devices. It is known to produce significant quantities of soot composed of carbon particulate. This soot is generated from Lexan by mechanisms similar to those that generate dust from graphite exposed to disruption heat loads. Therefore particulate produced from Lexan is of interest for the purpose of comparison with that produced by graphite, and because Lexan is a convenient substitute when graphite cannot be used, as with the carbon/metal tests.

IV.1.A. Lexan Polycarbonate Test Results

Tests were performed in SIRENS using Lexan as the carbon-based material. The following table displays total discharge energy, sample mass loss Δm, and particle size distribution parameters for two tests. Sample mass loss has been scaled to total discharge energy and total exposed length of material (e.g. for S760, 31.77 mg / 6.050 kJ / 8.8 cm = 0.597 mg/kJ/cm). Button mass increase from deposited carbon soot was negligible. Analysis for particle size distribution was performed on buttons 1, 3, and 9 for S760 and buttons 1, 5, and 9 for S761. These buttons sufficiently represent different locations for collection available in the expansion chamber. Although the mass of deposited material was negligible, button surfaces displayed a large number of particles when viewed in the SEM. The resulting particle size distribution found for button 1 of S760 is shown in Fig. 10. An important result is that generally for the Lexan tests the data ate reasonably well represented by a log-normal distribution, as reflected in the values of R^2.

TEST MATRIX FROM TWO LEXAN POLYCARBONATE TESTS

	Lexan Test 1 (Shot S760)			Lexan Test 2 (Shot S761)		
Energy (kJ)	6.050			6.423		
Δm (mg/kJ/cm)	0.597			0.676		
	CMD (μm)	GSD	R^2	CMD (μm)	GSD	R^2
Button 1	0.069	2.14	0.992	0.073	2.23	0.997
Button 3	-	-	-	0.079	2.06	0.997
Button 5	0.166	2.48	0.989	-	-	-
Button 9	0.097	2.58	0.994	0.081	1.96	0.987

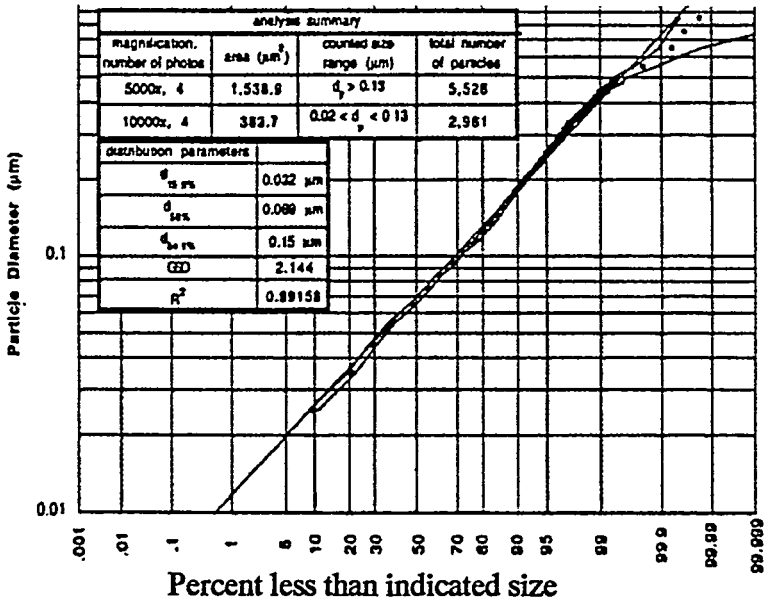

Fig. 10 Particle size distribution for Lexan in LX Test 1 button 1, SIRENS Shot S760

IV.1.B. Graphite Carbon Test results

Particulate production from graphitized carbon was investigated using two different grades of graphite: UTR-22 and ATJ. In order to generate sufficient quantities of particulate from graphite carbon materials, a high energy input to the source section was needed in order to provide high-energy density deposition. An input energy of 7 kJ was used for each test, and because graphite is electrically conductive, the source section configuration was slightly modified from that used for the Lexan tests. Following a series of exploratory tests, the most useful configuration placed short graphite sleeves near the exit of the source section. The following table shows a test matrix for graphites, where it is important to note that graphite sleeves were destroyed during the discharge, and thus no mass loss was obtained. This likely resulted from a current path developing within the conductive graphite at some point during the discharge. Resistive energy dissipation within the sample caused intense internal heating and vaporization, resulting in mechanical failure of the material. In fact, particulate collected near the end of the expansion chamber (buttons 7 and 9) for the ATJ graphite test appeared to consist of two general particle groups: very fine particles ($\tilde{}$ 0.1 μm) possibly associated with vaporized material, and very large particles ($\tilde{}$ 10+ μm) resulting from the fragmentation of solid graphite grains. The particle size distribution for button 9 of shot S764 (with ATJ graphite) is illustrated in Fig. 11. There is an apparent shift in the center of the distribution when compared to particulate collected much closer to the exit of the source section. A log-probability plot also shows that the overall shape is not well represented by a log-normal distribution. Size distributions for particulate collected close to the source exit of the ATJ test and particulate collected from the UTR-22 test reasonably compare to results of the Lexan tests. Average CMD for the Lexan tests was 0.094 $\pm$ 0.033 μm and the graphite tests (excluding buttons 7 and 9 of the ATJ test) gave 0.098 $\pm$ 0.014 μm as the average CMD.

TEST MATRIX FROM GRAPHITE CARBON TESTS

	UTR-22 Test (Shot S763)			ATJ Test (Shot S764)		
Energy (kJ)	7.195			7.162		
Δm (mg)	N/A Samples were destroyed			N/A Samples were destroyed		
	CMD (μm)	GSD	R^2	CMD (μm)	GSD	R^2
Button 1	0.102	2.33	0.993	0.115	2.13	0.996
Button 3	0.114	2.63	0.990	0.086	2.52	0.982
Button 5	-	-	-	0.075	2.97	0.996
Button 7	-	-	-	0.318	2.76	0.969
Button 9	0.096	3.57	0.966	0.544	3.464	0.969

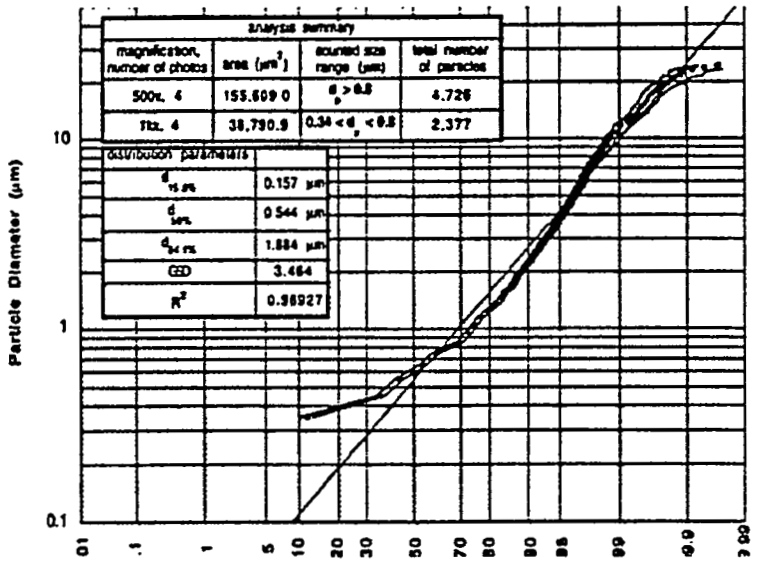

Fig. 11 Particle size distribution for carbon in ATJ graphite Test button 9, SIRENS Shot S764

IV.2 Carbon/Copper Mixture Test Results

Particle formation in the presence of two or more condensing species is of interest because several different materials are present in the interior of a fusion reactor's vacuum vessel, which may be exposed to heat loading and vaporization during disruptions. To investigate this situation, several tests have been performed on SIRENS with multiple materials placed in the source section and exposed to the high heat flux produced by the arc channel. The first of these tests involved a mixture of Lexan and copper. Lexan was chosen as the carbon-based material because of its convenience of use in the source section and the resulting carbon particles from the Lexan tests were of similar size and shape as the particles generated in the graphite tests.

Two different source section configurations, short and segmented, were tested with the Lexan-carbon/copper mixture, and the following table shows the test matrix results. Sample mass loss Δm of the Lexan for each test was greater than that found in tests with only Lexan in the source section (1.64 and 1.75 mg/kJ/cm versus 0.6 mg/kJ/cm). Total copper mass loss from the short configuration test (shot S765) was much greater than that from the segmented test (shot S769). Size distributions generated for particulate collected from the short configuration test have an average CMD (0.147 µm) slightly larger than that of the carbon-only tests (0.096 µm), indicating a small impact from the copper on overall particle size. Increasing the amount of copper in the source section, however, does have a noticeable effect on the resulting size distributions, as found in the results from the segmented configuration test. Here the CMD's are roughly a factor of 3 larger than that of the short configuration and carbon-only tests (average CMD of 0.29 µm vs. 0.096 µm).

TEST MATRIX FROM CARBON/COPPER MIXTURE TESTS

	Short Configuration Test (Shot S765)			Segmented Configuration Test (Shot S764)		
Energy (kJ)	6.822			7.143		
Carbon Δm	1.64 mg/kJ/cm			1.75 mg/kJ/cm		
Copper Δm	48.26 mg/kJ/cm			23.78 mg/kJ/cm		
	CMD (μm)	GSD	R^2	CMD (μm)	GSD	R^2
Button 1	0.123	2.31	0.997	0.356	2.45	0.995
Button 2	-	-	-	0.203	2.17	0.987
Button 3	0.119	2.23	0.995	0.246	2.19	0.993
Button 9	0.200	2.47	0.989	-	-	-
Button 17	-	-	-	0.353	2.95	0.992

IV.3 Carbon/Stainless Steel SS316 Mixture Test Results

The intended use of stainless steel type 316 (SS316) for many internal components of the ITER vacuum vessel, or any future fusion reactor, makes this material important in an investigation of disruption-induced mobilization and safety analysis. Testing in SIRENS of Lexan "as carbon simulator" and SS316 has been conducted in both the short and segmented source section configurations. The following table shows a test matrix for Lexan-SS316 test results. As with the carbon/copper tests, sample mass loss Δm of the Lexan carbon was greater than the mass loss found from tests with Lexan-only sleeves. Unlike the carbon/copper tests, however, the metal (SS316) mass loss for both short and segmented configurations match. Size distributions generated from collected particulate of the short configuration test (shot S766) are close to those found in the Lexan and graphite carbon tests. Particulate collected from the segmented configuration test have CMD values close to the carbon-only tests, but the GSD values are higher because of the contribution of large particles associated with the SS316 metal.

TEST MATRIX FROM LEXAN CARBON/STAINLESS STEEL MIXTURE TESTS

	Short Configuration Test (Shot S766)			Segmented Configuration Test (Shot S770)		
Energy (kJ)	6.822			7.143		
Carbon Δm	0.975 mg/kJ/cm			1.40 mg/kJ/cm		
SS316 Δm	25.65 mg/kJ/cm			24.36 mg/kJ/cm		
	CMD (μm)	GSD	R^2	CMD (μm)	GSD	R^2
Button 1	0.116	2.00	0.996	0.135	2.74	0.993
Button 2	0.116	2.13	0.998	-	-	-
Button 3	0.099	2.14	0.994	0.094	2.45	0.972
Button 5	0.113	1.20	0.997	-	-	-
Button 9	0.123	2.53	0.989	0.278	2.50	0.996

IV.4 Carbon/Tungsten Mixture Test Results

A single test, shot S767, has been performed in SIRENS with Lexan carbon and tungsten sleeves placed in the source section. Tungsten has been chosen as a material of interest in disruption-induced mobilization studies for ITER. The configuration used for this test was different from the short and segmented configurations of the other carbon/metal tests because only one sample sleeve length of tungsten was available (3.0 cm). The tested configuration consisted of sample sleeves in the lengths (ordered from cathode to anode ends): 4.3 cm Maycor insulator, 3.0 cm Lexan, 3.0 cm tungsten, and 1.5 cm length Maycor. The following table show test results for carbon/tungsten mixture, SIRENS shot S767 at 7.302 kJ.

TEST MATRIX FROM LEXAN CARBON/TUNGSTEN MIXTURE TESTS

	Carbon/Tungsten Test (Shot S766)		
	Energy (kJ)	7.302	
	Carbon Δm	0.82 mg/kJ/cm	
	Tungsten Δm	16.85 mg/kJ/cm	
	CMD (μm)	GSD	R^2
Button 1	0.097	2.03	0.992
Button 2	0.109	2.31	0.984
Button 3	-	-	-
Button 5	0.139	1.93	0.986
Button 9	0.121	2.49	0.985

Lexan sample mass loss (0.82 mg/kJ/cm) was less than values from the other carbon/metal tests, but agrees well with the mass loss from Lexan-only tests. Sample Δm of the tungsten sleeve was also lower than that found in other carbon/metal tests. Size distribution parameters of collected particulate match reasonably well with particulate from Lexan and graphite tests, possibly indicating that tungsten has an insignificant effect on particle formation.

IV.5 Carbon/Aluminum Mixture Test Results

Aluminum has been chosen to replace beryllium in the carbon/metal mixed material test. Lexan was used in this test to simulate carbon. Aluminum has thermo-physical properties close to those of beryllium, and beryllium is a material considered for ITER design. Because of difficulty in working with beryllium, aluminum has been used to simulate the thermal response of the low density, low melting point material when exposed to high heat flux. A single Lexan carbon and aluminum test (shot S768) was performed in SIRENS with sample material placed in the segmented source section configuration. The following table displays the test results of carbon/aluminum mixture. Lexan carbon sample Δm matches Lexan mass loss from the other carbon/metal tests and aluminum sample Δm is slightly higher. Size distribution parameters reflect the contribution of large particles to the overall population. CMD and GSD values are greater than those from Lexan and graphite carbon, similar to the carbon/copper and carbon/SS316 segmented configuration tests.

TEST MATRIX FROM LEXAN CARBON/ALUMINUM MIXTURE TESTS

	Carbon/Aluminum Test (Shot S768)		
	Energy (kJ)	7.068	
	Carbon Δm	1.50 mg/kJ/cm	
	Aluminum Δm	27.62 mg/kJ/cm	
	CMD (μm)	GSD	R^2
Button 1	0.281	3.08	0.995
Button 2	0.216	3.19	0.976
Button 3	0.154	2.42	0.977
Button 5	0.126	2.89	0.942
Button 9	0.153	3.176	0.970

V. CONCLUSION

The design of the SIRENS facility, and additional modifications to the electrothermal source section, has been proven to be a suitable simulator for disruption and abnormal transient events in tokamak fusion reactors. As a high heat flux facility, the primary mechanism by which energy is deposited on the surface of plasma-facing materials is by photon transport, and consequently the SIRENS source section is a radiation-dominated source. It has also been shown that SIRENS is a simulator for plasma-facing materials aerosol mobilization. Tests have shown that material vaporized in the modified source section of the device expands into the expansion chamber, where cooling and condensation occur. Aerosol particles of varying sizes have been produced, with average sizes in the 1-10 μm range. Production of particulates "aerosol" from the source section is a result of an ablation-controlled arc regime that heats the wall material by radiation from a blackbody plasma, and then allowing the plasma to jet outside of the source due to the large pressure gradient. It has also been shown that SIRENS has the relevance scalability to ITER, which allowed for investigation and determination of particulates for most materials relevant to ITER, and other future large tokamaks. A complete and detailed description of SIRENS facility, scoping for disruption-induced mobilization and wall material vaporization is attached in Part 1: "Scoping of SIRENS for Wall material Vaporization Studies", J.P. Sharpe and M.A. Bourham, EDF No. ITER/US/97/TE/SA-14, June 1997.

ITER, and for most other tokamaks, relevant metals have been tested under disruption-like conditions for particulate generation, specifically, copper, stainless steel SS316, tungsten and aluminum (simulator for beryllium). Particles were generated in the SIRENS source section and are allowed to expand into a collection cell "expansion chamber" and captured on substrates (buttons) distributed inside of the collection chamber. Each substrate was analyzed using electron microscopy to determine the underlying particle size distribution. The analysis shows that particle size distributions for each material has count median diameters (CMD) in the range of 0.3 μm to 3.0 μm; which means that particle generation in SIRENS is basically independent of the material tested. Although particles down to diameter of 0.075μm and up to diameter of 25 μm were observed, the majority of the particles in the underlying distributions existed at about 1.0 μm diameter. A complete and detailed description of experiments conducted on metals is attached in Part 2: "Characterization of Disruption-Induced Particulate from ITER Relevant Metals", J.P. Sharpe and M.A. Bourham, EDF No. ITER/US/97/TE/SA-21, November 1997.

With regard to carbon materials, Lexan polycarbonate has been used as a simulator for carbon, however, several tests were conducted on grades UTR-22 and ATJ graphitic carbon. additionally, tests experiments were conducted on carbon mixed with metals in either short or segmented configuration. Carbon/metal mixtures with Lexan carbon and each copper, stainless-steel SS3 16, tungsten, and aluminum were conducted. Particulate produced from each test was collected and analyzed to determine the underlying particle size distribution. Lexan and graphite carbon tests generated particles with comparable size distributions. Short configuration tests with Lexan carbon and metals generated particulate with CMD's slightly greater than those of carbon-only tests, although GSD's of the mixture tests were greater due to contribution of large particles. Segmented configuration tests generally displayed greater difference from the carbon-only tests, which displays the role of larger particles in the overall distribution.

VI. REFERENCES

SIRENS Facility and Disruption Simulation:

J. Gilligan, O. Auciello, M. Bourham, O.E. Hankins, B. Wehring, D. Hahn, R. Mohanti and J. Stock, "Theoretical and Experimental Studies of the Vapor Shielding Mechanism for Surfaces Subjected to High Heat Fluxes", Fusion Technology, Vol. 15, No.2, Part 2A, pp. 522-527, 1989.

J. Gilligan, K. Niemer, M. Bourham, C. Croessmann, O. Hankins, N. Orton, S. Tallavarjula and R. Mohanti, "Studies of High Heat-Flux and Runaway Electron Damage During a Plasma Disruption", J. of Nuclear Materials, Vol. 176&177, pp.779-785, 1991.

M. Bourham, J. Gilligan, O. Hankins, W. Eddy and J. Hurley, "Electrothermal Plasma Source as a High Heat Flux Simulator for Plasma-Facing Components and Launch Technology Studies", Proc. 9th International Conference on High Power Particle Beams, Washington, D.C., May 25-29 (1992), Vol. III, pp.1979-1983, 1992.

Y. Hirooka, M. Bourham, J. Brooks, R. Causey, G. Chevalier, R. Conn, W. Eddy, J. Gilligan, M. Khandagle and Y. Ra, "Evaluation of Tungsten as a Plasma-Facing Material for Steady State Magnetic Fusion Devices", J. Nuclear Materials, Vol. 196-198, pp. 149-158, 1992.

M.A. Bourham and J.G. Gilligan, "Surface Damage of Plasma-Facing Components Under Short Pulse and Intense High Heat Loading", Proc. 15th IEEE/NPSS-Symposium on Fusion Engineering, Hyannis, Cape Cod, MA, 11-15 October , 1993, Vol. 1, pp. 23-25, IEEE Cat. # 93CH3348-0, 1993.

J.G. Gilligan and M.A. Bourham, "The Use of an Electrothermal Plasma Gun to Simulate the Extremely High Heat Flux Conditions of a Tokamak Disruption", J. Fusion Energy, Vol.12, No.3, p. 113, 1993.

M.A. Bourham and J.G. Gilligan, "Erosion of Plasma-Facing Components Under Simulated Disruption-Like Conditions Using An Electrothermal Plasma Gun", Fusion Technology, Vol.26, pp.517-521, November 1994.

J.D. Hurley, M.A. Bourham and J.G. Gilligan, "Numerical Simulation and Experiment of Plasma Flow in the Electrothermal Launcher SIRENS", IEEE Trans. Magnetics, Vol. 31, pp.616-621, January 1995.

Disruption Simulation and Experiments:

A. HASSANEIN, "Erosion and Redeposition of Divertor and Wall Materials During Abnormal Events", Fusion Technology, Vol.19, p.1789, 1991.

V.R. Barabash et al., "Damage of Refractory Metals and Carbon-Based Materials Under Simulation of the Thermal Influence at Plasma Disruption," Fusion Engineering and Design, Vol. 18, p.145, 1991.

H. Bolt et al., "Performance of Carbon Materials Under Short and Intense Electron Beam Pulses in the JEBIS Facility," Fusion Technology, Vol. 20, p.231, 1991.

A. Hassanein, "Plasma Disruption Modeling and Simulation", Fusion Technology, Vol.26, p.532, 1994.

J.P. Sharpe, M.A. Bourham and J.G. Gilligan, "Preliminary Investigation Into Aerosol Mobilization Resulting From Fusion Reactor Disruptions", Fusion Technology, Vol. 30, pp.1424-1428, November 1996.

Particulate and Dust Generation, Experiments and Modeling:

J.P. Sharpe, M.A. Bourham and J.G. Gilligan, "Experimental Investigation of Disruption-Induced Aerosol Mobilization in Accident Scenarios of ITER", Proc. 17th IEEE NPSS Symposium on Fusion Engineering, San Diego, CA, 6-10 October 1997, Vol.1, pp.153-156, 1997.

W.J. Carmack, "DIII-D Dust Particulate Characterization", ITER EDF No. ITER/US/97/TE/SA-8, March 1997.

W.J. Carmack et al., "DIII-D Dust Particulate Characterization: June 1998 Vent", INEEL/EXT-1999-00095, January 1999.

R. Little, A. Costley, G. Federici, F. Heckendorn, S. J. Piet, "Minutes of the 1997 Dust Coordination Meeting," S 81 MI 16 07-06-18 R 0.2, July 2, 1997.

J.P. Sharpe, M.A. Bourham and J.G. Gilligan, "Generation and Characterization of Carbon Particulate in Disruption Simulations", Fusion Technology, Vol. 34, No. 3, Part 2, pp.634-639, November 1998.

W.J. Carmack, G.R. Smolik, R.A. Anderl, R.J. Pawelko and P.B. Hembree, "Tokamak Dust Particle Size and Surface Area Measurements", Fusion Technology, Vol. 34, No. 3, Part 2, pp.604-608, November 1998.

Overall View of ITER Safety:

D.A. Petti and K.A. McCarthy, "ITER Safety: Lessons Learned for the Future", Fusion Technology, Vol. 34, No. 3, Part 2, pp.390-396, November 1998.

Part 1

"Scoping of SIRENS for Wall material Vaporization Studies"

J.P. Sharpe and M.A. Bourham

EDF No. ITER/US/97/TE/SA-14, June 1997.

ENGINEERING DESIGN FILE

	**International Thermonuclear Experimental Reactor (ITER)** **U.S. Home Team** **Fusion Safety Program**	EDF No.: ITER/US/97/TE/SA-14 DATE: June 1997 TASK AREA: SAE-1

SUBJECT: Scoping of SIRENS for Wall Material Vaporization Studies

SUMMARY: This document describes scoping tests conducted in the SIRENS facility. These tests have been conducted prior to performance of experiments to investigate plasma disruption-induced mobilization of activated wall material in ITER. The SIRENS facility has been modified from its original configuration to accommodate the production and collection of material generated during the interaction of a high energy density plasma and a test material. The purpose of this document is to present key experimental parameters and quality control procedures associated with the generation of data and results in the SIRENS facility.

An existing electrothermal plasma gun (SIRENS) has been modified to simulate plasma disruption events in terms of power flux and produce mobilized particles in the same manner as expected in ITER. The sleeve section of the SIRENS electrothermal source has been changed to use ITER-relevant materials. An expansion chamber has been added to allow controlled collection of the resulting particulate. Preliminary tests have been successfully conducted on 316 stainless steel and copper, demonstrating the validity of the experiment in accomplishing the prescribed task. Resulting particle size distributions from scoping tests are reported, as well as insight gained from performing these tests.

Future work for this experiment includes detailed analysis of the condensation results for copper, stainless steel #316, tungsten, carbon, and certain combinations of these materials. After building this experimental database of resulting particle size distributions, modeling will be performed to aid in extrapolation of SIRENS results to ITER conditions.

Distribution (complete package): Project File, M. Bourham, W. J. Carmack, J. G. Gilligan, K. A. McCarthy, D. A. Petti, S. Piet, J. P. Sharpe

Author:	Date:	Reviewed:	Date	Approved:	Date:
J. Phillip Sharpe	6/16/97	K. A. McCarthy		D. A. Petti	
M. Bourham					6/15/97

Outline

1.0 Introduction

Evaluation of potential safety hazards from operation of the International Thermonuclear Experimental Reactor (ITER) is required for siting of the device. Continuous operation conditions such as high heat and neutron loads (up to 20 MW/m^2 and 1 MW/m^2, respectively)[1] degrade the performance of plasma facing components. Disruption events, which occur when the entire inventory of stored energy in the plasma is rapidly exhausted to the surrounding walls, will detrimentally affect wall material. A significant amount of mass can be lost from the wall due to vaporization and melting, generating particles (i.e. aerosols or dust) upon condensation and cooling. These particles are generally composed of activation products and are possibly chemically reactive (of concern for air/steam ingress accidents). Thus, wall material mobilization presents a potential safety hazard because of the possibility of particulate release.

To gauge the magnitude of hazard from disruption-induced material vaporization and subsequent condensation, disruption simulations must be performed on relevant materials at conditions expected in ITER. Extremely high energy fluxes are required for ITER simulation (20-100 GW/m^2 over 10 ms[1]). The SIRENS (Surface Interaction Experiment at North Carolina State) high heat flux facility at North Carolina State University (NCSU) can meet this requirement by producing energy fluxes on order of 50 GW/m^2 over a 50-150 μs time frame. The purpose of this report is to present the experimental procedures developed for use of SIRENS in disruption-induced mobilization studies and to show readiness for testing. The results of preliminary scoping tests will be presented. The measured parameters allow determination of aerosol transport properties, which are necessary to quantify the activation product source term, and evaluation of potential chemical reactions that could challenge confinement barriers.

Although SIRENS has been shown to be suitable for tokamak disruption studies and has an operating history that includes over 700 experimental runs[2], several changes in the mode of operation were necessary to produce mobilization data. Section 2 of this report outlines the SIRENS facility and the changes made for this application. Experiment procedure is covered in Section 3. Analytical techniques used to evaluate particulate data are described in Section 4, and scoping test results are presented in Section 5. Appendices are included describing documentation procedures and equipment calibration and maintenance.

2.0 Experiment Description

The SIRENS facility was developed in 1986 to investigate high heat flux exposure to various materials, providing quantitative data to many industries, such as fusion technology, aerospace, environmental waste, and defense[3-5]. The device is a small scale high energy density electrothermal (ET) plasma gun, capable of delivering 50 GW/m^2 for 50-150 μs. Useful heat flux originates in and is transported from an ET source section, then exposed to test material samples as a near-blackbody radiation source. Details of the nominal operation are discussed in Section 2.1. Aerosol formation from wall material vaporization, however, requires a somewhat different configuration. Heat flux for wall vaporization is in effect produced by the same mechanism as in the nominal case, but the material of interest is placed within the ET source section. Once the vaporized material exits the source section, it undergoes expansion and generates aerosol in a large chamber. This process and the necessary changes in SIREN's configuration are explained in detail in Section 2.2. Also discussed in that section is the relevance of the wall vaporization mechanism in SIRENS to similar mechanisms expected in an ITER disruption. Section 2.3 will show parametric equivalence of SIRENS and ITER, and describe relevant simulations on SIRENS.

2.1 SIRENS Facility

SIRENS was designed to utilize an electrothermal ablation-controlled arc to generate a high heat flux source for studying plasma-material interaction. The term electrothermal results from the arc discharge vaporizing and heating inner wall material, creating a hot, conductive gas (i.e. plasma). Figure 2.1.1 shows the configuration of the ET source section.

The ET source works as follows. An external circuit supplies high voltage and current to the point cathode, initiating an arc discharge to the associated circular anode. Arc initiation occurs as current arrives to the cathode in a time governed by supply circuit inductance, allowing potential to increase between the electrodes until dielectric breakdown of the intervening medium. In SIRENS, a polycarbonate capillary (e.g. Lexan) is generally filled with argon gas at an ambient pressure of 700 mTorr, the cathode material is either pure tungsten or a tungsten alloy (DIMETECH or HD-17), and the anode is situated at the end of the brass outer conductor. Breakdown voltage for this ET source section configuration

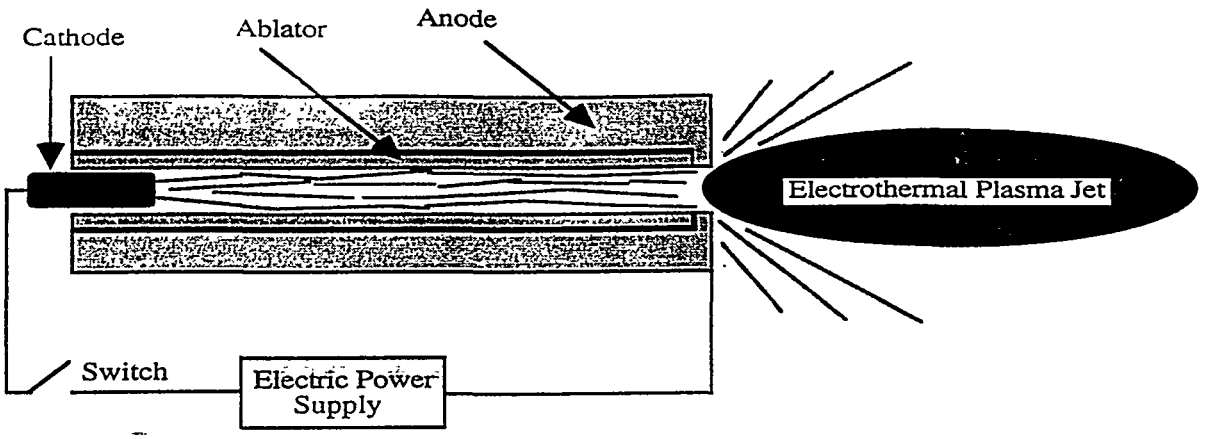

Figure 2.1.1 Electrothermal source configuration of SIRENS for nominal operation.

has been found to be approximately 1 kV in argon. Upon breakdown, the medium becomes conductive and enters a glow discharge regime. However with the presence of a high current source, the glow discharge very quickly transitions into the thermal arc regime. Electron current originates from the cathode by field emission, and the arc plasma can be shown to be in local thermodynamic equilibrium (LTE) because of high pressure achieved from vaporization of the capillary wall and the cathode[6]. The spectral emission takes on the characteristics of the vapor of the wall and cathode material rather than that of the fill gas[7]. This brute-force arc generation occurs in an estimated time on order of hundreds of nanoseconds, again being determined by the total circuit impedance.

The mechanism by which energy is transferred to the capillary wall is radiation. Since the arc plasma is in LTE (which means no net energy flows between volume elements, electron and arc gas temperatures are equivalent, and the plasma is optically thick), the surface will radiate as a black body. Heat flux to the surface is determined from the Stefan-Boltzmann radiation law, $q'' = \sigma T^4$, where σ is Stefan's constant ($5.7605E10^{-8}$ $W/m^2/K^4$). Ensuing wall vaporization from this incident heat flux results in energy removal by gas-dynamic jets[8]. As the capillary within the ET source provides a constrictive geometry, the gas is ejected into the arc region, partially ionized, and heated to thermodynamic equilibrium. This plasma continues to radiate, and pressure will increase due to mass addition. Since the capillary is open on one end, an axial pressure gradient exists which forces the plasma to jet out. This dynamic process assumes the relaxation time of thermodynamic equilibrium is much less than any characteristic time associated with gas-dynamic transport.

Once generated, plasma that exits the ET source may be utilized in a number of ways. It may be used, for example, to expose other surfaces external to the source to high radiative heat flux. The intense pressure generated within the capillary (~700 MPa) has also been used to launch a projectile. The combination of high heat flux and pressure could be used to significantly improve combustion in advanced propellants. SIRENS has been equipped to allow versatility in both energy output and diagnostic capabilities. Figure 2.1.2 displays the arrangement of the ET source with respect to the vacuum chamber and several diagnostic tools. Table 2.1.1 lists typical SIRENS operational characteristics. Table 2.1.2 gives a listing of some of the diagnostics available on the device. Equipment associated with SIRENS is maintained and calibrated at regular intervals by performing standards checks or following equipment manufacturer's guidelines. See Appendix B for details.

Table 2.1.1 SIRENS Operational Characteristics

Discharge Voltage	1 - 8 kV
Peak Current	20 -100 kA
Net Energy	1 -80 kJ
Discharge Period	100 -300 μs
Radiated Power	2 - 120 GW/m^2
Peak Pressure	100 - 700 MPa
Plasma Density	10^{24} - 10^{27} m^{-3}
Average Temperature	1 - 3 eV
Average Velocity	4 - 8 km/s

Table 2.1.2 Available Diagnostics on SIRENS

Temperature	conductivity probes, Langmuir probes,OMA*
Pressure	piezo-electric pressure transducers
Heat Flux	IR thermocouples
Velocity	break wires, opto-interuptors
Plasma Composition	OMA
Discharge Voltage	dividing high voltage probe
Discharge Current	Rogowski coil
Mass Loss	micro-balance scales

* - Optical Multi-channel Analyzer

One important diagnostic tool is a model developed specifically to describe the physics occurring in the source section. This model has been incorporated into a code named ODIN. Given an input of time-dependent current entering the source section, the code will predict several plasma parameters, such as temperature, density, pressure and total energy. This code has been empirically tested by numerous benchmarking experiments[9].

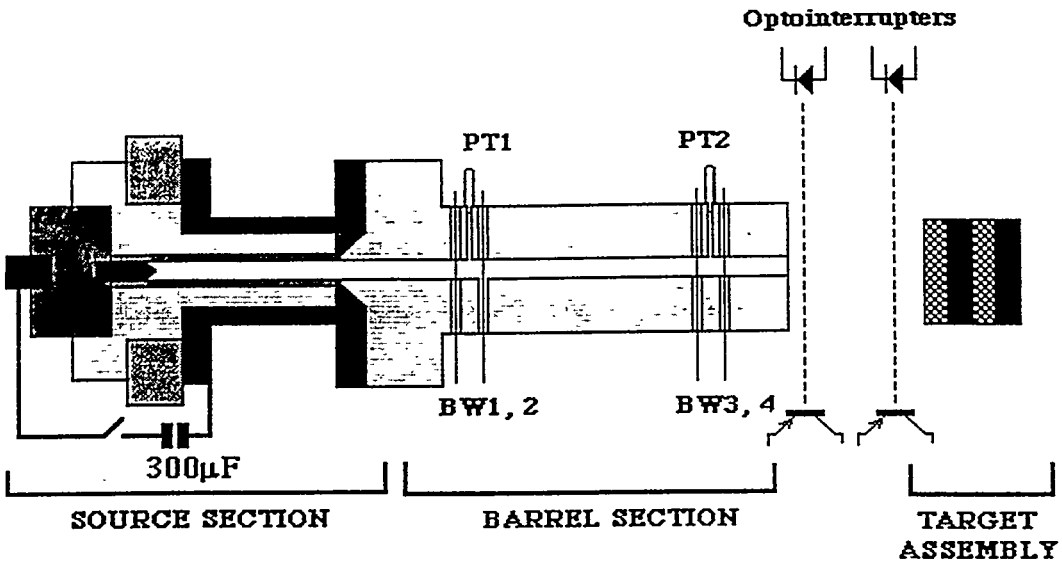

Figure 2.1.2. Layout of SIRENS, including various diagnostic tools for standard operation.

Power is delivered to the ET source of SIRENS by a pulsed-power network (PPN), shown in Figure 2.1.3. Operation of this inductance-capacitance-resistance (LCR) circuit is straightforward in that the output current and voltage are governed by the second-order differential equation describing the configuration. However, the time dependent nature of the plasma in the circuit generates a time dependence in the R and L components, acting to destabilize the governing equation and create a set of coupled equations (generally assumed to be linear). Detailed analysis of this circuit is important to ensure the system is near critically damped, otherwise a large voltage oscillation would send current back into the capacitor bank. The circuit designed for SIRENS has been tested and used for many experiments. See Figure 2.1.4 for examples of typical voltage (V) and current (I) traces. Varying pulse lengths, or time constants, are achieved by changing the amount of controllable inductance in the circuit. The present configuration is designed for pulse lengths of 50 μs and 250 μs. Bank charging is accomplished using an external circuit with a 100 mA high-voltage power supply. Once the desired charging voltage is achieved, the charging circuit is isolated and an independent high-voltage thyristron is used to trigger the spark gap switch.

Analysis of the V and I traces provides a convenient way to calculate the total energy discharged into the ET source section. Since power (P) is simply the product V*I, then total energy (E) is the integrated (numerically from the V*I product trace) power. This

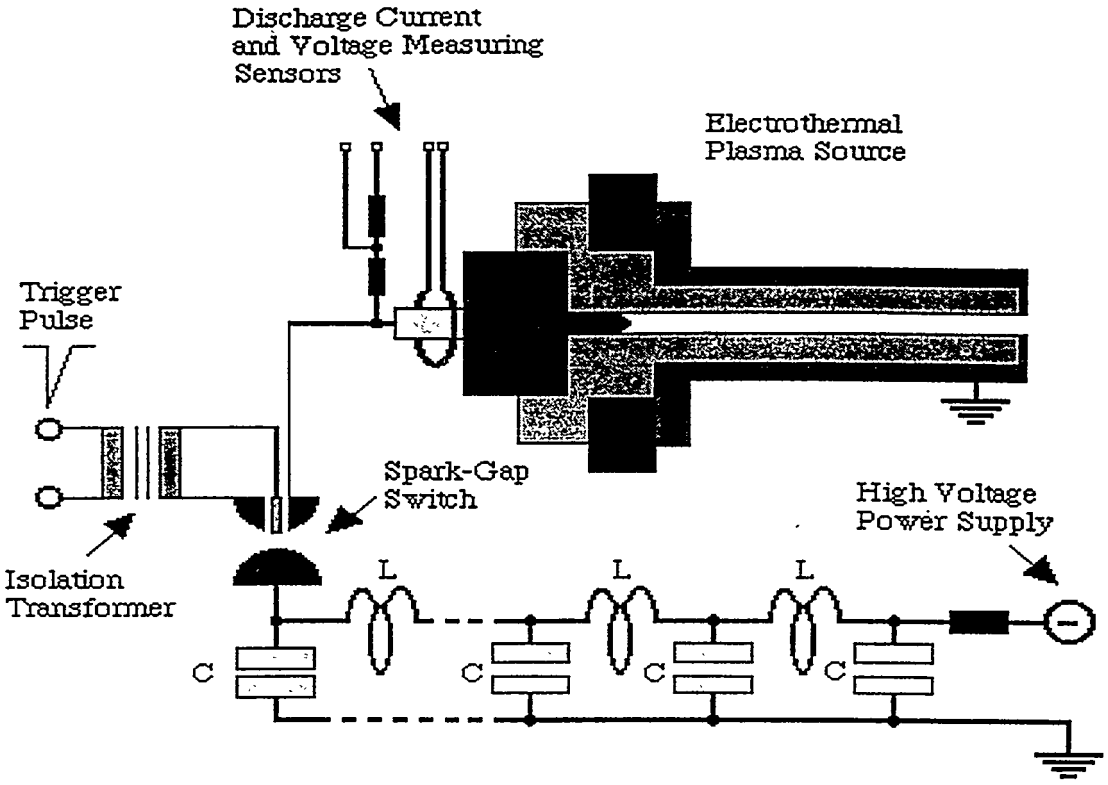

Figure 2.1.3. Pulsed-power network (PPN) which energizes SIRENS.

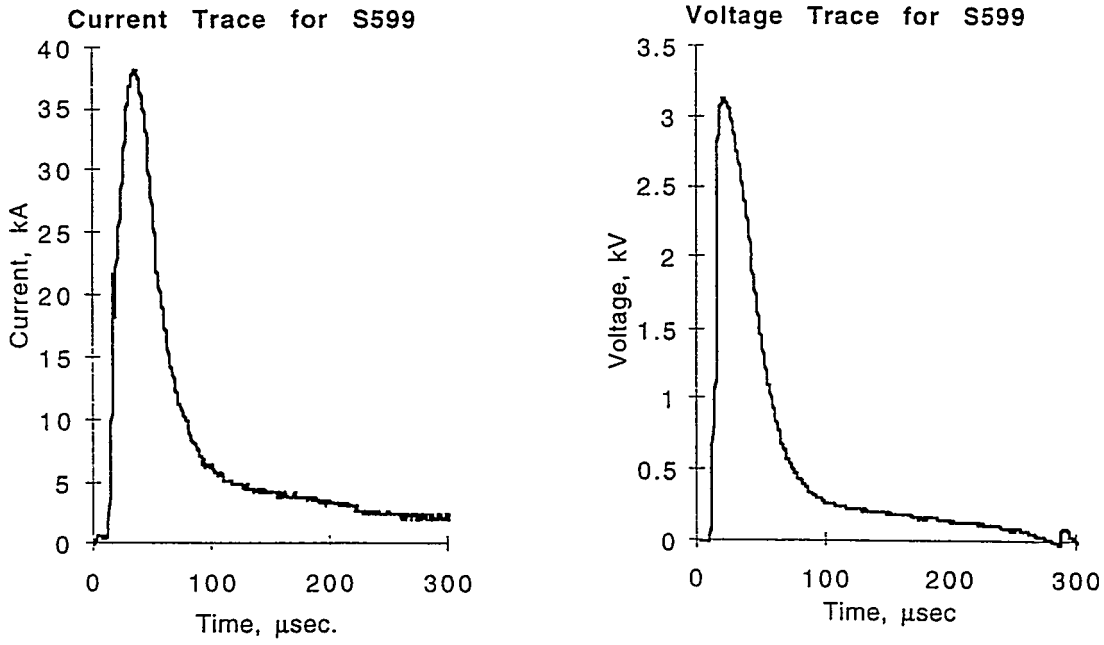

Figure 2.1.4. Voltage and current traces from the SIRENS PPN.

energy may then be compared with the change in energy stored in the capacitor bank. Table 2.1.3 displays a comparison of the energies determined for several shots. Occasionally, residual voltage remains on the capacitors after the shot because the plasma is generally extinguished after the first cycle of the discharge. The measured bank loss energy is the total energy available to the circuit from the capacitor bank. Integrated power determined from the voltage and current measurements is the amount of energy delivered to the source section and is typically within 2% of the value determined by the capacitor bank loss measurement. The ODIN code prediction is compared against the integrated power measurement as an indication of the accuracy of the model. The model estimate is generally within 12% of the integrated power measurement. The difference in measured and predicted discharge energy originates from the assumption in the model that conductivity in the ET plasma is ideal. An effort is currently being made to improve the model to include non-ideal conductivity terms. ODIN predictions of source mass loss and exit pressure are also compared to measurements (see attached publication in Appendix C). These comparisons are useful, but are not relied upon to provide key parameters in the experiment.

Table 2.1.3. Comparison of shot energy determined from three different methods.

Shot	Capacitor Bank Energy Loss (J)	Integrated Power (J)	ODIN Prediction (J)
S553	5930	3870*	5146
S599	5050	4923	5277
S641	6070	5350	5806
S705	9080	9010	7920

*-voltage probe out of calibration

2.2 *SIRENS Use for ITER Wall Vaporization Studies*

The versatility of SIRENS proves to be useful in the study of wall material vaporization relevant to ITER. The experiment is being used to study plasma disruption-induced activation product generation and transport, with the objectives described in the "Test Plan for Disruption Induced Aerosol Characterization for ITER Source Term Determination"[10]. Experiments are to be performed to determine size and chemical form of material mobilized during a plasma disruption. The data will contribute to determination of the overall activation product source term associated with postulated ITER accidents.

Disruption energy flux in ITER is expected to be 20 - 100 GW/m^2 (20 - 100 MJ/m^2 over 1 - 10 ms)[1], and SIRENS can generate energy fluxes in the range of 50 GW/m^2 (up to 12 MJ/m^2 over 0.25 ms). The primary mechanism of energy transfer to the walls in both ITER and SIRENS is blackbody radiation. Thus wall material vaporization occurs similarly in both devices. Vapor shielding is unimportant in this comparison because the overall energy deposited to the wall surface is of interest, not the heat flux which originates from the source. The temperature of the vapor shield (or plasma-surface interaction region) is, however, important because this is the source of radiation. In ITER, continual ablation of surfaces exposed to disruption plasma will feed mass into the interaction region, which is subsequently heated by the incoming flux of energetic particles[11]. This is in principle analogous to the ablation-controlled arc in the ET source of SIRENS.

Of particular interest in this investigation is what happens to vaporized material following the disruption. A significant amount of mass is vaporized by the disruption, generating high pressure expanding out against the kinetic pressure of the incoming disruption flux. After the disruption ceases, the portion of this vapor that is not intercepted by a cold wall (resulting in surface condensation) continues to expand into the large volume of the plasma chamber, cooling and condensing as it does so. Similarly in SIRENS, the vaporized wall material is ejected from the capillary into an expansion volume. Cooling and condensing in the expansion volume causes particles to be generated in SIRENS representative of those expected from an ITER disruption.

Table 2.2.1 displays a comparison between relevant ITER and SIRENS parameters. Major points displayed by the table are:

- disruption (or simulation) energies and pulse lengths are different
- affected areas are vastly different (SIRENS can accommodate only small samples)
- total power fluxes exposed to wall material are similar (within scale)
- ITER-relevant materials may be studied in SIRENS
- mixed materials effects may be studied
- adiabatic expansion volume ratios are within scale for a range of erosion depths

Expansion volume ratios (vol. of ablated wall material / available expansion vol.) are important because of the relevance to aerosol formation. ITER-relevant materials may be

studied in SIRENS, and mixed materials studies are easily performed. Beryllium could be tested but is beyond the scope of this investigation due to special handling requirements. Although the simulated disruption energy and pulse length are different from those expected in ITER, the total power flux (GW/m^2) achievable in SIRENS is comparable. Similarity in power flux is essential because pseudo-steady ablation rates of radiatively heated surfaces are directly dependent upon this parameter.

Table 2.2.1. Comparison of relevant ITER and SIRENS parameters.

Parameter		ITER (expected)	SIRENS	Scaling ITER : SIRENS
1. Disruption energy (MJ/m^2)		20 - 100	up to 12	1 : 2 - 1 : 10
2. Energy pulse duration (msec)		1 - 10*	up to 0.25**	1 : 4 - 1 : 100
3. Disruption power flux to walls (GW/m^2)		20 - 100	50	1 : 0.4 - 1 : 2
4. Affected area (m^2)		10 - 500	7.5E-4***	-
5. Expansion volume ratio	Erosion Depth			
	1 μm	7.69E-8	1.17E-7	1 : 1.5
	10 μm	7.69E-7	1.17E-6	1 : 1.5
	100 μm	7.69E-6	1.19E-5	1 : 1.5
6. Materials capability	Material	Important in ITER?	SIRENS capable	
	Copper	Yes	Yes	
	Tungsten	Yes	Yes	
	SS316	Yes	Yes	
	Carbon	Yes	Yes	
7. Mixed materials capability		Yes	Yes	

* ITER value from thermal quench time as given by ITER GDRD, March, 1996.
** longer pulse lengths can be achieved via PFN modification
*** after source section modification to SIRENS

Changes in the configuration of SIRENS to allow simulation of disruption-induced wall vaporization are made in the ET source section. Simply changing the capillary liner in the source section from polycarbonate to some material of interest allows ITER-relevant materials (listed in Table 2.2.1) to be investigated. Figure 2.2.1 details the modified ET source section. Two ceramic insulators are necessary to isolate conducting samples from the electrodes, thereby forcing the arc discharge through the capillary, rather than shorting in the sample. These insulators must be able to withstand high heat fluxes and have minimal ablation such that the vapor is composed mostly of sample material. Presently, the ceramic used is MAYCOR, which is easily machineable but very brittle when exposed to high temperatures.

Another significant change was the addition of the glass expansion chamber with one end connected to the ET source (Figure 2.2.2). This chamber is necessary to allow controlled collection of the particles formed upon condensation (see Section 4 for details on particulate collection). The chamber expansion volume is limited by the size constraints of the SIRENS vacuum vessel. Chamber dimensions are currently 100 mm in diameter and 400 mm in length (aspect ratio = D/L = 4). A new vacuum vessel and expansion chamber (with diameter of 180 mm and adjustable length up to 760 mm) will be used for future experiments. The adjustable chamber aspect ratio will allow scaling to any reasonable expansion volume ratio.

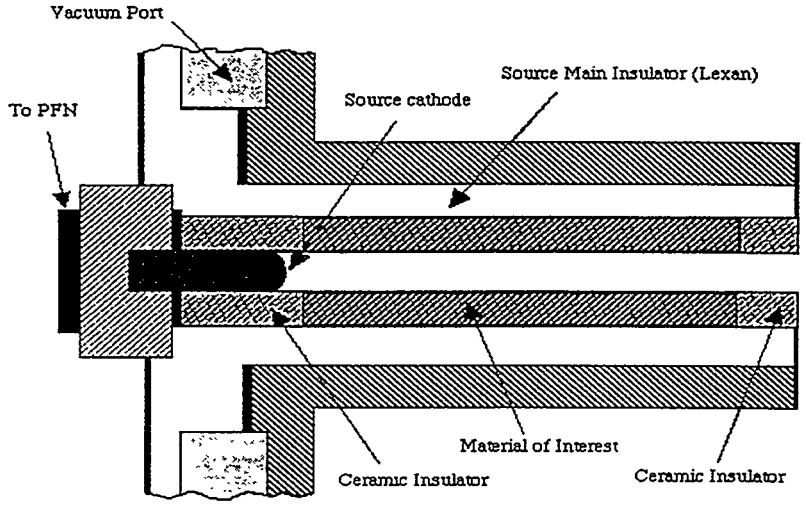

Figure 2.2.1. Modified SIRENS source section.

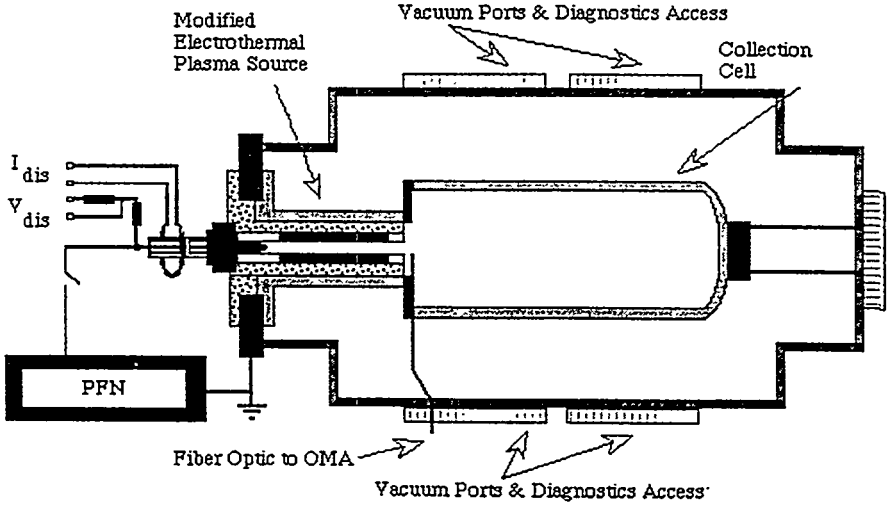

Figure 2.2.2. Modified SIRENS facility with the source section and expansion chamber.

3.0 Experimental Procedures

Experimental procedures have been developed for wall vaporization studies in SIRENS. This section will describe experimental and analytical procedures used for disruption simulation and wall vaporization studies in the SIRENS facility.

3.1 Preparation, Execution, and General Analysis of Experiments

Each time an experiment is performed using SIRENS, a list of preparatory actions must be followed. Typically the first step is to properly load all material samples and necessary diagnostics. For wall vaporization studies, this includes insertion of the expansion chamber into the vacuum vessel, connection of thermocouples and pressure transducers, and insertion of optical fiber for spectroscopic measurements. Note that during assembly of the expansion cell and source section, all relevant mass measurements are made. These measurements include initial weight of the sample in the source section, initial weight of the source cathode (to gauge potential contamination effects), and pre-test weights of all particle collection surfaces. Next, the modified source section is anchored to the vacuum vessel and coupled to the expansion chamber. Source section diagnostics (Rogowski coil and high-frequency HV probe) are then put in place. At this point all diagnostics and data acquisition systems are powered up and tested. Provided all tests are successful, the vessel is closed and pumped down to the vessel's ultimate pressure (~50 mTorr) using a roughing pump. Another test is performed to ensure no piece of equipment was damaged during pump down. The vessel is then back-filled to the appropriate test pressure. Throughout this entire procedure, all relevant information regarding diagnostics channels and experiment parameters are recorded on the run sheet. With all equipment in place, the experiment is ready for execution.

The first step in shot execution is to setup the trigger circuit, which includes adding a 20 μs delay to ensure the entire event will be recorded on all diagnostics channels. Next, the high-voltage supply for bank charging is powered up in safety mode (interlocked for no connection to bank). Inside the experiment room, all personnel leave the area, the grounding safety is disabled, and the cage is locked. In the control room, the trigger system is powered up. The high energy density capacitor bank may now be charged to the desired voltage (a experiment parameter) by disengaging the HV supply interlock and applying voltage. Upon reaching voltage, the interlock is switched to firing mode, the HV supply is switched off, and the trigger HV is activated. Manually triggering the delay

generator activates the spark-gap switch, allowing bank energy to discharge through the ET source section, in effect "firing the gun". Residual bank voltage is recorded and then dumped to ground through a dummy load for safety. Final chamber pressure is also recorded to indicate a potential leak resulting from the shot. The experiment room is re-opened, ground safety is re-established, all diagnostic equipment is secured, and the vessel is opened. The source and expansion chamber are carefully disassembled to allow post-shot analysis. Table 3.1.1 summarizes the shot execution steps described above.

Table 3.1.1. Procedural list for shot execution on SIRENS.

1. Install source, chamber, diagnostic inputs, record details on run sheet throughout procedure.
2. Pump system down to ultimate pressure (down to 50 mTorr).
3. Back-fill with argon to 700 mTorr.
4. Prepare data acquisition system, set trigger delay, secure interlocks on HV supply and trigger circuit.
5. Disable grounding safety and close cage.
6. Power up trigger system, heat filament.
7. Charge bank to V_o that gives desired energy input (not to exceed 50 mA rate from HV supply).
8. Upon reaching V_o : interlock to prepare to fire, switch off HV supply, set manual trigger on ADC module, activate trigger HV.
9. Trigger the delay generator... **FIRE!**
10. Record V_f and final vessel pressure.
11. Power down trigger circuit, deactivate delay generator, interlock to dump to ground, dump V_f to dummy load.
12. Open cage, establish ground safety, and disassemble source and chamber.

Following the successful execution of a shot, standard analysis is performed and includes inspection of the discharge voltage and current traces for unusual events (cracked insulator, etc.), determination of overall shot energy and duration, and simulation using the ODIN computer code. The following figures show the results of such an analysis of an experiment performed for high heat flux surface erosion studies.

Figure 3.1.1 displays the voltage and current traces for a shot in which the outer insulator surrounding the source section failed due to fatigue from multiple shots. This event provides very limited data because of the difficulty in characterizing the energy deposited into the source section. Appearance of a crack disrupts current flow into the capillary, which instantaneously changes circuit parameters, resulting in erratic current and voltage traces. The problem is easily avoidable by using new insulators after a set number of shots; experience has shown insulators survive 4 shots before failure.

Figures 3.1.2 displays results from an ODIN code simulation for the shot with current trace shown in Figure 2.1.4. The simulation calculates state variables such as pressure, temperature, and density, as well as kinetic, radiative, and total discharge energies. These parameters are compared to corresponding measurements in experiments for which these measurements are made.

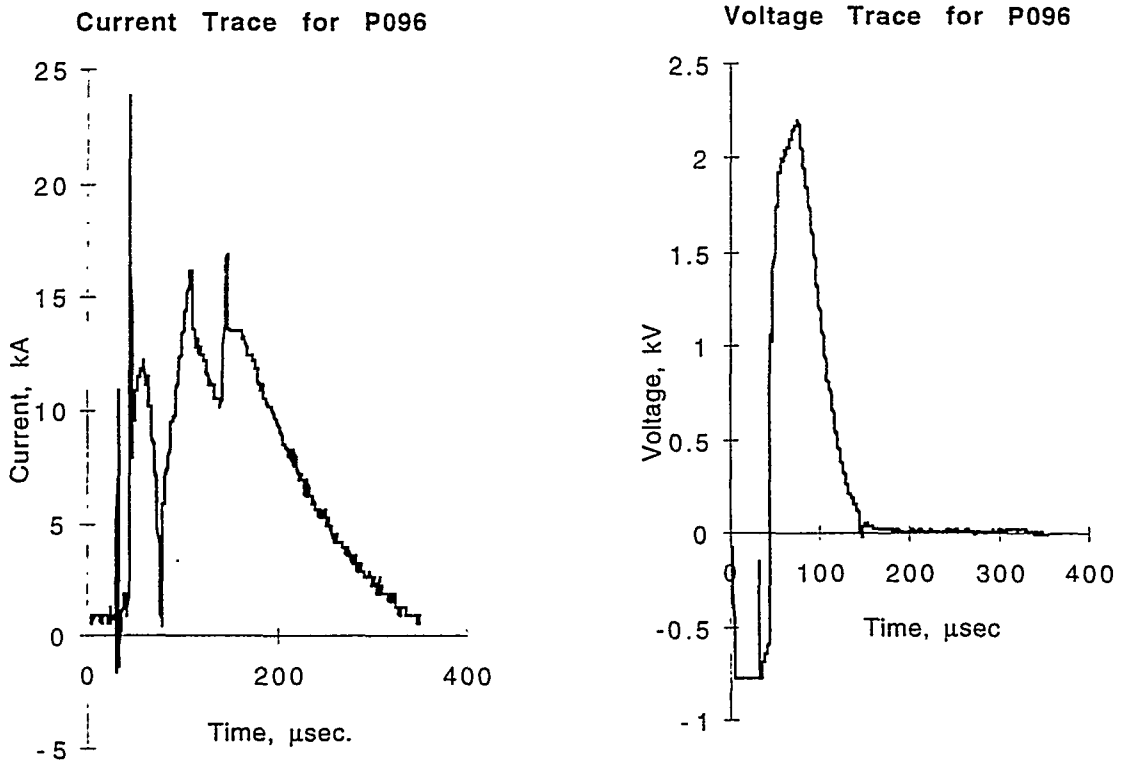

Figure 3.1.1. Current and voltage traces for a shot with insulator failure.

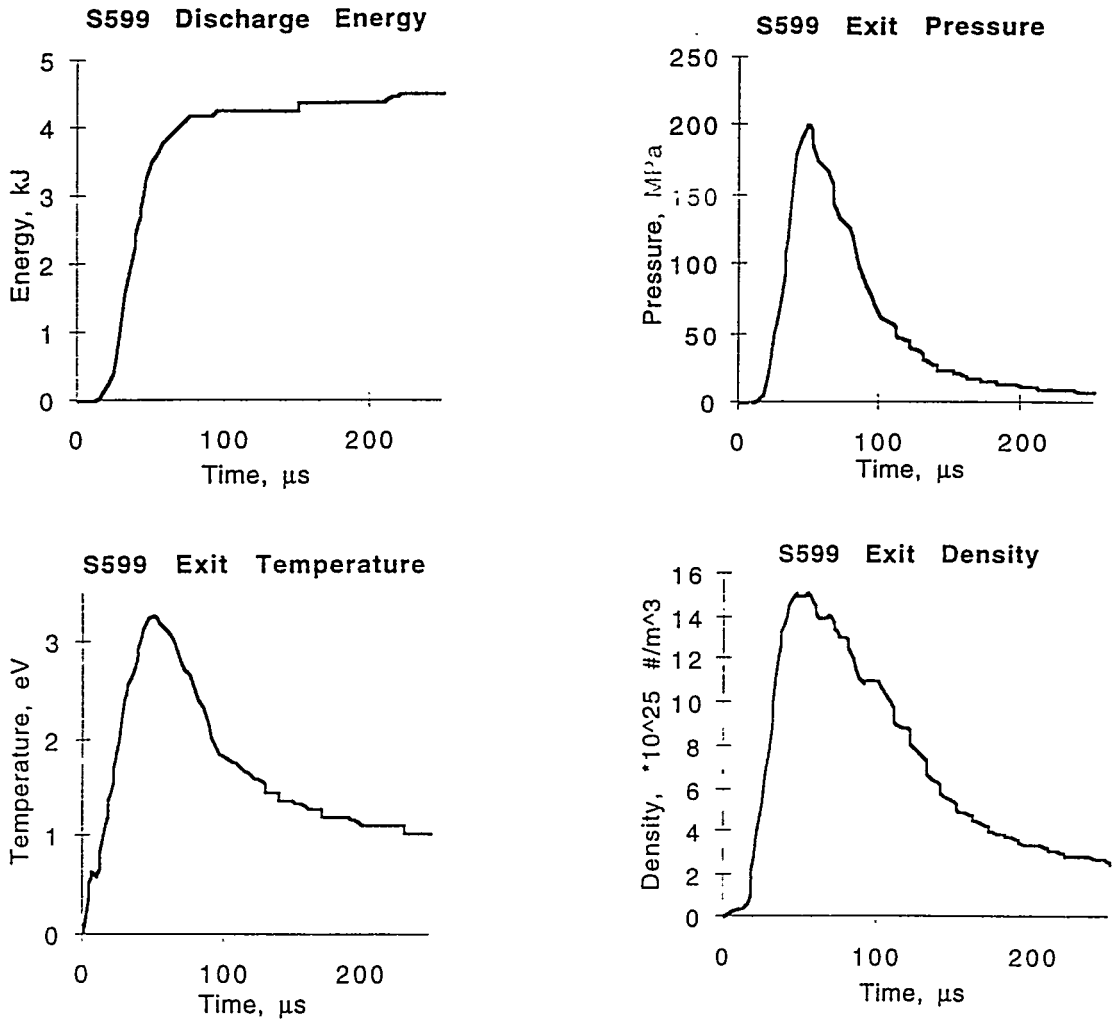

Figure 3.1.2. ODIN output parameters for typical shot analysis.

4.0 Particle Size Analysis

This section describes particulate collection in an experiment and construction of particle size distributions from the collected material.

4.1 Condensate Collection by Capture Buttons

As discussed in Section 2.2, vaporized material from the ET source expands out into a glass collection chamber. Upon expansion, energy is lost via thermal radiation (recall the vapor is still very hot when exiting the capillary) since the background gas at low pressure does not significantly contribute to convective cooling. When the vapor reaches the wall, conduction will also assist in cooling. During this expansion and cooling process, condensation will occur by one or more mechanisms. For example, homogeneous and/or heterogeneous nucleation may occur in the bulk expansion plume, while wall condensation (drop-wise or film) could occur on the peripheral boundary.

The expansion chamber has been analyzed assuming adiabatic expansion of an ideal gas at an initial pressure equivalent to the ET source exit pressure and a final pressure sufficient to ensure vapor supersaturation and subsequent condensation. No energy is lost from the vapor if the expansion process is considered adiabatic. The vapor temperature change occurs due to the change in internal energy from expansion. Thermal radiation cooling, however, does occur and drives the vapor into thermal non-equilibrium condensation at a faster rate than adiabatic expansion. An added complication is gas-dynamic non-equilibrium which results from free-jet expansion of the vapor from the source exit into the chamber. Occurrence of these non-equilibrium processes shows that vapor expansion from the source section is not adiabatic, and furthermore complicates modeling of the associated condensation physics. The volume required for adiabatic expansion will be used as a reference against which to compare the experimental expansion volume. For example, an initial pressure of 335 MPa (for 1 gram of Cu ablated in the source), and a final expansion pressure of 101.325 kPa (Cu is solid at 1 atmosphere), the required volume for adiabatic expansion of the ideal gas is 5.83×10^{-4} m^3. Applying the ideal gas equation of state gives a final vapor temperature of 180° C. Volume available to the real gas is 3.14×10^{-3} m^3 using the original chamber dimensions given in Section 2.2 (100 mm diameter and 400 mm length), which provides 5.4 times the adiabatic expansion volume. A larger chamber is

also available, providing an expansion volume of 1.94×10^{-2} m^3 (dimensions are 180 mm diameter and 762 mm length).

Once particles have formed within the chamber, they follow flow streamlines or diffuse to the wall. To collect these particles, 1.25 cm diameter metal discs (buttons) are distributed on the inner wall. For the preliminary investigation, stainless steel (SS316) was used for Cu source section samples and copper was used for SS316 samples. Button distribution for the original expansion chamber is shown in Figure 4.1.1. Vapor and particle momentum near the ET source exit are predominately directed along the chamber axis, resulting in fewer particles transported to the wall and increased mass deposition down the length of the chamber. Buttons approaching the end of the chamber are placed at offset locations that will eliminate deposition shadowing by upstream buttons. At the very end of the chamber, buttons are placed on a plastic end plate. Maximum mass deposition is expected at this location. Buttons are attached by adhering the discs to plastic backings (using rubber cement, which allows them to be easily removed with acetone). The backings are tapped to accept threaded rods that penetrate tiny holes in the chamber wall and are capped with small nuts (see inset in Figure 4.1.1). This arrangement allows for button installation prior to an experiment and removal following an experiment.

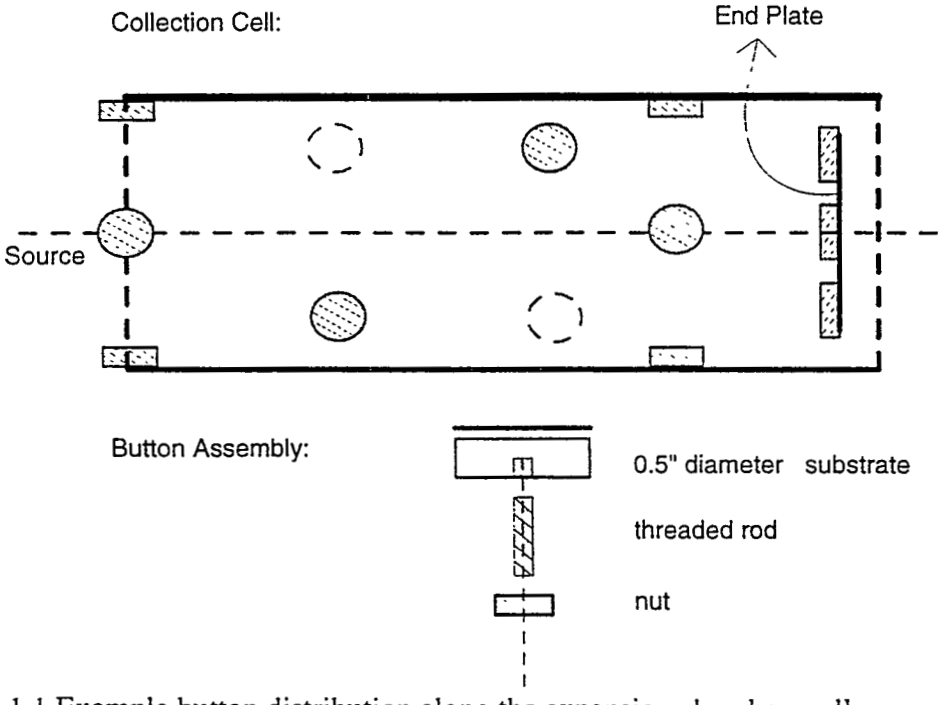

Figure 4.1.1 Example button distribution along the expansion chamber wall.

Condensate mass deposition onto each button is determined by measuring the weight of the button before and after each shot. This also gives fractional mass deposition as a function of position within the expansion chamber. Because the buttons are glued to plastic backings, care must be taken when making the weight measurements. To ensure that removing a button from its backing does not leave a glue residue, a test was performed. Each disc in a control set of 4 buttons was individually weighed, attached to the plastic backing, threaded with the rod, and attached to the chamber wall. An equivalent procedure is used in shot preparation. Next, the button sets were removed from the chamber, taken off the plastic backing, and re-weighed. Table 4.1.1 displays the initial and final weights measured during this test. The difference is within the uncertainty of the measurement (± 0.00003 g), thereby showing that mass deposition on buttons can be determined from weight measurements before and after exposure.

Table 4.1.1 Control button analysis.

Control Button	Initial Disc Weight* (grams)	Final Disc Weight* (grams)	% difference
1	0.58233	0.58231	0.003
2	0.58380	0.58382	0.003
3	0.58262	0.58260	0.003
4	0.58356	0.58354	0.003

*- average of 4 different measurements.

Once a shot is complete and particles have been deposited on the buttons, they are removed from the expansion chamber, weighed, and prepared for particulate size distribution analysis. Characterization of particle size and morphology using a scanning electron microscope (SEM) and an optical microscope will be discussed in detail in the following sections.

4.2 Observation of Particulate

Scanning electron microscopy (SEM) and optical microscope techniques have been developed for characterizing particulate from various sources.[12] Size distributions are readily obtained by counting the number of particles within a specified size range on the microscope images. Analysis of the particles produced during a disruption simulation on SIRENS will be accomplished in this manner. The capture buttons will serve as both collection surfaces and as analysis substrates.

Upon viewing the buttons in the SEM, appropriate magnification for counting is determined by the size and area density of particles on the button. At low magnification, many small particles present in the population may be overlooked, while with high magnification, too few particles will be on an image to represent the population. Imaging at various magnifications will provide a meaningful sample of the population. Scoping tests for this task show that 2 or 3 different SEM magnifications (selected from 350x, 500x, 1000x, 1200x, and 1500x) are sufficient to cover the range of particle sizes. Maximum size of an object viewable with the SEM is 1000 μm, while the minimum size based on SEM resolution is < 0.001 μm. Observations using the optical microscope are made at 50x, 100x, 500x, and 1000x, allowing a particle size range of 0.1 μm < d_p < 1000 μm. Incorrect combination of data from different magnifications could result in over counting the number of particles in size bins that are shared between the distributions from each magnification. The overall particle size distribution construction protocol is described in Section 4.3. The number of photographs necessary at a specified magnification is influenced by the observed particle density on the image. Many particles must be counted for sufficient counting statistics to ensure accurate representation of the size distribution. Generally, four areas should be examined and photographed at each magnification. (For the scoping tests, in many cases only one photograph was available.)

Figure 4.2.1 displays resulting SEM photographs of a particular button (S715 Button 11) used to collect particles in one of the scoping experiments. Part (a) of Figure 4.2.1 shows an SEM image at 500x, where many particles are present. Based on experience gained from using this method, this magnification would be used to count particles greater than 2.5 μm. Part (b) of the figure was taken at 1200x, which, for example, could be used to count particles between 0.625 μm and 2.5 μm. An image with magnification 3000x is shown in part (c). This magnification would be used to count particles in the size range of 0.1 μm to 0.625 μm. In this example, several images at 3000x would be required for analysis because there are relatively few particles present to contribute to the overall distribution. Generally, images obtained at magnifications higher than 3000x on the SEM are impractical because many photographs would be necessary to obtain a representative count of particles less than 0.1 μm. With both the SEM and optical microscope, the minimum counted particle size is dependent upon the highest magnification and the number of photographs taken at that magnification. If a sufficient population of extremely small particles (< about 0.25 μm) are observed, many photographs are made to accurately represent them in the overall distribution.

Figure 4.2.1. SEM micrographs from button 11 of scoping test S715.

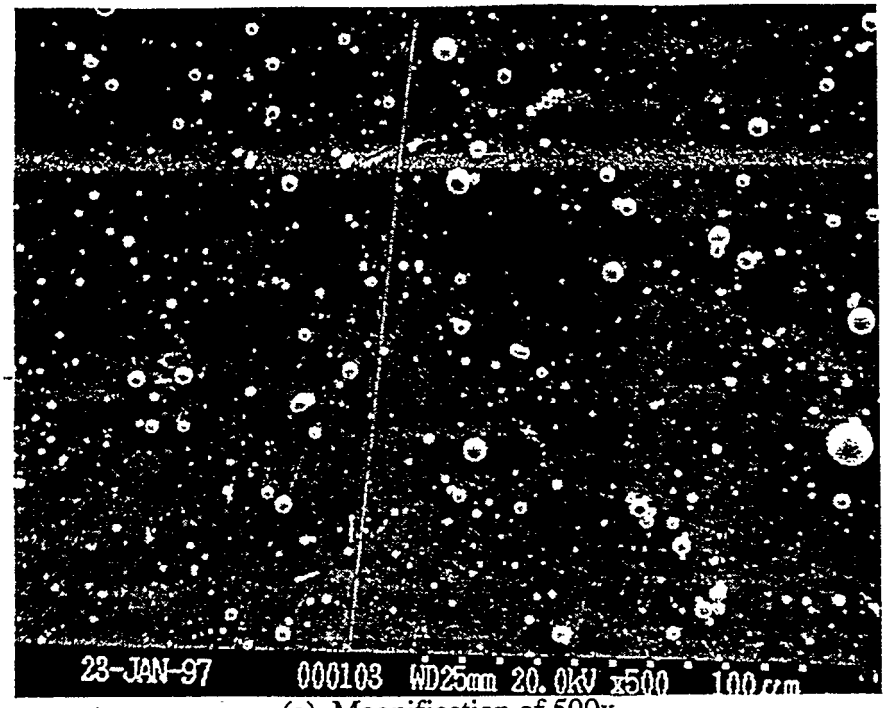

(a) Magnification of 500x

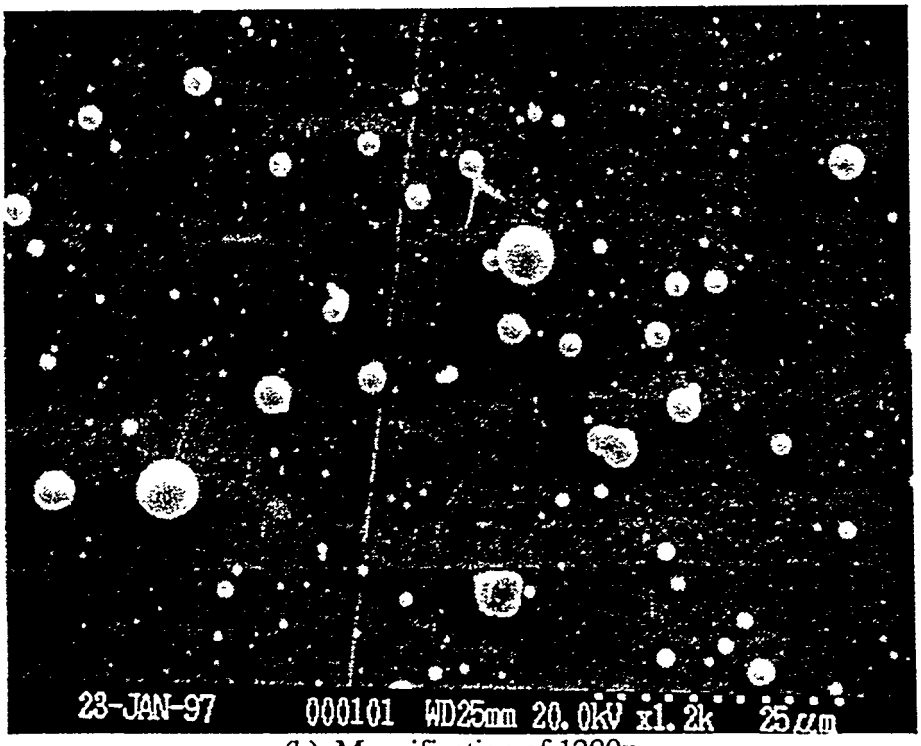

(b) Magnification of 1200x

Figure 4.2.1. cont.

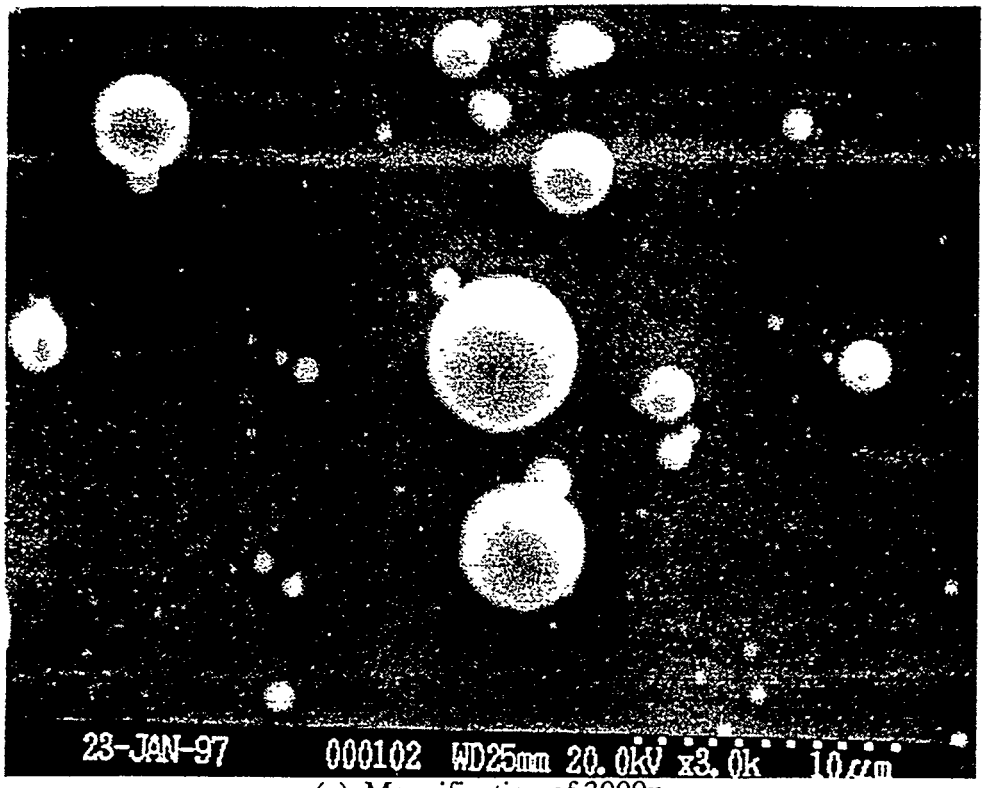

(c) Magnification of 3000x

Figure 4.2.2 shows the resulting 100x, 500x, and 1000x optical microscope photographs for button S715_10. The optical microscope can be used similar to the SEM microscope following the same guidelines for image quality and particle analysis.

Figure 4.2.2. Optical microscope photographs of button 10 from scoping test S715.

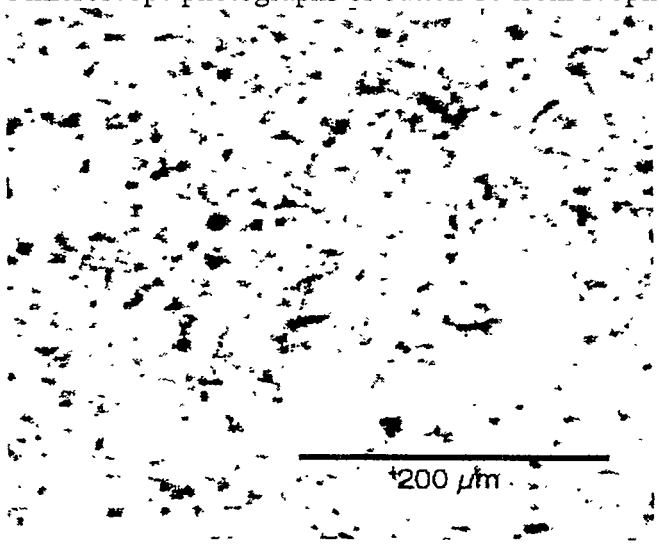

(a) 100x photo

Figure 4.2.2. cont.

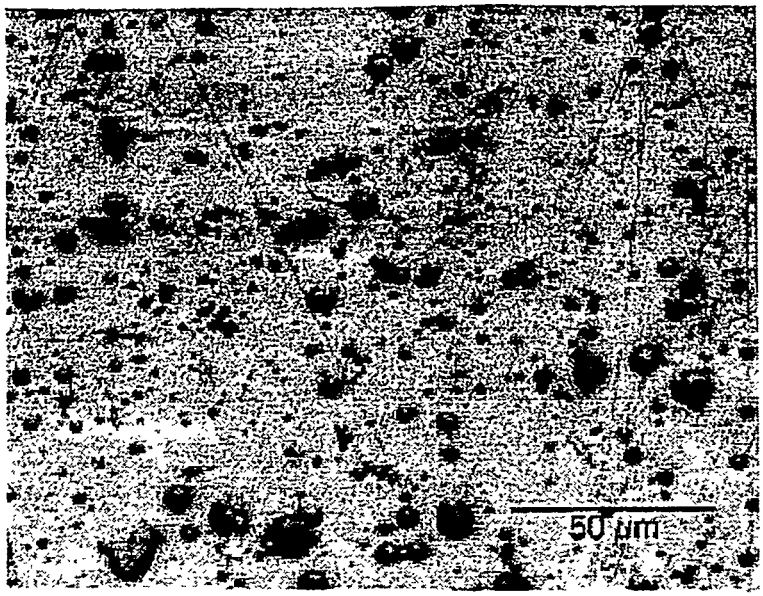

(b) 500x photo

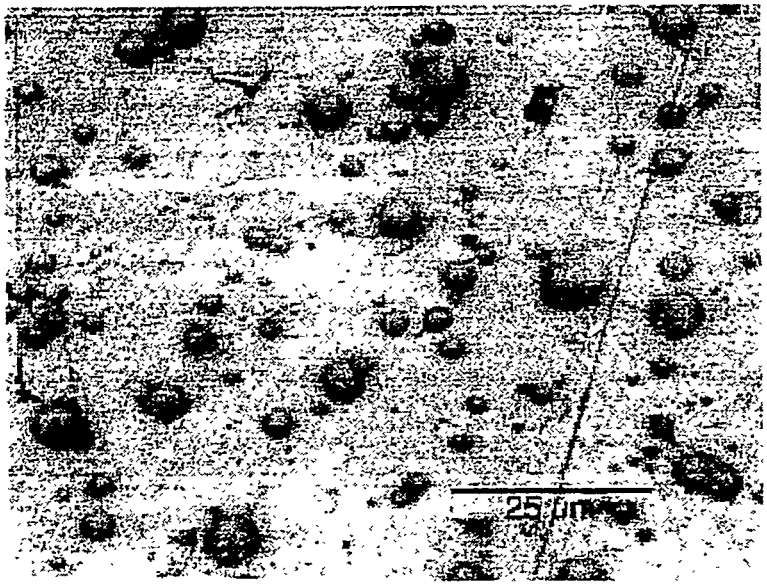

(c) 1000x photo

There are several considerations regarding image quality that must be addressed when using the SEM and optical microscopes. Specifically, analysis requires images which display bright, sharply focused particles with distinct edges. Operating parameters of the SEM, such as accelerator potential, working distance, and detector mode, must be optimized for the sample configuration. Image focus, astigmatism, brightness, and

contrast must also be adjusted to yield proper particle distinction. Neutral density and polarizing filters should be used on the optical microscope to improve the image quality for particle size determinations similar to the adjustments for SEM photographs. The actual particle analysis is to be performed using photographs on Polaroid film that are electronically scanned to obtain a digital image. Specialized image analysis software is used to count the particles. Although high resolution photographic image quality is expected from any SEM or optical microscope facility, particular attention must be given to these issues because of the sensitivity of the analysis software with respect to generating accurate particle size distributions.

4.3 Image Analysis and Distribution Generation

Image analysis and particle counting is accomplished using the method developed by Carmack et al.[12]. A schematic depiction of the technique is shown in Figure 4.3.1. As described in Section 4.2 the substrates are examined using a scanning electron microscope and an optical microscope. The images are analyzed using NIH-Image software, available as public domain from the National Institute of Health. Photograph images are scanned and converted to digital files that are used as input to the software. The digital image is prepared for object counting (i.e. scaling, thresholding, shadow removal, etc.) and the software is instructed to "analyze particles." Results for each particle on the image are returned and include projected area (from pixel-area scaling conversion), major and minor elliptical radii, and any user defined function, such as conversion of projected area to equivalent-sphere diameter. The resulting data from each individual photograph of a given substrate are combined and used to build the particle size distribution using spreadsheet software.

The first step following image acquisition and particle count involves performing a sampling test known as the Kruskal-Wallis test on data sets taken at the same magnification but at different locations on the substrate. This test determines if the data sets are representative of the overall underlying population. Data sets that fail this test are eliminated from the analysis. The next step is to define size bins for each magnification and count the number of particles that contribute to each bin range at each magnification. From this, cumulative percent of counted particles is determined for each magnification. These magnification distributions are then plotted in log-probability form and a linear fit applied. The count median diameter (CMD) and geometric standard deviation (GSD) are determined

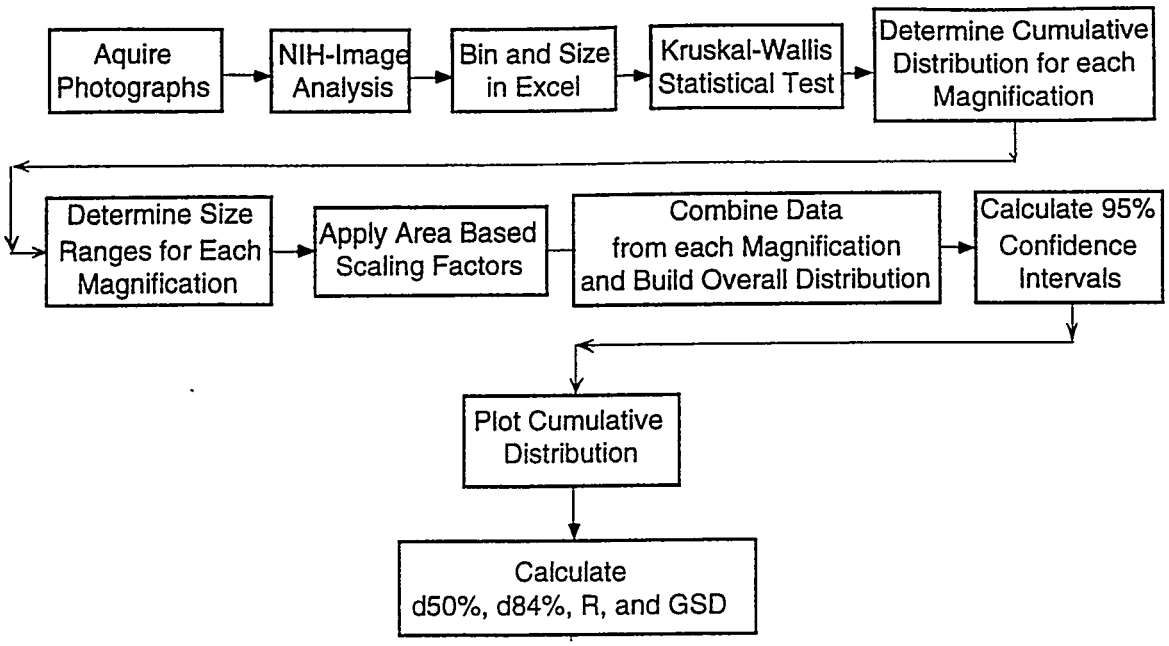

Figure 4.3.1 Schematic depiction of the size distribution construction technique.

from the fit parameters. The CMD, $d_{50\%}$, is the particle size corresponding to the 50 percent cumulative value and the $d_{84.1\%}$ is the particle size corresponding to the 84.1 percent cumulative value. The GSD is the $d_{84.1\%}$ value divided by the $d_{50\%}$ value. Using this distribution fit for individual magnifications, appropriate range selection for each magnification is made. Data in the appropriate size range for each magnification is then scaled by adjusting the number of counts in each bin based on the viewed area of that magnification. Table 4.3.1 shows the scaling factors used for various magnifications from both SEM analysis and optical microscope analysis. These scaled counts are then combined to produce the overall particle size distribution for the substrate under investigation. Ninety-five percent confidence intervals for the distribution are also calculated and plotted.

To check the distribution construction technique a particle size distribution was constructed from optical microscope photographs of sample Q1DV taken from the DIII-D vacuum vessel provided by the INEEL. Table 4.3.2 shows a summary of the relevant particle size distribution data generated for the comparison as well as the data reported by Carmack et al.[13] for the sample analyzed. Figure 4.3.2 shows the distribution constructed by NCSU from the DIII-D Q1DV photographs provided by the INEEL and the distibution generated from INEEL's separate analysis of the same data. Differences in the values obtained for $d_{50\%}$ (17%) and GSD (7%) result from different particle size screening criteria used in the

image analysis. Appropriate discrimination criteria are currently being investigated. The influence of the discrimination criteria on particle sizing results is expected to be smaller for SEM photographs than for optical photographs because the minimum resolvable pixel size corresponds to much smaller particle sizes for the SEM than for the optical microscope. The particle size distribution measurement has been benchmarked as outlined in Carmack et al.[13] using known particle size distribution material obtained from Duke Scientific, CA, USA. Presentation of this benchmark is provided by Carmack et al. in the same reference.

Table 4.3.1. Scale Factors for the optical microscope and the SEM microscope.

Magnification	Optical Microscope Scaling		SEM Microscope Scaling	
	(pixels/μm)[a]	Scale Factor	(pixels/μm)[a]	Scale Factor
50x	0.342	0.25	-	-
100x	0.679	1	-	-
350x	-	-	1.97	0.49
500x	3.4	25	2.95	1
700x	-	-	2.74	1.96
1000x	6.8	100	5.9	4
1200x	-	-	7.2	5.76
1500x	-	-	8.9	9
3000x	-	-	17.7	36
5000x	-	-	19.5	100

(a) Magnifications are constant as determined by the microscope hardware. Scale values may vary slightly if digitized at higher magnification than one. This is accounted for by the operator using NIH-Image by measuring the area of each photograph.

Table 4.3.2. Comparison of NCSU analysis verses INEEL analysis for DIII-D Q1DV.

	$d_{15.9\%}$	$d_{50\%}$	$d_{84.1\%}$	GSD	R^2
NCSU Analysis	0.25	0.64	1.65	2.69	0.9857
INEEL Analysis	0.35	0.53	1.52	2.88	0.9823

Figure 4.3.2. Log probability distribution constructed by NCSU and INEEL for DIII-D Q1DV dust.

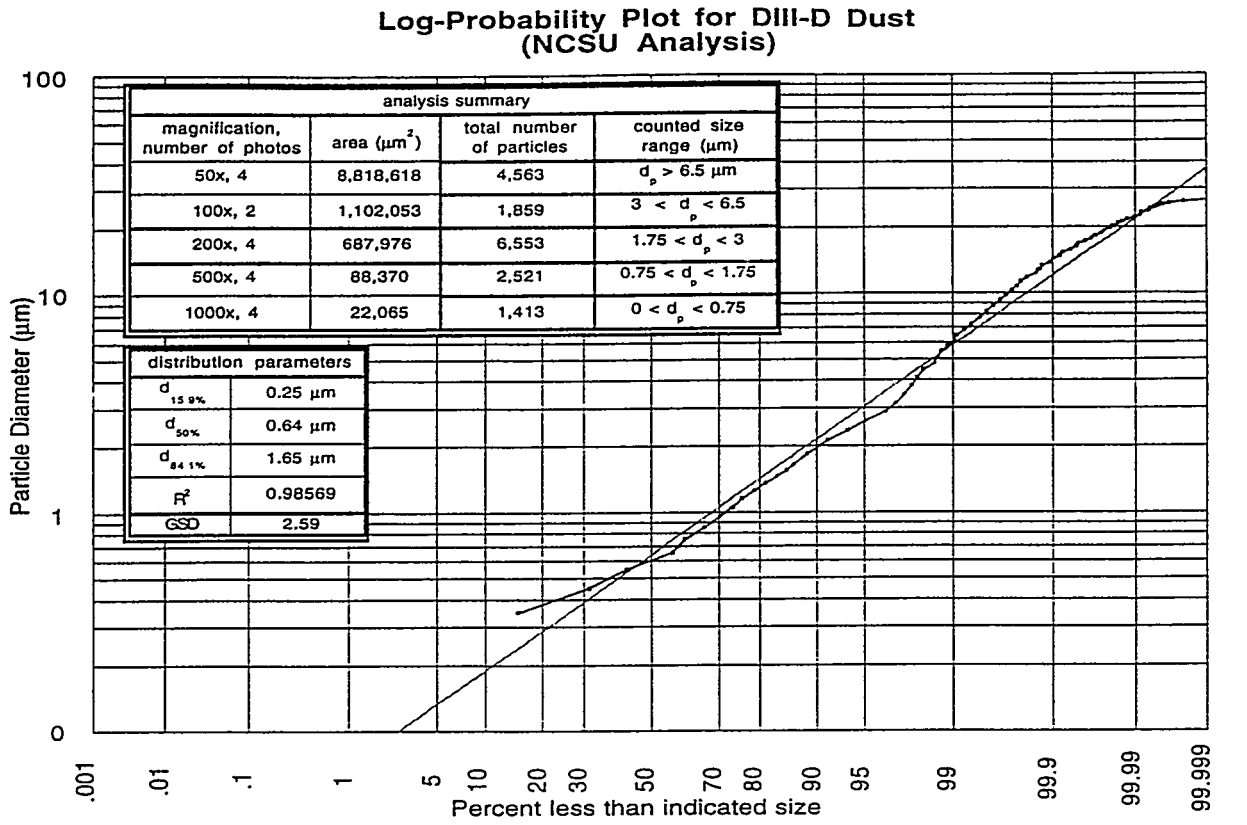

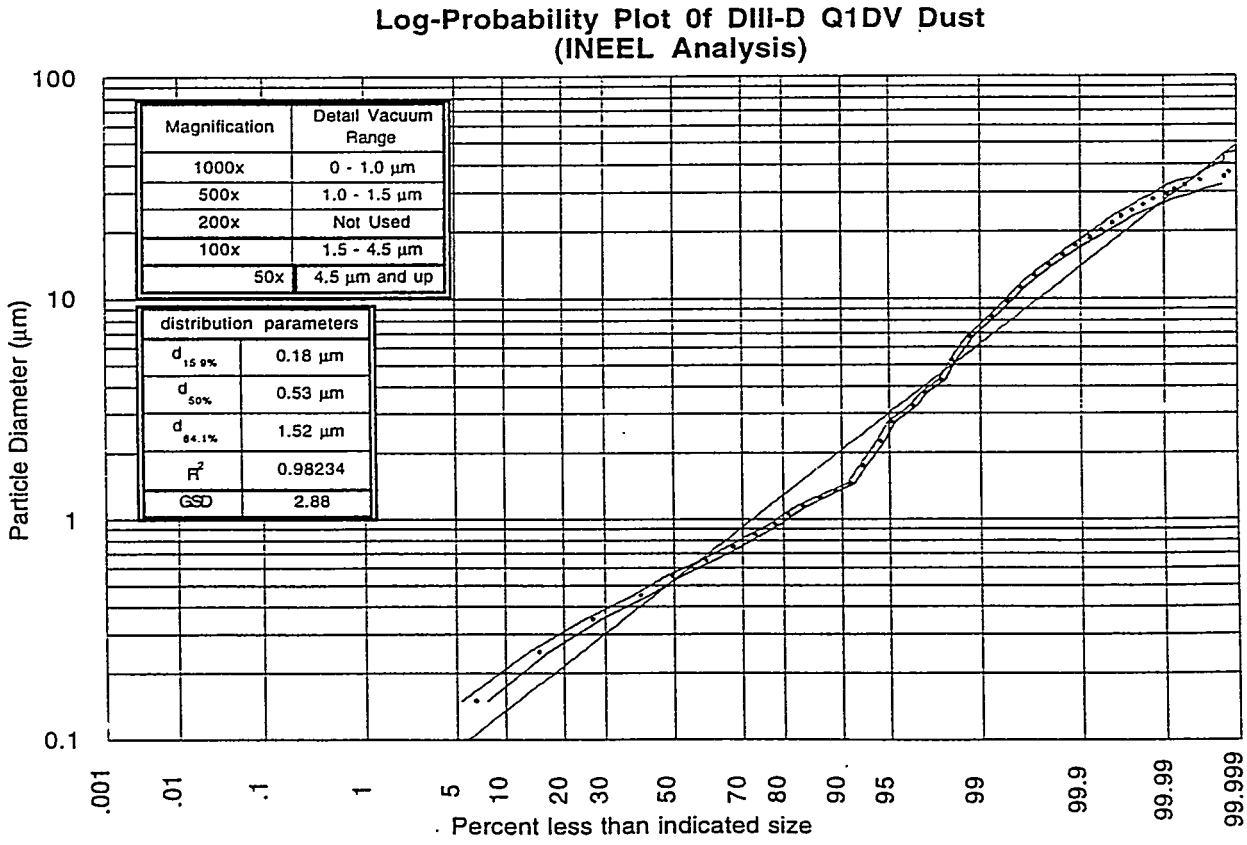

5.0 Scoping Test Results

The experimental and analytical techniques for this task have been performed in scoping tests. Four experimental runs, or "shots", were completed, with three producing particle size distribution results. Table 5.0.1 displays a summary of the scoping shots. Data recorded trigger failures hindered shot duration measurements (obtained from discharge current measurements)for S712 and S715. This problem has been corrected. Shot duration measured for S713 was 40 μs, producing an energy flux of 115 GW/m^2 incident on the sample material (Cu).

Table 5.0.1 Scoping Shots Summary

Shot Label	Energy (kJ)	Duration (μsec)	Sample	Sample Δm (mg)	comments
S710	2.5	10	Cu	100	exploding wire
S712	4.9	-	Cu	490	diagnostics trigger failed
S713	5.2	40	Cu	320	filter installed
S715	3	-	SS316	197	diagnostics trigger failed

5.1 Shot S710

The first test performed, S710, involved introducing a copper wire into the capillary of the ET source section. When sufficiently high current (10-20 kA) is passed through this wire, it is heated very quickly and vaporizes, or explodes. This mechanism generates an inventory of metal vapor within the capillary and is ejected due to the resulting pressure gradient. This process is somewhat similar to what occurs during generation of an electrothermal plasma. It is not, however, suitable as a method for disruption simulation because the mechanism of material heating is different from that in a disruption (i.e. Joule heating vs. radiative heat flux). This technique is, however, suitable to evaluate the expansion chamber for particulate collection.

The capillary with the exploding wire was directed to exhaust into the collection chamber. No collection buttons were used in this test. The decision to use collection buttons had not yet been made. Following shot execution, the cell was inspected for particulate. The entire wire did not vaporize because the end of the chamber was uniformly coated with solid copper. A large chunk of molten copper may have impacted the chamber's end and froze as it spread on the wall. Other regions of the wall appeared hazy from a covering of copper

dust, and with a magnifying glass spherical copper-colored objects were observed. These objects were the particulate of interest. although they possibly formed as small molten globules rather than vapor condensation. Initially the particles were to be removed from the wall by repeated baths in pure water and alcohol. however they were difficult to remove from the surface in a consistent manner. Resulting particle size distributions could not be generated because of the insufficient number of particles collected from the wall. An alternative method of collecting and analyzing the particles was developed using collection buttons attached to the wall of the expansion chamber, as described in Section 4. An acid bath was used to remove all the copper particles from the wall in this shot.

5.2 Shots S712 and S713

The first material to be tested in the modified ET source section was copper. Shots S712 and S713 were an attempt to generate, collect, and analyze copper particulate from a disruption simulation.

S712 was performed with buttons distributed along the collection chamber wall and also on a plastic plate attached to the end of the expansion chamber. The shot was performed at an energy level of 4.9 kJ (measured from bank loss), and resulted in 490 mg of mass removed from the copper sleeve in the source section. Unfortunately the manual diagnostics trigger on the delay generator failed to trigger the current and voltage recordings, so integrated power data and input for ODIN were not obtained. This problem can be attributed to the problems associated with the electronic data acquisition modules used to record the current and voltage. The problem has been corrected by repairing and recalibrating the data acquisition modules (LeCroy 6810). These shots were successful in that copper particulate were produced in the experiment and collected on the button substrates as depicted in Figure 4.1.1. In contrast to the exploding wire test, these particles were somewhat loosely attached to button surfaces and the chamber wall. A simple swipe with a Q-tip would displace and remove the dust from the wall, but not the buttons. Deposition along the wall (viewed as a slight copper-colored haze) was not uniform but tended to be thicker at the chamber's end. Dust appeared to pile in front of the buttons on the chamber wall. Deposition on the buttons varied, however there was a shadowing effect from other buttons upstream. To avoid this in future shots, axially consecutive buttons were rotated azimuthally. Also in this shot, the end section of the glass collection chamber broke into several pieces, indicating the existence of a significant pressure wave at that location some

time during the expansion. This broken end was removed and a steel backplate inserted, which has survived two subsequent shots (S713 and S715).

S713 provided an opportunity to perform a shot with a filter located at the end of the collection chamber. Copper was also used in this test and lost 320 mg of mass at an energy input of 5.2 kJ. Voltage and current traces for this shot were recorded and are displayed below in Figure 5.2.1. Shot duration was 40 μsec (measured as full pulse length). Figure 5.2.2 shows pressure, temperature, density, and mass loss calculated by ODIN. Note the predicted mass loss from ODIN is less than the measured value (90 mg predicted and 320 mg measured loss). This could be due to molten copper being transported away from the sleeve. However, no significant melt deposit was observed on the sleeve after the shot. The ODIN prediction may be incorrect due to the non-ideal plasma conditions that are not included in the model (see Section 2.1). A coating of dust similar to that of S712 was observed in the chamber following shot execution. Unfortunately the filter substrate (cellulose nitride) burned away. Future attempts with a filter will be performed with quartz filter substrate, which was unavailable during this test. Particulate deposition occurred on collection buttons distributed along the wall and end section around the filter housing.

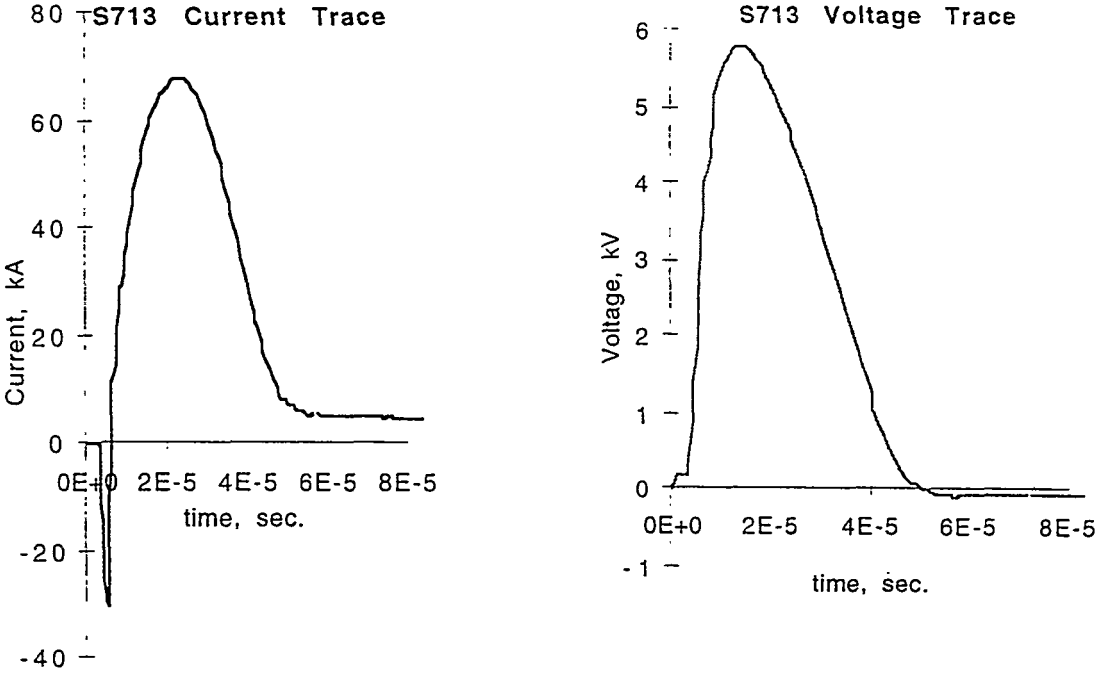

Figure 5.2.1. S713 current and voltage traces.

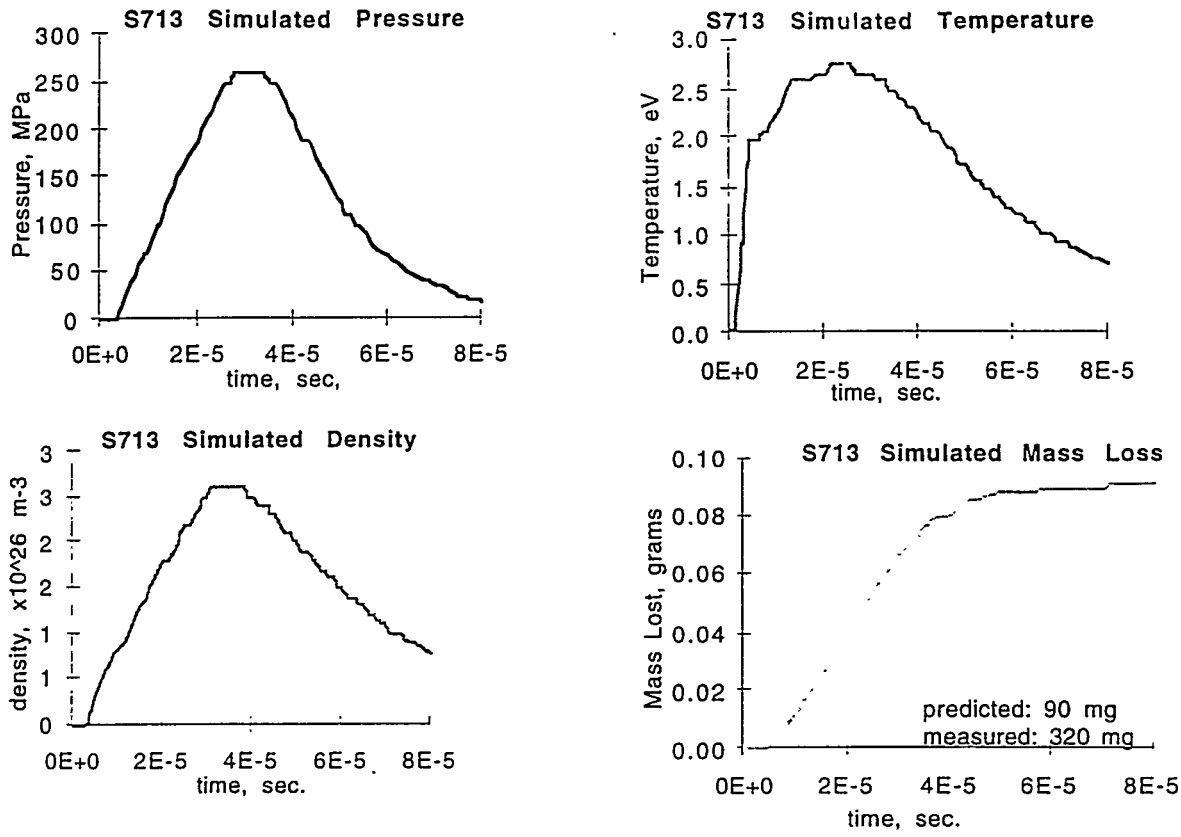

Figure 5.2.2. S713 ODIN simulation output.

Table 5.2.1 shows a summary of the particle size distribution data generated from the collected mass from a selection of button collection surfaces from Shots S712 and S713. Representative SEM micrographs from S712 and S713 are shown in Figure 5.2.3. After taking photos from several different buttons, the sizing and counting procedure was performed as described in Section 4. Figure 5.2.4 and Figure 5.2.5 show the resulting particle count distributions for S712 and S713, respectively.. The plot for S712 appears reasonable, and there were many particles in the measured population. Results from S713, however, are more suspect because SEM images from this shot were not optimized in brightness and contrast, and fewer images were obtained. This demonstrates the need for a large number of particles to be counted from many substrate photographs to obtain results representative of the underlying distribution. Shown in Figure 5.2.6 is the fractional mass gain of buttons versus axial position in the chamber. The shadowing effects associated with S712 are responsible for the observed decrease. Expected increase is observed for S713 because of the relocation of the buttons. Comparative mass loss between the source section and all collection buttons was performed for S713. The comparison was performed

by assuming mass deposition on the chamber surface was uniform in the regions between axial button locations and the average value of this area deposition was given by that measured on local collection buttons. The amount of mass deposited was found to be 60 mg. This result is less than the predicted mass loss from ODIN (90 mg) and much less than the mass loss measured from the source section (320 mg). Accounting for collection of all mass evolved from the source section is impractical because of the difficulty of accounting for mass deposited in a non-uniform fashion along the length of the expansion chamber.

Table 5.2.1. Summary of Particle Size Distribution Data for S712 and S713

S712 Button	Axial distance from source (cm)	$d_{15.9\%}$	$d_{50\%}$	$d_{84.1\%}$	GSD	R^2
14	40.6	0.57	1.15	2.31	2.01	0.9642
19	42.5 (end plate)	0.46	0.95	1.94	2.04	0.9868
20	42.5 (end plate)	0.22	0.47	1.01	2.15	0.9845
S713 Button	Axial distance from source (cm)	$d_{15.9\%}$	$d_{50\%}$	$d_{84.1\%}$	GSD	R^2
1	4.5	0.24	0.55	1.24	2.25	0.9858
11	40 (end plate)	0.15	0.51	1.67	3.27	0.9436

The resulting particle size distributions in shots S712 and S713 were obtained in a scoping context, as this was the first attempt by the authors to perform the particle size measurement protocol. Consequently, several parameters were not optimized in the early part of the analysis (specifically image quality and quantity). This must be kept in mind when interpreting the results. With experience gained in the analysis of S712 and S713, future experiments will yield results representative of the underlying distributions with greater accuracy. With this in mind, some interesting features of the analysis may be pointed out. The particles shown in the SEM photographs (Figure 5.2.3) for the most part appear spherical. This was generally the case regardless of button location on the expansion chamber wall. Particle number per area appeared to increase as a function of axial distance from source exit, similar to the fractional mass gain of the buttons in shot S713. Count distributions for S712 (Figure 5.2.4) are mostly linear, while kinks appear in the distributions for S713 (Figure 5.2.5). These kinks result from an inadequate number of photographs at mid-range magnifications (500x and 1000x), and do not represent the underlying distribution. One final feature to note regarding S712 is the larger mean diameter on a wall button (button 14) than on endplate buttons, and the difference of mean

diameters of buttons on the endplate (0.95 μm for button 19 and 0.47 μm for button 20). Unfortunately relative orientation of these buttons was not recorded for the experiment. Future tests performed for this task will explore these types of relations.

Figure 5.2.3. SEM micrographs from S712 and S713.

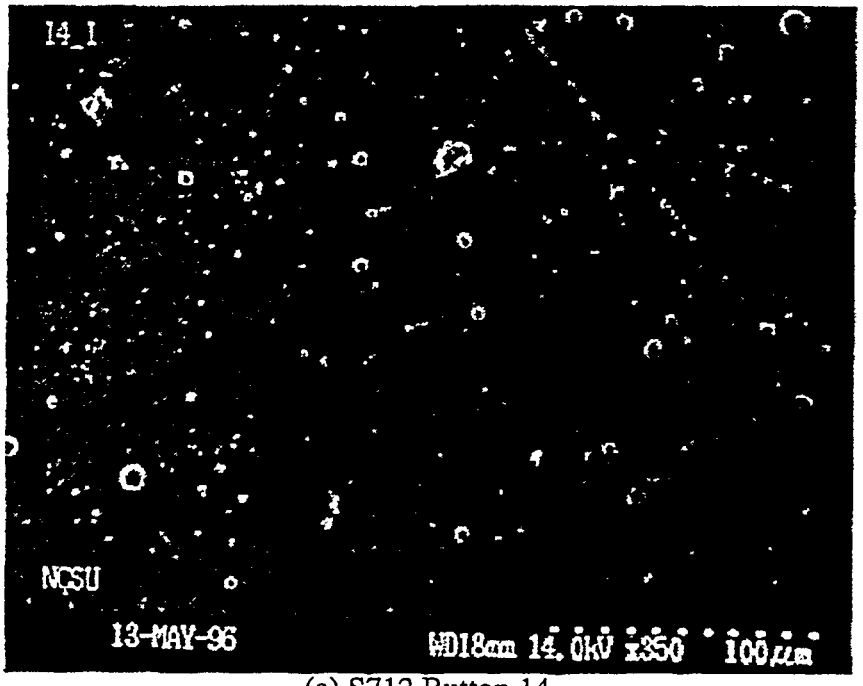

(a) S712 Button 14

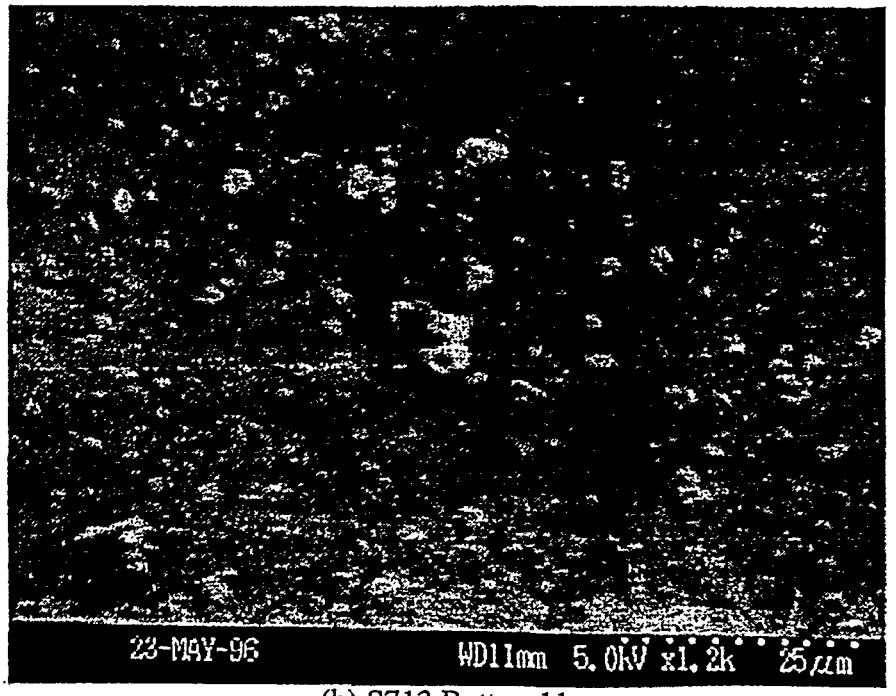

(b) S713 Button 11

Figure 5.2.4. Count distributions for Shot S712.

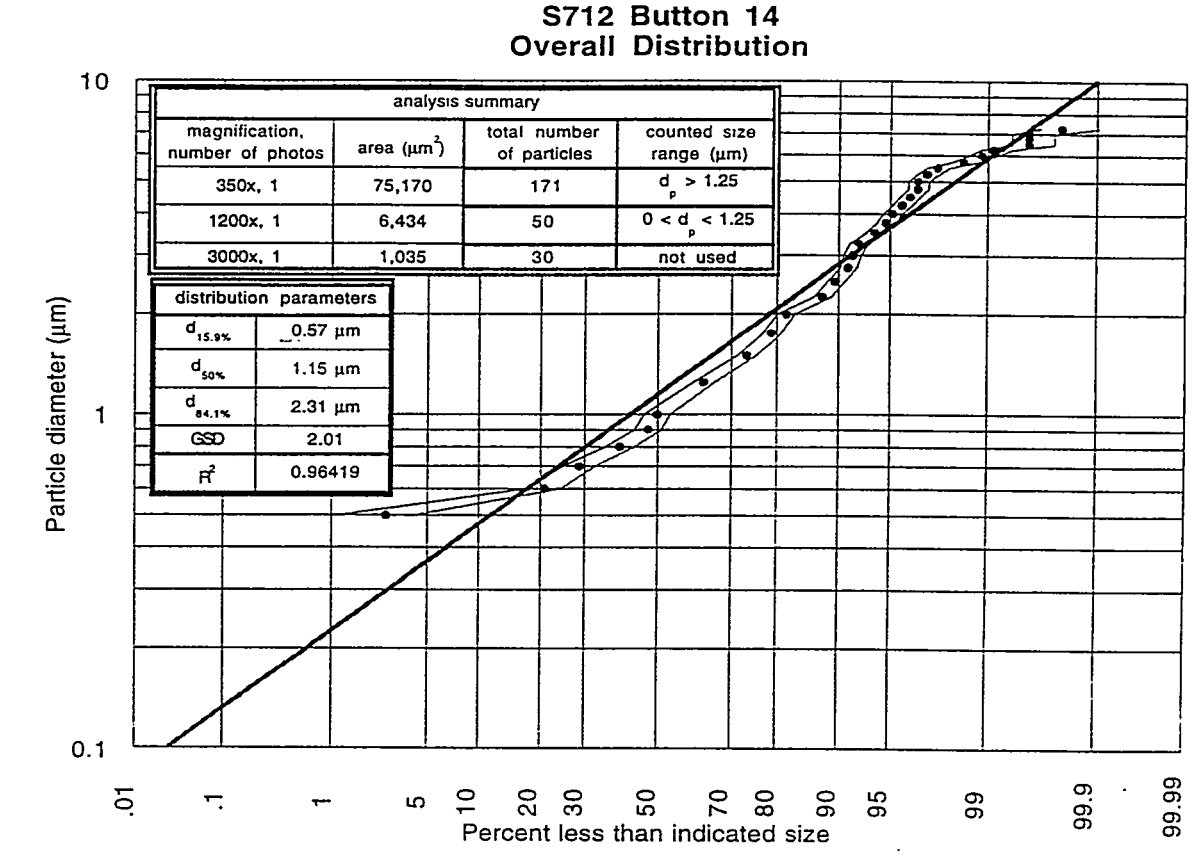

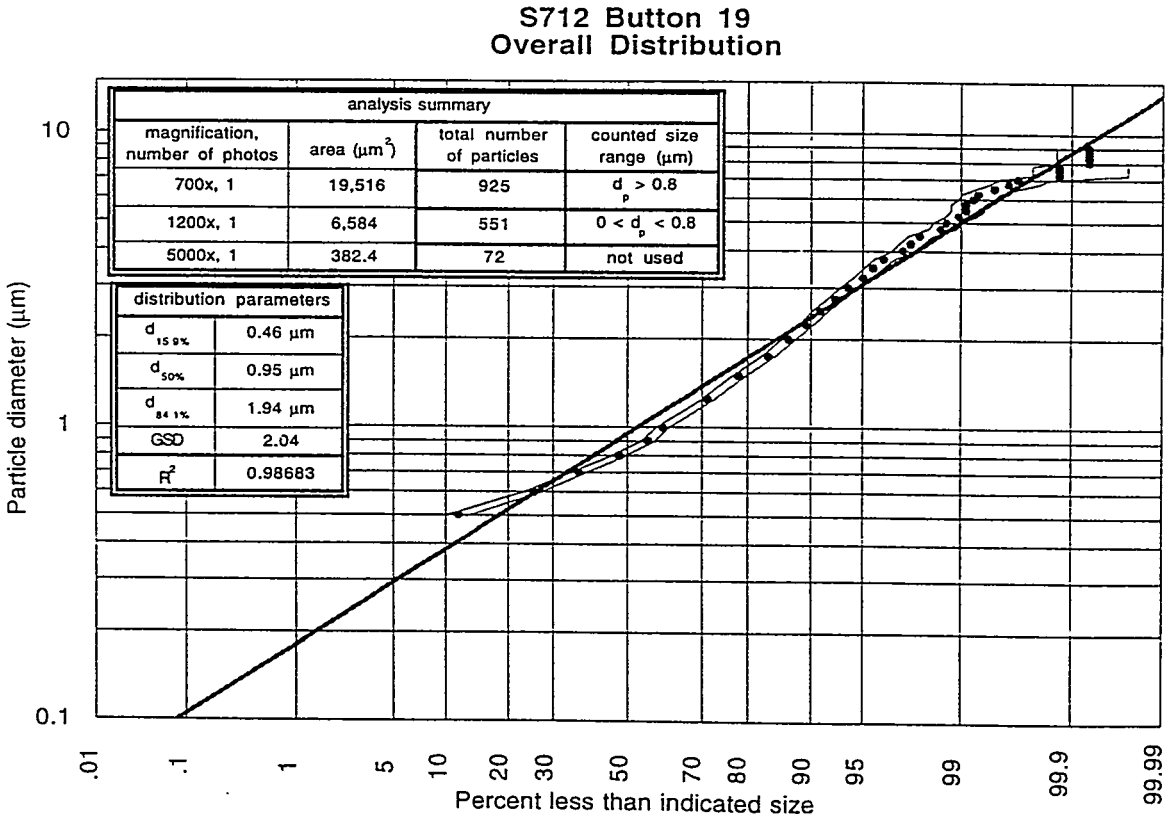

Figure 5.2.4.cont.

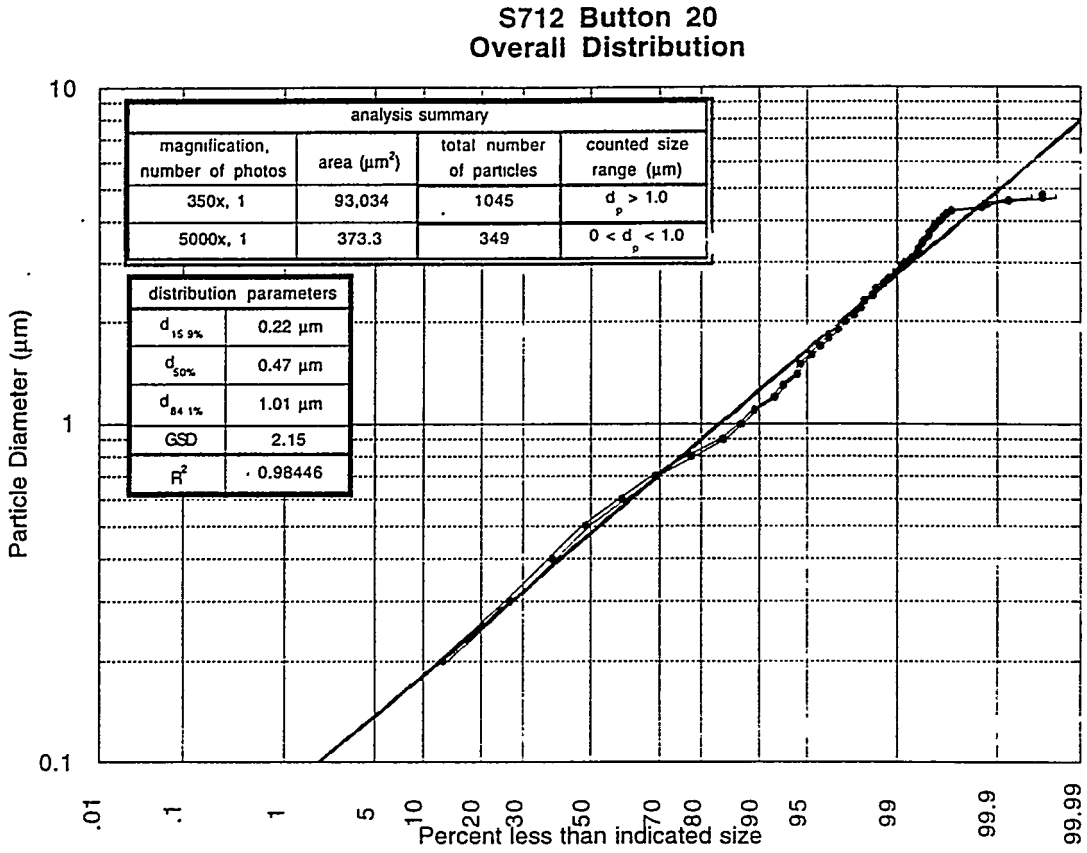

Figure 5.2.5. Count distributions for Shot S713.

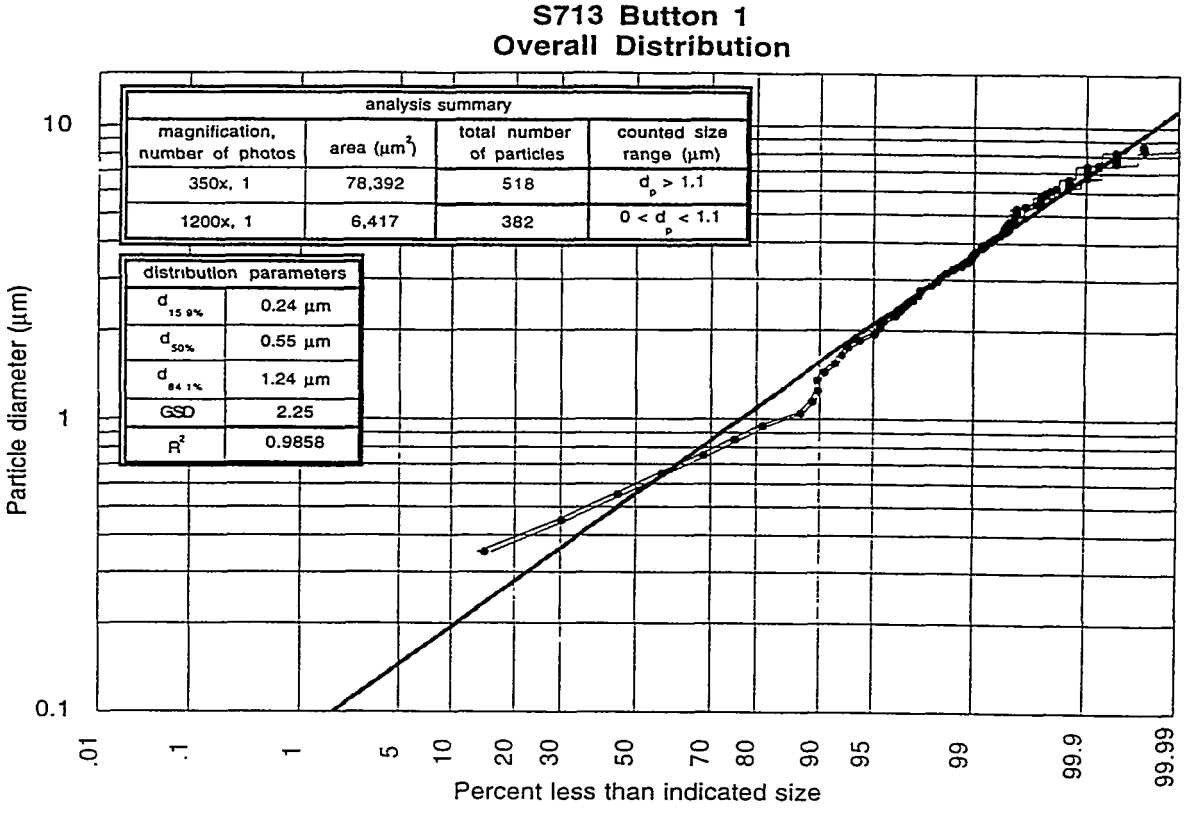

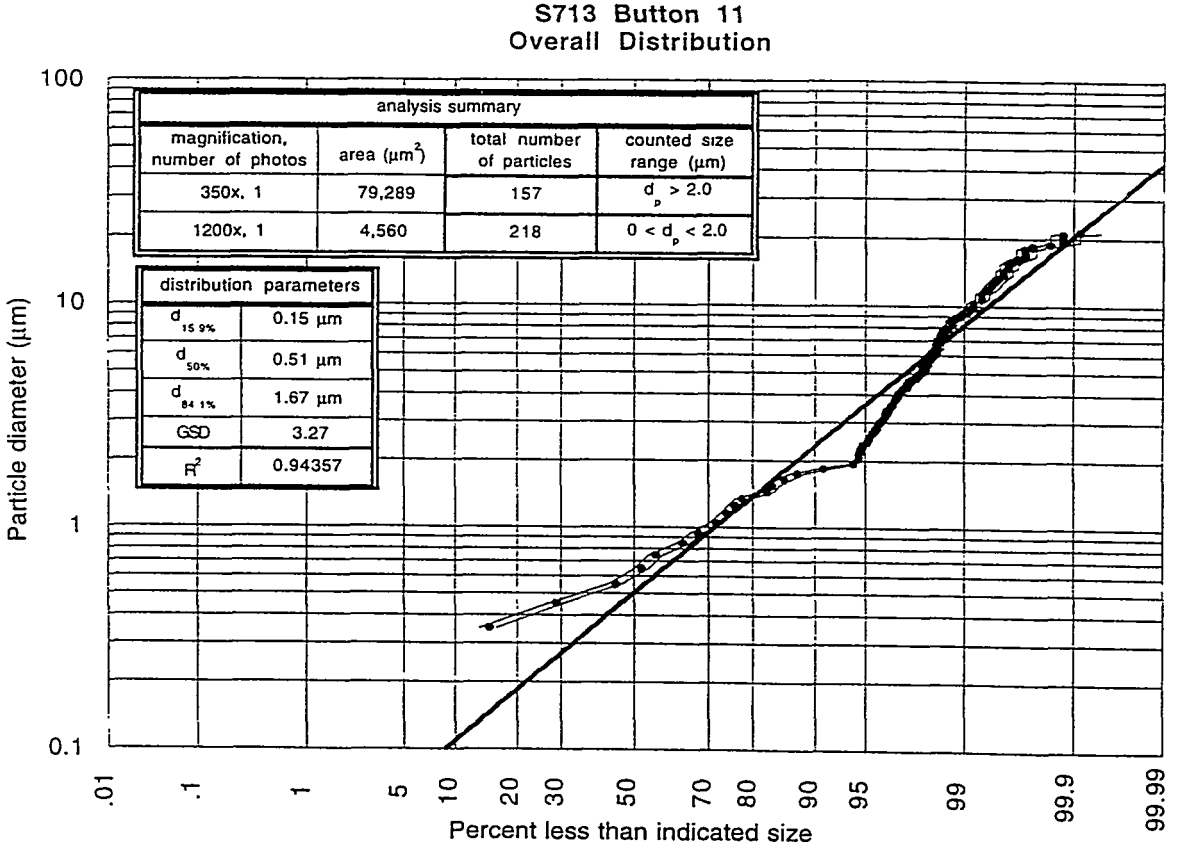

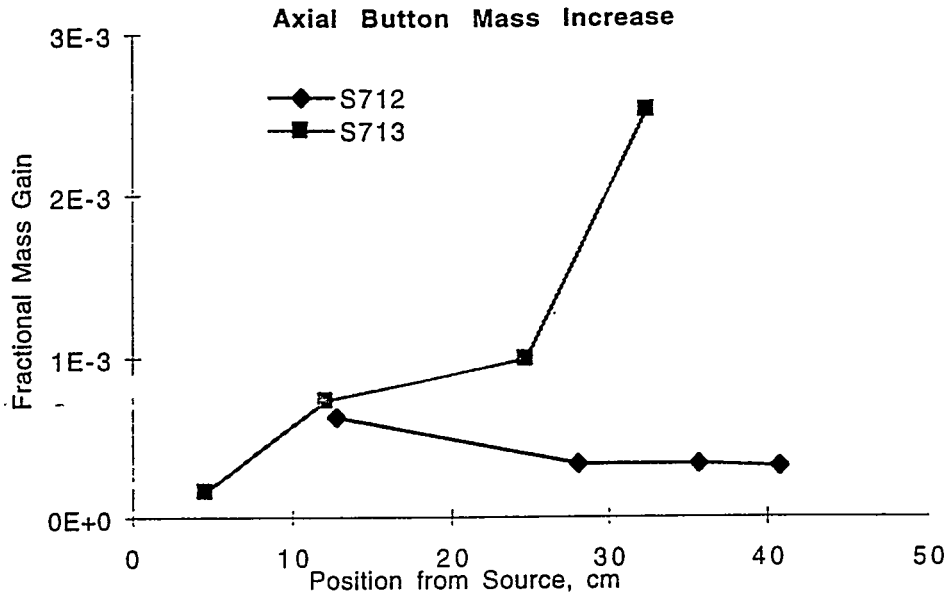

Figure 5.2.6. Axial mass deposition on collection buttons for S712 and S713.

5.3 Shot S715

Scoping test shot S715 was performed with stainless steel #316 (SS316). This experiment was prepared according to the procedure described in Section 3, with buttons along the collection cell wall and on the end plate. With an energy input of 3 kJ, the SS316 sleeve in the source section lost 197 mg of mass. The manual trigger failed to activate the data recorder modules prior to the shot, thus no current and voltage traces were obtained, and ODIN simulation could not be performed. Otherwise, shot execution was successful and produced the expected dust in the collection cell. Observations of this dust include: streaks from relatively large (possibly molten) blobs of SS316 were on the wall, visible deposition of silvery SS316 on the collection buttons, and flakes deposited on the collection chamber wall. Qualitatively, there appears to be varying deposition mechanisms on the walls at different locations, e.g. vapor-wall condensation versus gas-to-particle conversion in the flow stream. Different deposition types of this sort were not observed with the copper sample in tests S712 and S713. The expansion volume was insufficient to cool the vapor, and a larger chamber is to be installed for future experiments to provide a higher degree of expansion cooling.

Particles deposited on collection buttons were analyzed with the SEM and optical microscopes. Representative SEM micrographs are displayed in Figure 5.3.1, individual button size distributions are shown in Figure 5.3.2, and fractional mass gain of the buttons is plotted as a function of axial position in Figure 5.3.3. The sizing technique used in this analysis was that described in Section 4, and is much more accurate than the analysis for S712 and S713 due primarily to the experience gained in obtaining quality photographs from the SEM and optical microscope during the S712 and S713 analysis. Ninety-five percent confidence intervals are shown in the figures representing the statistical error of the distribution. The buttons represented were located 12.1 cm (button 3), 32.4 cm (button 8), and 37.4 cm (button 10) from the source exit. Relative button orientation was not recorded for this experiment, but will be recorded in future experiments to characterize the effect of gravity on particle collection. Table 5.3.1 displays a summary of the results obtained from the SEM and optical microscope analyses. Particle number per area, mean particle diameter, and fractional mass gain increase with button distance from the source exit. Button fractional mass gain (Figure 5.3.3) increases in a fashion similar to that observed in shot S713, however S715 mass gain is lower in magnitude. This is likely a result the difference in shot energy and test material (S713 was performed at 5.2 kJ on a copper sleeve and S715 at 3 kJ with a stainless steel sleeve), with the lower energy shot producing

less mobilized mass. There is not enough data at present to explain this mass gain effect, and this will be further investigated in future tests.

The primary difference between the SEM and optical microscope results for button 10 are attributed to the difference in imaging quality obtained with the optical microscope. Future use of the optical microscope for particle size distribution measurement will incorporate linear polarizers and filters for elimination of bright and dark inconsistencies in the particle image. These inconsistencies are due to the difference in light reflection from particle surfaces causing particles to have measured areas smaller than actual areas.

Compositional analysis was also performed using the SEM's energy-dispersive X-ray analysis (EDX) facility. Results displayed in Figure 5.3.4 indicate that the particles deposited on the button are of (nearly) the same composition as the source section material (i.e. SS316), based on relative mixtures of iron and chromium in the particles. This indicates that highly mixed-species vapor does not preferentially condense out individual components. Further investigation is required, specifically in terms for mixed-materials effects. This is to be investigated further during future experiments.

Table 5.3.1 Summary of Particle Size Distribution Data for S715.

S715 Button	Axial distance from source (cm)	$d_{15.9\%}$	$d_{50\%}$	$d_{84.1\%}$	GSD	R^2
3	12.1	0.47	0.94	1.91	2.03	0.9865
8	32.4	0.68	1.34	2.60	1.96	0.9901
10 (SEM)	37.4	0.69	1.46	3.1	2.12	0.9932
10 (optical)	37.4	0.32	0.80	2.01	2.50	0.9839

Figure 5.3.1. Representative SEM micrographs from S715.

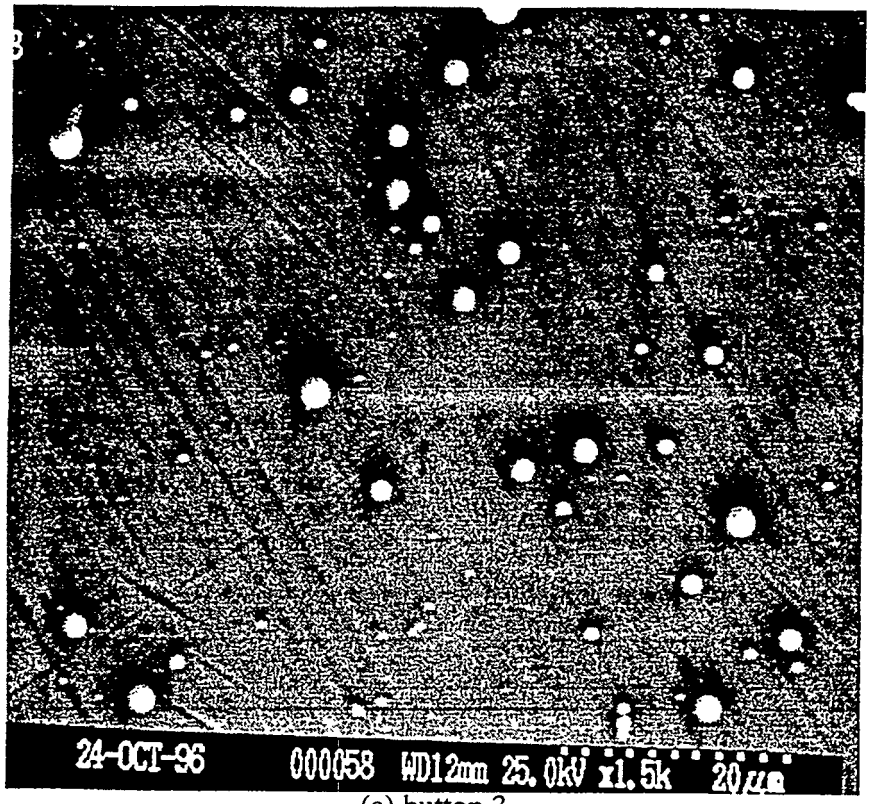

(a) button 3

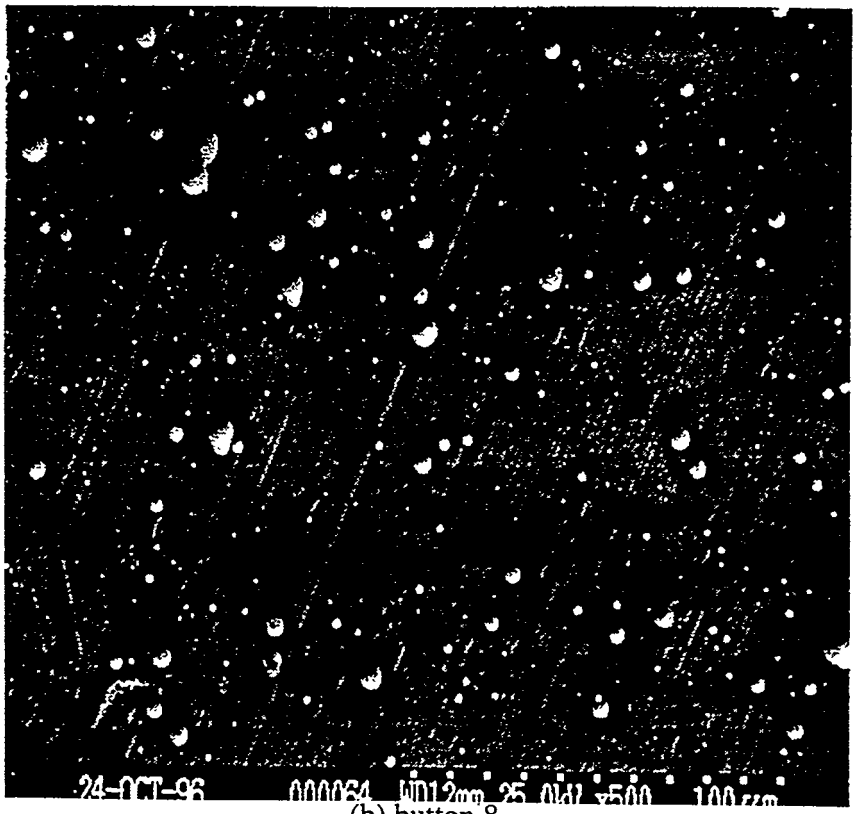

(b) button 8

Figure 5.3.1.cont.

(c) button 10

Figure 5.3.2. Particle size distributions from S715.

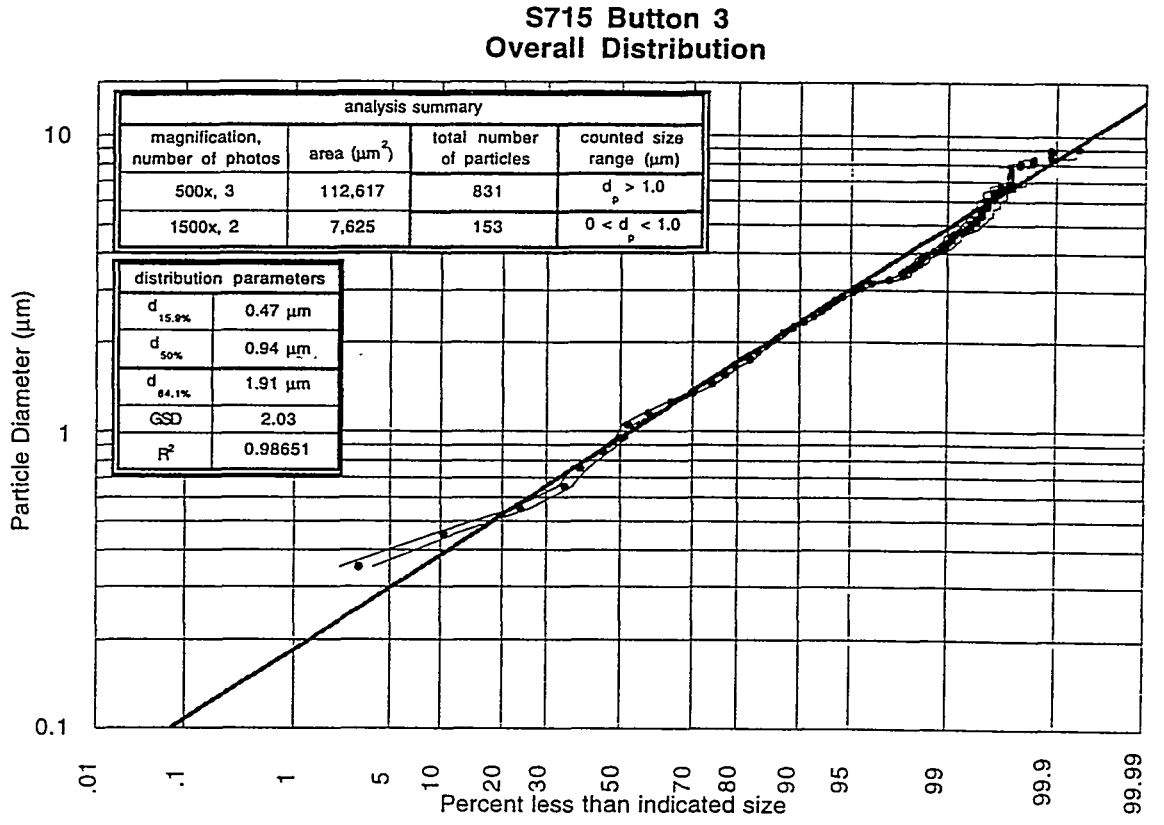

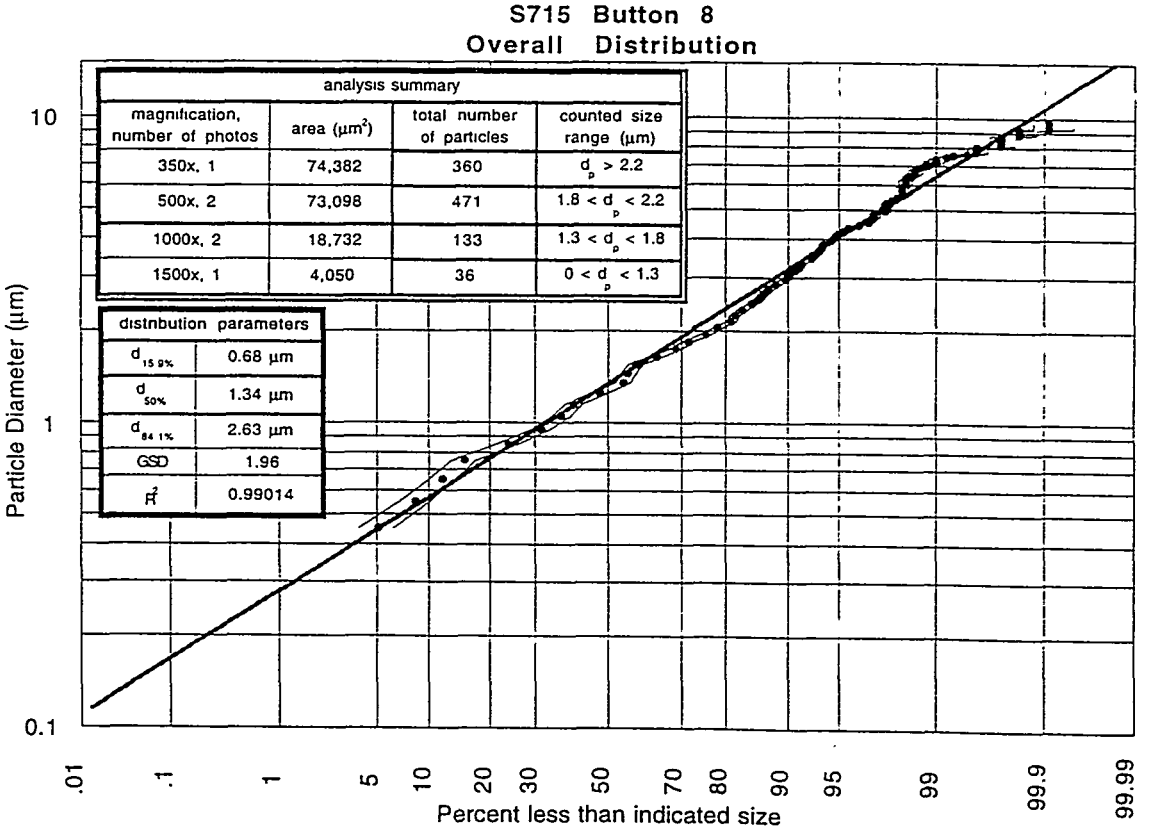

Figure 5.3.2.cont.

S715 Button 10 Overall Distribution (SEM analysis)

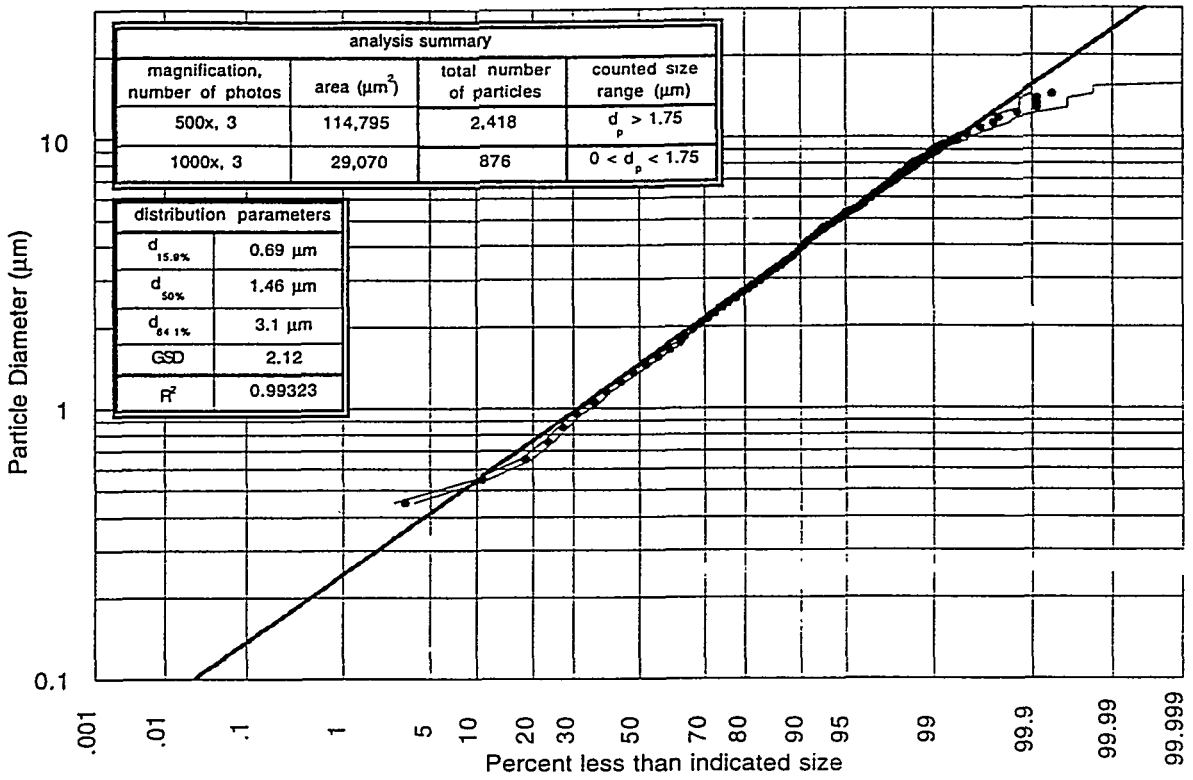

S715 Button 10 Overall Distribution (Optical Microscope Analysis)

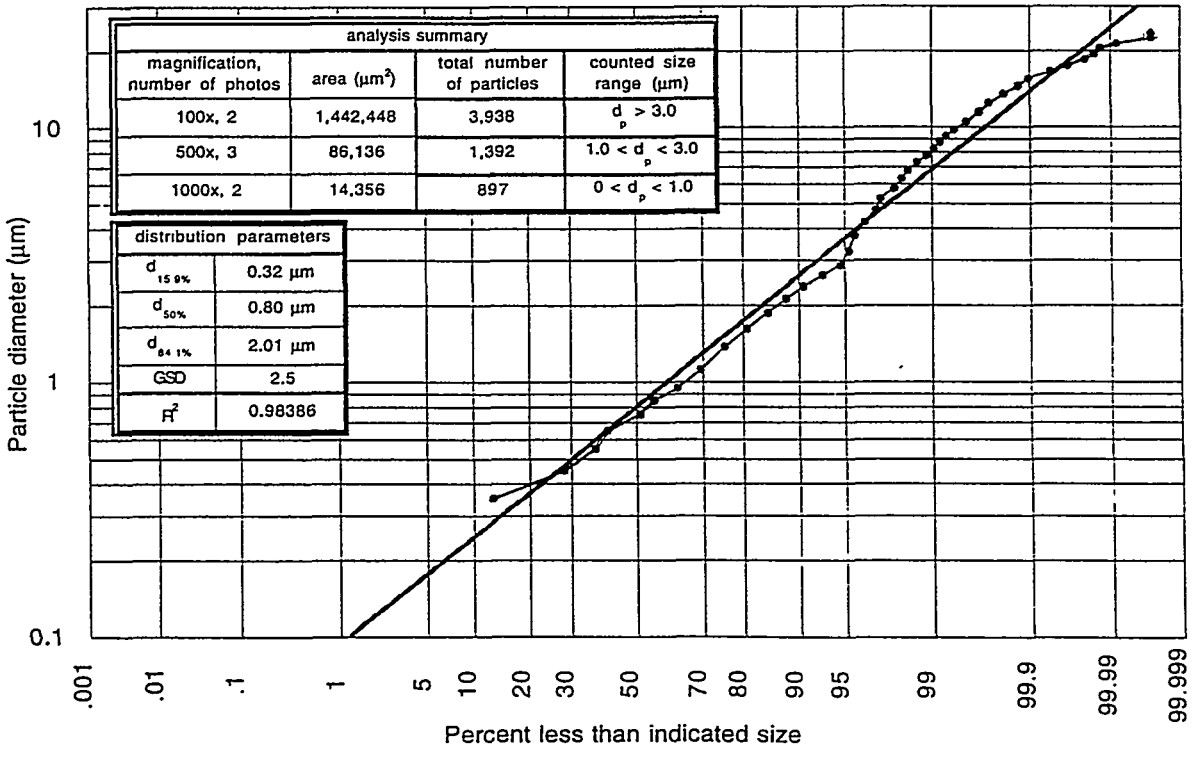

Figure 5.3.3. Axial mass deposition on collection buttons for S715.

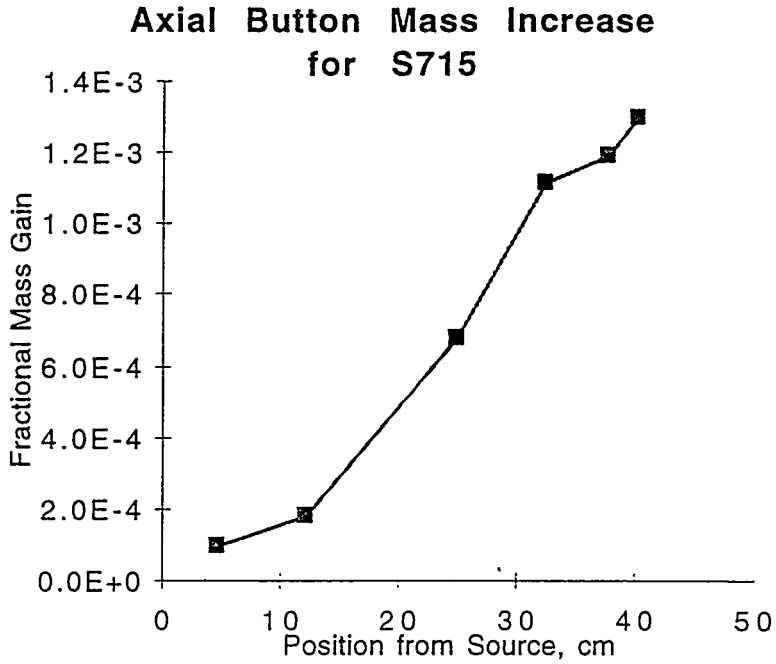

Figure 5.3.4. EDX images from button S715 Button 11.

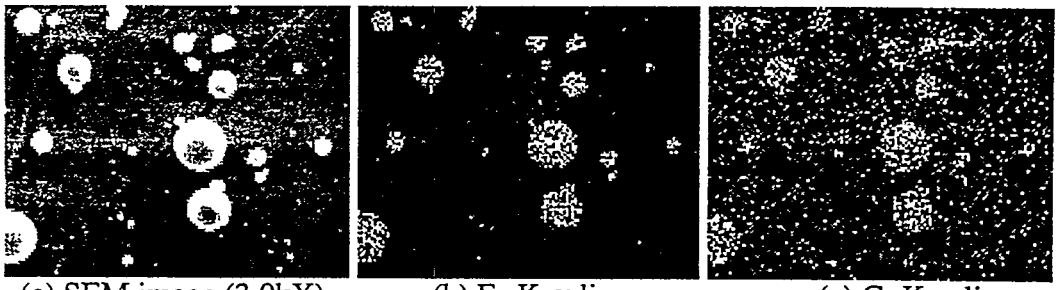

(a) SEM image (3.0kX) (b) Fe K-α line (c) Cr K-α line

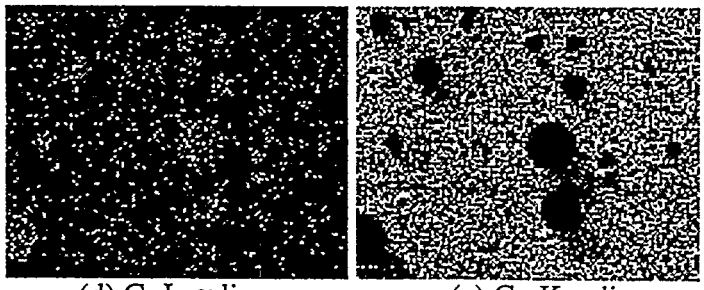

(d) Cr L-α line (e) Cu K-α line

6.0 Conclusion

This document describes an approach to investigate plasma disruption-induced mobilization of activated wall material in ITER. An existing electrothermal plasma gun has been modified to facilitate disruption simulation in terms of power flux and produce mobilized particles in the same manner as expected in ITER. The sleeve section of the ET source was changed to use ITER-relevant materials, and an expansion chamber was added to allow controlled collection of the resulting particulate. Preliminary tests have been successfully performed, demonstrating the readiness of the facility to accomplish the experiment series. Resulting particle size distributions from scoping tests were reported, as well as insight gained from performing these tests.

Future work for this task includes detailed analysis of the vapor condensation of copper, stainless steel #316, tungsten, carbon, and combinations of these materials. After building this experimental database of resulting particle size distributions, modeling will be performed and extrapolated to ITER.

7.0 Acknowledgments and Disclaimer

Sincere appreciation goes out to the Fusion Safety Program at the INEEL, specifically Kathryn A. McCarthy, David A. Petti, Galen R. Smolik, and William J. Carmack. This work is supported by US DOE, Director of Energy Research, Office of Fusion Energy, under grant C87-101407 task 007 and UCSD ITER 10112833.

This report is an account of work assigned to the U.S. Home Team under Task Agreement No. S81TT08 within the Agreement among the European Atomic Energy Community, the Government of Japan, the Government of the Russian Federation, and the Government of the United States of America on Cooperation in the Engineering Design Activities for the International Thermonuclear Experimental Reactor ("ITER EDA Agreement") under the auspices of the International Atomic Agency (IAEA). The report has not been reviewed by the ITER Publications Office.

References

1. ITER General Design Requirements, March 22, 1996, draft.
2. Gilligan, J.G., M.A.Bourham, "The Use of an Electrothermal Plasma Gun to Simulate the Extremely High Heat Flux Conditions of a Tokamak Disruption," *J. of Fusion Energy*, vol.12, p.311, 1993.
3. Bourham, M.A., J.G. Gilligan, O.E.Hankins, "Plasma-Material Interaction in Electrothermal and Electromagnetic Launchers," *AIAA 24th Plasmadynamics and Lasers Conference*, July 6-9, 1993, Orlando, Fl.
4. Kincaid, R.W., M.A. Bourham, "Electrothermal Plasma Gun as a Pellet Injector," *Fusion Technology*, vol.26, p.637, 1994.
5. Hurley, J.D., M.A. Bourham, J.G. Gilligan, "Modeling and Experiment of an Electrothermal Igniter for Electrothermal-Chemical Guns," *30th JANNAF Combustion Subcommittee Meeting, Vol.1*, November 15-19, 1993, Monterey, CA.
6. Roth, J.R., *Industrial Plasma Engineering, Vol. I*, Institute of Physics Publishing, 1995.
7. von Engel, A., *Ionized Gases*, Oxford University Press, 1965.
8. Rozanov, V.B., "Gas-Dynamic Model of a Capillary Discharge with Evaporative Walls," *High Temperature*, vol.8, p.895, 1971.
9. J.D. Hurley, M.A. Bourham and J.G. Gilligan,"Numerical Simulation and Experiment of Plasma Flow in the Electrothermal Launcher SIRENS," IEEE Trans. Magnetics, vol. 31, pp.616-621, January 1995.
10. Sharpe, J. P., M. Bourham, J. G. Gilligan, "Test Plan for Disruption Induced Aerosol Characterization for ITER Source Term Determination, ITER Task: S 81 TT 14 95-02-28 FU Part B," EDF No: ITER/US/95/TE/SA-22, September 6, 1995.
11. Hassanein, A., "Plasma Disruption Modeling and Simulation," *Fusion Technology*, vol.26, p.532, 1994.
12. Hinds,W.C., *Aerosol Technology: Properties, Behaviors, and Measurements of Airborne Particles*, John Wiley and Sons, 1982.
13. Carmack, W. J., Engelhardt, M. E., and Hembree, P. B. DIII-D Dust Particulate Characterization. ITER EDF# ITER/US/97/TE/SA-8. Idaho National Engineering and Environmental Laboratory, March 1997.

Appendix A. Documentation and Reporting Procedures

Experimental procedures, calibration records, and results from this task will be maintained in a laboratory notebook on site at N.C. State University, with copies sent quarterly during the progression of the task to the Fusion Safety Program (FSP) at the INEEL. Update reports will be issued monthly, or whenever important results are obtained. Final results of experiments will be presented in an ITER program engineering design file (EDF). Electronic copies of the images used for size analysis will be kept on site and with the INEEL FSP. A consistent file naming scheme will be used to indicate experiment test label, button of study, and the photograph number. For example S715_11_1 indicates photo 1 on button 11 in shot S715. Shot-specific information, such as button location, will be tabulated in relevant reports and in the laboratory notebooks.

Appendix B. Equipment Calibration Procedures and Certification

Maintaining reliable equipment during this experimental investigation is important to ensure valid results. All utilized equipment and diagnostic tools will be calibrated periodically. This appendix will describe the calibration schedule and include copies of the most recent calibration certificates for items calibrated by the manufacturer.

B.1 Calibration Schedule

All associated equipment is to be calibrated at regular intervals. Instrument sensitivity and robustness determines specific calibration periodicity. Table B.1.1 lists primary instruments for calibration along with required frequency and whether calibration is performed externally by the manufacturer or by personnel at NCSU. Calibration tracing and history is maintained on a form entitled "Equipment Availability and Calibration Schedule" found on site at the SIRENS facility in the Equipment Inventory Notebook. Attached to this appendix is a copy of the most recent form.

Table B.1.1.Equipment calibration information.

Equipment Item	Calibration Frequency	Date of Most Recent Calibration	Calibration Performance
microbalance	weekly	5/97	in-house
high voltage probe	monthly	5/97	in-house
Rogowski coil	semi-annually	5/97	in-house and externally
ADC modules	yearly	2/97	externally
Pressure Transducers	18 -24 months	12/96	externally
SEM	monthly	5/97	externally

B.2 Calibration Procedures

The microbalance, the Rogowski coil, and the high-voltage probe are calibrated using specific procedures according to the schedule shown above.

Accuracy in the microbalance is important because of the small mass loss or gain of various experimental components (e.g. source sleeve and buttons). Currently a Mettler AE240 Dual Range Balance is used. The device has a built in 100.0 gram calibration option, which may be used to benchmark the calibration curve on a frequent basis. This is generally performed at the beginning of each day of use. The microbalance is calibrated

weekly. Using a set of NIST-standard weights (1, 2, 5, 10, and 25 mg), mass measurements are obtained, recorded, and compared to actual weight. If a significant discrepancy is found (>0.1% difference or 0.1 mg from the standard), the internal calibration option is used to reset the balance table. This typically brings the device back into calibration. If not, as indicated by an uncorrectable difference, it may be in need of service from the manufacturer.

A high-frequency response high voltage probe (HVP) is important for determining the time-resolved energy density discharged into the ET source. The HVP in use on SIRENS is a Tektronix Model P6015A 1000X compensated voltage probe. Calibration of this device is performed as described in the associated manufacturer's manual. This procedure requires adjustment of the compensation capacitance for low, middle, and high frequency responses. Using a 1 MHz function generator with 50V peak-to-peak output allows for appropriate compensation in each frequency range. Bandwidth and rise time verification is performed to ensure correct compensation.

The Rogowski coil used to detect time-resolved high level current (> 1kA) was designed and built in-house. An associated integrator circuit allows the desired frequency response to be designed into the device. Initial calibration occurs by measuring high current discharges with the coil to be calibrated and with an externally calibrated standard coil. The SIRENS facility uses a coil calibrated by Maxwell Technologies, CA, USA. Recent calibration results are included in Section B.3. The calibration is essentially a verification that the integrator circuit functions as designed. This robust device does not require frequent calibration, but the standard coil is used with the normal coil on a random shot for comparison every 6 months.

B.3 Calibration Certificates

The attached calibration certificates are for instruments used for this task, which are LeCroy 6810 ADC converter modules, Kistler Ballistic Pressure Transducer Type 617C, Kistler charge amplifier type 5010B, and an externally calibrated integrator for the Rogowski coil.

Certificate of Calibration

LeCroy
Innovators in Instrumentation

Instrument Model Number 6810
Report Number RN18766
Calibration Date 2-5-97
Department LRSCS
Temperature (°C) 24°

Serial Number A61502
Description WAVEFORM RECORDER
Calibration Due Date 2-5-98
Location CHESTNUT RIDGE, NY
Humidity (%) 16 %

Condition Received
In Tolerance ☐
Out of Tolerance ☑
Operational Failure ☑

Condition Returned
Meets all Specs ☑
Limited Specs ☐
Other ☐

Out of Tolerance Description
GAINS & OFFSETS NO/GOOD

Comments

Certified Calibration Equipment Used

Manufacturer	Model Number	Serial Number	Cal Due Date
HP	8116A	2537A-01975	1-14-98
TEK	SG 5010	B010131	1-14-98
TEK	SG 503	B081574	1-14-98
TEK	SG 503	B079880	1-14-98
TEK	SG 503	B081570	1-14-98
TEK	SG 503	B081590	1-14-98
KEITHLEY	196 DMM	371556	1-15-98

LeCroy Corporation certifies that this instrument meets or exceeds all published specifications and has been calibrated using standards whose accuracies are traceable to the National Institute of Standards and Technology. The calibration system requirements are in compliance with MIL-STD 45662A.

2-05-97
Certification Date

LRS Customer Service Manager/Supervisor

Certificate of Calibration

LeCroy
Innovators in Instrumentation

Instrument Model Number 6810
Report Number RN18766
Calibration Date 2-5-97
Department LRSCS
Temperature (°C) 24°

Serial Number A68762
Description WAVEFORM RECORDER
Calibration Due Date 2-5-98
Location CHESTNUT RIDGE, NY
Humidity (%) 16%

Condition Received
- In Tolerance ☐
- Out of Tolerance ☑
- Operational Failure ☑

Condition Returned
- Meets all Specs ☑
- Limited Specs ☐
- Other ☐

Out of Tolerance Description
OFFSETS + GAINS NO/GOOD

Comments

Certified Calibration Equipment Used

Manufacturer	Model Number	Serial Number	Cal Due Date
HP	8116A	2537A-01975	1-14-98
TEK	SG-5010	B010131	1-14-98
TEK	SG 503	B081574	1-14-98
TEK	SG 503	B073280	1-14-98
TEK	SG 503	B081570	1-14-98
TEK	SG 503	B081572	1-14-98
KEITHLEY	196 DMM	371556	1-15-98

LeCroy Corporation certifies that this instrument meets or exceeds all published specifications and has been calibrated using standards whose accuracies are traceable to the National Institute of Standards and Technology. The calibration system requirements are in compliance with MIL-STD 45662A.

2-5-97
Certification Date

David Cyganski
LRS Customer Service Manager/Supervisor

Piezo Instrumentation KISTLER

Pressure Transducer Calibration Certificate

Model. 617C SN C104883 MAR 05 1996

Range (psi)	75000	45000	15000	Ambient Temperature 74°F (23°C) Ambient Humidity 35% 1 bar = 14.5037 psi 1 psi = 0.06894 bar
Sensitivity (pC/psi)	-0.0938	-0.0922	-0.0900	The calibration of all basic standards used in these test are traceable to the National Institute of Standards and Technology (N I S T).
				By: Michael P. Peters Date: 02-22-1996

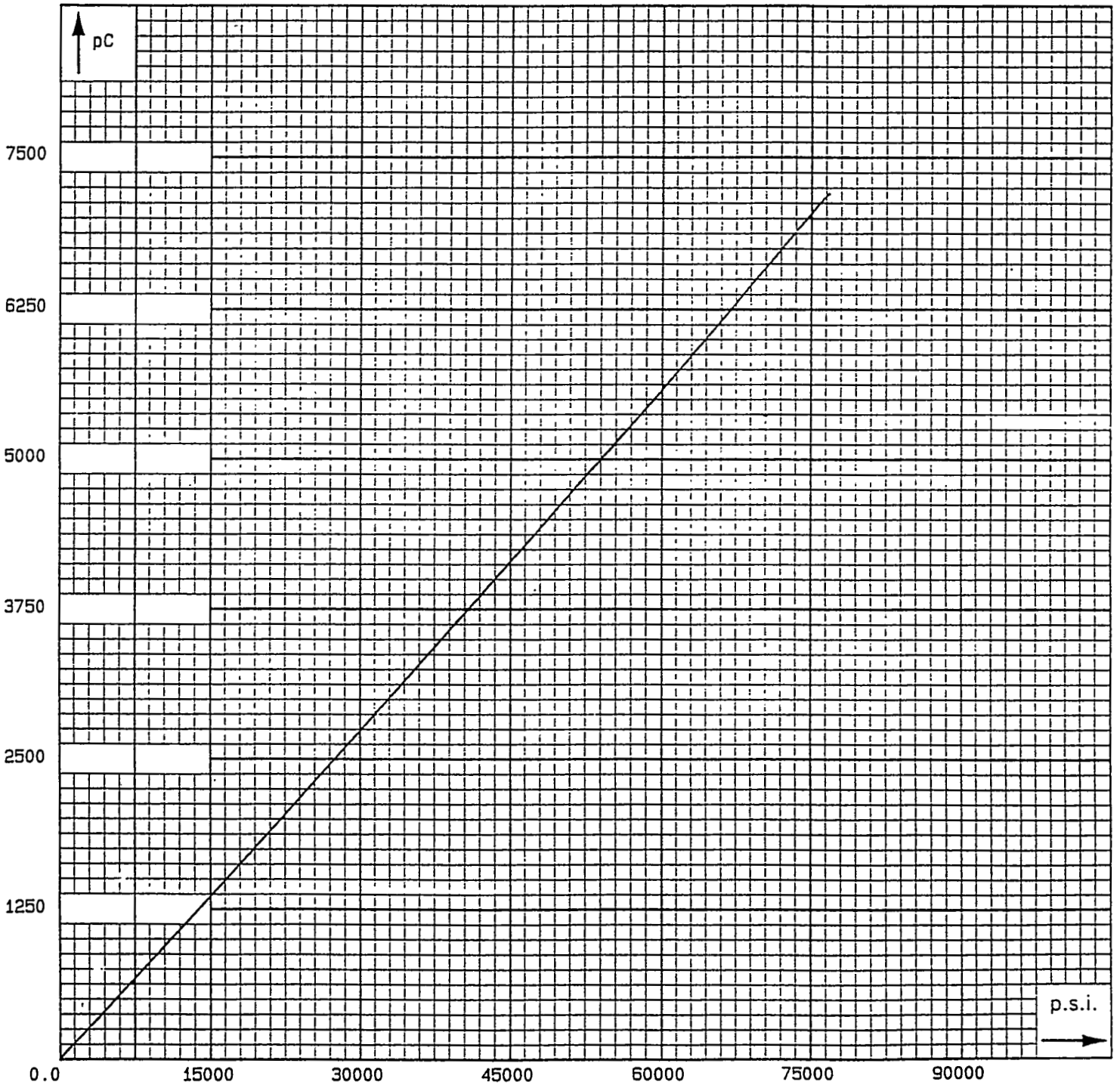

026 0600-001-REV. C, 1/95

Kistler Instrument Corporation • 75 John Glenn Drive • Amherst, NY 14228-2171

Piezo Instrumentation KISTLER

Pressure Transducer Calibration Certificate

Model 617C SN C104882 MAR 0.5 1996

Range (psi)	75000	45000	15000	Ambient Temperature 74°F (23°C) Ambient Humidity 35% 1 bar = 14.5037 psi 1 psi = 0.06894 bar
Sensitivity (pC/psi)	-0.0896	-0.0879	-0.0854	The calibration of all basic standards used in these test are traceable to the National Institute of Standards and Technology (N I S T).
				By: Michael F. Ferro Date: 02-22-1996

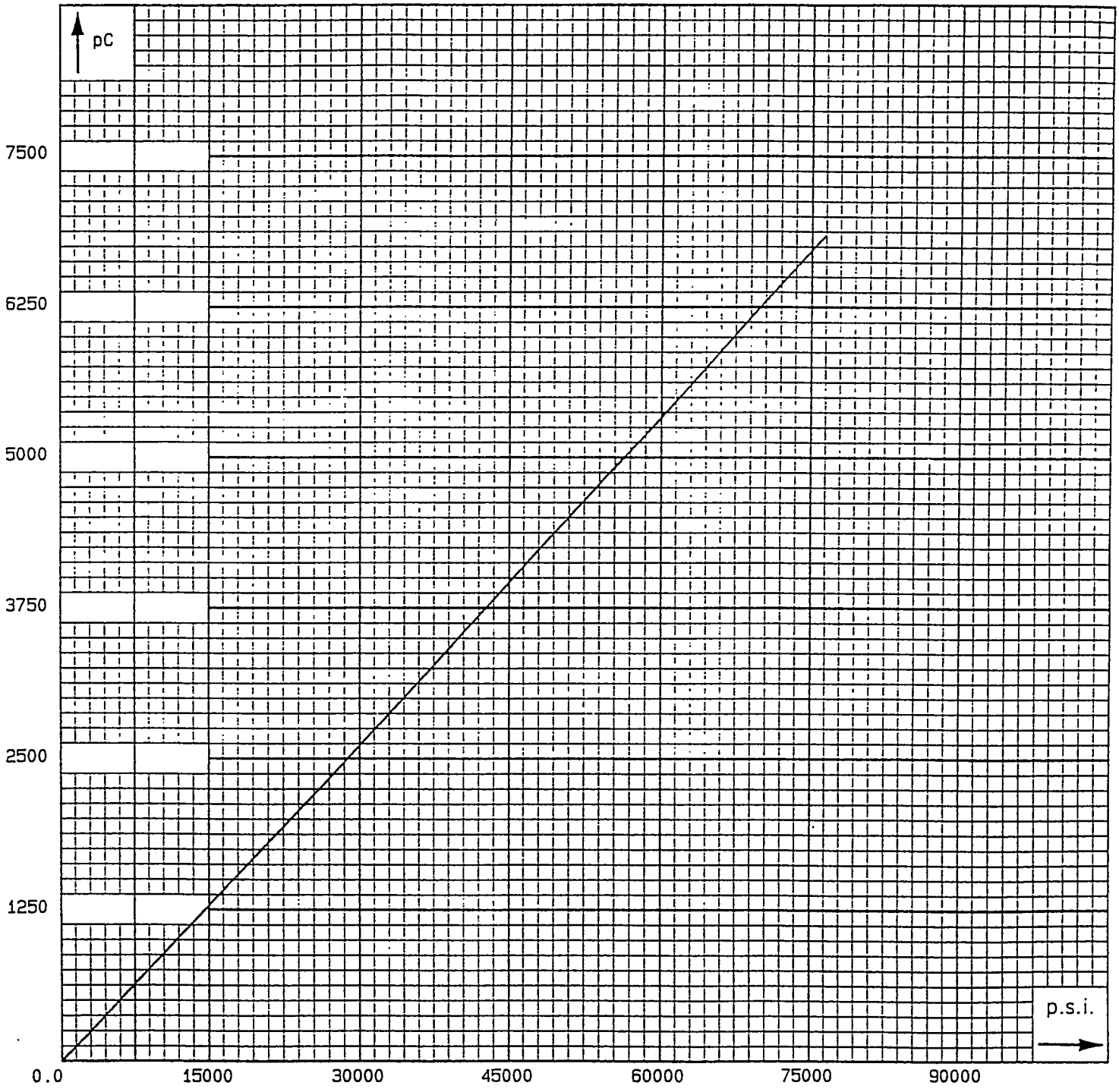

026 0600-001 REV C, 1/95

KISTLER
Kistler Instrument Corporation

75 John Glenn Drive
Amherst, NY 14228-2171
Phone 716-691-5100
Fax 716-691-5226

Certificate of Calibration

Model: 5010B
Serial Number: C72579
MIL-STD-45662A
Environmental Conditions: Temperature 72 deg.F +/- 7 deg.F
Rel. Humidity 30% +/- 25%

Date: 07-23-1996
Certificate No.: 072396-C72579

Test Equipment Used:
Keithley 199 DMM, SN 0548534
Philips PM5138 Funct. Generator, SN L0638319
Kistler Precision Calibrator, SN 441977

Tested by: Jeremy Block
Signature: 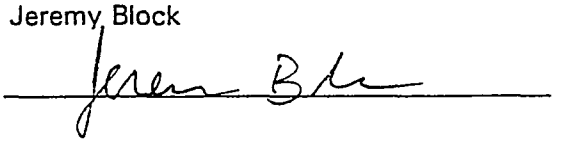

ACCURACY

Range (pC/MU)	Average Deviation	Maximum Measured Deviation
1.00 to 9.99	-0.01%	+0.05%
10.0 to 99.9	+0.02%	+0.07%
100.0 to 999.0	-0.03%	+0.05%
1000 to 9990	+0.02%	+0.04%
10000 to 99900	-0.01%	+0.04%

INTERNAL CALIBRATION CAPACITOR

Measured Value: 1033 pF

NOISE

Noise in Reset (at 1pC/V Range): 0.2 mV
Noise in Operate (at 1pC/V Range): 0.4 mV

DRIFT

Drift at each range within 0.03 pC/Second specification

PIEZOTRON CURRENT

Measured Value: 4.0 mA

Kistler Instrument Corp. hereby certifies that the above product was calibrated in compliance with Military Standard Calibration Systems Requirements MIL-STD-45662A using applicable Kistler procedures. Standards used are traceable to the National Institute of Standards and Technology (NIST), or another recognized National Standard, or have been derived from accepted values of natural physical constants, or have been derived by the ratio type of calibration, or by comparison to consensus standards.

KISTLER
Kistler Instrument Corporation

75 John Glenn Drive
Amherst, NY 14228-2171
Phone 716-691-5100
Fax 716-691-5226

Certificate of Calibration

Model: 5010B
Serial Number: C72411
MIL-STD-45662A
Environmental Conditions: Temperature 72 deg.F +/- 7 deg.F
Rel. Humidity 30% +/- 25%

Date: 07-11-1996
Certificate No.: 071196-C72411

Test Equipment Used:
Keithley 199 DMM, SN 0548534
Philips PM5138 Funct. Generator, SN L0638319
Kistler Precision Calibrator, SN 441977

Tested by: Kevin F. Kelly
Signature: 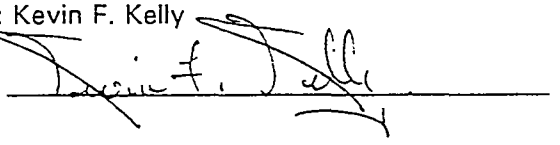

ACCURACY

Range (pC/MU)	Average Deviation	Maximum Measured Deviation
1.00 to 9.99	-0.02%	+0.06%
10.0 to 99.9	+0.02%	+0.06%
100.0 to 999.0	-0.03%	+0.08%
1000 to 9990	-0.05%	+0.09%
10000 to 99900	-0.02%	+0.10%

INTERNAL CALIBRATION CAPACITOR

Measured Value: 989 pF

NOISE

Noise in Reset (at 1pC/V Range): 0.2 mV
Noise in Operate (at 1pC/V Range): 0.2 mV

DRIFT

Drift at each range within 0.03 pC/Second specification

PIEZOTRON CURRENT

Measured Value: 4.0 mA

Kistler Instrument Corp. hereby certifies that the above product was calibrated in compliance with Military Standard Calibration Systems Requirements MIL-STD-45662A using applicable Kistler procedures. Standards used are traceable to the National Institute of Standards and Technology (NIST), or another recognized National Standard, or have been derived from accepted values of natural physical constants, or have been derived by the ratio type of calibration, or by comparison to consensus standards.

Maxwell TECHNOLOGIES

To: Chad Boyer
North Carolina State University
Department of Nuclear Engineering
Burlington Labs Box 7909
Raleigh, NC 27695

Chad:

We calibrated your Rogowski against our Pearson current probe model 1049. We used two different pulses to give you a variety to choose from. One pulse (PS-109) peaks in approximately 80 microseconds and the second one (PS-110) peaks in approximately 125 microseconds. You will note that the pulse starts before time zero because the data acquisition system was self trigged.

I have enclosed plots for each of the two tests with their scale factors listed. Their are three traces on each plot; The Pearson , the Raw signal from your rogowski integrated by computer, and your passive integrated output. You will note that the digitally integrated signal has a more consistent scale factor as is always the case.

Also enclosed is a floppy disk containing the raw and processed data files that you can manipulate yourself. The processed file is self explanatory with all three signals on it. The raw file consists of the three signals without processing.

Scale factors: Raw signals = 2.82468 E+7 A/v and 2.809E+7 A/v
Passively Integrated= 4.24195E+4 A/v and 4.0795E+4 A/v
Pearson Current probe= 500 A/v

I hope the data is a help to you. If you should need anything else please let me know.

Thankyou;

Paul Riedy
Maxwell Technologies
Green Farm Test Site
San Diego Ca. 92123
(619) 576-7857
Fax (619) 571-7194

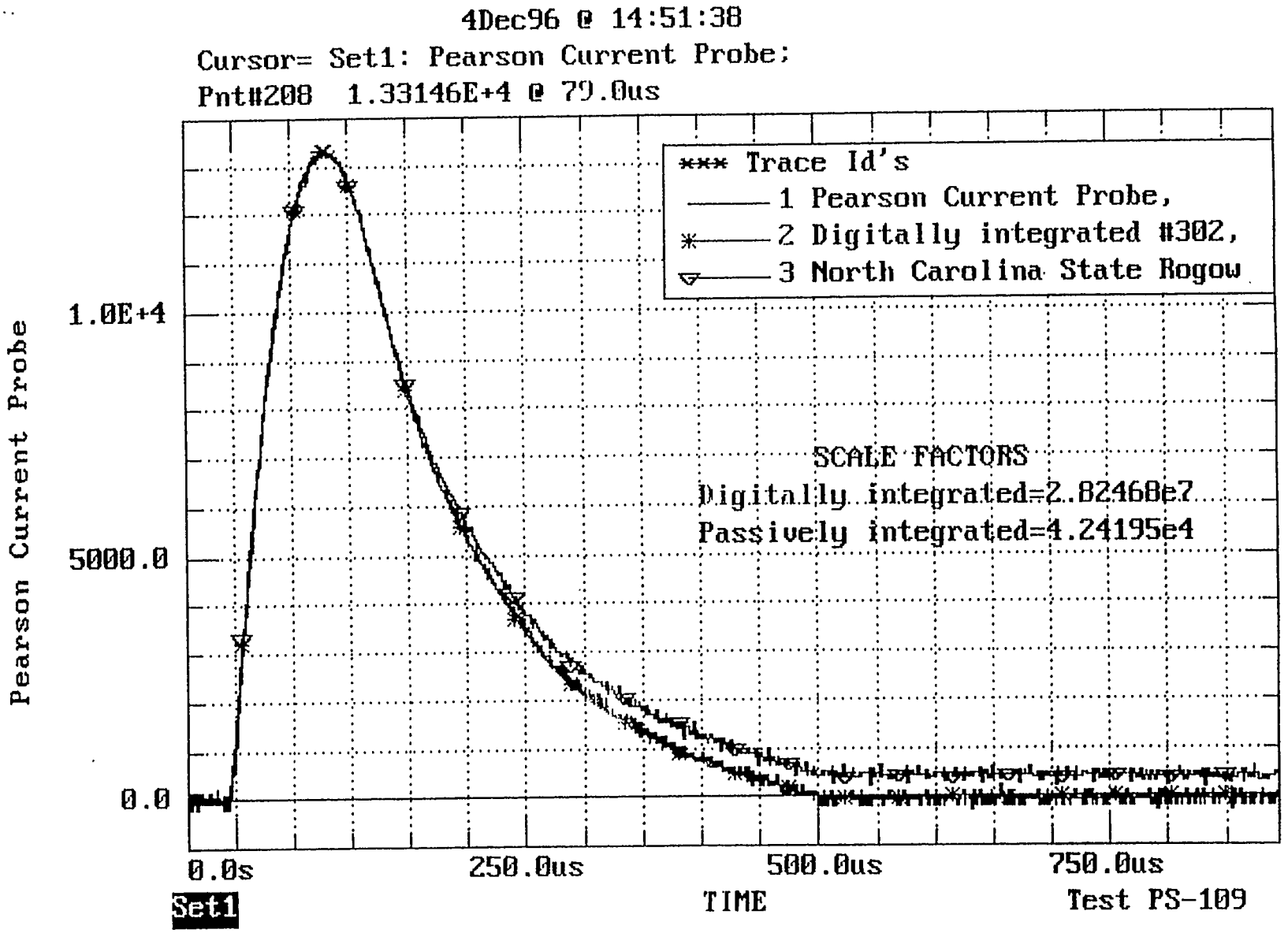
4Dec96 @ 14:51:38
Cursor= Set1: Pearson Current Probe:
Pnt#208 1.33146E+4 @ 79.0us
*** Trace Id's
1 Pearson Current Probe,
2 Digitally integrated #302,
3 North Carolina State Rogow
SCALE FACTORS
Digitally integrated=2.82468e7
Passively integrated=4.24195e4
Pearson Current Probe
1.0E+4
5000.0
0.0
0.0s
250.0us
500.0us
750.0us
TIME
Set1
Test PS-109

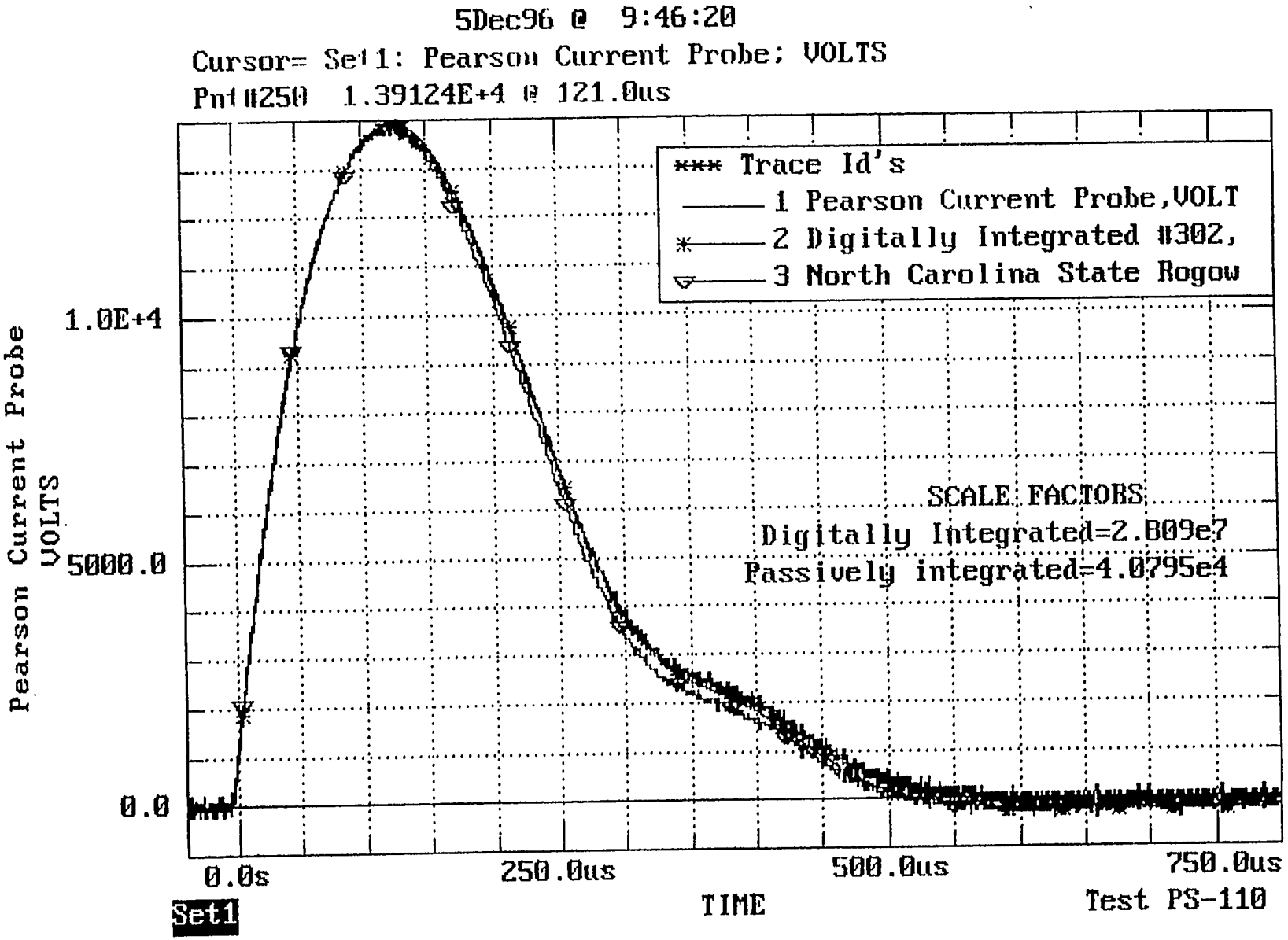
5Dec96 @ 9:46:20
Cursor= Set1: Pearson Current Probe; VOLTS
Pnt#250 1.39124E+4 @ 121.0us
*** Trace Id's
1 Pearson Current Probe,VOLT
2 Digitally Integrated #302,
3 North Carolina State Rogow
SCALE FACTORS
Digitally Integrated=2.809e7
Passively integrated=4.0795e4
Pearson Current Probe VOLTS
1.0E+4
5000.0
0.0
0.0s
250.0us
500.0us
750.0us
TIME
Set1
Test PS-110

Appendix C. Reference on ODIN Code[9]

Numerical Simulation and Experiment of Plasma Flow in the Electrothermal Launcher SIRENS

J.D. Hurley*, M.A. Bourham and J.G. Gilligan
North Carolina State University, Department of Nuclear Engineering, Raleigh, NC 27695-7909

Abstract— An electrothermal plasma source (ET) may be used as a launcher by itself, or as a pre-injector for electromagnetic launchers (railguns) or electrothermal-chemical (ETC) launchers. The characteristics of the injected plasma may affect the performance of the plasma armature (EM's) or the combustion process (ETC's). A 1-D, time-dependent fluid dynamics code, ODIN, has been developed to model the plasma formation and flow in the source and the barrel of the ET launcher SIRENS. The code models the energy transport, particle transport, plasma resistivity, plasma viscosity, and the equation-of-state. The measured mass loss of the ablating liner in the source section is in good agreement with that predicted by the code. Comparisons between the measured and predicted pressures inside the barrel are in good agreement.

I. INTRODUCTION

Electrothermal plasma sources have various applications in electric launchers technology. Electrothermal plasma sources are used as a launcher by itself, or as a pre-injector to form a plasma armature in railguns. In plasma-chemical launchers, the source injects the plasma into the propellant to control the burn rate. The operation of such devices may be greatly affected by the characteristics of the injected plasma (temperature, pressure, flow velocity, etc.) that is produced from the electrothermal source [1-3]. An electrothermal source produces, usually, a high-density (10^{25}-10^{26}/m^3), low-temperature (1-3 eV) plasma flow that can serve as an external high heat flux source [4-6]. The heat fluence S of most electrothermal plasmas can be modeled as a blackbody source. The heat flux that reaches the surface of the liner or the wall of the barrel is represented by $q'' = f\,S$, where f is the energy transmission factor through the vapor layer [6,7,10]. Several models have been proposed to describe the plasma formation in electrothermal plasma sources and ablation-controlled arcs [4-10]. However, modeling of the plasma expansion through the barrel is important for the operation of electric launchers that utilize a pre-injected ET plasma. A 1-D time dependent code, ODIN, has been developed to calculate the variation in the plasma parameters using the source discharge current, liner material properties, and the source and barrel geometry. The code accounts for the time and axial variation in the energy transmission factor, f, time and axial variation in the viscous and ablation drags, and time and axial variation in the plasma parameters. The code results are compared to experimental results obtained from the SIRENS ET launcher [6,11,12].

Manuscript received April 13, 1994.
This Work is supported by the US Army Research Office Contract DAAL03-92-G-0051, the US Army Space and Strategic Defense Command Contract DASG60-90-C-0028, and the US Army Ballistic Missile Defense Organization Contract DASG60-93-C-0029.
* Present address: Naval Research Laboratory, Code 6750, Washington, D.C. 20375-5356.

II. EXPERIMENTAL FACILITY

The electrothermal launcher SIRENS [6,11,12] has been designed to produce a low-temperature (1-3 eV), high-density (10^{25}-10^{26} /m^3) plasma. The plasma is formed inside the capillary (4 mm inner diam.) by the ablation of the Lexan liner, with currents up to 100 kA. The produced plasma is allowed to expand into the barrel (6 mm inner diam.) that is attached directly to the source. The heat flux can be varied from 2 to 70 GW/m^2 over a 100 μsec duration for input energies of 1-8 kJ. Fig. 1 shows the conceptual design of the electrothermal launcher SIRENS, the diagnostic setup for measuring the pressure and velocity, and a typical oscillogram of the discharge current at 1.17 kJ input energy.

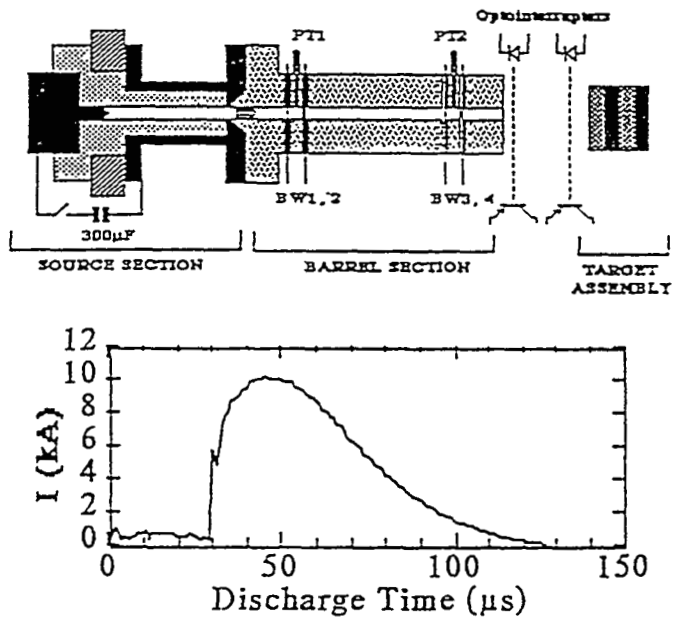

Fig. 1 Conceptual drawing of the SIRENS ET launcher, and a typical oscillogram of the discharge current at 1.17 kJ input energy.

An external Rogowski coil is used to measure the discharge current, and the discharge potential is measured via a compensated capacitively-coupled potential divider. The plasma velocity is measured via a photodiode array that is interfaced to a data acquisition system. The absolute pressure inside the expansion barrel is measured at two locations, 6 cm and 12 cm from the barrel entrance, using Kistler absolute pressure transducers coupled to charge amplifiers and interfaced to the data acquisition system [6,13].

III. CODE FORMULATION

The 1-D, time-dependent code ODIN [13] has been developed from the 0-D, time-dependent code ZEUS [7] that models the plasma formation inside the capillary of ET sources. In addition, ODIN models the plasma flow and expansion through the barrel of electrothermal plasma launchers. The code models the energy transport, particle transport, plasma resistivity, plasma viscosity, and equation-of-state. The source and barrel sections are broken into a specific number of cells and each cell is considered to be in local thermodynamic equilibrium (LTE), with the plasma modeled as a viscous fluid. The LTE and fluid model are used due to the highly collisional, low-temperature, high-density plasma that is produced by the ablation controlled arc inside the ET source. The viscous drag forces are varied according to the Reynolds number of each cell. As the Reynolds number increases, the modeled drag forces change accordingly from laminar to turbulent. Nonlinear fluid equations have been used due to the ionization, radiation, and drag effects. The specific internal energy of the plasma is computed as a function of the temperature assuming that the ablated material is completely dissociated. The energy transmission factor, f, through the vapor shield is internally computed, which allows for the time and axial variations of the vapor shield effect in the source and the barrel. The set of nonlinear equations are solved using the Bulirsch-Stoer method, which uses rational function extrapolation. It has been found that this method is computationally faster than the fourth-order Runge-Kutta method used in the ZEUS code. Error control is used in the code by monitoring the internal consistency, and adapting the stepsize to keep a prescribed bound on the local truncation error. Several simplifying assumptions are considered in the model. The plasma parameters are assumed to be constant across the cross section of the capillary. The plasma is assumed to be an ideal plasma, which is an acceptable assumption at higher values of input energy to the source (> 4 kJ), where the plasma temperature is about 3 eV. Electrothermal plasmas tend to be weakly nonideal, and the Spitzer resistivity model may yield inaccurate results. The ablated material in the source is assumed to be totally dissociated into the constituent atoms. The heat loss due to conduction inside both the source and the barrel is assumed to be negligible. The axial radiation transport is assumed to be negligible inside the source section where the plasma temperature is fairly isothermal [5]. However, at the interface between the source and the barrel, and inside the barrel, the axial temperature gradient can be large. The radial radiation transport will be included in future work. The self magnetic pressure due to the arc current is assumed to be less than the kinetic pressure of the plasma particles [8]. The set of governing equation are given in detail in Refs. 13 and 14.

A. *Conservation of Mass*

The rate of change in the particle density in each cell is the difference between the rate at which particles are introduced into the cell from ablation of the wall and the rate at which particles enter and leave the cell. The equation of continuity for each cell is given by [9]:

$$\frac{\partial n}{\partial t} = \dot{n}_a - \frac{\partial (vn)}{\partial z} \tag{1}$$

where n is the number density of plasma particles (atoms/m^3), $\dot{n}_a$ is the time rate of change of the number density of ablated material from the cell wall (atoms/m^3 sec), and v is the plasma velocity (m/sec). The time rate of change of the number density of ablated material from the cell wall is [7]:

$$\dot{n}_a = \frac{2q''}{H_{sub} A_p R} \tag{2}$$

where q" is the radiation heat flux incident on the wall surface (W/m^2), A_p is the mass of the atoms that constitute the plasma (kg/atom), R is the radius of the cell (meters) , and H_{sub} is the heat of sublimation. The radiation heat flux q" incident on the wall surface is modeled as a fraction f of the blackbody radiation $q'' = f\sigma_s T^4$ emitted from the hot plasma core [6,11,12], where f is the energy transmission factor through the vapor shield, σ_s is the Stefan-Boltzmann constant (5.670×10^{-8} W/m^2 K^4), and T is the plasma temperature (°K). The energy transmission factor, f, is given by [7,9]:

$$f = \frac{\rho H_{sub}}{P + \rho U + \rho H_{sub}} \tag{3}$$

where P is the plasma pressure (N/m^2), ρ is the plasma density (kg/m^3), and U is the internal energy of the plasma (Joules). The term $0.5\rho^2 v^2$ has been added to the denominator of the equation for f for one run of the code to account for the effect of the flow velocity on f. This term had virtually no effect on the value of f and was not include in the formula in all other calculations. The plasma pressure for an ideal plasma is given by $P = nkT(1 + \bar{Z})$, where k is the Boltzmann's constant (1.3807×10^{-23} J/K), and $\bar{Z}$ is the effective non-integral charge state.

B. *Conservation of Momentum*

The change in velocity in each cell is due to the pressure forces, the kinetic energy of particles entering and leaving the cell, and the ablation and viscous drags. The equation for the time rate of change of the velocity in each cell is given by [7,9]:

$$\frac{\partial v}{\partial t} = -\frac{1}{\rho}\frac{\partial P}{\partial z} - \frac{1}{2}\frac{\partial v^2}{\partial z} - \frac{v\dot{n}_a}{n} - \frac{2\tau_w}{\rho R} \tag{4}$$

where τ_w is the viscous drag at the wall (N/m^2). The first term on the right hand side is the change in velocity due to the axial pressure gradient. The second term is the change in velocity due to the kinetic energy gradient. The third term is the velocity loss due to the increase in the number density from ablated material (ablation drag). The fourth term is the velocity loss due to the viscous drag at the wall. The viscous drag for steady fully developed incompressible fluid flow was used in the calculations and is given by:

$$\tau_w = \frac{1}{2} C_f \rho v^2 \tag{5}$$

where C_f is the friction factor.

The friction factor is adjusted internally in the code based on the Reynolds number, Re, of each cell. The friction factor used for Reynolds numbers less than 2500 is the Darcy friction factor, $C_f = 16/R_e$, where the plasma flow is assumed laminar. The friction factor used for Reynolds numbers ranging from 2500 to 30 x 10^5 is from the model developed by Wieghardt [15] for turbulent flow in smooth pipes. This friction factor model is based on the power-law velocity profile for fully-developed turbulent flow and is given by:

$$v = V_{max} \cdot \left(\frac{R - r}{r}\right)^{\frac{1}{n}} \tag{6}$$

where V_{max} is the velocity at the center of the pipe, r is the radial distance from the center, and n is the parameter that depends on the Reynolds number of the flow. The resulting friction factor is given by:

$$C_f = K_4 \cdot (Re)^{-2/(n+1)} \tag{7}$$

where K_4 is a parameter that depends on n [13-15]. The friction factor used for Reynolds numbers greater than 6.0 x 10^6 is given by [15]:

$$\frac{1}{\sqrt{C_f}} = 4\log_{10}\left(3.7\frac{D}{\varepsilon}\right) \tag{8}$$

where ε = 2.0 x 10^{-5} m [15], is the roughness of a plastic pipe.

C. Conservation of Energy

The rate of change of the internal energy in each cell in the source section is due to Joule heating, radiation, flow work, changes in density, internal energy entering or leaving the cell due to particle transport, and frictional heating. The time rate of change of internal energy in each cell in the source is given by [7,9]:

$$n\frac{\partial U}{\partial t} = \eta j^2 - \frac{2q''}{R} - P\frac{\partial v}{\partial z} + \frac{1}{2}\dot{\rho}_a v^2 - \dot{n}_a U - v\frac{\partial (nU)}{\partial z} \tag{9}$$

where η is the plasma resistivity (Ω-m), and j is the discharge current density (A/m^2). The first term on the right hand side is the increase in internal energy due to joule heating. The second term is the loss in internal energy due to thermal radiation and the (2/R) factor is due to the conversion of surface heat flux to volume radiation. The third term is the change in internal energy due to work done by the plasma (flow work). The fourth term is the increase in internal energy due to friction from ablation. The fifth term is the loss in internal energy due to the cold ablated material entering the plasma. The sixth term is the change in internal energy due to particles entering and leaving the cell. The rate of change of the internal energy of each cell in the barrel section is identical to that in the source except for the absence of the joule heating term. The internal energy of an ideal plasma is given by [7]:

$$U = 1.5kT(1 + \bar{Z}) + \bar{I} + H_{sub} \tag{10}$$

where the first term on the right hand side is the internal energy due to thermal motion, and $\bar{I}$ is the internal energy due to ionization. The ionization energy is the sum of all ionization potentials up to the integer value of the charge state, m (m=integer($\bar{Z}$)). An additional correction term is added to account for the next higher ionization potential. The ionization potentials and the effective charge state are determined using the method proposed by Zeldovich and Raizer [16]:

$$\bar{I} = \sum_{i=0}^{m} I_i + (\bar{Z} - m) I_{m+1} \tag{11}$$

The Saha-Boltzmann equation is modified to account for the transformation from integral charge states to the non-integral states [16]:

$$I_Z(\bar{Z}+.5) = kT \ln\left\{\frac{AT^{1.5}}{Zn}\right\} \tag{12}$$

and A = 4.834 x 10^{21} K$^{-1.5}$ m^{-3} is a constant.

The plasma resistivity has been determined using the model $\eta = \eta_{ea} + \eta_{ei}$, where η_{ea} is the resistivity due to electron-neutral collisions and η_{ei} is the resistivity due to electron-ion collisions [17]. The resistivity due to electron-neutral collisions, η_{ea}, is:

$$\eta_{ea} = \frac{m_e}{e^2 n_e}\langle \upsilon_{ea} \rangle$$

where the average collision frequency due to the elastic interactions of electrons and neutral atoms, for a Maxwellian plasma, is: $\langle \upsilon_{ea} \rangle = \frac{2n_a \nabla_e}{3}\bar{Q}_{ea}$;

and n_a is the number density of neutrals, and $\bar{Q}_{ea}$ is the average momentum cross-section. The average momentum cross-section is determined by taking the weighted molar averages of the momentum cross-sections of the constituent atoms of the Lexan insulator ($C_{16}H_{14}O_3$). The resistivity due to electron-ion collisions, η_{ei}, is determined from the Spitzer Resistivity model [18]:

$$\eta_{ei} = \frac{38\bar{Z}\ln(\Lambda)}{\alpha_e T^{1.5}} \tag{13}$$

where α_e is the correction factor to the resistivity to account for the electron-electron collisions and is a function of the charge state. The plasma viscosity is $\mu = \mu_a + \mu_i$, where μ_a and μ_i are the viscosity due to the neutral atoms [19] and ions, respectively. The neutral viscosity μ_a is given by:

$$\mu_a = \frac{1}{3}\rho_a \lambda_a c_a \tag{14}$$

where ρ_a is the neutral atom density, c_a is the thermal velocity of the neutral atoms, and λ_a is the neutral mean free path. The ion viscosity μ_i is given by [19]:

$$\mu_i = \frac{1}{3}\rho_i \lambda_i c_i \tag{15}$$

where ρ_i is the ion mass density, c_i is the ion thermal velocity, and λ_i is the ion mean free path.

The equation for the internal energy does not depend explicitly on the plasma temperature. Therefore, the equations must be transformed so that the plasma temperature can be determined. The transformation used in ODIN is the same as that used in the ZEUS code [7,20]. A 2x2 matrix is formed from the time derivative of Eqn. 10 and Eqn. 12, which allows the explicit time variation of the temperature and charge state to be obtained.

IV. CODE RESULTS

The time evolution of the plasma parameters has been determined for input energies between 1 and 5 kJ. The plasma parameters averaged over the axial distance of the source and barrel, for input energies from 1 to 5 kJ, have been previously discussed [13]. The following is an analysis of a 1.17 kJ shot to show the time evolution of the plasma formation and flow in the source and barrel. The time evolution of the source density is shown in Fig. 2, where the density is fairly uniform along the length of the source with a slight decrease at the exit due to particle transport into the barrel. The density peaks at about 75 μs and then steadily decreases because the particle loss due to transport into the barrel is greater than the particle gain due to ablation. The time evolution of the barrel density is shown in Fig. 3. The transport of the particle density into the barrel section is shown, with the barrel density reaching its maximum value at about 105 μs. The barrel density then steadily decreases and flattens as the particles flow from the denser barrel entrance region to the barrel exit. The density profile also begins to oscillate as it reaches its peak value and these oscillations continue as the density decreases. The oscillations are due to compression waves that form in the barrel after the main driving force of the discharge is terminated.

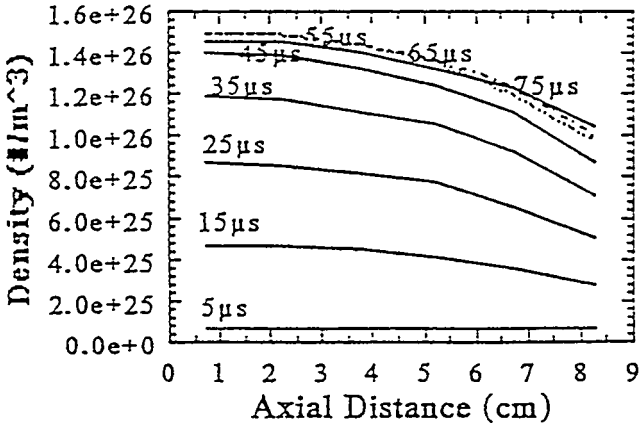

Fig. 2 Axial time evolution of the plasma density inside the source for 1.17 kJ input energy.

The time evolution of the source temperature is shown in Fig. 4. The source temperature reaches its maximum value at 15 μsec, which corresponds to the maximum of the discharge current. The source temperature is fairly isothermal, dropping slightly at the exit due to transport losses into the barrel. After reaching its peak value, the source temperature drops steadily due to cold ablated material entering the volume and the transport losses.

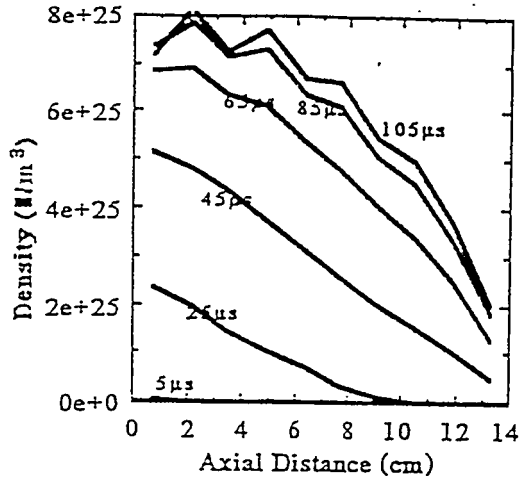

Fig. 3 Axial time evolution of the plasma density inside the barrel fo 1.17 kJ input energy.

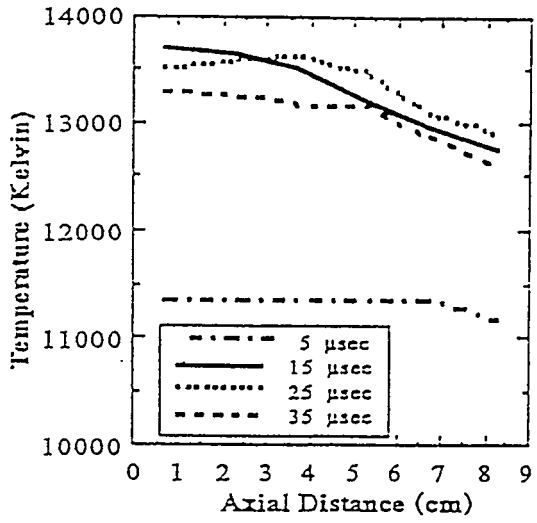

Fig. 4 Axial time evolution of the plasma temperature inside the source for 1.17 kJ input energy.

The time evolution of the barrel temperature is shown in Fig. 5, where the temperature gradients are large as the plasma begins its expansion down the length of the barrel. However, once the plasma reaches the barrel exit, the temperature is fairly constant along the barrel length and steadily drops due to ablated material entering the plasma and transport losses. The time evolution of the plasma pressure in the source section is shown in Fig. 6. The source pressure reaches its maximum value at approximately 45 μs. This time is approximately halfway between the time of peak temperature and peak density. This occurs due to the pressure being linearly dependent on both the temperature and the density. After the source pressure reaches its peak value, it steadily decreases due to the drop in temperature and density.

The progression of the pressure into the barrel section, up to 65 μs, is shown in Fig. 7. After this time the pressure profile begins to flatten out and drop as the plasma exits the barrel. The pressure profile exhibits the same types of

oscillations that were present in the density profile, which are due to the compression waves that the plasma experiences once the main driving force of the discharge is over.

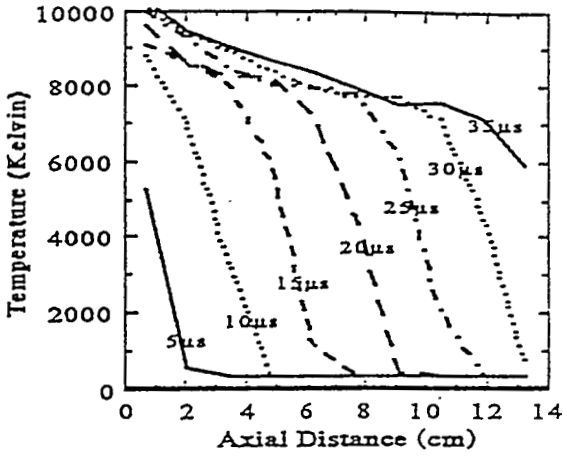

Fig. 5 Axial time evolution of the plasma temperature inside the barrel for 1.17 kJ input energy.

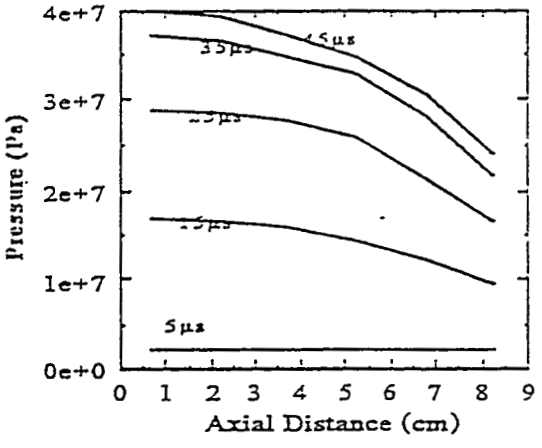

Fig. 6 Axial time evolution of the plasma pressure inside the source for 1.17 kJ input energy.

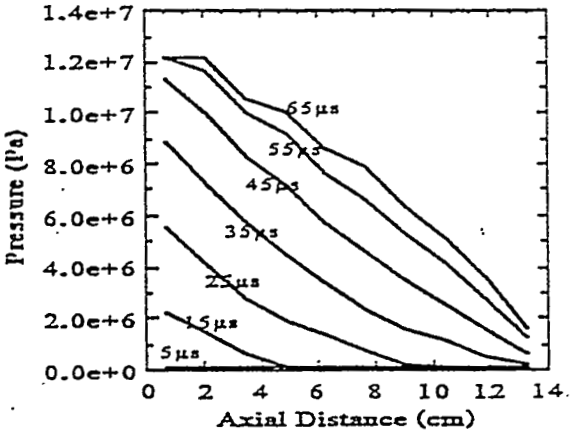

Fig. 7 Axial time evolution of the plasma pressure inside the barrel for 1.17 kJ input energy.

The time evolution of the source velocity is shown in Fig. 8. The velocity at the exit achieves the highest value due to the large pressure gradient between the source and barrel sections. After 55 μs, the velocity decreases steadily and flattens out as the pressure difference between the source and barrel drops. The time evolution of the velocity in the barrel section, up to 55 μs, is shown in Fig. 9. It is clear that the velocity is much larger at the barrel entrance and exit. The large velocities at the entrance are due to the large pressure gradient between the source exit and the barrel entrance. The velocities are large at the barrel exit due to the free expansion of the plasma into the vacuum chamber. The velocity profile is constant in the rest of the barrel, once the plasma has reached the exit.

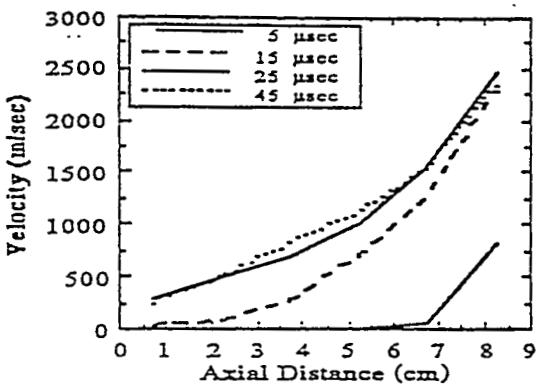

Fig. 8 Axial time evolution of the plasma velocity inside the source for 1.17 kJ input energy.

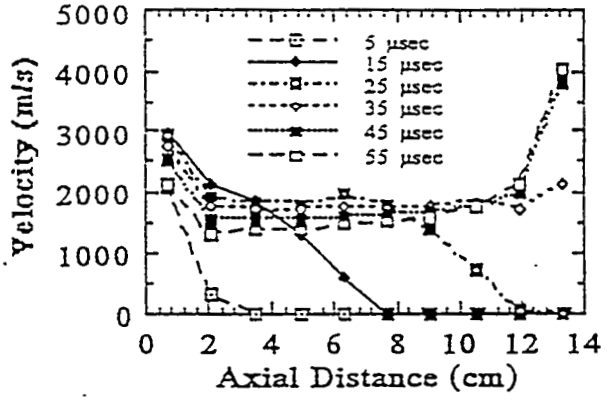

Fig. 9 Axial time evolution of the plasma velocity inside the barrel for 1.17 kJ input energy.

V. EXPERIMENTAL RESULTS

A comparison between the calculated mass loss and the measured mass loss in the source section is shown in Fig. 10. The error bars for the measured data represents the standard deviation of the data. The measured and calculated mass losses agreed fairly well for all input energies. The calculated and measured values were very close for the higher input energy shots. The reason for this is that the assumptions made in the modeling of the source are better approximations at higher energies [5]. The pressure in the barrel section was measured at two locations, 6 cm and 12 cm from the barrel entrance using piezoelectric pressure transducers. The calculated pressure was obtained from the code at these two locations b

fitting the calculated pressure of the barrel cells with a polynomial curve. Fig. 11 shows the measured and calculated pressure traces at the first location for an input energy of 4.10 kJ. The calculated pressure trace agrees well with the measured pressure trace, which was the case for all input energies.

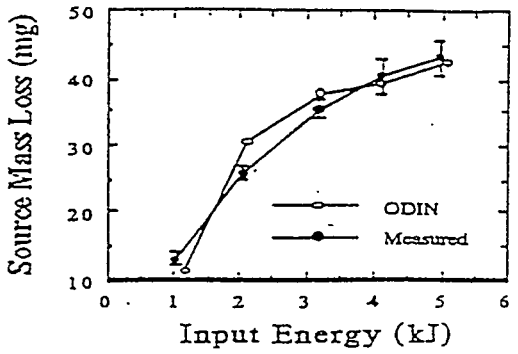

Fig. 10 A comparison between the measured and calculated mass loss in the source section.

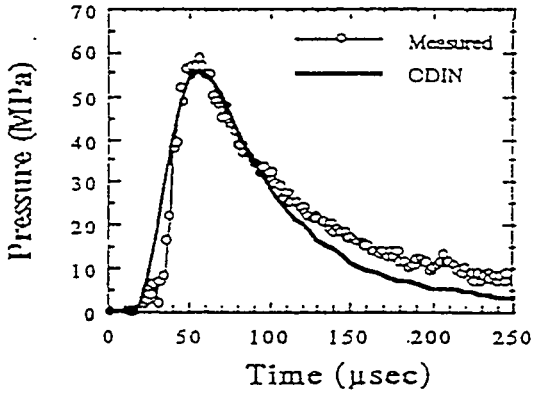

Fig. 11 Comparison between the measured and calculated pressure at 6.0 cm from the barrel entrance for an input energy of 4.10 kJ.

A comparison between the measured and calculated average resistivity for an input energy of 4.10 kJ is shown in Fig. 12. Electrothermal plasmas tend to be weakly nonideal, and the Spitzer resistivity model [18], may yield inaccurate results [4,11]. Corrections to the ideal plasma transport and thermodynamic properties for resistivity and charge state must be included.

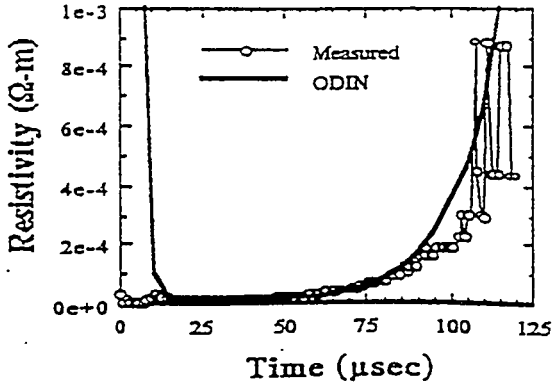

Fig. 12 A comparison between the measured and calculated average resistivity in the source section for an input energy of 4.10 kJ

CONCLUSIONS

A 1-D time-dependent fluid dynamics code, ODIN, has been developed to model the plasma formation and flow in electrothermal launchers. The time evolution of the plasma parameters has been determined for a range of input energies between 1 and 5 kJ. The code results compare favorably with experimental measurements.

REFERENCES

[1] A. Juhasz, "Activities in electrothermal gun propulsion," Technology Efforts in ETC Gun Propulsion, US Army Ballistic Research Laboratory, FY89, vol. 2, Aberdeen, Maryland, 1989.

[2] W.F. Morrison, J.D. Knapton and M.J. Bulman, "Gun propulsion technology," Progress in Astronautics and Aeronautics, American Institute of Aeronautics and Astronautics, vol. 109, p. 414, 1988.

[3] R.L. Burton, B.K. Hilko and F.D. Witherspoon, "Heating of a liquid/vapor mixture by a pulsed electric discharge," GT-Devices Rep. GTD 90-7, Final Technical Report, Air Force Office of Scientific Research, August 1990.

[4] A. Loeb and Z. Kapian, "A theoretical model for the physical processes in the confined high pressure discharges of electrothermal launchers," *IEEE Trans. on Magnetics*, vol. 25, pp. 342-346, January 1989.

[5] E. Z. Ibrahim, "The ablation dominated polymethyimethacrylate arc," *J. Phys. D.: Appl. Phys.*, vol.13, p. 2045, 1980.

[6] M. Bourham, J. Gilligan, O. Hankins, W. Eddy and J. Hurley, "Electrothermal Plasma Source as a High Heat Flux Simulator for Plasma-Facing Components and Launch Technology Studies," Proc. 9th International Conference on High Power Particle Beams, Washington, D.C., 25-29 May 1992, vol. III, p. 1979, 1992.

[7] J. G. Gilligan and R. B. Mohanti, "Time-dependent numerical simulation of ablation-controlled arcs," *IEEE Trans. Magn.*, vol. 18, No. 21, p. 190, April 1990.

[8] C. B. Ruchti and L. Niemeyer, "Ablation controlled arcs," *IEEE Trans. Plasma Sci.*, vol. 14, p. 423, August 1986.

[9] J. D. Powell, A. E. Zielinski, "Theory and experiment for an ablating-capillary discharge and application to electrothermal-chemical guns," Tech. Report BRL-TR-3355, June 1992.

[10] R. B. Mohanti, J. G. Gilligan and M. A. Bourham, "Time dependent simulation of weakly nonideal plasmas in electrothermal launchers," *Physics of Fluids B*, vol. 3, p. 3046, November 1991.

[11] M.A. Bourham, O.E. Hankins, J.G. Gilligan, J.D. Hurley and J.R. Earnhart, "Comparative study of component erosion for electromagnetic and electrothermal launchers," *IEEE Trans. Magnetics*, vol. 29, p.1107, January 1993.

[12] M.A. Bourham, J.G. Gilligan and O.E. Hankins, "Plasma-material interaction in electrothermal and electromagnetic launchers," The 24th AIAA Plasmadynamics & Lasers Conference, Orlando, FL, AIAA 93-3172, July 1993.

[13] J.D. Hurley, M.A. Bourham and J.G. Gilligan, "Modeling and experiment of an electrothermal igniter for electrothermal-chemical guns," Proc. 30th JANNAF Combustion Meeting, CPIA, 3V6, Monterey, CA, 15-19 November 1993.

[14] J.D. Hurley, "In-bore diagnostics and modeling of an electrothermal plasma launcher," Ph.D. Thesis, North Carolina State University, Raleigh, NC, May 1993.

[15] A. J. Ward-Smith, Internal fluid flow : The fluid dynamics of flow in pipes and ducts, Oxford University Press, NY, 1980.

[16] Ya. B. Zeldovich, and Yu. P. Raizer, Physics of shock waves and high temperature hydrodynamic phenomena, vol. I, Academic Press, NY, 1963 .

[17] A. B. Cambel, Plasma physics and magneto-fluidmechanics, McGraw- Hill, NY, 1963.

[18] L. Spitzer, Jr. and R. Harm, "Transport phenomena in a completely ionized gas," *Phys. Rev.*, vol. 80, No. 2, p. 230, Oct. 1950.

[19] J. W. Bond, K. M. Watson, and J. A. Welch, Jr., Atomic theory of gas dynamics, Addison-Wesley Publishing Co., NY, 1965.

[20] R.B. Mohanti, Time dependent numerical simulation of nonideal plasmas in ablation controlled arcs, Ph.D. Thesis, North Carolina State University, Raleigh, 1990.

Part 2

"Characterization of Disruption-Induced Particulate from ITER Relevant Metals"

J.P. Sharpe and M.A. Bourham

EDF No. ITER/US/97/TE/SA-21, November 1997.

ENGINEERING DESIGN FILE

	**International Thermonuclear Experimental Reactor (ITER)** **U.S. Home Team** **Fusion Safety Program**	EDF No.: ITER/US/97/TE/SA-21 DATE: November 1997 TASK AREA: SAE-1

SUBJECT: Characterization of Disruption-Induced Particulate from ITER Relevant Metals

SUMMARY: The SIRENS high heat flux facility at North Carolina State University has been used to simulate the erosion and mobilization effects on ITER-relevant materials exposed to hard disruption conditions. Specifically, size distributions of various particulate resulting from surface vaporization and subsequent condensation under vacuum conditions have been produced. This document presents fundamental data obtained from a set of experiments performed with copper, stainless steel, tungsten, and aluminum (to simulate beryllium).

For this experimental investigation, particulate were generated from test material mobilized in the SIRENS electrothermal source section. Material exiting the source section was then introduced into a large controlled volume (cylindrical glass tube) upon which collection substrates (buttons) were mounted. Selected buttons were observed with a scanning electron microscope (SEM); the buttons generally displayed a significant population of particles deposited on the exposed surface. Using the SEM, photographs of a given button were obtained and analyzed for the number and size of deposited particles. This data was then fit to the log-normal distribution function, generating the overall particle size distribution for the selected button.

Particulate collected and analyzed from the various metals studied in this task displayed count median diameters from 0.3 μm to 3.0 μm. The minimum and maximum observed particle sizes where 0.075 μm and 50 μm, respectively. The majority of the particles in the underlying distributions, however, were ~1 μm in diameter.

In the near future, carbon and mixed-material tests will be performed. Later on, modeling of particulate generation and the necessary extrapolation to ITER will also be performed. The database resulting from this experimental task may be used to test models predicting the size of particulate mobilized during possible ITER disruptions.

Distribution (complete package): Project File, M. Bourham, W. J. Carmack, J. G. Gilligan, K. A. McCarthy, D. A. Petti, S. Piet, J. P. Sharpe

Author:	Date:	Reviewed:	Date:	Approved:	Date:
J. Phillip Sharpe		K. A. McCarthy		D. A. Petti	
M. Bourham		K.A. McCarthy	11/25/97	DA Petti	11/25/97

Outline

1.0 Introduction

The SIRENS high heat flux facility at NCSU has been used to simulate the erosion and mobilization effects on ITER-relevant materials exposed to hard disruption conditions. Specifically, size distributions of various particulate resulting from surface vaporization and subsequent condensation under vacuum conditions have been produced. Such information is necessary for ITER safety analyses involving disruption-induced mobilization of activated component material. This report presents fundamental data obtained from a set of experiments performed with copper, stainless steel, tungsten, and aluminum, and includes discussions on important observations, difficulties encountered, and significance of the tests to the overall task[1]. Each material tested will be discussed in separate sections, followed by a general conclusion comparing the overall results.

2.0 Experimental Procedure

The experimental configuration follows that described in the ITER EDF "Scoping of SIRENS for Wall Material Vaporization Studies"[2]. The test material was fabricated into a cylindrical sleeve of 0.397 cm ID, 0.714 cm OD, and 6 cm length, and placed into a Lexan inner insulator of 0.714 cm ID and 11.9 cm length. A ceramic (Maycor) insulator was used to isolate the electrically conducting test sleeves, thus forcing the arc discharge of SIRENS through the inside of the test sleeve (capillary) and exposing the inner surface of the test material to radiant heat flux. The entire assembly of test sleeve, ceramic insulator, Lexan inner and outer insulators, cathode, and anode housing is called the source section for each test in this series. Energy deposited on the surface from the intense arc releases material from the test sleeve by vaporization or ablation; this mobilized mass flows from the capillary into a large glass expansion cell (17.8 cm ID, 76.2 cm length). During the expansion process, the vapor cools well into supersaturation and condenses, forming the particulate of interest. This particulate is transported to the wall of the expansion cell and is intercepted at certain locations by circular collection substrates (buttons). Following the test, buttons are removed, weighed for relative mass gain, and observed under high magnification of a Scanning Electron Microscope (SEM). Photographic images of a button's surface are obtained, and the particles are sized and counted from these images, generating the particulate size distribution for that button[3].

The following items are included for reference: Figure 2.1 shows the source section configuration, Table 2.1 tabulates button locations within the expansion cell and on the end plate, Figure 2.2 displays schematically the button distribution in the expansion chamber, and Table 2.2 contains reference material for the various materials used in this series of experiments.

Figure 2.1. SIRENS source section configuration.

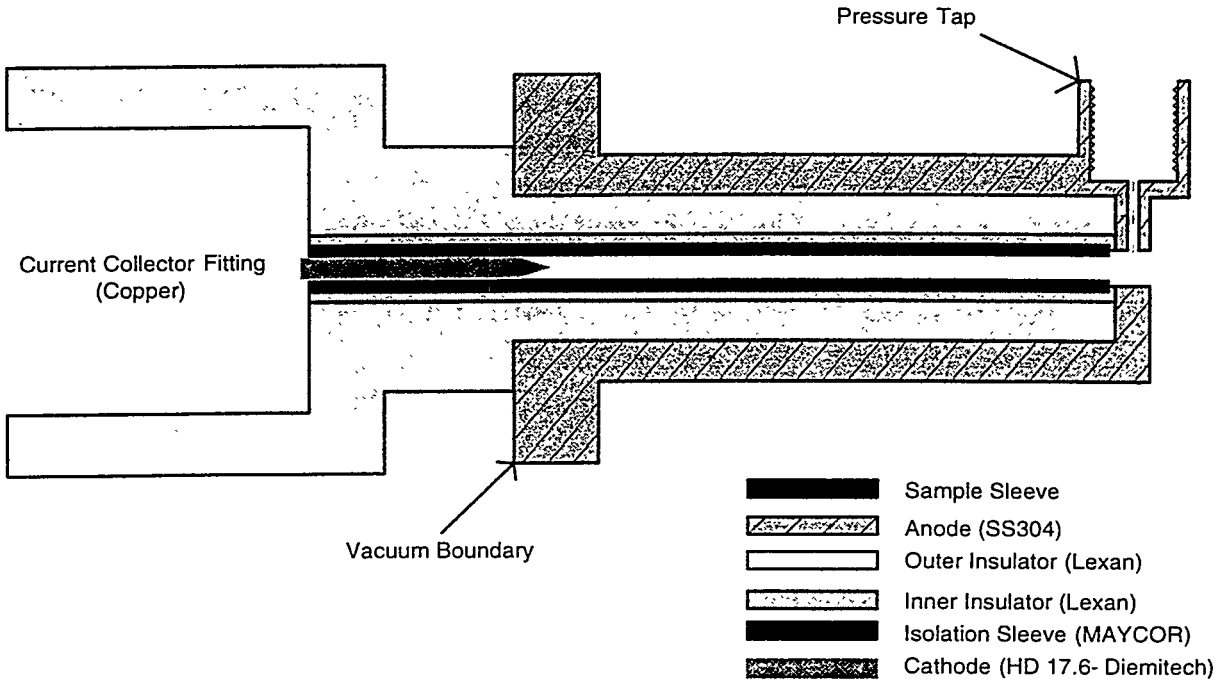

Table 2.1. Tabulated button distribution.

Button	Axial distance from source (cm)	θ (deg.) *
1	12.7	0
2	12.7	180
3	31.75	45
4	31.75	225
5	50.8	90
6	50.8	270
7	69.9	135
8	69.9	315
	End plate at 73.66 cm	
	radius (cm)	angle (deg.) **
9	3.0	0
10	4.5	45
11	7.0	90
12	7.0	180
13	3.0	225
14	4.5	270
15	7.0	315
16	4.5	135
17	4.5	224

* chamber top aligned to 0°

** end plate 90° aligned to chamber 0°

Figure 2.2. Schematic button distribution.

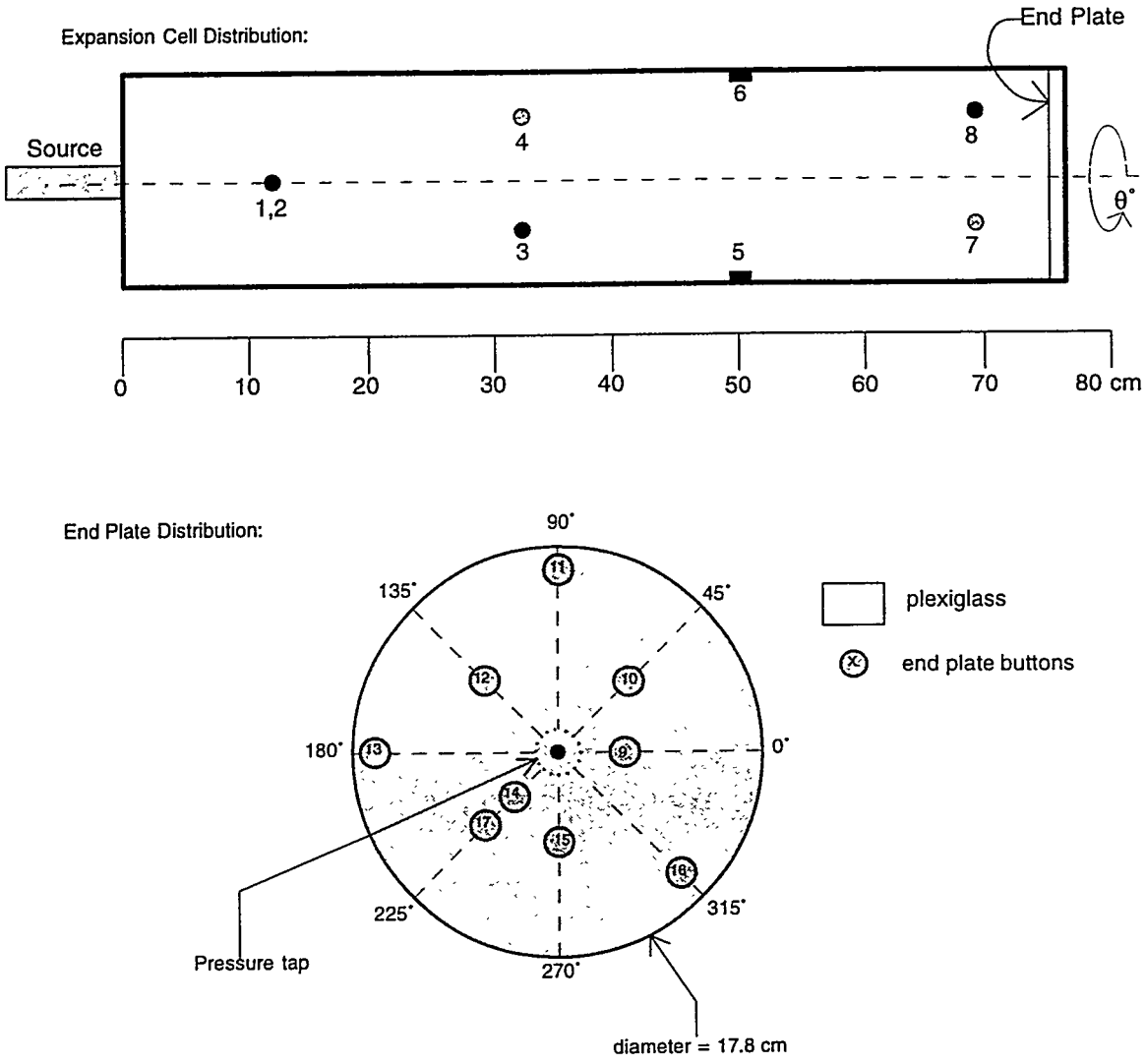

Table 2.2. Materials reference. [4,5]

Material	density (kg/m^3)	T_{melt} (K)	T_{boil} (K)	STP c_p (J/K/kg)	STP k (W/m/K)	STP σ ($1/\Omega/m \times 10^6$)	ΔH-fus (kJ/kg)	ΔH-vap (kJ/kg)
Al	2,700	933.5	2,792	897	237	36.4	397	10,896
Cu	8,960	1,357	2,835	383.1	401	59.2	207	6,577
Fe	7,870	1,811	3,134	452	80.4	10.3	247	6,094
W	19,300	3,695	5,828	134.4	173	18.6	250	4,486
SS304	7,820	1,700	3,000	478	19.4	~10	*	*
SS316	7,500	1,700	3,200	500	30.0	8.47	280	6,800
Lexan ($C_{16}H_{14}O_3$)	1,180	-	665(s)	1,200	3.0	0	-	54,000(s)
Maycor	2,500	-	*	*	*	0	-	*
HD-17.6 (diemitech)	17,600	*	*	*	27.0	14.0*	*	*

Notes:

(1) All properties are equilibrium properties at appropriate standards. STP is 101325 Pa and 298.15 K.

Notation:
- c_p specific heat capacity
- k thermal conductivity
- σ electrical conductivity
- ΔH-fus enthalpy of fusion
- ΔH-vap enthalpy of vaporization

(2) Subscript s denotes sublimation property.

(3) Dash (-) signifies non-existant data, asterisk (*) denotes data not available.

(4) All figures displayed to reported accuracy.

(5) Materials composition:

Maycor:
- SiO_2 @ 40-50 wt%
- AlO @ 10-25 wt%
- BO @ 5-10 wt%
- KO @ 5-10 wt%
- MgO @ 10-25 wt%
- F @ 5-10 wt%

HD 17.6:
- W @ 92.5 wt%
- Ni, Fe, Mo balance

SS304:
- C @ 0.08 wt%
- Mn @ 2.00 wt%
- Si @ 1.00 wt%
- Cr @ 16.0 - 18.0 wt%
- Ni @ 8.0 - 10.5 wt%
- Fe balance

SS316:
- C @ 0.08 wt%
- Mn @ 2.00 wt%
- Si @ 1.00 wt%
- Cr @ 16.0 - 18.0 wt%
- Ni @ 10.0 - 14.0 wt%
- Mo @ 2.0 - 3.0 wt%
- Fe balance

3.0 Copper Test Results

Two independent tests were performed in SIRENS using Cu as the test material: shots S734 and S737. These shots were prepared and performed using the procedure given in Reference 2. Table 3.0.1 displays a summary of mass loss data and particulate size distributions from the two Cu tests. Sample mass loss was consistent for shots of nearly equivalent discharge energies, and cathode mass loss was also about the same. Differences observed in particulate size distributions, especially on end-plate buttons, are a direct result of differences in SEM image quality. Images obtained from buttons used in Cu Test #1 were not optimized and displayed significant levels of noise because proper operational parameters of the SEM had not yet been established. Smaller particles were lost in the noise and the resulting size distributions were biased to larger sizes. Images from buttons used in Cu Test #2, however, were fully optimized and displayed negligible noise levels.

Table 3.0.1 Cu tests comparison summary.

	Cu Test 1 (S734)				Cu Test 2 (S737)			
Energy (J)	4260				4458			
Sample Δm (mg)	436.67				451.13			
Cathode Δm (mg)	30.9				26.45			
	Δm (mg)	$d_{50\%}$ (μm)	GSD	R^2	Δm (mg)	$d_{50\%}$ (μm)	GSD	R^2
Button 1	0.09	0.66	1.77	0.966	0.11	0.58	2.17	0.988
Button 2	0.05	*	*	*	0.12	*	*	*
Button 3	0.03	*	*	*	0.06	*	*	*
Button 4	0.20	*	*	*	0.15	*	*	*
Button 5	0.43	*	*	*	0.11	*	*	*
Button 6	0.39	0.78	2.13	0.986	0.13	0.630	2.43	0.989
Button 7	0.15	0.55	2.38	0.962	0.25	0.505	2.57	0.983
Button 8	0.39	*	*	*	0.29	*	*	*
Button 9	0.15	0.77	2.07	0.984	0.41	0.426	2.63	0.991
Button 10	0.18	*	*	*	0.44	*	*	*
Button 11	0.68	*	*	*	0.76	*	*	*
Button 12	0.28	0.97	2.04	0.988	0.52	0.366	3.06	0.989
Button 13	0.17	*	*	*	0.33	*	*	*
Button 14	0.08	0.84	2.27	0.970	0.28	0.381	2.70	0.981
Button 15	0.39	*	*	*	0.67	*	*	*
Button 16	0.23	*	*	*	0.42	*	*	*
Button 17	0.22	*	*	*	0.35	*	*	*

Note: Asterisk (*) denotes buttons for which the analysis was not performed.

3.1 S734: Cu Test #1

The first Cu test was performed with the large glass expansion chamber containing stainless steel collection buttons distributed as shown in Figure 2.2, and a SS304 housing containing the source section. Voltage and current traces are shown in Figure 3.1.1. The current trace is not representative of the discharge current; what is displayed is the dI/dt attenuated by the filter resistance. The voltage trace shows a delay in the discharge of about 50 μs after trigger initiation, and large voltage swings during the discharge. This result was unexpected, and raised concerns about the diagnostic probes and data recorders. Similar unusual traces appear with other tests in this series, and a large effort is currently underway to correct these problems, including the purchase of new equipment (specifically, a new current monitor for accurate current measurement). However, this series of materials tests does not rely heavily on these particular diagnostics, so the series was continued. The most significant diagnostic is the net discharge energy supplied by the capacitor bank, which is easily obtained by recording the net voltage drop of the bank. Recent tests on the SIRENS power delivery system have shown transmission line losses to be negligible, meaning that most (~98%) of the discharge energy is deposited in the arc in the source capillary. Improper function of the diagnostics means that information is lost regarding temporal discharge characteristics, such as plasma conductance, temperature history, and charge state, which are useful when developing models of the metal-vapor plasma.

Another measurement attempted during this test was the incident pressure upon the expansion chamber end-plate. The resulting trace is displayed in Figure 3.1.2. This particular trace appears believable, but other tests in the series in which a pressure measurement was attempted produced pressure traces that were extremely noisy. Various techniques for acquiring the pressure measurements are under investigation. The use of peizo-electric transducers in an electrical environment is very difficult due to the sensitivity of the charge generated in the peizo-crystal to stray EM fields. The SIRENS triggering system generates such fields and is likely the cause of this problem; other shielding configurations for this system are being investigated.

Following the shot, the buttons were removed and weighed to determine the amount of material deposited. These measurements are shown in Table 3.1.1. Small measured Δm's exist because of the large difference in collection area of the buttons and deposit area on the inner surface of the chamber (single button surface area / total chamber surface area = 0.007%). Also, the measurement resolution was on order of the measured value (Micro-balance measurements are good to 0.05 mg in the averaged quantity). A clearly increasing trend is seen in the data down the length of the chamber, while no definite trend is observed from the data on end-plate buttons.

Analysis for particle size distribution was performed using buttons 1, 6, 7, 9, 12, and 14. These buttons were chosen because they best represent the different locations for collection available in the expansion chamber. Images from the SEM were obtained and analyzed using the normal protocol. The images were not optimized to the highest quality for analysis due to lack of experience in obtaining appropriate SEM operating parameters. However the quality was sufficient to allow counting with some sacrifice in the minimum resolvable particle size due to necessary discrimination settings. SEM parameters requiring adjustment for image optimization are contrast and background levels, as well as SEM operation in secondary electron mode. Figure 3.1.3 shows representative SEM images of Button 9 from Cu Test #1. Stainless steel was used for button material in this test. Incorrect contrast and brightness levels allowed clear imaging of the grain boundaries. Presence of such distinct background features tends to interfere with the ability of the size analysis software to recognize individual particles. The problem is corrected by reducing the background brightness until the grain boundaries disappear from the image. Corresponding brightness reduction of imaged particles is countered by increasing the contrast level, enhancing the particles since they are of different composition than the substrate.

Figures 3.1.4-9 display the resulting particle size distributions obtained from this test. Included in each figure are analysis summary tables, data points, a straight line showing the best linear fit, and 95% confidence boundaries about the data.

Minimum equivalent diameter was used as the discrimination criteria because of its effect on image noise reduction.[6] This criteria requires that an object in the image must contain a certain number of pixels before it is counted as a particle. The empirical factor 3.25 was found to provide acceptable noise reduction and accurate sizing of the particles. A different factor (2.25) was used on tests later in the series because of significant improvement in image quality. Preliminary sensitivity studies have shown that factors below 2.25 do not affect the distributions representing the data in the high quality images.

Also shown in the summary tables are the Kruskal-Wallis (KW) statistical test results from the particle diameter data from each available magnification. The reported z-value is a root mean square variance test showing the relative discrepancy of each individual image data to the total group data for each magnification. Significant variation in data from one image indicates the non-compliance of that data to the hypothesis distribution. Another value from the K-W test is the significance probability, or p-value. This value is an overlay of a chi-square distribution on the hypothesis distribution for the total data population. A p-value of less than 0.05 (5%) indicates a large discrepancy within the population, requiring the elimination of one dataset (starting with the highest associated z-value) until the p-value rises above the 5% set-point. This entire process helps ensure the final combined distribution truly represents the underlying particle size population on the button.

Figure 3.1.1. Cu Test #1 voltage and current traces.

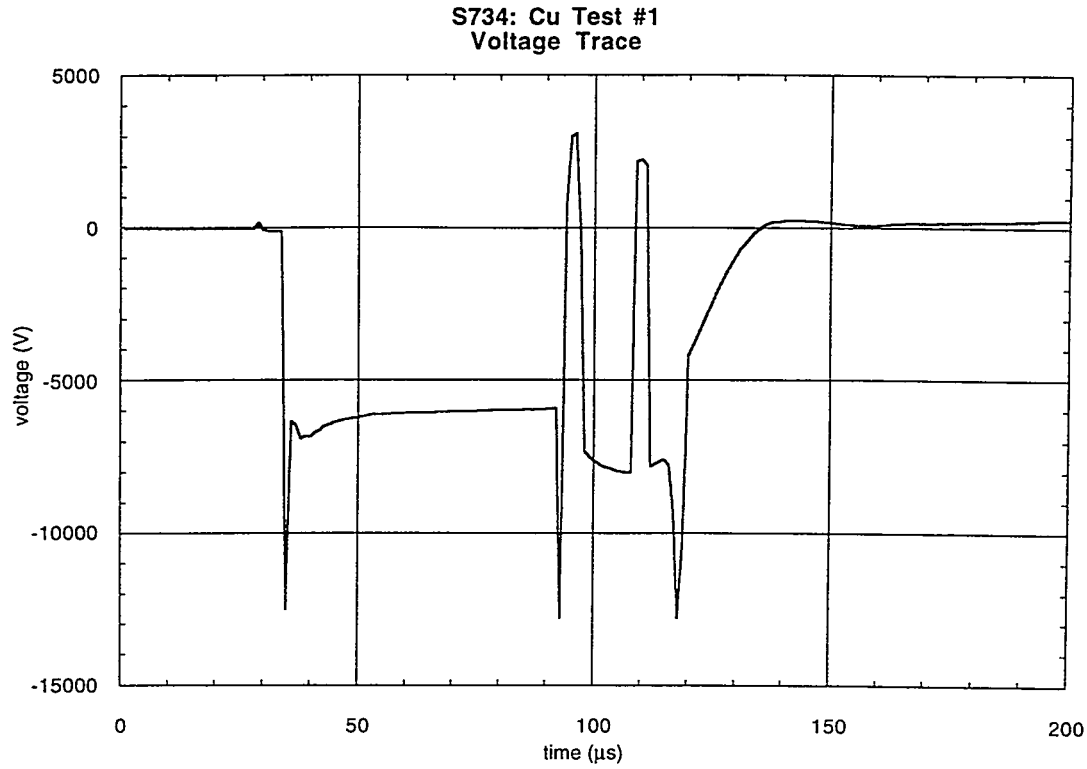

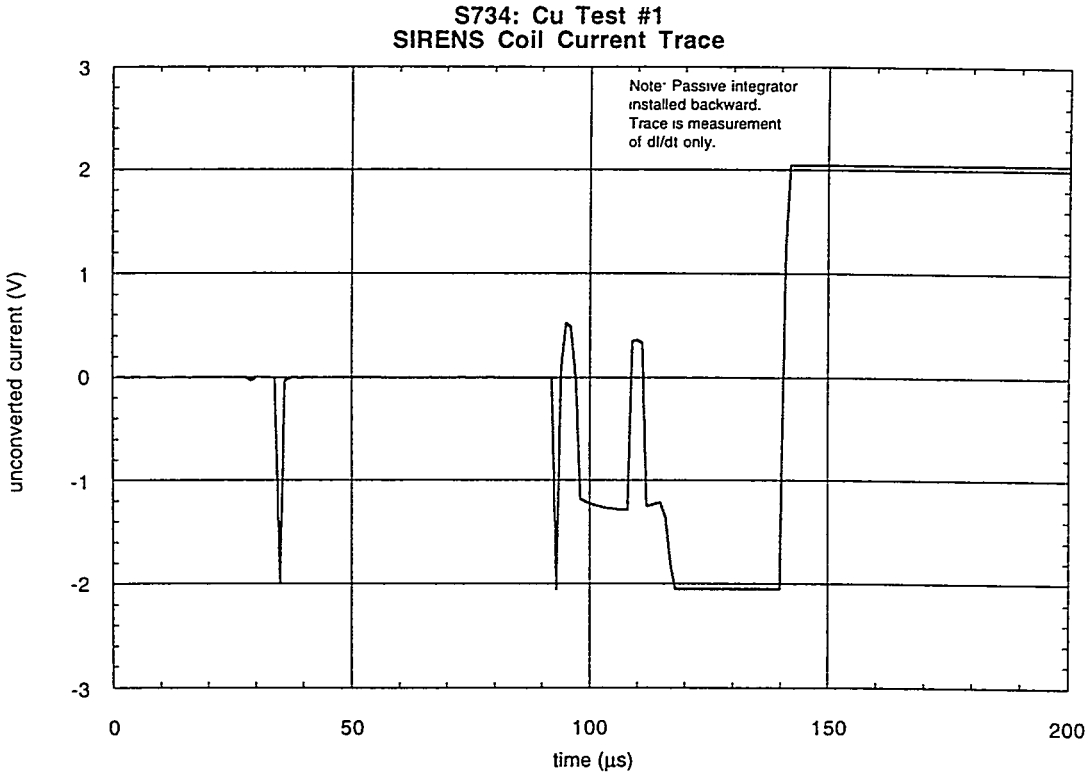

Figure 3.1.2. Cu Test #1 end-plate P transducer trace.

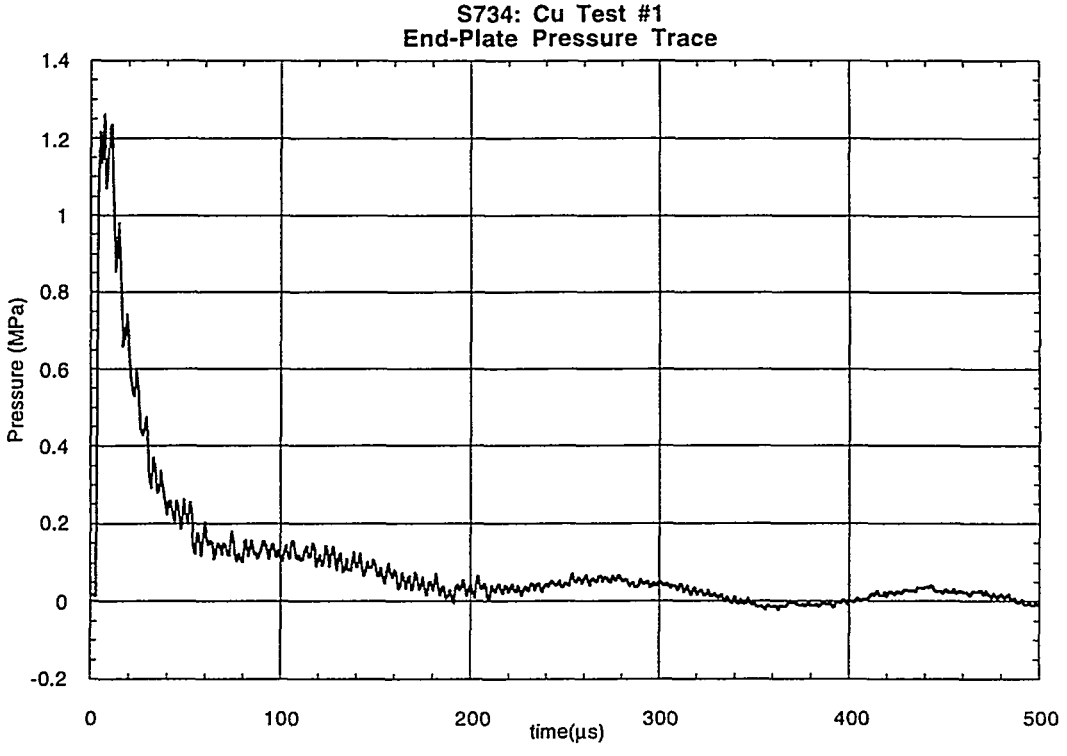

Table 3.1.1. S734 mass measurements.

Source Section Components: component	pre-test wt. (g)	post-test wt. (g)	Δ wt. (mg, ± 0.05)
short insulator	1.01902	-	-
long insulator	2.91962	-	-
cathode (dimetech)	9.14178	9.11092	30.86
Cu sleeve	14.62702	14.19034	436.67

Substrate Components: wall button	pre-test wt. (g)	post-test wt. (g)	Δ wt. (mg)	end-plate button	pre-test wt (g)	post-test wt. (g)	Δ wt. (mg)
1	0.58686	0.58695	0.09	9	0.58350	0.58365	0.15
2	0.58667	0.58672	0.05	10	0.58360	0.58379	0.18
3	0.58710	0.58713	0.03	11	0.58313	0.58381	0.68
4	0.58355	0.58375	0.20	12	0.58707	0.58735	0.28
5	0.58736	0.58780	0.43	13	0.58759	0.58776	0.17
6	0.58345	0.58384	0.39	14	0.58269	0.58277	0.08
7	0.58750	0.58765	0.15	15	0.58373	0.58412	0.39
8	0.58422	0.58461	0.39	16	0.58288	0.58311	0.23
				17	0.58320	0.58342	0.22

Notes:
(1) All weight measurements are taken 3+ times and averaged.
(2) Δm uncertainty is ± 0.05 mg.

Figure 3.1.3. SEM images from Cu Test #1 showing the distinct substrate grain boundaries which tend to interfere with image analysis.

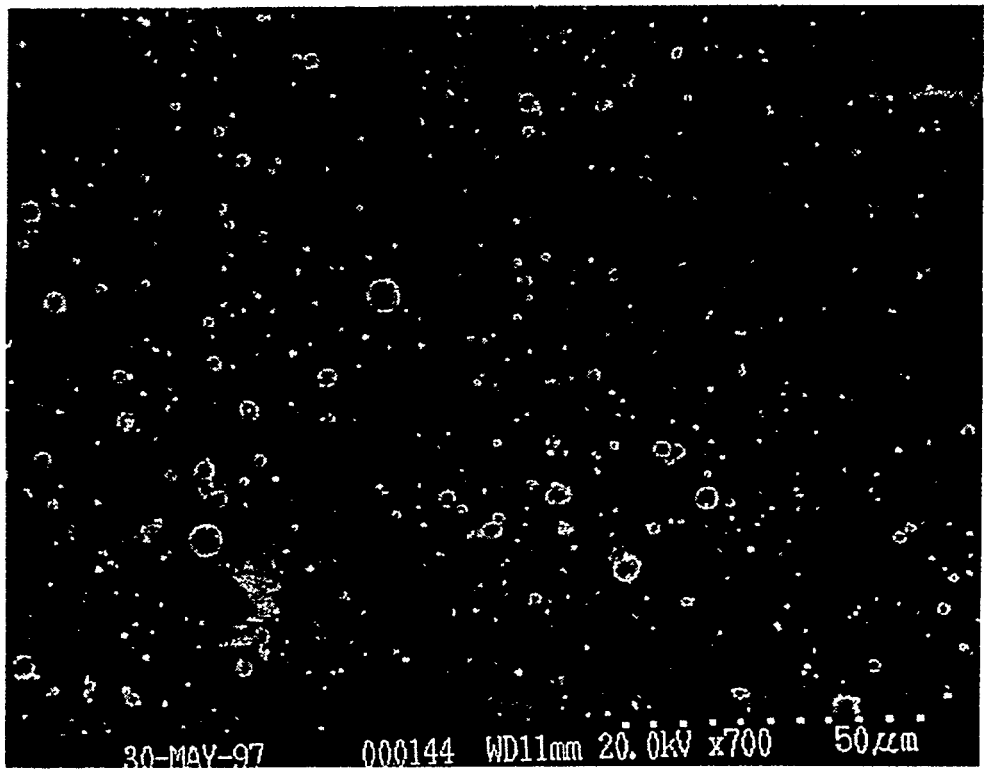

(a) location on Button 9 at 700x

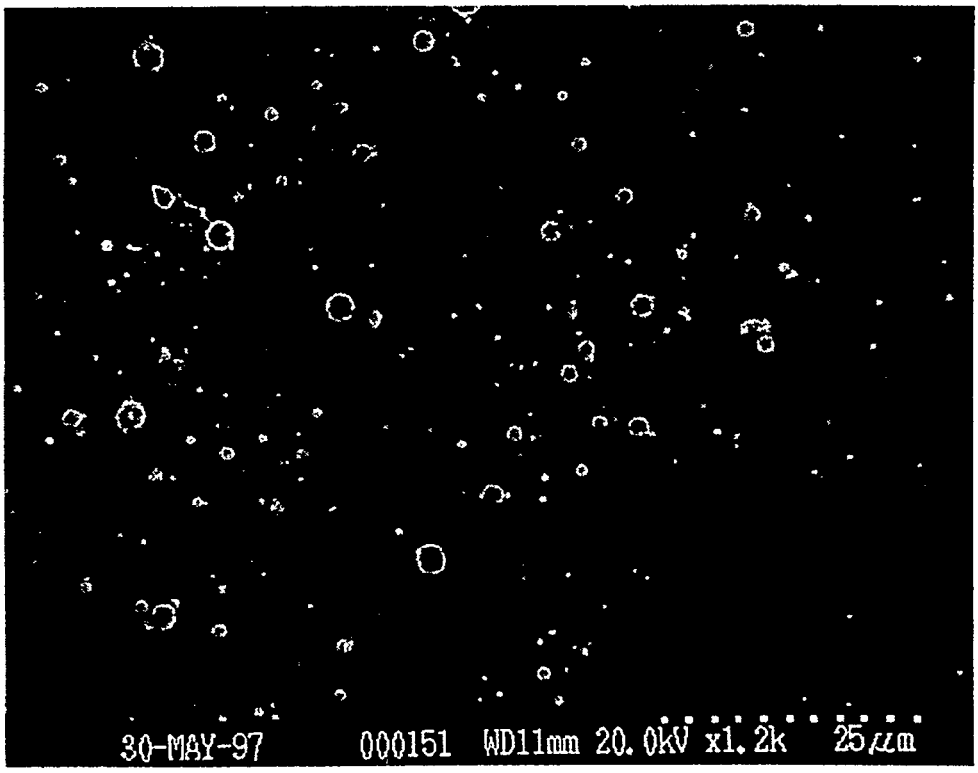

(b) different location on Button 9 at 1200x

Figure 3.1.4. Cu Test #1, Button 1 particle size distribution, with linear fit and 95% confidence intervals.

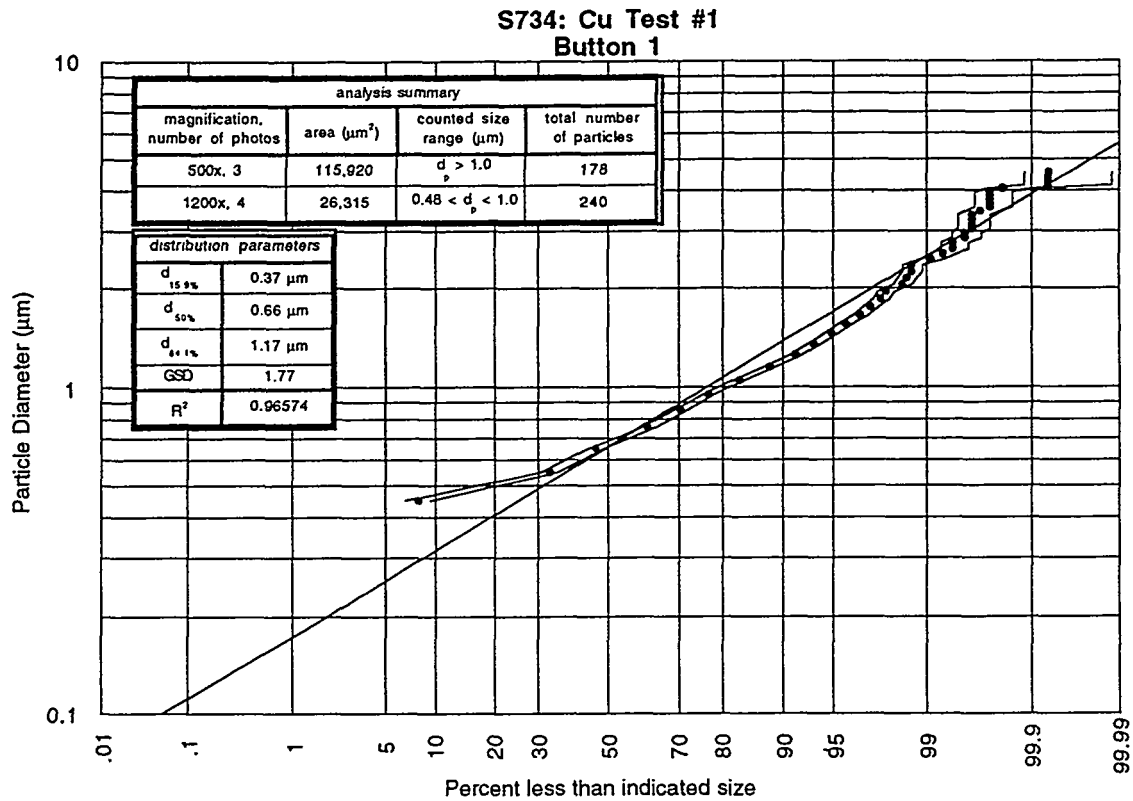

Data Summary Table:

photo	mag	scale (pixel/μm)	size (μm²)	min. d_{eq} (μm)*	# of particles	scale factor	KW Test z-value	Overall p-value
734_1_1	500x	2.82	230x168	1.15	50	1	0.37	0.109
734_1_2**	500x	2.82	230x167	1.15	-	-	-	
734_1_3	500x	2.82	230x170	1.15	57	1	1.71	
734_1_4	500x	2.82	230x166	1.15	71	1	-1.97	
734_1_5	1200x	6.8	95x70	0.48	75	5.76	1.11	0.321
734_1_6	1200x	6.8	95x69	0.48	55	5.76	0.22	
734_1_7	1200x	6.8	95x70	0.48	60	5.76	-1.81	
734_1_8	1200x	6.8	95x68	0.48	50	5.76	0.44	

* equivalent minimum diameter particle counted having an area of at least 3.25 x 1/scale on a side.
** image was of poor quality and not used for analysis

Figure 3.1.5. Cu Test #1, Button 6 particle size distribution, with linear fit and 95% confidence intervals.

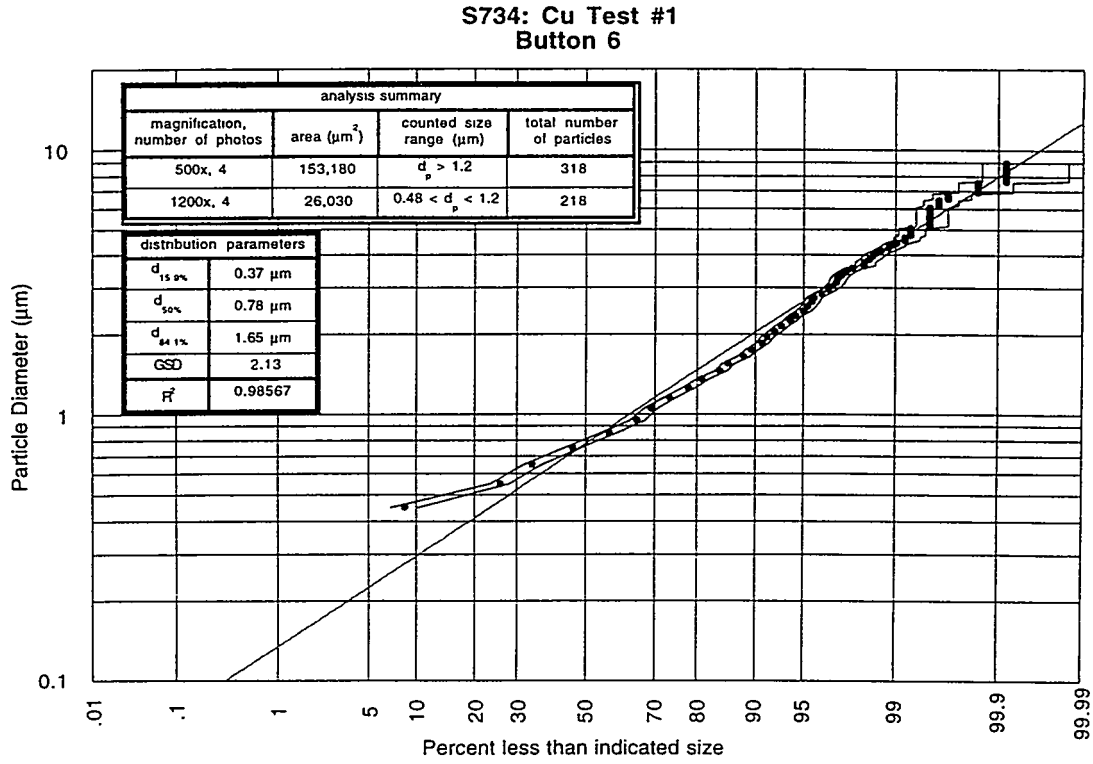

Data Summary Table:

photo	mag	scale (pixel/µm)	size (µm²)	min. d_{eq} (µm)*	# of particles	scale factor	KW Test z-value	Overall p-value
734_6_1	500x	2.82	230x163	1.15	85	1	-0.26	0.900
734_6_2	500x	2.82	230x167	1.15	79	1	0.75	
734_6_3	500x	2.82	230x167	1.15	82	1	-0.37	
734_6_4	500x	2.82	230x167	1.15	72	1	-0.11	
734_6_5	1200x	6.8	95x68	0.48	37	5.76	1.28	0.392
734_6_6	1200x	6.8	95x68	0.48	62	5.76	-0.10	
734_6_7	1200x	6.8	95x70	0.48	65	5.76	0.39	
734_6_8	1200x	6.8	95x68	0.48	54	5.76	-1.42	

* equivalent minimum diameter particle counted having an area of at least 3.25 x 1/scale on a side.

Figure 3.1.6. Cu Test #1, Button 7 particle size distribution, with linear fit and 95% confidence intervals.

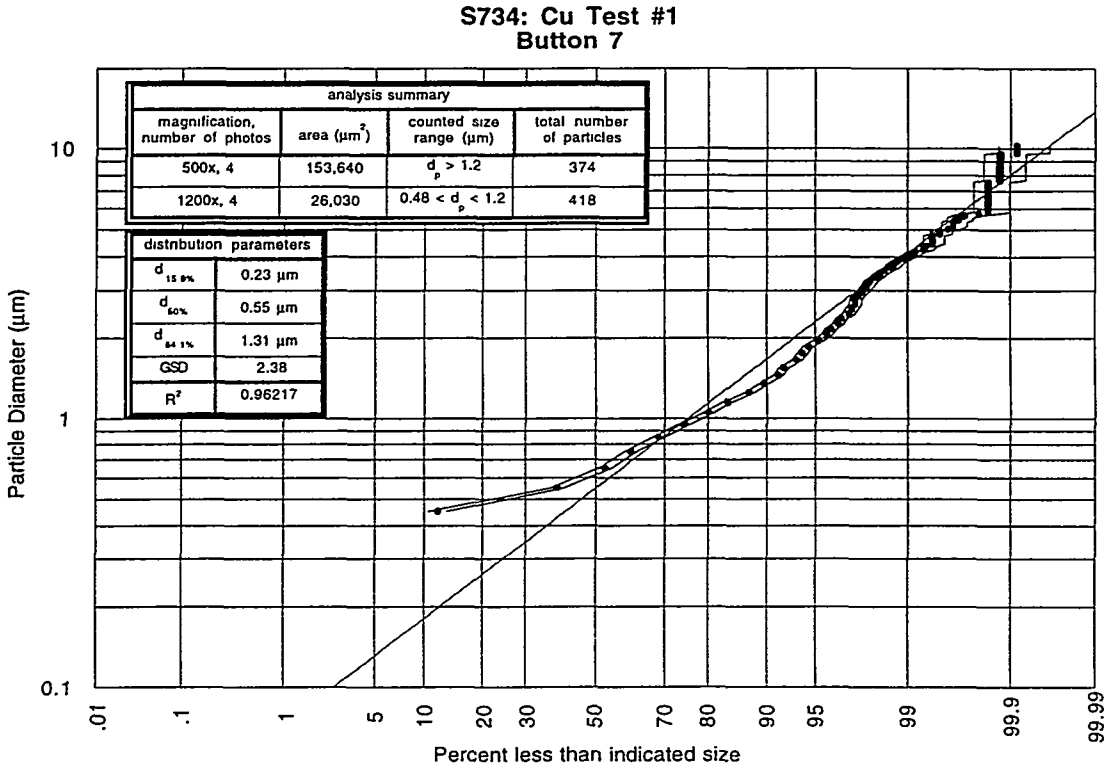

Data Summary Table:

photo	mag	scale (pixel/µm)	size (µm²)	min. d_{eq} (µm)*	# of particles	scale factor	KW Test z-value	Overall p-value
734_7_1	500x	2.82	230x166	1.15	75	1	1.09	0.335
734_7_2	500x	2.82	230x167	1.15	84	1	1.68	
734_7_3	500x	2.82	230x167	1.15	116	1	-0.57	
734_7_4	500x	2.82	230x168	1.15	99	1	-1.67	
734_7_5	1200x	6.8	95x68	0.48	82	5.76	0.33	0.535
734_7_6	1200x	6.8	95x68	0.48	130	5.76	-0.45	
734_7_7	1200x	6.8	95x69	0.48	117	5.76	1.18	
734_7_8	1200x	6.8	95x69	0.48	89	5.76	-1.10	

* equivalent minimum diameter particle counted having an area of at least 3.25 x 1/scale on a side.

Figure 3.1.7. Cu Test #1, Button 9 particle size distribution, with linear fit and 95% confidence intervals.

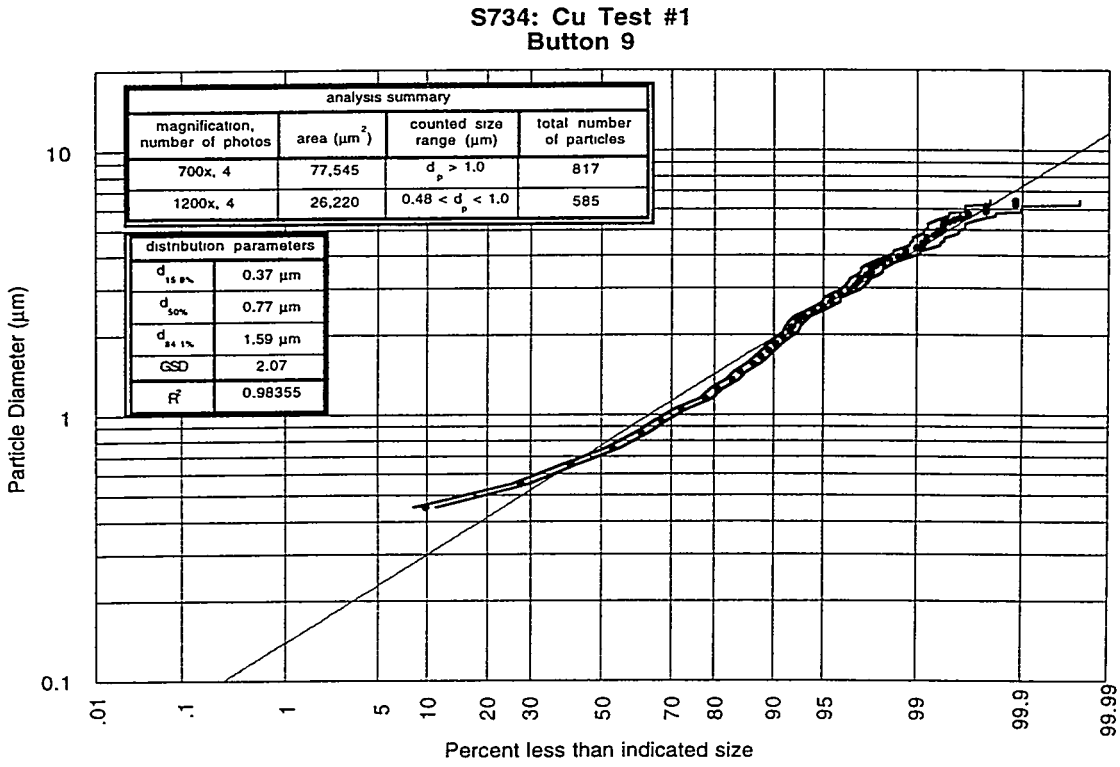

Data Summary Table:

photo	mag	scale (pixel/µm)	size (µm²)	min. d_{eq} (µm)*	# of particles	scale factor	KW Test z-value	Overall p-value
734_9_1	700x	3.96	163x119	0.82	163	1	-1.81	0.051
734_9_2	700x	3.96	164x120	0.82	227	1	0.67	
734_9_3	700x	3.69	163x117	0.82	212	1	2.23	
734_9_4	700x	3.96	163x119	0.82	215	1	-1.26	
734_9_5	1200x	6.8	95x69	0.48	134	2.939	-0.13	0.932
734_9_6	1200x	6.8	95x70	0.48	152	2.939	-0.47	
734_9_7	1200x	6.8	95x69	0.48	154	2.939	0.02	
734_9_8	1200x	6.8	95x69	0.48	145	2.939	0.59	

* equivalent minimum diameter particle counted having an area of at least 3.25 x 1/scale on a side.

Figure 3.1.8. Cu Test #1, Button 12 particle size distribution, with linear fit and 95% confidence intervals.

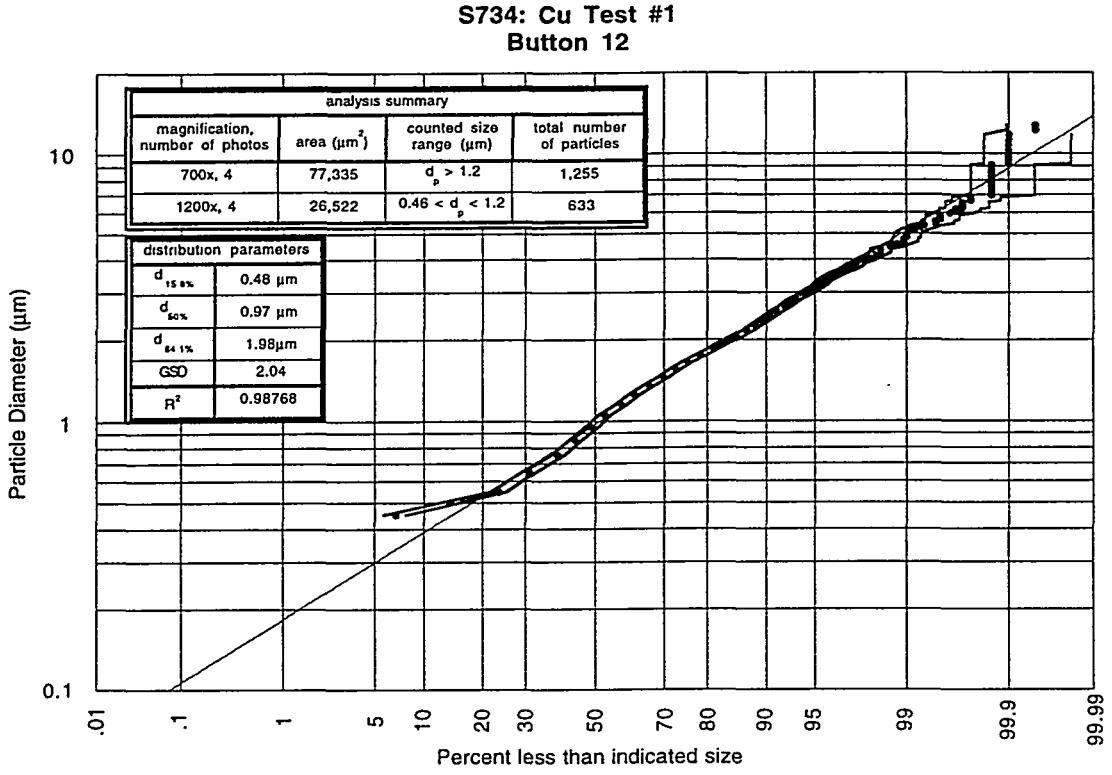

Data Summary Table:

photo	mag	scale (pixel/μm)	size (μm²)	min. d_{eq} (μm)*	# of particles	scale factor	KW Test z-value	Overall p-value
734_12_1	700x	4.14	163x117	0.79	331	1	0.99	0.550
734_12_2	700x	4.14	163x120	0.79	317	1	-1.10	
734_12_3	700x	4.14	164x119	0.79	297	1	-0.52	
734_12_4	700x	4.14	164x117	0.79	310	1	0.61	
734_12_5	1200x	7.08	96x69	0.46	171	2.939	-0.27	0.870
734_12_6	1200x	7.08	96x69	0.46	152	2.939	0.78	
734_12_7	1200x	7.08	96x69	0.46	152	2.939	0.03	
734_12_8	1200x	7.08	96x70	0.46	158	2.939	-0.51	

* equivalent minimum diameter particle counted having an area of at least 3.25 x 1/scale on a side.

Figure 3.1.9. Cu Test #1, Button 14 particle size distribution, with linear fit and 95% confidence intervals.

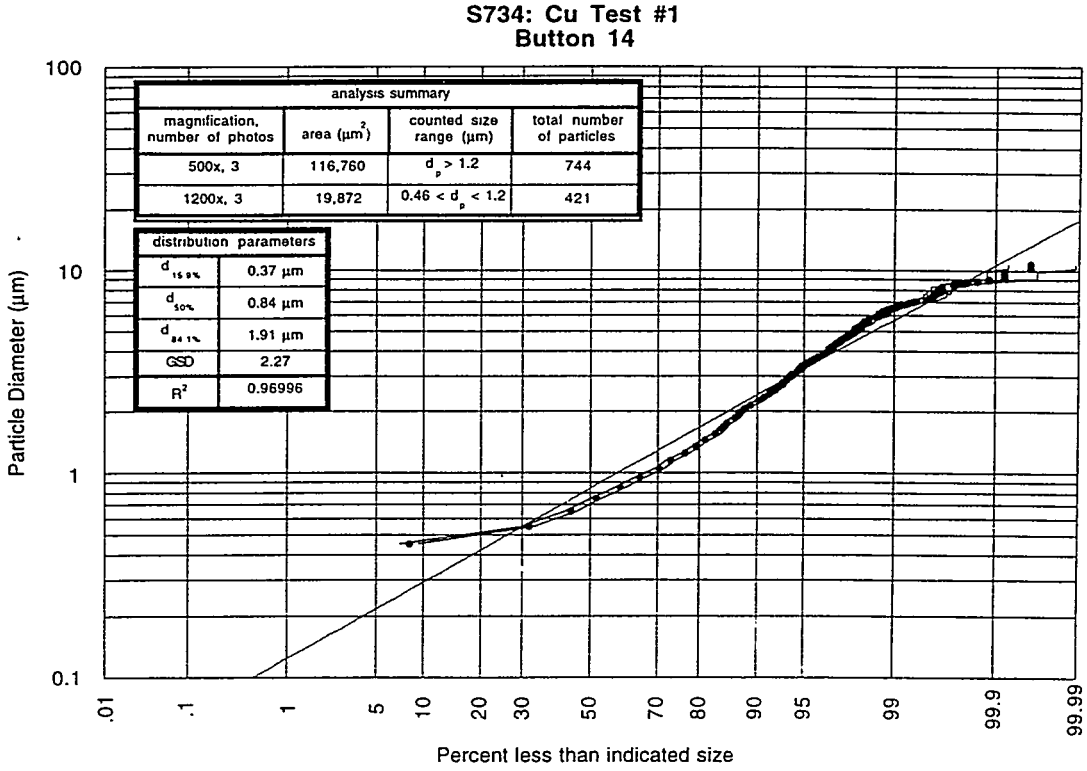

Data Summary Table:

photo	mag	scale (pixel/µm)	size (µm²)	min. d_{eq} (µm)*	# of particles	scale factor	KW Test z-value	Overall p-value
734_14_1	500x	2.93	232x167	1.11	200	1	0.36	0.873
734_14_2	500x	2.93	231x168	1.11	324	1	-0.51	
734_14_3	500x	2.93	232x169	1.11	220	1	0.21	
734_14_4	500x	2.93	232x168	1.11	209	1	failed	
734_14_5	1200x	7.08	96x69	0.46	144	5.76	0.60	0.682
734_14_6	1200x	7.08	96x69	0.46	123	5.76	0.28	
734_14_7	1200x	7.08	96x69	0.46	114	5.76	failed	
734_14_8	1200x	7.08	96x69	0.46	154	5.76	0.86	

* equivalent minimum diameter particle counted having an area of at least 3.25 x 1/scale on a side.

3.2. S737: Cu Test #2

A second copper test was performed to check consistency with the data obtained from the first test. This test was setup and performed in the same fashion as Cu Test #1, with the exception that the original source anode was replaced with the new anode containing a nozzle pressure tap. A Kistler 617C pressure transducer was inserted into the tap fitting, and the arrangement was tested by flowing compressed air through the source capillary. One other addition for this test was the installation of 0.1 mm diameter SS wire across the expansion chamber diameter, with the intent of capturing material (either particulate or vapor) using the wire as a single fiber filter. These wires were installed through holes drilled into the glass chamber at wall button locations, rotated around the chamber by 90°.

The shot was performed at a discharge energy of 4,458 J. This energy is slightly higher (~5%) than that of Cu Test #1 because the discharge did not occur at the original charging potential (5.2 kV). The discharge was successful at a charging potential of 5.32 kV; a higher voltage was required because this was the first shot attempted on the new anode section, which also has a slightly different geometry. Voltage and current traces for Cu Test #2 are displayed in Figure 3.2.1. A delay in the discharge is apparent in both traces (~250 μs). This delay possibly results from air contamination in the vacuum fill gas. The vacuum chamber was leaking slightly and the argon back-fill pressure was unsteady. Argon is necessary as the back-fill gas because it allows a discharge in the source section geometry at the charging voltage for the desired energy. Air requires a much larger charging voltage for breakdown (~6.5 kV). The discharge delay is of no consequence in this test series, and the presence of air at ~3 Torr is not expected to affect particulate formation mechanisms. The current trace for this test appears to have an incorrectly digitized magnitude because the normal calibrated Rogowski coil sensitivity factor (668.2 A/mV) gives unreasonably high current values (3.3 MA at 5000 mV). Because the sensitivity factor is in question, the trace is displayed in digitized value of mV rather than converted to Amps. A new scaling factor of 5.5 A/mV was found by matching integrated power to that measured for all shots in the test series, but this value is very different from that predicted by theory for the delay cable of 40 turns/inch from which the Rogowski coil was constructed (~650 A/mV). This large discrepancy is possibly attributable to EM interference across the digitizer channels. Although the scaled value of current traces given in this report are likely incorrect, the traces were included because they contain temporal information about the discharge.

Figure 3.2.2 shows the resulting measurements from the pressure transducers located at the source exit and at the chamber end plate. The signals appear to be only noise generated by the discharge EM pulse. Both transducers are strongly affected because of their close proximity to the discharge region. Transducer sensitivities set in corresponding charge amplifiers give unreasonable pressure magnitudes, and the time response displayed in the

signal does not follow that expected from a gas flow measurement. The pressure measurement experiment will be redesigned because of the importance of this diagnostic to future gas flow / condensation modeling attempts. Preliminary tests have shown that improved shielding of the transmission line and charge amplifiers tends to reduce interference. Care must also be taken to avoid grounding loops, to which these pressure transducers are particularly sensitive.

Resulting measurements of button weight increase following mass deposit are shown in Table 3.2.1. The average mass deposited on buttons on the end plate is greater than the average mass deposited on the wall. Buttons 7 and 8, on the chamber wall 70 cm from the source exit, had greater amounts of material deposition compared to other buttons on the chamber wall. Also, buttons located on the end plate at the largest available radial position showed larger amounts of mass deposited than buttons closer to the center. This general deposition pattern was also observed in Cu Test #1 (see Table 3.1.1).

Particulate collected on buttons 1, 6, 7, 9, 12, and 14 were imaged and analyzed using the normal protocol. Results are shown in Figures 3.2.3-8. The images obtained for this analysis were optimized for the counting procedure, and the equivalent minimum diameter discrimination factor was set to 2.25. The $d_{50\%}$ and GSD's for Cu Test #2 are generally smaller and larger, respectively, than those from Cu Test #1 because the improved image quality allowed accurate counting of the smaller particles. The goodness-of-fit parameter R^2 is also closer to 1.0 for Cu Test #2, indicating a stronger linear correlation in the associated data. However, both Cu tests show that particle sizes are generally in the range of $0.1\ \mu m < d_p < \sim 5\ \mu m$.

The SEM facility used to generate the images used for this and other tests includes an x-ray detector for energy-dispersive x-ray analysis (EDXA). Use of the EDXA instrument allows particle composition to be determined. Two regions on button 9 were analyzed, and the resulting spectra are shown in Figure 3.2.9. Region (a) was a location devoid of copper particles; the resulting spectra gives confirmation as only the elements associated with SS316 produced x-ray peaks. Elemental peak ratios from the analysis of k-shell x-rays are Fe @ 72.69%, Ni @ 11.42%, and Cr @ 15.89%, corresponding roughly to the known composition of SS316 (Fe @ 61.9 - 68.9%, Ni @ 10 - 14%, and Cr @ 16 - 18%). Region (b) on the button contained a single Cu particle ~1.2 μm in diameter. The x-ray spot was placed over the particle, and the resulting spectra (Figure 3.2.9 (b)) shows strong Cu peaks (k-shell peak ratio for Cu is 88.6%). The other, small peaks result from electron scatter from the source into the surrounding substrate. From this the particle is shown to be copper. Other particles on this button were observed and also shown to be copper.

The final feature of this test is the collection wires placed across the width of chamber. None of the wires melted or broke, and significant deposits were observed (via optical microscope) on all wires. Characterizing the type of deposited material was difficult because a smooth coating of material seemed to have lumps of particles intermixed. A greater amount of material was deposited on the wires close to the source exit.

Figure 3.2.1. Cu Test #2 voltage and current traces.

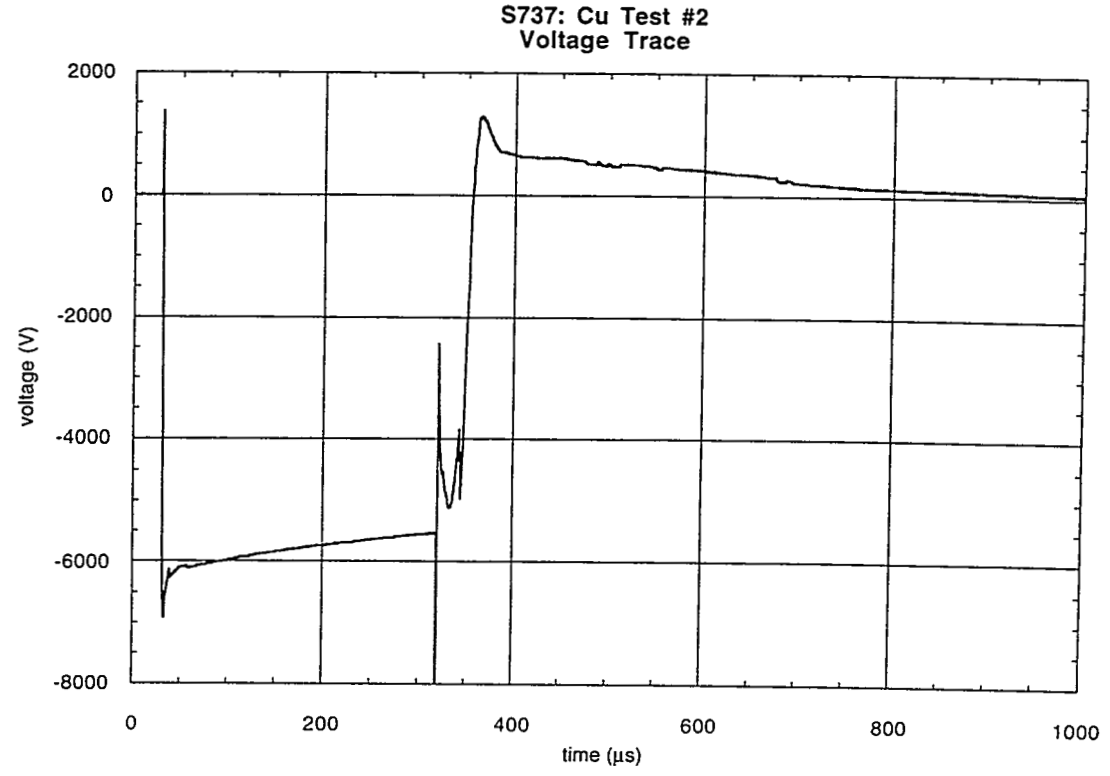

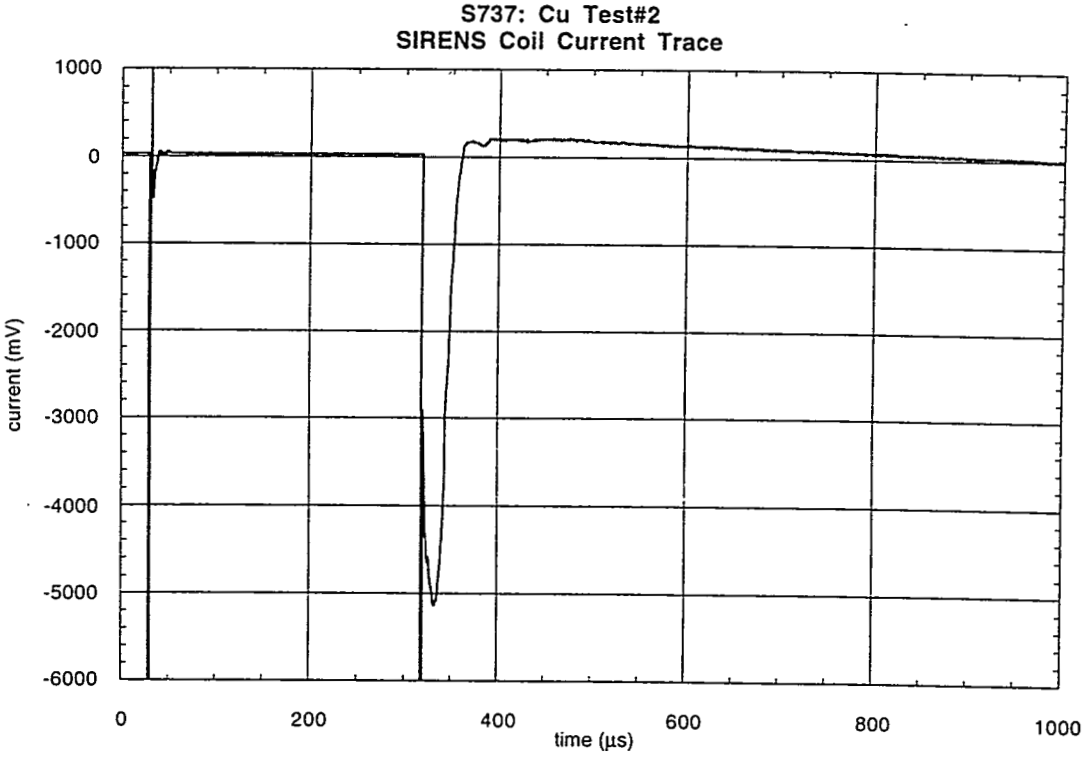

Figure 3.2.2. Cu Test #2 source and end-plate P transducer traces.

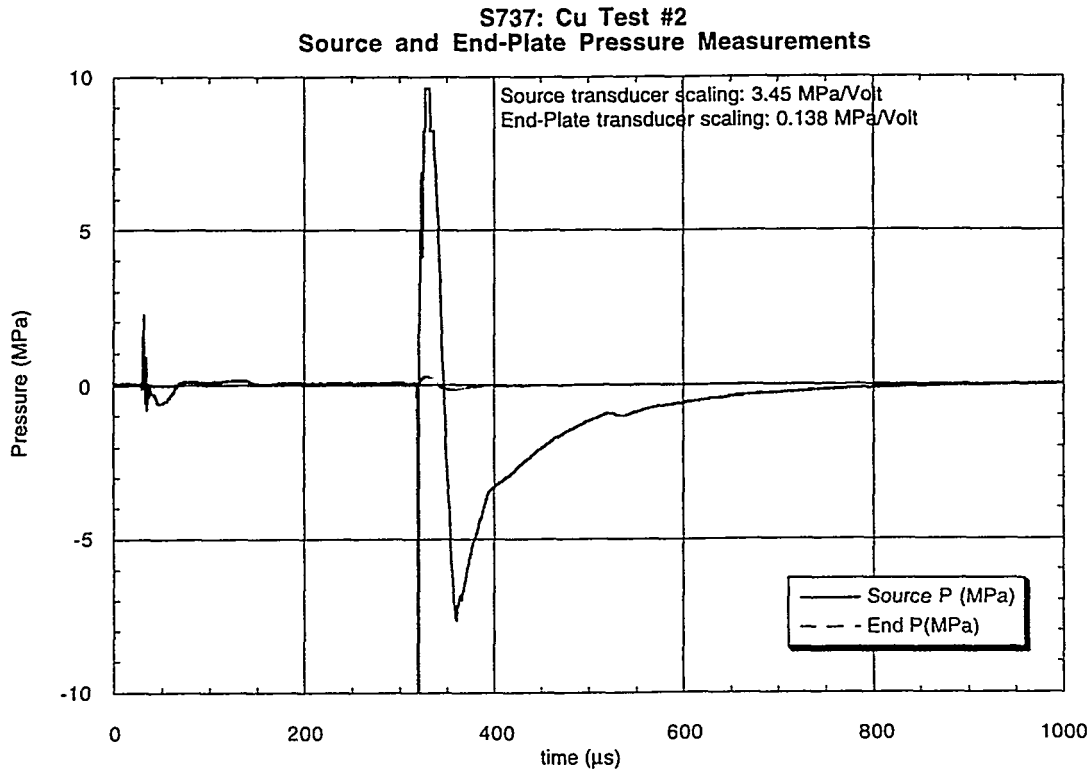

Table 3.2.1. S737 mass measurements.

Source Section Components: component	pre-test wt. (g)	post-test wt. (g)	Δ wt. (mg, ± 0.05)
short insulator	1.02568	-	-
long insulator	2.92292	-	-
cathode (dimetech)	9.07753	9.05108	26.45
Cu sleeve	14.60324	14.15211	451.13

Substrate Components: wall button	pre-test wt. (g)	post-test wt. (g)	Δ wt. (mg)	end-plate button	pre-test wt (g)	post-test wt. (g)	Δ wt. (mg)
1	0.58260	0.58271	0.11	9	0.58285	0.58326	0.41
2	0.58267	0.58279	0.12	10	0.58355	0.58400	0.44
3	0.58748	0.58754	0.06	11	0.58264	0.58339	0.76
4	0.58362	0.58377	0.15	12	0.58385	0.58437	0.52
5	0.58357	0.58368	0.11	13	0.58336	0.58369	0.33
6	0.58715	0.58728	0.13	14	0.58395	0.58422	0.28
7	0.58734	0.58759	0.25	15	0.58745	0.58813	0.67
8	0.58272	0.58301	0.29	16	0.58726	0.58768	0.42
				17	0.58244	0.58278	0.35

Notes:
(1) All weight measurements are taken 3+ times and averaged.
(2) Δm uncertainty is ± 0.05 mg.

Figure 3.2.3. Cu Test #2, Button 1 particle size distribution, with linear fit and 95% confidence intervals.

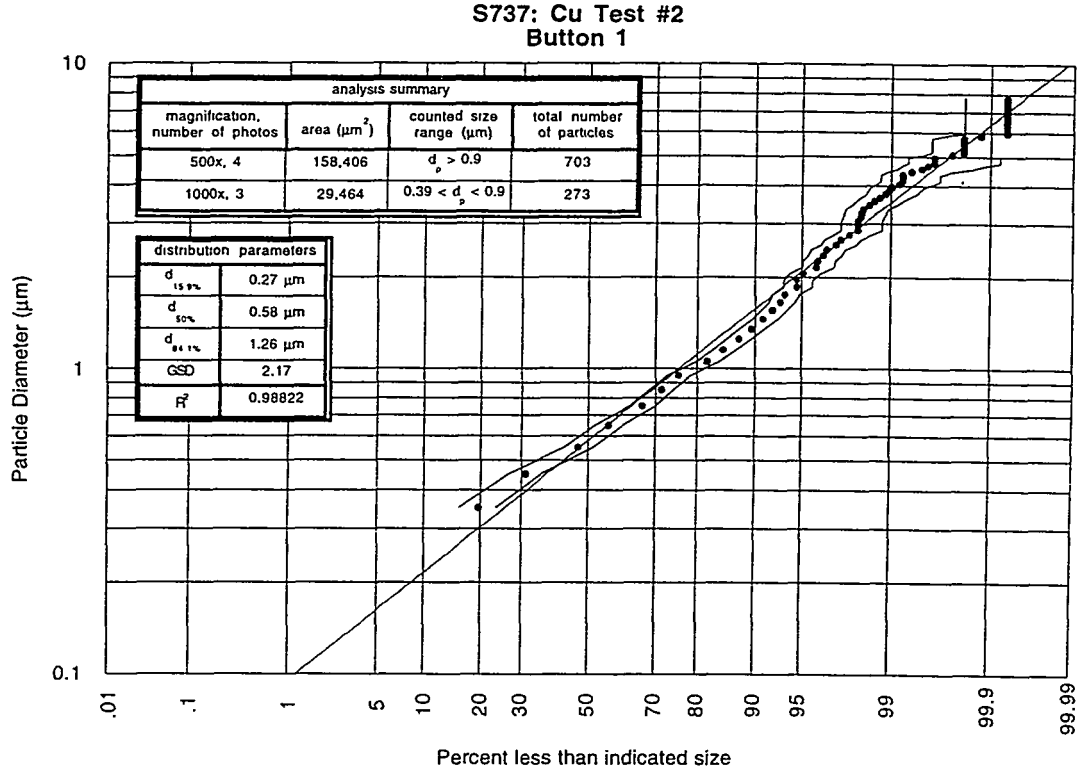

Data Summary Table:

photo	mag	scale (pixel/μm)	size (μm²)	min. d_{eq} (μm)*	# of particles	scale factor	KW Test z-value	Overall p-value
737_1_1	500x	2.92	231x170	0.77	171	1	0.73	0.630
737_1_2	500x	2.92	231x171	0.77	178	1	-1.27	
737_1_3	500x	2.92	231x173	0.77	173	1	0.23	
737_1_4	500x	2.92	232x171	0.77	181	1	0.31	
737_1_5	1000x	5.84	115x84	0.39	92	4	-1.35	0.242
737_1_6	1000x	5.84	116x85	0.39	79	4	1.51	
737_1_7	1000x	5.84	116x85	0.39	102	4	-0.09	

* equivalent minimum diameter particle counted having an area of at least 2.25 x 1/scale on a side.

Figure 3.2.4. Cu Test #2, Button 6 particle size distribution, with linear fit and 95% confidence intervals.

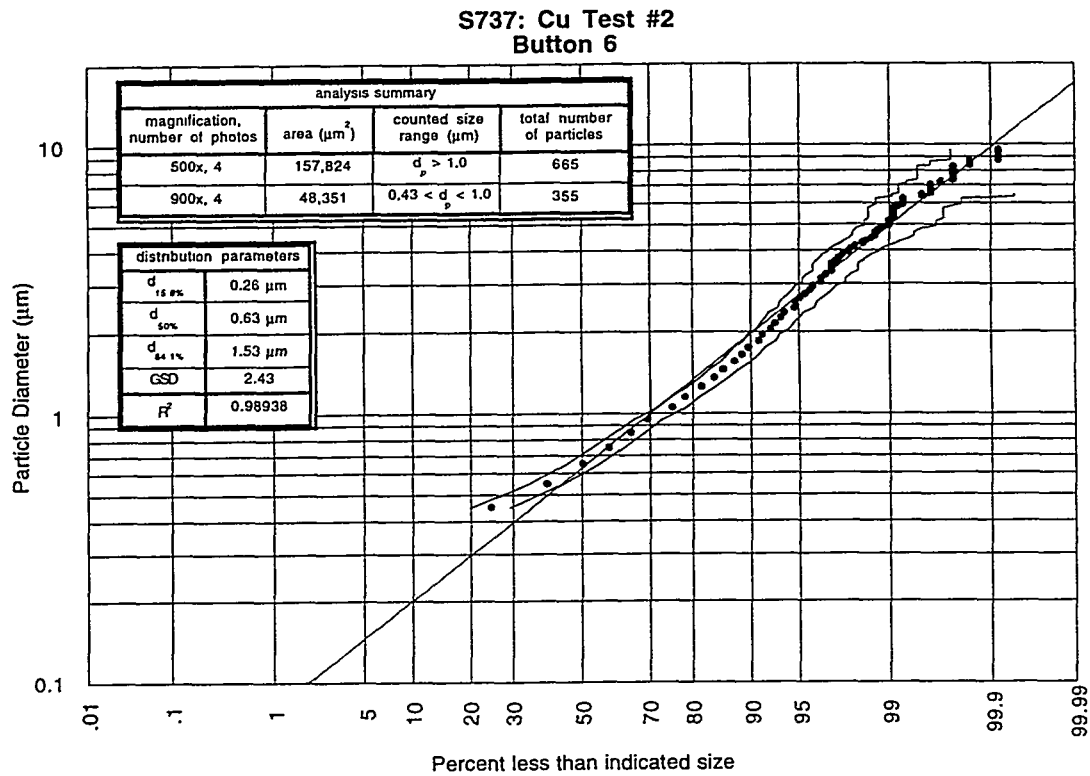

Data Summary Table:

photo	mag	scale (pixel/μm)	size (μm²)	min. d_{eq} (μm)*	# of particles	scale factor	KW Test z-value	Overall p-value
737_6_1	500x	2.92	233x170	0.77	172	1	0.02	0.230
737_6_2	500x	2.92	232x171	0.77	150	1	0.26	
737_6_3	500x	2.92	232x171	0.77	197	1	-1.74	
737_6_4	500x	2.92	230x169	0.77	146	1	1.64	
737_6_5	900x	5.26	129x94	0.43	87	3.24	1.67	0.063
737_6_6	900x	5.26	128x94	0.43	97	3.24	-2.14	
737_6_7	900x	5.26	128x94	0.43	89	3.24	-0.76	
737_6_8	900x	5.26	129x95	0.43	82	3.24	1.35	

* equivalent minimum diameter particle counted having an area of at least 2.25 x 1/scale on a side.

Figure 3.2.5. Cu Test #2, Button 7 particle size distribution, with linear fit and 95% confidence intervals.

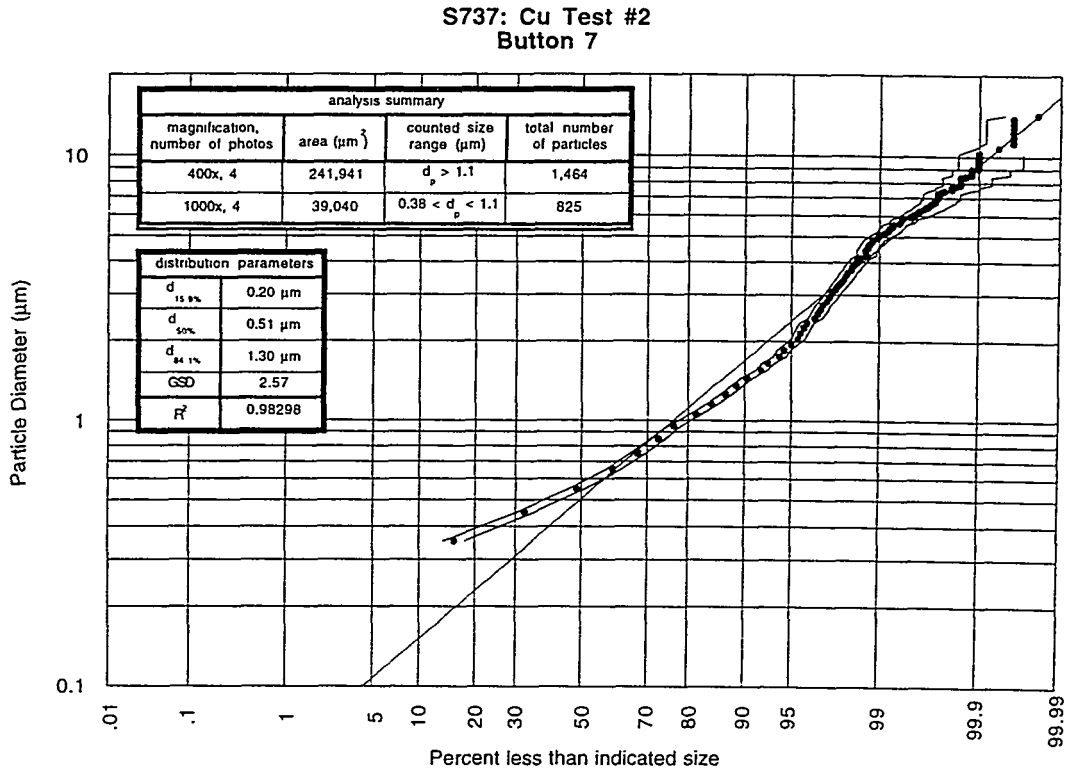

Data Summary Table:

photo	mag	scale (pixel/μm)	size (μm²)	min. d_{eq} (μm)*	# of particles	scale factor	KW Test z-value	Overall p-value
737_7_1	400x	2.35	287x212	0.96	397	1	-1.94	0.088
737_7_2	400x	2.35	287x212	0.96	320	1	-0.13	
737_7_3	400x	2.35	287x209	0.96	335	1	2.20	
737_7_4	400x	2.35	287x210	0.96	412	1	-0.02	
737_7_5	1000x	5.86	116x85	0.38	181	6.25	-1.37	0.479
737_7_6	1000x	5.86	115x84	0.38	193	6.25	-0.32	
737_7_7	1000x	5.86	116x85	0.38	188	6.25	0.87	
737_7_8	1000x	5.86	115x84	0.38	263	6.25	0.72	

* equivalent minimum diameter particle counted having an area of at least 2.25 x 1/scale on a side.

Figure 3.2.6. Cu Test #2, Button 9 particle size distribution, with linear fit and 95% confidence intervals.

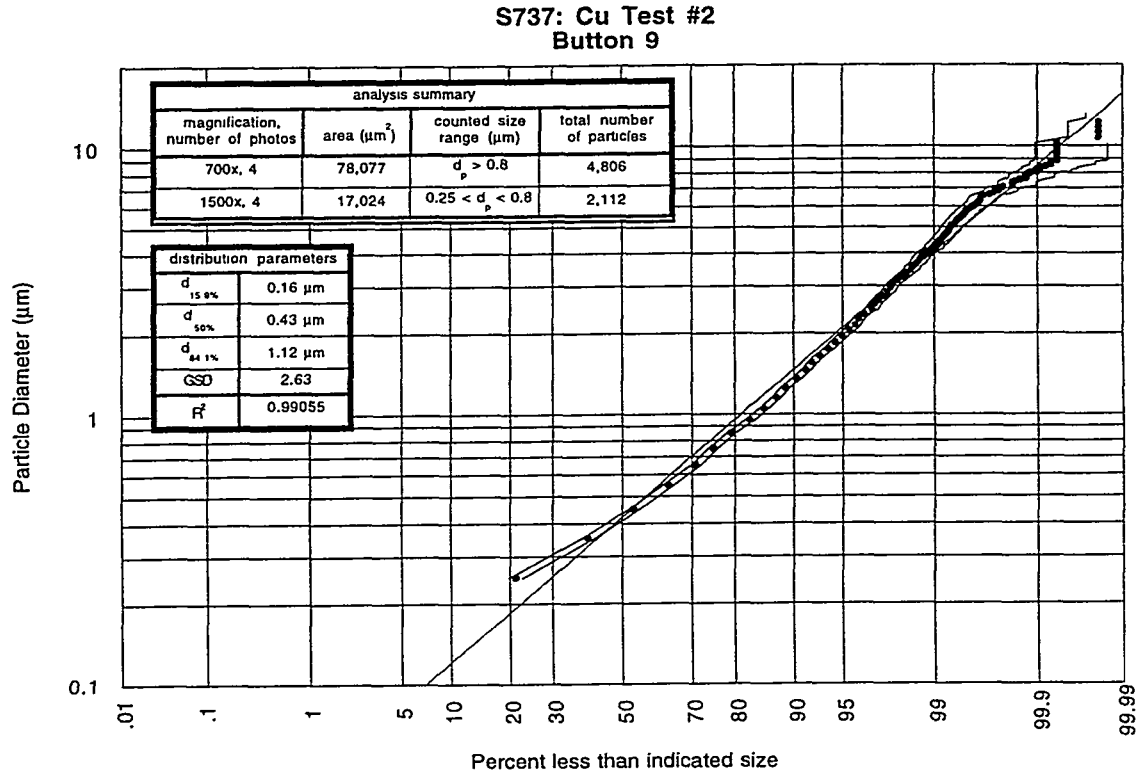

Data Summary Table:

photo	mag	scale (pixel/µm)	size (µm²)	min. d_{eq} (µm)*	# of particles	scale factor	KW Test z-value	Overall p-value
737_9_1	700x	4.14	163x120	0.54	1112	1	1.79	0.052
737_9_2	700x	4.14	163x120	0.54	1200	1	1.39	
737_9_3	700x	4.14	163x120	0.54	1139	1	-1.01	
737_9_4	700x	4.14	163x119	0.54	1355	1	-2.05	
737_9_5	1500x	8.9	76x56	0.25	574	4.59	-0.77	0.801
737_9_6	1500x	8.9	76x56	0.25	471	4.59	0.85	
737_9_7	1500x	8.9	76x56	0.25	550	4.59	0.08	
737_9_8	1500x	8.9	76x56	0.25	517	4.59	-0.11	

* equivalent minimum diameter particle counted having an area of at least 2.25 x 1/scale on a side.

Figure 3.2.7. Cu Test #2, Button 12 particle size distribution, with linear fit and 95% confidence intervals.

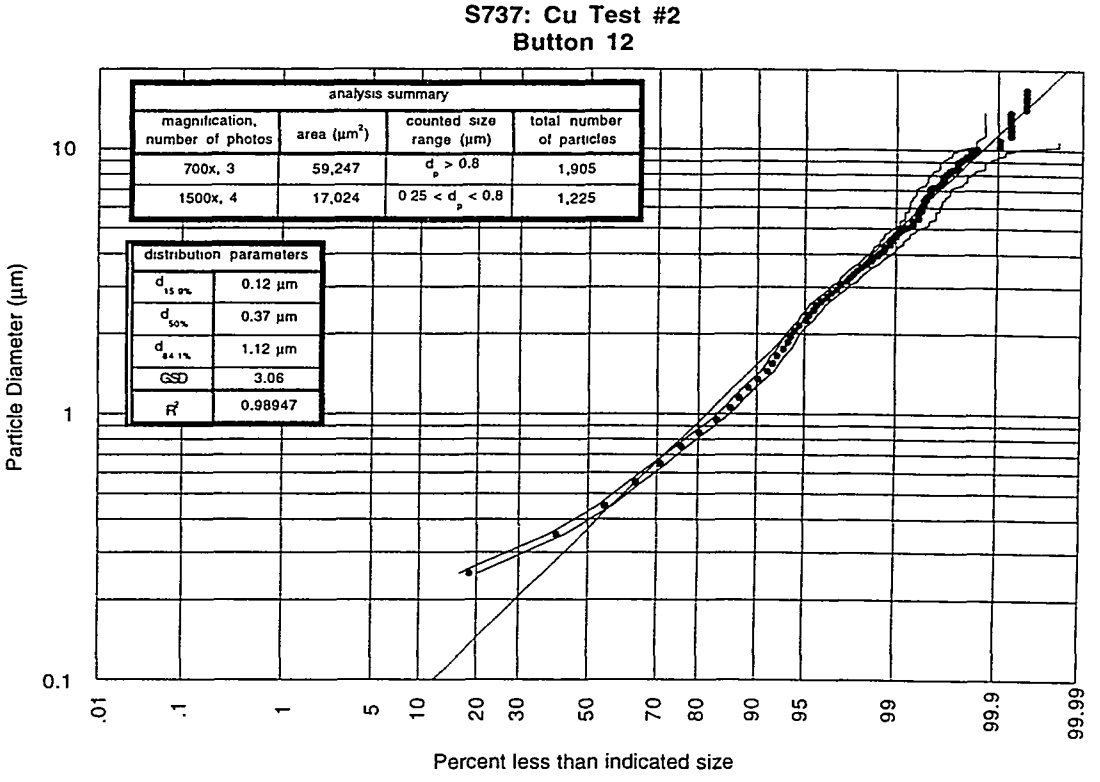

Data Summary Table:

photo	mag	scale (pixel/µm)	size (µm²)	min. d_{eq} (µm)*	# of particles	scale factor	KW Test z-value	Overall p-value
737_12_1	700x	4.14	164x121	0.54	675	1	-1.54	0.104
737_12_2	700x	4.14	164x120	0.54	638	1	-0.43	
737_12_3	700x	4.14	163x121	0.54	589	1	2.04	
737_12_4	700x	4.14	164x120	0.54	-	-	failed	
737_12_5	1500x	8.9	76x56	0.25	272	4.59	-0.70	0.552
737_12_6	1500x	8.9	76x56	0.25	313	4.59	-0.71	
737_12_7	1500x	8.9	76x56	0.25	328	4.59	1.35	
737_12_8	1500x	8.9	76x56	0.25	312	4.59	0.00	

* equivalent minimum diameter particle counted having an area of at least 2.25 x 1/scale on a side.

Figure 3.2.8. Cu Test #2, Button 14 particle size distribution, with linear fit and 95% confidence intervals.

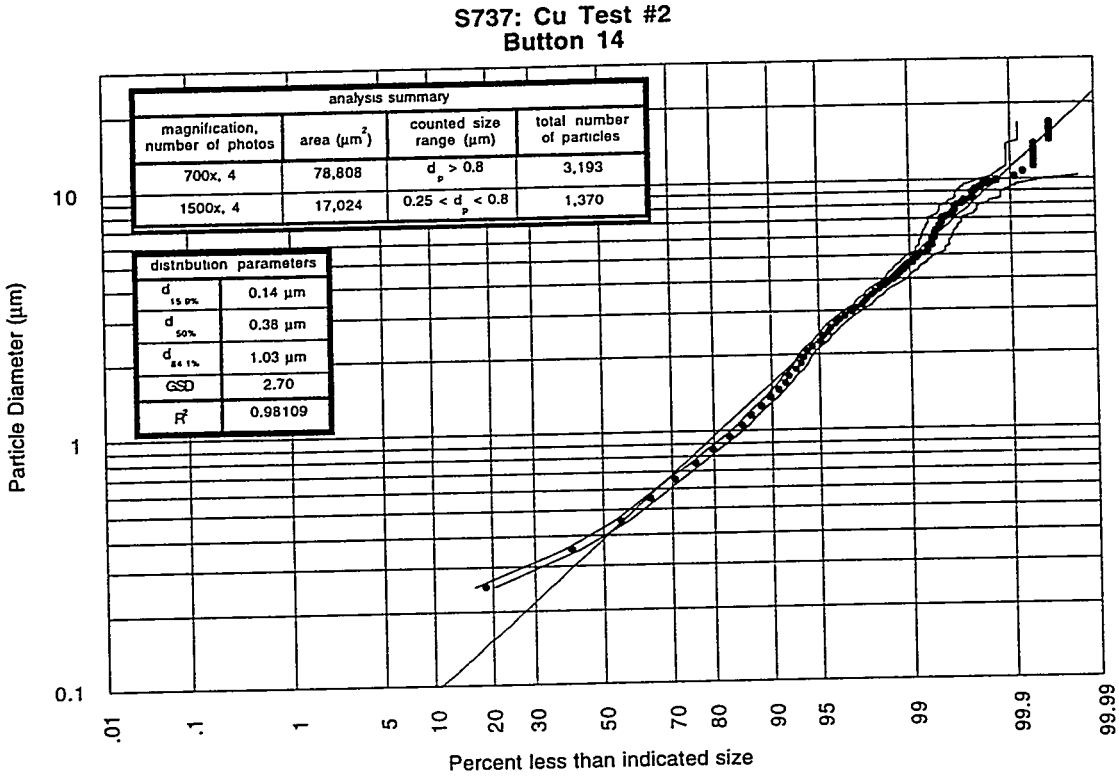

Data Summary Table:

photo	mag	scale (pixel/μm)	size (μm²)	min. d_{eq} (μm)*	# of particles	scale factor	KW Test z-value	Overall p-value
737_14_1	700x	4.14	163x120	0.54	731	1	-0.10	0.118
737_14_2	700x	4.14	164x121	0.54	965	-	-0.30	
737_14_3	700x	4.14	163x120	0.54	769	1	-1.70	
737_14_4	700x	4.14	164x121	0.54	728	1	2.16	
737_14_5	1500x	8.9	76x56	0.25	342	4.59	0.41	0.942
737_14_6	1500x	8.9	76x56	0.25	308	4.59	-0.53	
737_14_7	1500x	8.9	76x56	0.25	321	4.59	-0.15	
737_14_8	1500x	8.9	76x56	0.25	399	4.59	0.23	

* equivalent minimum diameter particle counted having an area of at least 2.25 x 1/scale on a side.

Figure 3.2.9. EDXA spectra from 2 different regions on Button 9 in Cu Test #2. Region (a).

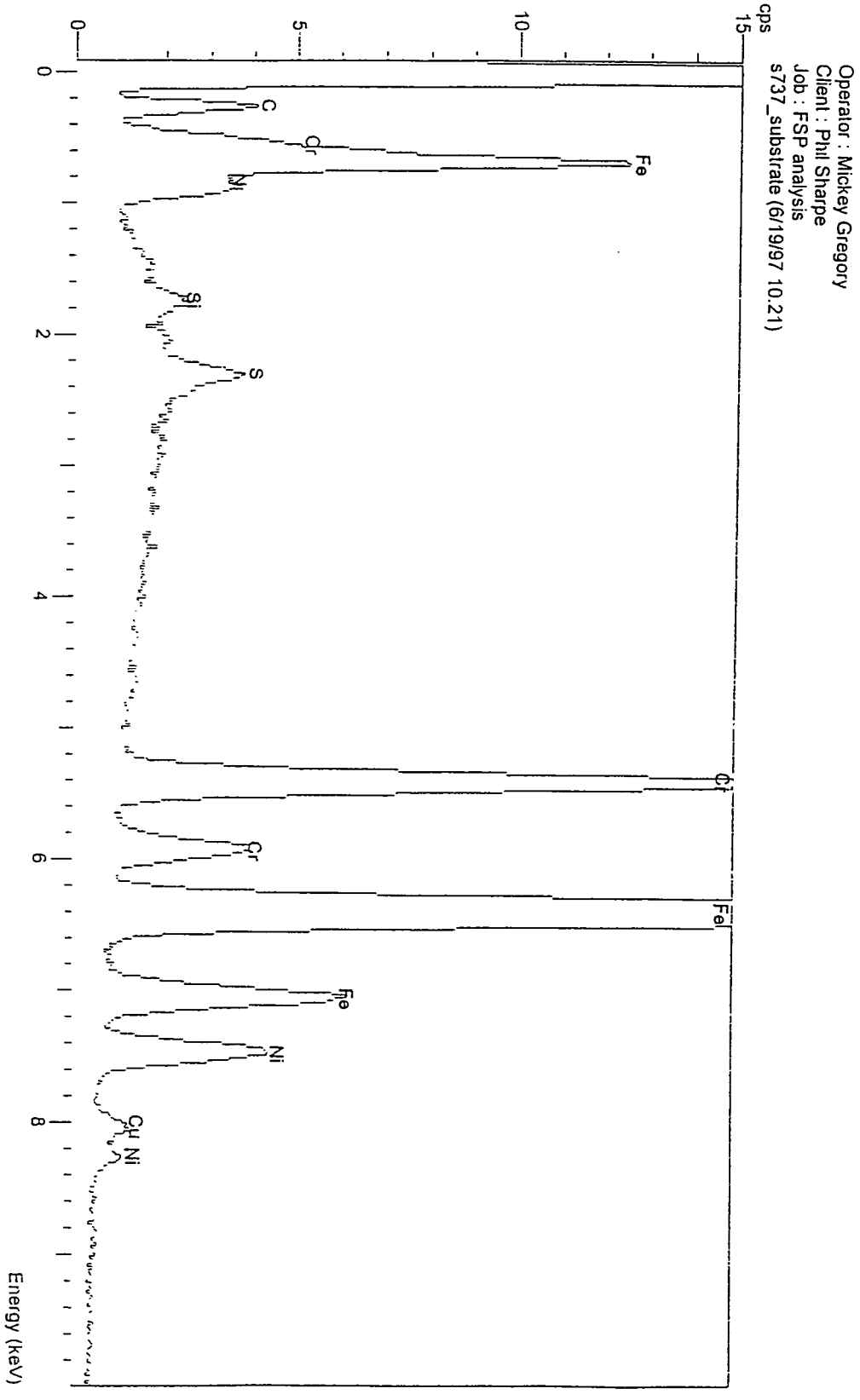

Figure 3.2.9.continued.

Region (b).

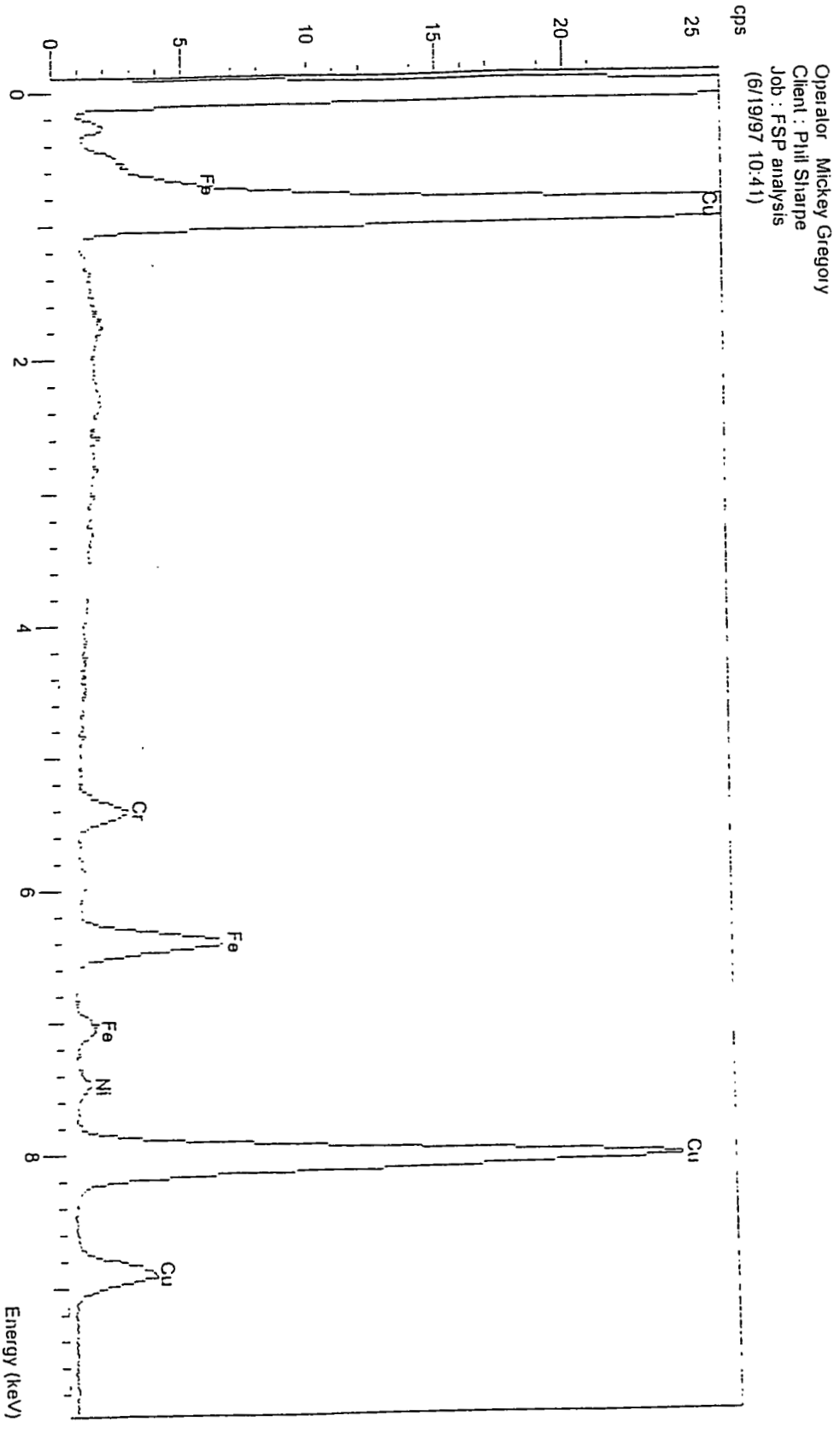

4.0 Stainless Steel 316 Test Results

Stainless steel 316 (SS316) was another ITER relevant material examined in the SIRENS high heat flux facility. Two separate tests were performed using SS316 test sleeves in the SIRENS source section; the tests were designated S735 and S738. Table 4.0.1 displays a summary of mass loss data and particulate size distributions from the two SS316 tests. Sample mass loss was consistent for shots performed at nearly equivalent energy levels, although cathode mass loss was different by a factor of 2. Particulate size distributions for buttons at the same location for the two different tests are generally consistent, all having $d_{50\%} < \sim 1.3$ μm.

Table 4.0.1 SS316 tests comparison summary.

	SS316 Test 1 (S735)				SS316 Test 2 (S738)			
Energy (J)	4259				4260			
Sample Δm (mg)	349.93				367.61			
Cathode Δm (mg)	12.38				21.57			
	Δm (mg)	$d_{50\%}$ (μm)	GSD	R^2	Δm (mg)	$d_{50\%}$ (μm)	GSD	R^2
Button 1	0.05	0.45	1.78	0.955	0.12	0.45	1.94	0.986
Button 2	0.03	*	*	*	0.12	*	*	*
Button 3	0.14	*	*	*	0.07	*	*	*
Button 4	0.15	*	*	*	0.12	*	*	*
Button 5	0.07	*	*	*	0.12	*	*	*
Button 6	0.01	1.31	1.69	0.996	0.10	0.75	2.21	0.991
Button 7	0.42	0.84	2.14	0.992	0.15	1.46	2.10	0.994
Button 8	0.13	*	*	*	0.09	*	*	*
Button 9	0.28	0.92	1.78	0.984	0.24	0.618	2.27	0.993
Button 10	0.09	*	*	*	0.21	*	*	*
Button 11	0.19	*	*	*	0.16	*	*	*
Button 12	0.23	0.54	2.33	0.980	0.23	0.75	2.37	0.995
Button 13	0.10	*	*	*	0.16	*	*	*
Button 14	0.20	0.73	1.87	0.989	0.06	0.62	2.29	0.974
Button 15	0.34	*	*	*	0.45	*	*	*
Button 16	0.17	*	*	*	0.16	*	*	*
Button 17	0.18	*	*	*	0.31	*	*	*

Note: Asterisk (*) denotes analysis not performed.

4.1 S735: SS316 Test #1

The first SS316 test was performed with a discharge energy of 4,259 J. The source housing without the pressure fitting was used because the new housing was not yet available. Copper buttons were used as the particulate collection substrate in the expansion chamber, and they were distributed as described in Figure 2.2. Voltage and current traces are displayed in Figure 4.1.1. The high voltage probe was re-calibrated prior to this shot. Upon close evaluation of the two traces, the digitized signals have nearly equivalent time and magnitude responses. The measured peak voltage was ~ -10,000 V, but the charging potential was only -5,200 V. This is obviously wrong because the inductive load of the arc does not produce negative reactance at a level twice as high as the input voltage, especially given the associated current signal. These traces could be large noise levels generated by an EM pulse from the discharge, which inductively couples to the instrumentation channels. This problem is currently being investigated.

A pressure transducer was installed on the center of the end-plate for this test. The pressure signal from the previous Cu test had shown significant levels of noise. Changes in the pressure diagnostic for this test included connecting the pressure transducer to the charge amplifier with a double shielded cable and changing the sensitivity level on the charge amplifier to a lower level. The resulting trace is shown in Figure 4.1.2. The initial spike feature is noise from the discharge, but the feature at ~ 8 ms is possibly the arrival of a pressure wave at the end plate. Assuming this is the pressure wave associated with the shock front of the expanding metal vapor from the source section exit, the front propagation speed was ~100 m/s (recall the back-fill gas pressure roughly 2 Torr).

Button mass increase data are displayed in Table 4.1.1. An important observation regarding mass deposit on the buttons is that the leading edge of wall buttons, as well as the surface, were coated with material. The amount of mass deposited on each wall button was not exactly uniform across the button surface. It is impossible to determine what fraction was deposited on the top surface only. Also, the entire inner surface of the expansion chamber was coated with a thin layer of silver-gray colored material. An attempt was made to remove particulate from the glass surface using replicating tape. Analysis of this tape has not yet been successful.

Particulate size distributions obtained from SEM images of selected buttons (1, 6, 7, 9, 12, and 14) are displayed in Figures 4.1.3-8. All images were optimized for the counting procedure, and the minimum equivalent diameter factor was set to 2.25. Analysis summary tables are included in each figure. Figure 4.1.9 shows representative SEM images from Button 7 of this test.

Some interesting features were observed on the images. Buttons on the end plate contained extraordinary numbers of distinct particles. Several larger particles had smaller particles attached (~5-20% diameter of the large particle; for example, one particular particle ~6 μm in diameter on Button 14 had two satellites attached, one of 0.6 μm diameter and another of 1.0 μm diameter). The counting process does not distinguish different particles among these agglomerates. Another noted feature includes buttons located on the side wall contained several 'streakers' with tails all pointing in the same general direction. The tails were approximately 2.5 - 3 times as long as the particles were wide. This indicates the incident particle had a molten surface layer that froze as it was deposited along the surface. This feature was also observed with the Cu tests, but not to the same extent.

Figure 4.1.1. SS316 Test #1 voltage and current traces.

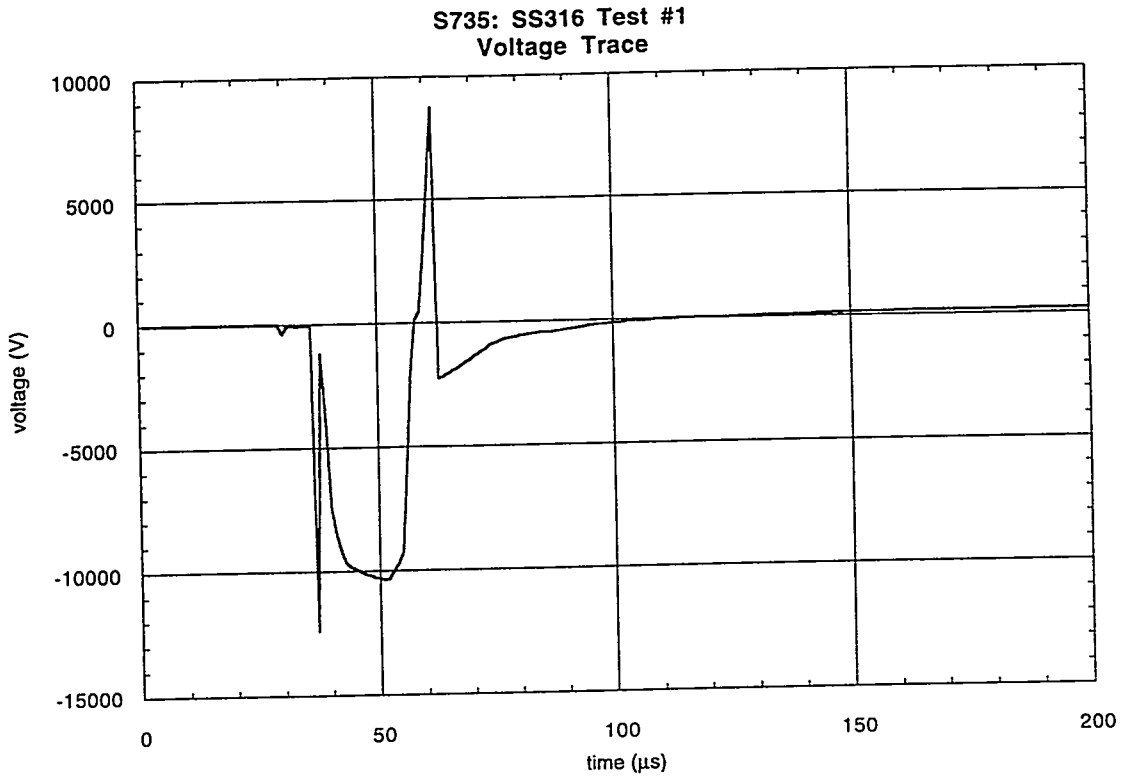

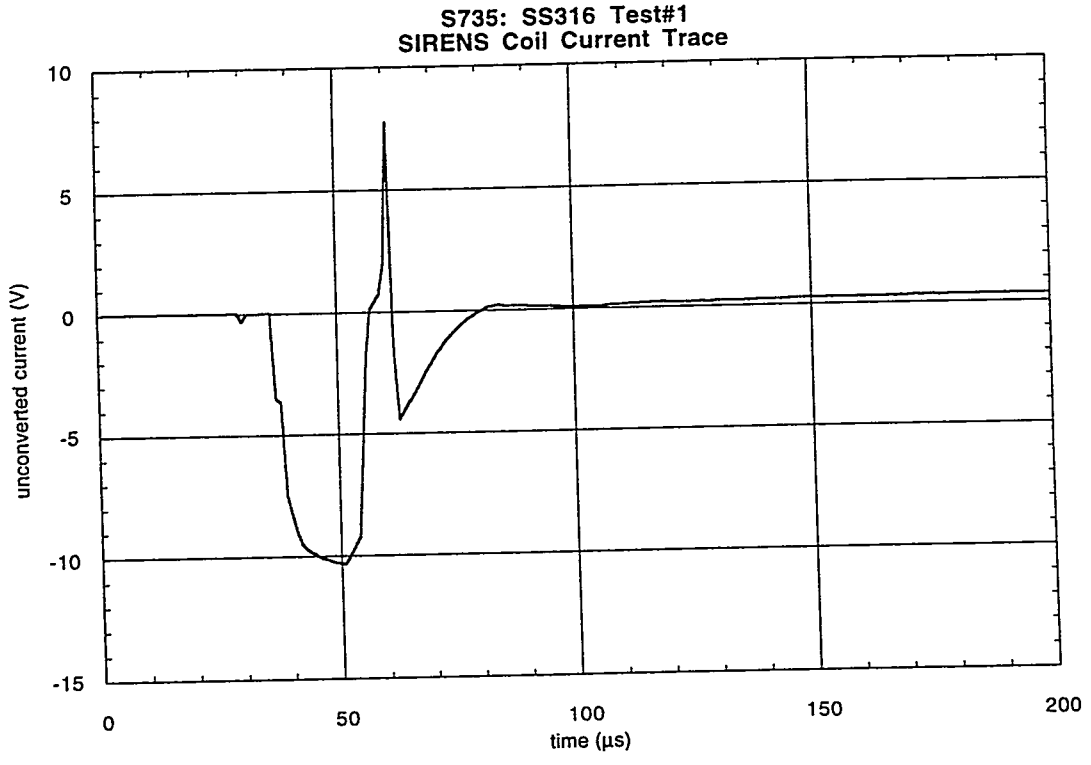

Figure 4.1.2. SS Test #1 end-plate P transducer trace.

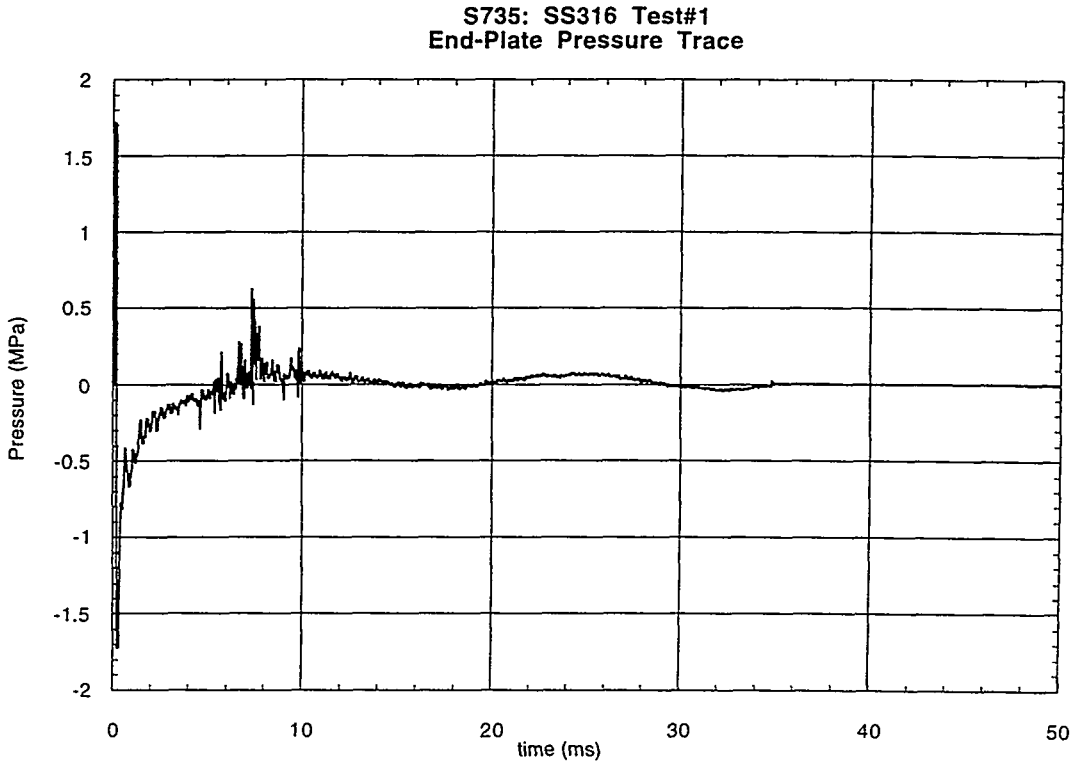

Table 4.1.1. S735 mass measurements.

Source Section Components: component	pre-test wt. (g)	post-test wt. (g)	Δ wt. (mg, ± 0.05)
short insulator	1.02244	-	-
long insulator	2.92527	-	-
cathode (dimetech)	9.11094	9.09856	12.38
SS316 sleeve	12.28635	11.93641	349.93

Substrate Components: wall button	pre-test wt. (g)	post-test wt. (g)	Δ wt. (mg)	end-plate button	pre-test wt (g)	post-test wt. (g)	Δ wt. (mg)
1	0.90458	0.90463	0.05	9	0.89931	0.89958	0.28
2	0.90557	0.90560	0.03	10	0.90351	0.90359	0.09
3	0.89782	0.89796	0.14	11	0.90687	0.90706	0.19
4	0.89954	0.89969	0.15	12	0.89970	0.89992	0.23
5	0.91348	0.91355	0.07	13	0.89489	0.89499	0.10
6	0.89779	0.89780	0.01	14	0.91374	0.91394	0.20
7	0.90872	0.90914	0.42	15	0.90244	0.90279	0.34
8	0.90929	0.90942	0.13	16	0.89757	0.89774	0.17
				17	0.90456	0.90473	0.18

Notes:
(1) All weight measurements are taken 3+ times and averaged.
(2) Δm uncertainty is ± 0.05 mg.

Figure 4.1.3. SS316 Test #1, Button 1 particle size distribution, with linear fit and 95% confidence intervals.

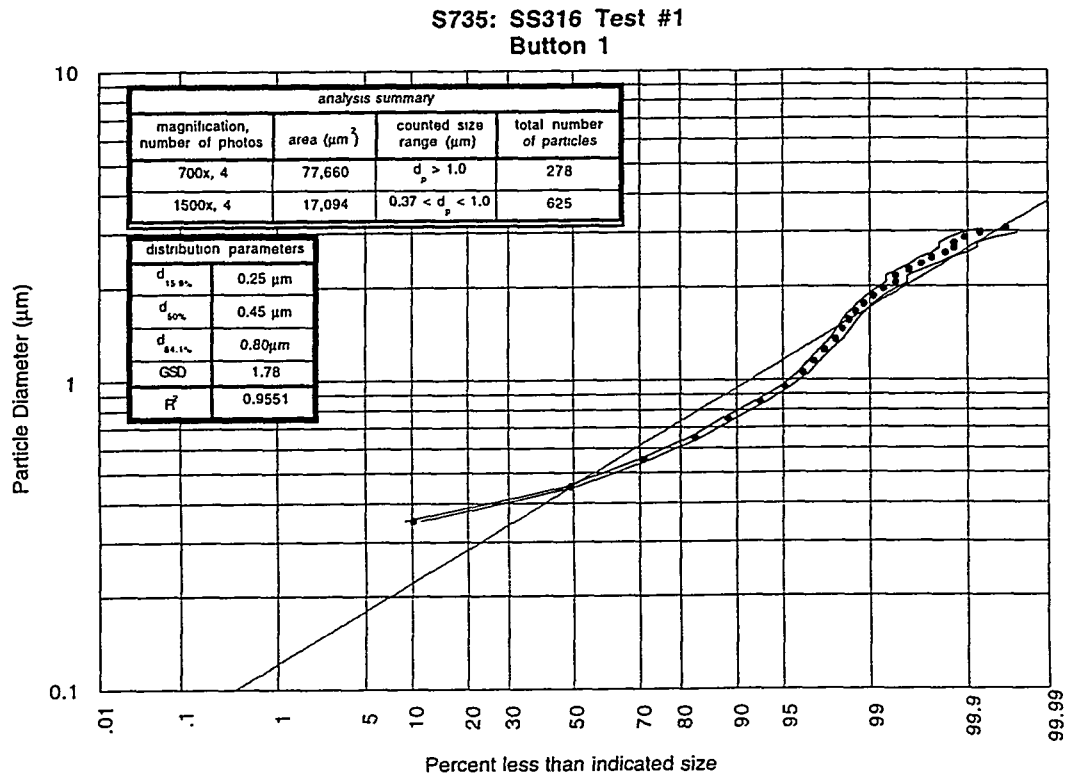

Data Summary Table:

photo	mag	scale (pixel/μm)	size (μm²)	min. d_{eq} (μm)*	# of particles	scale factor	KW Test z-value	Overall p-value
735_1_1	700x	4.14	164x119	0.79	58	1	0.77	0.555
735_1_2	700x	4.14	164x119	0.79	104	1	-1.41	
735_1_3	700x	4.14	1164x118	0.79	60	1	0.63	
735_1_4	700x	4.14	162x120	0.79	56	1	0.27	
735_1_5	1500x	8.85	77x56	0.37	115	4.592	0.97	0.248
735_1_6	1500x	8.85	77x56	0.37	133	4.592	-1.28	
735_1_7	1500x	8.85	77x55	0.37	102	4.592	1.44	
735_1_8	1500x	8.85	77x55	0.37	275	4.592	-0.78	

* equivalent minimum diameter particle counted having an area of at least 2.25 x 1/scale on a side.

Figure 4.1.4. SS316 Test #1, Button 6 particle size distribution, with linear fit and 95% confidence intervals.

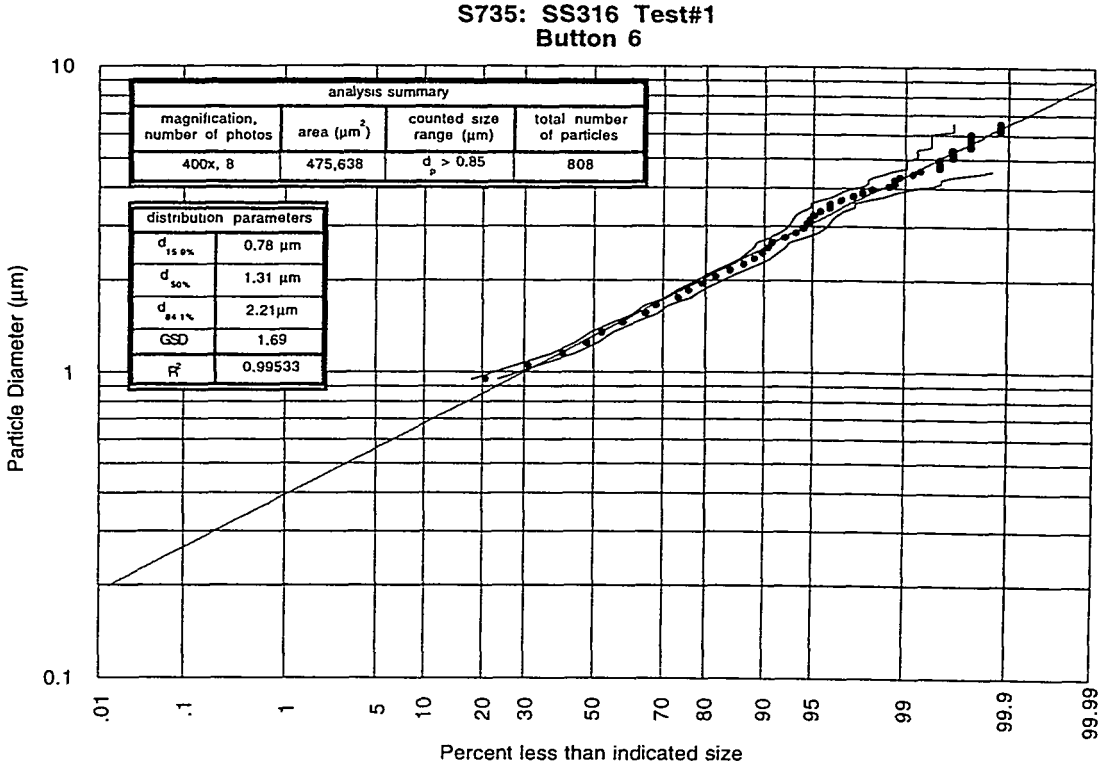

Data Summary Table:

photo	mag*	scale (pixel/µm)	size (µm²)	min. d_{eq} (µm)**	# of particles	scale factor	KW Test z-value	Overall p-value
735_6_1	400x	2.36	287x206	0.85	78	1	2.07	0.155
735_6_2	400x	2.36	286x207	0.85	90	1	1.97	
735_6_3	400x	2.36	289x207	0.85	127	1	-0.41	
735_6_4	400x	2.36	286x208	0.85	113	1	-1.48	
735_6_5	400x	2.36	286x208	0.85	81	1	0.04	
735_6_6	400x	2.36	286x207	0.85	121	1	-0.36	
735_6_7	400x	2.36	287x207	0.85	103	1	-0.28	
735_6_8	400x	2.36	288x208	0.85	95	1	-1.11	

* 400x was determined to be the only magnification necessary for this analysis because no particles of size smaller then min. d_{eq} were observed, even at higher magnifications.

** equivalent minimum diameter particle counted having an area of at least 2.25 x 1/scale on a side.

Figure 4.1.5. SS316 Test #1, Button 7 particle size distribution, with linear fit and 95% confidence intervals.

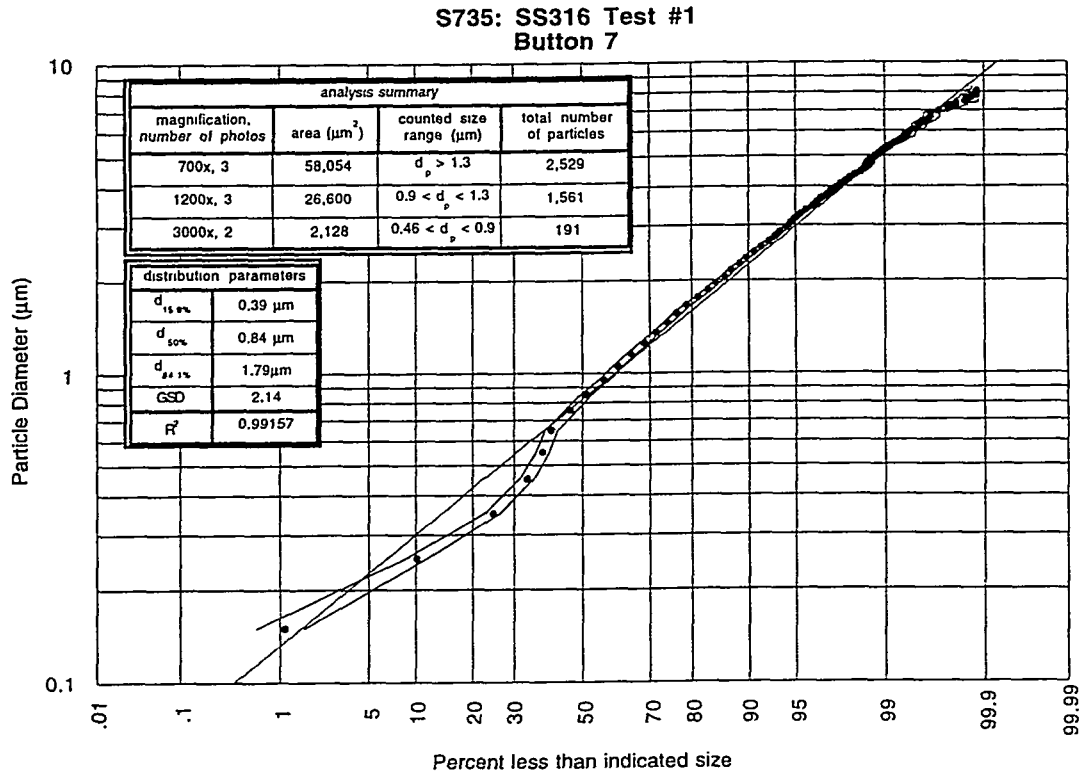

Data Summary Table:

photo	mag	scale (pixel/μm)	size (μm²)	min. d_{eq} (μm)*	# of particles	scale factor	KW Test z-value	Overall p-value
735_7_1	700x	4.14	164x118	0.79	958	1	-1.13	0.053
735_7_2	700x	4.14	163x118	0.79	-	-	failed	
735_7_3	700x	4.14	163x119	0.79	898	1	-1.09	
735_7_4	700x	4.14	165x117	0.79	673	1	2.43	
735_7_5	1200x	7.08	95x70	0.46	-	-	failed	0.168
735_7_6	1200x	7.08	95x70	0.46	447	2.939	-1.16	
735_7_7	1200x	7.08	95x70	0.46	441	2.939	-0.74	
735_7_8	1200x	7.08	95x70	0.46	470	2.939	1.88	
735_7_9	3000x	17.7	38x28	0.18	102	18.37	-0.15	0.878
735_7_10	3000x	17.7	38x28	0.18	89	18.37	0.15	

* equivalent minimum diameter particle counted having an area of at least 2.25 x 1/scale on a side.

Figure 4.1.6. SS316 Test #1, Button 9 particle size distribution, with linear fit and 95% confidence intervals.

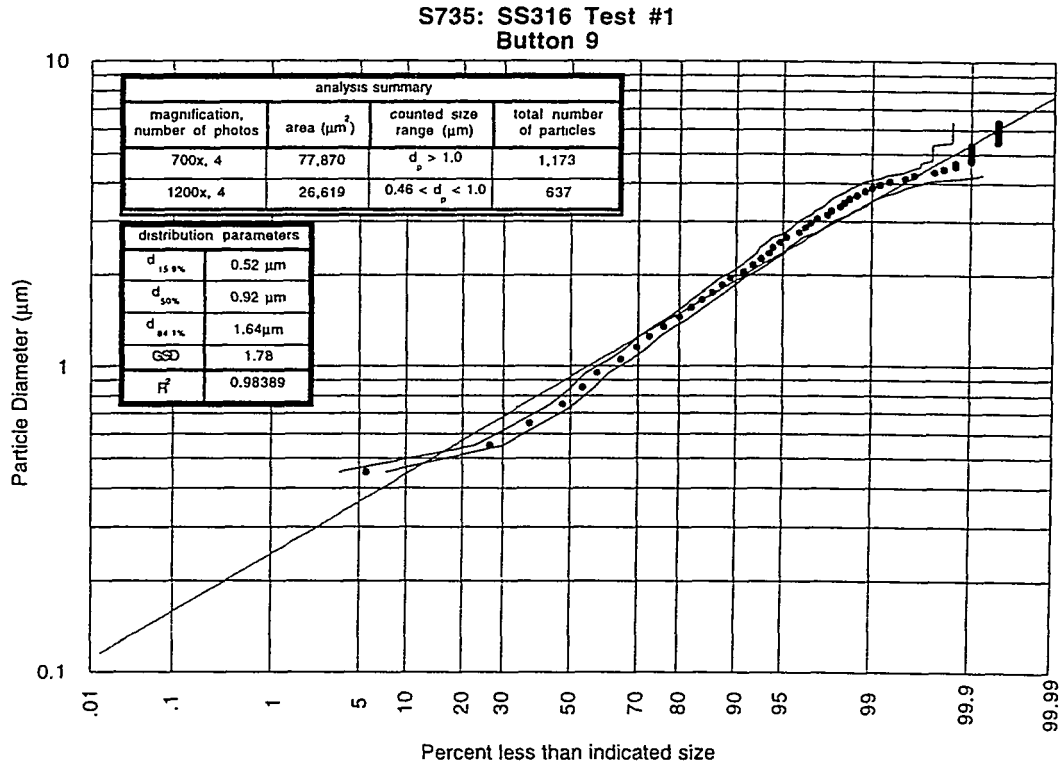

Data Summary Table:

photo	mag	scale (pixel/μm)	size (μm²)	min. d_{eq} (μm)*	# of particles	scale factor	KW Test z-value	Overall p-value
735_9_1	700x	4.14	163x119	0.79	242	1	-1.59	0.419
735_9_2	700x	4.14	163x119	0.79	293	1	0.07	
735_9_3	700x	4.14	163x120	0.79	284	1	0.32	
735_9_4	700x	4.14	164x119	0.79	354	1	1.03	
735_9_5	1200x	7.08	95x69	0.46	162	2.939	-1.96	0.102
735_9_6	1200x	7.08	96x70	0.46	155	2.939	0.57	
735_9_7	1200x	7.08	96x70	0.46	169	2.939	1.96	
735_9_8	1200x	7.08	96x69	0.46	151	2.939	-0.62	

* equivalent minimum diameter particle counted having an area of at least 3.25 x 1/scale on a side.

Figure 4.1.7. SS316 Test #1, Button 12 particle size distribution, with linear fit and 95% confidence intervals.

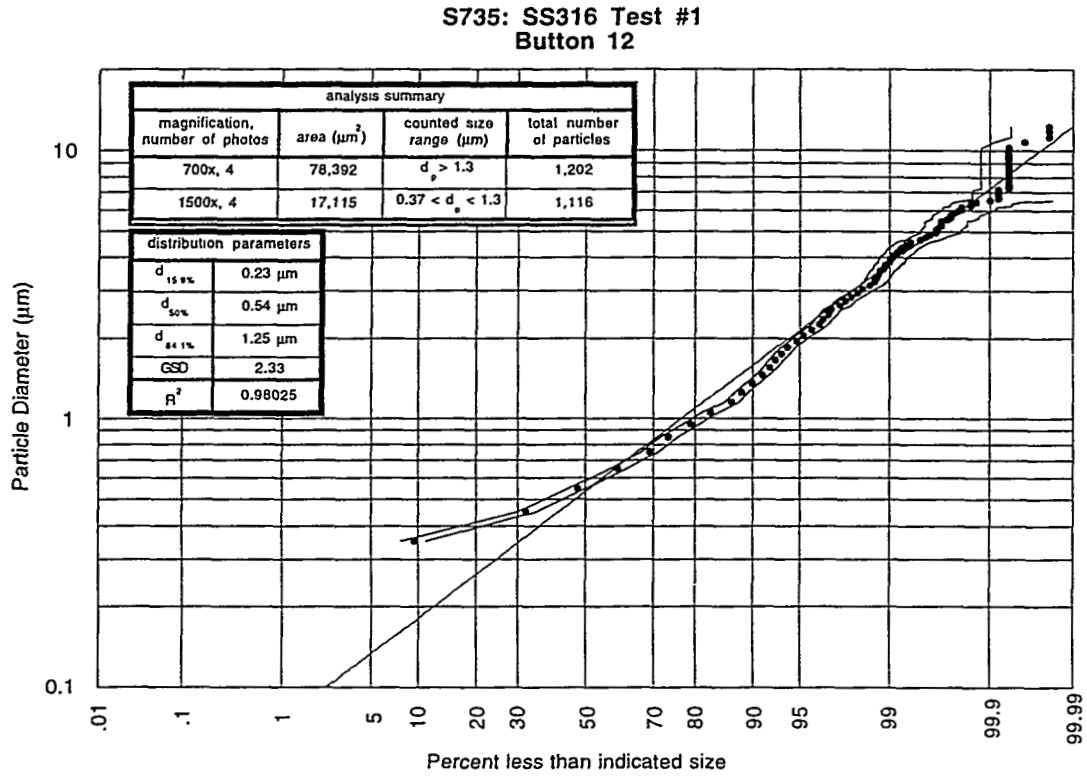

Data Summary Table:

photo	mag	scale (pixel/μm)	size (μm²)	min. d_{eq} (μm)*	# of particles	scale factor	KW Test z-value	Overall p-value
735_12_1	700x	4.14	164x121	0.79	342	1	-0.01	0.131
735_12_2	700x	4.14	164x120	0.79	244	1	1.01	
735_12_3	700x	4.14	164x118	0.79	277	1	1.37	
735_12_4	700x	4.14	164x119	0.79	339	1	-2.17	
735_12_5	1500x	8.85	76x56	0.37	249	4.592	0.34	0.08
735_12_6	1500x	8.85	77x55	0.37	177	4.592	0.93	
735_12_7	1500x	8.85	77x56	0.37	377	4.592	1.40	
735_12_8	1500x	8.85	77x56	0.37	313	4.592	-2.55	

* equivalent minimum diameter particle counted having an area of at least 2.25 x 1/scale on a side.

Figure 4.1.8. SS Test #1, Button 14 particle size distribution, with linear fit and 95% confidence intervals.

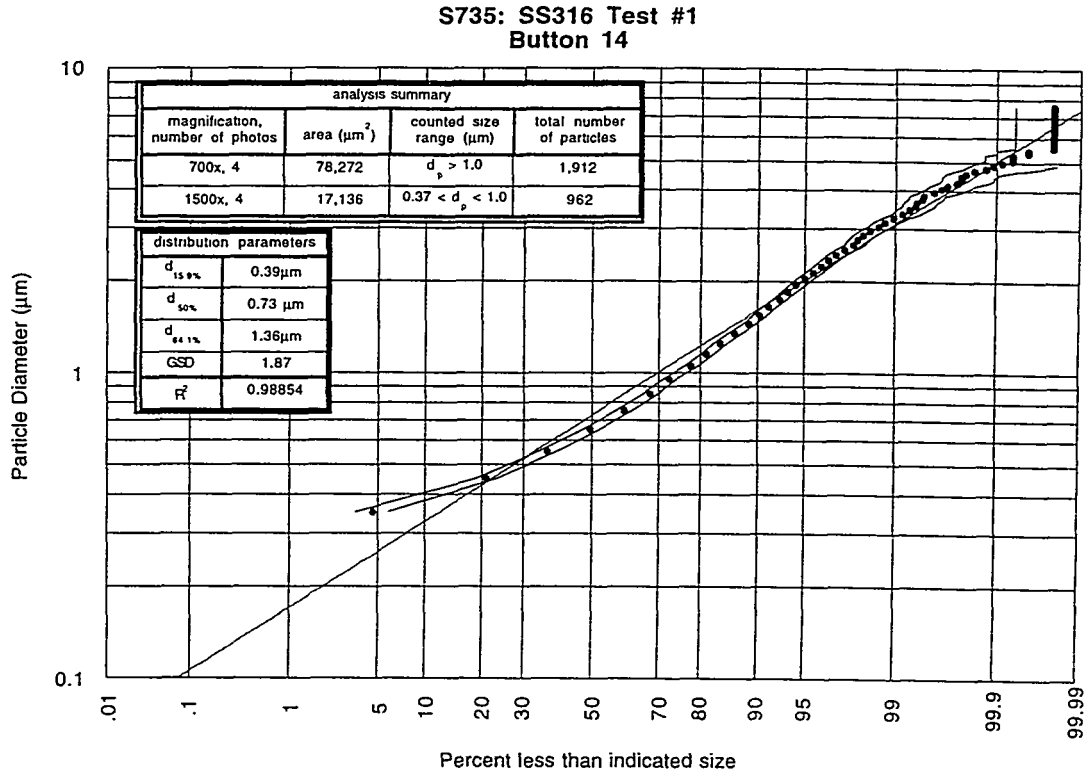

Data Summary Table:

photo	mag	scale (pixel/μm)	size (μm²)	min. d_{eq} (μm)*	# of particles	scale factor	KW Test z-value	Overall p-value
735_14_1	700x	4.14	163x120	0.79	469	1	0.49	0.259
735_14_2	700x	4.14	164x119	0.79	504	1	-1.20	
735_14_3	700x	4.14	164x119	0.79	437	1	-0.98	
735_14_4	700x	4.14	164x120	0.79	502	1	1.66	
735_14_5	1500x	8.85	76x56	0.37	216	4.592	-0.67	0.551
735_14_6	1500x	8.85	76x56	0.37	240	4.592	1.00	
735_14_7	1500x	8.85	77x56	0.37	263	4.592	0.62	
735_14_8	1500x	8.85	77x56	0.37	243	4.592	-0.99	

* equivalent minimum diameter particle counted having an area of at least 2.25 x 1/scale on a side.

Figure 4.1.9. Representative SEM images from Button 7, SS316 Test #1. Note the presence of streakers on the substrate depicted in (a)

.

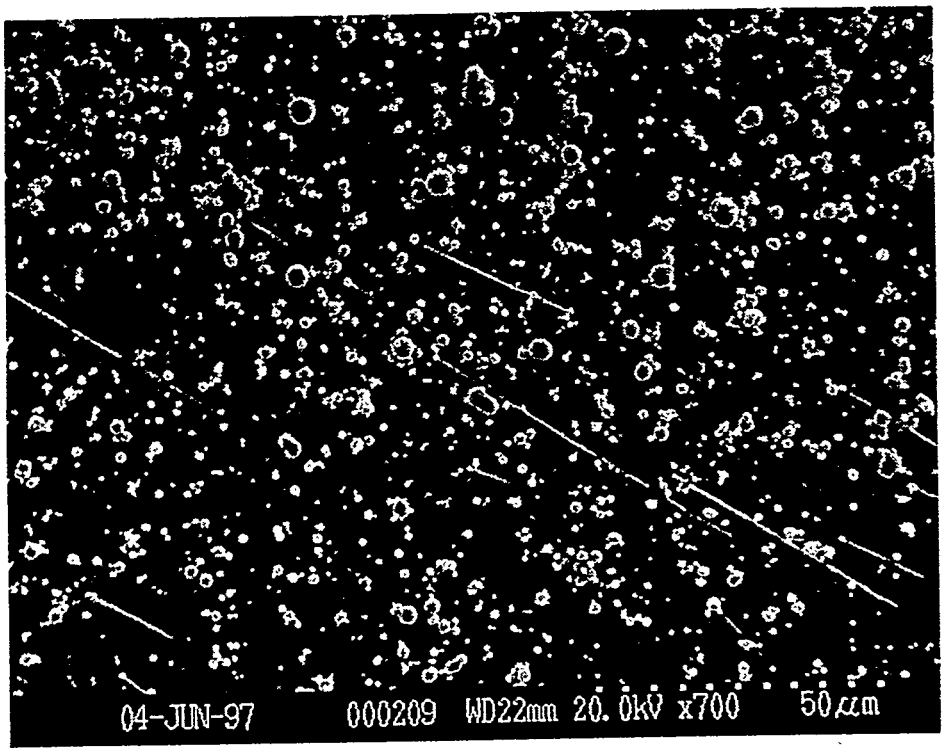

(a) 700x

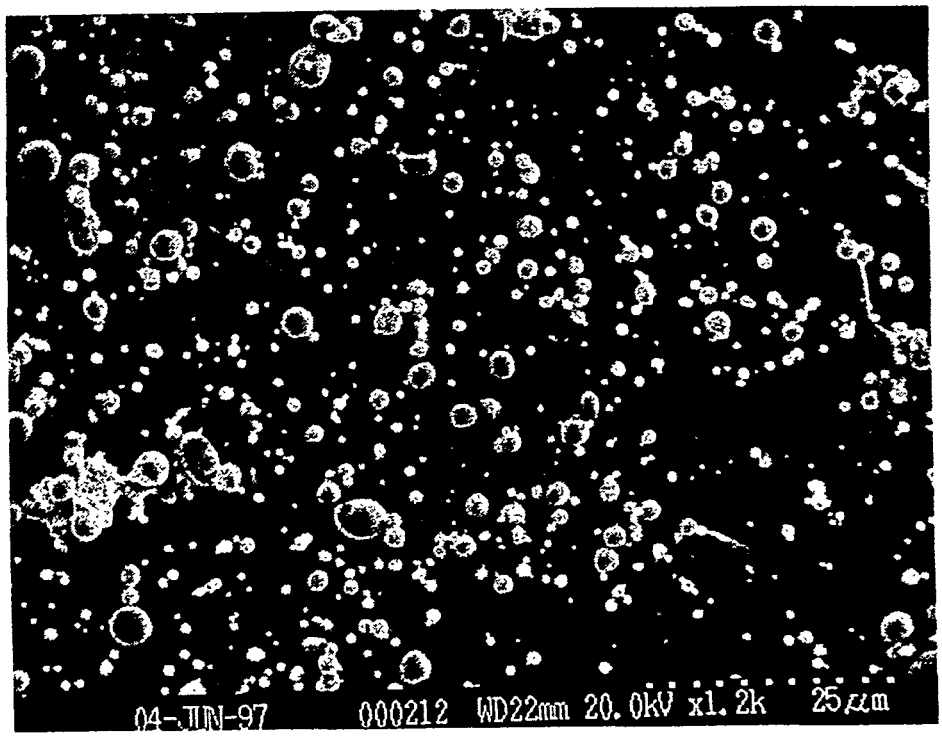

(b) 1200x

Figure 4.1.9.continued.

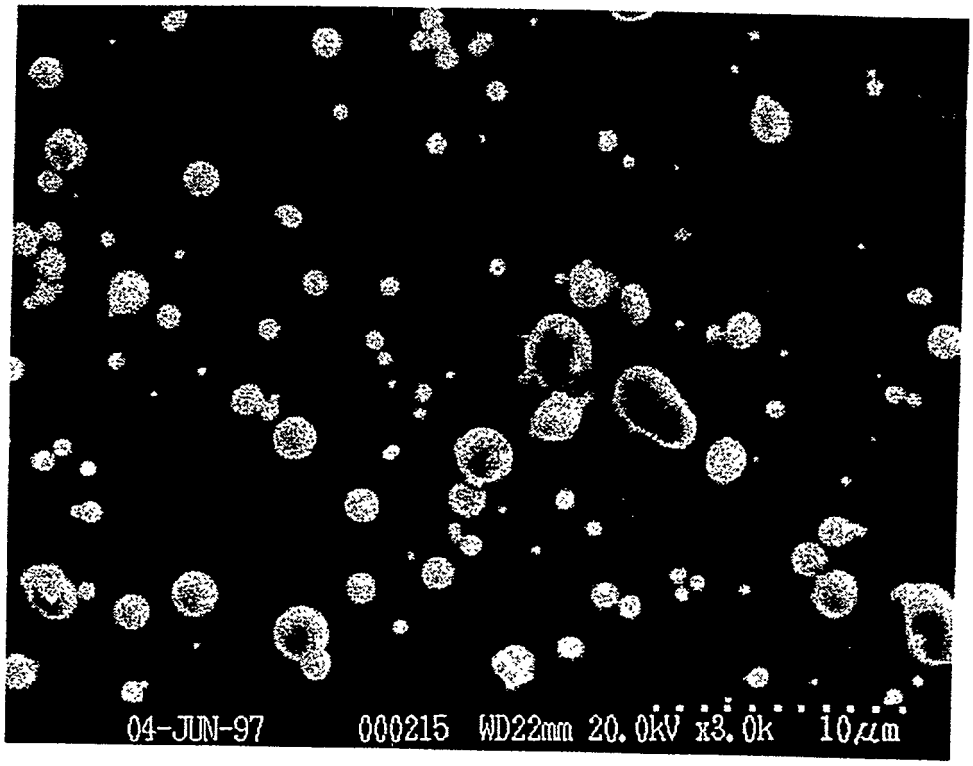

(c) 3000x

4.2. S738: SS316 Test #2

A second test using stainless steel 316 was performed with a discharge energy of 4,260 J. Voltage and current traces are displayed on Figure 4.2.1, and the same problems with the digitized signal occur in this shot as with the previous SS316 test. A pressure measurement was also attempted at the chamber end-plate, and the resulting trace is shown in Figure 4.2.2. Noise from the discharge saturated the data recorder input within the first 10 μs, so the remainder of the trace contains no information. This measurement was attempted using the same pressure diagnostic configuration as SS316 Test #1, however it apparently failed for this shot. The source anode with a pressure tap was not used in this shot because of damage observed on the transducer following Cu Test #2. Testing indicated the transducer was still functioning properly, however the decision was made not to risk complete damage of the transducer, and wait until a new source exit pressure measurement configuration could be investigated. Table 4.2.1 contains button mass increase data, from which no apparent trend in material deposition was observed.

Particulate size distributions measured from buttons 1, 6, 7, 9, 12, and 14 are displayed in Figures 4.2.3-8. Many of the same features from SS316 Test #1 (such as high particle numbers on end plate buttons and streaking on wall buttons) were observed with this test. All images made for analysis were optimized for counting, and the equivalent minimum diameter factor was set to 2.25. Analysis summary tables are included in each figure.

Figure 4.2.1. SS316 Test #2 voltage and current traces.

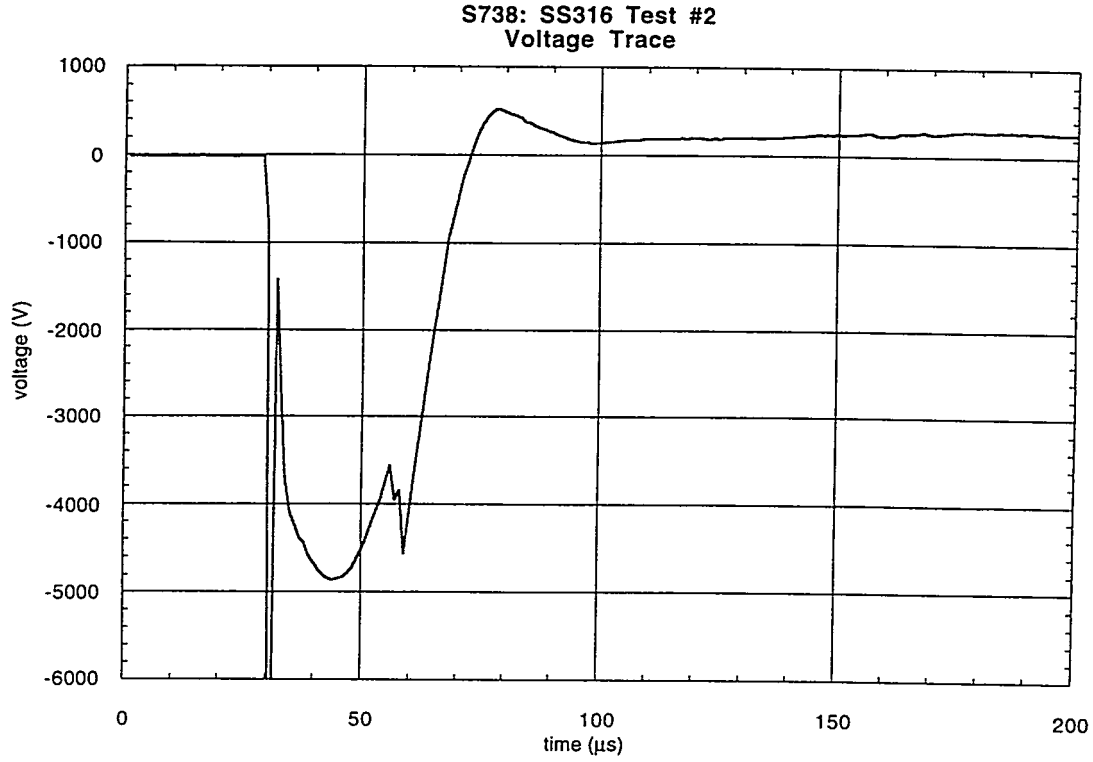

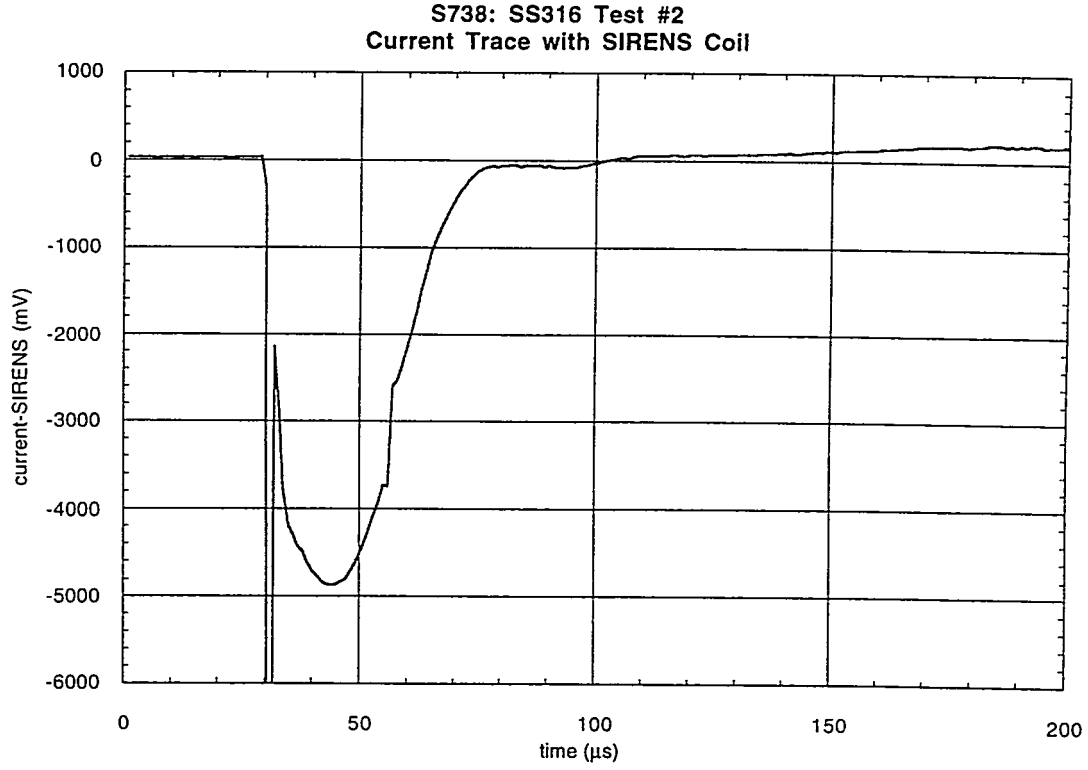

Figure 4.2.2. SS316 Test #2 end-plate P transducer trace.

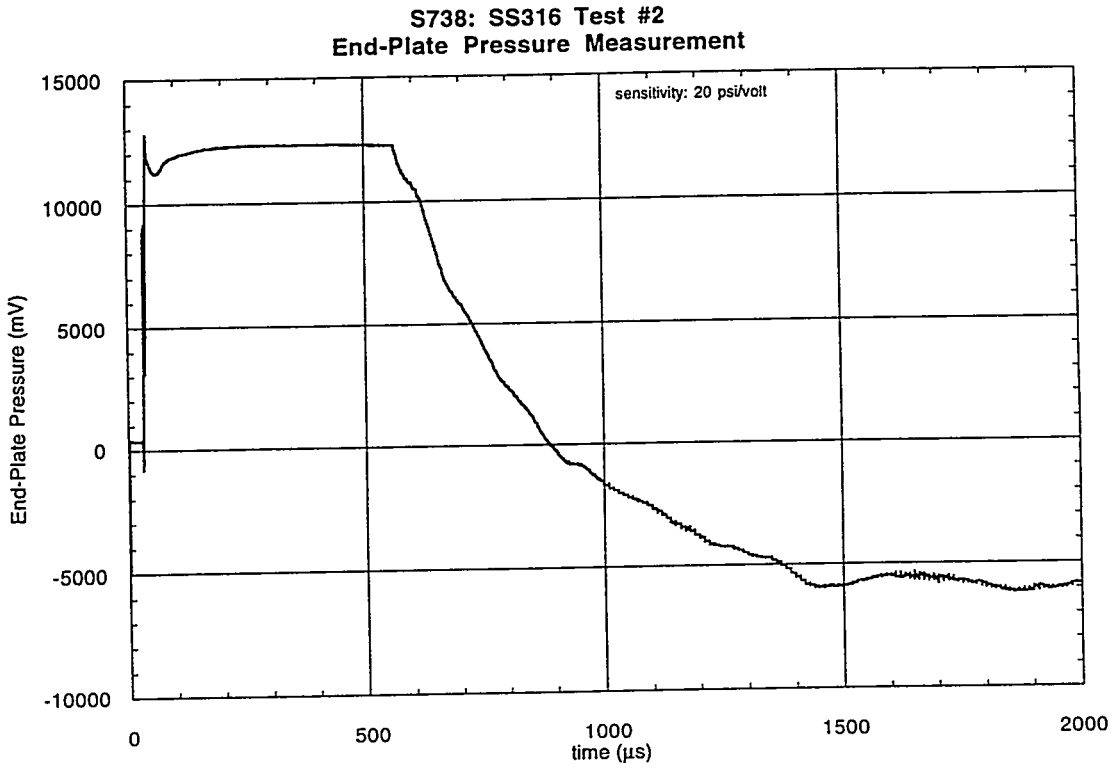

Table 4.2.1. S738 mass measurements.

Source Section Components: component	pre-test wt. (g)	post-test wt. (g)	Δ wt. (mg, ± 0.05)
short insulator	1.01268	-	-
long insulator	3.00177	-	-
cathode (dimetech)	9.0511	9.02957	21.57
SS316 sleeve	12.29986	11.93225	367.61

Substrate Components: wall button	pre-test wt. (g)	post-test wt. (g)	Δ wt. (mg)	end-plate button	pre-test wt (g)	post-test wt. (g)	Δ wt. (mg)
1	0.92385	0.92396	0.12	9	0.91708	0.91733	0.24
2	0.91990	0.92002	0.12	10	0.91988	0.92002	0.21
3	0.91677	0.91684	0.07	11	0.91498	0.91513	0.16
4	0.91986	0.91998	0.12	12	0.91357	0.91380	0.23
5	0.92076	0.92088	0.12	13	0.91810	0.91827	0.16
6	0.92260	0.92270	0.10	14	0.92119	0.92125	0..06
7	0.92288	0.92303	0.15	15	0.91864	0.91909	0.45
8	0.91463	0.91472	0.09	16	0.91706	0.91722	0.16
				17	0.91784	0.91815	0.31

Notes:
(1) All weight measurements are taken 3+ times and averaged.
(2) Δm uncertainty is ± 0.05 mg.

Figure 4.2.3. SS316 Test #2, Button 1 particle size distribution, with linear fit and 95% confidence intervals.

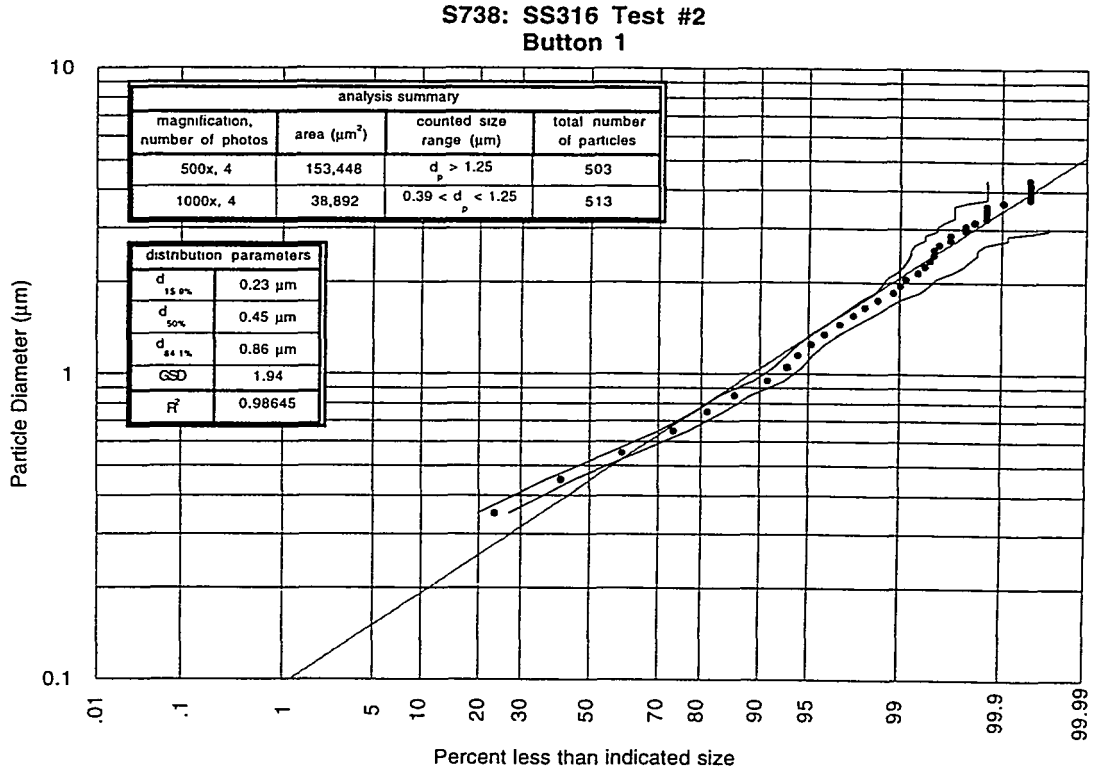

Data Summary Table:

photo	mag	scale (pixel/µm)	size (µm²)	min. d_{eq} (µm)*	# of particles	scale factor	KW Test z-value	Overall p-value
738_1_1	500x	2.92	233x166	0.77	168	1	-2.39	0.076
738_1_2	500x	2.92	231x166	0.77	125	1	1.89	
738_1_3	500x	2.92	230x167	0.77	112	1	0.30	
738_1_4	500x	2.92	229x166	0.77	98	1	0.46	
738_1_5	1000x	5.84	117x84	0.39	104	4	-0.12	0.882
738_1_6	1000x	5.84	116x84	0.39	115	4	0.57	
738_1_7	1000x	5.84	115x84	0.39	138	4	-0.85	
738_1_8	1000x	5.84	115x84	0.39	156	4	0.41	

* equivalent minimum diameter particle counted having an area of at least 2.25 x 1/scale on a side.

Figure 4.2.4. SS316 Test #2, Button 6 particle size distribution, with linear fit and 95% confidence intervals.

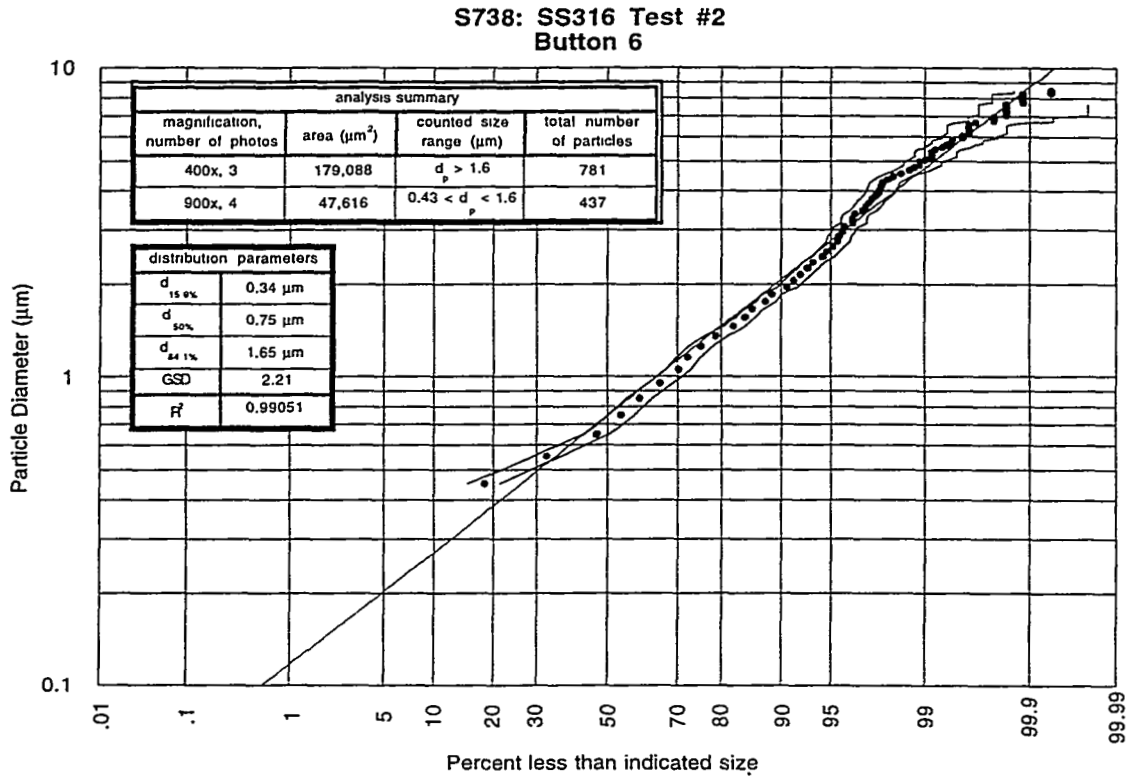

Data Summary Table:

photo	mag	scale (pixel/μm)	size (μm²)	min. d_{eq} (μm)*	# of particles	scale factor	KW Test z-value	Overall p-value
738_6_1	400x	2.94	287x208	0.96	238	1	-0.37	0.371
738_6_2	400x	2.94	287x209	0.96	-	-	failed	
738_6_3	400x	2.94	287x207	0.96	248	1	-1.04	
738_6_4	400x	2.94	288x209	0.96	295	1	1.35	
738_6_5	900x	5.28	128x93	0.43	101	5.0625	1.25	0.557
738_6_6	900x	5.28	129x93	0.43	104	5.0625	-0.74	
738_6_7	900x	5.28	128x93	0.43	120	5.0625	0.25	
738_6_8	900x	5.28	128x93	0.43	112	5.0625	-0.74	

* equivalent minimum diameter particle counted having an area of at least 2.25 x 1/scale on a side.

Figure 4.2.5. SS316 Test #2, Button 7 particle size distribution, with linear fit and 95% confidence intervals.

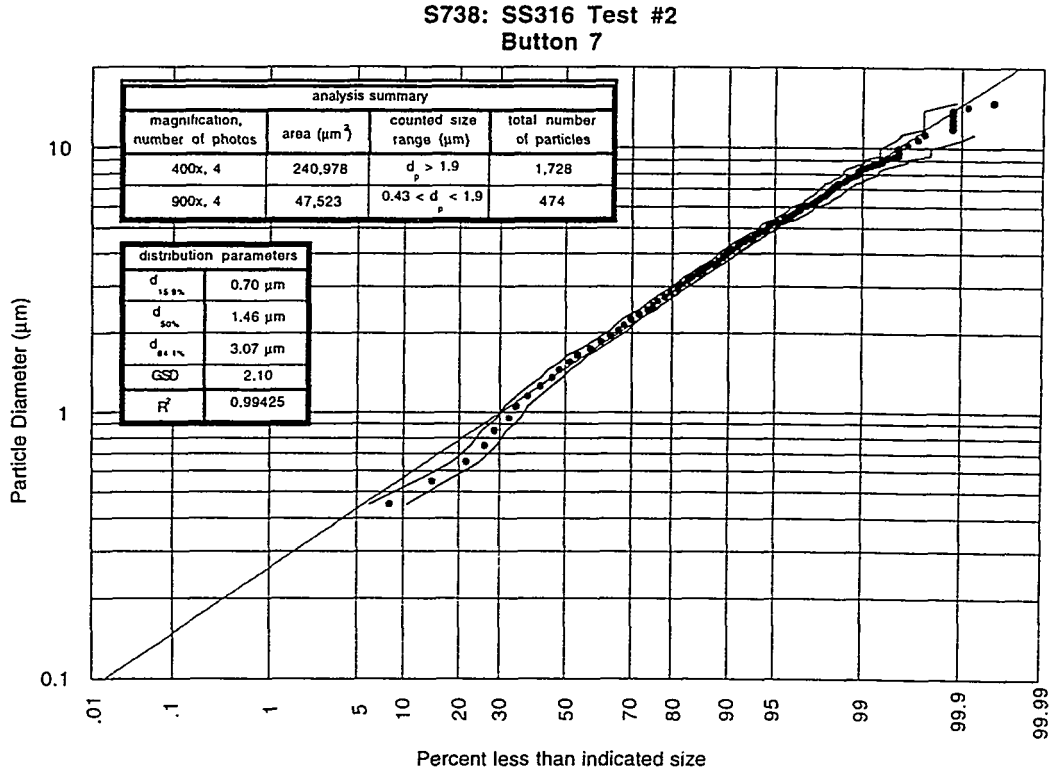

Data Summary Table:

photo	mag	scale (pixel/μm)	size (μm²)	min. d_{eq} (μm)*	# of particles	scale factor	KW Test z-value	Overall p-value
738_7_1	400x	2.35	288x209	0.96	424	1	-0.98	0.217
738_7_2	400x	2.35	289x208	0.96	468	1	-1.41	
738_7_3	400x	2.35	289x210	0.96	428	1	1.27	
738_7_4	400x	2.35	288x209	0.96	408	1	1.18	
738_7_5	900x	5.28	128x92	0.43	124	5.0625	-1.50	0.097
738_7_6	900x	5.28	127x93	0.43	103	5.0625	1.28	
738_7_7	900x	5.28	128x93	0.43	125	5.0625	-1.35	
738_7_8	900x	5.28	128x94	0.43	122	5.0625	1.66	

* equivalent minimum diameter particle counted having an area of at least 2.25 x 1/scale on a side.

Figure 4.2.6. SS316 Test #2, Button 9 particle size distribution, with linear fit and 95% confidence intervals.

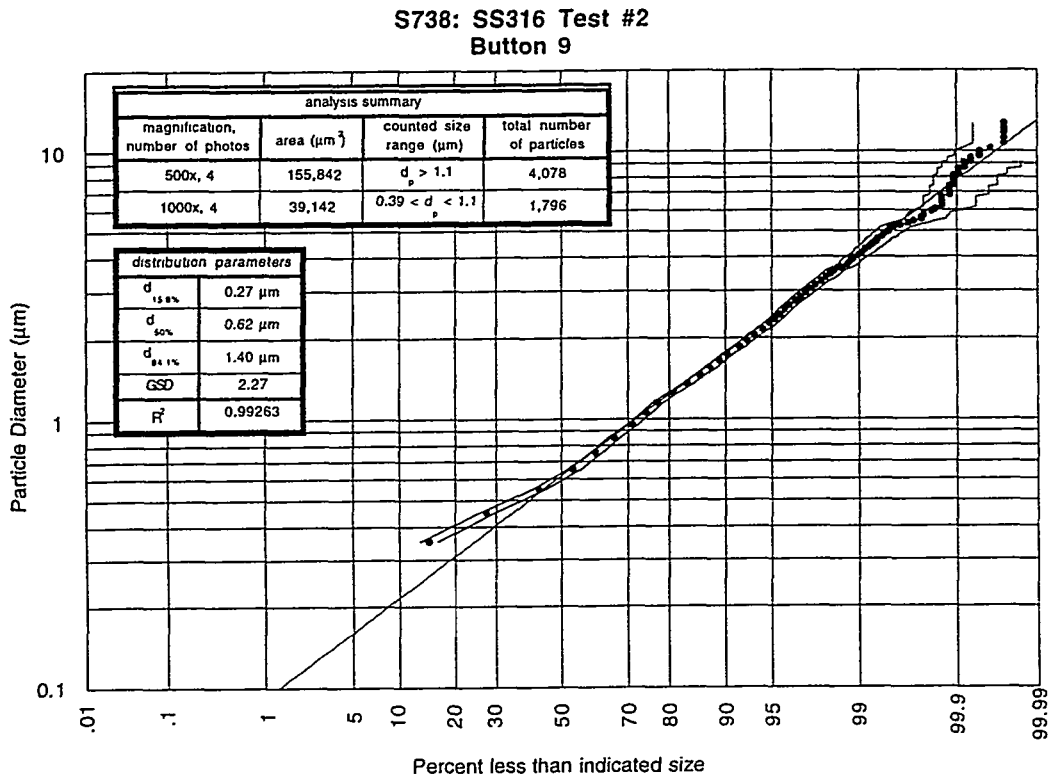

Data Summary Table:

photo	mag	scale (pixel/µm)	size (µm²)	min. d_{eq} (µm)*	# of particles	scale factor	KW Test z-value	Overall p-value
738_9_1	500x	2.92	232x167	0.77	1115	1	-1.83	0.236
738_9_2	500x	2.92	232x166	0.77	938	1	0.16	
738_9_3	500x	2.92	232x168	0.77	908	1	1.49	
738_9_4	500x	2.92	233x170	0.77	1117	1	0.29	
738_9_5	1000x	5.84	116x86	0.39	438	4	0.59	0.804
738_9_6	1000x	5.84	118x83	0.39	425	4	-0.94	
738_9_7	1000x	5.84	116x83	0.39	454	4	0.20	
738_9_8	1000x	5.84	116x84	0.39	479	4	0.14	

* equivalent minimum diameter particle counted having an area of at least 2.25 x 1/scale on a side.

Figure 4.2.7. SS316 Test #2, Button 12 particle size distribution, with linear fit and 95% confidence intervals.

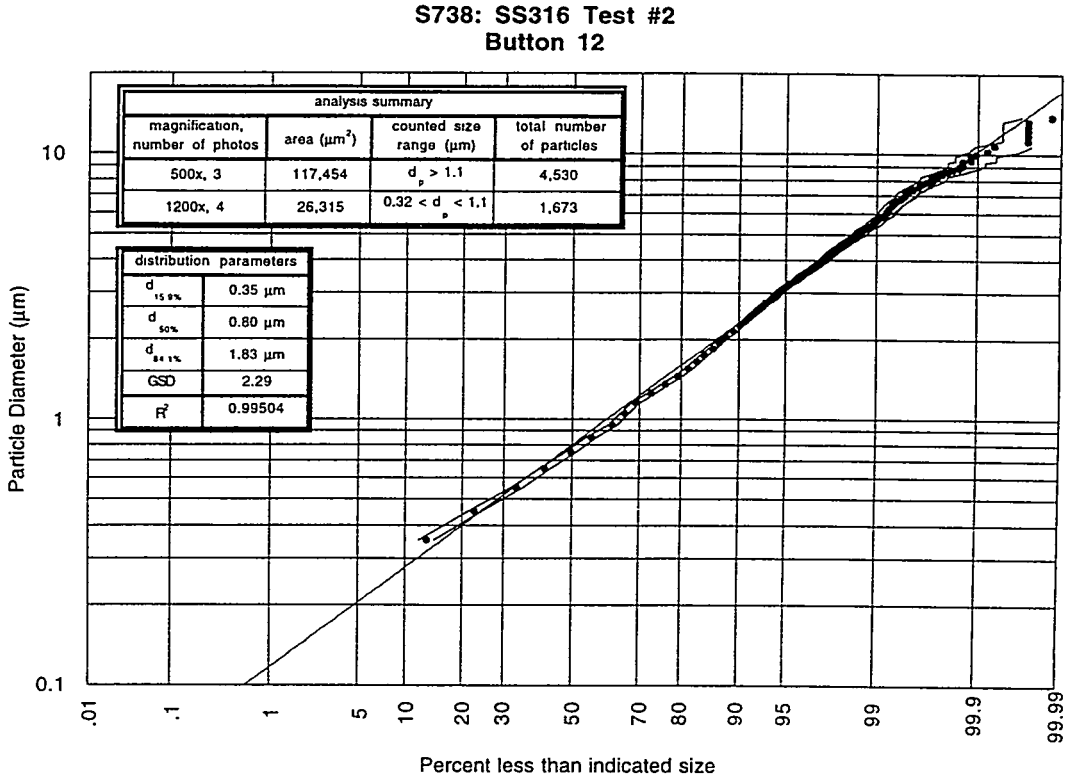

Data Summary Table:

photo	mag	scale (pixel/µm)	size (µm²)	min. d_{eq} (µm)*	# of particles	scale factor	KW Test z-value	Overall p-value
738_12_1	500x	2.92	231x168	0.77	1462	1	-1.47	0.275
738_12_2	500x	2.92	231x170	0.77	1339	1	0.09	
738_12_3	500x	2.92	231x170	0.77	-	-	failed	
738_12_4	500x	2.92	232x169	0.77	1729	1	1.34	
738_12_5	1200x	7.08	95x69	0.32	367	5.76	-0.74	0.701
738_12_6	1200x	7.08	96x69	0.32	516	5.76	0.72	
738_12_7	1200x	7.08	95x70	0.32	412	5.76	0.60	
738_12_8	1200x	7.08	95x69	0.32	378	5.76	-0.69	

* equivalent minimum diameter particle counted having an area of at least 2.25 x 1/scale on a side.

Figure 4.2.8. SS316 Test #2, Button 14 particle size distribution, with linear fit and 95% confidence intervals.

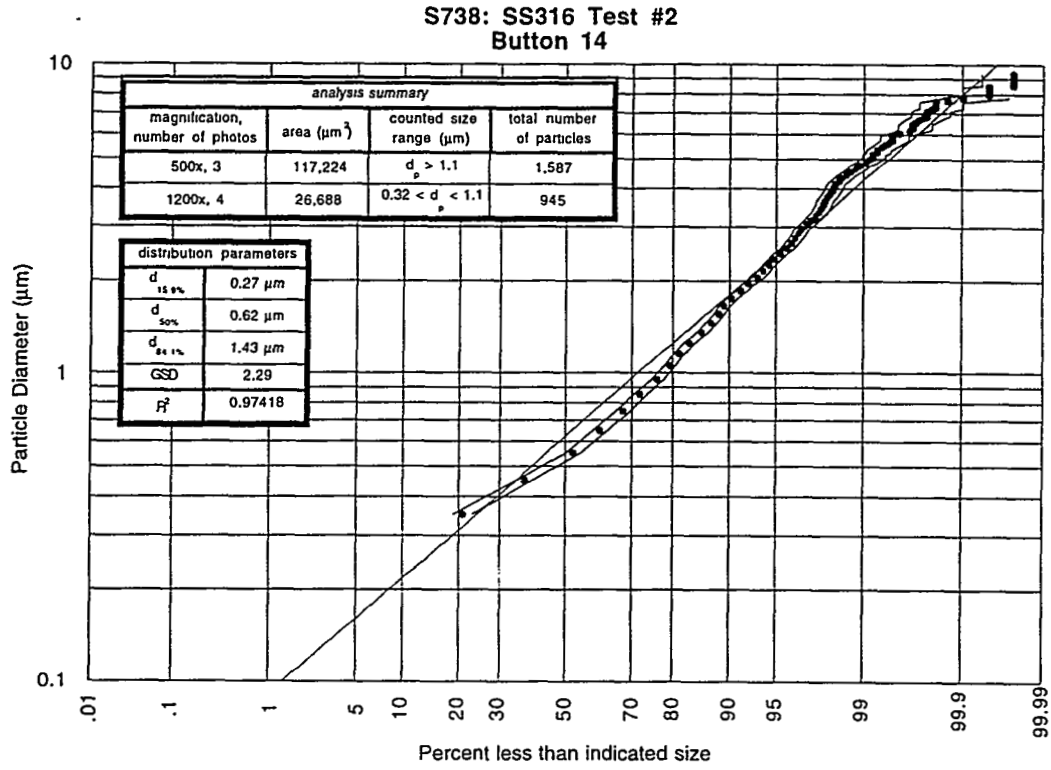

Data Summary Table:

photo	mag	scale (pixel/μm)	size (μm²)	min. d_{eq} (μm)*	# of particles	scale factor	KW Test z-value	Overall p-value
738_14_1	500x	2.92	231x168	0.77	538	1	1.10	0.398
738_14_3	500x	2.92	231x169	0.77	519	1	0.14	
738_14_4	500x	2.92	233x169	0.77	530	1	-1.24	
738_14_5	1200x	7.08	96x69	0.32	236	5.76	-0.96	0.676
738_14_6	1200x	7.08	96x69	0.32	238	5.76	-0.28	
738_14_7	1200x	7.08	96x70	0.32	230	5.76	0.24	
738_14_8	1200x	7.08	96x70	0.32	241	5.76	0.99	

* equivalent minimum diameter particle counted having an area of at least 2.25 x 1/scale on a side.

5.0 Tungsten Test Results

Another ITER-relevant metal investigated under the disruption simulation conditions available in SIRENS was pure tungsten. Two separate tests were prepared and performed in the usual fashion, as described in [2]. Table 5.0.1 contains a summary of important test data: sample mass loss, button weight gain, and particulate size distribution parameters. The sample sleeves from both tests shattered due to the brittle nature of W, and the reported sample mass losses are best estimates from weighing all pieces collected from the shattered sleeves. Changes in button mass were very small, often lower than the accuracy resolution of the balance (± 0.05 mg). Difficulties were encountered in analyzing particulate size distributions on end-plate buttons from W Test #2 because of substrate pitting or cratering from W particle impaction. An alternate technique for analyzing W particles on these buttons is currently being investigated.

Table 5.0.1 W tests comparison summary.

	W Test 1 (S736)				W Test 2 (S739)			
Energy (J)	4260				4259			
Sample Δm (mg)	154.85(1)				241.93(1)			
Cathode Δm (mg)	21.18				25.13			
	Δm (mg)	$d_{50\%}$ (μm)	GSD	R^2	Δm (mg)	$d_{50\%}$ (μm)	GSD	R^2
Button 1	0.03	0.30	1.97	0.997	0.06	0.38	1.99	0.974
Button 2	0.10	*	*	*	0.07	*	*	*
Button 3	0.03	*	*	*	0.01	*	*	*
Button 4	0.06	*	*	*	0.07	*	*	*
Button 5	0.05	*	*	*	0.05	*	*	*
Button 6	0.10	0.50	1.76	0.996	0.02	0.30	2.11	0.986
Button 7	-0.03	0.70	1.65	0.980	0.13	0.36	2.15	0.992
Button 8	0.08	*	*	*	0.05	*	*	*
Button 9	0.04	1.05	2.59	0.965	0.01	*	*	*
Button 10	0.08	*	*	*	0.04	*	*	*
Button 11	0.12	*	*	*	0.01	*	*	*
Button 12	0.04	0.66	2.49	0.974	0.02	*	*	*
Button 13	0.10	*	*	*	0.03	*	*	*
Button 14	-0.01	0.80	2.49	0.968	0.09	*	*	*
Button 15	0.05	*	*	*	0.17	*	*	*
Button 16	0.08	*	*	*	0.18	*	*	*
Button 17	0.00	*	*	*	0.14	*	*	*

Notes:
(1) Sample Δm's are best estimate because sleeves shattered in both tests.
(2) Asterisk (*) denotes buttons for which the analysis was not performed.

5.1 S736: W Test #1

The first tungsten test was performed with a discharge energy of 4,260 J. Copper capture buttons were placed in the glass chamber in the normal configuration (see Figure 2.2). Figure 5.1.1 shows the resulting voltage and current traces. Signal acquisition problems similar to previous tests plagued this shot. Figure 5.1.2 displays the signal obtained from the end-plate pressure transducer, showing again no information except for noise from the discharge EM pulse. The new source housing with pressure tap was not used for this test because a reliable pressure diagnostic configuration had not been developed. Table 5.1.1 gives mass data for the sample sleeve and buttons. The amount of mass deposited on the buttons was insufficient to show any trends.

One significant result from this test is that the W sleeve cracked and broke. The source exit end of the sleeve had broken into 4 circumferential segments, each about 1.5 cm in length. The mechanism responsible for breaking the sleeve has not been found, however 2 different scenarios offer possible answers. Heat and exit pressure may have propagated microcracks from machining in the sleeve's end. Also, the sleeve may have been cracked during the extraction procedure following the shot.

Particulate size distributions from selected buttons (1, 6, 7, 9, 12, and 14) are shown in Figures 5.1.3-8. The images obtained for this analysis were optimized for the counting procedure, and the minimum equivalent diameter discrimination factor was set to 2.25 for most cases. A value of 3.25 was used for some high magnification images to discriminate features that were not particles. A feature that interfered with the particle counting technique was cratering or pitting that resulted from impact of W particles on the Cu substrate. Edges of the craters were significantly distinct, and in the particle characterization procedure they were counted as particles and skewed the resulting distribution. Cratering was not severe in W Test #1, but was so abundant in W Test #2 that end-plate buttons could not be analyzed.

Figure 5.1.9 shows representative SEM images of Button 12 on the end-plate from W Test #1. The first image was taken at 200x to obtain information about the larger particles (10 - 15 μm) on the button. Subsequent images were taken at 700x and 1200x, and smaller particles were recorded. Craters appear on the higher magnification images, and are on the order of the particle sizes. These craters were investigated on the SEM to prove that the substrate surface was deformed. Two images taken at different angles were used to generate a relief image that showed the craters to be indentation's into the surface and particles to be bodies on the surface. Also, the EDXA facility in the SEM proved the particles were W, and the crater edges were analyzed for material other than that of the substrate. No other material was found.

Figure 5.1.1. W Test #1 voltage and current traces.

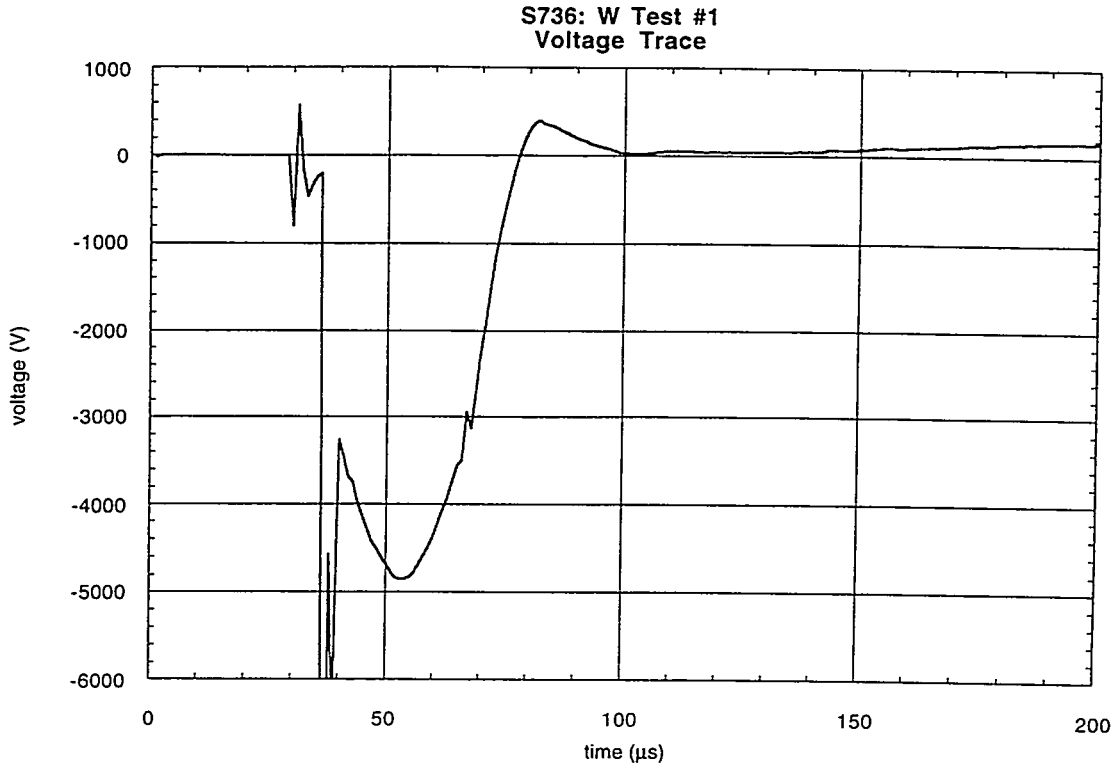

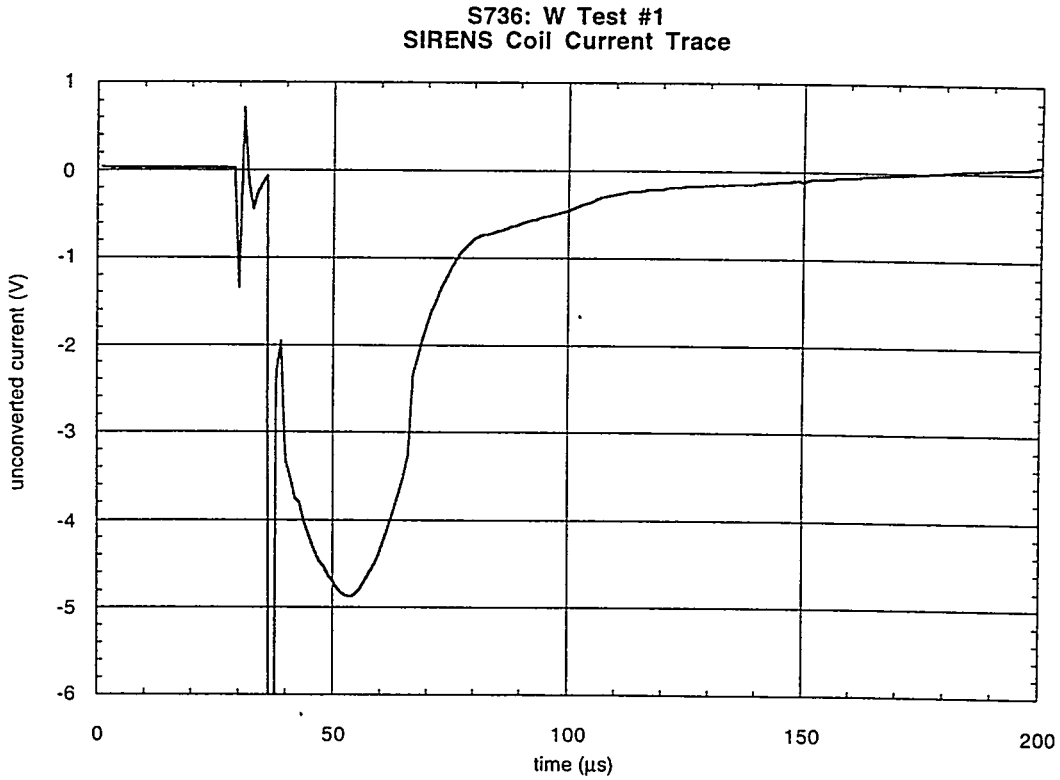

Figure 5.1.2. W Test #1 end-plate P transducer trace.

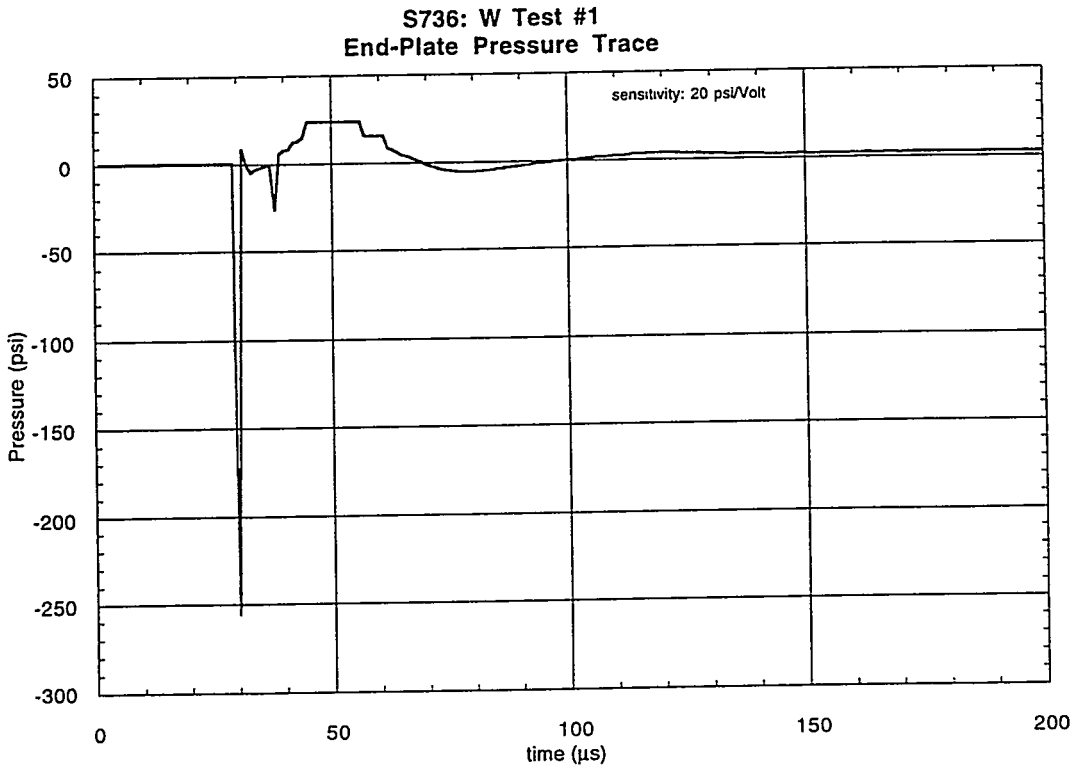

Table 5.1.1. S736 mass measurements.

Source Section Components: component	pre-test wt. (g)	post-test wt. (g)	Δ wt. (mg, ± 0.05)
short insulator	1.02145	-	-
long insulator	2.91280	-	-
cathode (dimetech)	9.09866	9.07748	21.18
W sleeve	31.38996	31.23531(3)	154.85

Substrate Components: wall button	pre-test wt. (g)	post-test wt. (g)	Δ wt. (mg)	end-plate button	pre-test wt (g)	post-test wt. (g)	Δ wt. (mg)
1	0.90284	0.90286	0.03	9	0.90865	0.90869	0.04
2	0.90120	0.90130	0.10	10	0.91047	0.91055	0.08
3	0.90387	0.90390	0.03	11	0.91374	0.91386	0.12
4	0.89696	0.89702	0.06	12	0.91422	0.91426	0.04
5	0.89873	0.89878	0.05	13	0.91120	0.91130	0.10
6	0.91494	0.91504	0.10	14	0.90500	0.90499	-0.01
7	0.90120	0.90117	-0.03	15	0.91163	0.91162	0.05
8	0.91375	0.91384	0.08	16	0.91415	0.91423	0.08
				17	0.91013	0.91013	0.00

Notes:
(1) All weight measurements are taken 3+ times and averaged.
(2) Δm uncertainty is ± 0.05 mg.
(3) Measurement of all pieces of shattered sleeve.

Figure 5.1.3. W Test #1, Button 1 particle size distribution, with linear fit and 95% confidence intervals.

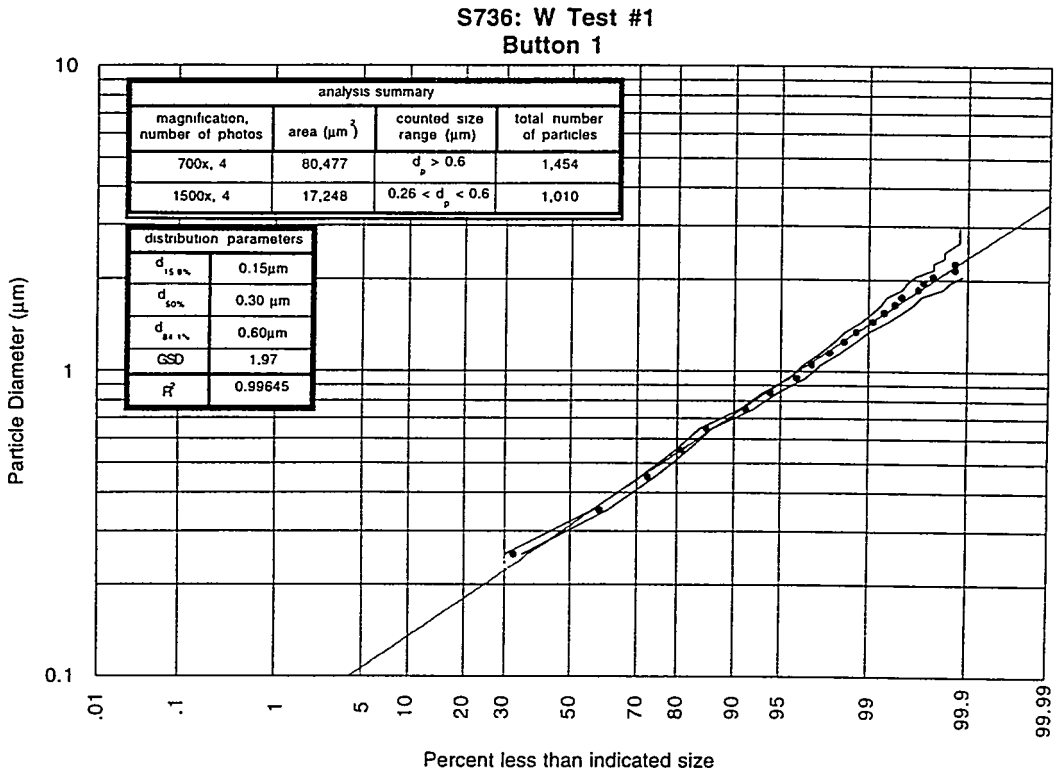

Data Summary Table:

photo	mag	scale (pixel/μm)	size (μm²)	min. d_{eq} (μm)*	# of particles	scale factor	KW Test z-value	Overall p-value
736_1_1	700x	3.94	165x122	0.57	422	1	-0.84	0.829
736_1_2	700x	3.94	166x122	0.57	372	1	0.15	
736_1_3	700x	3.94	165x121	0.57	403	1	0.70	
736_1_4	700x	3.94	165x122	0.57	257	1	-0.00	
736_1_5	1500x	8.5	77x56	0.26	267	4.592	1.44	0.465
736_1_6	1500x	8.5	77x56	0.26	278	4.592	-1.06	
736_1_7	1500x	8.5	77x56	0.26	219	4.592	-0.49	
736_1_8	1500x	8.5	77x56	0.26	246	4.592	0.10	

* equivalent minimum diameter particle counted having an area of at least 2.25 x 1/scale on a side.

Figure 5.1.4. W Test #1, Button 6 particle size distribution, with linear fit and 95% confidence intervals.

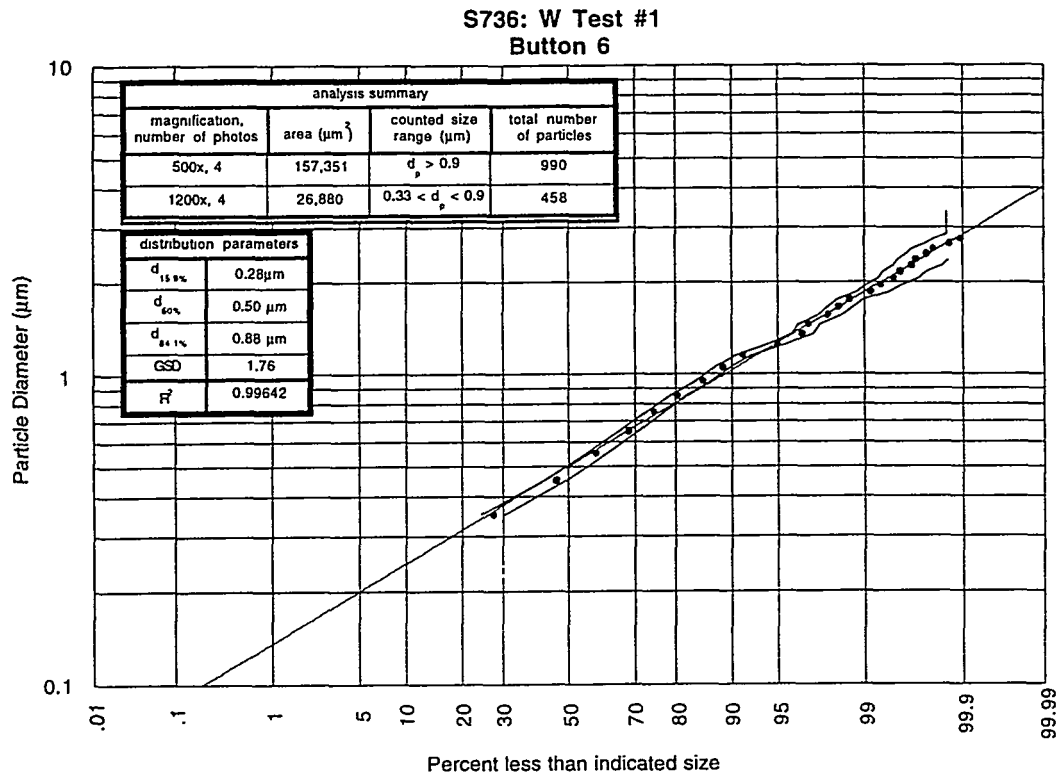

Data Summary Table:

photo	mag	scale (pixel/μm)	size (μm²)	min. d_{eq} (μm)*	# of particles	scale factor	KW Test z-value	Overall p-value
736_6_1	500x	2.81	232x170	0.80	251	1	0.27	0.980
736_6_2	500x	2.81	231x171	0.80	255	1	-0.28	
736_6_3	500x	2.81	233x166	0.80	260	1	-0.21	
736_6_4	500x	2.81	231x172	0.80	224	1	0.23	
736_6_6	1200x	6.8	97x70	0.33	110	5.76	-0.28	0.087
736_6_7	1200x	6.8	96x70	0.33	147	5.76	-1.44	
736_6_8	1200x	6.8	96x70	0.33	98	5.76	-0.60	
736_6_9	1200x	6.8	96x70	0.33	103	5.76	2.49	

* equivalent minimum diameter particle counted having an area of at least 2.25 x 1/scale on a side.

Figure 5.1.5. W Test #1, Button 7 particle size distribution, with linear fit and 95% confidence intervals.

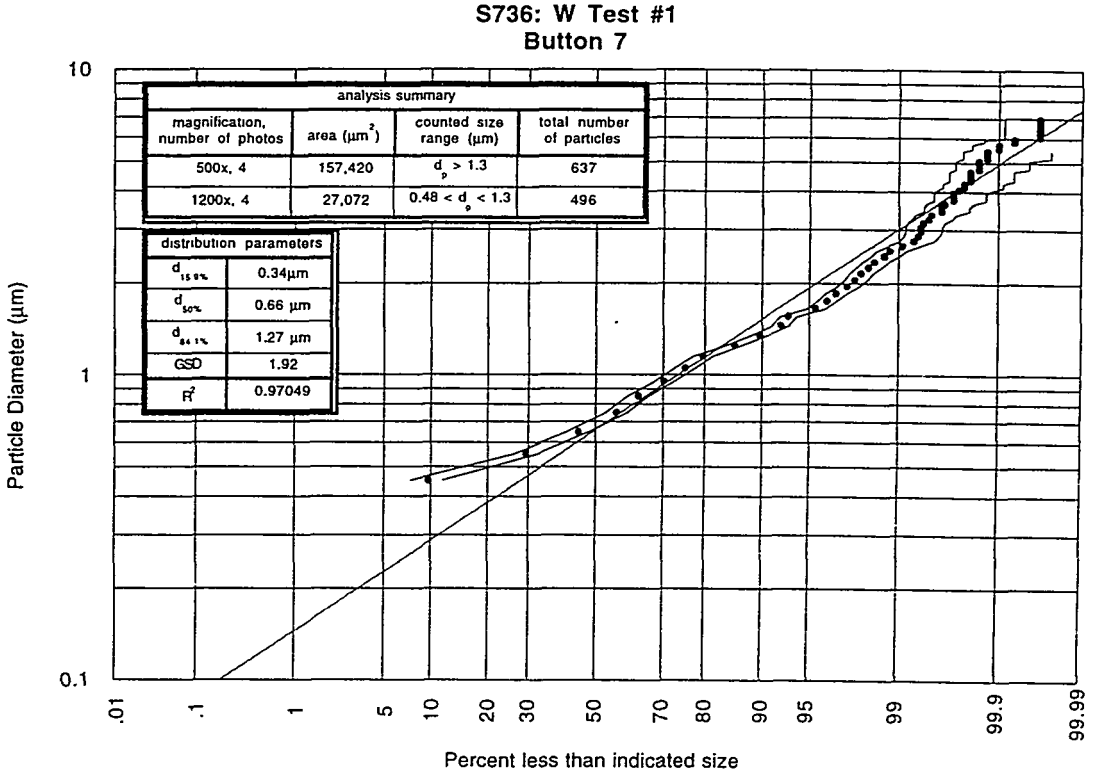

Data Summary Table:

photo	mag	scale (pixel/μm)	size (μm²)	min. d_{eq} (μm)*	# of particles	scale factor	KW Test z-value	Overall p-value
736_7_1	500x	2.82	232x170	1.15	151	1	0.94	0.643
736_7_2	500x	2.82	232x170	1.15	191	1	0.08	
736_7_3	500x	2.82	231x170	1.15	138	1	-1.12	
736_7_4	500x	2.82	231x170	1.15	157	1	0.07	
736_7_5	1200x	6.8	96x70	0.48	107	5.76	-0.85	0.439
736_7_6	1200x	6.8	96x71	0.48	146	5.76	0.14	
736_7_7	1200x	6.8	96x70	0.48	123	5.76	-0.80	
736_7_8	1200x	6.8	96x71	0.48	120	5.76	1.47	

* equivalent minimum diameter particle counted having an area of at least 3.25 x 1/scale on a side.

Figure 5.1.6. W Test #1, Button 9 particle size distribution, with linear fit and 95% confidence intervals.

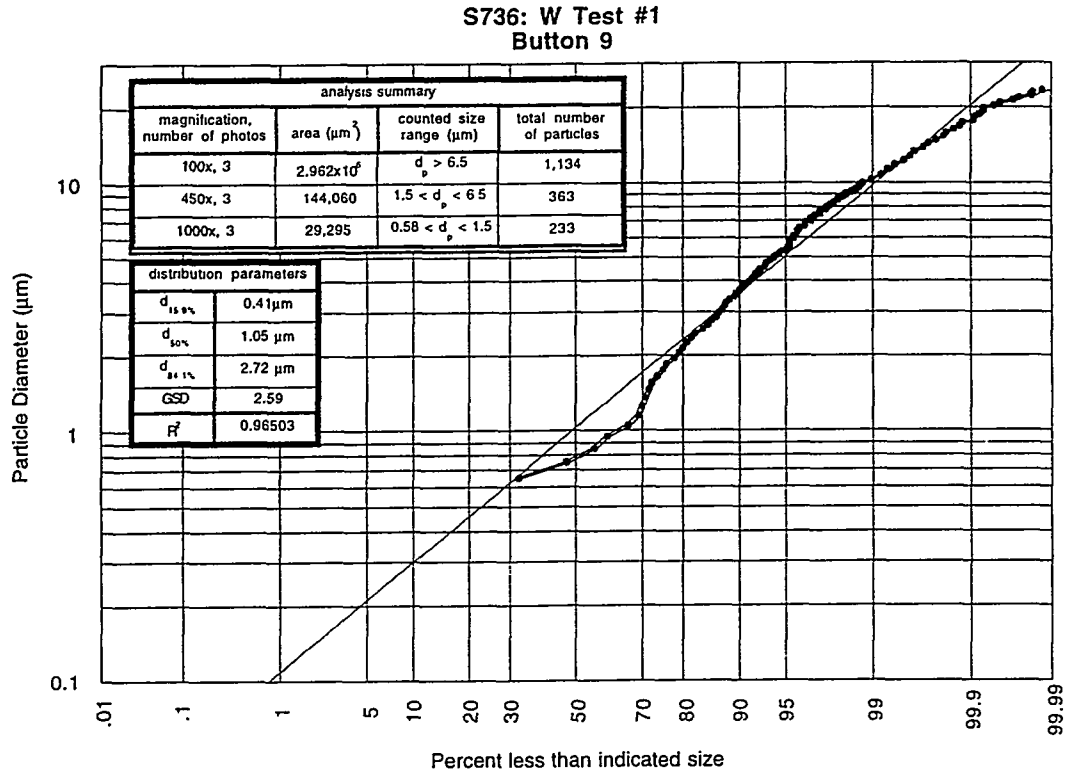

Data Summary Table:

photo	mag	scale (pixel/μm)	size (μm²)	min. d_{eq} (μm)*	# of particles	scale factor	KW Test z-value	Overall p-value
736_9_1	100x	0.564	1158x855	5.76	361	1	1.35	0.144
736_9_2	100x	0.564	1156x851	5.76	397	1	-1.92	
736_9_3	100x	0.564	1158x853	5.76	376	1	0.61	
736_9_4	450x	2.54	257x188	1.28	124	20.25	0.65	0.719
736_9_5	450x	2.54	257x187	1.28	121	20.25	-0.75	
736_9_6	450x	2.54	256x187	1.28	118	20.25	0.10	
736_9_7	1000x	5.64	115x85	0.58	78	100	-1.21	0.061
736_9_8	1000x	5.64	115x84	0.58	81	100	-1.11	
736_9_9	1000x	5.64	116x85	0.58	74	100	2.37	

* equivalent minimum diameter particle counted having an area of at least 3.25 x 1/scale on a side.

Figure 5.1.7. W Test #1, Button 12 particle size distribution, with linear fit and 95% confidence intervals.

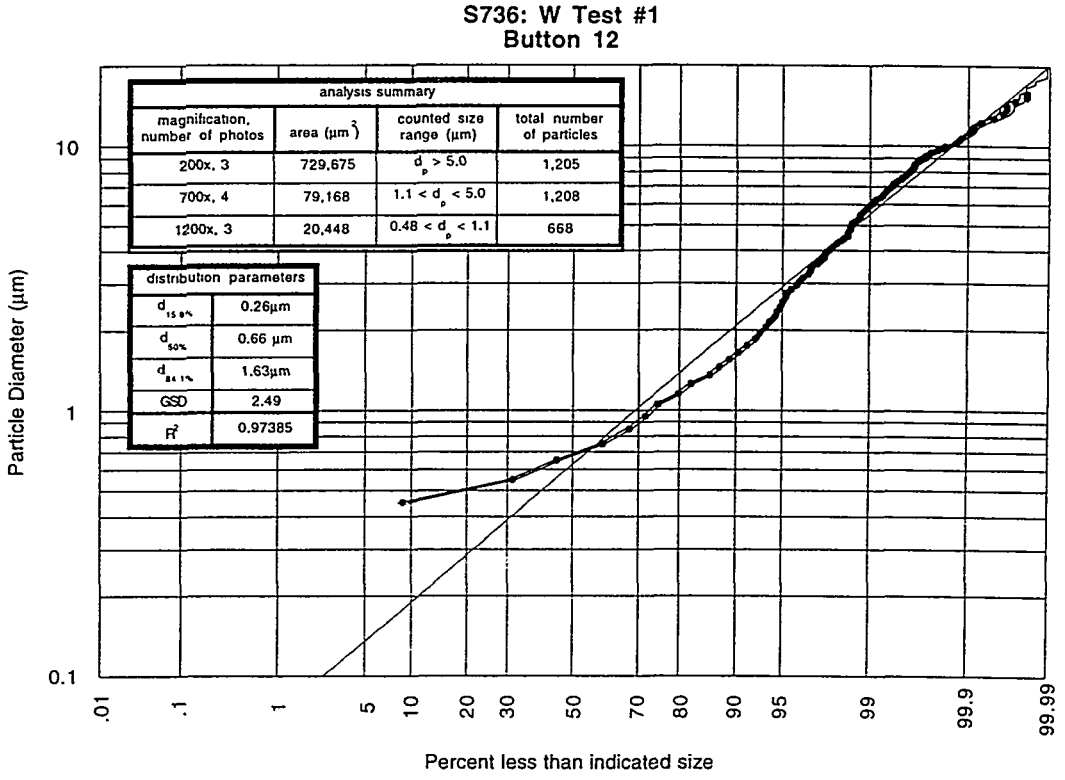

Data Summary Table:

photo	mag	scale (pixel/μm)	size (μm²)	min. d_{eq} (μm)*	# of particles	scale factor	KW Test z value	Overall p-value
736_12_1	200x	1.13	575x423	2.88	445	1	0.02	0.567
736_12_2	200x	1.13	575x422	2.88	334	1	0.93	
736_12_3	200x	1.13	575x424	2.88	426	1	-0.89	
736_12_4	700x	3.96	164x120	0.82	267	12.25	-0.18	0.562
736_12_5	700x	3.96	164x121	0.82	321	12.25	-0.57	
736_12_6	700x	3.96	164x121	0.82	289	12.25	-0.69	
736_12_7	700x	3.96	165x120	0.82	331	12.25	1.40	
736_12_8	1200x	6.8	96x71	0.48	216	36	-0.35	0.857
736_12_9	1200x	6.8	96x71	0.48	206	36	0.55	
736_12_10	1200x	6.8	96x71	0.48	246	36	-0.19	

* equivalent minimum diameter particle counted having an area of at least 3.25 x 1/scale on a side.

Figure 5.1.8. W Test #1, Button 14 particle size distribution, with linear fit and 95% confidence intervals.

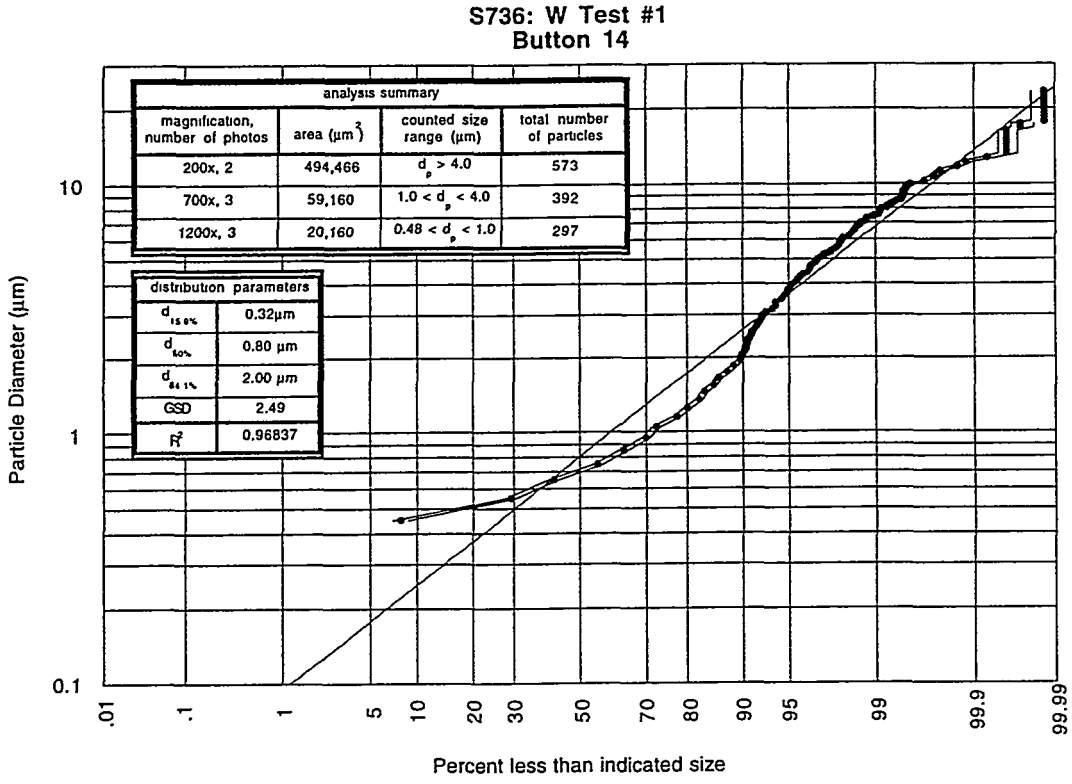

Data Summary Table:

photo	mag	scale (pixel/μm)	size (μm²)	min. d_{eq} (μm)*	# of particles	scale factor	KW Test z-value	Overall p-value
736_14_1	200x	1.125	579x429	2.89	287	1	0.89	0.371
736_14_2	200x	1.125	579x425	2.89	286	1	-0.89	
736_14_3	700x	3.96	164x120	0.82	140	12.25	-1.36	0.385
736_14_4	700x	3.96	164x120	0.82	120	12.25	0.86	
736_14_5	700x	3.96	165x120	0.82	132	12.25	0.54	
736_14_6	1200x	6.8	96x70	0.48	95	36	1.55	0.163
736_14_7	1200x	6.8	96x70	0.48	108	36	0.15	
736_14_8	1200x	6.8	96x70	0.48	94	36	-1.71	

* equivalent minimum diameter particle counted having an area of at least 3.25 x 1/scale on a side.

Figure 5.1.9. Representative SEM images from W Test #1, Button 12. Craters appear in (c) as bright rings with dark interiors.

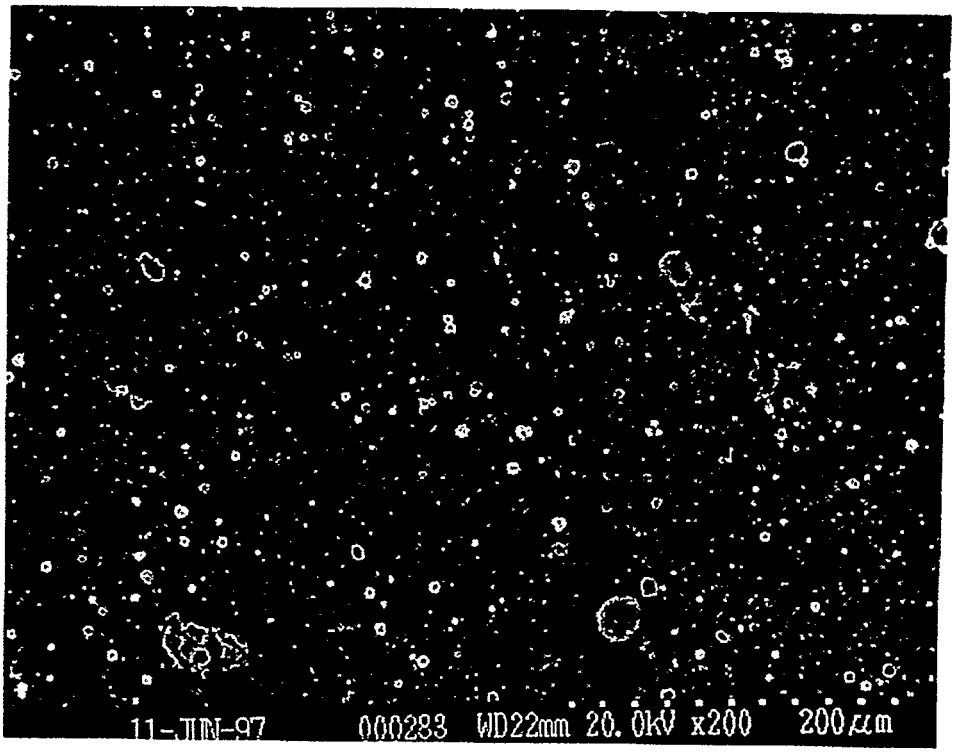

(a) 200x

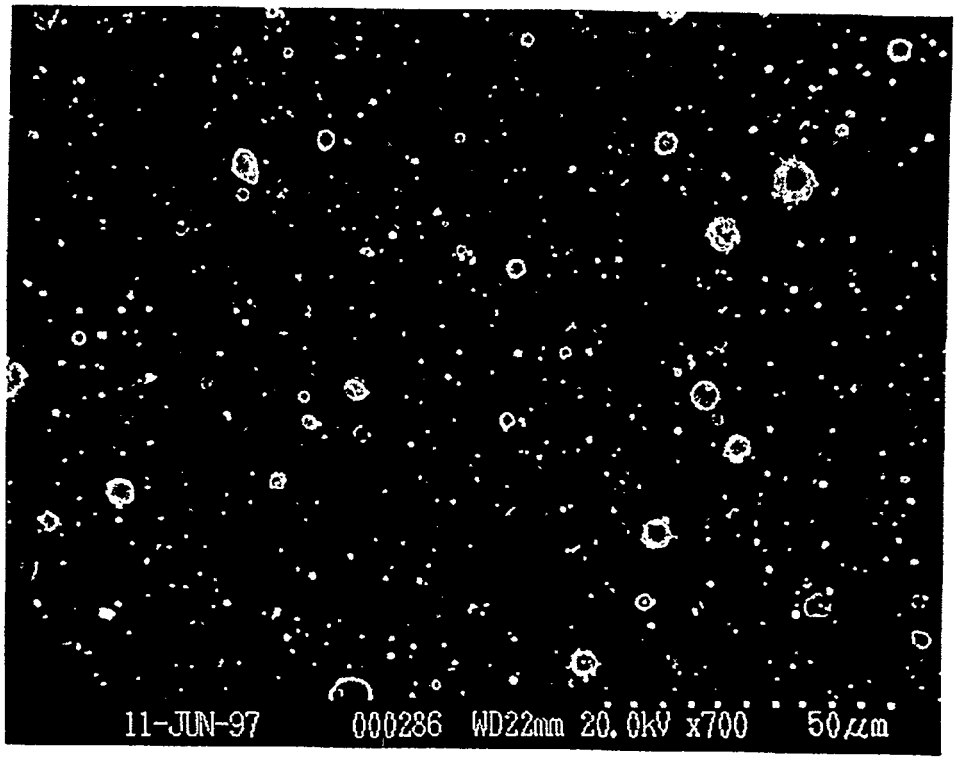

(b) 700x

Figure 5.1.9.continued.

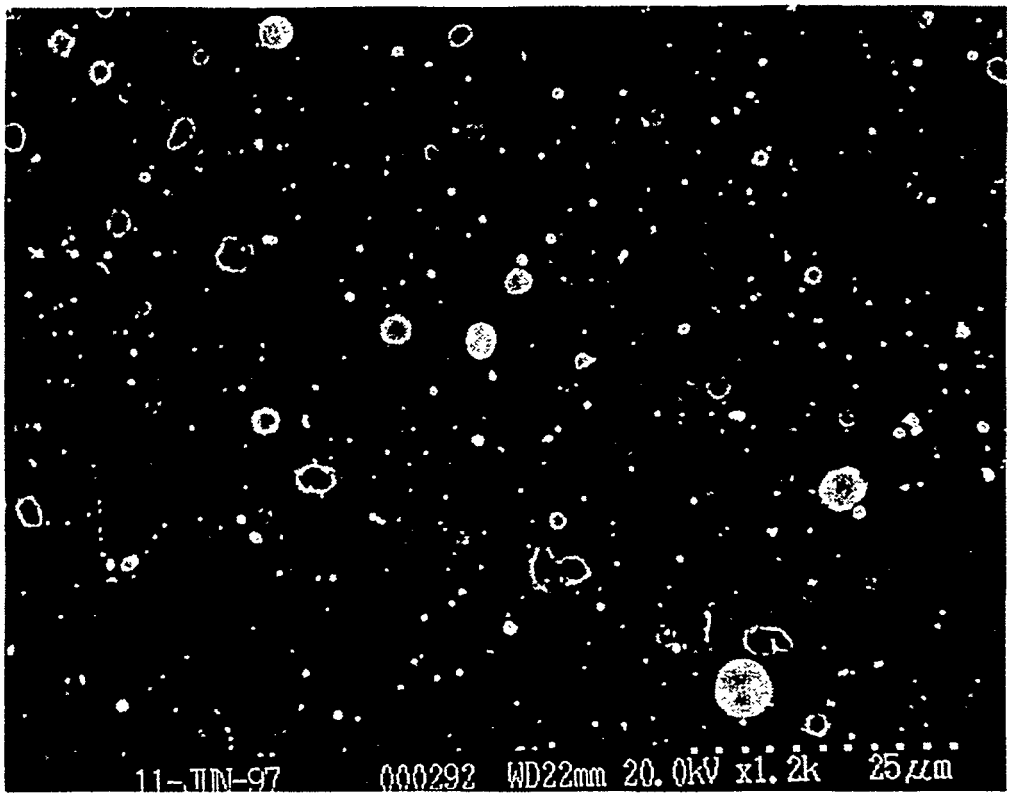

(c) 1200x

5.2. *S739: W Test #2*

The second tungsten test was performed with a discharge energy of 4,259 J. Copper and stainless steel capture buttons were placed in the glass chamber in the normal configuration (see Figure 2.2). Copper buttons were placed on the chamber wall, while copper and stainless steel were used on the end plate to investigate differences in susceptibility to cratering from impact of the W particles. Figure 5.2.1 shows the resulting voltage and current traces. Signal acquisition problems similar to previous tests plagued this shot. Figure 5.2.2 displays the signal obtained from the end-plate pressure transducer, showing again no information except for noise from the discharge EM pulse. The new source section housing with pressure tap was not used in this test. Table 5.2.1 gives mass data for the sample sleeve and buttons. The amount of mass deposited on the buttons was insufficient to show any trends.

As in W Test #1, the tungsten sample sleeve used in W Test #2 broke. Since the Lexan inner insulator housing the sample sleeve is transparent, cracks were observed prior to attempting extraction of the sleeve. The break pattern for this test, however, was significantly different from Test #1. Cracks ran down the entire length of the sleeve, as well as around the circumference; the sleeve was shattered into many pieces. The material deposited on buttons did not appear to have resulted from this shattering, though. The generally spherical shape of the material on the buttons did not match the shape of debris collected from around the shattered sleeve. Further investigation into the response of tungsten (specifically embrittlement) to high heat loading should be performed.

Particulate size distributions from selected buttons (1, 6, 7, 9, 12, and 14) are shown in Figures 5.2.3-8. The images obtained for this analysis were optimized for the counting procedure, and the minimum equivalent diameter discrimination factor was set to 2.25 for most cases. Significant cratering was observed on end-plate buttons, regardless of the substrate material. Wall-mounted buttons were not cratered. The cratering problem was so severe on end-plate buttons that accurate particle size distributions were not obtained. Different steps, such as running in backscatter mode and varying levels of contrast, were attempted with the SEM to generate acceptable images, but without success.

Figure 5.2.1. W Test #2 voltage and current traces.

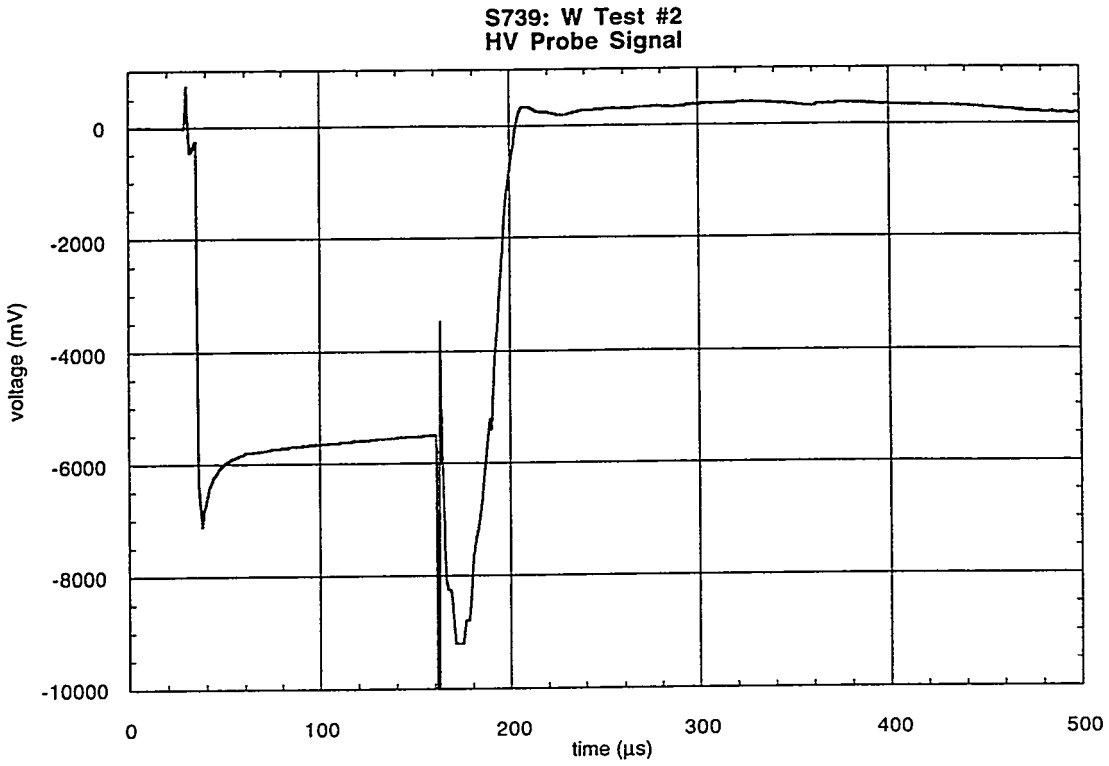

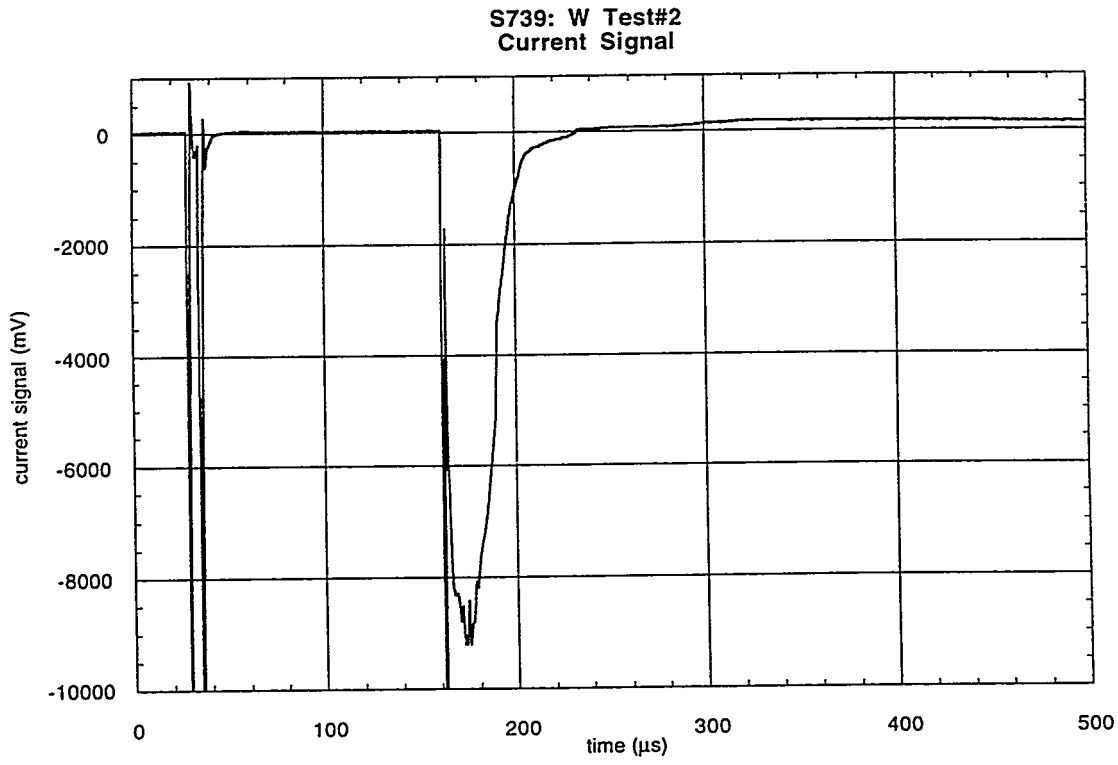

Figure 5.2.2. W Test #2 end-plate P transducer trace.

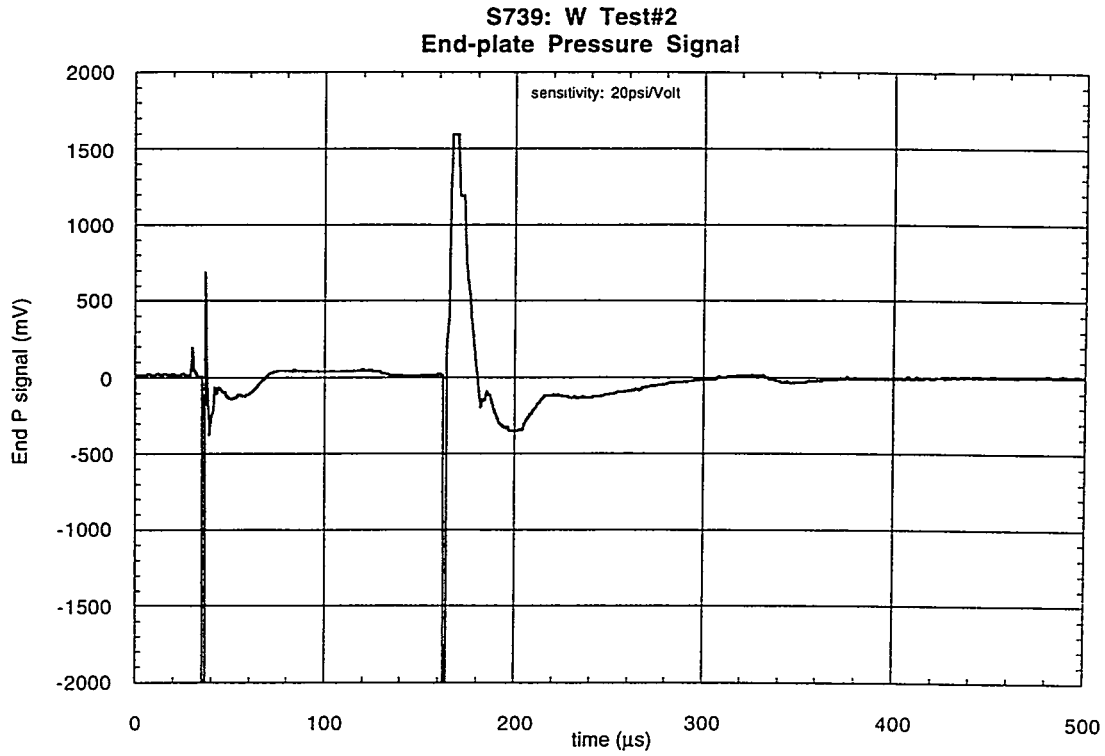

Table 5.2.1. S739 mass measurements.

Source Section Components:			
component	pre-test wt. (g)	post-test wt. (g)	Δ wt. (mg, ± 0.05)
short insulator	1.01828	-	-
long insulator	2.91518	-	-
cathode (dimetech)	9.02951	9.00438	25.13
W sleeve	30.78820	30.57327(3)	214.93

Substrate Components:							
wall button	pre-test wt. (g)	post-test wt. (g)	Δ wt. (mg)	end-plate button	pre-test wt (g)	post-test wt. (g)	Δ wt. (mg)
1	0.58696	0.58703	0.06	9	0.58758	0.58759	0.01
2	0.58703	0.58711	0.07	10	0.58250	0.58254	0.04
3	0.58257	0.58258	0.01	11	0.58369	0.58370	0.01
4	0.58377	0.58384	0.07	12	0.58309	0.58311	0.02
5	0.58372	0.58376	0.05	13	0.58314	0.58317	0.03
6	0.58688	0.58691	0.02	14	0.91983	0.91992	0.09
7	0.91841	0.91853	0.13	15	0.92456	0.92473	0.17
8	0.91858	0.91863	0.05	16	0.91772	0.91790	0.18
				17	0.91717	0.91731	0.14

Notes:
(1) All weight measurements are taken 3+ times and averaged.
(2) Δm uncertainty is ± 0.05 mg.
(3) Measurement of all pieces of shattered sleeve.

Figure 5.2.3. W Test #2, Button 1 particle size distribution, with linear fit and 95% confidence intervals.

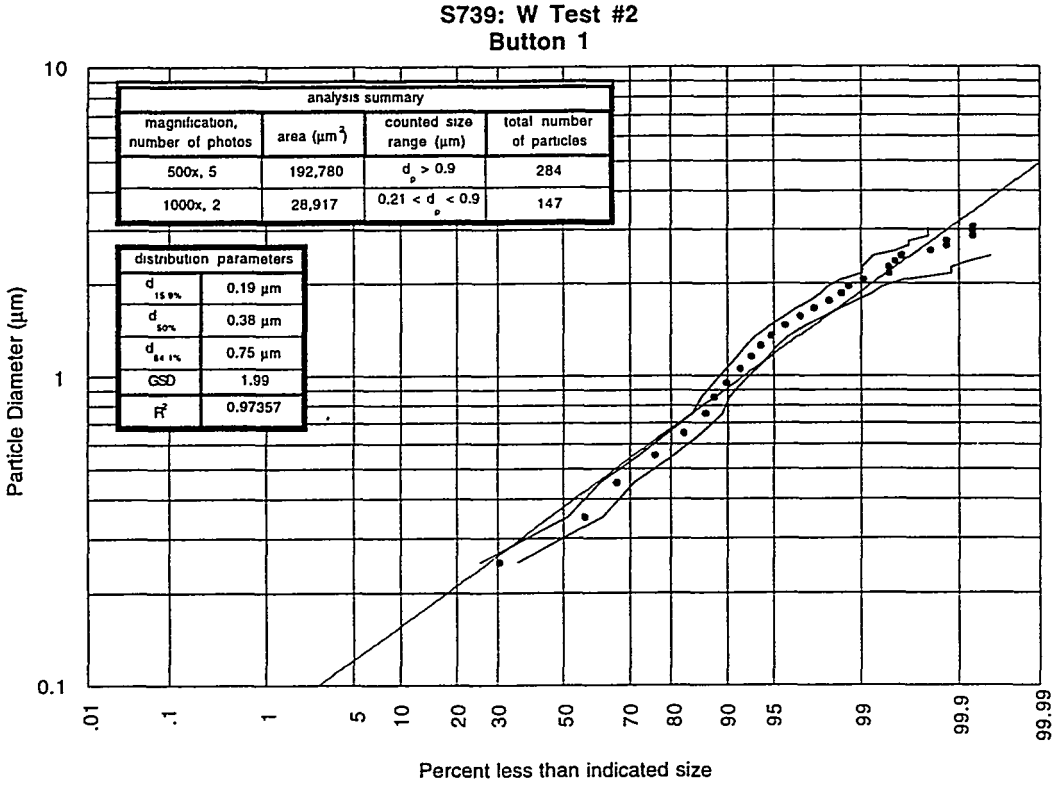

Data Summary Table:

photo	mag	scale (pixel/μm)	size (μm²)	min. d_{eq} (μm)*	# of particles	scale factor	KW Test z-value	Overall p-value
739_1_1	500x	2.92	231x171	0.77	-	-	failed	0.719
739_1_2	500x	2.92	231x168	0.77	64	1	-1.16	
739_1_3	500x	2.92	231x167	0.77	55	1	0.23	
739_1_4	500x	2.92	230x169	0.77	64	1	020	
739_1_7	500x	2.92	231x165	0.77	47	1	1.00	
739_1_8	500x	2.92	230x167	0.77	54	1	-0.20	
739_1_5	1000x	5.84	15x83	0.21**	57	4	1.15	0.242
739_1_6	1000x	5.84	116x83	0.21**	90	4	-1.15	

* equivalent minimum diameter particle counted having an area of at least 2.25 x 1/scale on a side.
** equivalent minimum diameter particle counted having an area of at least 1.25 x 1/scale on a side.

Figure 5.2.4. W Test #2, Button 6 particle size distribution, with linear fit and 95% confidence intervals.

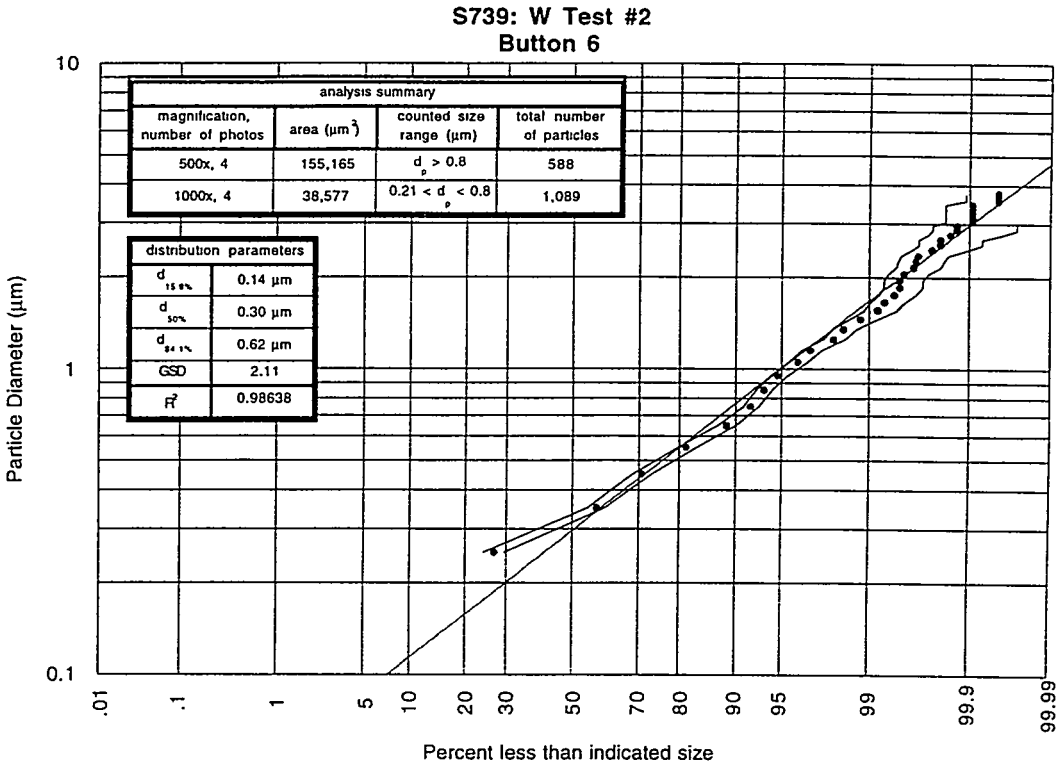

Data Summary Table:

photo	mag	scale (pixel/μm)	size (μm²)	min. d_{eq} (μm)*	# of particles	scale factor	KW Test z-value	Overall p-value
739_6_1	500x	2.92	232x166	0.77	143	1	1.25	0.531
739_6_2	500x	2.92	230x170	0.77	121	1	-0.17	
739_6_3	500x	2.92	231x167	0.77	146	1	-1.12	
739_6_4	500x	2.92	232x168	0.77	171	1	0.04	
739_6_5	1000x	5.84	115x83	0.21**	232	4	1.49	0.075
739_6_6	1000x	5.84	116x84	0.21**	194	4	1.66	
739_6_7	1000x	5.84	116x83	0.21**	326	4	-0.96	
739_6_8	1000x	5.84	115x84	0.21**	337	4	-1.75	

* equivalent minimum diameter particle counted having an area of at least 2.25 x 1/scale on a side.

** equivalent minimum diameter particle counted having an area of at least 1.25 x 1/scale on a side.

Figure 5.2.5. W Test #2, Button 7 particle size distribution, with linear fit and 95% confidence intervals.

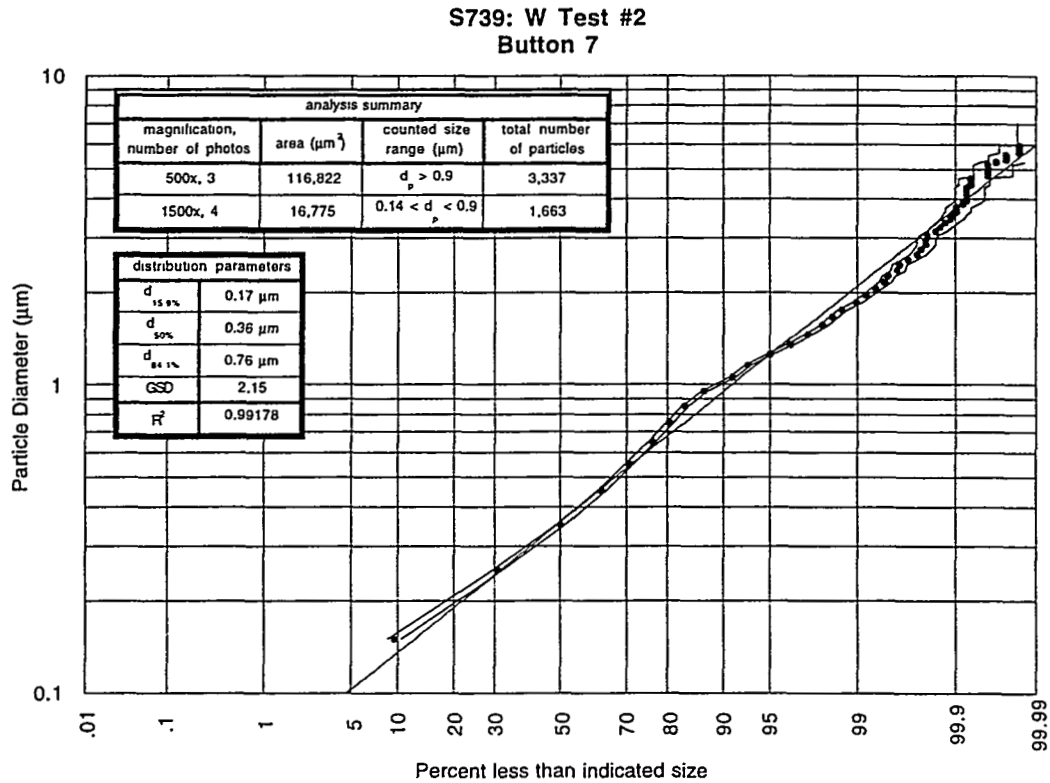

Data Summary Table:

photo	mag	scale (pixel/μm)	size (μm²)	min. d_{eq} (μm)*	# of particles	scale factor	KW Test z-value	Overall p-value
739_7_2	500x	2.92	232x167	0.77	1137	1	0.52	0.857
739_7_3	500x	2.92	231x170	0.77	1147	1	-0.11	
739_7_4	500x	2.92	231x168	0.77	1053	1	-0.42	
739_7_5	1500x	8.85	76x55	0.14**	377	9	0.00	0.843
739_7_6	1500x	8.85	76x55	0.14**	414	9	-0.61	
739_7_7	1500x	8.85	76x55	0.14**	415	9	-0.25	
739_7_8	1500x	8.85	77x55	0.14**	457	9	0.83	

* equivalent minimum diameter particle counted having an area of at least 2.25 x 1/scale on a side.
** equivalent minimum diameter particle counted having an area of at least 1.25 x 1/scale on a side.

6.0 Aluminum Test Results

The final ITER-relevant metal investigated under the disruption simulation conditions available in SIRENS was aluminum. Aluminum is relevant to because it has thermophysical properties similar to those of beryllium (a candidate for first wall and divertor tile coatings). Beryllium is not easily handled because of its toxic nature, and aluminum is often used to simulate beryllium in the context of thermal response. Two separate tests in SIRENS were performed with aluminum sleeves. Table 6.0.1 contains a summary of important test data: sample mass loss, button weight gain, and particulate size distribution parameters.

Table 6.0.1 Al tests comparison summary.

	Al Test 1 (S744)				Al Test 2 (S745)			
Energy (J)	4226				4260			
Sample Δm (mg)	526.41				493.40			
Cathode Δm (mg)	32.46				33.73			
	Δm (mg)	$d_{50\%}$ (μm)	GSD	R^2	Δm (mg)	$d_{50\%}$ (μm)	GSD	R^2
Button 1	0.20	*	*	*	0.40	*	*	*
Button 2	0.20	*	*	*	0.43	*	*	*
Button 3	0.14	1.90	2.15	0.989	0.28	2.29	2.01	0.972
Button 4	0.17	*	*	*	0.43	*	*	*
Button 5	0.22	*	*	*	0.89	*	*	*
Button 6	0.19	*	*	*	0.44	*	*	*
Button 7	0.12	3.01	2.04	0.978	0.96	1.60	2.19	0.991
Button 8	0.02	*	*	*	0.37	*	*	*
Button 9	0.45	0.847	2.48	0.991	0.82	1.27	2.29	0.984
Button 10	**	**	**	**	**	*	*	*
Button 11	**	**	**	**	**	*	*	*
Button 12	0.86	*	*	*	1.52	*	*	*
Button 13	0.79	*	*	*	**	*	*	*
Button 14	0.84	*	*	*	0.45	*	*	*
Button 15	0.89	*	*	*	**	*	*	*
Button 16	**	**	**	**	0.87	*	*	*
Button 17	0.66	*	*	*	**	*	*	*

Notes:
(1) Asterisk (*) denotes analysis not performed.
(2) Double asterisk (**) indicates button locations not used in the test.

6.1 S744: Al Test #1

The first aluminum test was performed with a discharge energy of 4,226 J. Copper capture buttons were placed in the glass chamber in the normal configuration (see Figure 2.2). Figure 6.1.1 shows the resulting voltage and current traces, both showing the same problems seen throughout this entire test series. Table 6.1.1 gives mass data for the sample sleeve and buttons. Relatively large amounts of mass were deposited on end-plate buttons, and these buttons visually appeared to be coated with aluminum. The side-wall buttons displayed similar amounts of mass gain as seen in the other materials tests, but the visual appearance was significantly different. Many long streaks of aluminum were visible with the unaided eye. Similar streaks were visible only under magnification in the other materials tests.

Particulate size distributions from selected buttons (3, 7 and 9) are shown in Figures 6.1.3-5. Fewer buttons were analyzed in for the Al tests because apparent variation in deposited material occurred only between wall and end-plate buttons, and because the nature of the Al coating to flake off made reliable analysis difficult for some buttons. Regions covered by flakes (that subsequently fell off) were typically devoid of particles. Flakes ranged in size from roughly 1 mm to 25 mm in equivalent diameter.

Representative SEM images from button 7 are shown in Figure 6.1.6. The particles deposited on side wall and end-plate buttons for this test were generally larger than particles from other materials. Lower magnifications were suitable to view the entire particle size range, and no particles smaller than ~1 μm were observed even at high magnifications (1000x).

One notable feature of each distribution from the various buttons in this test is the distribution component from the large particles strays from the linear shape typically observed with the other materials. This deviation from linearity suggests the underlying distribution for each button is bimodal. A physical interpretation of this observation comes about when the low melting temperature of Al is considered. It is possible that the normally small amount of transmitted heat flux into the test sleeve is sufficient to increase the temperature of a surface layer of Al beyond the melting point. The pressure associated with the mass vaporization in the sleeve could then eject molten Al from the surface, entraining relatively large molten particles in the flow. These particles are not generated by condensation and growth, and could be larger than those that are generated by condensation and growth. The resulting distributions then have at least two particle types generated by different mechanisms, thus skewing the log-normal approximation of the overall distribution. This effect was not observed in tests with other materials because of their higher melting temperatures. Further investigation is required.

Figure 6.1.1. W Test #1 voltage and current traces.

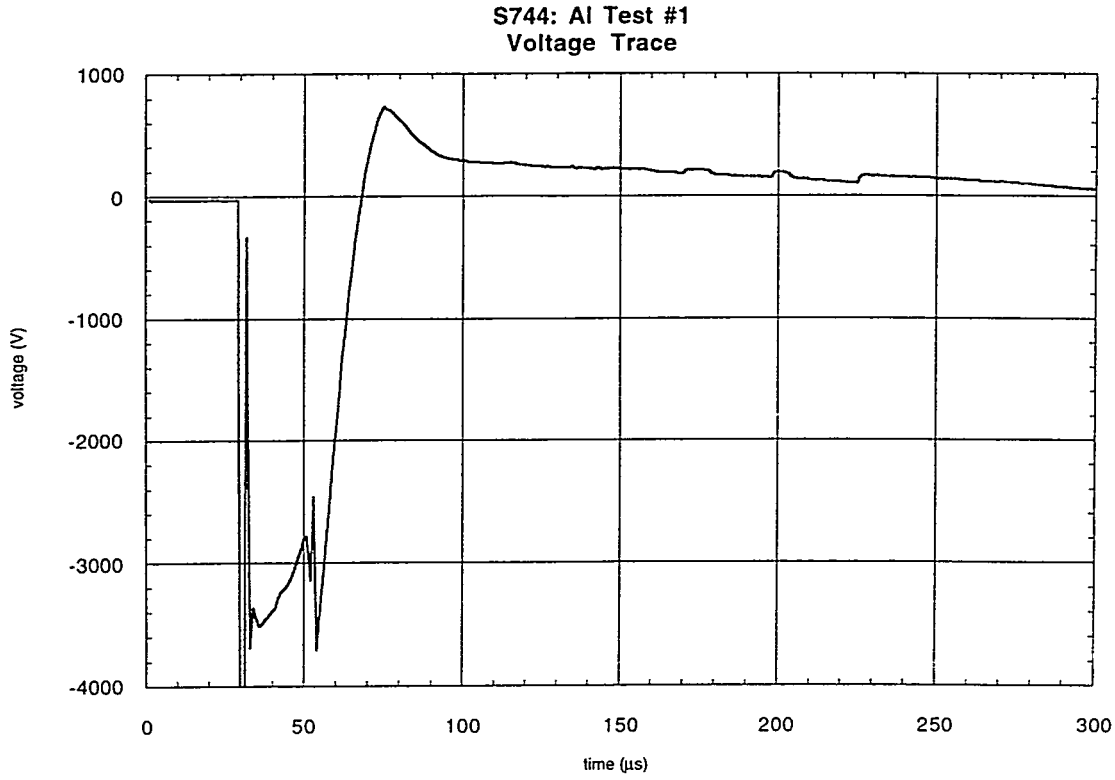

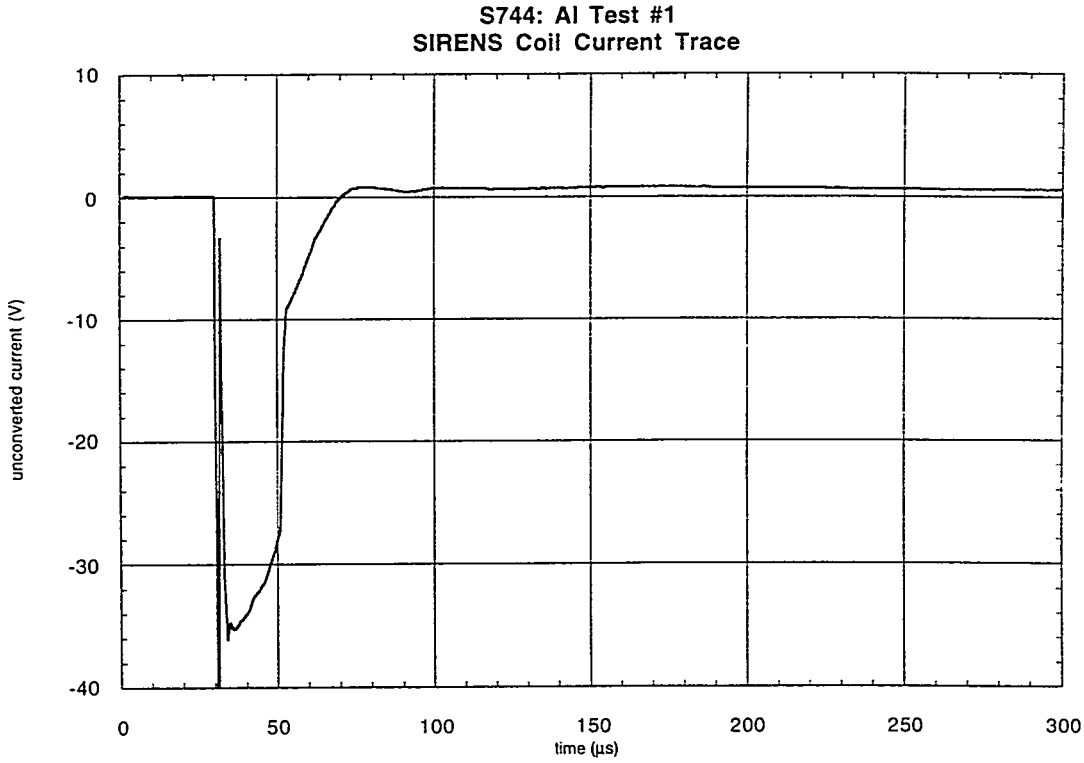

Table 6.1.1. S734 mass measurements.

Source Section Components:

component	pre-test wt. (g)	post-test wt. (g)	Δ wt. (mg, ± 0.05)
short insulator	1.0256	-	-
long insulator	2.93625	-	-
cathode (dimetech)	8.96390	8.93145	32.46
Al sleeve	4.42097	3.89456	526.41

Substrate Components:

wall button	pre-test wt. (g)	post-test wt. (g)	Δ wt. (mg)	end-plate button	pre-test wt (g)	post-test wt. (g)	Δ wt. (mg)
1	0.91550	0.91570	0.20	9	0.92273	0.92317	0.45
2	0.92263	0.92283	0.20	10	**	**	**
3	0.91826	0.91840	0.14	11	**	**	**
4	0.91335	0.91351	0.17	12	0.91966	0.92052	0.86
5	0.92108	0.92130	0.22	13	0.91851	0.91930	0.79
6	0.91929	0.91948	0.19	14	0.92024	0.92108	0.84
7	0.91567	0.91579	0.12	15	0.92070	0.92159	0.89
8	0.90451	0.90453	0.02	16	**	**	**
				17	0.91455	0.91521	0.66

Notes:

(1) All weight measurements are taken 3+ times and averaged.

(2) Δm uncertainty is ± 0.05 mg.

(3) Double asterisk (**) denotes buttons not used in this test.

Figure 6.1.3. Al Test #1, Button 3 particle size distribution, with linear fit and 95% confidence intervals.

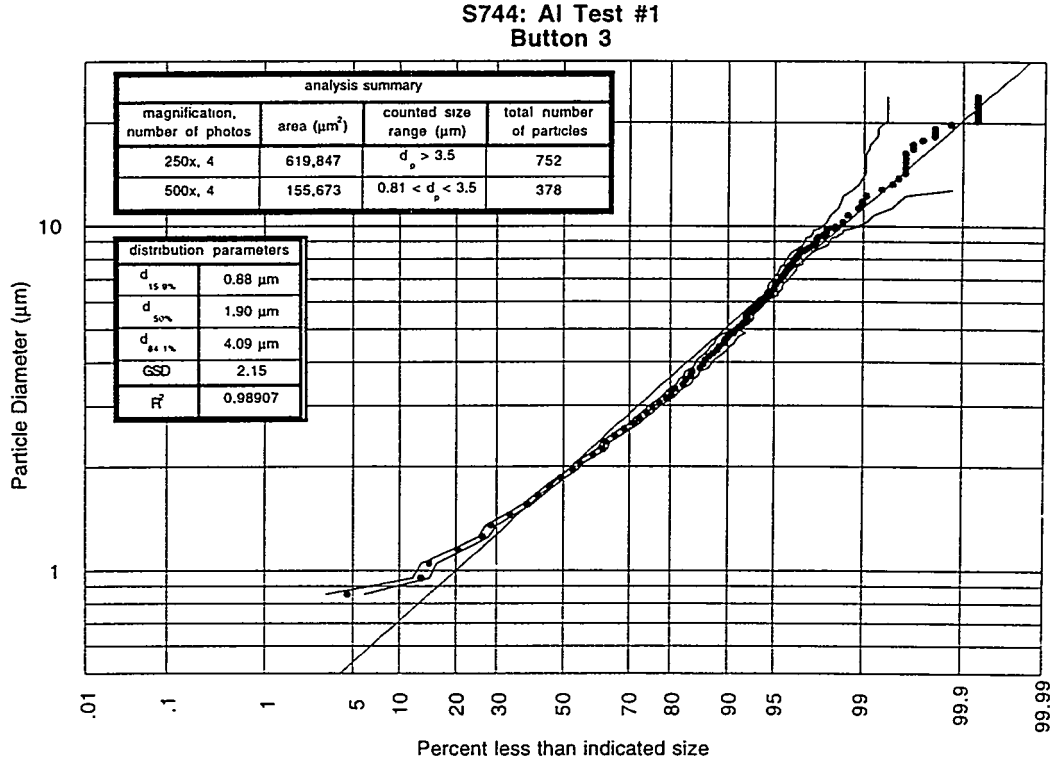

Data Summary Table:

photo	mag	scale (pixel/μm)	size (μm²)	min. d_{eq} (μm)*	# of particles	scale factor	KW Test z-value	Overall p-value
744_3_1	250x	1.39	465x334	1.62	241	1	-1.20	0.610
744_3_2	250x	1.39	466x334	1.62	178	1	0.02	
744_3_3	250x	1.39	464x332	1.62	152	1	0.31	
744_3_4	250x	1.39	465x333	1.62	181	1	1.01	
744_3_5	500x	2.78	232x167	0.81	66	4	0.88	0.730
744_3_6	500x	2.78	233x168	0.81	89	4	0.44	
744_3_7	500x	2.78	231x167	0.81	22	4	-0.39	
744_3_8	500x	2.78	232x169	0.81	112	4	-0.75	

* equivalent minimum diameter particle counted having an area of at least 2.25 x 1/scale on a side.

Figure 6.1.4. Al Test #1, Button 7 particle size distribution, with linear fit and 95% confidence intervals.

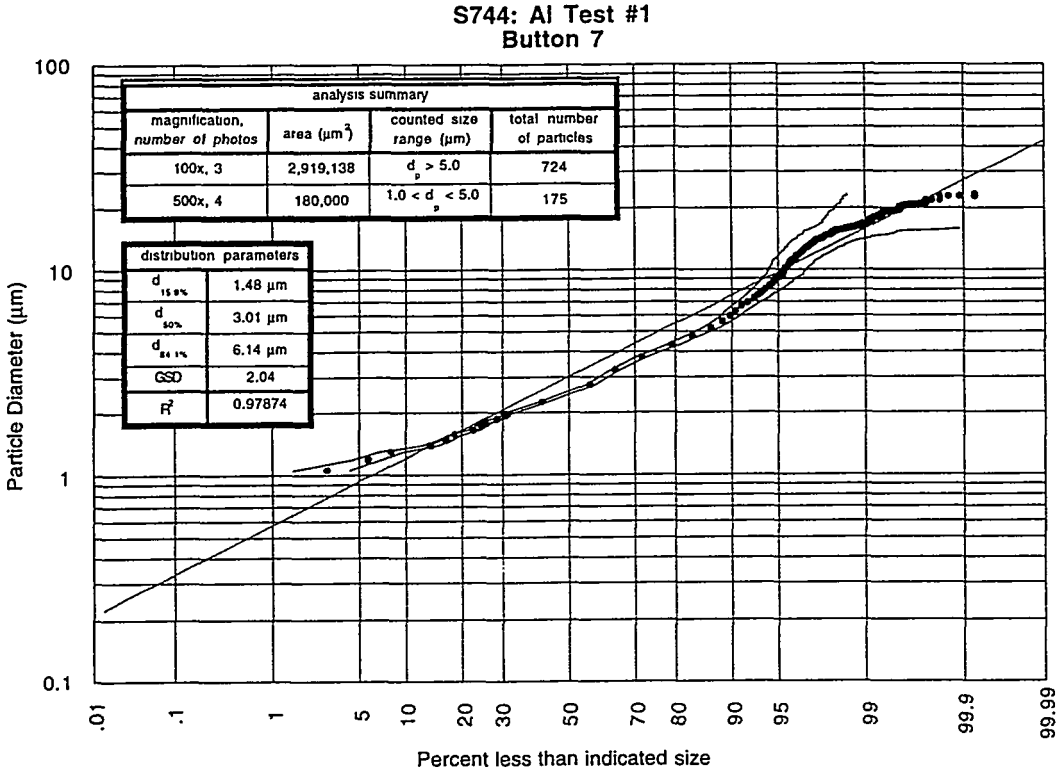

Data Summary Table:

photo	mag	scale (pixel/μm)	size (μm²)	min. d_{eq} (μm)*	# of particles	scale factor	KW Test z-value	Overall p-value
744_7_1	100x	0.556	1164x832	4.05	271	1	-0.97	0.255
744_7_2	100x	0.556	1165x842	4.05	288	1	1.65	
744_7_3	100x	0.556	1160x836	4.05	165	1	-0.81	
744_7_6	400x	2.24	288x209	1.00	45	16	0.56	0.362
744_7_7	400x	2.24	288x207	1.00	51	16	1.00	
744_7_8	400x	2.24	288x209	1.00	79	16	-1.41	

* equivalent minimum diameter particle counted having an area of at least 2.25 x 1/scale on a side.

Figure 6.1.5. Al Test #1, Button 9 particle size distribution, with linear fit and 95% confidence intervals.

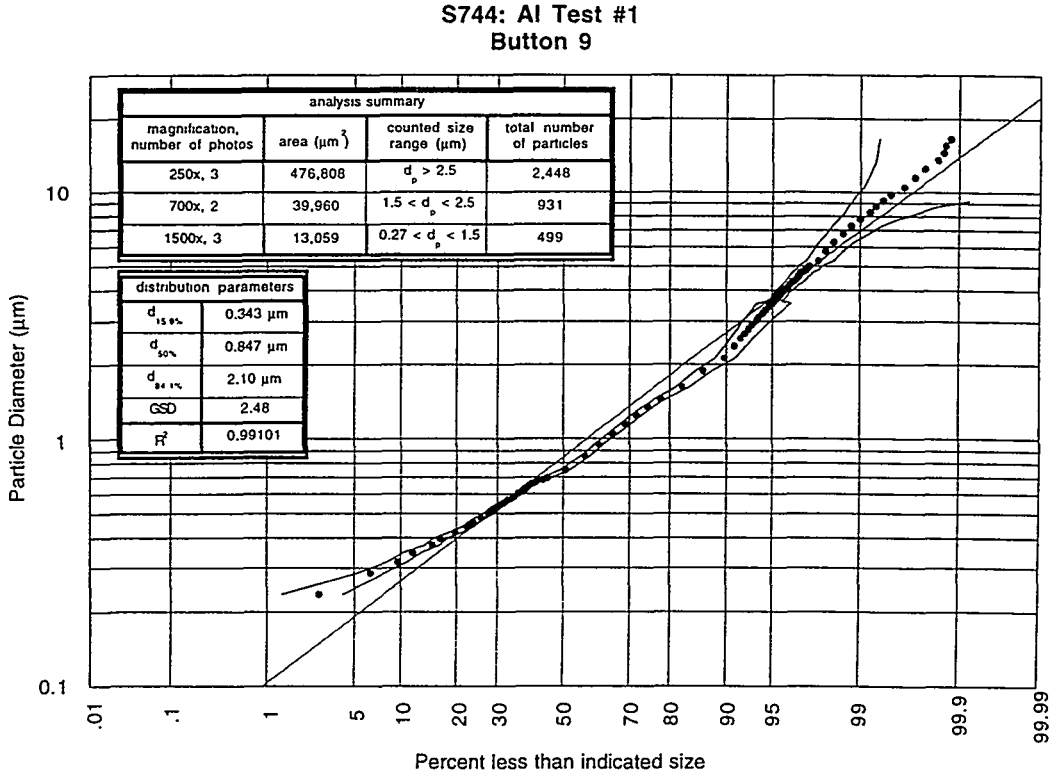

Data Summary Table:

photo	mag	scale (pixel/μm)	size (μm²)	min. d_{eq} (μm)*	# of particles	scale factor	KW Test z-value	Overall p-value
744_9_1	250x	1.39	466x340	1.62	656	1	-1.31	0.417
744_9_2	250x	1.39	467x340	1.62	957	1	0.75	
744_9_3	250x	1.39	468x341	1.62	835	1	0.46	
744_9_4	700x	3.92	167x120	0.576	439	7.84	0.12	0.901
744_9_5	700x	3.92	166x121	0.576	492	7.84	-0.12	
744_9_6	700x	3.92	166x120	0.576	315	7.84	failed	
744_9_7	1500x	8.40	77.4x56.3	0.269	180	36	0.18	0.644
744_9_8	1500x	8.40	77.6x56.4	0.269	155	36	0.70	
744_9_9	1500x	8.40	77.5x55.8	0.269	164	36	-0.58	

* equivalent minimum diameter particle counted having an area of at least 2.25 x 1/scale on a side.

Figure 6.1.6. Representative SEM images from Al Test #1, Button 7.

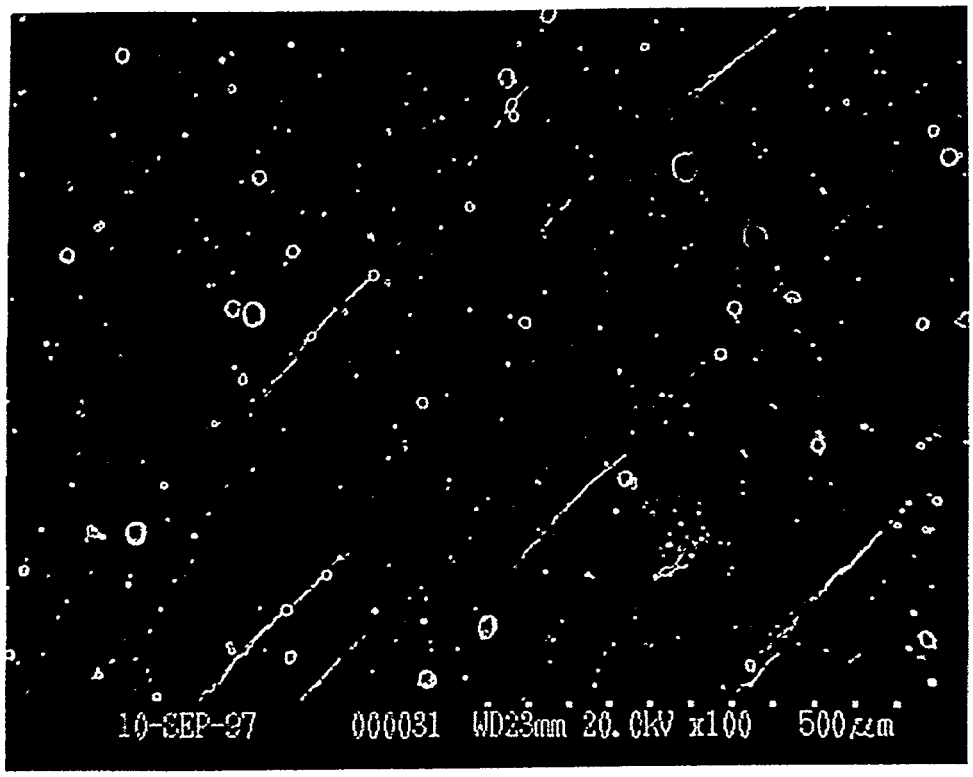

(a) 100x

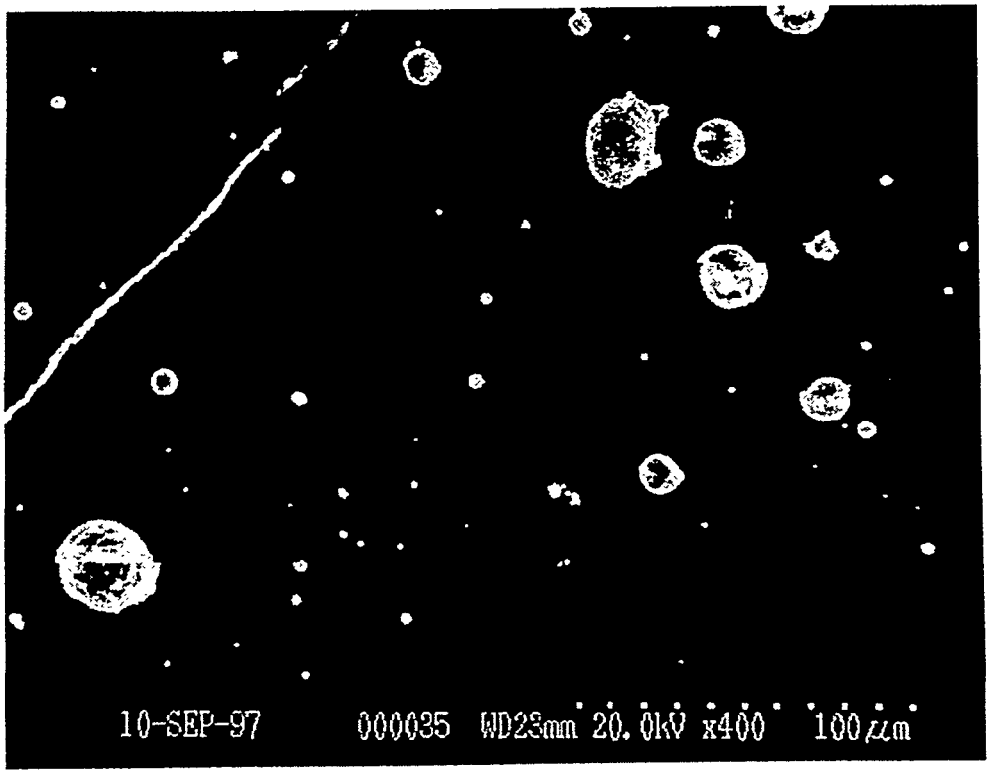

(b) 400x

6.2. *S745: Al Test #2*

The second aluminum test was performed with a discharge energy of 4,260 J. Copper capture buttons were placed in the glass chamber in the normal configuration (see Figure 2.2). Voltage and current traces were not obtained for this test because the digitizer failed to trigger prior to the discharge. Table 6.2.1 gives mass data for the sample sleeve and buttons. Noticeably more mass was deposited on the wall buttons in this test; it is not clear why this occurred since the mass loss from the Al sleeves for each shot was approximately equal (526 mg for Al Test #1 compared to 493 mg for Al Test #2).

Particulate size distributions from selected buttons (3, 7, and 9) are shown in Figures 6.2.3-5. The images obtained for this analysis were optimized for the counting procedure, and the minimum equivalent diameter discrimination factor was set to 2.25 for all cases. The non-linear shapes of the distributions are again observed in this test (see Section 6.1).

Table 6.2.1. S745 mass measurements.

Source Section Components: component	pre-test wt. (g)	post-test wt. (g)	Δ wt. (mg, ± 0.05)
short insulator	1.02609	-	-
long insulator	2.92392	-	-
cathode (dimetech)	8.93149	8.89776	33.73
Al sleeve	4.40913	3.91573	493.40

Substrate Components: wall button	pre-test wt. (g)	post-test wt. (g)	Δ wt. (mg)	end-plate button	pre-test wt (g)	post-test wt. (g)	Δ wt. (mg)
1	0.91512	0.91552	0.40	9	0.92264	0.92345	0.82
2	0.91776	0.91819	0.43	10	**	**	**
3	0.92195	0.92223	0.28	11	**	**	**
4	0.91931	0.91974	0.43	12	0.91598	0.91749	1.52
5	0.92428	0.92517	0.89	13	**	**	**
6	0.91855	0.91900	0.44	14	0.91715	0.91760	0.45
7	0.91741	0.91837	0.96	15	**	**	**
8	0.91981	0.92017	0.37	16	0.92043	0.92130	0.87
				17	**	**	**

Notes:
(1) All weight measurements are taken 3+ times and averaged.
(2) Δm uncertainty is ± 0.05 mg.
(3) Double asterisk (**) denotes buttons not used in this test.

Figure 6.2.3. Al Test #2, Button 3 particle size distribution, with linear fit and 95% confidence intervals.

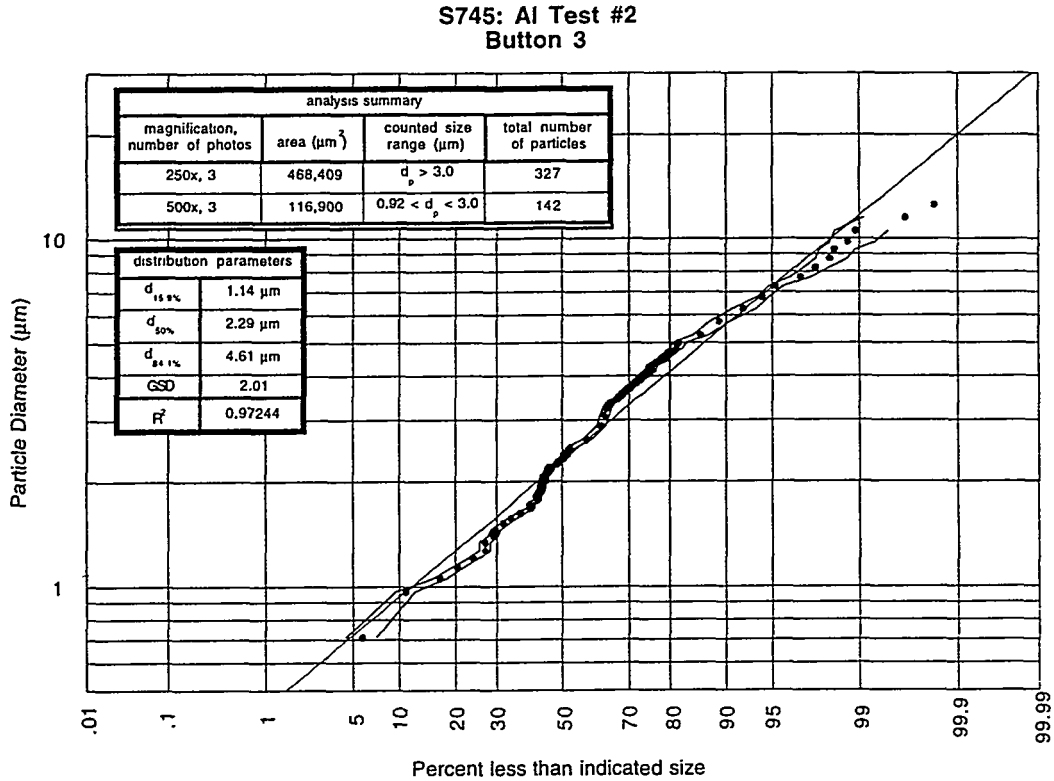

Data Summary Table:

photo	mag	scale (pixel/μm)	size (μm²)	min. d_{eq} (μm)*	# of particles	scale factor	KW Test z-value	Overall p-value
745_3_1	250x	1.39	466x332	1.83	118	1	-1.79	0.190
745_3_2	250x	1.39	469x337	1.83	99	1	0.57	
745_3_3	250x	1.39	466x334	1.83	110	1	1.27	
745_3_4	500x	2.78	234x167	0.92	50	4	1.03	0.06
745_3_5	500x	2.78	233x169	0.92	41	4	1.44	
745_3_6	500x	2.78	233x165	0.92	51	4	-2.38	

* equivalent minimum diameter particle counted having an area of at least 2.25 x 1/scale on a side.

Figure 6.2.4. Al Test #2, Button 7 particle size distribution, with linear fit and 95% confidence intervals.

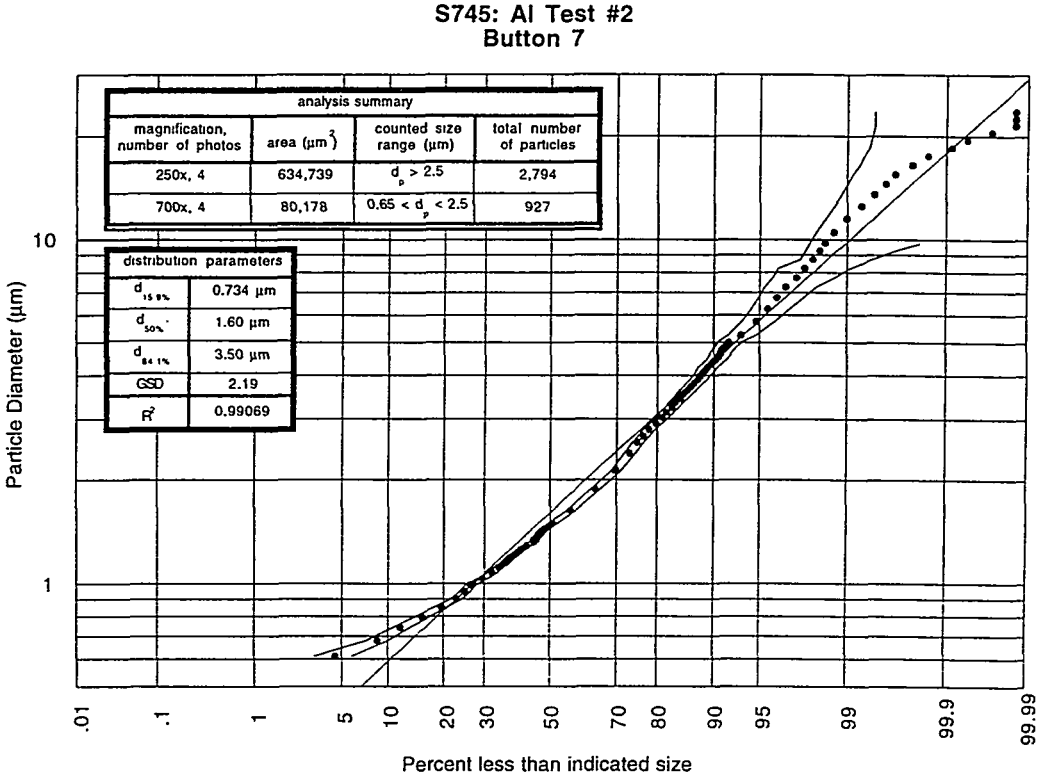

Data Summary Table:

photo	mag	scale (pixel/μm)	size (μm²)	min. d_{eq} (μm)*	# of particles	scale factor	KW Test z-value	Overall p-value
745_7_1	250x	1.39	467x337	1.83	587	1	-2.54	0.053
745_7_2	250x	1.39	468x342	1.83	622	1	1.77	
745_7_3	250x	1.39	468x335	1.83	763	1	0.39	
745_7_9	250x	1.39	468x343	1.83	822	1	0.27	
745_7_4	700x	3.92	166x120	0.65	189	7.84	2.06	0.116
745_7_5	700x	3.92	166x121	0.65	229	7.84	-1.69	
745_7_7	700x	3.92	166x121	0.65	191	7.84	0.46	
745_7_8	700x	3.92	166x121	0.65	318	7.84	-0.60	

* equivalent minimum diameter particle counted having an area of at least 2.25 x 1/scale on a side.

Figure 6.2.5. Al Test #2, Button 9 particle size distribution, with linear fit and 95% confidence intervals.

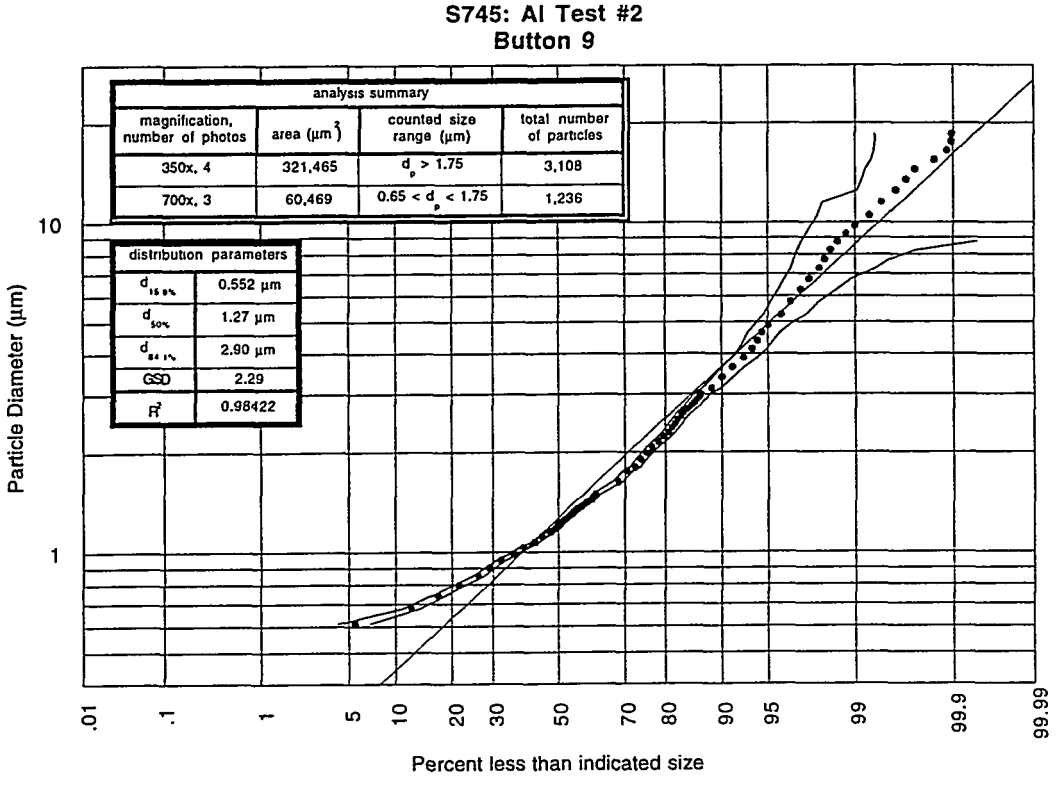

Data Summary Table:

photo	mag	scale (pixel/μm)	size (μm²)	min. d_{eq} (μm)*	# of particles	scale factor	KW Test z-value	Overall p-value
745_9_2	350x	1.96	332x241	1.30	680	1	-0.34	0.293
745_9_3	350x	1.96	332x242	1.30	952	1	-1.66	
745_9_4	350x	1.96	332x243	1.30	698	1	1.05	
745_9_5	350x	1.96	331x243	1.30	778	1	1.07	
745_9_6	700x	3.92	166x122	0.65	370	4	2.21	0.085
745_9_7	700x	3.92	165x121	0.65	413	4	-1.20	
745_9_8	700x	3.92	166x121	0.65	245	4	failed	
745_9_9	700x	3.92	166x122	0.65	453	4	-0.93	

* equivalent minimum diameter particle counted having an area of at least 2.25 x 1/scale on a side.

7.0 Conclusion

The ITER-relevant metals of copper, stainless steel, tungsten, and aluminum (to simulate beryllium) have been tested under disruption-like conditions for particulate generation. Particles were successfully generated in the SIRENS experiment and captured on substrates (or buttons) distributed in a collection chamber. Each substrate was analyzed using electron microscopy to determine the underlying particle size distribution. Table 7.1 shows a summary of the measured size distributions on buttons at equivalent locations for different tests of the various materials. The analysis shows that particle size distributions for each material has count median diameters (CMD or $d_{50\%}$) in the range of 0.3 μm to 3.0 μm. This indicates that particle generation in this experiment is basically independent of the material tested. Although particles down to diameter of 0.075 μm and up to diameter of ~50 μm were observed, the bulk of the particles in the underlying distributions were ~ 1 μm diameter.

Future work in the investigation of disruption-induced particulate mobilization with the SIRENS facility includes:

- improved characterization of the arc discharge in the materials source section
- measurement of the expansion pressure at the exit of the source section, on the centerline of the end-plate, and other locations within the collection chamber
- development of diagnostics to measure parameters associated with the mechanisms of energy deposit on the sample material in the source section
- investigation of condensation and growth mechanisms responsible for the particulate size distributions observed in these tests
- investigation of other ITER-relevant materials, specifically carbon and mixed materials
- further study into the behavior of the metal vapor plasma produced in the ET source section.

Table 7.1. Summary test data and particle size distribution parameters.

	Cu Test 1 (S734)			Cu Test 2 (S737)		
Energy (J)	4260			4458		
Sample Δm (mg)	436.67			451.13		
	$d_{50\%}$ (μm)	GSD	R^2	$d_{50\%}$ (μm)	GSD	R^2
Button 1	0.66	1.77	0.966	0.58	2.17	0.988
Button 3	*	*	*	*	*	*
Button 6	0.78	2.13	0.986	0.63	2.43	0.989
Button 7	0.55	2.38	0.962	0.505	2.57	0.983
Button 9	0.77	2.07	0.984	0.426	2.63	0.991
Button 12	0.97	2.04	0.988	0.366	3.06	0.989
Button 14	0.84	2.27	0.970	0.381	2.70	0.981

	SS316 Test 1 (S735)			SS316 Test 2 (S738)		
Energy (J)	4259			4260		
Sample Δm (mg)	349.93			367.61		
	$d_{50\%}$ (μm)	GSD	R^2	$d_{50\%}$ (μm)	GSD	R^2
Button 1	0.45	1.78	0.955	0.45	1.94	0.986
Button 3	*	*	*	*	*	*
Button 6	1.31	1.69	0.996	0.75	2.21	0.991
Button 7	0.84	2.14	0.992	1.46	2.10	0.994
Button 9	0.92	1.78	0.984	0.618	2.27	0.993
Button 12	0.54	2.33	0.980	0.75	2.37	0.995
Button 14	0.73	1.87	0.989	0.62	2.29	0.974

	W Test 1 (S736)			W Test 2 (S739)		
Energy (J)	4260			4259		
Sample Δm (mg)	154.85			241.93		
	$d_{50\%}$ (μm)	GSD	R^2	$d_{50\%}$ (μm)	GSD	R^2
Button 1	0.30	1.97	0.997	0.38	1.99	0.974
Button 3	*	*	*	*	*	*
Button 6	0.50	1.76	0.996	0.30	2.11	0.986
Button 7	0.70	1.65	0980	0.36	2.15	0.992
Button 9	1.05	2.59	0.965	*	*	*
Button 12	0.66	2.49	0.974	*	*	*
Button 14	0.80	2.49	0.968	*	*	*

	Al Test 1 (S744)			Al Test 2 (S745)		
Energy (J)	4226			4260		
Sample Δm (mg)	526.41			493.40		
	$d_{50\%}$ (μm)	GSD	R^2	$d_{50\%}$ (μm)	GSD	R^2
Button 1	*	*	*	*	*	*
Button 3	1.90	2.15	0.989	2.29	2.01	0.972
Button 6	*	*	*	*	*	*
Button 7	3.01	2.04	0.978	1.60	2.19	0.991
Button 9	0.847	2.48	0.991	1.27	2.29	0.984
Button 12	*	*	*	*	*	*
Button 14	*	*	*	*	*	*

8.0 Acknowledgments and Disclaimer

Sincere appreciation goes out to the Fusion Safety Program at the INEEL, specifically Kathryn A. McCarthy, David A. Petti, Galen R. Smolik, and William J. Carmack. This work is supported by US DOE, Director of Energy Research, Office of Fusion Energy, under grant C87-101407 task 007 and UCSD ITER 10112833.

This report is an account of work assigned to the U.S. Home Team under Task Agreement No. S81TT08 within the Agreement among the European Atomic Energy Community, the Government of Japan, the Government of the Russian Federation, and the Government of the United States of America on Cooperation in the Engineering Design Activities for the International Thermonuclear Experimental Reactor ("ITER EDA Agreement") under the auspices of the International Atomic Agency (IAEA). The report has not been reviewed by the ITER Publications Office.

This report is an account of work undertaken within the framework of the ITER EDA Agreement. Neither the ITER Director, the Parties to the ITER Agreement, the U.S. DOE, the U.S. Home Team Leader, the U.S. Home Team, the IAEA or any agency thereof, or any of their employees, makes any warranty, express or implied, or assumes any legal liability or responsibility for the accuracy, completeness, or usefulness of any information, apparatus, product, or process disclosed, or represents that its use would not infringe privately owned rights. Reference herein to any specific commercial product, process, or service by trade name, trademark, manufacturer, or otherwise, does not necessarily constitute or imply its endorsement, recommendation, or favoring by the parties to the ITER EDA Agreement, the IAEA or any agency thereof.

The views and opinions of authors expressed herein do not necessarily state or reflect those of the ITER Director, the Parties to the ITER Agreement, the U.S. DOE, the U.S. Home Team Leader, the U.S. Home Team, the IAEA or any agency thereof.

References

1. Sharpe, J.P., M. Bourham, J.G. Gilligan, "Test Plan for Disruption Induced Aerosol Characterization for ITER Source Term Determination, ITER Task: S 81 TT 14 95-02-28 FU Part B," EDF No. ITER/US/95/TE/SA-22, September 6, 1995.

2. Sharpe, J.P., M. Bourham, " Scoping of SIRENS for Wall Material Vaporization Studies," EDF No. ITER/US/97/TE/SA-14, June, 1997.

3. Carmack,W.J, et al., "DIII-D Dust Particulate Characterization," EDF No. ITER/US/97/TE/SA-8, March 1997.

4. CRC Handbook of Thermophysical and Themochemical Data, CRC Press, Boston, 1994.

5. CRC Handbook of Physical and Chemical Sciences, CRC Press, Boston, 1992.

6. Russ, John C., Image Processing Handbook, CRC Press, Boston, 1995.

Part 3

"Characterization of Carbon-Based Particulate from Disruption Simulations"

J.P. Sharpe and M.A. Bourham

EDF No. ITER/US/98/TE/SA-11, June 1998.

ENGINEERING DESIGN FILE

	International Thermonuclear Experimental Reactor (ITER) **U.S. Home Team** **Fusion Safety Program**	EDF No.: ITER/US/98/TE/SA-11 DATE: June 1998 TASK AREA: SAE-1

SUBJECT: Characterization of Carbon-Based Particulate from Disruption Simulations

SUMMARY: Carbon and carbon / metal particulate has been generated in the SIRENS disruption simulator at North Carolina State University for the purpose of simulating disruption-induced particulate mobilization in ITER. Material tested includes Lexan polycarbonate, UTR-22 grade graphite, ATJ grade graphite, Lexan / copper mixture, Lexan / stainless-steel 316 mixture, Lexan / tungsten mixture, and Lexan / aluminum mixture. Each of these materials and combinations are either directly relevant to ITER or are appropriate substitutes for determination of mechanisms responsible for particle generation.

Particulate generation is achieved in SIRENS by exposing test material to the high heat flux of a confined electric arc. Mobilization results from this exposure by surface ablation, vaporization, and possible melt layer liquefaction of metal components. The mobilized mass flows from the high heat flux region into a large expansion volume; cooling of the vapor during expansion allows particle condensation and growth. Collection substrates (buttons) at discrete locations on the wall of the expansion chamber intercept particulate for analysis.

This report presents results of the analysis of collected particulate. Particle size distributions were generated from images of button surfaces obtained with a scanning electron microscope. Count Median Diameters (CMD) for the Lexan and graphite tests ranged from 0.069 μm to 0.54 μm and Geometric Standard Deviations (GSD) varied from 1.96 to 3.57. Lexan / copper tests produced particulate of GMD's between 0.12 μm and 0.35 μm, and corresponding GSD's from 2.17 to 2.95. Particulate collected in the Lexan / SS316 tests ranged from 0.099 μm to 0.28 μm in CMD and 2.00 to 2.74 in GSD. Lexan / tungsten produced particles sized from 0.097 μm to 0.14 μm in CMD and 1.93 to 2.49 in GSD. Finally, the Lexan / aluminum test generated particles with CMD's between 0.15 μm and 0.28 μm with GSD's between 2.42 and 3.18. Overall particle sizes for all carbon and carbon/metal mixtures are less than particle sizes produced in previous tests with metallic material only.

Distribution (complete package): Project File,

Authors: Date:	Reviewed: Date: 7/1/98	Approved: Date:
J. Phillip Sharpe M. Bourham D.A. Petti for J.P. Sharpe	K. A. McCarthy L. C. Cadwallader for K. A. McCarthy	D. A. Petti D.A. Petti 7/1/98

Outline

1.0 Introduction

An investigation into the production of carbon-based particulate at conditions relevant to expected ITER disruption thermal energy loads has been performed on the SIRENS facility at North Carolina State University. Various carbon materials and carbon / metal mixtures exposed to high heat flux generated in the SIRENS plasma source section include: Lexan polycarbonate (polymeric chain $C_{16}H_{14}O_3$), UTR-22 grade graphite, ATJ grade graphite, Lexan / copper mixture (both short and segmented configuration), Lexan / stainless-steel 316 (SS316) mixture (short and segmented configurations), Lexan / tungsten mixture, and Lexan / aluminum mixture (segmented configuration only). Particulate of interest results from test surface mobilization followed by expansion cooling of vaporized material and subsequent condensation in vacuum conditions. Particle samples are collected at discrete positions within a controlled volume and used to generate representative size distributions. Such information is necessary for ITER safety analyses involving disruption-induced mobilization of reactor component material[1]. This report presents data from the carbon-based material tests and the resulting particulate size distributions, and includes discussion on important observations, difficulties encountered, and significance of the tests to the overall task. Each material tested will be discussed in separate sections, followed by a general conclusion comparing the overall results.

2.0 Experimental Procedure

The experimental configuration for the carbon-based materials tests follows that described in [2,3]. For completeness, important experimental parameters are re-stated here, and necessary changes in sample configuration for carbon / metal tests are explained.

The SIRENS facility allows various configurations of sample material exposure to high heat flux. Optimal configuration for particulate generation required placement of the sample material within the SIRENS plasma source section (see Figure 2.1). To this end, sample material is fabricated into a cylindrical sleeve of 0.397 cm ID, 0.714 cm OD, and a length specified by application, and placed into a Lexan inner insulator of 0.714 cm ID and 11.8 cm length. These components are placed in a Lexan outer insulator and then into a SS304 anode housing that is bolted to a large vacuum chamber and connected to a pulse power delivery system. This entire assembly is referred to as the SIRENS source section. High heat flux exposure to the inner surface of the sample material is achieved by drawing an intense electrical arc between the point cathode and annular anode, separated by a length of 8.8 cm. Similar to the expected response of an exposed surface in an ITER disruption, radiant energy deposited on the sample surface mobilizes material by ablation, vaporization, and possible melt layer liquefaction of metal components. This mobilized mass flows from the open end of the source section into a large glass expansion cell (17.8 cm ID, 76.2 cm length). Cooling of the vapor during expansion allows particle condensation and growth. This particulate is transported to the wall of the expansion cell and is intercepted at certain locations by

circular collection substrates (buttons). Following the test, buttons are removed, weighed for relative mass gain, and observed under high magnification of a Scanning Electron Microscope (SEM). Photographic images of a button's surface are obtained, and the particles are sized and counted from these images, generating the particle size distribution for that button. These measured size distributions are then fitted to the log-normal distribution. The reported values are the fitted size distribution parameters: count median diameter (CMD), geometric standard deviation (GSD), and linear correlation coefficient (R^2). This methodology for generating sizes distributions follows that presented by Carmack, et al. in [4].

Successful generation of carbon particulate required utilizing various configurations in the placement, or "stacking order", of test material within the inner insulator. Tests with Lexan-only sleeves were performed with the entire exposed length (8.8 cm) consisting of Lexan. For graphite, a series of tests was performed with different configurations to find a stacking order that generated a sufficient amount of particulate. Difficulties with the graphite tests will be thoroughly discussed in Section 3. In fact, these difficulties influenced the choice of the carbon material used for carbon / metal mixture tests. Using Lexan as the carbon-based material in these tests is justifiable given that sufficient heat flux is available to completely dissociate the polycarbonate into its elemental constituents. Atomic and molecular hydrogen, oxygen (H, H_2, O and O_2), and potentially molecular methane (CH_4) are non-condensables that have no impact on particle formation of the dominant condensable species, i.e. carbon. Appreciable quantities of water vapor are unlikely to form because of the molecular mixture of H and O. Two primary configurations were used in the carbon / metal mixture tests: a "short" configuration test to characterize the particles formed when the condensing species is predominately carbon, and a "segmented" configuration test to characterize particles formed from roughly equivalent surface areas of carbon and metal exposed to a high heat flux.. The short configuration consisted of a 1 cm length of metal surrounded by two Lexan sleeves 3 cm and 3.5 cm in length. The segmented configuration was made of three sets of Lexan / metal pairs with each component 1.0 cm in length, giving a total exposed length of 6.0 cm. Figure 2.2 depicts both configurations.

Expansion chamber geometry and button location are shown in Figure 2.3 and Table 2.1, respectively. Only button locations 1, 2, 3, 4, 5, 7, 9, and 17 were used in this experiment campaign because they adequately represent varying locations for investigating differences in particle deposition. Buttons were constructed from 0.5 in. (1.27 cm) diameter glass slides 0.1 mm thick mounted onto an equivalent diameter washer (for structural support). Note the non-conductive nature of the glass required a 200 nm layer of sputtered gold coating on the button surface for analysis in the SEM. This procedure was performed on an unexposed button and no particles or surface features were observed during SEM analysis. This coating process does not to affect particle size analysis.

Figure 2.1. Cross-section through the SIRENS source section.

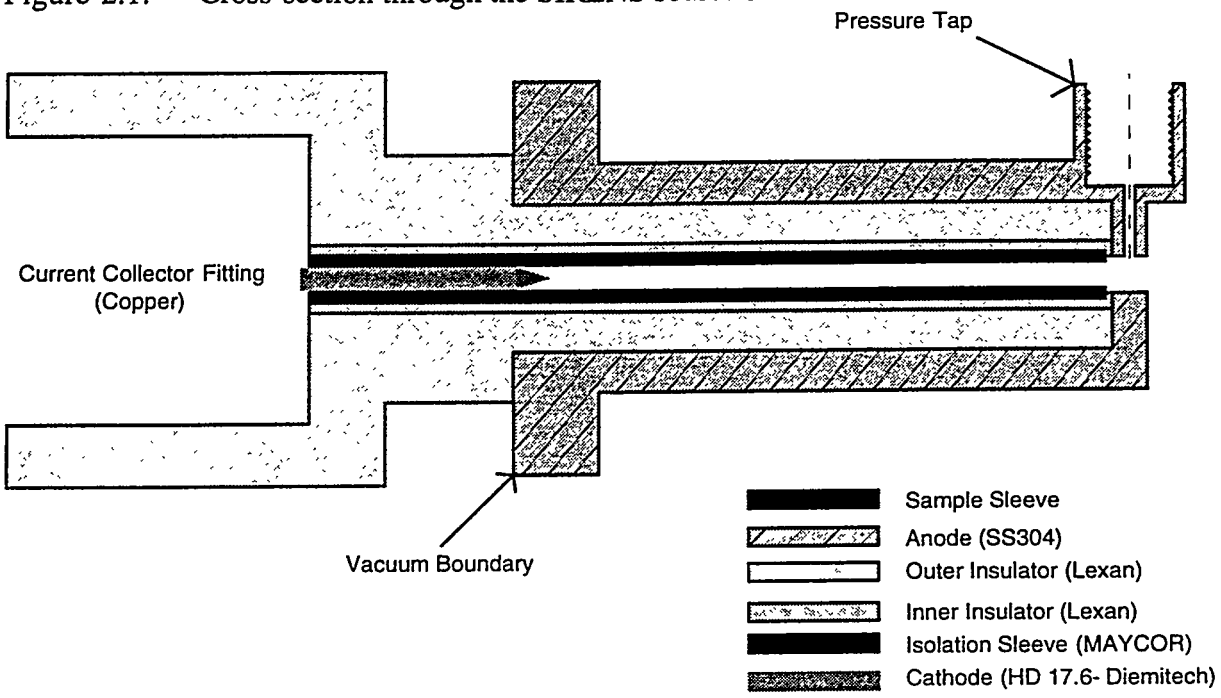

Figure 2.2. Carbon / metal mixture test sleeve configurations.

Short Configuration

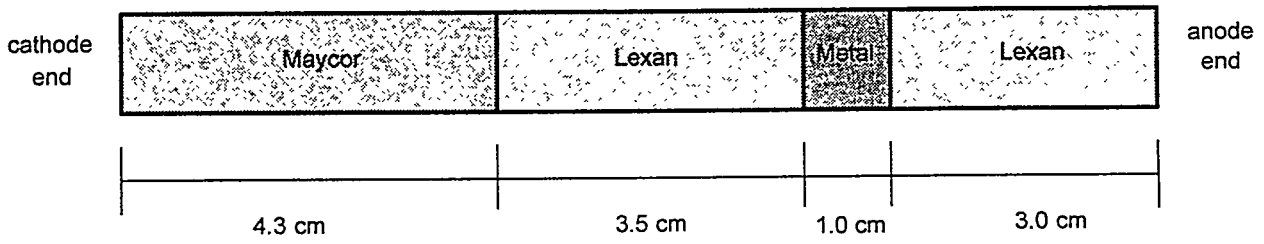

Segmented Configuration

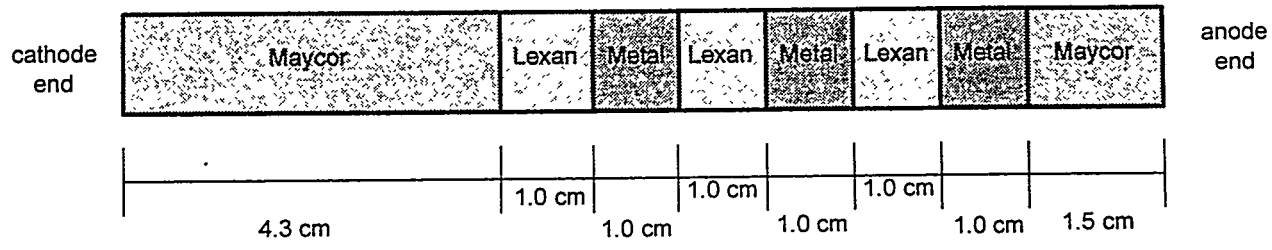

Figure 2.3. Expansion chamber geometry and button distribution.

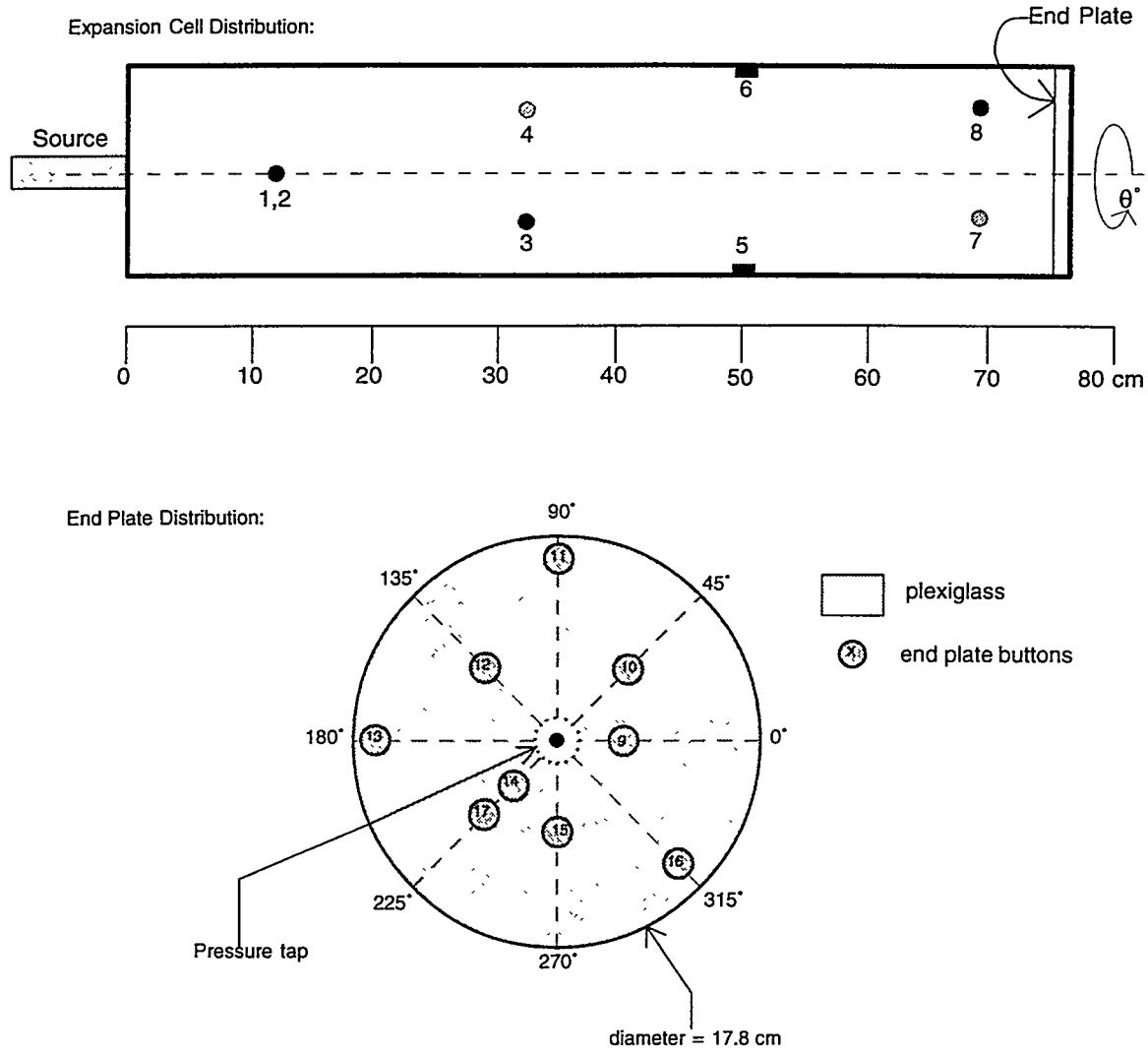

Table 2.1. Tabulated button distribution.

Wall Buttons

Button	Axial distance from source (cm)	θ (deg.)
1	12.7	0
2	12.7	180
3	31.75	45
4	31.75	225
5	50.8	90
6	50.8	270
7	69.9	135
8	69.9	315

End-Plate Buttons

Button	Radius (cm)	Angle (deg.)
9	3.0	0
10	4.5	45
11	7.0	90
12	7.0	180
13	3.0	225
14	4.5	270
15	7.0	315
16	4.5	135
17	4.5	224

Notes: (1) End plate at 73.66 cm from source exit.
(2) Chamber top aligned to 0°.
(3) End plate 90° aligned to chamber 0°.

3.0 Carbon Test Results

Experimental investigation into the production of carbon particulate from thermal loading conditions similar to those expected in an ITER disruption has been performed using carbon-based materials of Lexan polycarbonate, UTR-22 grade graphite and ATJ grade graphite. These materials were prepared and tested as described by the procedure in [2]. Table 3.0.1 displays a summary of mass loss data and particulate size distributions from the carbon tests.

Table 3.0.1. Carbon tests comparison summary.

	Lexan Test 1 (S760)				Lexan Test 2 (S761)			
Energy (J)	6050				6423			
Fluence (MJ/m^2)	5.51				5.85			
Duration (μs)	50				80			
Sample Δm (mg)	31.77				38.22			
Scaled Δm (mg/kJ/cm)	0.597				0.676			
Cathode Δm (mg)	42.45				37.25			
	Δm (mg)	$d_{50\%}$ (μm)	GSD	R^2	Δm (mg)	$d_{50\%}$ (μm)	GSD	R^2
Button 1	*	0.069	2.144	0.992	-0.04	0.073	2.230	0.997
Button 2	*	*	*	*	-0.06	*	*	*
Button 3	*	*	*	*	-0.28	0.079	2.056	0.997
Button 4	*	*	*	*	0.89	*	*	*
Button 5	*	0.166	2.480	0.989	0.23	*	*	*
Button 7	*	*	*	*	-0.06	*	*	*
Button 9	*	0.097	2.584	0.994	-0.13	0.081	1.96	0.987
Button 17	*	*	*	*	0.06	*	*	*
	UTR-22 Graphite Test (S763)				ATJ Graphite Test (S764)			
Energy (J)	7195				7162			
Fluence (MJ/m^2)	6.56				6.53			
Duration (μs)	40				40			
Sample Δm (mg)	-destroyed-				-destroyed-			
Cathode Δm (mg)	46.70				80.24			
	Δm (mg)	$d_{50\%}$ (μm)	GSD	R^2	Δm (mg)	$d_{50\%}$ (μm)	GSD	R^2
Button 1	1.81	0.102	2.330	0.993	0.06	0.115	2.130	0.996
Button 2	0.02	*	*	*	0.19	*	*	*
Button 3	0.43	0.114	2.630	0.990	0.18	0.086	2.521	0.982
Button 4	0.02	*	*	*	0.09	*	*	*
Button 5	0.08	*	*	*	0.06	0.075	2.970	0.996
Button 7	0.08	*	*	*	0.37	0.318	2.762	0.980
Button 9	-0.21	0.096	3.568	0.966	-1.64	0.544	3.464	0.969
Button 17	0.01	*	*	*	-8.21	*	*	*

Note: Asterisk (*) denotes buttons for which the analysis was not performed.

3.1 Lexan Tests: S760 and S761

The first carbon-based tests were performed using full-length sleeves of Lexan within the SIRENS source section. The large ablation threshold of Lexan (54 MJ/kg) required a high energy electrical discharge (~6 kJ) for production of sufficient quantity of particulate for analysis. Voltage and current traces from the discharge in both S760 and S761 are shown in Figures 3.1.1. The voltage trace displayed for S761 is off-scale due to an inadvertent offset added to the voltage channel in the data collection instrument. The resulting power and energy trace for S760 is shown in Figure 3.1.2. The fact that integrated power (from V and I measurements) results in a discharge energy within 2% of the measured energy loss from the charging capacitor bank indicates that the value of electrical energy released by the arc is equivalent to the stored electrical energy. Power and energy could not be determined for test S761 because the voltage trace for this test was off-scale.

A detailed summary of mass measurements of the various components from the tests is displayed in Table 3.1.1. Mass loss from the Lexan sleeves was found to be 0.597 mg/kJ/cm for S760 and 0.676 mg/kJ/cm for S761. These values were obtained by scaling the measured mass loss in milligrams to total discharge energy as determined from capacitor bank energy loss and total sleeve length exposed to the electrical discharge (8.8 cm for full-length Lexan sleeves). Post-test button weights and corresponding Δm's are unavailable for S760 because the glass buttons tended to crack and break off from the holder on which they were mounted. This problem was alleviated by permanently mounting the glass buttons on a metal washer of equal diameter. Although increasing the overall weight, this arrangement provides sufficient rigidity for the buttons' glass surfaces to be installed and removed from inside of the expansion chamber. The button weight differences associated with S761 show that deposited mass is undetectable, given that many of the measurements display a Δm on the order of detection uncertainty ($\pm$ 0.05 mg). The relatively large mass increase for buttons 4 and 5 is likely not due to deposit of carbon material. Mass loss observed on buttons 3 and 9 resulted from small portions of the button's glass surface being chipped and removed.

Although the mass of deposited material was negligible (within measurement error), button surfaces displayed a large number of particles when viewed in the SEM. Figure 3.1.3 gives representative mircographs from Lexan test 2 (S761) button 3 at 5 kx and 10 kx. Images such as these were obtained for buttons 1, 3, and 9 for Lexan test 1 (S760) and buttons 1, 5, and 9 for Lexan test 2 (S761). Smaller particles in these images appear roughly circular, while larger particles have more irregular shapes. Neither flakes nor large, flat structures were observed. Figures 3.1.4-9 display the resulting particle size distributions. Included in each figure are the analysis summary table and the overall log-probability plot displaying the cumulative distribution, best fit line, and 95% confidence bounds. Particle counts obtained at varying magnifications were combined using scaling factors derived from dividing imaged area at a given magnification by a the area of an image obtained at a standard magnification (1 kx)[4]. Data variance, and hence the 95%

confidence bounds, is determined from a weighting process dependent on total number of particles in the population, width of each particle size bin, number of particles in each size bin, and magnification-specific scaling factors. An important result from this analysis of Lexan test data is that generally the data are well represented by a log-normal distribution curve.

Also shown in the summary tables are the Kruskal-Wallis (K-W) statistical test results from the particle diameter data from each available magnification. The reported z-value is a root mean square variance test showing the relative discrepancy of each individual image data to the total group data for each magnification. Significant variation in data from one image indicates the non-compliance of that data to the hypothesis distribution. Another value from the K-W test is the significance probability, or p-value. This value is an overlay of a chi-square distribution on the hypothesis distribution for the total data population. A p-value of less than 0.05 (5%) indicates a large discrepancy within the population, requiring the elimination of one dataset (starting with the highest associated z-value) until the p-value rises above the 5% set-point. This entire process helps ensure the final combined distribution truly represents the underlying particle size population on the button. There are a few instances, however, in which all datasets at a given magnification fail this test. Rather than eliminate the important data from these magnifications, the overall distributions were generated using data from the failed images in order to produce a better representation of the underlying distribution than if the data were excluded. This exception was enacted for analysis of the following datasets: S760 button 5, S761 button 3, S761 button 9, S764 button 1, S764 button 9, S767 button 1, S767 button 5, and S768 button 5. If 2 or more datasets passed the K-W test, they were used in the analysis. The analysis summary table for each button indicates datasets not used by the remark 'failed' in the K-W Test z-value column.

Figure 3.1.1. Voltage and current traces for both Lexan tests.

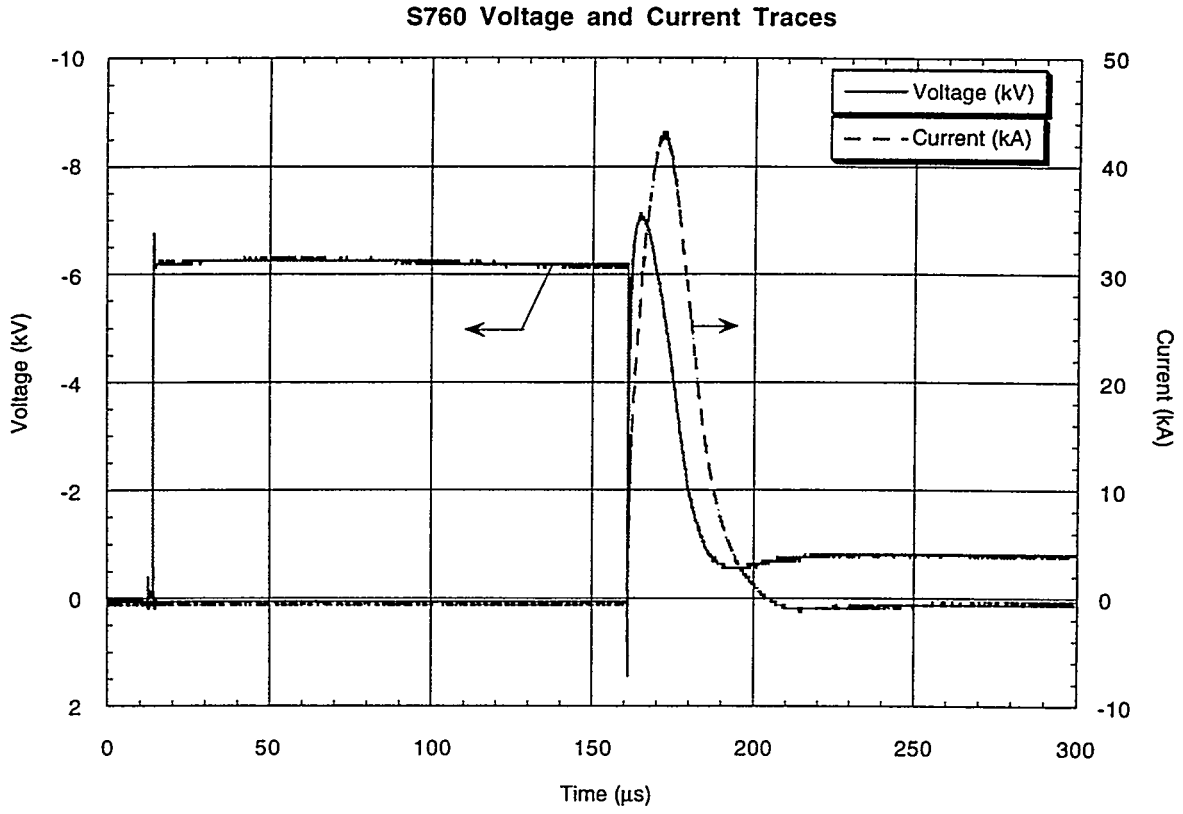

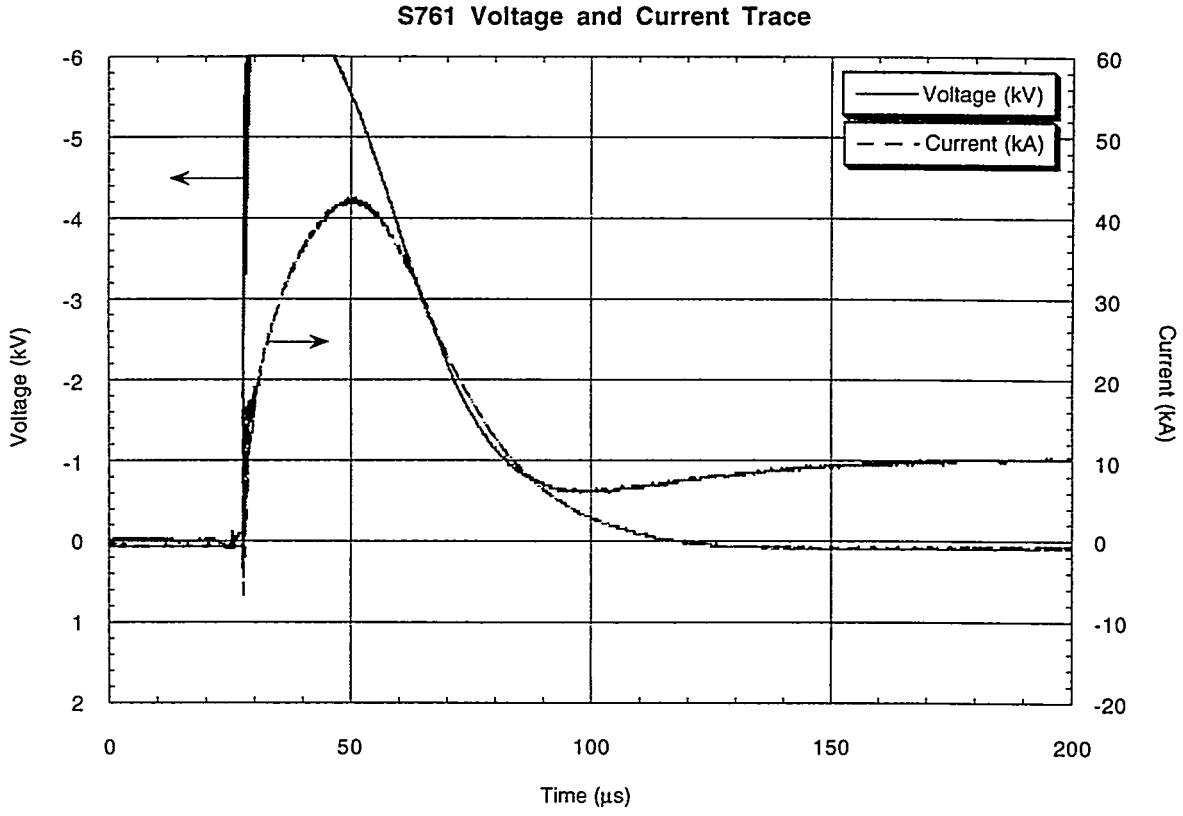

Figure 3.1.2. Power and energy traces for Lexan test S760.

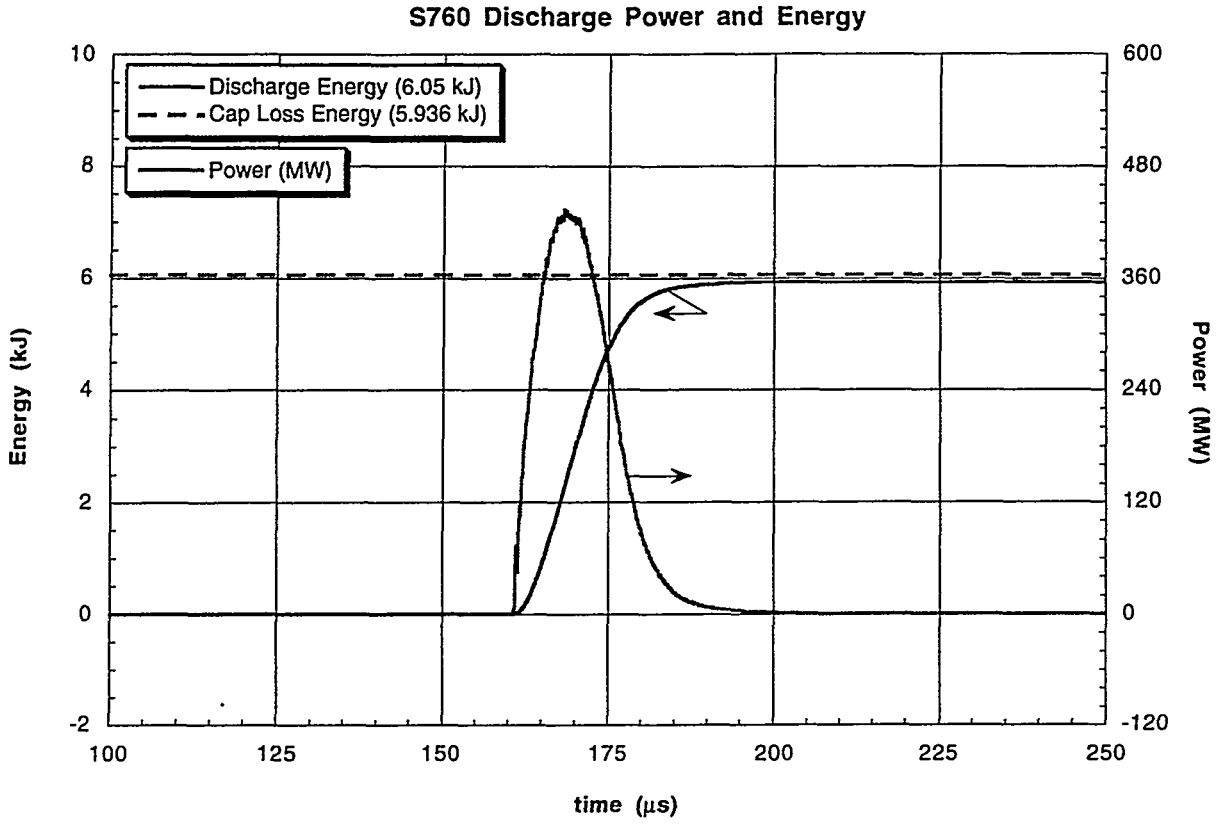

Table 3.1.1. Lexan test mass measurements.

S760: Lexan Test 1

Source Section Components:			
component	pre-test wt. (g)	post-test wt. (g)	Δ wt. (mg)
short insulator	N/A	N/A	N/A
long insulator	N/A	N/A	N/A
cathode	10.00565	9.96023	42.45
Lexan sleeve	3.89196	3.83019	31.77

Substrate Components:			
wall button	pre-test wt. (g)	post-test wt. (g)	Δ wt. (mg)
1	0.04326	-	-
2	0.04390	-	-
3	0.04230	-	-
4	0.04375	-	-
5	0.04269	-	-
7	0.04252	-	-
9	0.04233	-	-
17	0.04301	-	-

Notes: (1) All weight measurements are taken 3+ times and averaged.
(2) Δm uncertainty is ± 0.05 mg.
(3) post-test weights not obtained due to fragility of glass buttons. See text.

S761: Lexan Test 2

Source Section Components:			
component	pre-test wt. (g)	post-test wt. (g)	Δ wt. (mg)
short insulator	N/A	N/A	N/A
long insulator	N/A	N/A	N/A
cathode	9.91358	9.87632	37.25
Lexan sleeve	3.85441	3.81618	38.22

Substrate Components:			
wall button	pre-test wt. (g)	post-test wt. (g)	Δ wt. (mg)
1	0.49243	0.49239	-0.04
2	0.45905	0.45899	-0.06
3	0.48967	0.48939	-0.28
4	0.44315	0.44404	0.89
5	0.47920	0.47943	0.23
7	0.44671	0.44665	-0.06
9	0.43032	0.43019	-0.13
17	0.48897	0.48903	0.06

Notes: (1) All weight measurements are taken 3+ times and averaged.
(2) Δm uncertainty is ± 0.05 mg.

Figure 3.1.3. Representative SEM micrographs of button 3 from Lexan test 2, S761.

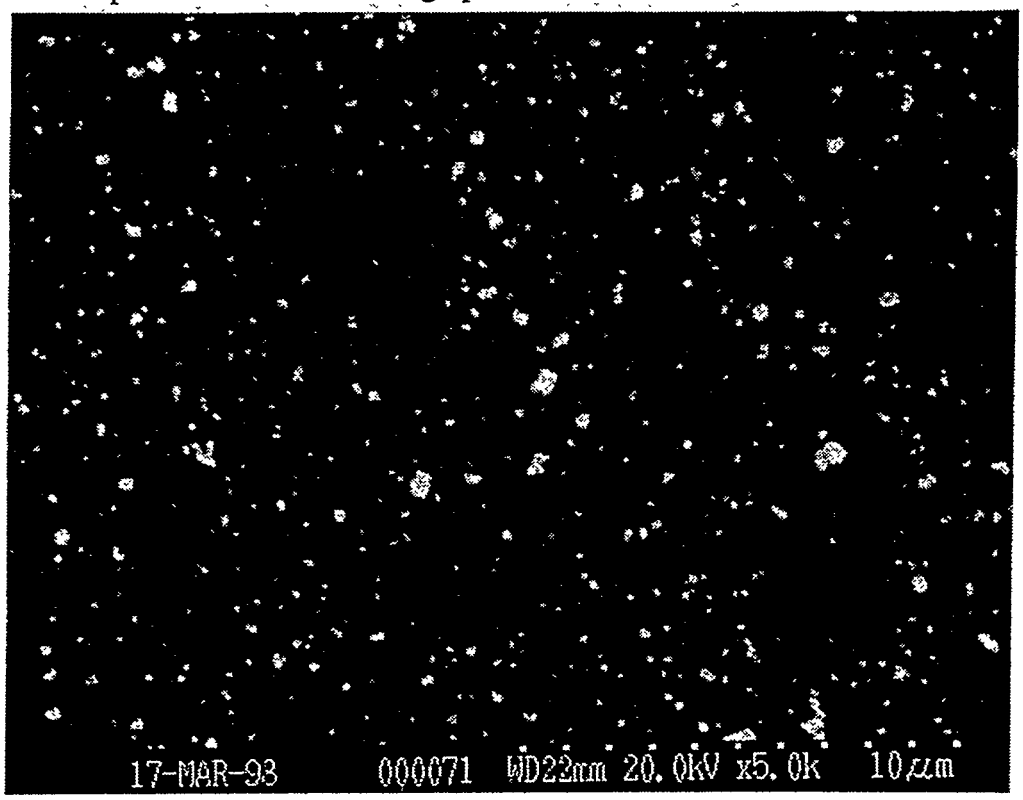

(a) 5 kx

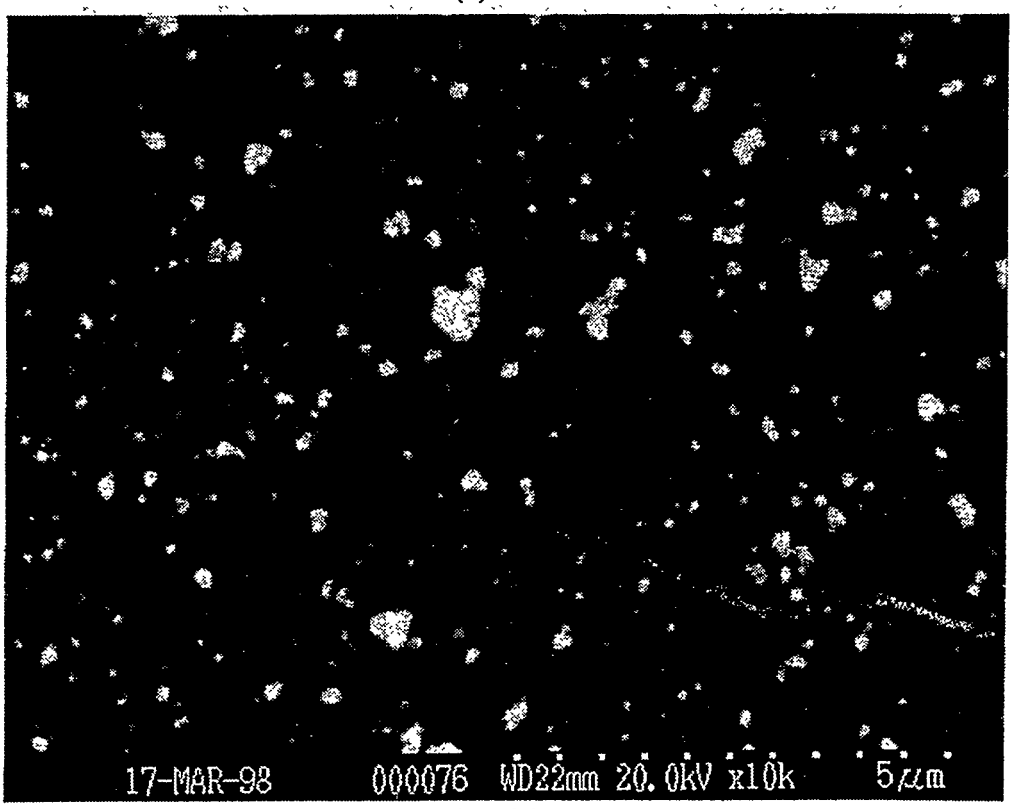

(b) 10 kx

Figure 3.1.4. Lexan test 1 (S760) button 1 particle size distribution.

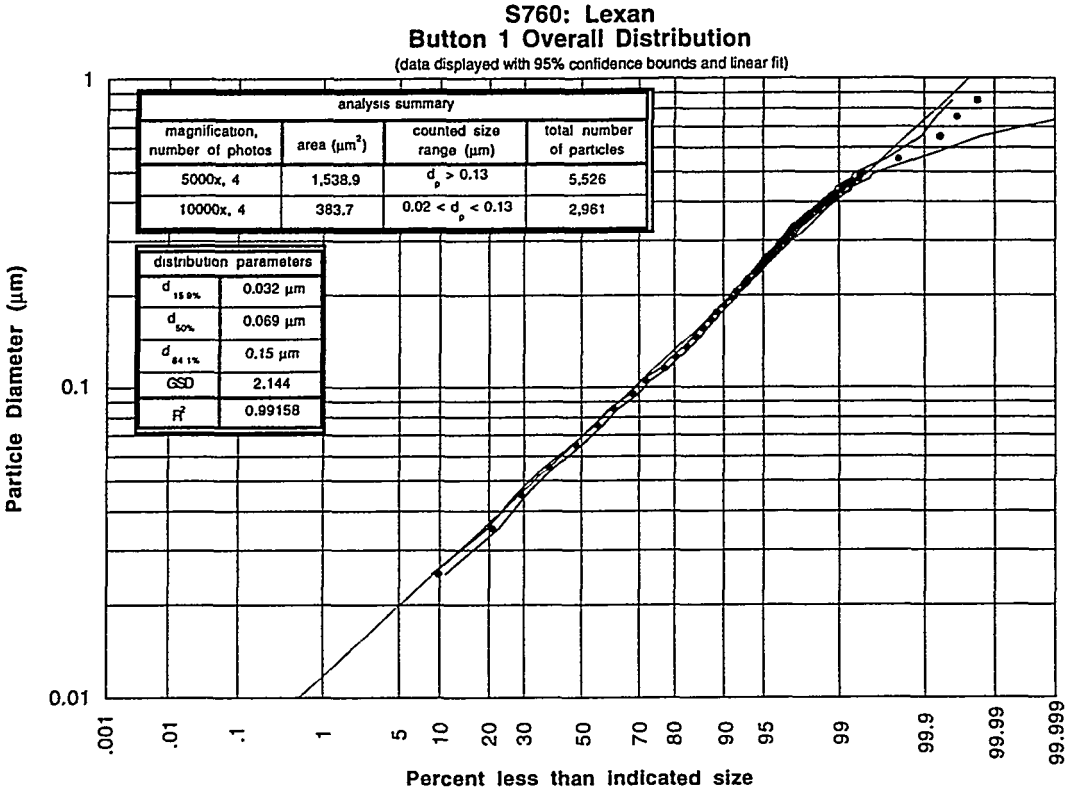

Data Summary Table:

photo	mag	scale (pixel/µm)	size (µm²)	min. d_{eq} (µm)	# of particles	scale factor	KW Test z-value	Overall p-value
760_1_1	5 kx	29.4	23.0x16.8	0.057[a]	1304	1	-1.61	0.045
760_1_2	5 kx	29.4	22.9x16.8	0.057[a]	1448	1	1.71	
760_1_3	5 kx	29.4	22.8x16.9	0.057[a]	1484	1	-1.66	
760_1_4	5 kx	29.4	22.9x16.7	0.057[a]	1290	1	1.58	
760_1_5	10 kx	58.8	11.5x8.37	0.02[b]	741	4	0.33	0.911
760_1_6	10 kx	58.8	11.4x8.4	0.02[b]	798	4	0.42	
760_1_7	10 kx	58.8	11.4x8.37	0.02[b]	749	4	-0.66	
760_1_8	10 kx	58.8	11.5x8.37	0.02[b]	673	4	0.10	

a. equivalent minimum diameter particle counted having an area of at least 2.25 x 1/scale on a side.
b. equivalent minimum diameter particle counted having an area of at least 1.1 x 1/scale on a side.

Figure 3.1.5. Lexan test 1 (S760) button 5 particle size distribution.

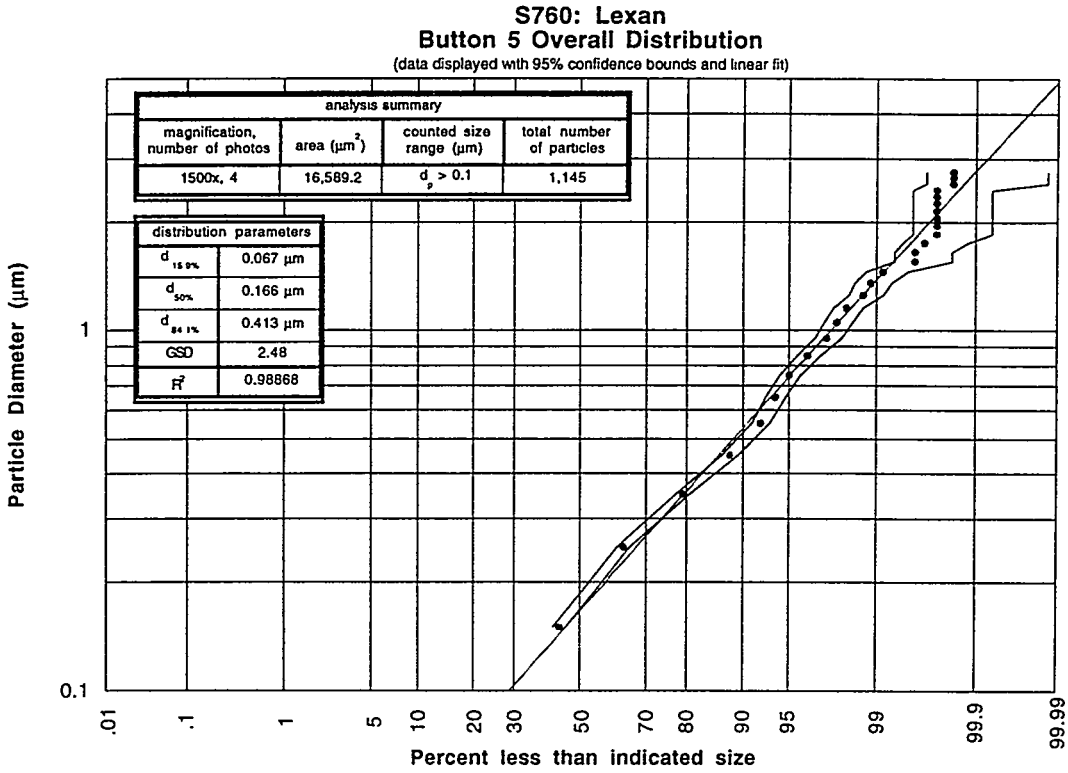

Data Summary Table:

photo	mag	scale (pixel/µm)	size (µm²)	min. d_{eq} (µm)	# of particles	scale factor	KW Test z-value	Overall p-value
760_5_1[a]	500x	2.94	229x168	0.340[b]	690	-	2.93	0.000
760_5_2[a]	500x	2.94	229x166	0.340[b]	696	-	7.33	
760_5_3[a]	500x	2.94	230x166	0.340[b]	863	-	-8.86	
760_5_4[a]	500x	2.94	229x166	0.340[b]	735	-	-0.74	
760_5_5	1.5 kx	8.9	75.8x53.8	0.112[c]	741	1	0.33	0.911
760_5_6	1.5 kx	8.9	75.8x54.8	0.112[c]	798	1	0.42	
760_5_7	1.5 kx	8.9	75.6x55.0	0.112[c]	749	1	-0.66	
760_5_8	1.5 kx	8.9	75.8x55.4	0.112[c]	673	1	0.10	

a. Images obtained at 500x were ineffective in collecting usable particle size data, as reflected in the Kruskal-Wallis test results. Therefore, these images were not used in generating the particle size distribution for this button.

b. no minimum equivalent diameter required.

c. minimum equivalent diameter particle counted having an area of at least 5.9 x 1/scale on a side.

Figure 3.1.6. Lexan test 1 (S760) button 9 particle size distribution.

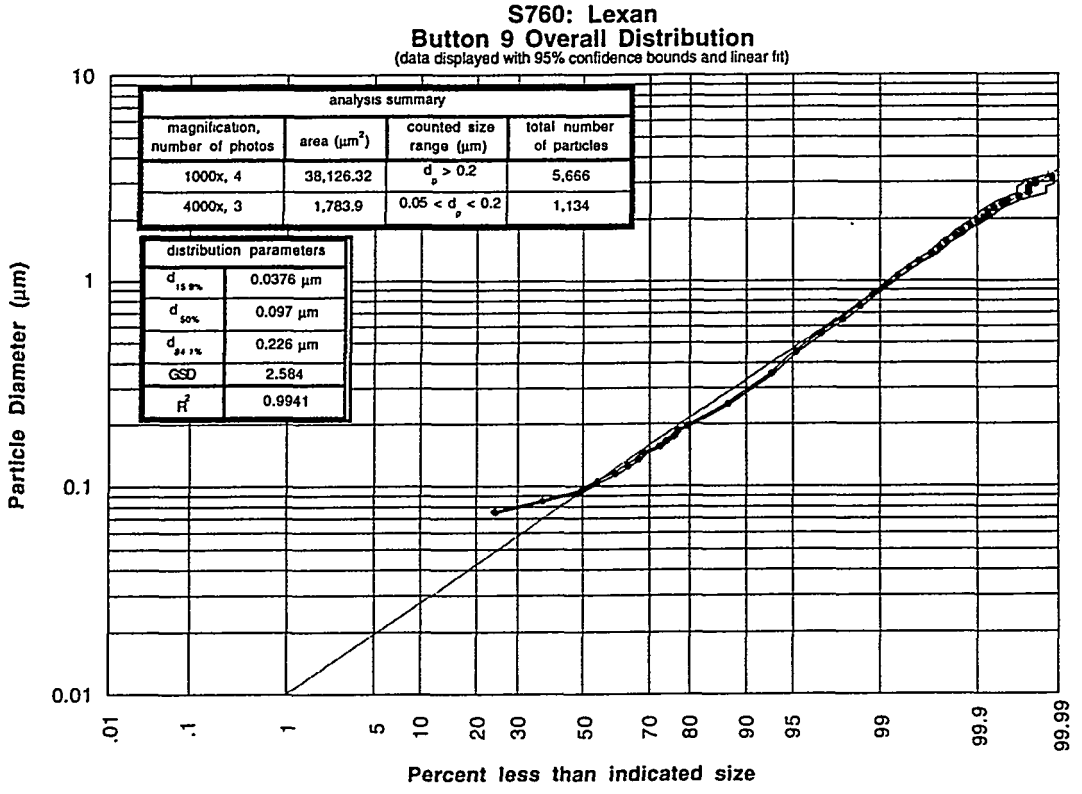

Data Summary Table:

photo	mag	scale (pixel/μm)	size (μm²)	min. d_{eq} (μm)	# of particles	scale factor	KW Test z-value	Overall p-value
760_9_1	1 kx	5.88	114.8x83.2	0.192[a]	1176	1	0.76	0.225
760_9_2	1 kx	5.88	114.8x83.2	0.192[a]	1290	1	-0.90	
760_9_3	1 kx	5.88	114.6x83.0	0.192[a]	1272	1	-1.37	
760_9_4	1 kx	5.88	114.6x83.0	0.192[a]	1328	1	1.51	
760_9_5	4 kx	23.5	28.7x20.7	0.048[a]	369	16	1.24	0.409
760_9_6	4 kx	23.5	28.6x20.8	0.048[a]	437	16	-1.08	
760_9_7	4 kx	23.5	28.6x20.8	0.048[a]	328	16	-0.12	
760_9_8	4 kx	23.5	28.8x20.7	0.048[a]	435	-	failed	

a. minimum equivalent diameter particle counted having an area of at least 1.1 x 1/scale on a side.

Figure 3.1.7. Lexan test 2 (S761) button 1 particle size distribution.

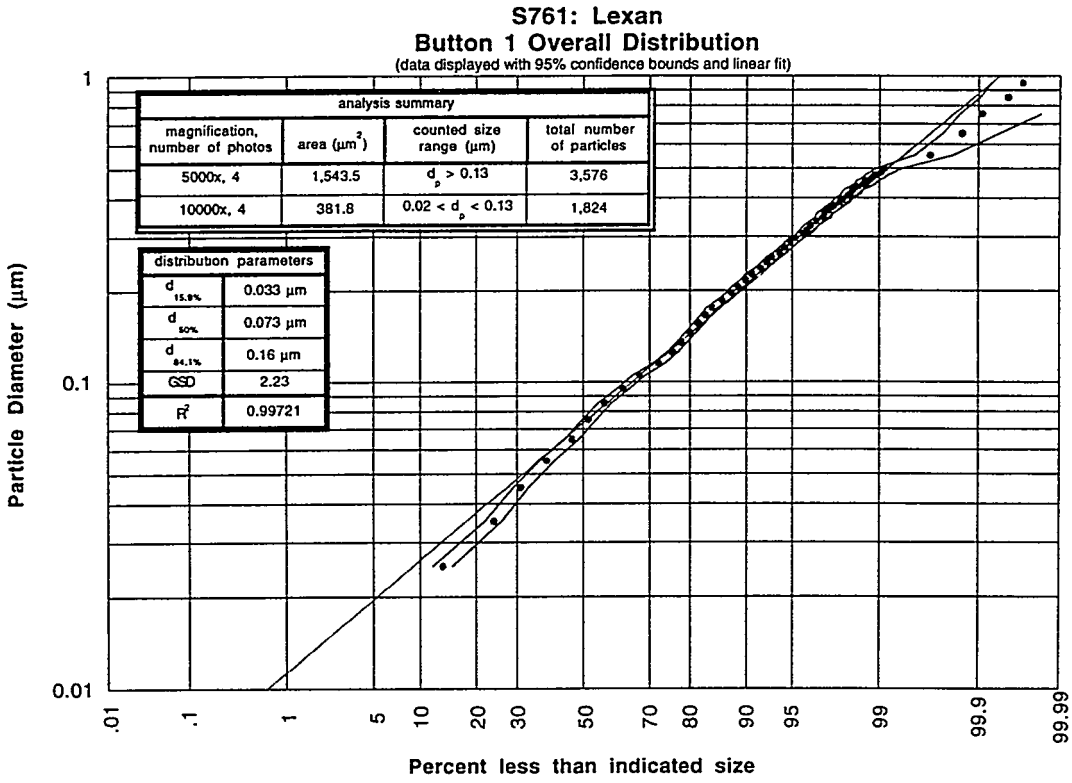

Data Summary Table:

photo	mag	scale (pixel/μm)	size (μm²)	min. d_{eq} (μm)	# of particles	scale factor	KW Test z-value	Overall p-value
761_1_1	5 kx	29.4	22.9x16.9	0.038[a]	493	1	-1.58	0.161
761_1_2	5 kx	29.4	22.9x16.9	0.038[a]	877	1	1.65	
761_1_3	5 kx	29.4	22.9x16.8	0.038[a]	1335	-	-failed-	
761_1_4	5 kx	29.4	22.9x16.8	0.038[a]	871	1	-0.31	
761_1_5	10 kx	58.8	11.4x8.33	0.0192[a]	280	4	1.89	0.161
761_1_6	10 kx	58.8	11.4x8.44	0.0192[a]	461	4	-0.49	
761_1_7	10 kx	58.8	11.4x8.37	0.0192[a]	569	-	-failed-	
761_1_8	10 kx	58.8	11.4x8.35	0.0192[a]	514	4	-1.11	

a. minimum equivalent diameter particle counted having an area of at least 1.1 x 1/scale on a side.

Figure 3.1.8. Lexan test 2 (S761) button 3 particle size distribution.

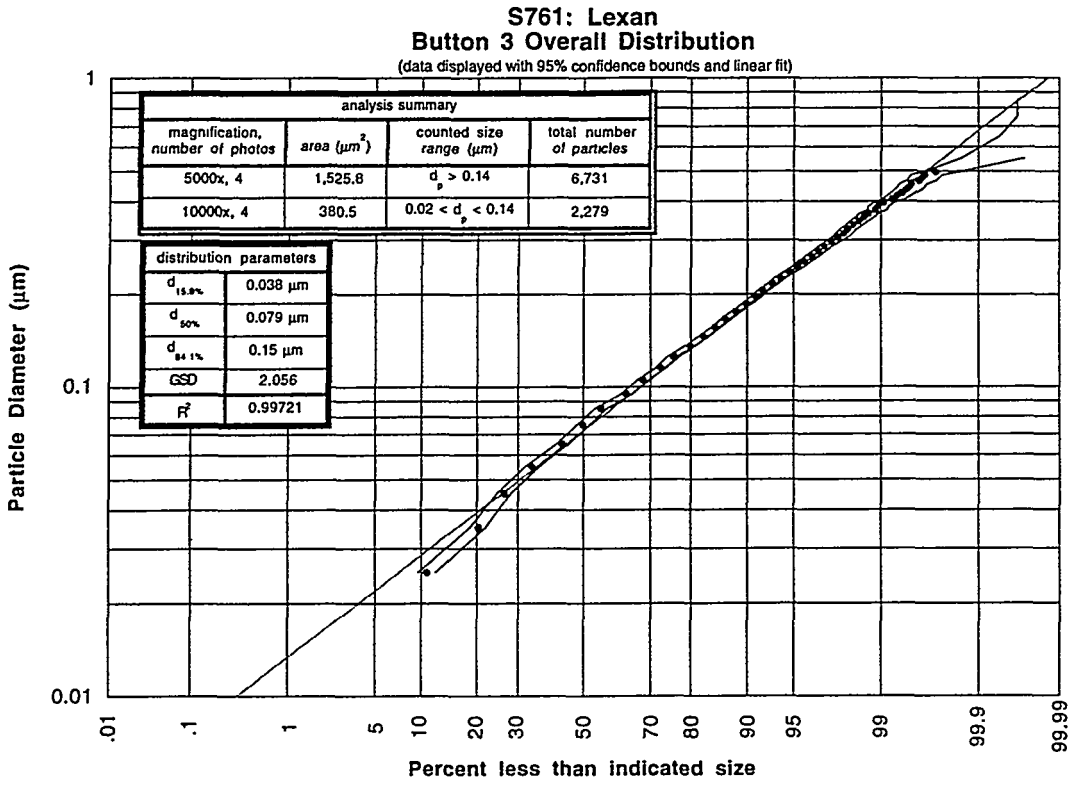

Data Summary Table:

photo	mag	scale (pixel/μm)	size (μm²)	min. d_{eq} (μm)	# of particles	scale factor	KW Test z-value	Overall p-value
761_3_1	5 kx	29.4	22.9x16.6	0.038[a]	1790	1	-1.56	0.117
761_3_2	5 kx	29.4	22.9x16.7	0.038[a]	1821	1	-0.99	
761_3_3	5 kx	29.4	22.9x16.7	0.038[a]	1431	1	0.61	
761_3_4	5 kx	29.4	22.8x16.7	0.038[a]	1689	1	2.03	
761_3_5[b]	10 kx	58.8	11.4x8.4	0.0192[a]	474	4	-1.14	0.000
761_3_6[b]	10 kx	58.8	11.4x8.35	0.0192[a]	693	4	-5.57	
761_3_7[b]	10 kx	58.8	11.3x8.35	0.0192[a]	555	4	1.91	
761_3_8[b]	10 kx	58.8	11.4x8.35	0.0192[a]	557	4	5.13	

a. minimum equivalent diameter particle counted having an area of at least 1.1 x 1/scale on a side.
b. All images obtained at 10 kx failed the Kruskal-Wallis test (i.e. $p < 0.05$) but were used in generation of the overall size distribution.

Figure 3.1.9. Lexan test 2 (S761) button 9 particle size distribution.

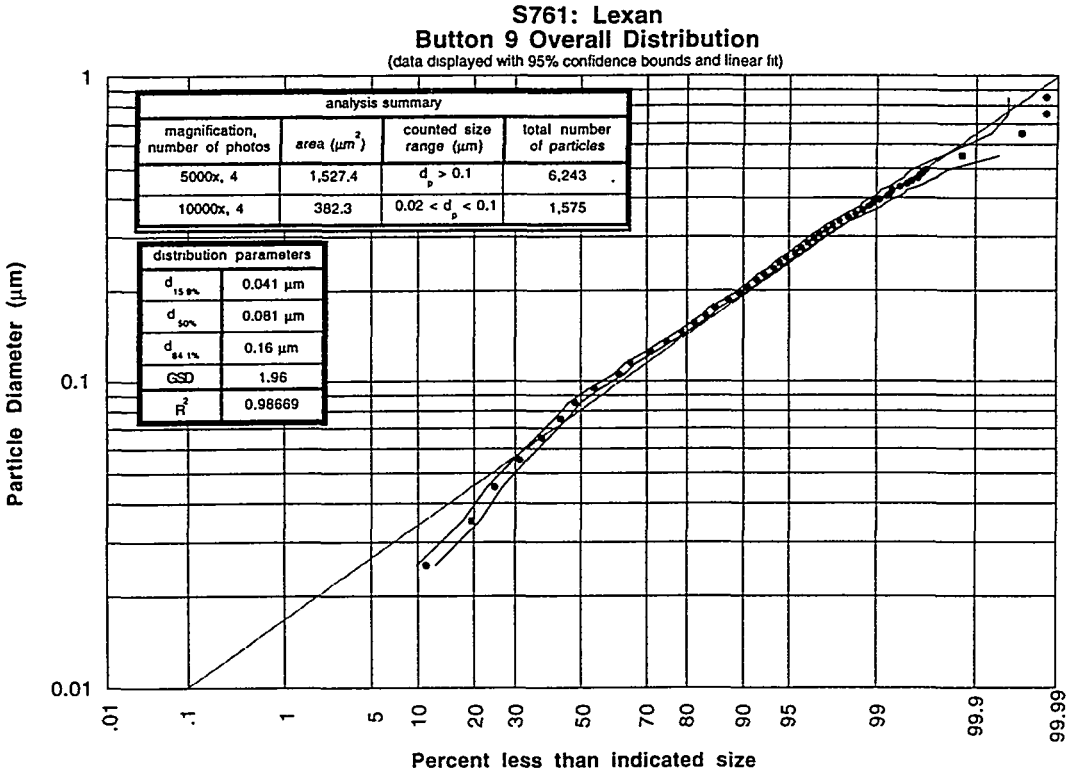

Data Summary Table:

photo	mag	scale (pixel/μm)	size (μm²)	min. d_{eq} (μm)	# of particles	scale factor	KW Test z-value	Overall p-value
761_9_1[a]	5 kx	29.4	22.9x16.7	0.038[a]	1711	1	-2.25	0.000
761_9_2[a]	5 kx	29.4	22.9x16.6	0.038[a]	1520	1	-3.17	
761_9_3[a]	5 kx	29.4	22.9x16.7	0.038[a]	1920	1	3.79	
761_9_4[a]	5 kx	29.4	22.9x16.7	0.038[a]	1092	1	1.61	
761_9_5	10 kx	58.8	11.4x8.33	0.0192[a]	364	4	1.30	0.142
761_9_6	10 kx	58.8	11.4x8.37	0.0192[a]	353	4	-0.31	
761_9_7	10 kx	58.8	11.4x8.38	0.0192[a]	441	4	1.11	
761_9_8	10 kx	58.8	11.5x8.38	0.0192[a]	417	4	-2.08	

a. All images obtained at 5 kx failed the Kruskal-Wallis test (i.e. $p < 0.05$) but were used in generation of the overall size distribution.

b. minimum equivalent diameter particle counted having an area of at least 1.1 x 1/scale on a side.

3.2 *Graphite Tests: S763 and S764*

Particulate production from graphitized carbon was investigated with two different graphite grades: UTR-22 and ATJ. Generating sufficient quantities of particulate required electrical discharges of ~7 kJ, and because graphite is electrically conductive, source section configuration was slightly modified compared to that used for the Lexan tests. Following a series of exploratory tests, the most useful configuration placed the graphite sample sleeves near the exit of the source section. The configurations used for S763 and S764 are shown in Figure 3.2.1. Voltage and current traces for S763 and S764 are displayed in Figure 3.2.2; power and energy traces are shown in Figure 3.2.3.

Table 3.2.1 summarizes mass measurements of source section and button components. In both graphite tests, the sample sleeves were destroyed during the discharge. This likely resulted from a current path developing within the conductive graphite at some point during the discharge. Resistive energy dissipation within the sample caused intense internal heating and vaporization, resulting in mechanical failure of the material. In fact, particulate collected from locations near the end plate of the expansion chamber appeared to consist of two distinct particle groups: very fine particles (~0.1 μm) possibly associated with vaporized material and very large particles (~10+ μm) resulting from the fragmentation of solid graphite grains. These unequal-size populations are accordingly found in the overall distributions generated for collection buttons near the end plate of the expansion chamber. These particle size distributions appear bimodal, as indicated by sharp differences in the slope of the cumulative distrubution curve. Similar observations have been made in disruption simulations in the Russian Federation[5]. Particle size distributions for buttons near the source section exit and mid-length of the expansion chamber do not display a bimodal characteristic.

Representative SEM micrographs from button 3 of both S763 and S764 are given in Figures 3.2.4 and 3.2.5, respectively. No significant difference is observed in the shape and general size of the particles collected from these tests of different graphite grades. With the exception of the larger sized particles found near the chamber's end plate, particles from graphite tests and Lexan tests are indistinguishable. They also appear similar in size and shape to carbon particulate collected from the DIII-D tokamak[4] at GA in San Diego and the TFTR tokamak[6] at PPPL in Princeton.

Particulate collected from buttons 1, 3, and 9 of the UTR-22 graphite test (S763) were analyzed and the resulting size distributions displayed in Figures 3.2.6-8. Similarly, buttons 1, 3, 5, 7, and 9 of the ATJ graphite test (S754) were analyzed and those size distributions are shown in Figures 3.2.9-13.

Figure 3.2.1. Optimal source section configuration for carbon tests S763 and S764.

Source Configuration for S763: UTR-22 Graphite

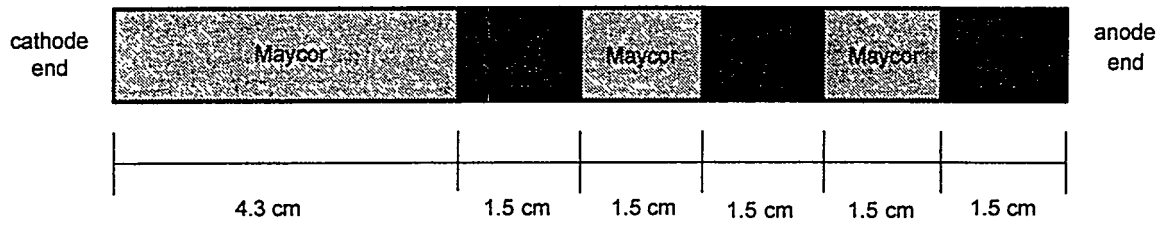

Source Configuration for S764: ATJ Graphite

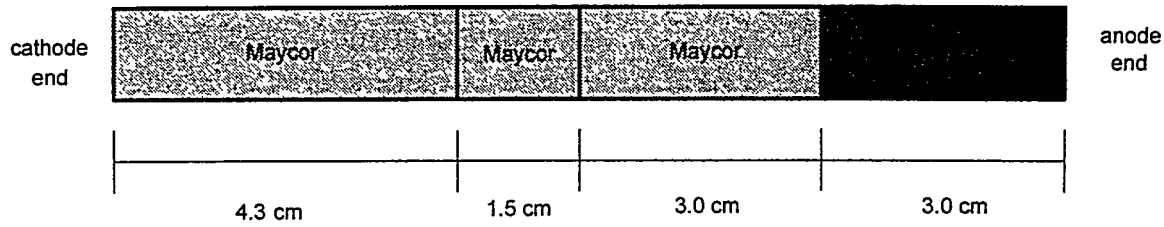

Table 3.2.1. Graphite carbon test mass measurements.

S763: UTR-22 Graphite Test

Source Section Components:			
component	pre-test wt. (g)	post-test wt. (g)	Δ wt. (mg)
cathode	9.74988	9.70318	46.70
long maycor	2.92346	-	-
graphite sleeve #1	0.74283	-destroyed-	-
short maycor #1	1.00869	-	-
graphite sleeve #2	0.69232	-destroyed-	-
short maycor #2	1.02274	-	-
graphite sleeve #3	0.79147	-destroyed-	-

Substrate Components:			
wall button	pre-test wt. (g)	post-test wt. (g)	Δ wt. (mg)
1	0.43523	0.43705	1.81
2	0.48540	0.48543	0.02
3	0.48568	0.48610	0.43
4	0.48102	0.48104	0.02
5	0.49460	0.49468	0.08
7	0.48119	0.48127	0.08
9	0.49318	0.49298	-0.21
17	0.48288	0.48289	0.01

Notes: (1) All weight measurements are taken 3+ times and averaged.
(2) Δm uncertainty is ± 0.05 mg.

S764: ATJ Graphite Test

Source Section Components:			
component	pre-test wt. (g)	post-test wt. (g)	Δ wt. (mg)
cathode	9.70319	9.62295	80.24
long maycor	2.91887	-	-
short maycor #1	1.02892	-	-
short maycor #2	2.03493	-	-
graphite sleeve	1.47408	-destroyed-	-

Substrate Components:			
wall button	pre-test wt. (g)	post-test wt. (g)	Δ wt. (mg)
1	0.48505	0.48511	0.06
2	0.48833	0.48852	0.19
3	0.43966	0.43984	0.18
4	0.48424	0.48433	0.09
5	0.48458	0.48464	0.06
7	0.48317	0.48354	0.37
9	0.48481	0.48317	-1.64
17	0.49066	0.48245	-8.21
control	0.45921	0.45918	-0.02

Notes: (1) All weight measurements are taken 3+ times and averaged.
(2) Δm uncertainty is ± 0.05 mg.

Figure 3.2.2. Voltage and current traces for graphite carbon tests S763 and S764.

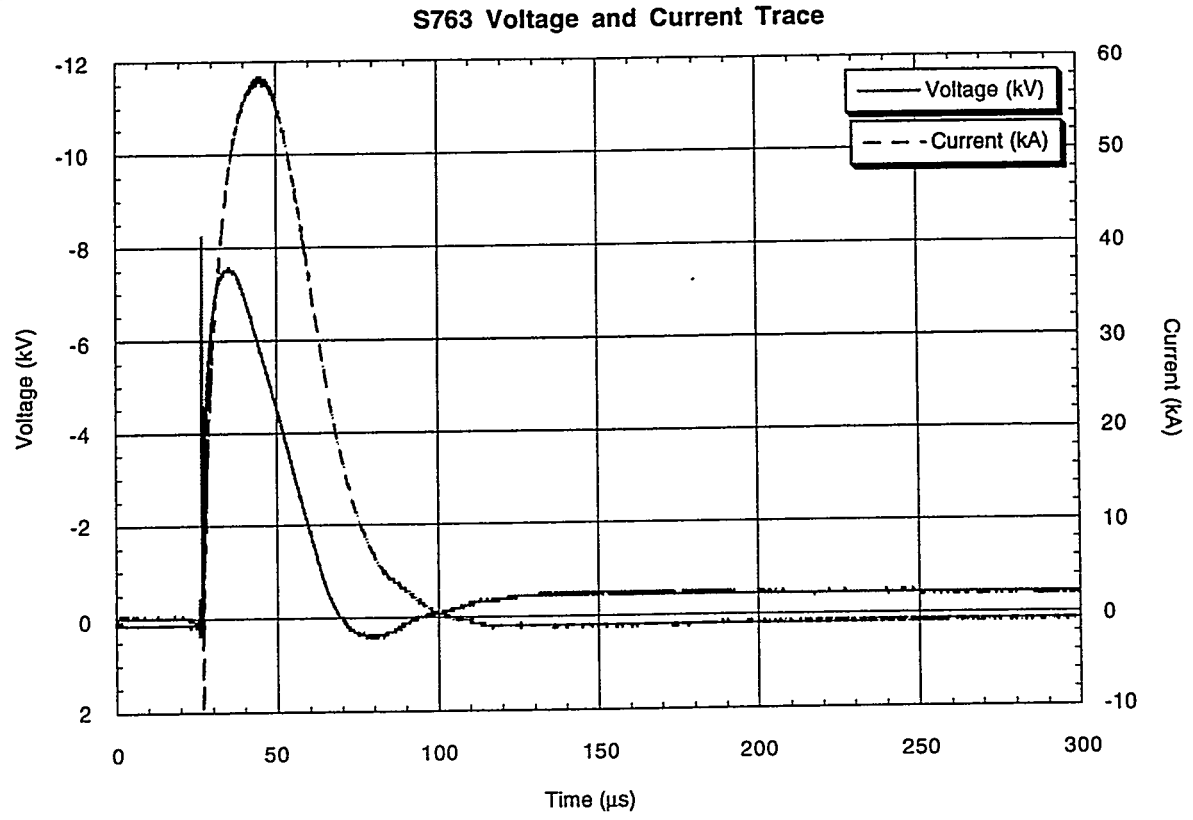

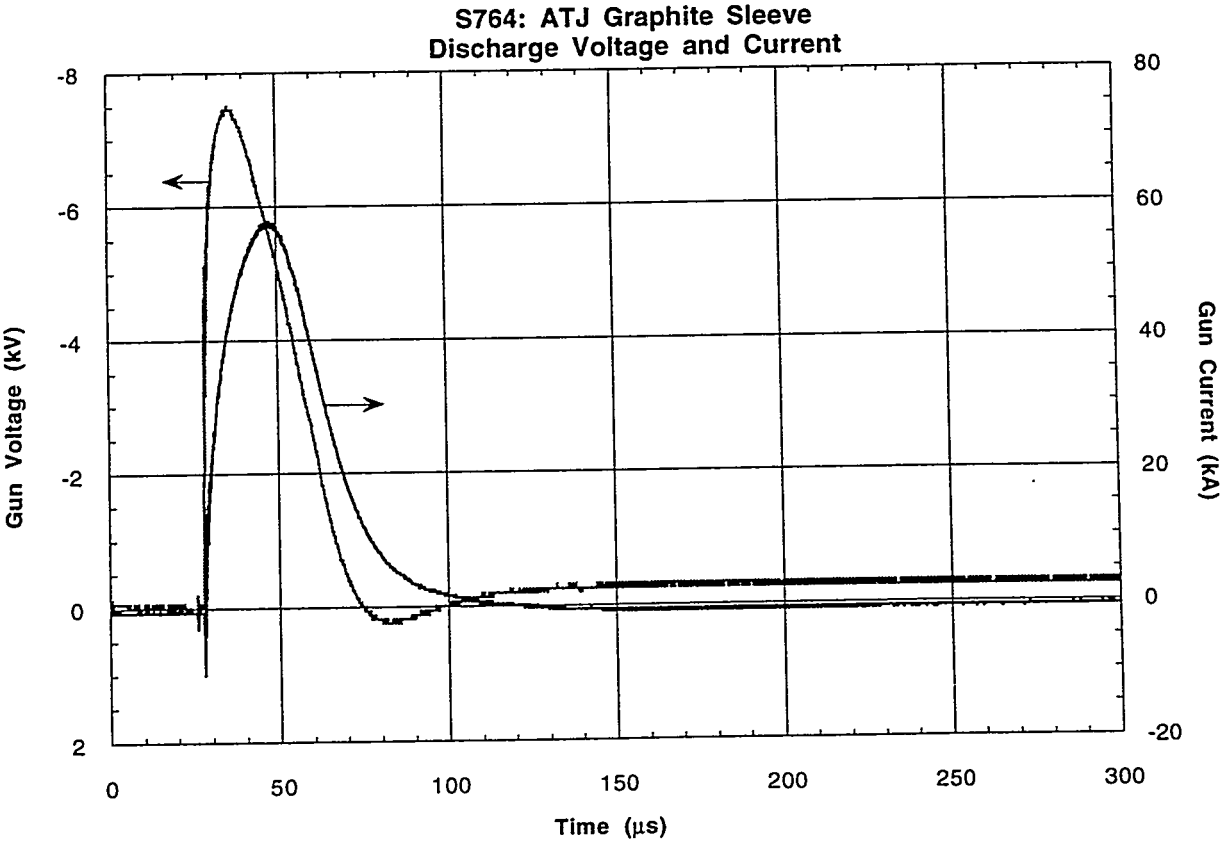

Figure 3.2.3. Power and energy traces for graphite carbon tests S763 and S764.

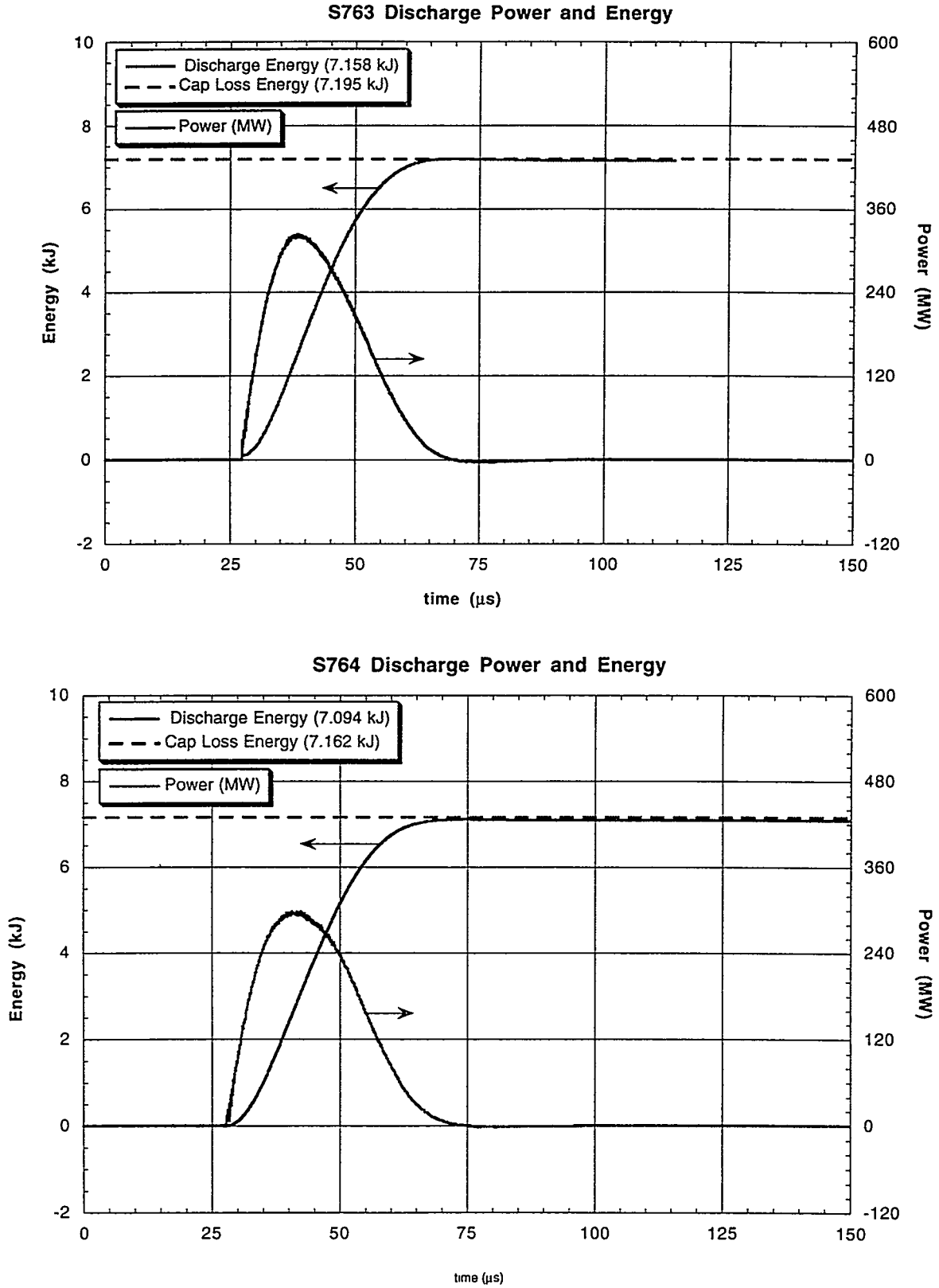

Figure 3.2.4. Representative SEM micrographs of button 3 from UTR-22 graphite test S763.

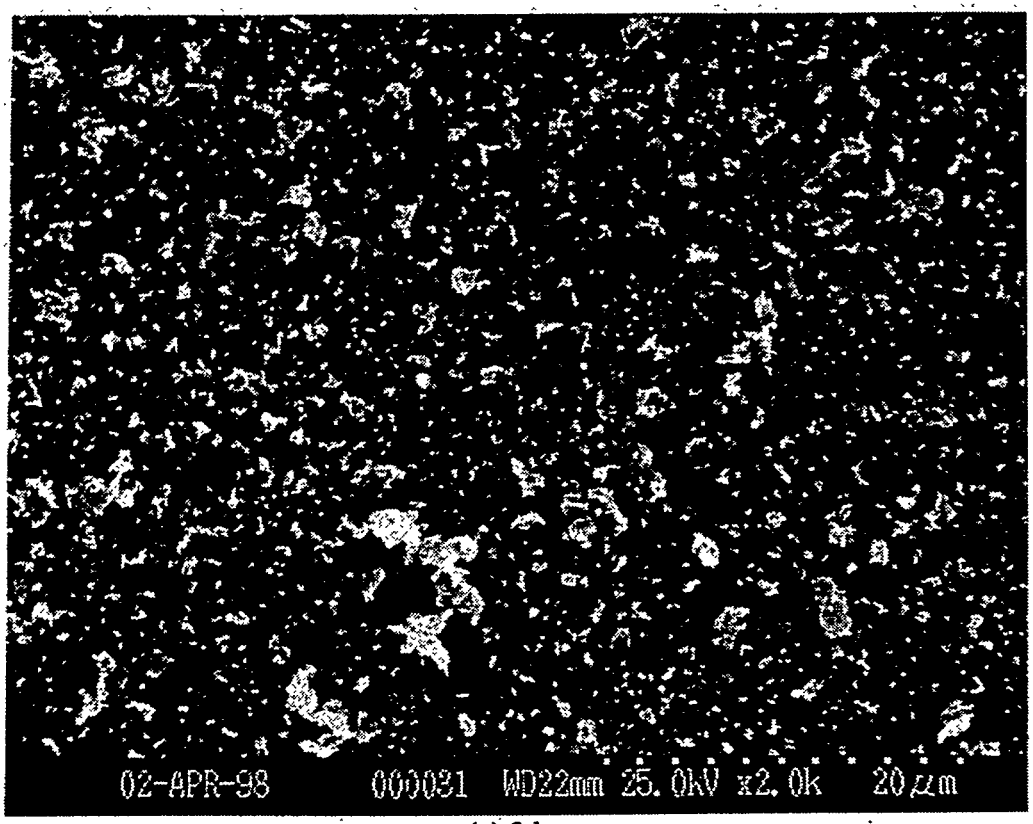

(a) 2 kx

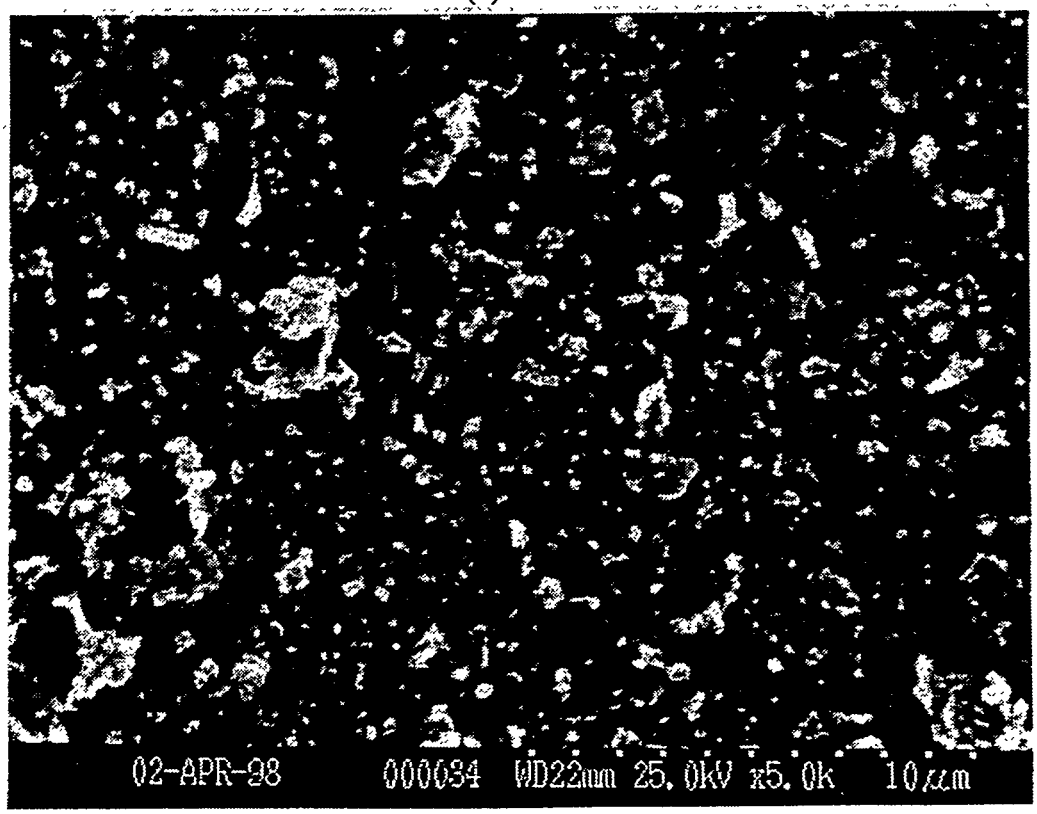

(b) 5kx

Figure 3.2.4. cont.

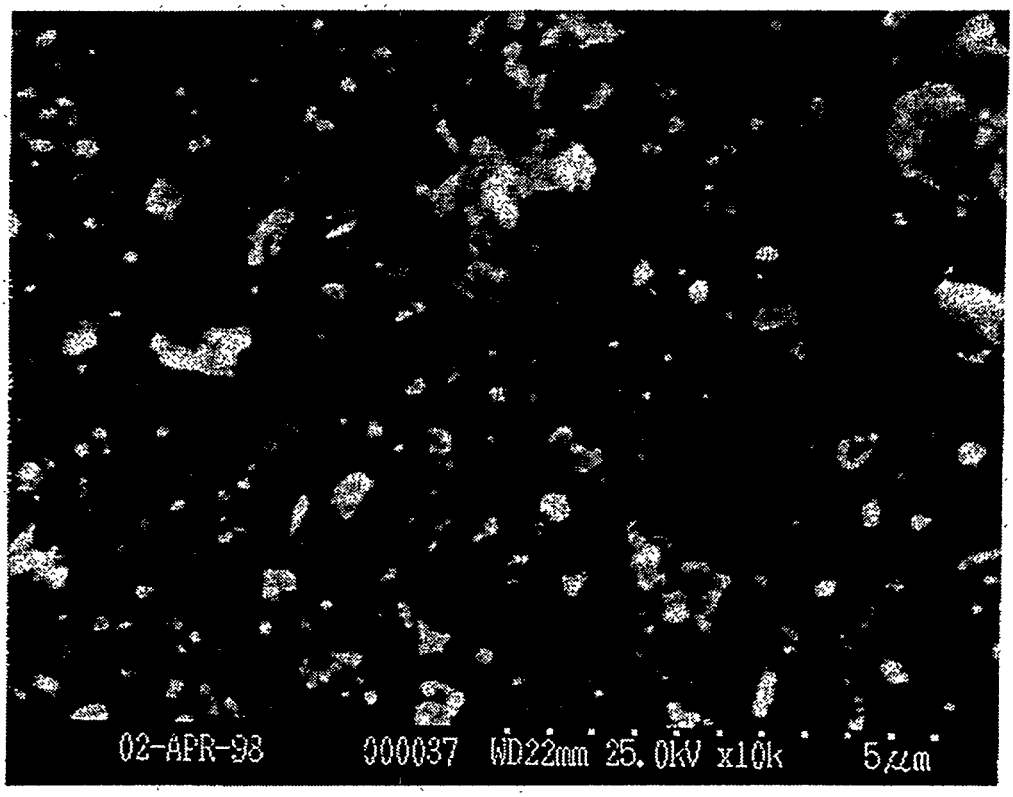

(c) 10 kx

Figure 3.2.5. Representative SEM micrographs of button 3 from ATJ graphite test S764.

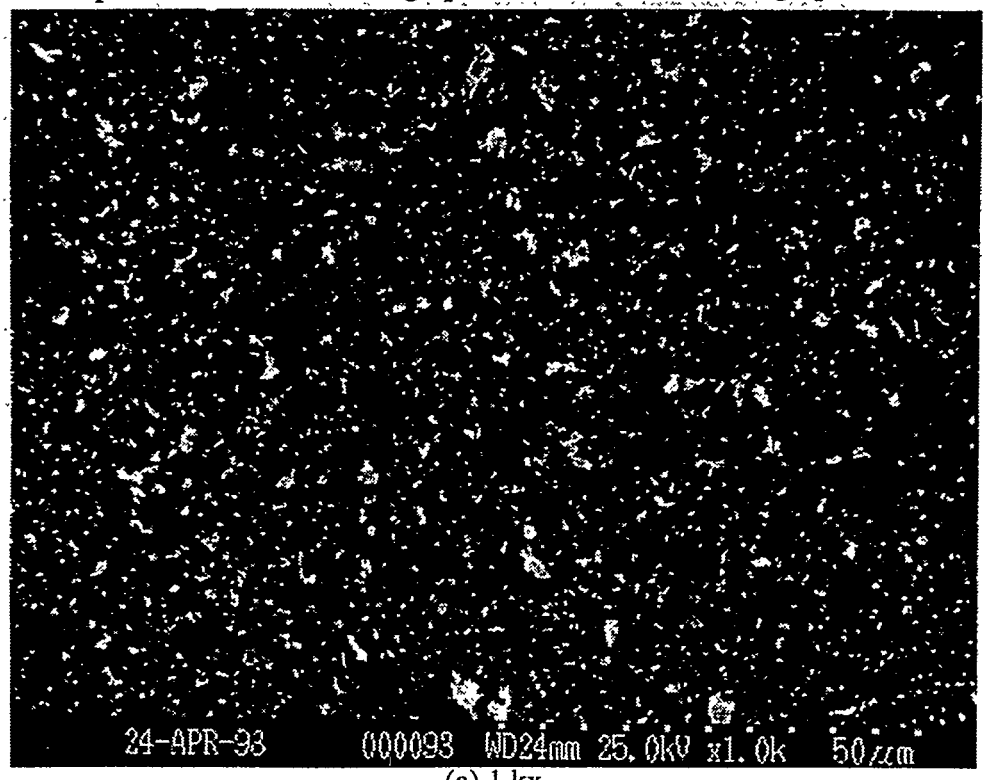

(a) 1 kx

Figure 3.2.5.cont.

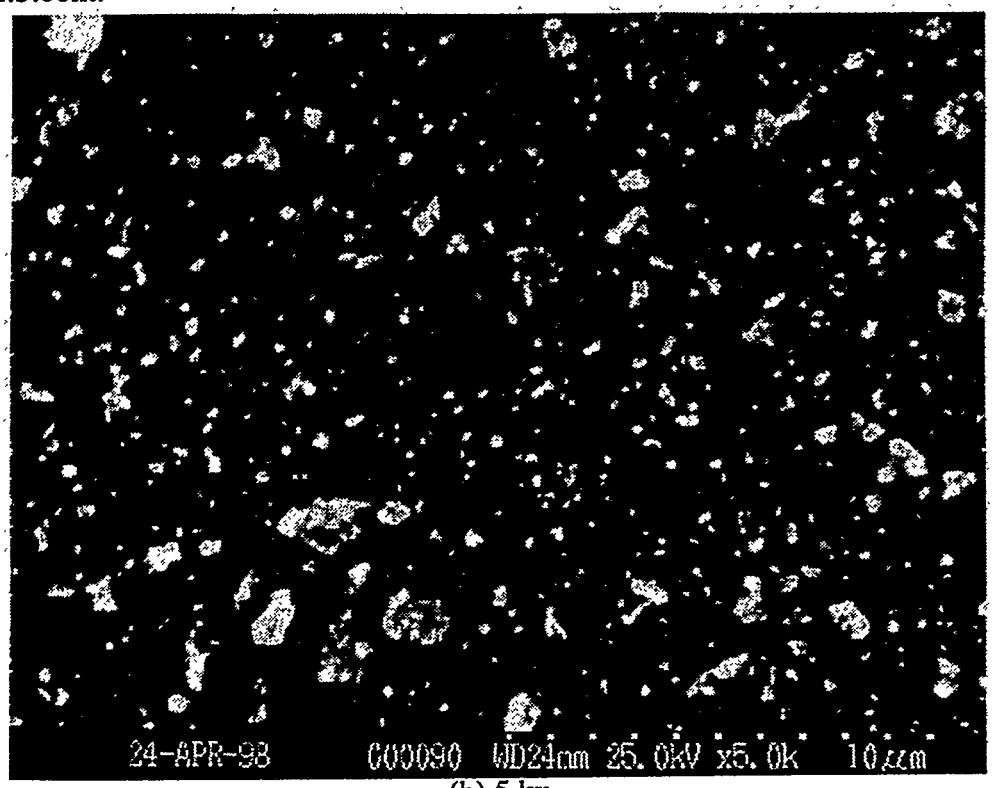

(b) 5 kx

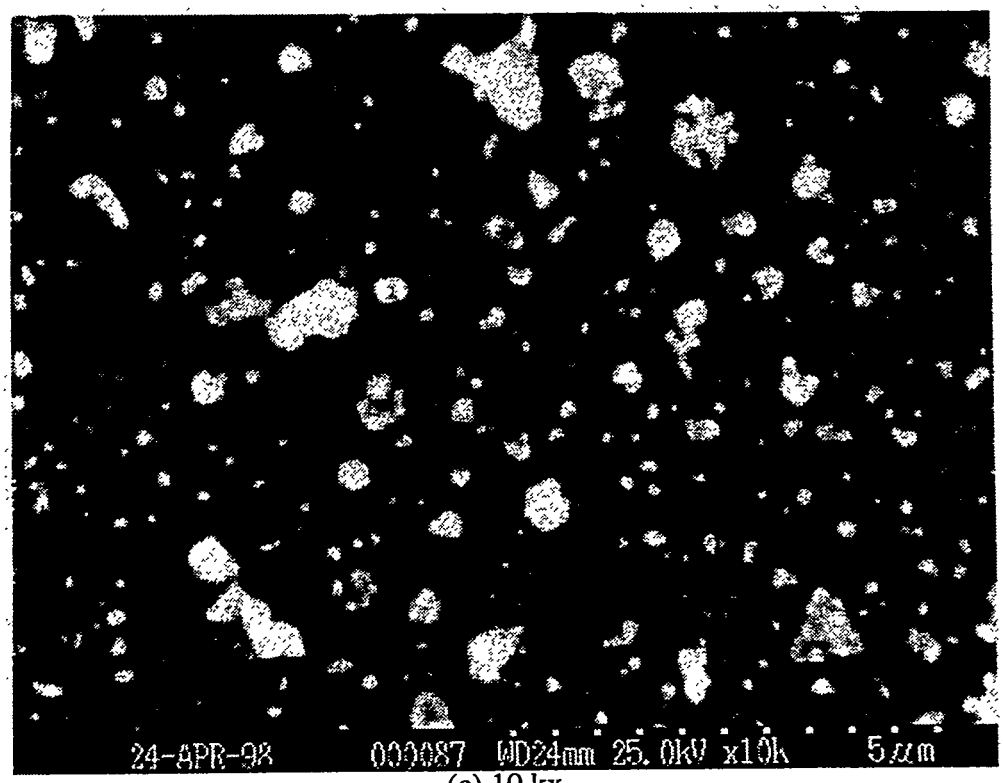

(c) 10 kx

Figure 3.2.6. UTR-22 graphite test (S763) button 1 particle size distribution.

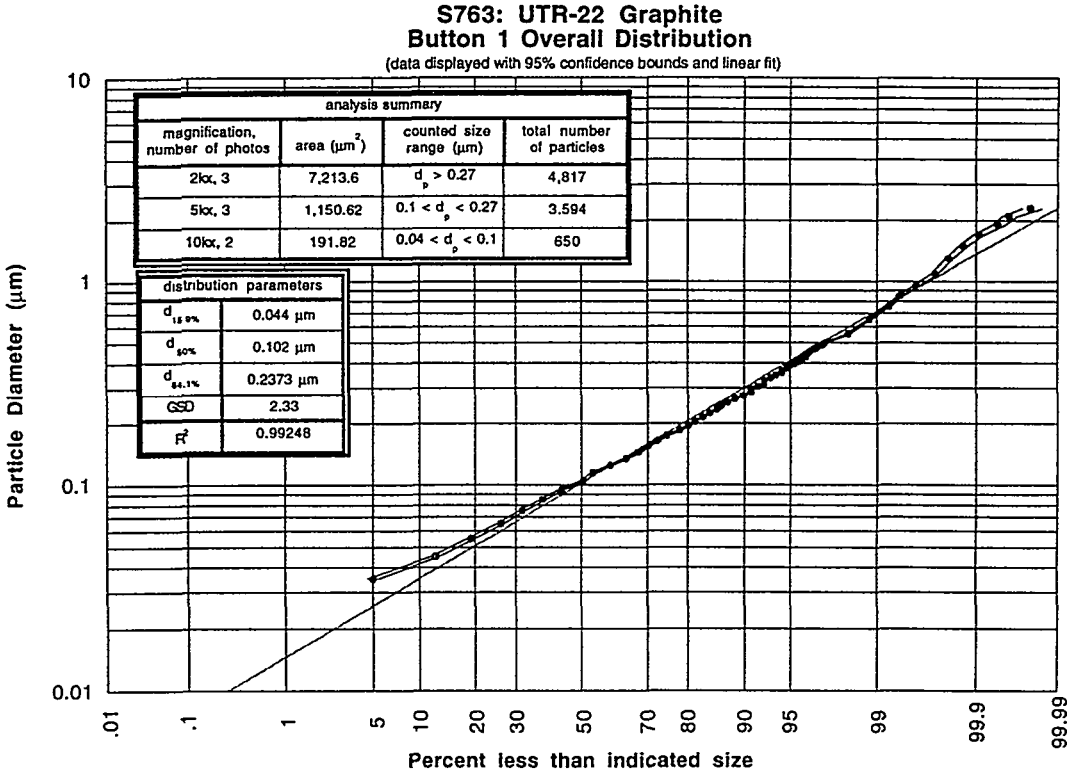

Data Summary Table:

photo	mag	scale (pixel/μm)	size (μm²)	min. d_{eq} (μm)	# of particles	scale factor	KW Test z-value	Overall p-value
763_1_1	2 kx	11.75	57.5x41.9	0.2[a]	1736	1	0.20	0.971
763_1_2	2 kx	11.75	57.3x41.9	0.2[a]	1691	1	-0.20	
763_1_3	2 kx	11.75	57.5x41.9	0.2[a]	1390	1	0.00	
763_1_4	5 kx	29.4	22.9x16.8	0.068[b]	1283	6.25	0.88	0.672
763_1_5	5 kx	29.4	23.0x16.7	0.068[b]	1141	6.25	-0.55	
763_1_6	5 kx	29.4	23.0x16.6	0.068[b]	1170	6.25	-0.36	
763_1_7	10 kx	58.8	11.5x8.38	0.038[b]	275	25	-failed-	0.611
763_1_8	10 kx	58.8	11.5x8.33	0.038[b]	360	25	0.511	
763_1_9	10 kx	58.8	11.5x8.35	0.038[b]	290	25	-0.511	

a. minimum equivalent diameter particle counted having an area of at least 5.1 x 1/scale on a side.
b. minimum equivalent diameter particle counted having an area of at least 3.1 x 1/scale on a side.

Figure 3.2.7. UTR-22 graphite test (S763) button 3 particle size distribution.

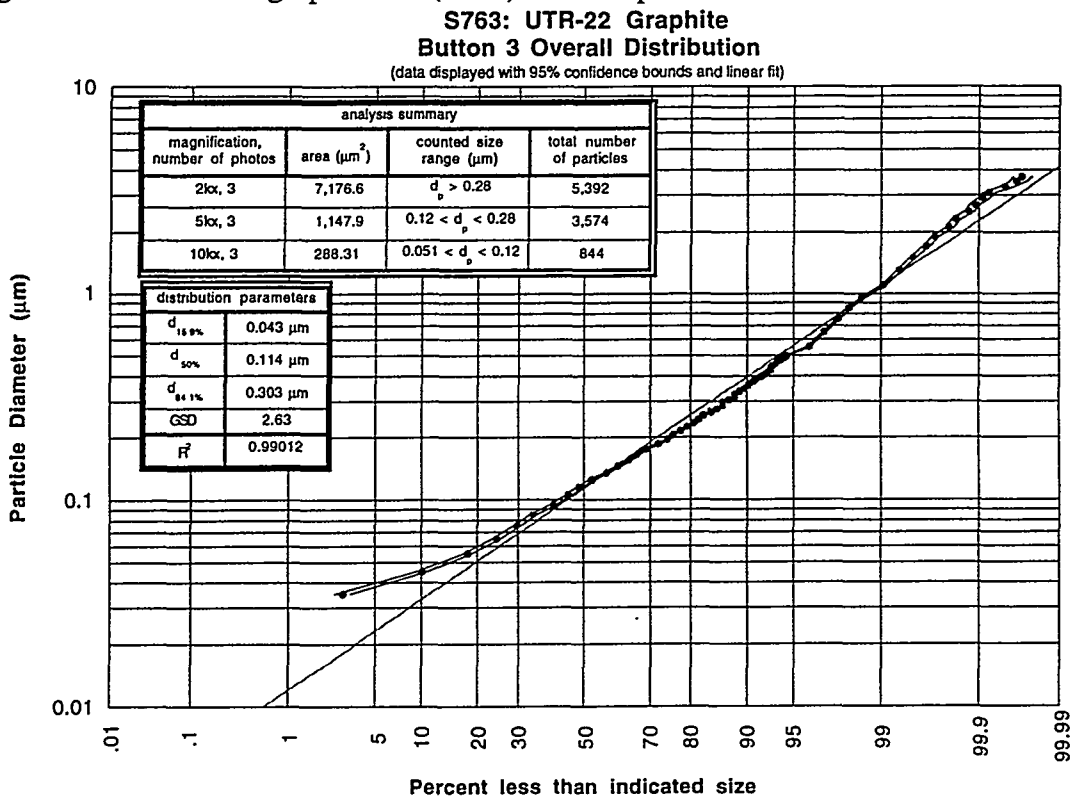

Data Summary Table:

photo	mag	scale (pixel/µm)	size (µm²)	min. d_{eq} (µm)	# of particles	scale factor	KW Test z-value	Overall p-value
763_3_1	2 kx	11.75	57.4x41.8	0.2[a]	1535	1	0.82	0.355
763_3_2	2 kx	11.75	57.3x41.5	0.2[a]	1780	1	0.70	
763_3_3	2 kx	11.75	57.4x41.8	0.2[a]	2077	1	-1.43	
763_3_4	5 kx	29.4	22.9x16.7	0.068[b]	1207	6.25	0.79	0.394
763_3_5	5 kx	29.4	22.8x16.8	0.068[b]	1255	6.25	-1.36	
763_3_6	5 kx	29.4	22.9x16.7	0.068[b]	1112	6.25	0.60	
763_3_7	10 kx	58.8	11.5x8.32	0.038[b]	226	25	0.76	0.741
763_3_8	10 kx	58.8	11.5x8.4	0.038[b]	323	25	-0.24	
763_3_9	10 kx	58.8	11.5x8.35	0.038[b]	295	25	-0.46	

a. minimum equivalent diameter particle counted having an area of at least 5.1 x 1/scale on a side.
b. minimum equivalent diameter particle counted having an area of at least 3.1 x 1/scale on a side.

Figure 3.2.8. UTR-22 graphite test (S763) button 9 particle size distribution.

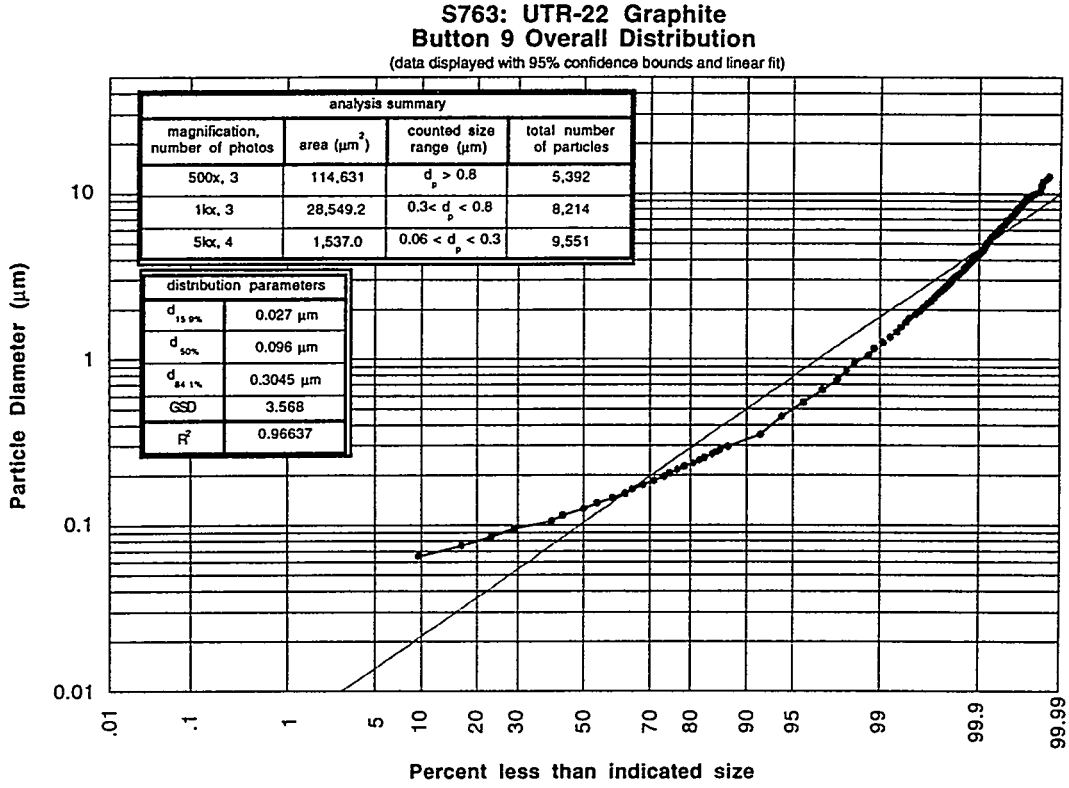

Data Summary Table:

photo	mag	scale (pixel/µm)	size (µm²)	min. d_{eq} (µm)	# of particles	scale factor	KW Test z-value	Overall p-value
763_9_2	5 kx	29.4	22.9x16.7	0.065[a]	904	100	0.02	0.980
763_9_3	5 kx	29.4	23.0x16.7	0.065[a]	503	-	-failed-	
763_9_4	5 kx	29.4	23.0x16.8	0.065[a]	832	100	-0.02	
763_9_5	5 kx	29.4	23.0x16.7	0.065[a]	1094	-	-failed-	
763_9_6	1 kx	5.88	114.8x82.3	0.278[b]	2534	4	-0.15	0.057
763_9_7	1 kx	5.88	114.6x83.5	0.278[b]	2583	4	2.20	
763_9_8	1 kx	5.88	115.4x82.6	0.278[b]	3097	4	-1.96	
763_9_9	500 x	2.94	229.5x166.3	0.654[b]	3422	1	1.73	0.219
763_9_10	500 x	2.94	230x167	0.654[b]	2678	1	-0.70	
763_9_11	500 x	2.94	229.3x166	0.654[b]	3451	1	-1.08	

a. minimum equivalent diameter particle counted having an area of at least 3.1 x 1/scale on a side.
b. minimum equivalent diameter particle counted having an area of at least 2.1 x 1/scale on a side.

Figure 3.2.9. ATJ graphite test (S764) button 1 particle size distribution.

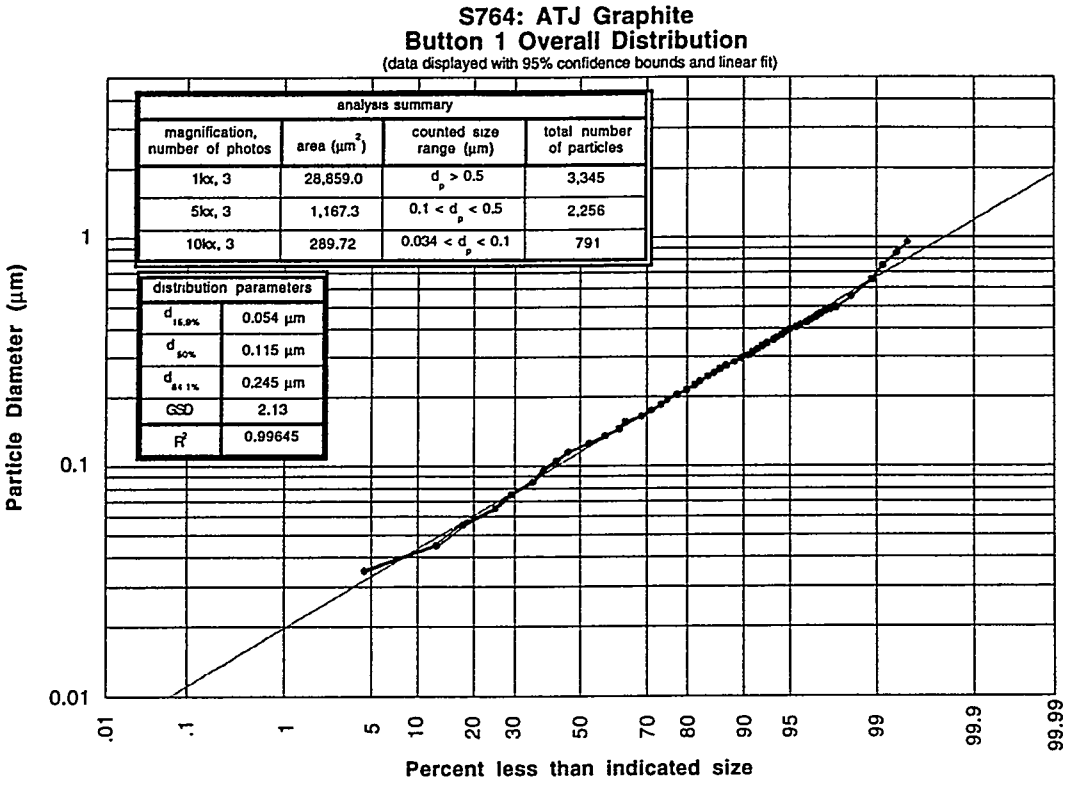

Data Summary Table:

photo	mag	scale (pixel/μm)	size (μm²)	min. d_{eq} (μm)	# of particles	scale factor	KW Test z-value	Overall p-value
764_1_1[a]	10 kx	56.4	11.45x8.35	0.034[b]	201	100	5.07	0.000
764_1_2[a]	10 kx	56.4	11.49x8.44	0.034[b]	221	100	1.20	
764_1_3[a]	10 kx	56.4	11.51x8.44	0.034[b]	369	100	-5.50	
764_1_4[a]	5 kx	28.2	23.04x16.77	0.090[c]	991	25	-5.27	0.000
764_1_5[a]	5 kx	28.2	23.09x16.95	0.090[c]	729	25	1.64	
764_1_6[a]	5 kx	28.2	22.98x16.95	0.090[c]	536	25	4.35	
764_1_7	1 kx	5.64	115.1x83.51	0.35[b]	449	1	0.18	0.625
764_1_8	1 kx	5.64	115.3x83.87	0.35[b]	1199	1	0.60	
764_1_9	1 kx	5.64	114.9x83.87	0.35[b]	697	1	-0.93	

a. All images obtained at 10 kx and 5 kx failed the Kruskal-Wallis test (i.e. $p < 0.05$) but were used in generation of the overall size distribution.
b. minimum equivalent diameter particle counted having an area of at least 3.1 x 1/scale on a side.
c. minimum equivalent diameter particle counted having an area of at least 5.1 x 1/scale on a side.

Figure 3.2.10. ATJ graphite test (S764) button 3 particle size distribution.

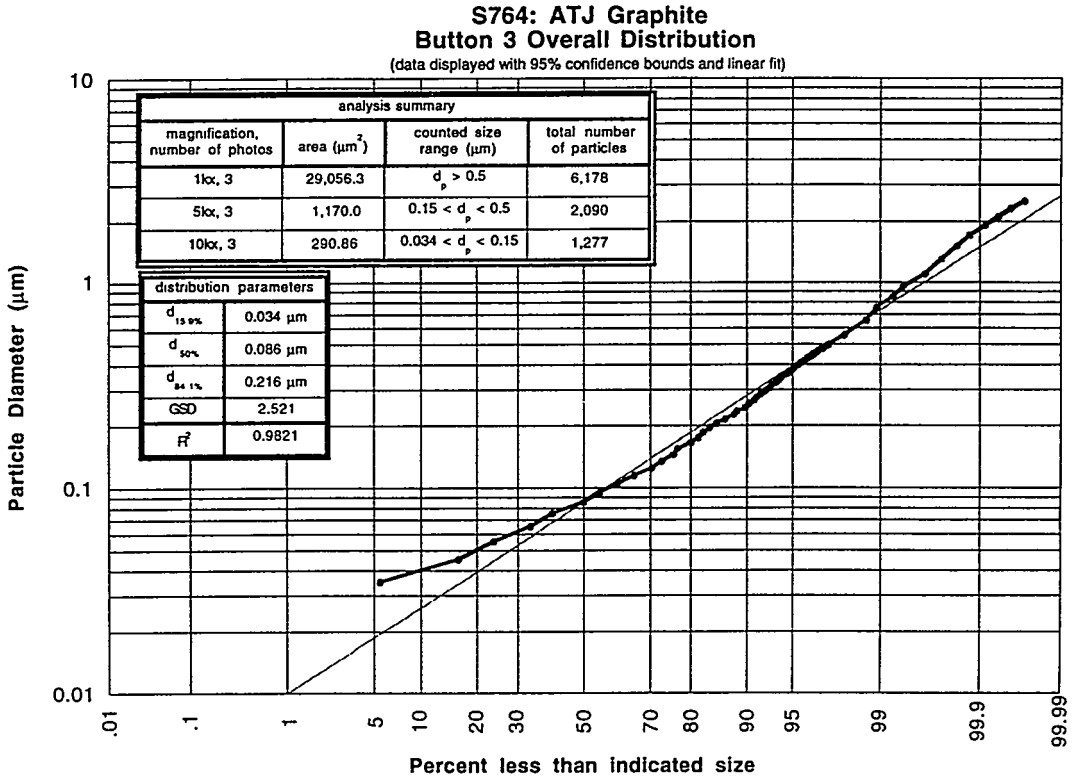

Data Summary Table:

photo	mag	scale (pixel/µm)	size (µm²)	min. d_{eq} (µm)	# of particles	scale factor	KW Test z-value	Overall p-value
764_3_1	10 kx	56.4	11.52x8.46	0.034[a]	430	100	0.76	0.448
764_3_2	10 kx	56.4	11.49x8.33	0.034[a]	400	100	-0.76	
764_3_3	10 kx	56.4	11.52x8.48	0.034[a]	447	-	-failed-	
764_3_4	5 kx	28.2	22.98x16.99	0.090[b]	651	25	-0.11	0.737
764_3_5	5 kx	28.2	23.05x16.84	0.090[b]	623	25	0.74	
764_3_6	5 kx	28.2	23.09x16.95	0.090[b]	816	25	-0.59	
764_3_7	1 kx	5.64	114.5x84.4	0.35[a]	2238	1	-1.21	0.161
764_3_8	1 kx	5.64	115.4x83.87	0.35[a]	1861	1	1.88	
764_3_9	1 kx	5.64	115.3x84.75	0.35[a]	2079	1	0.60	

a. minimum equivalent diameter particle counted having an area of at least 3.1 x 1/scale on a side.
b. minimum equivalent diameter particle counted having an area of at least 5.1 x 1/scale on a side.

Figure 3.2.11. ATJ graphite test (S764) button 5 particle size distribution.

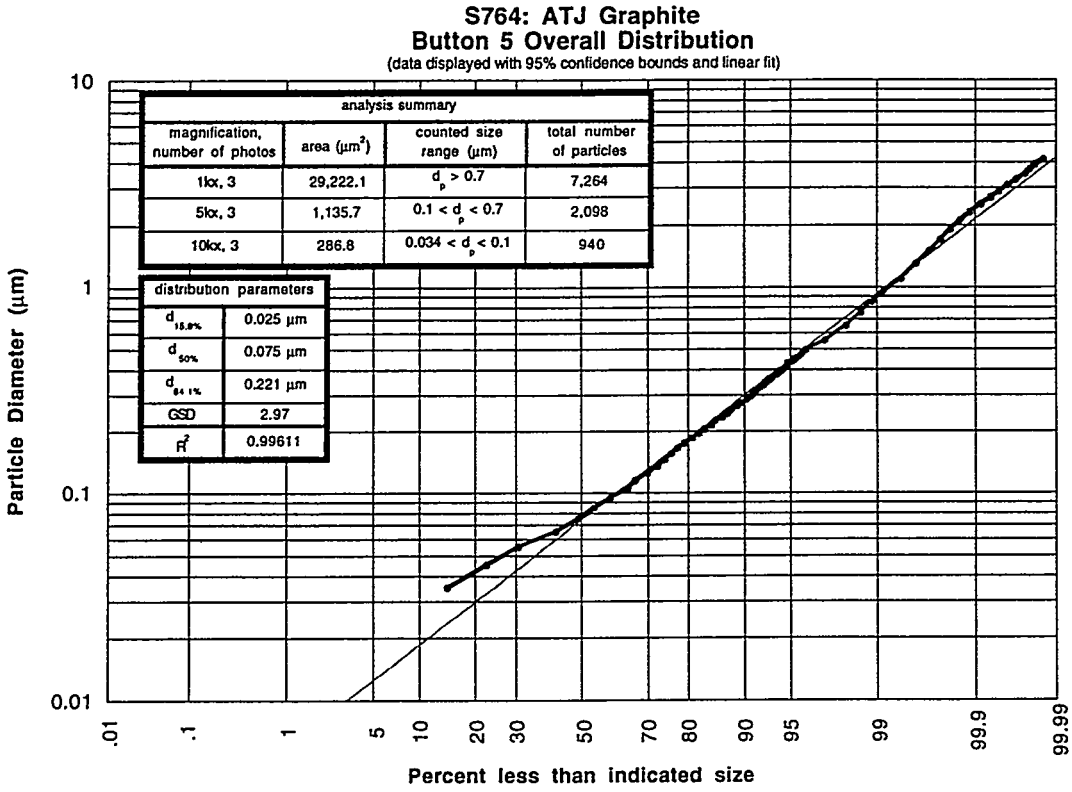

Data Summary Table:

photo	mag	scale (pixel/μm)	size (μm²)	min. d_{eq} (μm)[a]	# of particles	scale factor	KW Test z-value	Overall p-value
764_5_1	1 kx	5.88	114.5x84.7	0.34	2202	1	0.87	0.649
764_5_2	1 kx	5.88	114.5x84.7	0.34	2611	1	-0.16	
764_5_3	1 kx	5.88	115.6x84.8	0.34	2451	1	-0.69	
764_5_4	5 kx	29.4	22.82x16.73	0.07	666	25	0.33	0.382
764_5_5	5 kx	29.4	22.93x16.67	0.07	731	25	1.01	
764_5_6	5 kx	29.4	22.96x16.19	0.07	701	25	-1.32	
764_5_7	10 kx	58.8	11.46x8.40	0.034	286	100	-0.43	0.220
764_5_8	10 kx	58.8	11.45x8.27	0.034	301	100	1.70	
764_5_9	10 kx	58.8	11.36x8.44	0.034	353	100	-1.23	

a. minimum equivalent diameter particle counted having an area of at least 3.1 x 1/scale on a side.

Figure 3.2.12. ATJ graphite test (S764) button 7 particle size distribution.

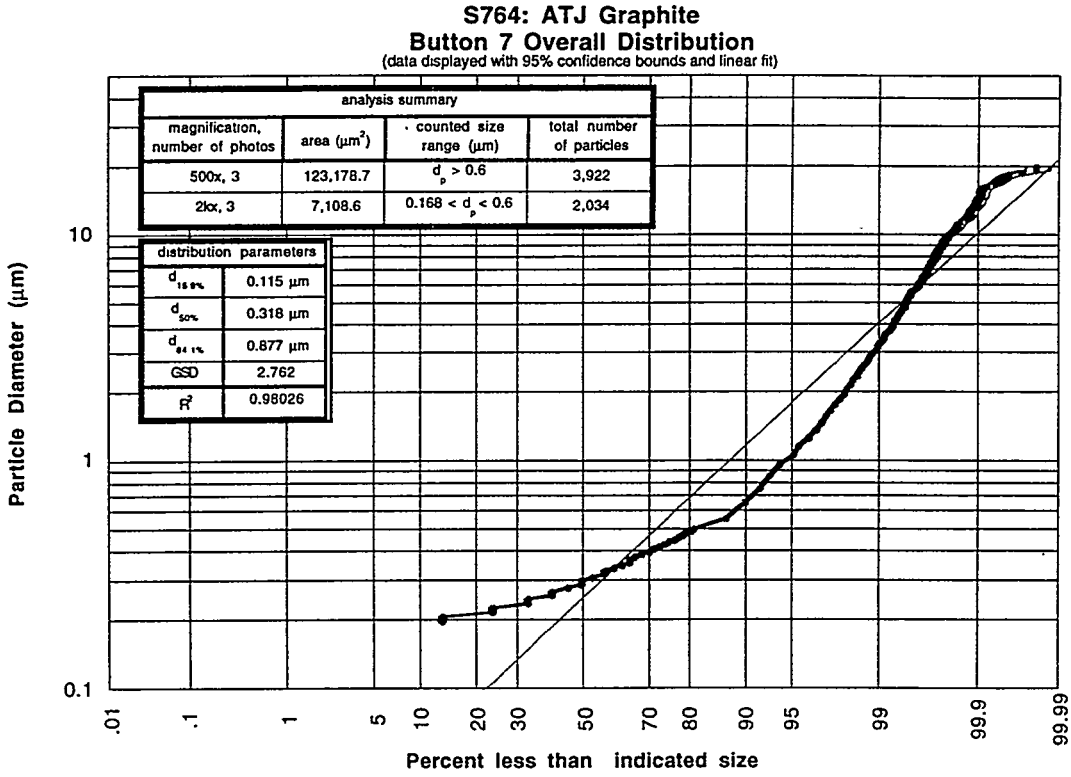

Data Summary Table:

photo	mag	scale (pixel/μm)	size (μm²)	min. d_{eq} (μm)[a]	# of particles	scale factor	KW Test z-value	Overall p-value
764_7_1	500 x	2.94	282.2x167.4	0.65	1231	1	1.39	0.161
764_7_2	500 x	2.94	227.6x167.3	0.65	1303	1	0.48	
764_7_3	500 x	2.94	231.0x163.9	0.65	1388	1	-1.83	
764_7_4	2 kx	11.8	57.46x41.27	0.168	600	16	-0.45	0.141
764_7_5	2 kx	11.8	57.2x41.19	0.168	493	16	1.96	
764_7_6	2 kx	11.8	57.46x41.11	0.168	941	16	-1.22	

a. minimum equivalent diameter particle counted having an area of at least 3.1 x 1/scale on a side.

Figure 3.2.13. ATJ graphite test (S764) button 9 particle size distribution.

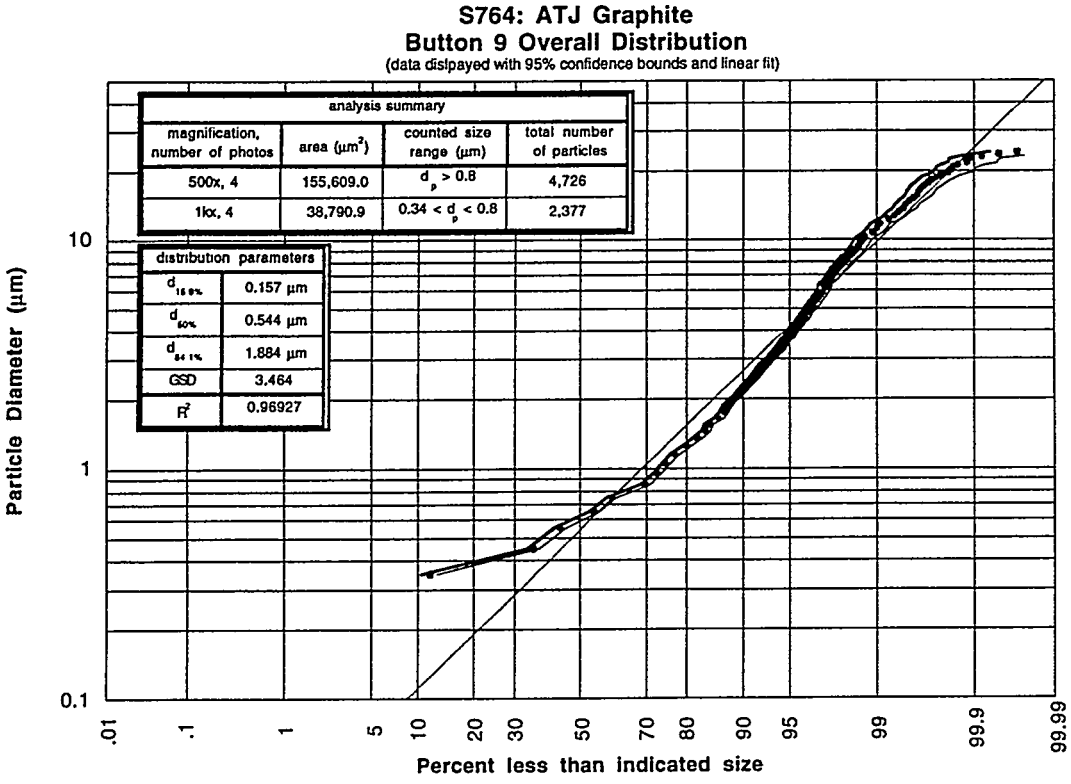

Data Summary Table:

photo	mag	scale (pixel/μm)	size (μm²)	min. d_{eq} (μm)[b]	# of particles	scale factor	KW Test z-value	Overall p-value
764_9_1	500 x	2.82	229.8x168.8	0.68	1346	1	-2.16	0.066
764_9_2	500 x	2.82	230.1x169.9	0.68	1421	1	1.92	
764_9_3	500 x	2.82	230.1x168.4	0.68	1124	1	0.22	
764_9_4	500 x	2.82	230.9x168.8	0.68	835	-	-failed-	
764_9_5[a]	1 kx	5.64	115.2x84.4	0.34	707	4	-4.27	0.000
764_9_6[a]	1 kx	5.64	115.4x84.93	0.34	433	4	5.94	
764_9_7[a]	1 kx	5.64	115.1x84.0	0.34	444	4	4.04	
764_9_8[a]	1 kx	5.64	115.4x83.16	0.34	793	4	-4.08	

a. All images obtained at 1 kx failed the Kruskal-Wallis test (i.e. $p < 0.05$) but were used in generation of the overall size distribution.

b. minimum equivalent diameter particle counted having an area of at least 2.9 x 1/scale on a side.

4.0 Carbon / Copper Tests

Particle formation in the presence of two or more condensing species is of interest because several different materials are present in the interior of a fusion reactor's vacuum vessel that may be exposed to heat loading and vaporization during disruptions. To investigate this situation, several tests have been performed in SIRENS with multiple materials placed in the source section and exposed to the high intensity arc. The first of these tests involved a mixture of Lexan (providing the carbon species) and copper. Lexan was chosen as the carbon-based material because of its convenience of use in the source section and the resulting carbon particles from the Lexan tests were of similar size and shape as the particles generated in the graphite tests. Two different configurations were chosen for the carbon / copper tests: a "short" configuration test to characterize the particles formed when the condensing species is predominately carbon, and a "segmented" configuration test to characterize particles formed from roughly equivalent surface areas of carbon and copper exposed to a high heat flux. Table 4.0.1 displays a summary of mass loss data and particle size distributions from the carbon / copper tests.

Table 4.0.1. Carbon / Copper tests comparison summary.

	Short C/Cu Test (S765)				*Segmented C/Cu Test (S769)*			
Energy (J)	6822				7143			
Fluence (MJ/m^2)	6.22				6.51			
Duration (μs)	80				60			
Lexan sleeve #1 Δm (mg)	37.16				12.56			
Copper sleeve #1 Δm (mg)	329.21				146.29			
Lexan sleeve #2 Δm (mg)	35.67				12.73			
Copper sleeve #2 Δm (mg)	-				166.75			
Lexan sleeve #3 Δm (mg)	-				12.21			
Copper sleeve #3 Δm (mg)	-				196.5			
Scaled Copper Δm (mg/kJ/cm)	48.26				23.78			
Scaled Lexan Δm (mg/kJ/cm)	1.64				1.75			
Cathode Δm (mg)	59.36				63.8			
	Δm (mg)	$d_{50\%}$ (μm)	GSD	R^2	Δm (mg)	$d_{50\%}$ (μm)	GSD	R^2
Button 1	0.17	0.123	2.313	0.997	0.77	0.356	2.451	0.995
Button 2	0.11	*	*	*	0.43	0.203	2.173	0.987
Button 3	0.15	0.119	2.232	0.995	0.74	0.246	2.190	0.993
Button 4	0.13	*	*	*	0.62	*	*	*
Button 5	0.33	*	*	*	0.33	*	*	*
Button 7	0.16	*	*	*	0.33	*	*	*
Button 9	0.45	0.200	2.468	0.989	-5.25	*	*	*
Button 17	0.15	*	*	*	1.11	0.353	2.954	0.992

Note: Asterisk (*) denotes analysis not performed.

4.1 Short Configuration: S765

The short configuration carbon / copper test was performed at a discharge energy of 6.82 kJ. Voltage and current traces are displayed in Figure 4.1.1, followed by power and energy in Figure 4.1.2. These traces are not smooth because the data collection system was inadvertently set to sample values every 10 μs rather than the usual 0.1 μs. Discharge energy calculated from integrated power (6.45 kJ) is less than the energy loss from the capacitor bank (6.82 kJ) because of the unaccounted area in the power curve from the slower sample rate. These values, however, remain within 5% agreement.

Table 4.1.1 summarizes mass measurements of source section and button components associated with S765. Mass loss from the copper sleeve was roughly ten times the loss from either of the two Lexan sleeves, although some fraction of this mass loss may have resulted from melt layer removal. Some sample material may melt if the arc comes in contact with its surface. An investigation of the impact of this melting is presently underway. In normalized units, the copper sleeve mass loss was 48.26 mg/kJ/cm, much higher than the value obtained in reference [3] for a copper-only sleeve in the source section (17 mg/kJ/cm). Scaled mass loss of the Lexan sleeves (1.64 mg/kJ/cm) is also greater in this tests than with Lexan-only sleeves in the source section (0.6 mg/kJ/cm). The general mass increase observed on the buttons from this test is greater than that seen in the pure-carbon tests. This indicates deposition in some form of the heavier copper species on button surfaces during the test.

Representative SEM micrographs of button 3 (Figure 4.1.3) shows the existence of somewhat larger particles residing on the button's surface, as compared to particles from the Lexan tests. A qualitative indication that many of these larger particles contain copper is provided by Energy Dispersive X-ray Analysis (EDXA). This analysis was performed on a region of button 2, and the results are shown in Figure 4.1.4. From the secondary electron (SE) image taken at 2 kx, a relatively large particle is observed on the mid-lower left side. EDXA image mapping showed this region to be predominately Cu (in part b of the figure where more dark pixels appear), while the surrounding area is significantly silicon from the glass substrate (in part c of the figure where fewer lighter pixels appear). Unfortunately, carbon is not readily detectable with the EDXA technique; as a result no carbon X-ray lines were present in this image spectrum.

Particle size distributions were obtained for buttons 1, 3, and 9 of S765 and are shown in Figures 4.1.5-8. The count median diameters resulting from a log-normal distribution fit are slightly larger than those seen for the Lexan-only tests, and the distribution widths as measured by the geometric standard deviation (GSD) are roughly the same.

Figure 4.1.1. Voltage and current traces for C/Cu short test (S765).

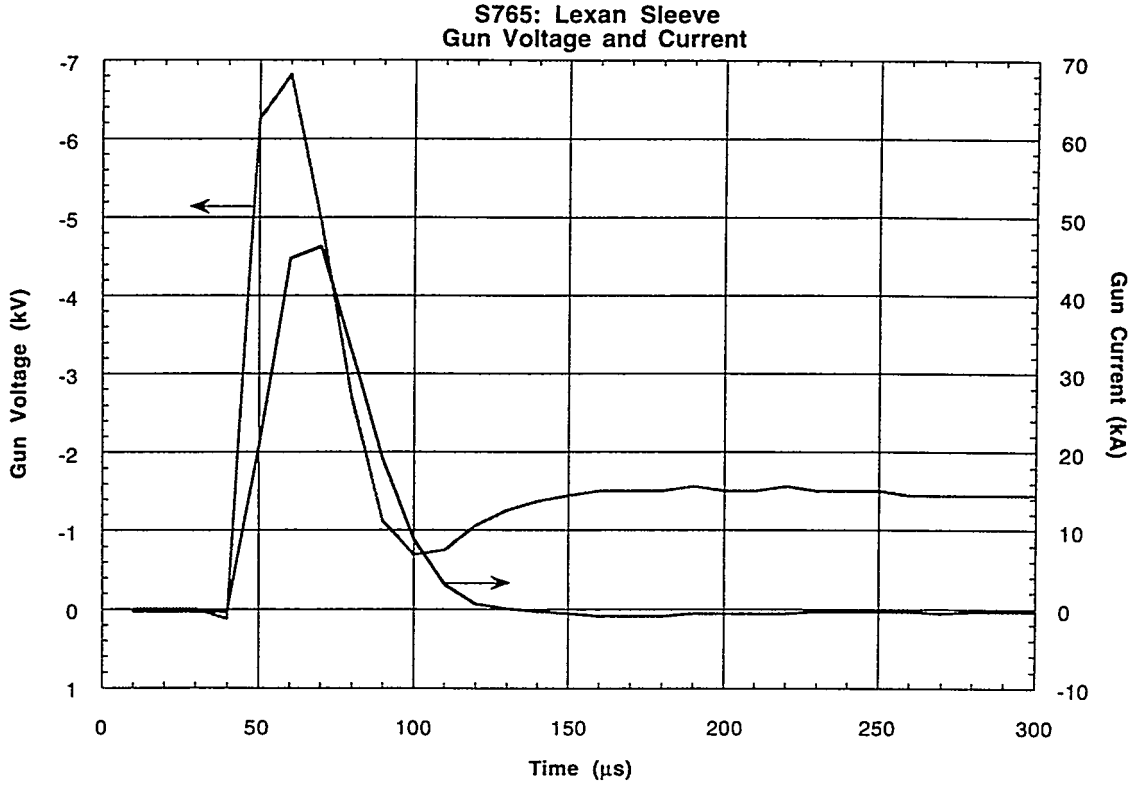

Figure 4.1.2. Power and energy traces for C/Cu short test (S765).

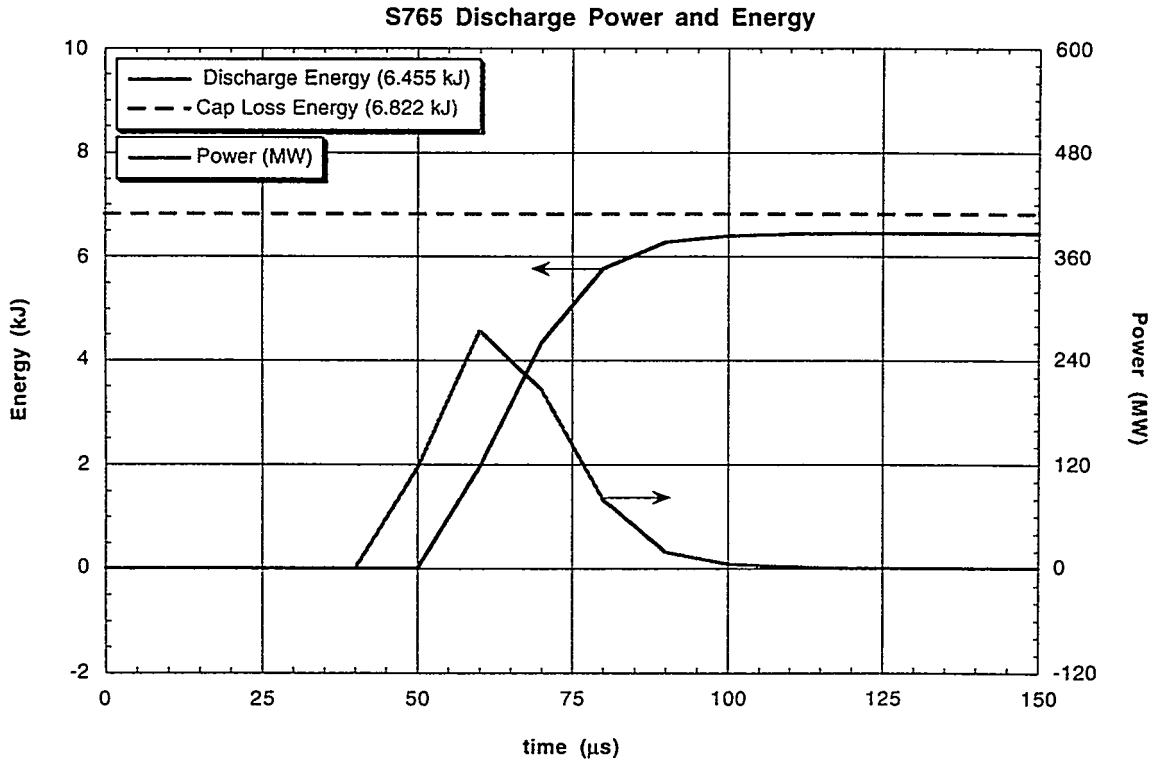

Table 4.1.1. C/Cu short test mass measurements.

S765: C / Cu Short Configuration

Source Section Components: component	pre-test wt. (g)	post-test wt. (g)	Δ wt. (mg)
cathode	9.58260	9.52324	59.36
long maycor	2.91699	-destroyed-	-
Lexan sleeve #1	1.13513	1.09797	37.16
copper sleeve	2.44184	2.11263	329.21
Lexan sleeve #2	0.96891	0.93324	35.67

Substrate Components: wall button	pre-test wt. (g)	post-test wt. (g)	Δ wt. (mg)
1	0.48208	0.48225	0.17
2	0.44300	0.44311	0.11
3	0.46595	0.46610	0.15
4	0.43984	0.43996	0.13
5	0.48477	0.48510	0.33
7	0.47846	0.47862	0.16
9	0.43916	0.43961	0.45
17	0.48941	0.48956	0.15

Notes: (1) All weight measurements are taken 3+ times and averaged.
(2) Δm uncertainty is ± 0.05 mg.

Figure 4.1.3. Representative SEM micrographs from button 3 of S765.

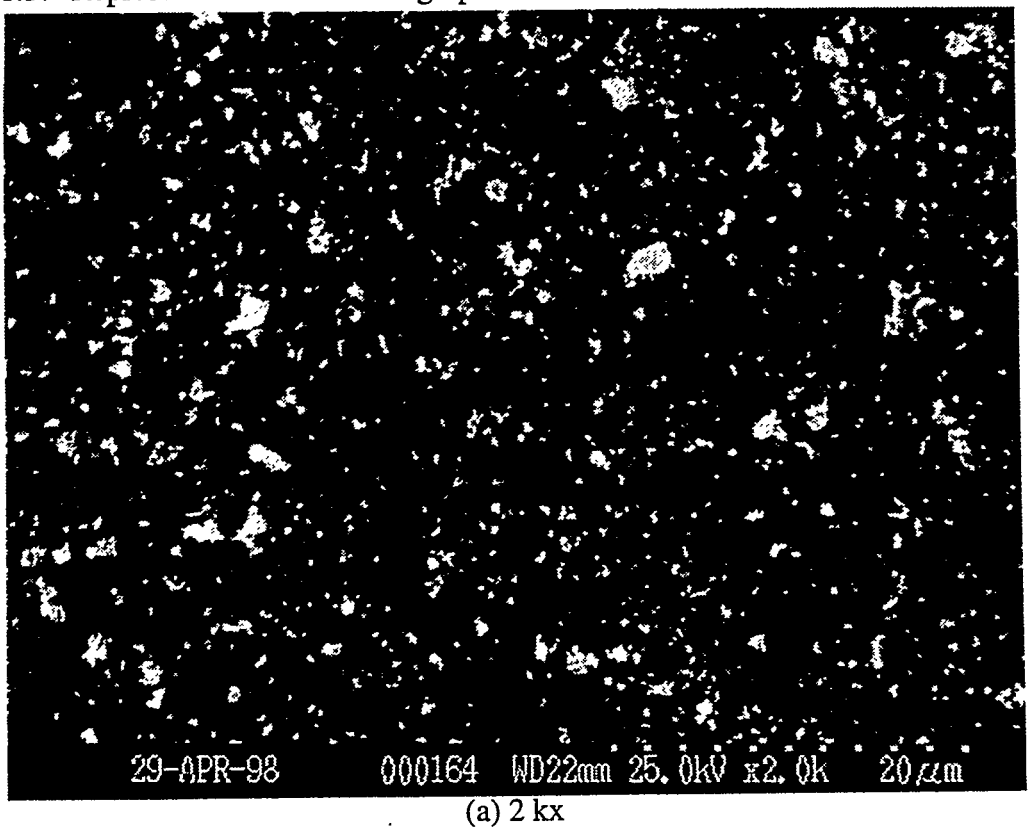

(a) 2 kx

Figure 4.1.3.cont.

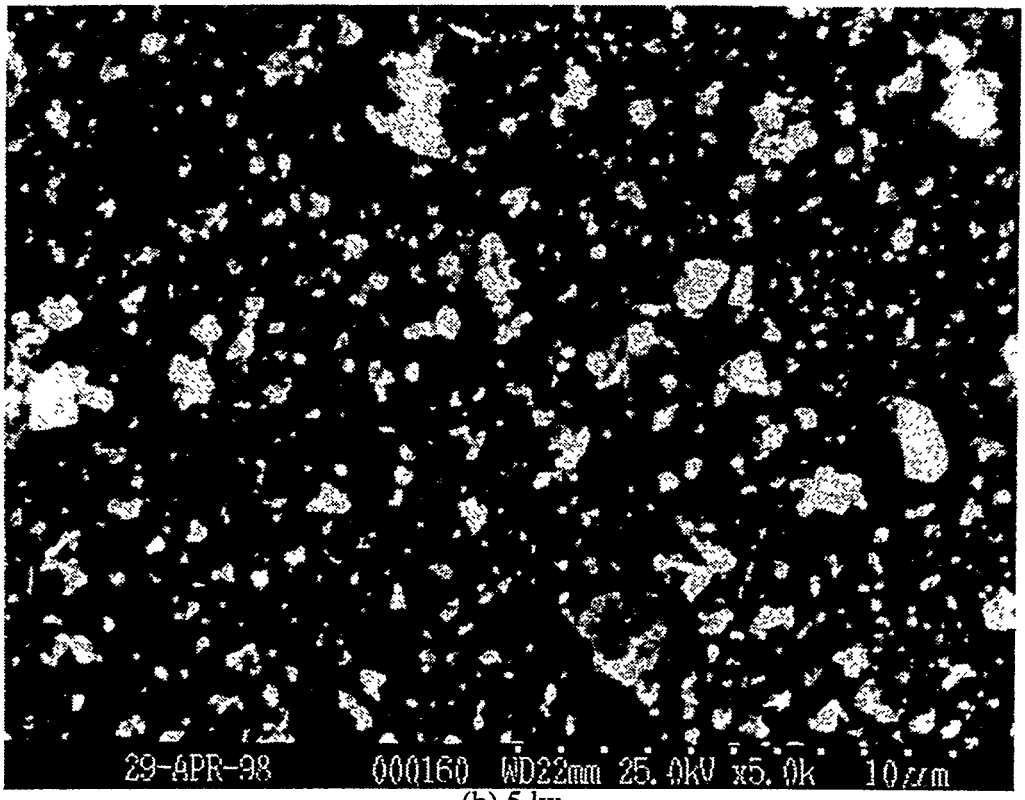

(b) 5 kx

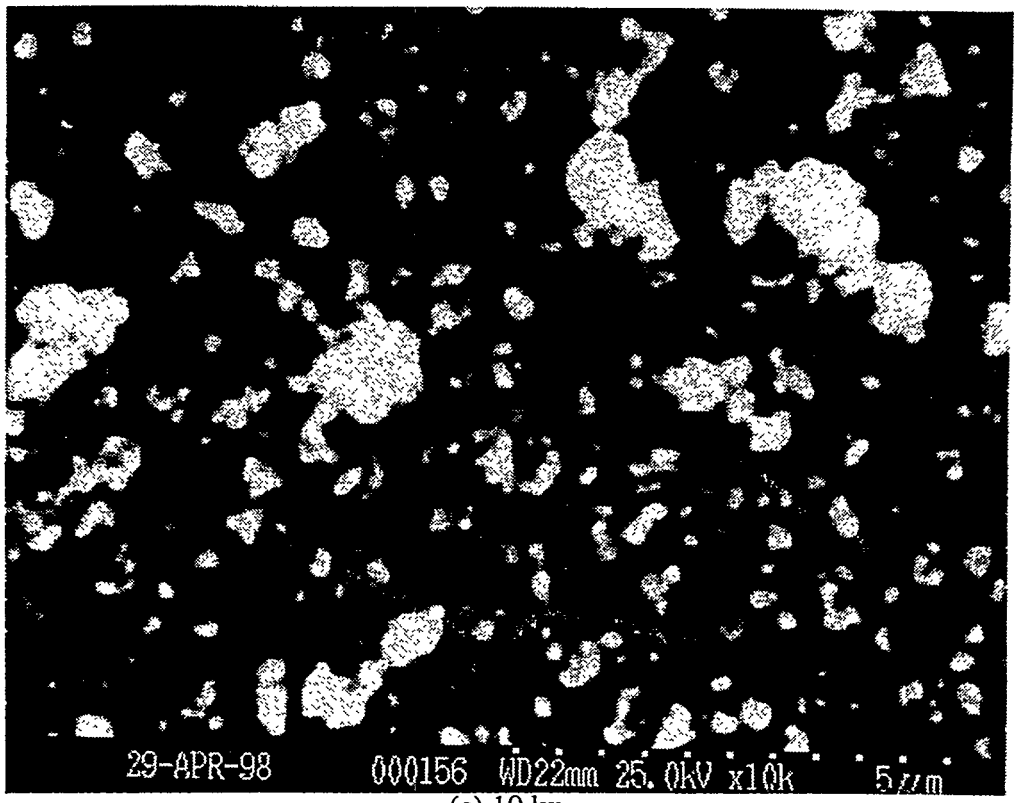

(c) 10 kx

Figure 4.1.4. EDXA mapping results of a button 2 region containing a Cu particle.

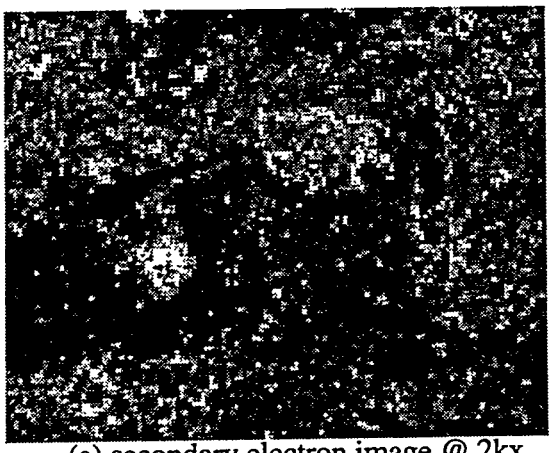

(a) secondary electron image @ 2kx

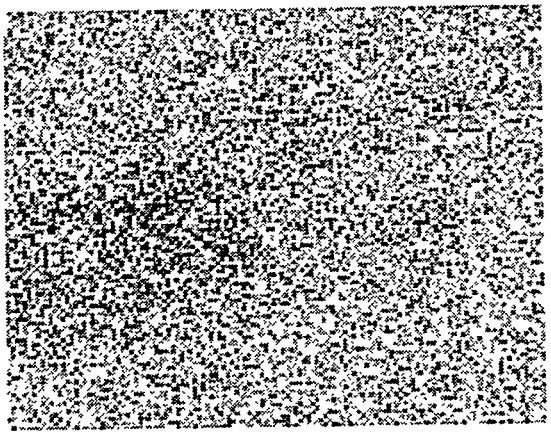

(b) Cu Kα mapping

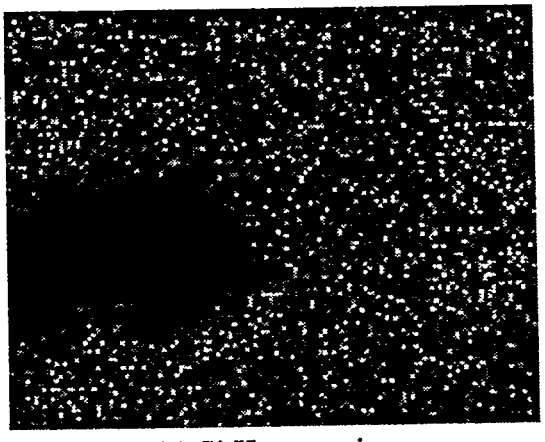

(c) Si Kα mapping

Figure 4.1.5. Carbon / Copper short test (S765) button 1 particle size distribution.

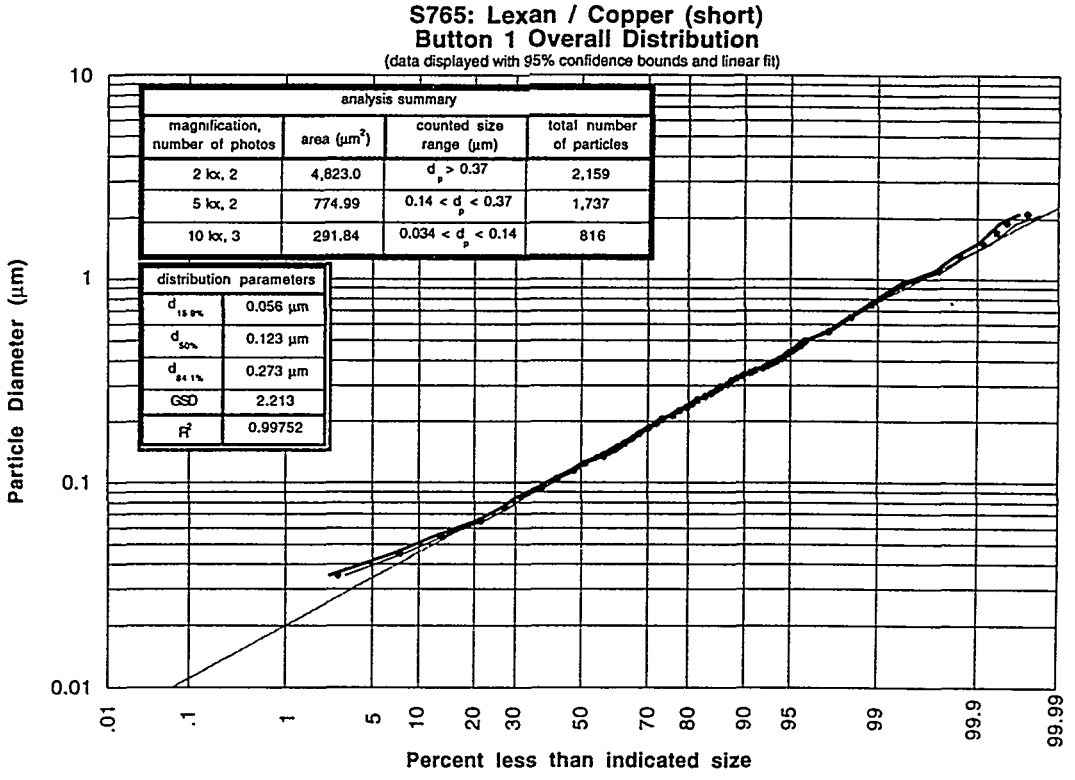

Data Summary Table:

photo	mag	scale (pixel/μm)	size (μm²)	min. d_{eq} (μm)	# of particles	scale factor	KW Test z-value	Overall p-value
765_1_1	10 kx	58.8	11.5x8.49	0.034[a]	192	25	-1.56	0.249
765_1_2	10 kx	58.8	11.46x8.47	0.034[a]	332	25	0.20	
765_1_3	10 kx	58.8	11.51x8.44	0.034[a]	292	25	1.18	
765_1_4	10 kx	58.8	11.48x8.40	0.034[a]	362	-	-failed-	
765_1_5	5 kx	29.4	22.99x16.87	0.068[a]	1054	6.25	0.17	0.863
765_1_7	5 kx	29.4	22.99x16.84	0.068[a]	683	6.25	-0.17	
765_1_11	5 kx	29.4	23.06x16.94	0.068[a]	803	-	-failed-	
765_1_8	2 kx	11.8	57.29x41.86	0.22[b]	1154	1	0.54	0.591
765_1_9	2 kx	11.8	57.2x41.86	0.22[b]	1210	-	-failed-	
765_1_10	2 kx	11.8	57.46x42.2	0.22[b]	1005	1	-0.54	

a. minimum equivalent diameter particle counted having an area of at least 3.1 x 1/scale on a side.
b. minimum equivalent diameter particle counted having an area of at least 5.1 x 1/scale on a side.

Figure 4.1.6. Carbon / Copper short test (S765) button 3 particle size distribution.

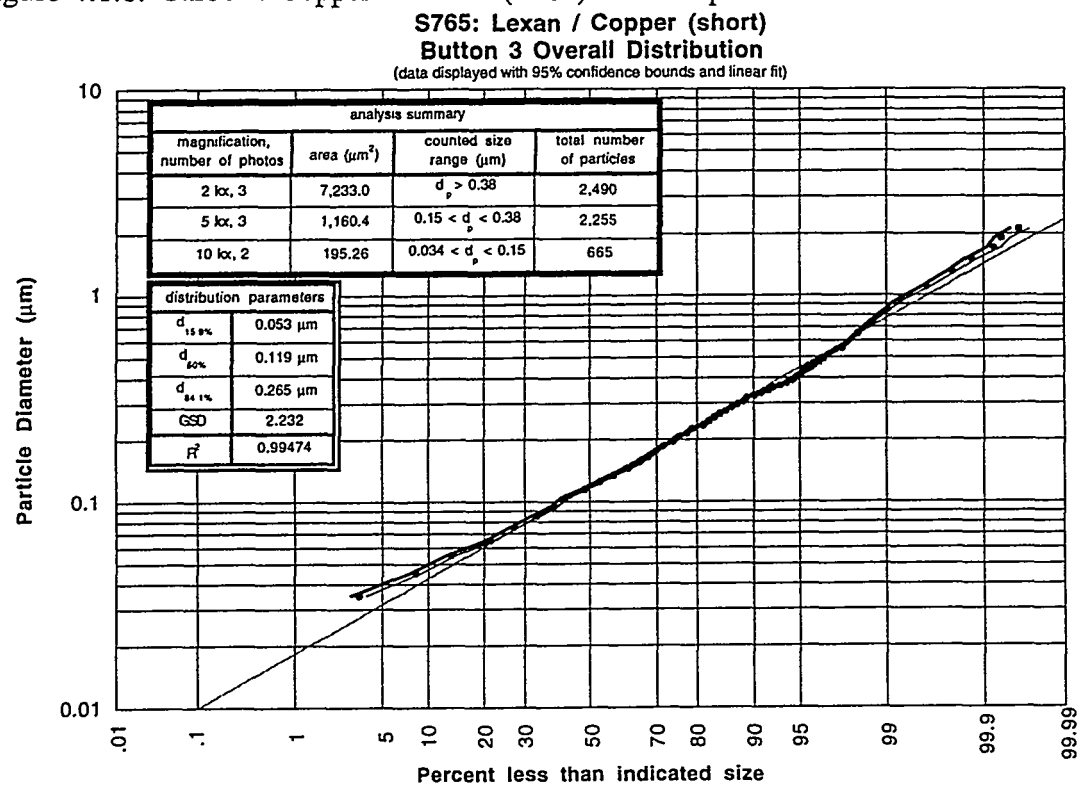

Data Summary Table:

photo	mag	scale (pixel/μm)	size (μm²)	min. d_{eq} (μm)	# of particles	scale factor	KW Test z-value	Overall p-value
765_3_1	10 kx	58.8	11.50x8.50	0.034[a]	212	-	-failed-	0.879
765_3_2	10 kx	58.8	11.53x8.45	0.034[a]	298	25	0.16	
765_3_3	10 kx	58.8	11.51x8.50	0.034[a]	367	25	-0.16	
765_3_4	5 kx	29.4	22.96x16.84	0.068[a]	826	6.25	-2.27	0.076
765_3_5	5 kx	29.4	22.96x16.97	0.068[a]	780	6.25	1.39	
765_3_6	5 kx	29.4	22.99x16.84	0.068[a]	649	6.25	0.96	
765_3_7	2 kx	11.8	57.29x41.69	0.22[b]	831	1	-0.76	0.418
765_3_8	2 kx	11.8	57.2x42.2	0.22[b]	939	1	-0.49	
765_3_9	2 kx	11.8	57.37x42.37	0.22[b]	726	1	1.31	

a. minimum equivalent diameter particle counted having an area of at least 3.1 x 1/scale on a side.
b. minimum equivalent diameter particle counted having an area of at least 5.1 x 1/scale on a side.

Figure 4.1.7. Carbon / Copper short test (S765) button 9 particle size distribution.

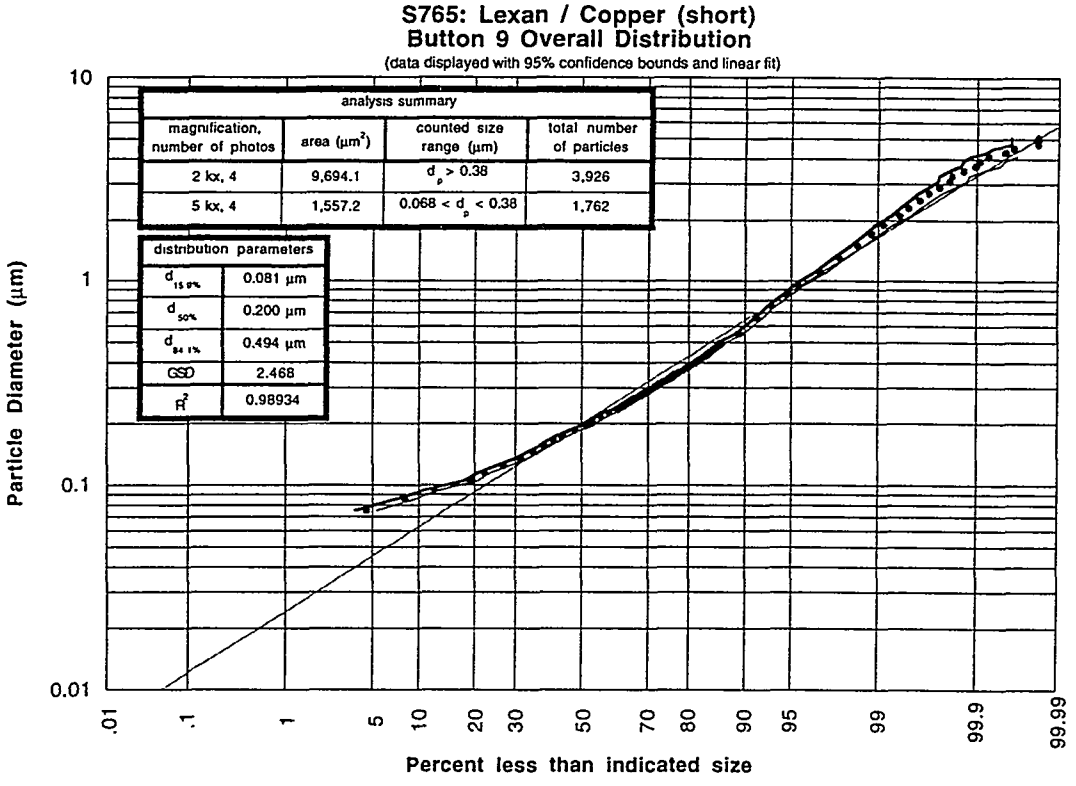

Data Summary Table:

photo	mag	scale (pixel/μm)	size (μm²)	min. d_{eq} (μm)	# of particles	scale factor	KW Test z-value	Overall p-value
765_9_1	5 kx	29.4	23.13x16.77	0.068[a]	422	6.25	0.60	0.0533
765_9_2	5 kx	29.4	23.03x17.07	0.068[a]	502	6.25	-2.21	
765_9_3	5 kx	29.4	22.99x16.87	0.068[a]	426	6.25	2.23	
765_9_4	5 kx	29.4	23.06x16.84	0.068[a]	412	6.25	-0.49	
765_9_5	2 kx	11.8	57.2x42.12	0.22[b]	1040	1	-0.65	0.426
765_9_6	2 kx	11.8	57.2x42.46	0.22[b]	957	1	1.65	
765_9_7	2 kx	11.8	57.29x42.63	0.22[b]	1067	1	-0.71	
765_9_8	2 kx	11.8	57.2x42.2	0.22[b]	862	1	-0.26	

a. minimum equivalent diameter particle counted having an area of at least 3.1 x 1/scale on a side.
b. minimum equivalent diameter particle counted having an area of at least 5.1 x 1/scale on a side.

4.2 Segmented Configuration: S769

A different test was performed using Lexan-carbon and copper in equal proportions within the source section. This segmented configuration was exposed to an electric discharge with an energy of 7.143 kJ. Voltage and current traces are displayed in Figure 4.2.1, and power and energy traces are given in Figure 4.2.2. Note the energy determined from integrated power is larger than the value calculated from capacitor bank energy loss, although only by 1.3%. This difference is within measurement error (~5%), even though typically the integrated power value is lower than the capacitor bank loss value.

Mass measurement information from S769 is summarized in Table 4.2.1. Each Lexan segment in the source section lost approximately equal amounts of mass, while the copper segments were observed to lose increasing amounts closer to the source exit. The total amount of copper material removed from all sleeves at this energy (7.14 kJ) was 509.54 mg. This may be compared with a result for a pure copper sleeve tested in reference [3] (i.e. S737, with 450 mg of mass lost from a copper sleeve 6.0 cm length at an energy of 4.46 kJ). In terms of mass loss per unit energy per unit length, S769 produced a copper mass loss of 23.78 mg/kJ/cm, while the data from [3] gives 17.0 mg/kJ/cm. The Lexan sleeves' mass loss value is also greater than the loss measured for a Lexan-only sleeve (1.75 mg/kJ/cm versus 0.6 mg/kJ/cm) and is comparable to that measured in the C / Cu short configuration test. The higher mass loss values from S765 and S769 possibly resulted from improved heating of the surface due to the presence of hot carbon / copper mixed species plasma in the arc. Another important mass difference was measured on the collection buttons. Mass increases on the buttons from S769 with the segmented source configuration were significantly greater than those associated with the short configuration of S765. This was expected due to the greater amount of copper exposed to arc-plasma heat flux. For the buttons on the chamber walls, mass gain decreases for locations further away from the source exit. End plate button 17 showed a relatively large increase in mass (1.11 mg), while button 9 was decreased in mass by 5.25 mg. This was caused by a large piece of the glass surface breaking away during the test, possibly from an impact with debris.

Figure 4.2.3 contains micrographs from the surface of button 3, taken at different locations and magnifications. These images show the distinct influence of increasing the amount of copper in the region exposed to high heat flux. Many larger and non-spherical particles are observed, and EDXA mapping indicates that some of the larger particles may contain both carbon and copper components (Figure 4.2.4). This evidence is only qualitative because of the ineffectiveness of EDXA to accurately detect carbon, as the carbon x-rays (0.281 and 0.291 keV) are at the edge of low energy noise in the EDXA system. As seen in Figure 4.2.5, evidence provided by optical emission spectroscopy obtained from the vaporized material expanding from the source section does indicate a significant amount of hot copper vapor, leading to the possibility that carbon and copper may both contribute to growth of individual particles. Carbon again goes undetected in

optical spectroscopy because no emission lines exist in the spectral region investigated. Finally, the resulting particle size distributions from buttons 1, 2, 3, and 17 are shown in Figures 4.2.6-9.

Figure 4.2.1. Voltage and current traces for C/Cu segmented test (S769).

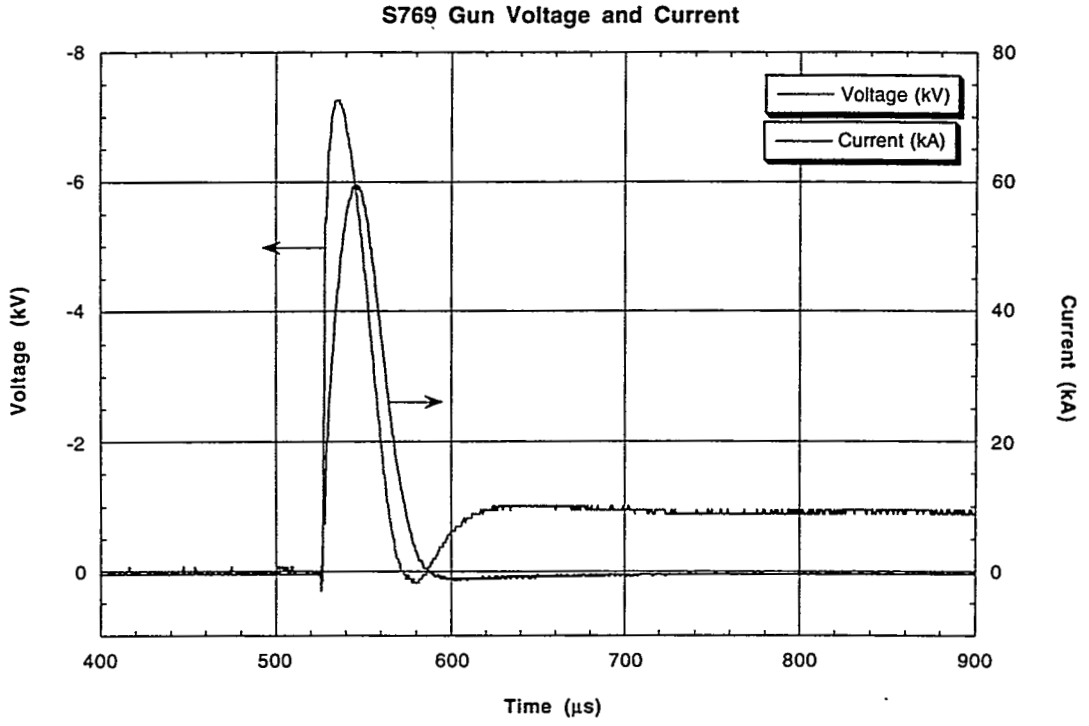

Figure 4.2.2. Power and energy traces for C/Cu segmented test (S769).

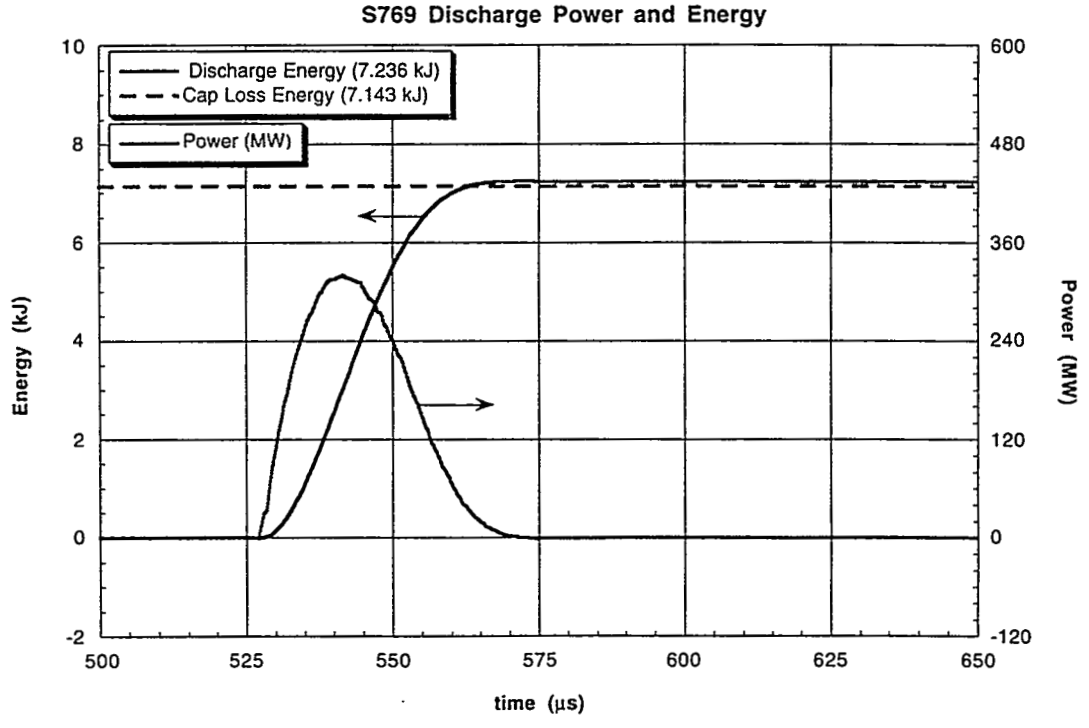

Table 4.2.1. Carbon / Copper segmented test mass measurements.

S769: Carbon / Copper Segmented Configuration

Source Section Components:			
component	pre-test wt. (g)	post-test wt. (g)	Δ wt. (mg)
cathode	10.34379	10.27999	63.80
long maycor	2.93284	-destroyed-	-
Lexan sleeve #1	0.33996	0.32740	12.56
copper sleeve #1	2.43863	2.29234	146.29
Lexan sleeve #2	0.33675	0.32401	12.73
copper sleeve #2	2.44141	2.27466	166.75
Lexan sleeve #3	0.33584	0.32363	12..21
copper sleeve #3	2.42624	2.22974	196.50
short maycor	1.02954	-destroyed-	-

Substrate Components:			
wall button	pre-test wt. (g)	post-test wt. (g)	Δ wt. (mg)
1	1.26395	1.26472	0.77
2	1.23819	1.23861	0.43
3	1.29614	1.29688	0.74
4	1.19472	1.19534	0.62
5	1.19061	1.19094	0.33
7	1.20527	1.20560	0.33
9	1.27968	1.27444	-5.25
17	1.24502	1.24613	1.11

Notes: (1) All weight measurements are taken 3+ times and averaged.
(2) Δm uncertainty is ± 0.05 mg.

Figure 4.2.3. Representative SEM micrographs from button 2 of S769.

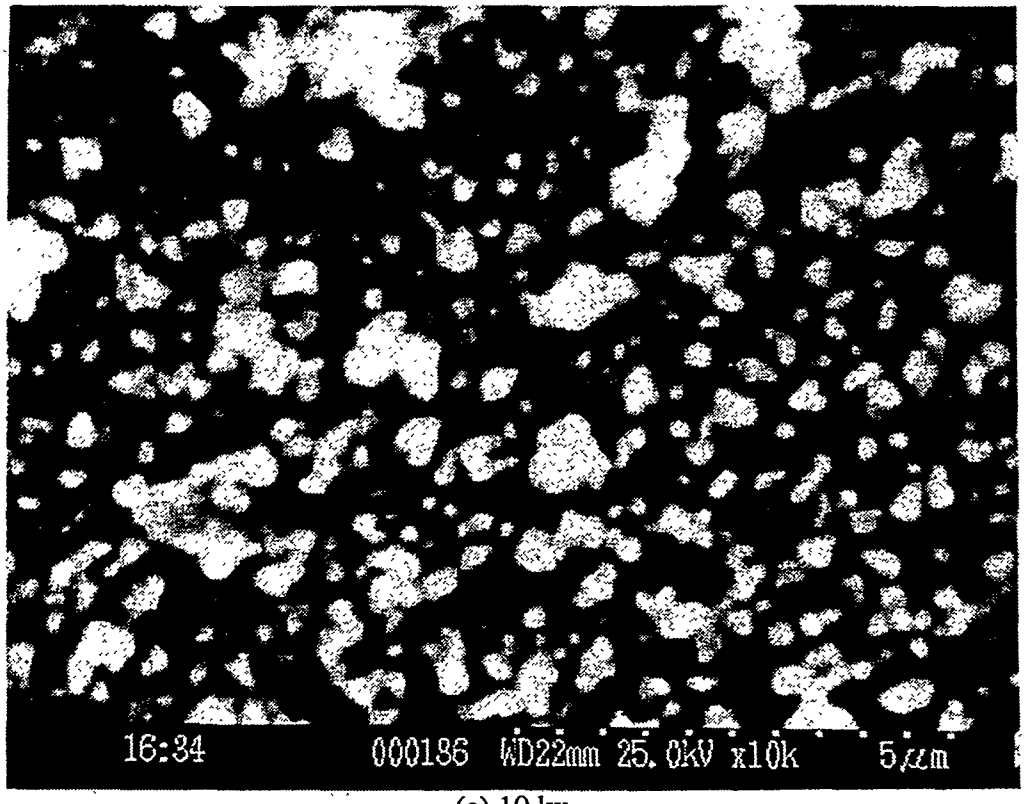

(a) 10 kx

Figure 4.2.3.cont.

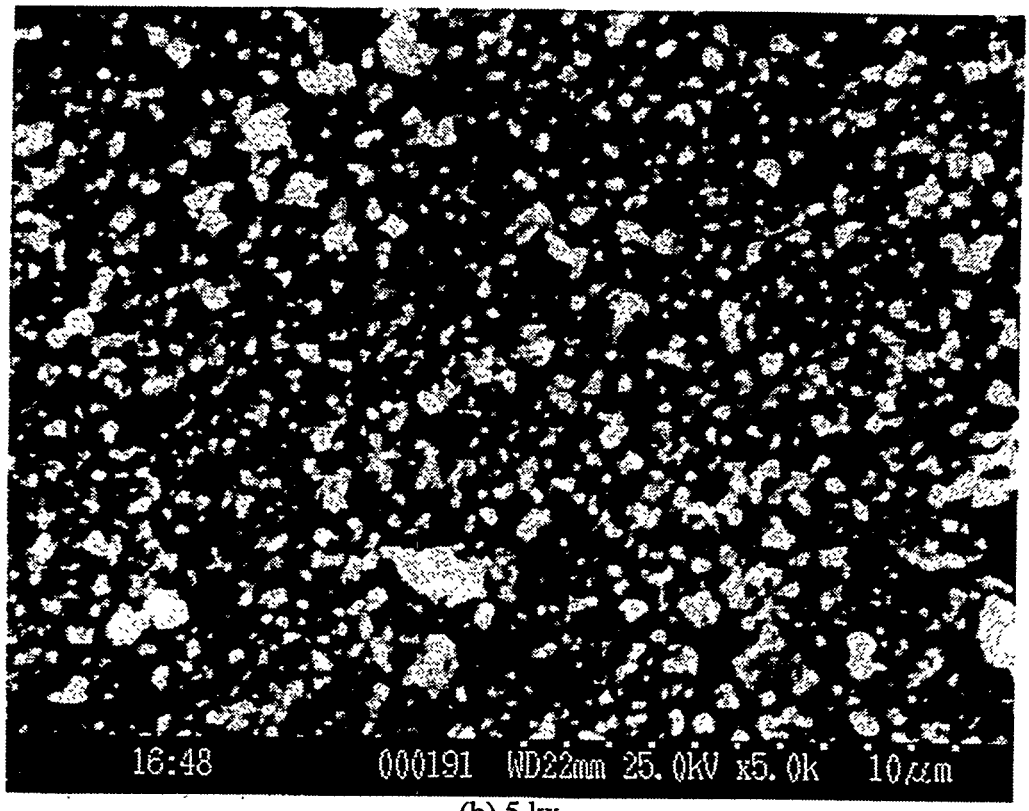

(b) 5 kx

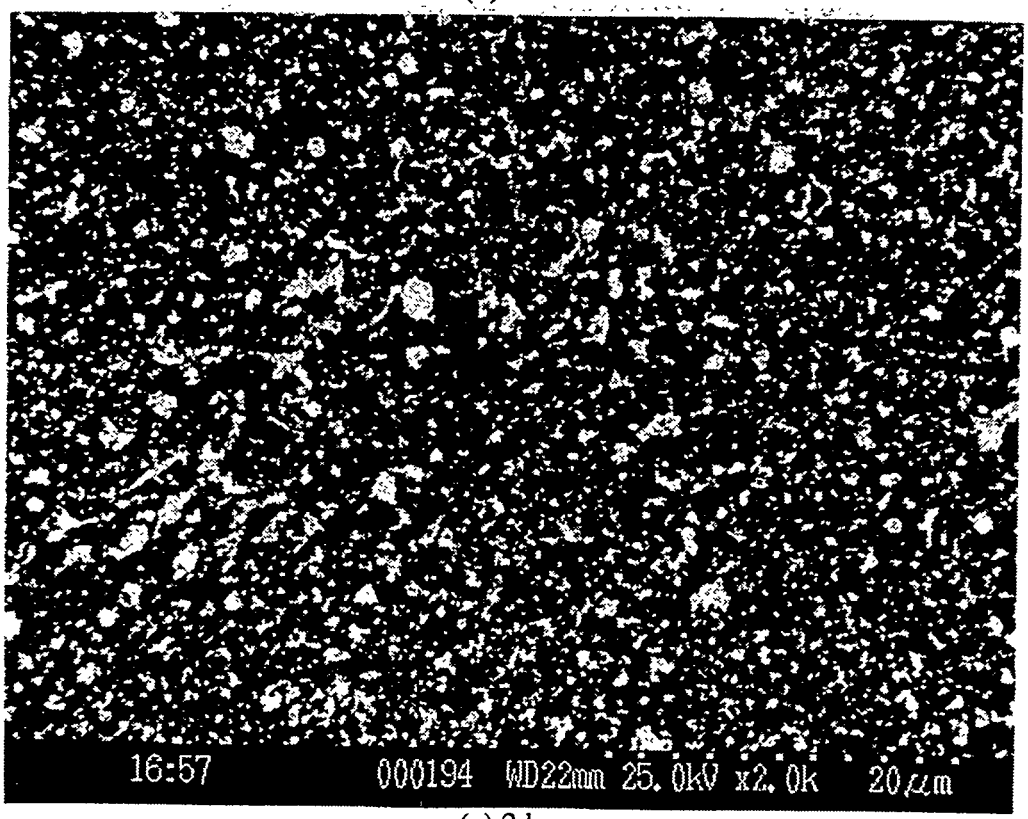

(c) 2 kx

Figure 4.2.4. EDXA mapping results of a button 2 region containing a Cu particle.

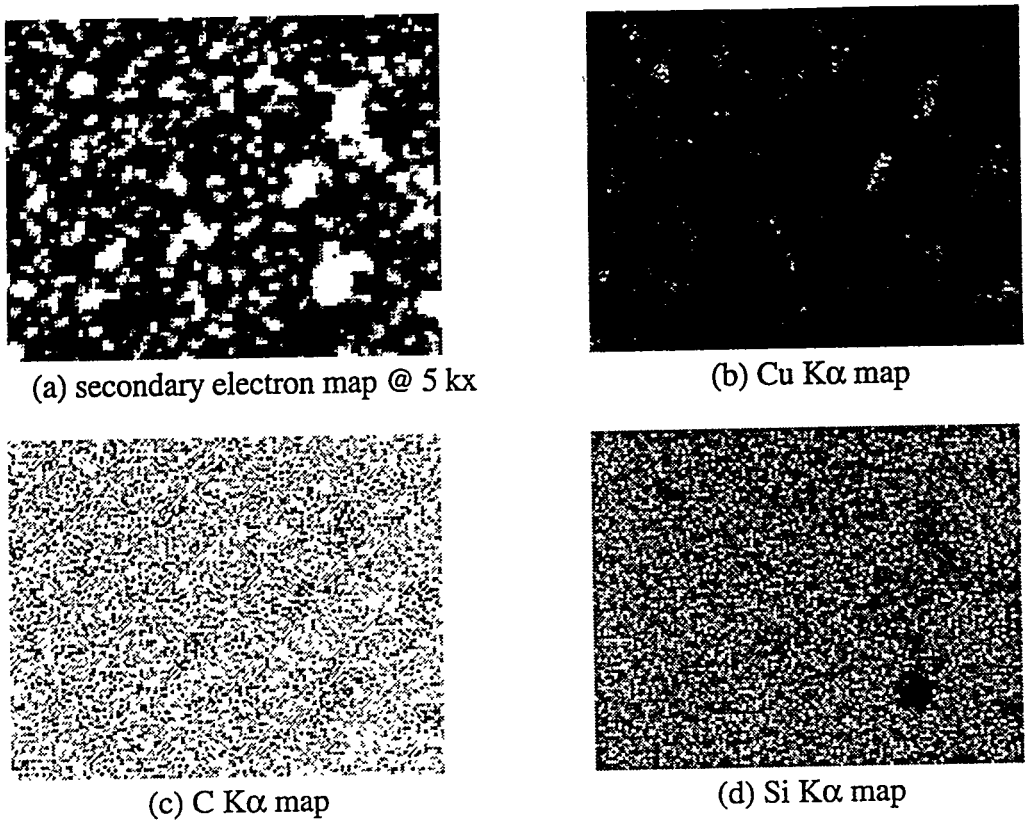

(a) secondary electron map @ 5 kx

(b) Cu Kα map

(c) C Kα map

(d) Si Kα map

Figure 4.2.5. Optical spectra of the expanding vapor from the S769 source section.

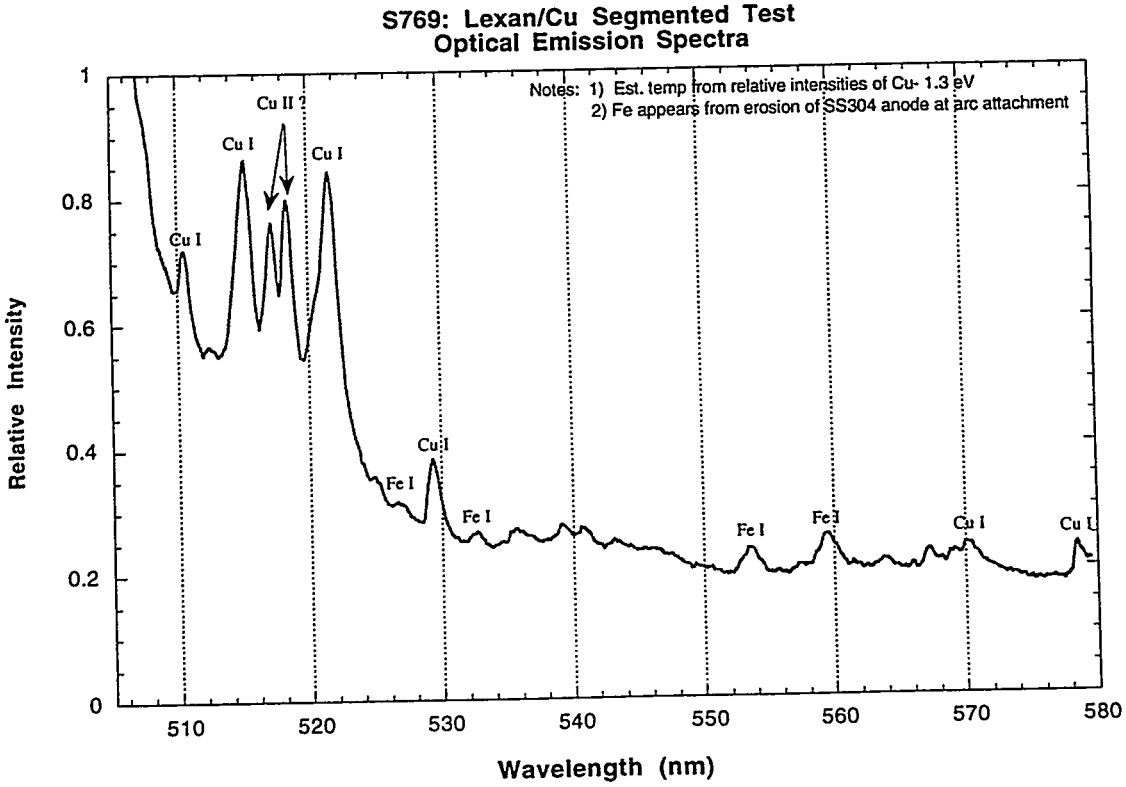

Figure 4.2.6. Carbon / Copper segmented test (S769) button 1 particle size distribution.

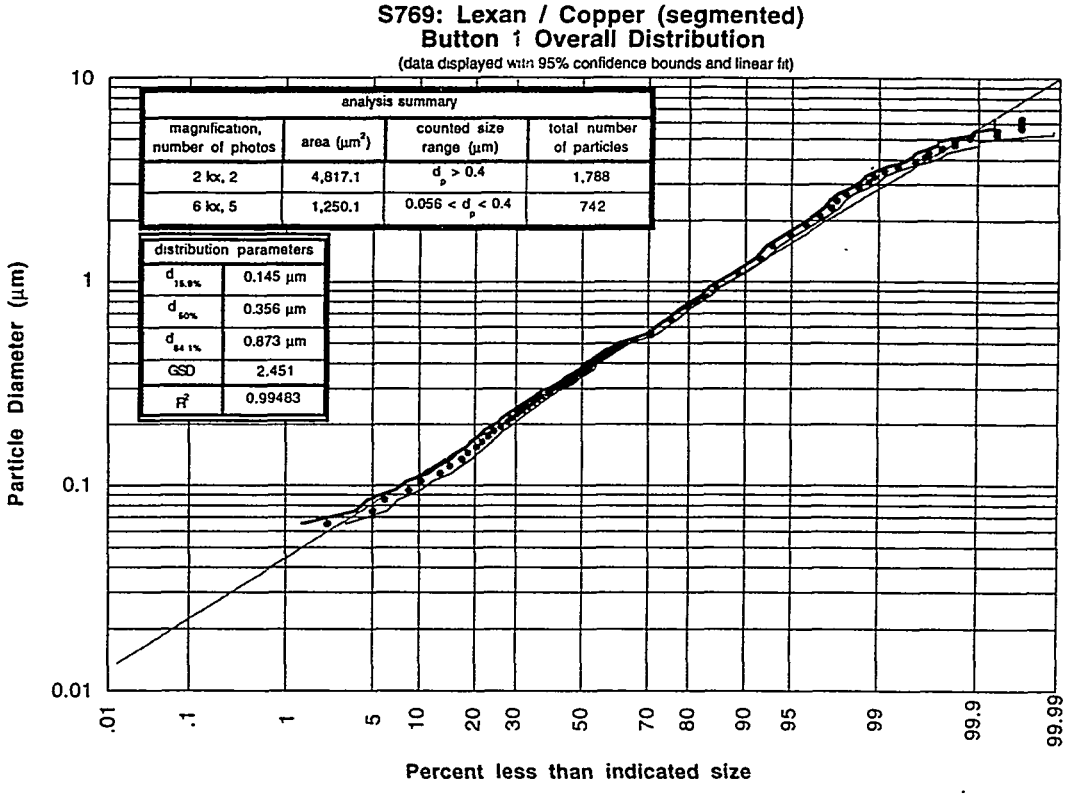

Data Summary Table:

photo	mag	scale (pixel/μm)	size (μm²)	min. d_{eq} (μm)	# of particles	scale factor	KW Test z-value	Overall p-value
769_1_1	6 kx	35.4	19.04x13.95	0.056[a]	87	9	1.66	0.113
769_1_2	6 kx	35.4	19.07x14.07	0.056[a]	129	9	-0.84	
769_1_3	6 kx	35.4	19.10x13.90	0.056[a]	160	9	-0.38	
769_1_4	6 kx	35.4	19.21x13.98	0.056[a]	200	9	-1.72	
769_1_5	6 kx	35.4	19.18x13.87	0.056[a]	166	9	1.69	
769_1_6	2 kx	11.8	57.46x41.02	0.22[b]	762	-	-failed-	0.08
769_1_7	2 kx	11.8	57.29x41.86	0.22[b]	868	1	-0.28	
769_1_8	2 kx	11.8	57.20x42.29	0.22[b]	902	1	0.28	

a. minimum equivalent diameter particle counted having an area of at least 3.1 x 1/scale on a side.
b. minimum equivalent diameter particle counted having an area of at least 5.1 x 1/scale on a side.

Figure 4.2.7. Carbon / Copper segmented test (S769) button 2 particle size distribution.

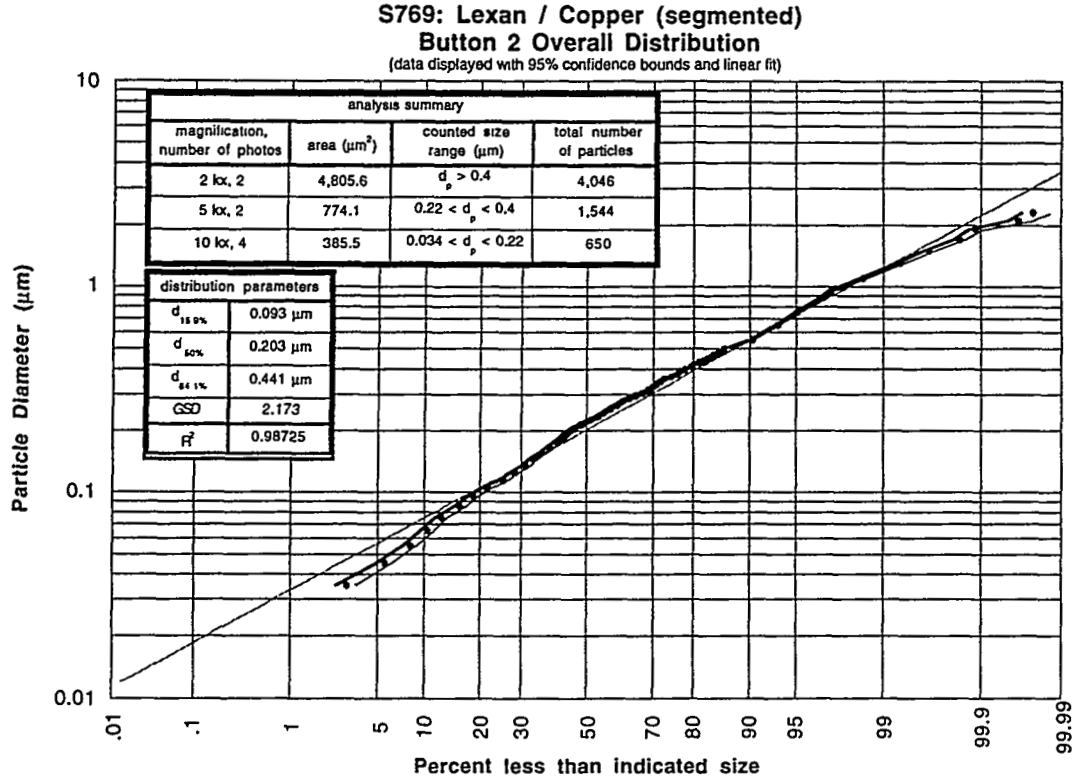

Data Summary Table:

photo	mag	scale (pixel/μm)	size (μm²)	min. d_{eq} (μm)	# of particles	scale factor	KW Test z-value	Overall p-value
769_2_1	10 kx	58.8	11.51x8.35	0.034[a]	180	25	-0.84	0.464
769_2_2	10 kx	58.8	11.56x8.35	0.034[a]	164	25	-0.71	
769_2_3	10 kx	58.8	11.55x8.38	0.034[a]	133	25	1.43	
769_2_4	10 kx	58.8	11.51x8.35	0.034[a]	173	25	0.24	
769_2_5	5 kx	29.4	23.03x16.84	0.068[a]	509	-	-failed	0.056
769_2_6	5 kx	29.4	23.10x16.84	0.068[a]	848	6.25	-1.91	
769_2_7	5 kx	29.4	23.06x16.70	0.068[a]	696	6.25	1.91	
769_2_8	2 kx	11.8	57.54x42.03	0.22[b]	2090	1	0.75	0.450
769_2_9	2 kx	11.8	57.29x41.95	0.22[b]	1721	-	-failed-	
767_9_10	2 kx	11.8	57.37x41.61	0.22[b]	1956	1	-0.75	

a. minimum equivalent diameter particle counted having an area of at least 3.1 x 1/scale on a side.
b. minimum equivalent diameter particle counted having an area of at least 5.1 x 1/scale on a side.

Figure 4.2.8. Carbon / Copper segmented test (S769) button 3 particle size distribution.

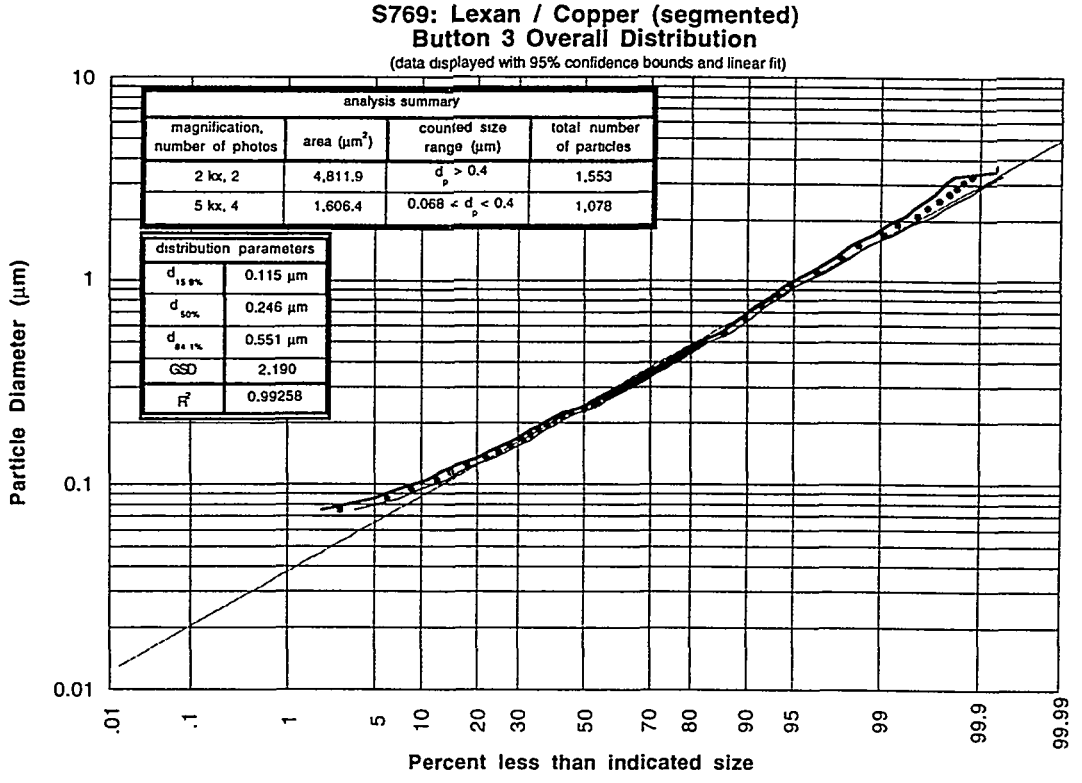

Data Summary Table:

photo	mag	scale (pixel/μm)	size (μm²)	min. d_{eq} (μm)	# of particles	scale factor	KW Test z-value	Overall p-value
769_3_1	5 kx	29.4	23.03x16.67	0.068[a]	247	6.25	0.66	0.193
769_3_2	5 kx	29.4	22.96x17.04	0.068[a]	293	6.25	-1.96	
769_3_3	5 kx	29.4	23.03x16.46	0.068[a]	259	6.25	-0.10	
769_3_4	5 kx	29.4	26.96x16.94	0.068[a]	279	6.25	1.46	
769_3_5	2 kx	11.8	57.29x41.86	0.22[b]	984	-	-failed-	0.480
769_3_6	2 kx	11.8	57.46x41.86	0.22[b]	833	1	0.71	
769_3_7	2 kx	11.8	57.37x42.12	0.22[b]	720	1	-0.71	

a. minimum equivalent diameter particle counted having an area of at least 3.1 x 1/scale on a side.
b. minimum equivalent diameter particle counted having an area of at least 5.1 x 1/scale on a side.

Figure 4.2.9. Carbon / Copper segmented test (S769) button 17 particle size distribution.

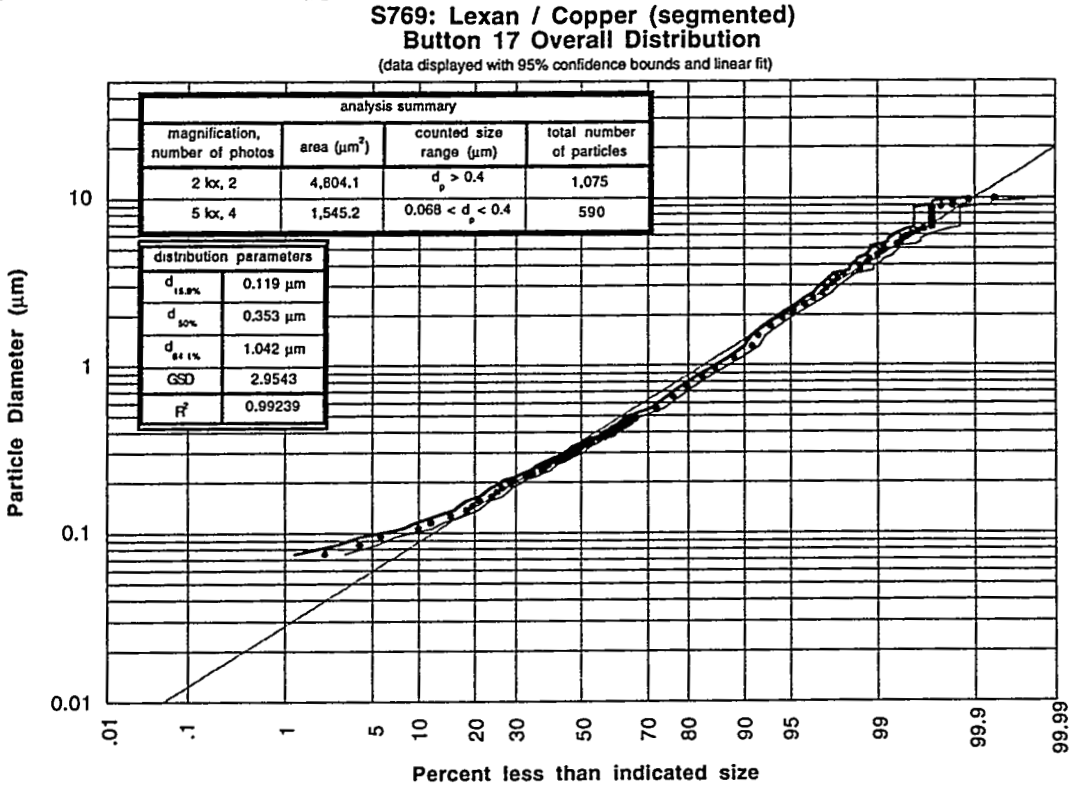

Data Summary Table:

photo	mag	scale (pixel/µm)	size (µm²)	min. d_{eq} (µm)	# of particles	scale factor	KW Test z-value	Overall p-value
769_17_1	5 kx	29.4	22.99x16.84	0.068[a]	101	6.25	0.49	0.290
769_17_2	5 kx	29.4	22.99x16.80	0.068[a]	127	6.25	0.93	
769_17_3	5 kx	29.4	22.99x16.80	0.068[a]	160	6.25	0.78	
769_17_4	5 kx	29.4	23.13x16.67	0.068[a]	202	6.25	-1.92	
769_17_5	2 kx	11.8	57.46x41.95	0.22[b]	701	-	-failed-	0.844
769_17_6	2 kx	11.8	57.12x42.03	0.22[b]	515	1	-0.20	
769_17_7	2 kx	11.8	57.29x41.95	0.22[b]	560	1	0.20	

a. minimum equivalent diameter particle counted having an area of at least 3.1 x 1/scale on a side.
b. minimum equivalent diameter particle counted having an area of at least 5.1 x 1/scale on a side.

5.0 Carbon / SS316 Tests

The intended use of stainless steel type 316 (SS316) for many components internal to the ITER vacuum vessel makes this material important in an investigation of disruption-induced mobilization and safety analysis. Similar to the tests performed with Lexan carbon and copper, testing in SIRENS of Lexan carbon and SS316 has been done in both the short and segmented source section configurations. Stainless steel 316 is quite different from copper, however, because the alloy is composed of several different elements (16-18% Cr, 10-14% Ni, 2-3% Mo, 2% Mn, 1% Si, 0.08% C, with Fe as the remaining quantity) rather than a single element with copper. An interesting question concerns the effect will various materials in SS316 have on particle formation and growth. This issue will be qualitatively addressed in the following sections based on EDXA mappings of particulate generated from the carbon / SS316 tests.

Displayed in Table 5.0.1 is a summary of mass loss data and particle size distributions from the Lexan carbon / SS316 tests.

Table 5.0.1. Carbon / SS316 tests comparison summary.

	Short C/SS316 Test (S766)				Segmented C/SS316 Test (S770)			
Energy (J)	7.127				7.055			
Fluence (MJ/m^2)	6.50				6.43			
Duration (μs)	80				60			
Lexan sleeve #1 Δm (mg)	19.74				8.17			
SS316 sleeve #1 Δm (mg)	182.82				159.42			
Lexan sleeve #2 Δm (mg)	25.43				9.89			
SS316 sleeve #2 Δm (mg)	-				178.99			
Lexan sleeve #3 Δm (mg)	-				11.51			
SS316 sleeve #3 Δm (mg)	-				177.08			
Scaled SS316 Δm (mg/kJ/cm)	25.65				24.36			
Scaled Lexan Δm (mg/kJ/cm)	0.975				1.40			
Cathode Δm (mg)	64.35				51.30			
	Δm (mg)	$d_{50\%}$ (μm)	GSD	R^2	Δm (mg)	$d_{50\%}$ (μm)	GSD	R^2
Button 1	0.56	0.116	2.003	0.996	0.47	0.135	2.742	0.993
Button 2	0.18	0.116	2.133	0.998	0.52	*	*	*
Button 3	0.48	0.099	2.141	0.994	0.63	0.094	2.445	0.972
Button 4	0.16	*	*	*	0.73	*	*	*
Button 5	0.85	0.113	1.998	0.997	0.36	*	*	*
Button 7	0.08	*	*	*	0.48	*	*	*
Button 9	0.71	0.123	2.533	0.989	0.78	0.278	2.495	0.996
Button 17	0.27	*	*	*	0.85	*	*	*

Note: Asterisk (*) denotes analysis not performed.

5.1 Short Configuration: S766

The short configuration Lexan carbon / SS316 test was performed with a discharge energy of 7.127 kJ. Resulting voltage and current traces are shown in Figure 5.1.1, followed by power and energy in Figure 5.1.2. These traces are typical for this experiment configuration.

A summary of test component mass measurements is given in Table 5.1.1. Total mass loss from the two Lexan sleeves in this test was lower than the corresponding loss associated with the carbon / copper short test S765, although discharge energy for S766 was larger. Mass loss of the SS316 sleeve, at 25.65 mg/kJ/cm, is lower than that observed in the carbon / copper short configuration test (48.26 mg/kJ/cm), possibly because the sublimation enthalpy for Cu is lower than that for Fe (5.7 kJ/kg versus 7.1 kJ/kg). For comparison, reference [3] gives a mass loss for a pure SS316 sample in the source section as 14 mg/kJ/cm. Again the presence of carbon / metal species in the plasma seems to increase effective mass loss from the metal surface. Mass increase of collection buttons was also observed, although unevenly for buttons at equal axial positions but different azimuthal positions (e.g. buttons 1 at 0.56 mg versus button 2 at 0.18 mg). Both end plate buttons displayed a significant increase. Relatively large gains in mass on these buttons indicate deposition of heavy particles. Representative micrographs of button 3 are included in Figure 5.1.3 and show the presence of a few larger particles somewhat spherical in shape. EDXA mapping (Figure 5.1.4) indicates these particles to consist of a mixture of the SS316 components rather than particles of the individual species.

Particle size distributions were obtained for buttons 1, 2, 3, 5, and 9 of S766 and are shown in Figures 5.1.5-9. Count median diameters of the fitted log-normal distributions are close to values obtained for most all tests in which Lexan was a component in the source section. Although a few larger particles may be observed in the images, the underlying populations are dominated by smaller particles of a size range corresponding those measured for Lexan carbon-only tests.

Figure 5.1.1. Voltage and current traces for C/SS316 short test (S766).

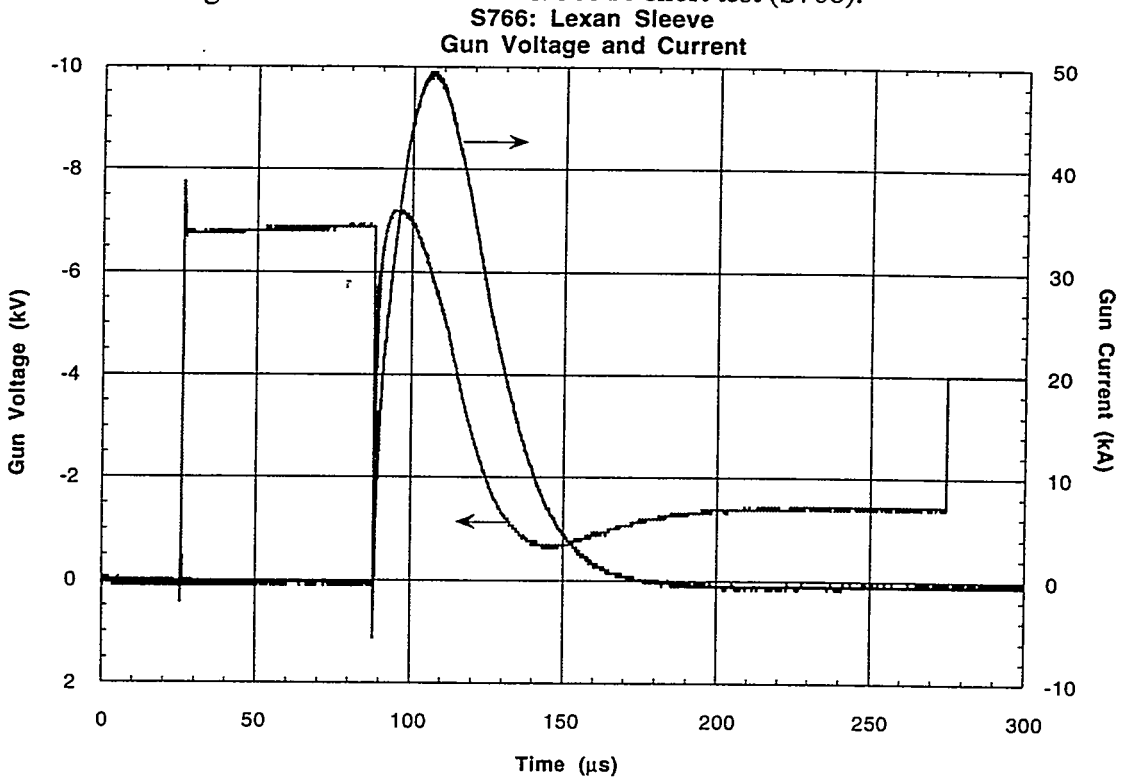

Figure 5.1.2. Power and energy traces for C/SS316 short test (S766).

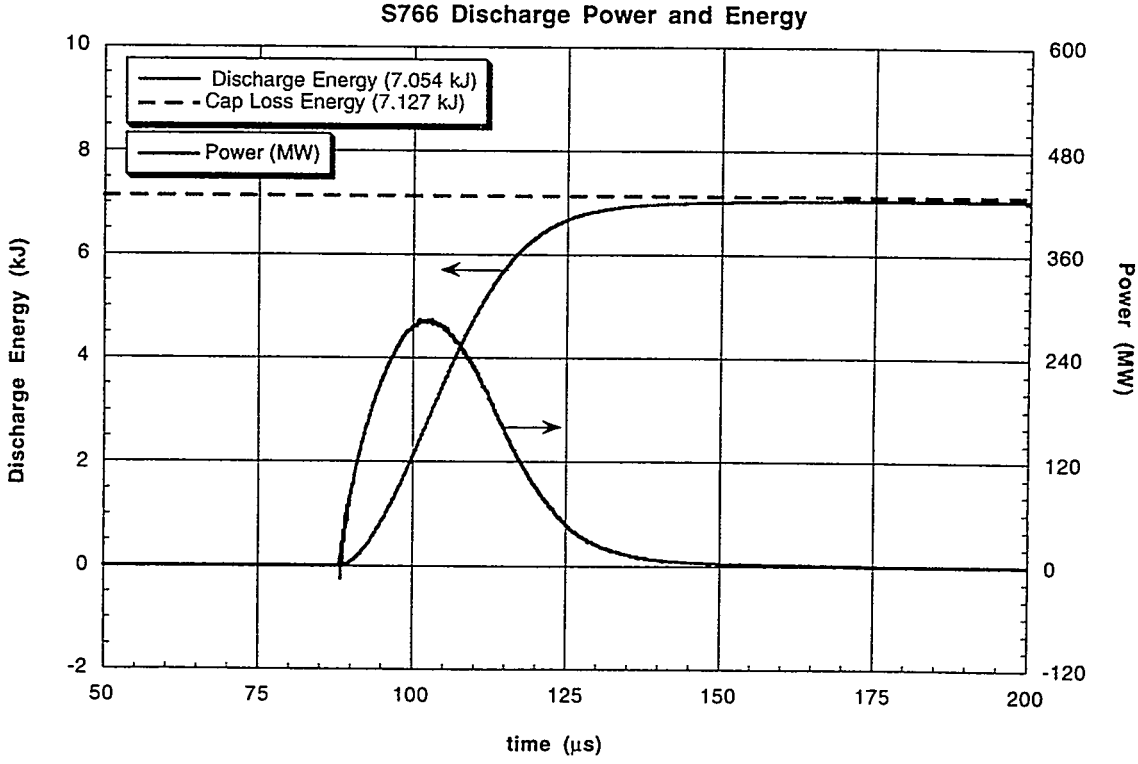

Table 5.1.1. *C/SS316* short test mass measurements.

S766: C / SS316 Short Configuration

Source Section Components: component	pre-test wt. (g)	post-test wt. (g)	Δ wt. (mg)
cathode	9.49281	9.42846	64.35
long maycor	2.92476	-destroyed-	-
Lexan sleeve #1	1.12123	1.10149	19.74
SS316 sleeve	2.15291	1.97009	182.82
Lexan sleeve #2	0.97372	0.94829	25.43

Substrate Components: wall button	pre-test wt. (g)	post-test wt. (g)	Δ wt. (mg)
1	1.25112	1.25168	0.56
2	1.16817	1.16835	0.18
3	1.22033	1.22081	0.48
4	1.30634	1.30651	0.16
5	1.23040	1.23125	0.85
7	1.22881	1.22888	0.08
9	1.20821	1.20892	0.71
17	1.23684	1.23711	0.27

Notes: (1) All weight measurements are taken 3+ times and averaged.
(2) Δm uncertainty is ± 0.05 mg.

Figure 5.1.3. Representative SEM micrographs from button 3 of S765.

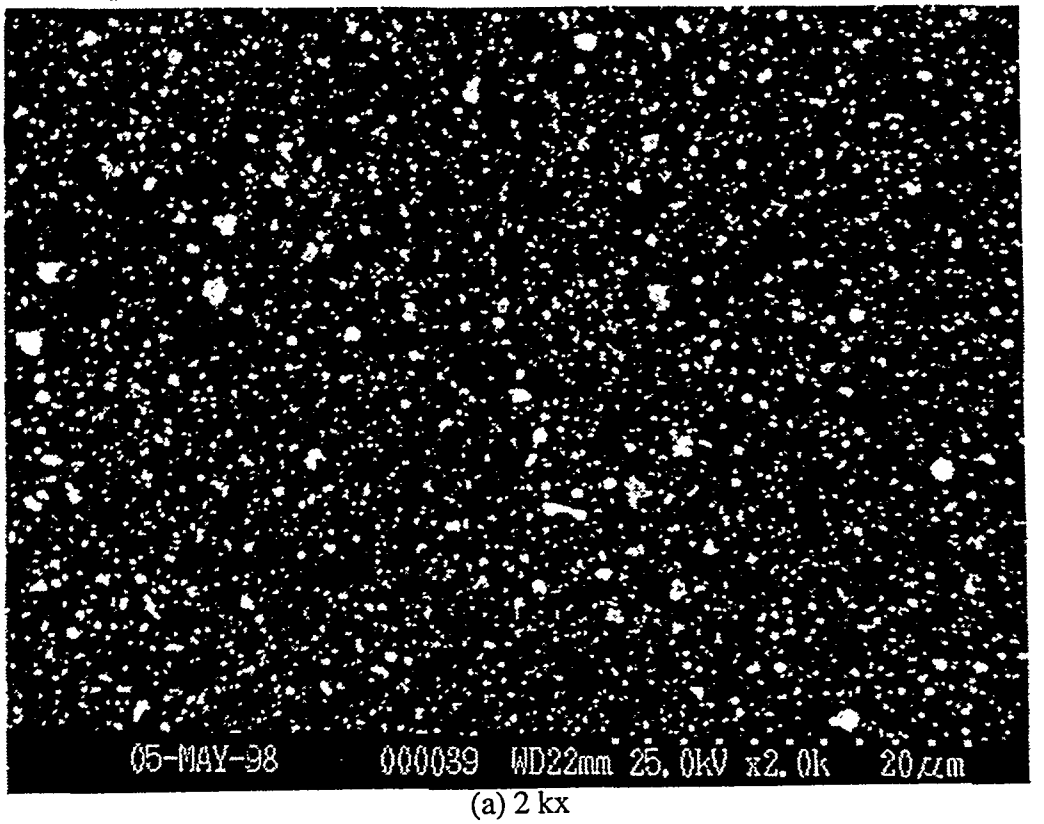

(a) 2 kx

Figure 5.1.3.cont.

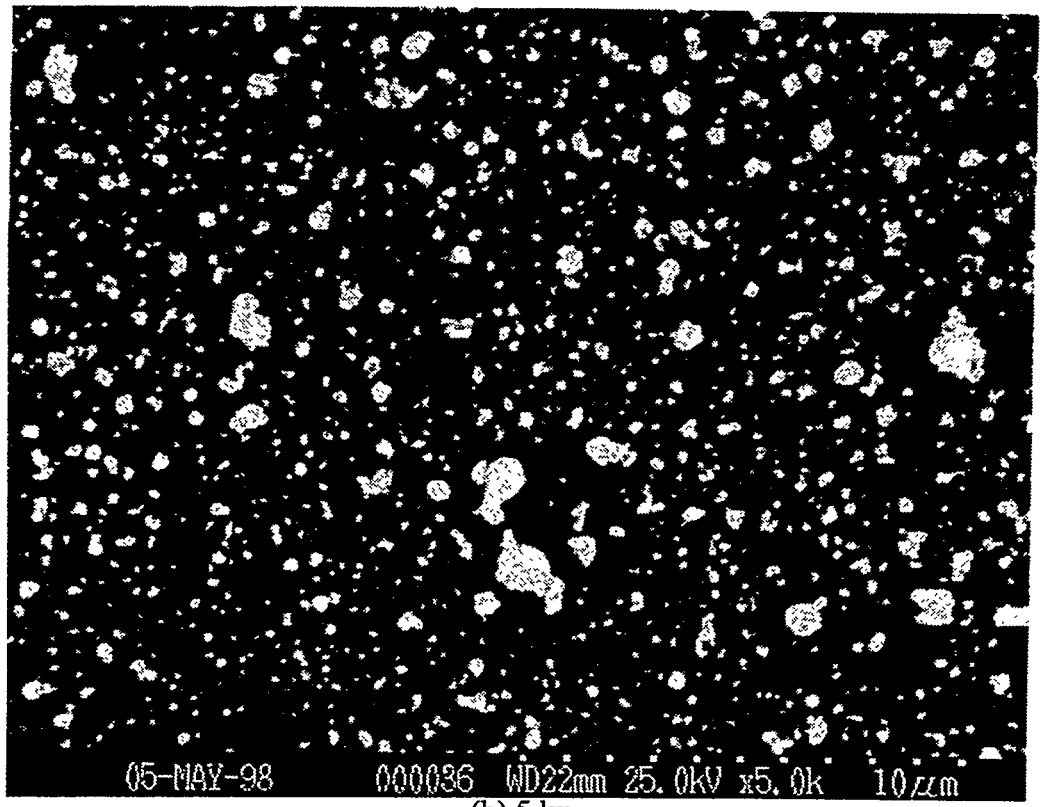

(b) 5 kx

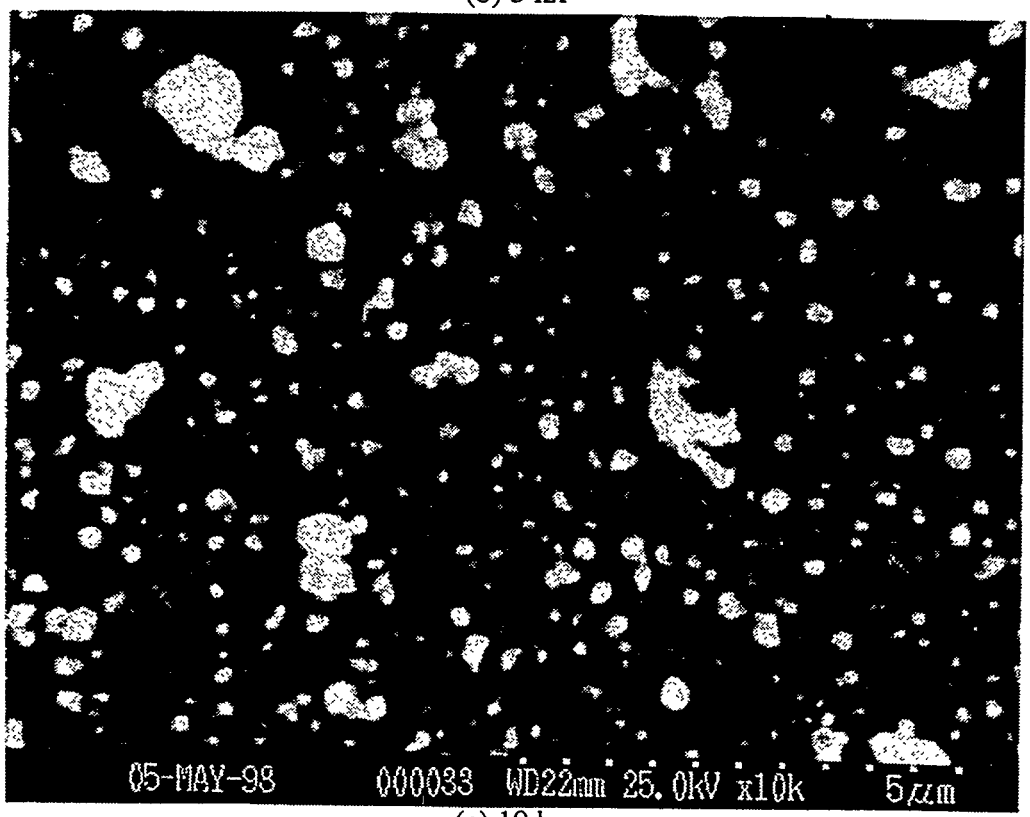

(c) 10 kx

Figure 5.1.4. EDXA mapping results of a region on button 2 containing SS316 particles.

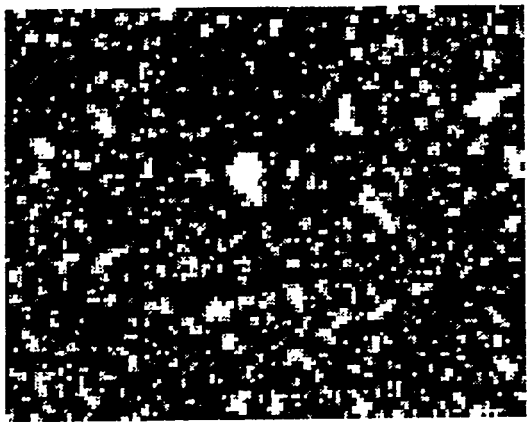

(a) secondary electron map @ 10 kx

(b) Fe Kα map

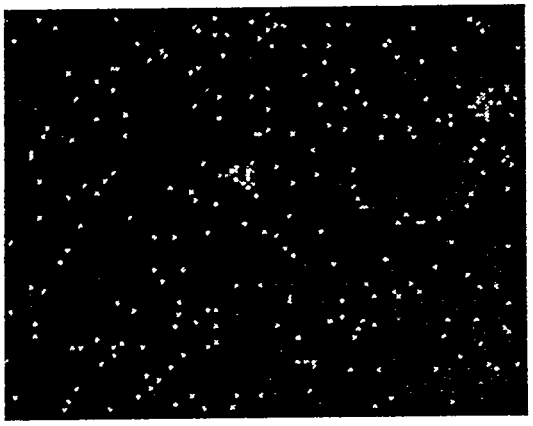

(c) Cr Kα map

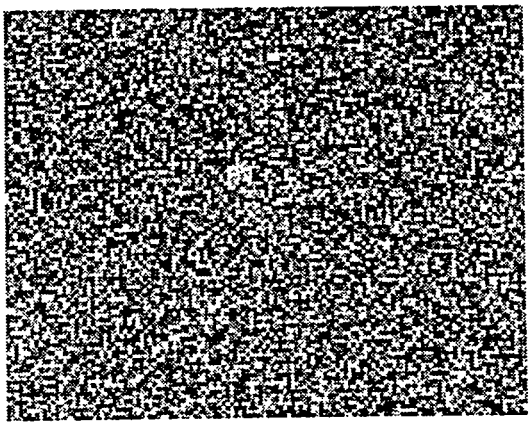

(d) Si Kα map

Figure 5.1.5. Carbon / SS316 short test (S766) button 1 particle size distribution.

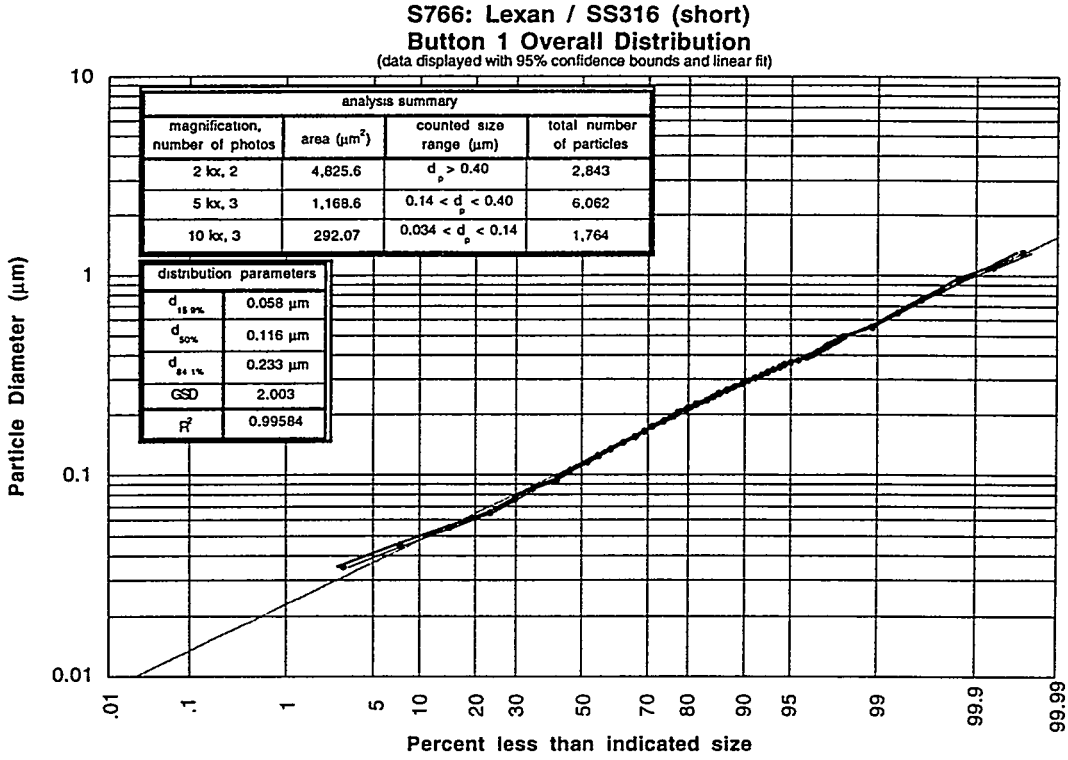

Data Summary Table:

photo	mag	scale (pixel/μm)	size (μm²)	min. d_{eq} (μm)	# of particles	scale factor	KW Test z-value	Overall p-value
766_1_1	10 kx	58.8	11.51x8.45	0.034[a]	639	25	-0.24	0.266
766_1_2	10 kx	58.8	11.5x8.42	0.034[a]	687	-	-failed-	
766_1_3	10 kx	58.8	11.45x8.5	0.034[a]	465	25	-1.33	
766_1_10	10 kx	58.8	11.46x8.38	0.034[a]	408	-	-failed-	
766_1_11	10 kx	58.8	11.51x8.47	0.034[a]	660	25	1.45	
766_1_4	5 kx	29.4	23.03x16.9	0.068[a]	2067	6.25	1.16	0.073
766_1_5	5 kx	29.4	23.06x16.9	0.068[a]	2010	6.25	-2.29	
766_1_6	5 kx	29.4	22.96x16.97	0.068[a]	1985	6.25	1.12	
766_1_7	2 kx	11.8	57.46x41.53	0.22[b]	2148	-	-failed-	0.780
766_1_8	2 kx	11.8	57.12x42.03	0.22[b]	1336	1	0.28	
765_3_9	2 kx	11.8	57.46x42.20	0.22[b]	1507	1	-0.28	

a. minimum equivalent diameter particle counted having an area of at least 3.1 x 1/scale on a side.
b. minimum equivalent diameter particle counted having an area of at least 5.1 x 1/scale on a side.

Figure 5.1.6. Carbon / SS316 short test (S766) button 2 particle size distribution.

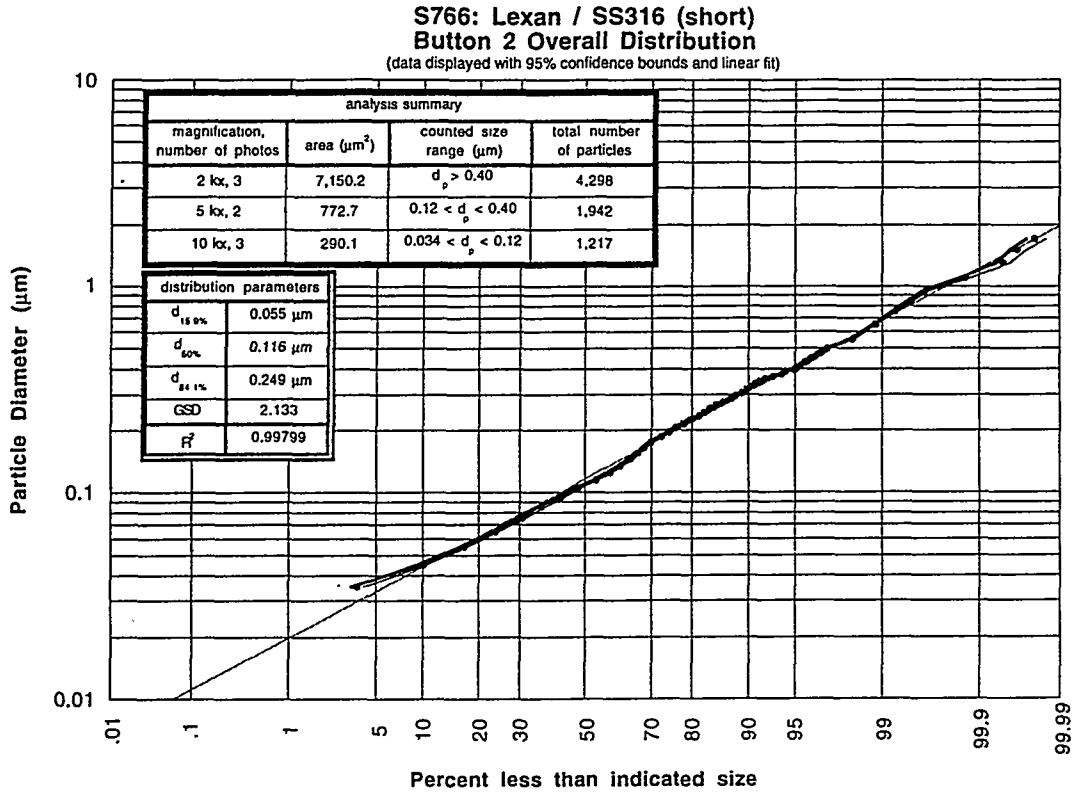

Data Summary Table:

photo	mag	scale (pixel/μm)	size (μm²)	min. d_{eq} (μm)	# of particles	scale factor	KW Test z-value	Overall p-value
766_2_1	10 kx	58.8	11.46x8.42	0.034[a]	336	25	0.48	0.270
766_2_2	10 kx	58.8	11.55x8.30	0.034[a]	445	-	-failed-	
766_2_3	10 kx	58.8	11.53x8.47	0.034[a]	313	-	-failed-	
766_2_4	10 kx	58.8	11.51x8.44	0.034[a]	468	25	-1.58	
766_2_5	10 kx	58.8	11.55x8.35	0.034[a]	413	25	1.18	
766_2_6	5 kx	29.4	22.96x16.63	0.068[a]	1132	-	-failed-	0.082
766_2_7	5 kx	29.4	22.93x16.63	0.068[a]	907	6.25	1.74	
766_2_8	5 kx	29.4	22.93x16.97	0.068[a]	1035	6.25	-1.74	
766_2_9	2 kx	11.8	57.54x41.36	0.22[b]	1538	1	-1.52	0.198
766_2_10	2 kx	11.8	57.12x41.86	0.22[b]	1616	1	1.67	
765_2_11	2 kx	11.8	57.29x41.53	0.22[b]	1147	1	-0.18	

a. minimum equivalent diameter particle counted having an area of at least 3.1 x 1/scale on a side.
b. minimum equivalent diameter particle counted having an area of at least 5.1 x 1/scale on a side.

Figure 5.1.7. Carbon / SS316 short test (S766) button 3 particle size distribution.

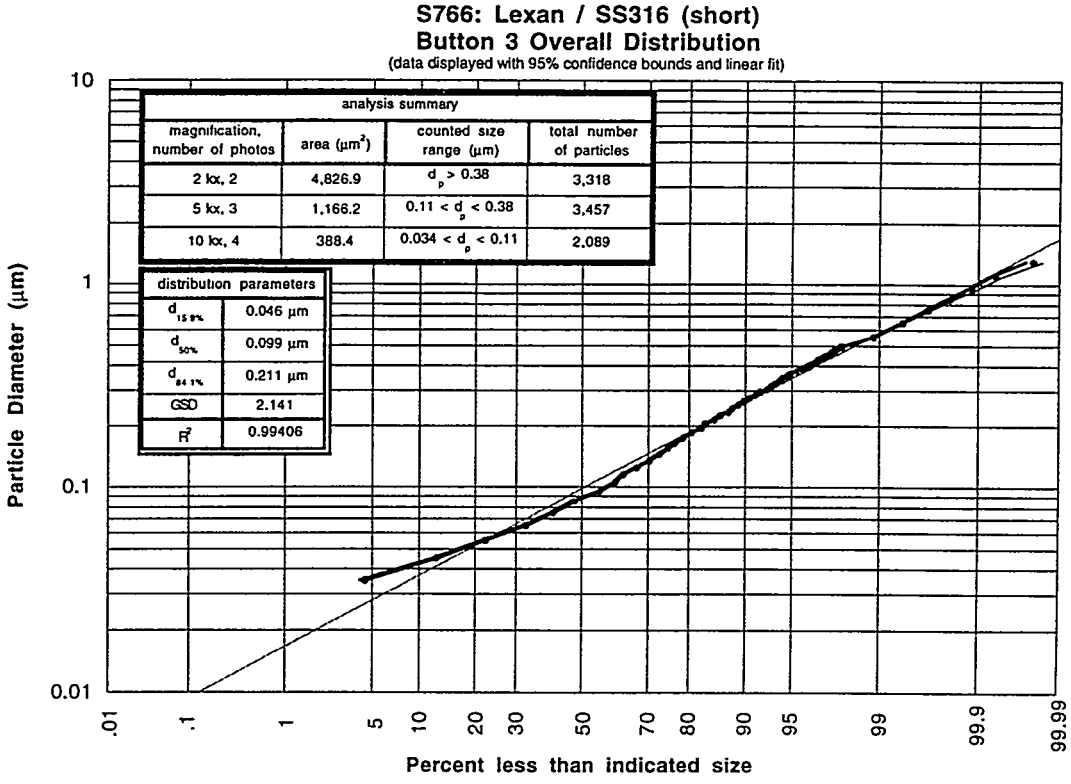

Data Summary Table:

photo	mag	scale (pixel/μm)	size (μm²)	min. d_{eq} (μm)	# of particles	scale factor	KW Test z-value	Overall p-value
766_3_1	10 kx	58.8	11.48x8.49	0.034[a]	623	25	-2.00	0.239
766_3_2	10 kx	58.8	11.5x8.38	0.034[a]	521	25	0.36	
766_3_3	10 kx	58.8	11.5x8.42	0.034[a]	455	25	1.07	
766_3_4	10 kx	58.8	11.5x8.5	0.034[a]	490	25	0.74	
766_3_5	10 kx	58.8	11.51x8.44	0.034[a]	604	-	-failed-	
766_3_6	5 kx	29.4	22.93x16.97	0.068[a]	1184	6.25	-1.06	0.450
766_3_7	5 kx	29.4	23.03x16.97	0.068[a]	1203	6.25	1.14	
766_3_8	5 kx	29.4	22.99x16.8	0.068[a]	1070	6.25	-0.09	
766_3_9	2 kx	11.8	57.2x42.29	0.22[b]	1485	1	-2.72	0.07
766_3_10	2 kx	11.8	57.29x42.12	0.22[b]	1833	1	2.72	
765_3_11	2 kx	11.8	57.12x41.86	0.22[b]	1869	-	-failed-	

a. minimum equivalent diameter particle counted having an area of at least 3.1 x 1/scale on a side.
b. minimum equivalent diameter particle counted having an area of at least 5.1 x 1/scale on a side.

Figure 5.1.8. Carbon / SS316 short test (S766) button 5 particle size distribution.

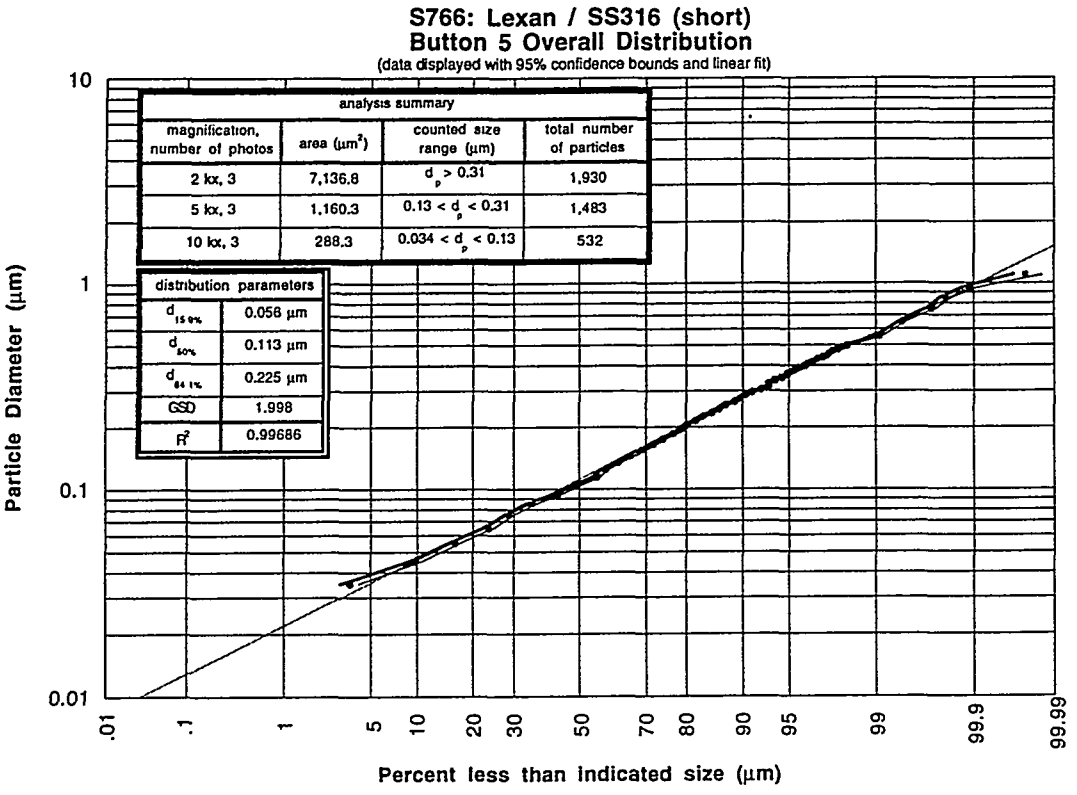

Data Summary Table:

photo	mag	scale (pixel/μm)	size (μm²)	min. d_{eq} (μm)	# of particles	scale factor	KW Test z-value	Overall p-value
766_5_1	10 kx	58.8	11.50x8.30	0.034[a]	145	25	-0.16	0.412
766_5_2	10 kx	58.8	11.45x8.44	0.034[a]	195	25	-1.10	
766_5_3	10 kx	58.8	11.48x8.38	0.034[a]	192	25	1.25	
766_5_4	5 kx	29.4	23.03x16.8	0.068[a]	488	6.25	-0.64	0.459
766_5_5	5 kx	29.4	23.03x16.8	0.068[a]	467	6.25	1.25	
766_5_6	5 kx	29.4	23.10x16.73	0.068[a]	528	6.25	-0.58	
766_5_7	2 kx	11.8	57.37x41.36	0.22[b]	644	1	0.43	0.217
766_5_8	2 kx	11.8	57.29x42.20	0.22[b]	588	1	-1.70	
765_5_9	2 kx	11.8	57.20x41.02	0.22[b]	698	1	1.20	

a. minimum equivalent diameter particle counted having an area of at least 3.1 x 1/scale on a side.
b. minimum equivalent diameter particle counted having an area of at least 5.1 x 1/scale on a side.

Figure 5.1.9. Carbon / SS316 short test (S766) button 9 particle size distribution.

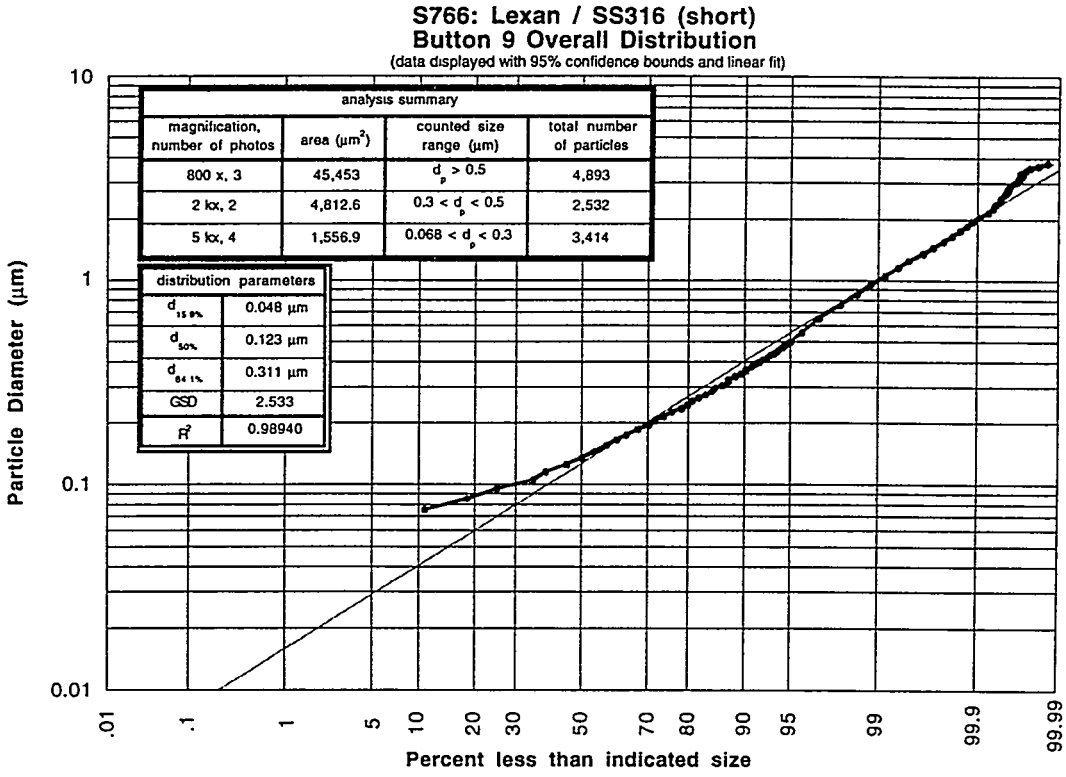

Data Summary Table:

photo	mag	scale (pixel/µm)	size (µm²)	min. d_{eq} (µm)	# of particles	scale factor	KW Test z-value	Overall p-value
766_9_1	5 kx	29.4	22.96x16.94	0.068[a]	861	39.1	-2.57	0.071
766_9_2	5 kx	29.4	22.99x16.84	0.068[a]	757	39.1	0.17	
766_9_3	5 kx	29.4	23.03x17.01	0.068[a]	577	39.1	1.00	
766_9_4	5 kx	29.4	23.06x16.87	0.068[a]	1219	39.1	1.40	
766_9_5	2 kx	11.8	57.37x42.95	0.22[b]	1224	6.25	0.49	0.627
766_9_6	2 kx	11.8	57.12x42.46	0.22[b]	1050	-	-failed-	
766_9_7	2 kx	11.8	57.12x42.12	0.22[b]	1308	6.25	-0.49	
766_9_8	800 x	4.72	143.6x104.2	0.54[b]	1721	1	2.13	0.102
766_9_9	800 x	4.72	143.6x105.3	0.54[b]	1523	1	-1.20	
765_9_10	800 x	4.72	143.9x106.8	0.54[b]	1649	1	-0.97	

a. minimum equivalent diameter particle counted having an area of at least 3.1 x 1/scale on a side.
b. minimum equivalent diameter particle counted having an area of at least 5.1 x 1/scale on a side.

5.2 *Segmented Configuration: S770*

A second test was performed with Lexan carbon and SS316 combined in the segmented configuration of the source section. The discharge energy for this test (S770) was 7.055 kJ. Voltage and current traces are displayed in Figure 5.2.1, and power and energy traces are shown in Figure 5.2.2. These traces are typical for this type of test.

Measured mass loss data for S770 are given in Table 5.2.1. The Lexan segments lost slightly more mass towards the exit of the source section, and the first SS316 component lost less mass than the remaining two by 19 mg. Significant difference in measured mass loss from the Lexan and SS316 segments results from the much lower sublimation energy of SS316, based on a value of 7.14 MJ/kg for the Fe component of SS316 compared to 54 MJ/kg for Lexan. In normalized units, total mass loss from the SS316 sleeve (24.36 mg/kJ/cm) compares favorably to the results from the short configuration test (S766 with 25.65 mg/kJ/cm) and is higher than that observed for a SS316 sleeve only in the source (14 mg/kJ/cm from [3]). Lexan mass loss is also greater than that observed for a Lexan-only sleeve. Measured mass increase of the buttons, however, does not follow the trend found in the short test configuration, as the values of deposited mass are generally greater and appear to peak around the mid-length distance. A somewhat similar deposition distribution was observed in the segmented carbon / copper test S769.

Figure 5.2.3 gives representative micrographs from button 3 of S770. Larger particles are found more frequently in this test than in the short segment test S766. This is expected because a larger quantity of SS316 exiting from the source section has a greater influence on the particle population. Many more spherical particles were found in this test compared to previous carbon / metal tests. As with the short test configuration of Lexan / SS316, particles seem to be a mixture of component material from the source section rather than particles of individual species, as shown in the EDXA maps provided in Figure 5.2.4. Optical emission spectroscopy, however, indicates the presence of individual components in the vapor plume exiting the source section during the shot (Figure 5.2.5). Mechanisms of particle formation and growth in this situation are very complicated.

Resulting overall distributions for buttons 1, 3, and 9 from S770 are given in Figures 5.2.6-8. The count median diameters from log-normal distribution fits are very close to those observed for the Lexan carbon-only tests. GSD values are somewhat greater, indicating a broader span of particle sizes in the underlying distributions.

Figure 5.2.1. Voltage and current traces for C/SS316 segmented test (S770).

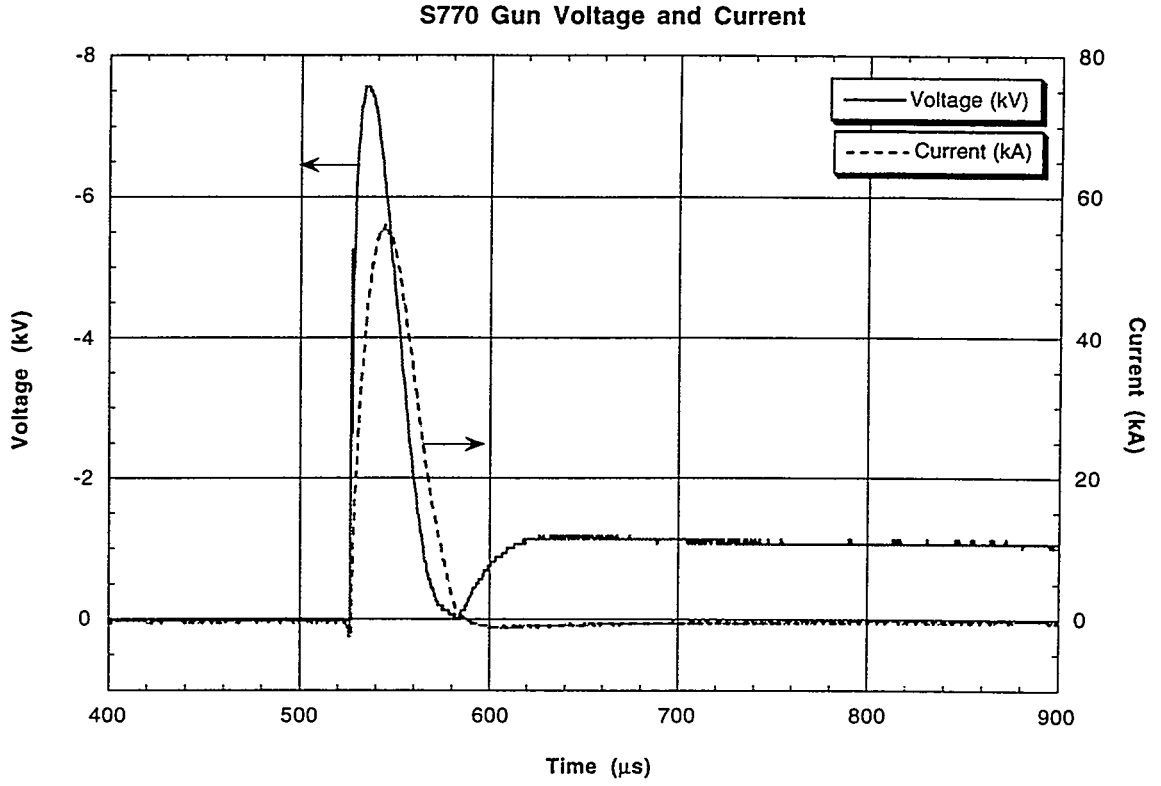

Figure 5.2.2. Power and energy traces for C/SS316 segmented test (S770).

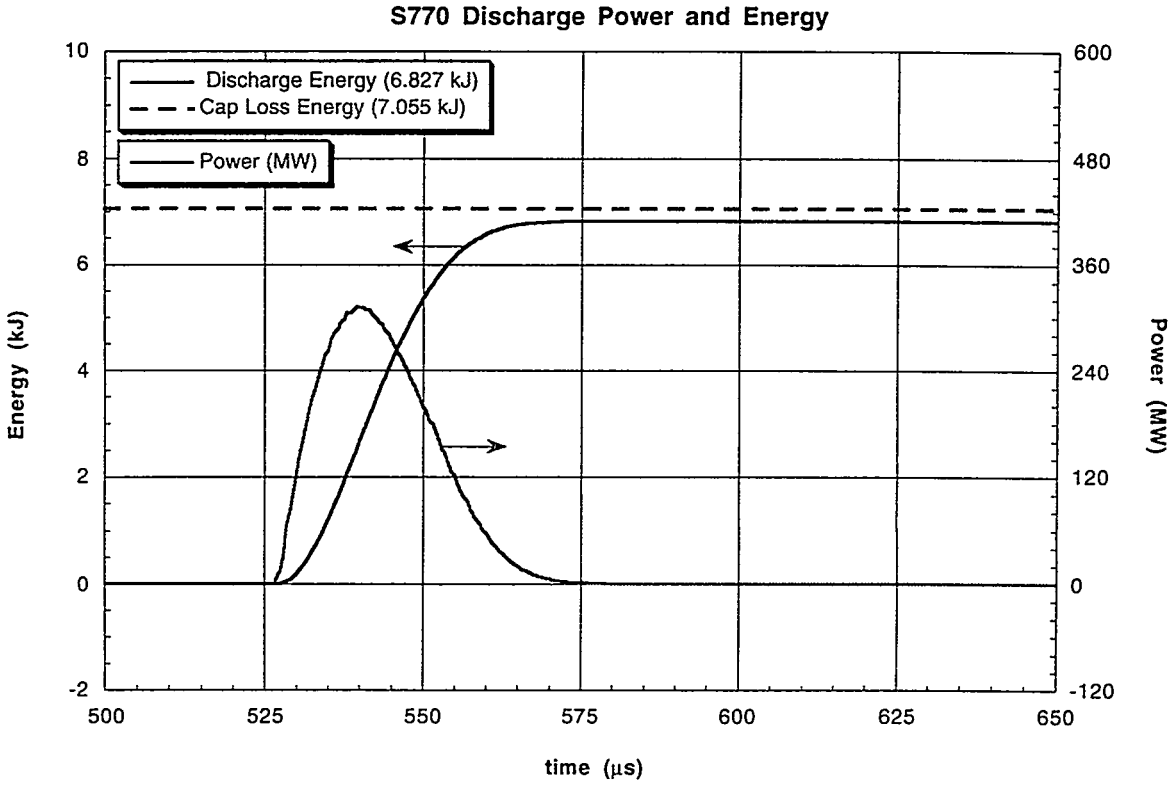

Table 5.2.1. Carbon / SS316 segmented test mass measurements.

S770: Carbon / SS316 Segmented Configuration

Source Section Components:			
component	pre-test wt. (g)	post-test wt. (g)	Δ wt. (mg)
cathode	10.21376	10.16247	51.30
long maycor	2.91160	-destroyed-	-
Lexan sleeve #1	0.32056	0.31239	8.17
SS316 sleeve #1	2.14681	1.98739	159.42
Lexan sleeve #2	0.31582	0.30593	9.89
SS316 sleeve #2	2.14767	1.96868	178.99
Lexan sleeve #3	0.33396	0.32245	11.51
SS316 sleeve #3	2.14418	1.96710	177.08
short maycor	1.02825	-destroyed-	-

Substrate Components:			
wall button	pre-test wt. (g)	post-test wt. (g)	Δ wt. (mg)
1	1.29144	1.29190	0.47
2	1.01519	1.01571	0.52
3	1.24010	1.24072	0.63
4	1.21681	1.21753	0.73
5	1.16535	1.16571	0.36
7	1.18280	1.18329	0.48
9	1.31203	1.31281	0.78
17	1.31206	1.31291	0.85

Notes: (1) All weight measurements are taken 3+ times and averaged.
(2) Δm uncertainty is ± 0.05 mg.

Figure 5.2.3. Representative SEM micrographs from button 3 of S770.

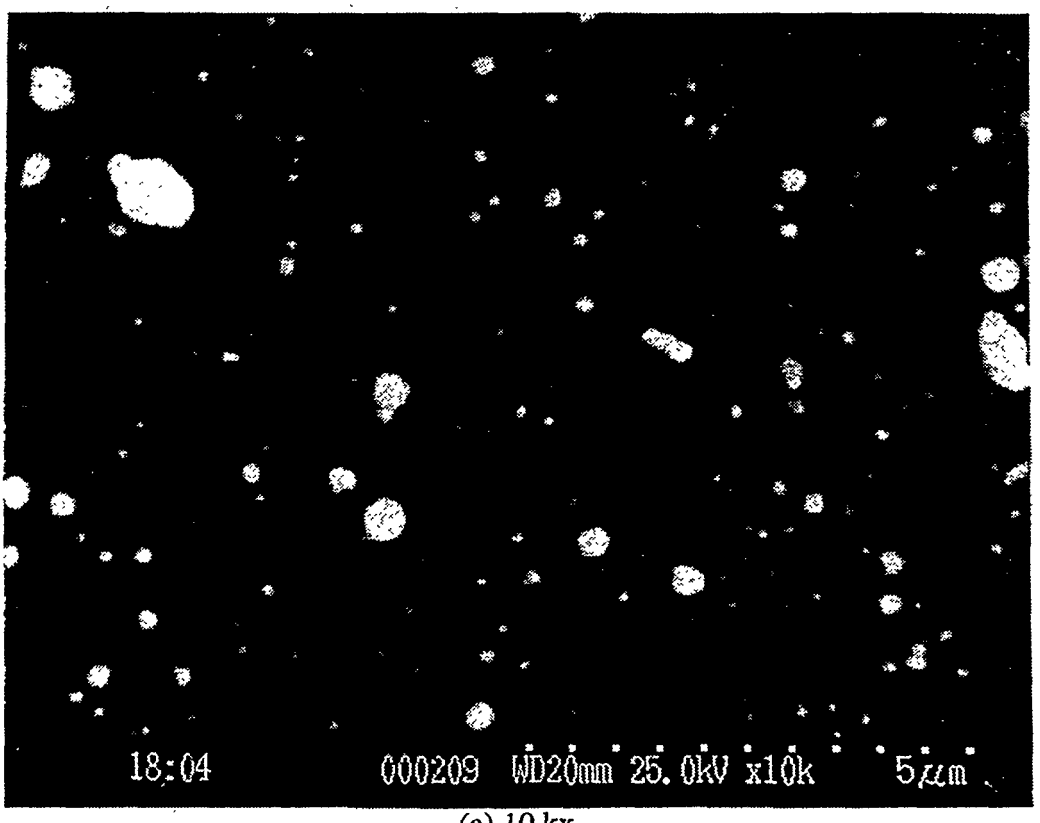

(a) 10 kx

Figure 5.2.3.cont.

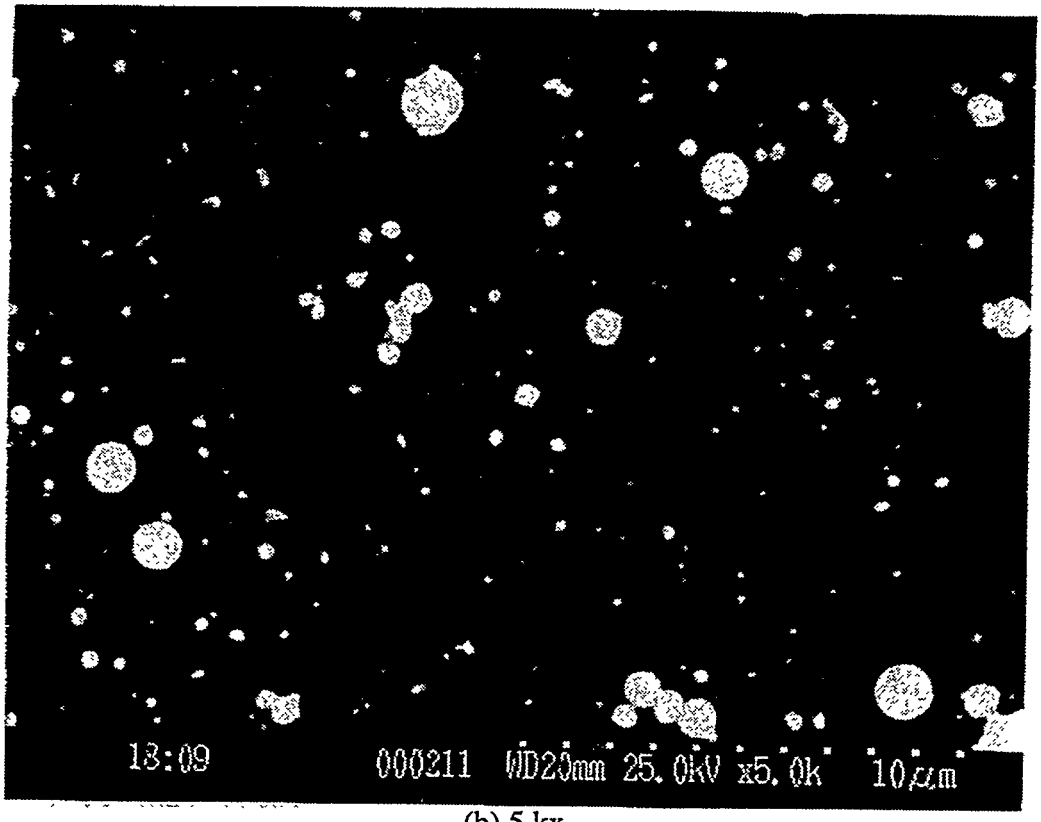

(b) 5 kx

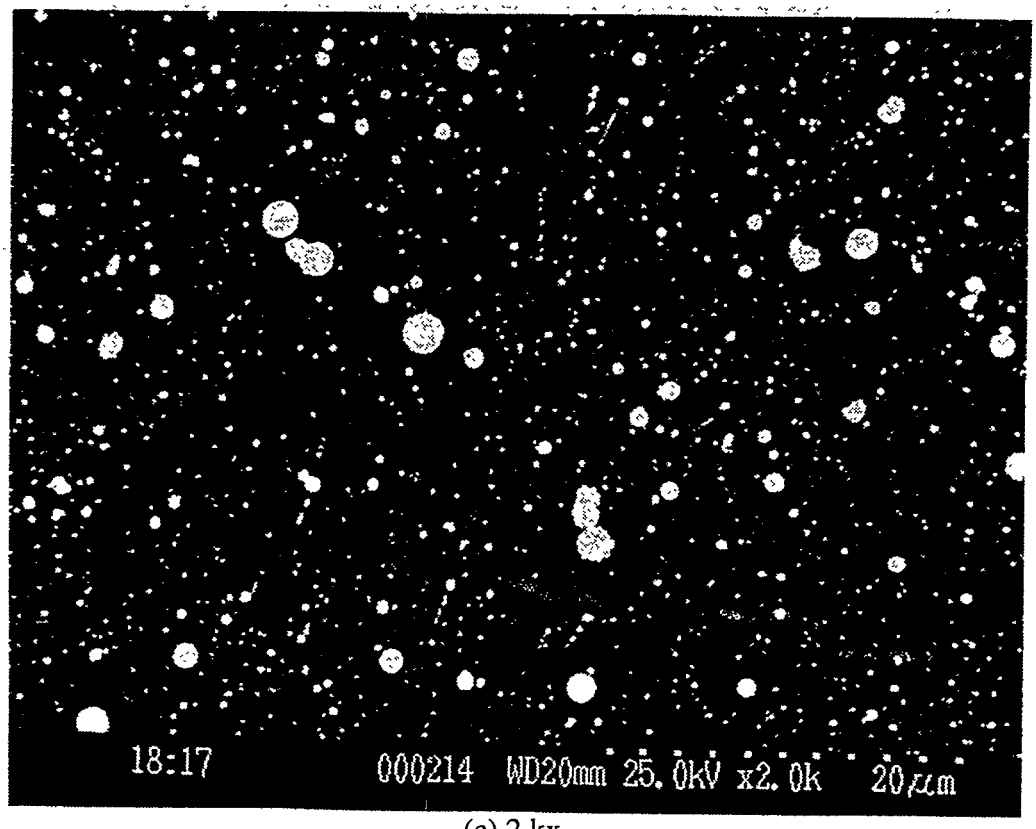

(c) 2 kx

Figure 5.2.4. EDXA mapping results of a button 9 region containing SS316 particles.

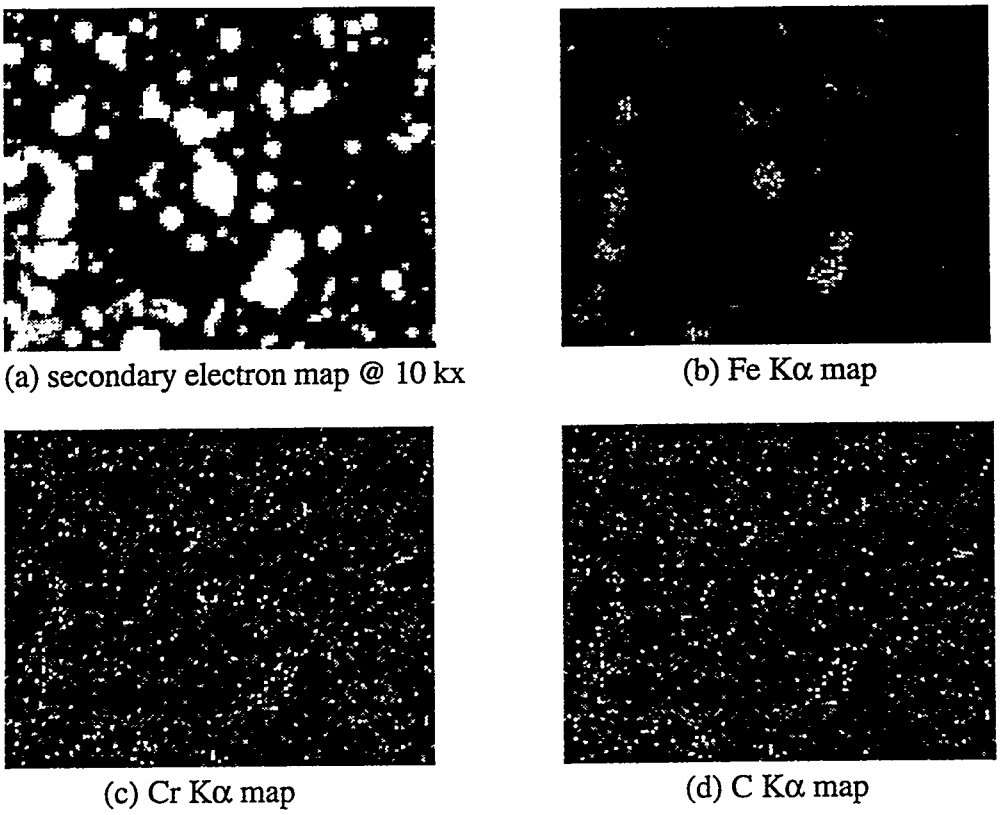

(a) secondary electron map @ 10 kx

(b) Fe Kα map

(c) Cr Kα map

(d) C Kα map

Figure 5.2.5. Optical spectra of the expanding vapor from the S770 source section.

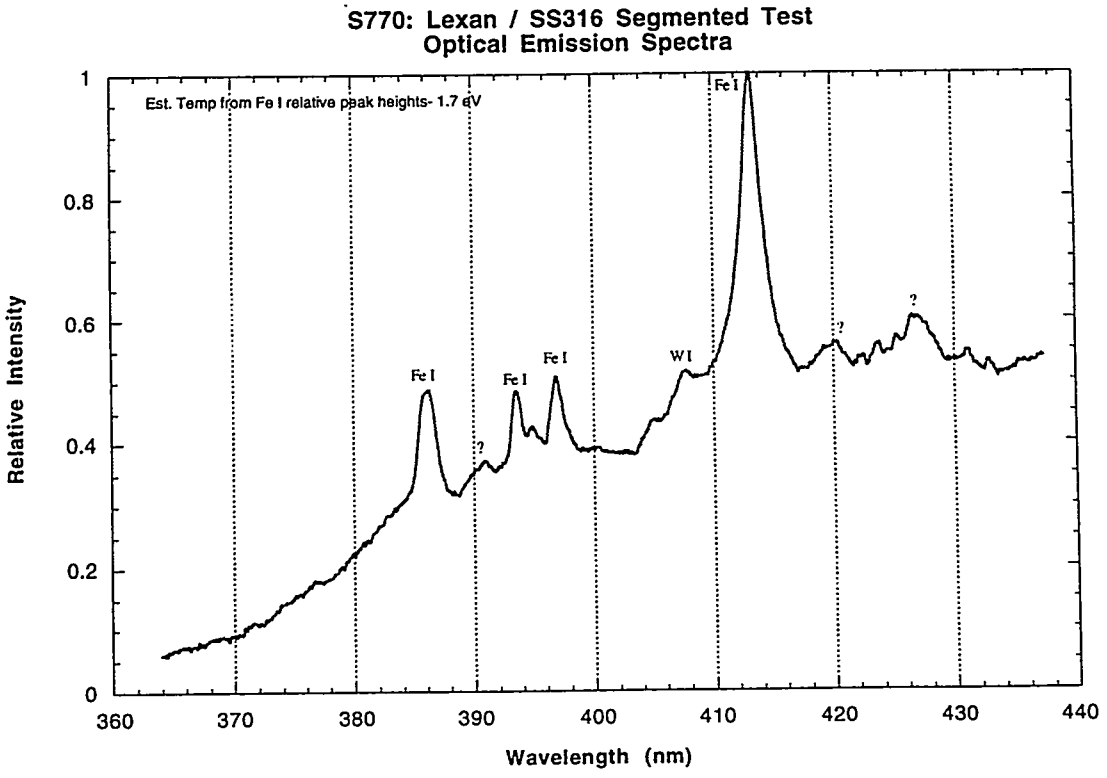

Figure 5.2.6. Carbon / SS316 segmented test (S770) button 1 particle size distribution.

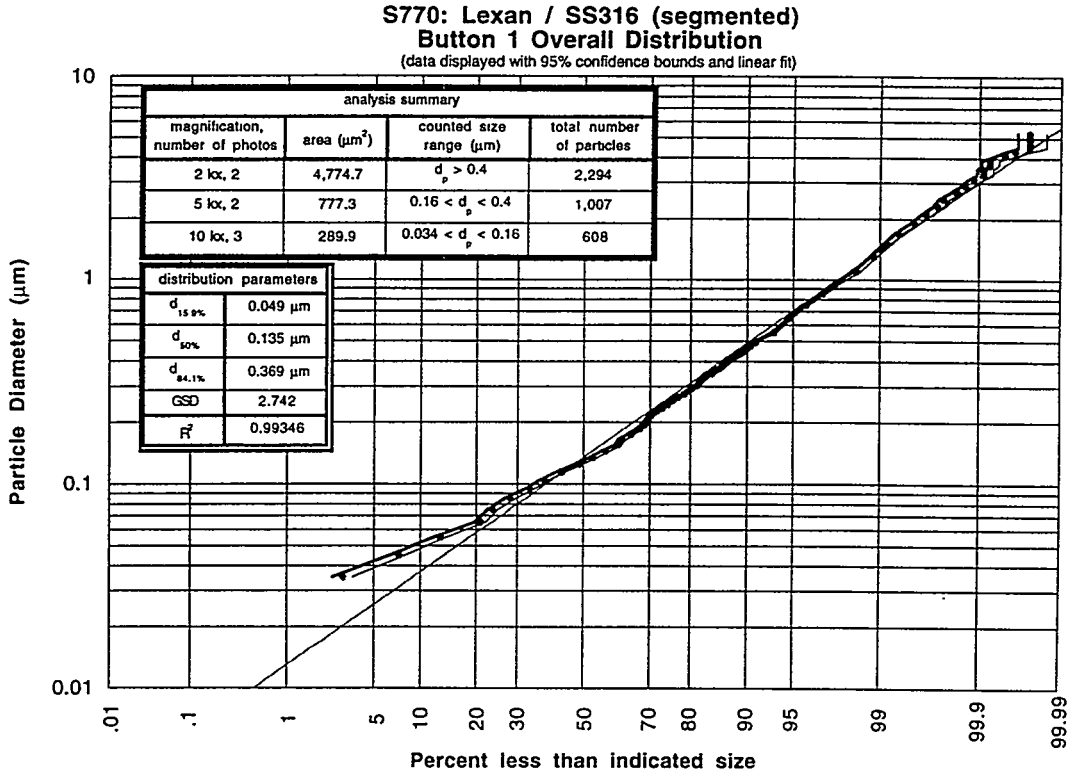

Data Summary Table:

photo	mag	scale (pixel/μm)	size (μm²)	min. d_{eq} (μm)	# of particles	scale factor	KW Test z-value	Overall p-value
770_1_1	10 kx	58.8	11.56x8.40	0.034[a]	205	25	0.68	0.664
770_1_2	10 kx	58.8	11.63x8.20	0.034[a]	207	25	0.16	
770_1_3	10 kx	58.8	11.53x8.45	0.034[a]	196	25	-0.85	
770_1_4	10 kx	58.8	11.50x8.42	0.034[a]	236	-	-failed-	
770_1_5	5 kx	29.4	23.03x16.80	0.068[a]	438	6.25	-0.50	0.618
770_1_6	5 kx	29.4	23.06x16.87	0.068[a]	569	6.25	0.50	
770_1_7	5 kx	29.4	23.03x16.73	0.068[a]	487	-	-failed-	
770_1_8	2 kx	11.8	57.29x41.69	0.22[b]	1075	1	0.46	0.649
770_1_9	2 kx	11.8	57.37x42.20	0.22[b]	562	-	-failed-	
770_1_10	2 kx	11.8	57.46x41.53	0.22[b]	1219	1	-0.46	

a. minimum equivalent diameter particle counted having an area of at least 3.1 x 1/scale on a side.
b. minimum equivalent diameter particle counted having an area of at least 5.1 x 1/scale on a side.

Figure 5.2.7. Carbon / SS316 segmented test (S770) button 3 particle size distribution.

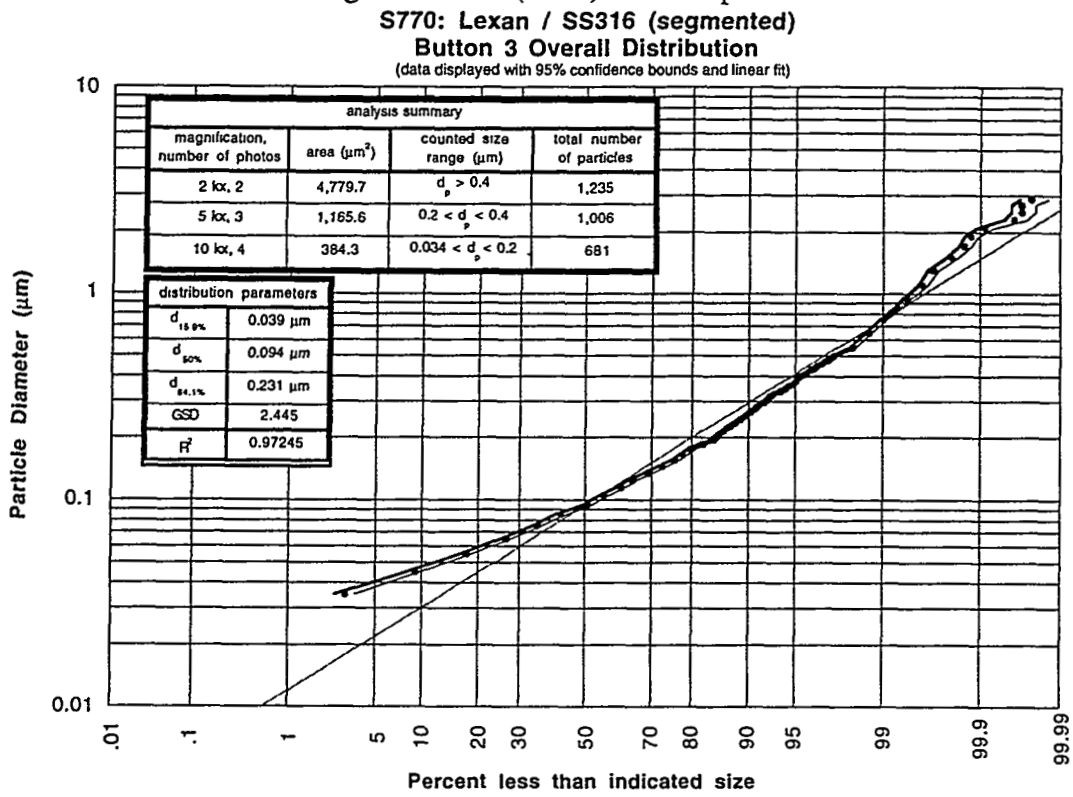

Data Summary Table:

photo	mag	scale (pixel/μm)	size (μm²)	min. d_{eq} (μm)	# of particles	scale factor	KW Test z-value	Overall p-value
770_3_1	10 kx	58.8	11.48x8.32	0.034[a]	258	25	0.12	0.268
770_3_2	10 kx	58.8	11.51x8.42	0.034[a]	166	25	0.57	
770_3_3	10 kx	58.8	11.58x8.33	0.034[a]	103	25	1.22	
770_3_4	10 kx	58.8	11.5x8.3	0.034[a]	154	25	-1.77	
770_3_5	5 kx	29.4	23.03x17.04	0.068[a]	367	6.25	-0.43	0.904
770_3_6	5 kx	29.4	23.03x16.77	0.068[a]	301	6.25	0.10	
770_3_7	5 kx	29.4	23.13x16.73	0.068[a]	338	6.25	0.34	
770_3_8	2 kx	11.8	57.03x42.2	0.22[b]	591	-	-failed-	0.445
770_3_9	2 kx	11.8	57.03x41.61	0.22[b]	646	1	-0.76	
770_3_10	2 kx	11.8	57.37x41.95	0.22[b]	589	1	0.76	

a. minimum equivalent diameter particle counted having an area of at least 3.1 x 1/scale on a side.
b. minimum equivalent diameter particle counted having an area of at least 5.1 x 1/scale on a side.

Figure 5.2.8. Carbon / SS316 segmented test (S770) button 9 particle size distribution.

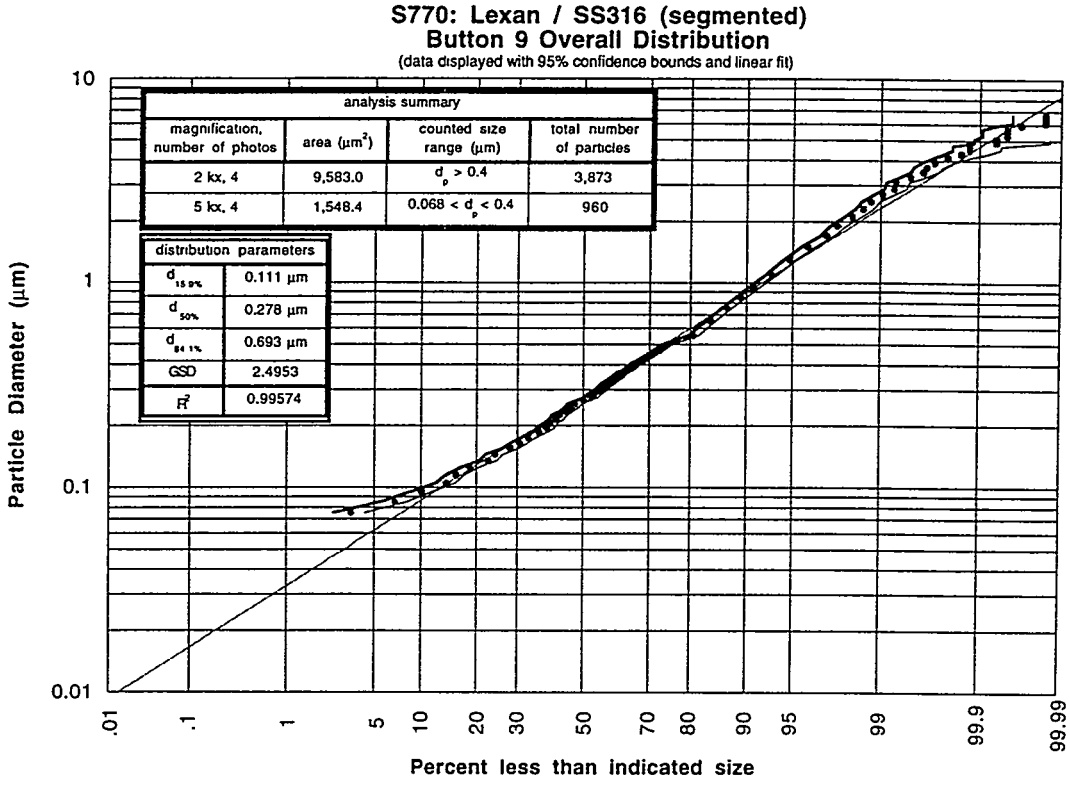

Data Summary Table:

photo	mag	scale (pixel/μm)	size (μm²)	min. d_{eq} (μm)	# of particles	scale factor	KW Test z-value	Overall p-value
770_9_1	5 kx	29.4	23.13x16.77	0.068[a]	213	6.25	-0.70	0.353
770_9_2	5 kx	29.4	22.96x16.80	0.068[a]	247	6.25	1.77	
770_9_3	5 kx	29.4	23.06x16.70	0.068[a]	250	6.25	-0.83	
770_9_4	5 kx	29.4	23.06x16.90	0.068[a]	250	6.25	-0.27	
770_9_5	2 kx	11.8	57.46x41.69	0.22[b]	944	1	-0.29	0.288
770_9_6	2 kx	11.8	57.12x42.20	0.22[b]	1042	1	-1.70	
770_9_7	2 kx	11.8	57.37x41.95	0.22[b]	907	1	0.96	
770_9_8	2 kx	11.8	57.20x41.44	0.22[b]	980	1	1.09	

a. minimum equivalent diameter particle counted having an area of at least 3.1 x 1/scale on a side.
b. minimum equivalent diameter particle counted having an area of at least 5.1 x 1/scale on a side.

6.0 Carbon / Tungsten Test: S767

Another material of interest in disruption-induced mobilization studies is tungsten. A single test, S767, has been performed in SIRENS with Lexan carbon and tungsten sleeves placed in the source section. The configuration used for this test was different from the short and segmented configurations of the other carbon / metal tests because only one sample sleeve length of tungsten was available (3.0 cm). Figure 6.1 displays the source section configuration used for this test. Table 6.1 gives the test summary.

Figure 6.1. Source section configuration used in C/W test S767.

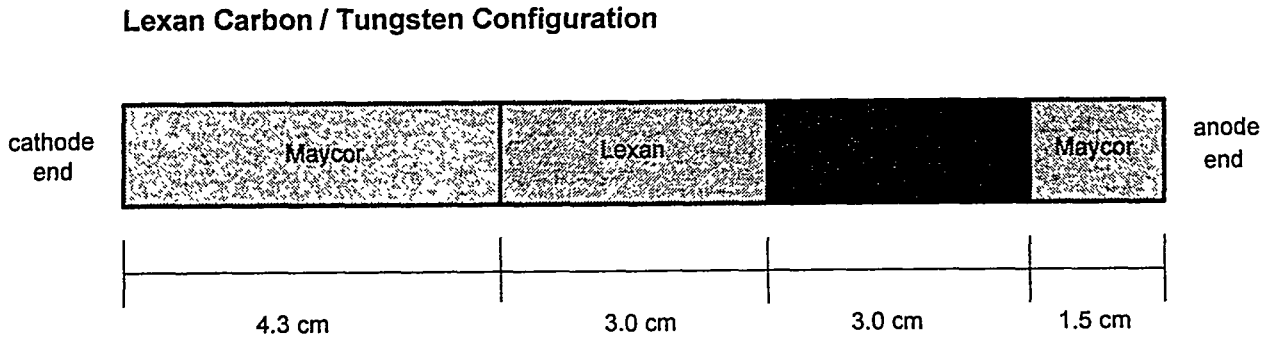

Table 6.1. Carbon / Tungsten test results summary.

	C / W Test (S767)			
Energy (J)	7.302			
Fluence (MJ/m^2)	6.66			
Duration (μs)	60			
Lexan sleeve Δm (mg)	17.89			
Tungsten sleeve Δm (mg)	369.03			
Scaled Tungsten Δm (mg/kJ/cm)	16.85			
Scaled Lexan Δm (mg/kJ/cm)	0.82			
Cathode Δm (mg)	58.21			
	Δm (mg)	$d_{50\%}$ (μm)	GSD	R^2
Button 1	0.13	0.097	2.028	0.992
Button 2	0.42	0.109	2.309	0.984
Button 3	0.52	*	*	*
Button 4	0.45	*	*	*
Button 5	0.07	0.139	1.927	0.986
Button 7	0.32	*	*	*
Button 9	-5.99	0.121	2.493	0.985
Button 17	-0.04	*	*	*

Note: Asterisk (*) denotes analysis not performed.

The Lexan carbon / tungsten test was performed with a discharge energy of 7.302 kJ. Figure 6.2 shows the voltage and current traces resulting from the discharge, and Figure 6.3 displays the electrical power and energy produced by the discharge. Integrated power gives a discharge energy of 7.751 kJ, while only 7.302 kJ was measured as loss from the capacitor bank. The source of this 6% discrepancy has not been found. Instruments used to measure the voltage and current were found to be in calibration, and the signal recorder displayed negligible gain and offset.

Table 6.2 presents a summary of mass measurements from this test. Normalized mass loss from the tungsten sleeve was found to be 16.85 mg/kJ/cm, and the Lexan sleeve normalized mass loss was 0.82 mg/kJ/cm. Collection buttons mounted on the expansion chamber wall showed a detectable level of mass gain from particulate deposit, appearing to peak at chamber mid-length. Both end plate buttons were found to have lost mass as a result of chipping and breaking away of the glass surfaces. Button 9 lost more mass (6 mg) because large pieces of the surface had been removed, while button 17 lost nearly as much mass from glass breakage as was gained from particulate deposit.

Representative SEM micrographs from button 2 of this carbon / tungsten test are given in Figure 6.4. These images show a large population to small, irregular particles at high magnification and fewer large spherical particles at lower magnifications. EDXA was unavailable at the time these images were obtained, thus distinguishing composition of these particles could not be achieved. Particle size distributions for buttons 1, 2, 5, and 9 are given in Figures 6.5-8. The influence of the many smaller sized particles may be seen in the count median diameter values ($d_{50\%}$); these values are on the order of sizes obtained from Lexan carbon-only tests.

Figure 6.2. Voltage and current traces for carbon / tungsten test S767.

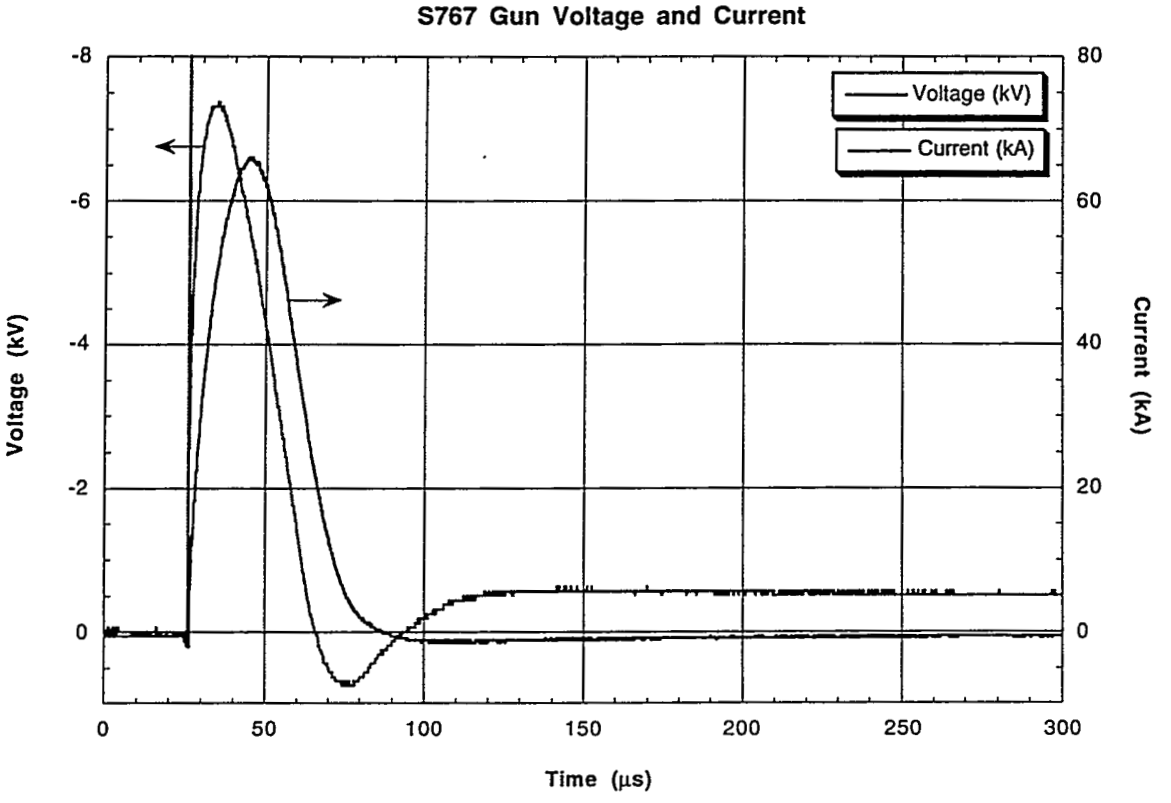

Figure 6.3. Power and energy traces for carbon / tungsten test S767.

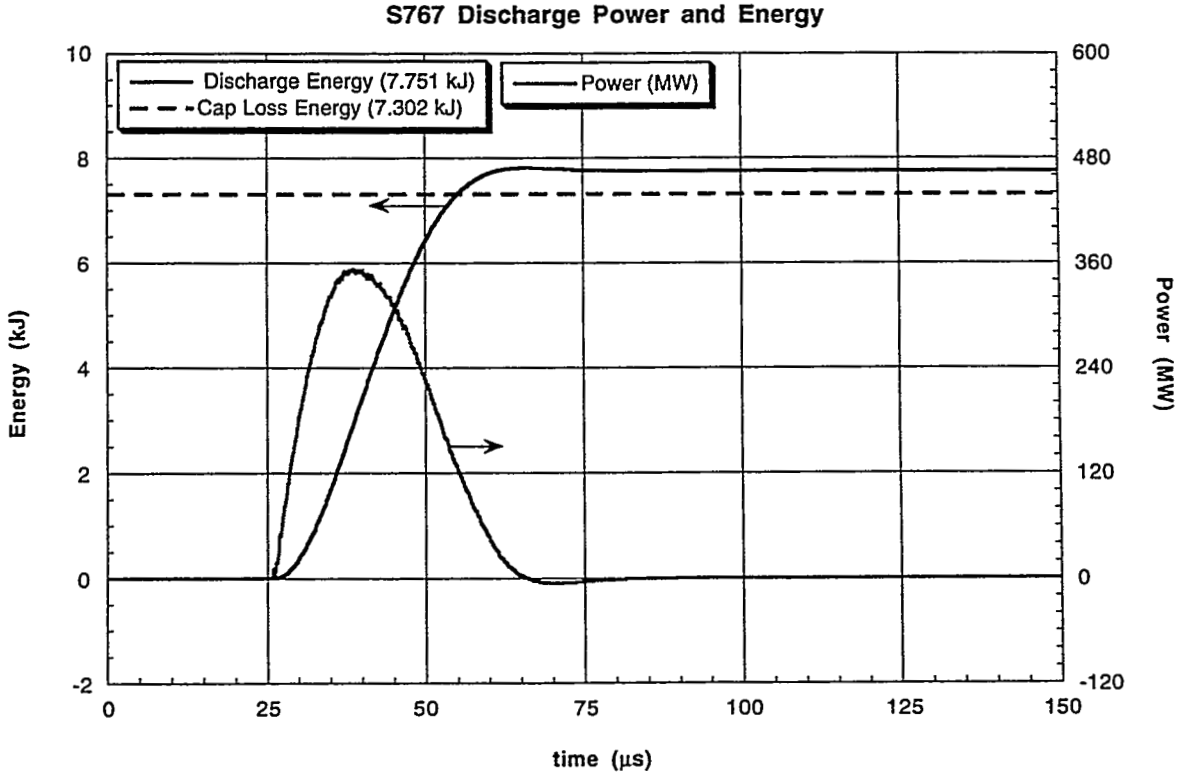

Table 6.2. Lexan carbon / tungsten test mass measurements.

S767: C / W Modified Configuration

Source Section Components:			
component	pre-test wt. (g)	post-test wt. (g)	Δ wt. (mg)
cathode	10.54769	10.48949	58.21
long maycor	2.91174	-destroyed-	-
Lexan sleeve	0.97291	0.95502	17.89
tungsten sleeve	15.51723	15.14819	369.03
short maycor	1.02590	-destroyed-	-

Substrate Components:			
wall button	pre-test wt. (g)	post-test wt. (g)	Δ wt. (mg)
1	1.24013	1.24027	0.13
2	1.28643	1.28685	0.42
3	1.32915	1.32967	0.52
4	1.29388	1.29433	0.45
5	1.29123	1.29130	0.07
7	1.25020	1.25052	0.32
9	1.24658	1.24059	-5.99
17	1.20150	1.20146	-0.04

Notes: (1) All weight measurements are taken 3+ times and averaged.

(2) Δm uncertainty is ± 0.05 mg.

Figure 6.4 Representative SEM micrographs from button 2 of S767.

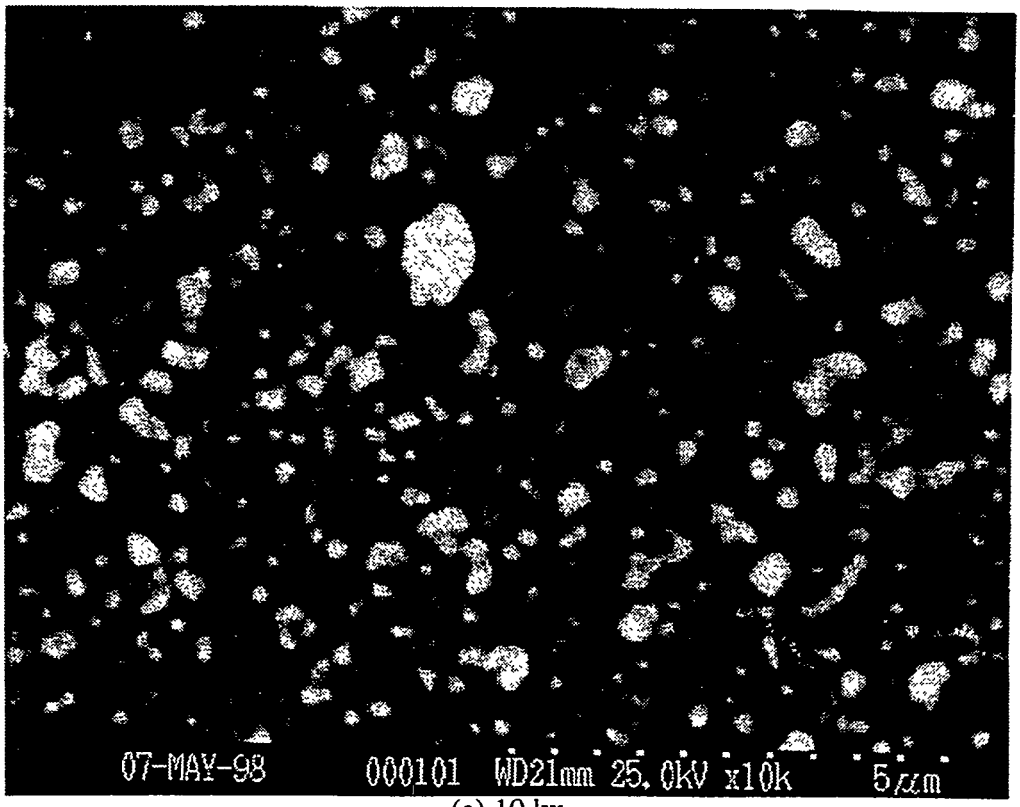

(a) 10 kx

Figure 6.4.cont.

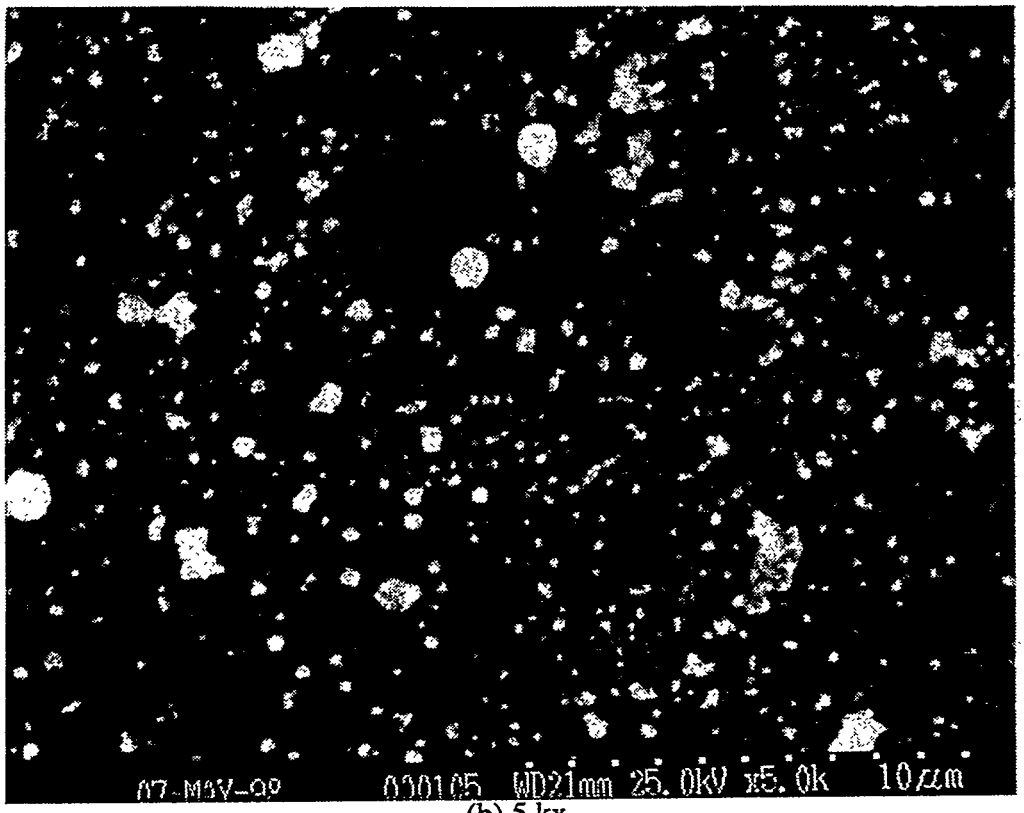

(b) 5 kx

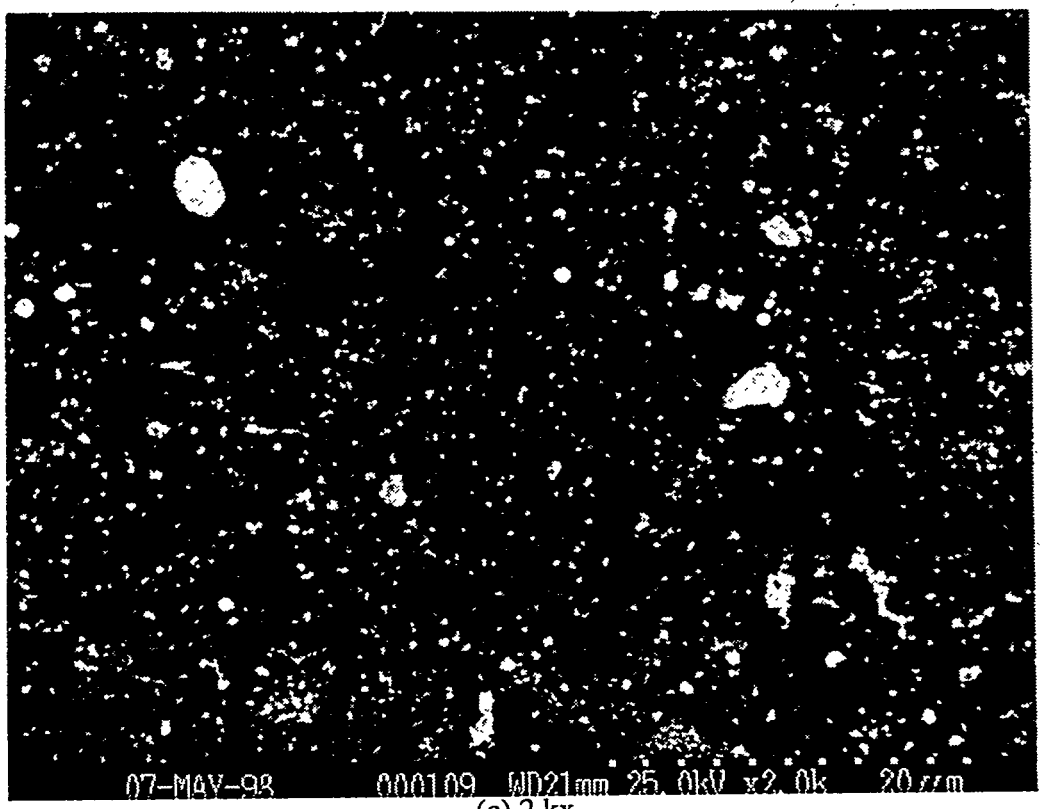

(c) 2 kx

Figure 6.5. Carbon / Tungsten test (S767) button 1 particle size distribution.

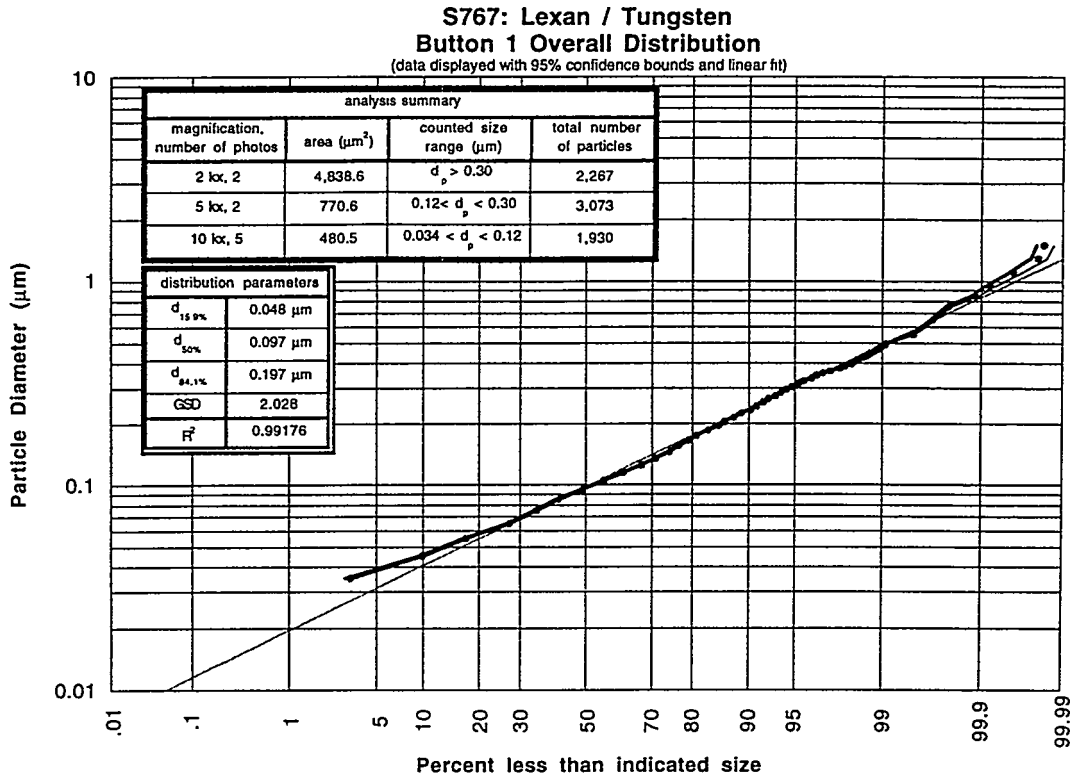

Data Summary Table:

photo	mag	scale (pixel/μm)	size (μm²)	min. d_{eq} (μm)	# of particles	scale factor	KW Test z-value	Overall p-value
767_1_1	10 kx	58.8	11.5x8.33	0.034[b]	798	25	3.95	0.000
767_1_2	10 kx	58.8	11.48x8.35	0.034[b]	623	25	-0.27	
767_1_3	10 kx	58.8	11.56x8.30	0.034[b]	581	25	-0.50	
767_1_4	10 kx	58.8	11.56x8.33	0.034[b]	416	25	1.72	
767_1_5	10 kx	58.8	11.5x8.4	0.034[b]	776	25	-4.64	
767_1_6	5 kx	29.4	22.99x16.77	0.068[b]	1583	6.25	-1.05	0.294
767_1_7	5 kx	29.4	23.13x16.53	0.068[b]	1169	-	-failed-	
767_1_8	5 kx	29.4	22.96x16.77	0.068[b]	1490	6.25	1.05	
767_1_9	2 kx	11.8	57.37x41.78	0.22[c]	1223	1	0.06	0.948
767_1_10	2 kx	11.8	57.37x42.37	0.22[c]	1161	-	-failed-	
767_1_11	2 kx	11.8	57.29x42.03	0.22[c]	1044	1	-0.06	

a. All images obtained at 10 kx failed the Kruskal-Wallis test (i.e. $p < 0.05$) but were used in generation of the overall size distribution.
b. minimum equivalent diameter particle counted having an area of at least 3.1 x 1/scale on a side.
c. minimum equivalent diameter particle counted having an area of at least 5.1 x 1/scale on a side.

Figure 6.6. Carbon / Tungsten test (S767) button 2 particle size distribution.

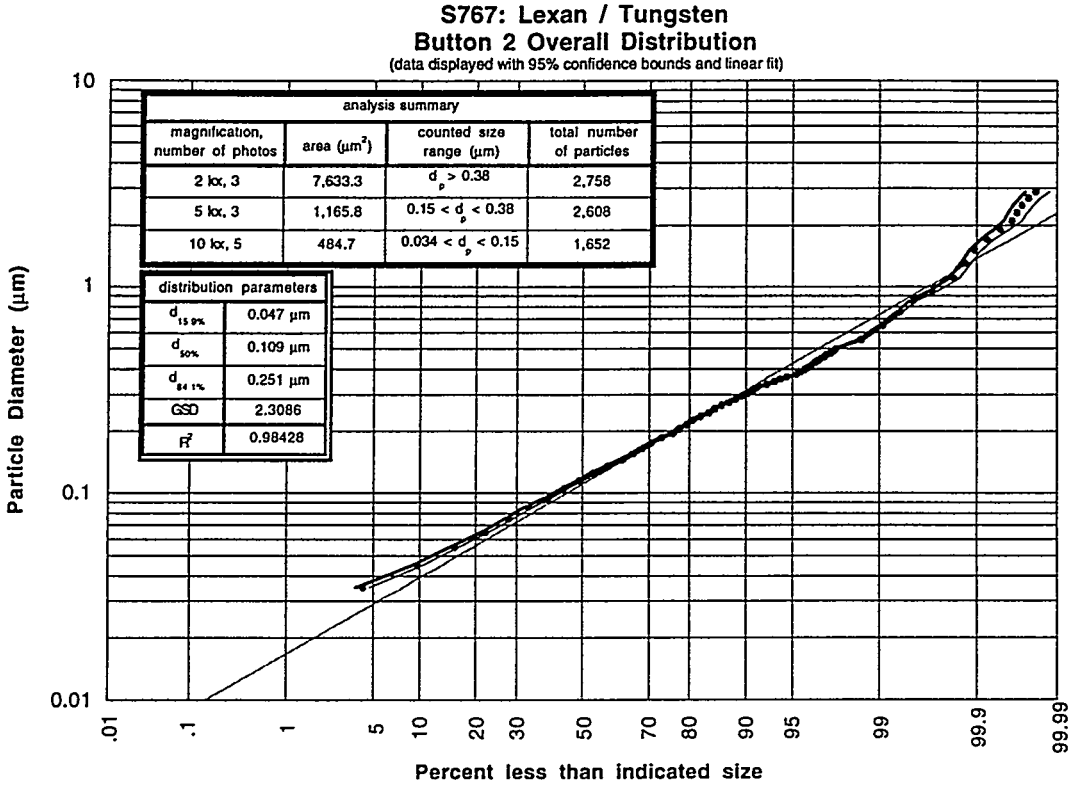

Data Summary Table:

photo	mag	scale (pixel/μm)	size (μm²)	min. d_{eq} (μm)	# of particles	scale factor	KW Test z-value	Overall p-value
767_2_1	10 kx	58.8	11.51x8.42	0.034[a]	322	25	1.05	0.279
767_2_2	10 kx	58.8	11.48x8.44	0.034[a]	396	25	-1.19	
767_2_3	10 kx	58.8	11.48x8.42	0.034[a]	650	25	1.65	
767_2_4	10 kx	58.8	11.46x8.55	0.034[a]	361	25	-0.75	
767_2_5	10 kx	58.8	11.56x8.33	0.034[a]	223	25	-0.80	
767_2_6	5 kx	29.4	23.06x16.94	0.068[a]	781	6.25	0.67	0.800
767_2_7	5 kx	29.4	22.96x16.94	0.068[a]	968	6.25	-0.34	
767_2_8	5 kx	29.4	22.96x16.94	0.068[a]	859	6.25	-0.30	
767_2_9	2 kx	11.8	56.95x42.12	0.22[b]	1031	1	0.10	0.742
767_2_10	2 kx	11.8	57.46x42.03	0.22[b]	813	1	0.62	
767_2_11	2 kx	11.8	57.2x42.54	0.22[b]	914	1	-0.70	

a. minimum equivalent diameter particle counted having an area of at least 3.1 x 1/scale on a side.
b. minimum equivalent diameter particle counted having an area of at least 5.1 x 1/scale on a side.

Figure 6.7. Carbon / Tungsten test (S767) button 5 particle size distribution.

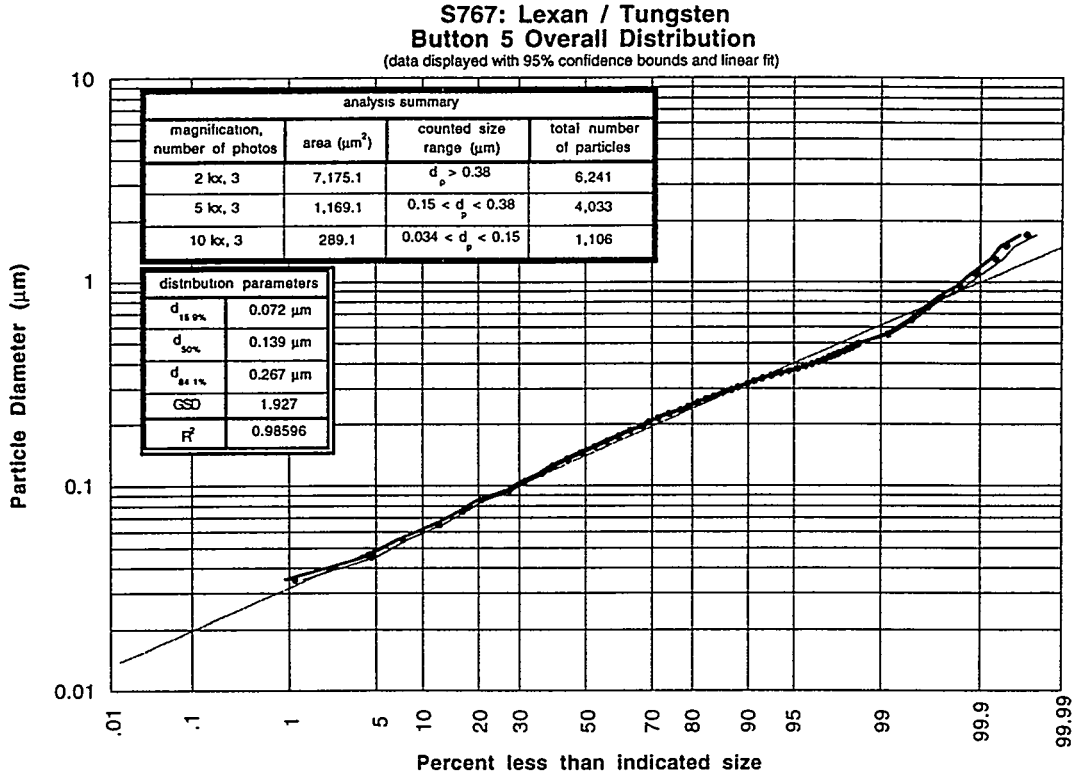

Data Summary Table:

photo	mag	scale (pixel/μm)	size (μm²)	min. d_{eq} (μm)	# of particles	scale factor	KW Test z-value	Overall p-value
767_5_1	10 kx	58.8	11.41x8.37	0.034[b]	327	25	-1.42	0.278
767_5_2	10 kx	58.8	11.46x8.45	0.034[b]	380	-	-failed-	
767_5_3	10 kx	58.8	11.51x8.42	0.034[b]	374	25	1.31	
767_5_4	10 kx	58.8	11.53x8.37	0.034[b]	405	25	0.06	
767_5_5	10 kx	58.8	11.55x8.47	0.034[b]	338	-	-failed-	
767_5_6	5 kx	29.4	23.10x16.97	0.068[b]	1467	6.25	-1.24	0.109
767_5_7	5 kx	29.4	22.99x16.80	0.068[b]	1349	6.25	2.10	
767_5_8	5 kx	29.4	23.03x16.97	0.068[b]	1217	6.25	-0.86	
767_5_9[a]	2 kx	11.8	57.12x41.61	0.22[c]	1580	1	-3.84	0.000
767_5_10[a]	2 kx	11.8	57.54x41.61	0.22[c]	2233	1	-0.87	
767_5_11[a]	2 kx	11.8	57.2x42.03	0.22[c]	2428	1	4.28	

a. All images obtained at 2 kx failed the Kruskal-Wallis test (i.e. $p < 0.05$) but were used in generation of the overall size distribution.
b. minimum equivalent diameter particle counted having an area of at least 3.1 x 1/scale on a side.
c. minimum equivalent diameter particle counted having an area of at least 5.1 x 1/scale on a side.

Figure 6.8. Carbon / Tungsten test (S767) button 9 particle size distribution.

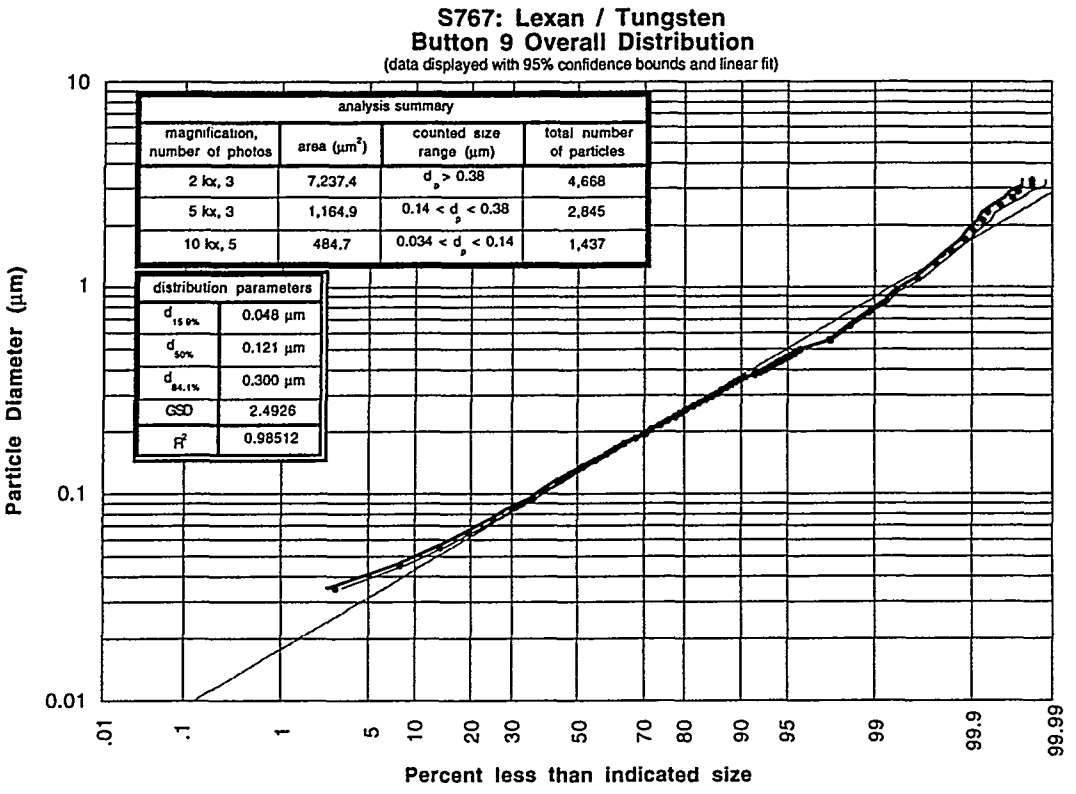

Data Summary Table:

photo	mag	scale (pixel/μm)	size (μm²)	min. d_{eq} (μm)	# of particles	scale factor	KW Test z-value	Overall p-value
767_9_1	10 kx	58.8	11.56x8.21	0.034[a]	206	25	2.73	0.052
767_9_2	10 kx	58.8	11.45x8.5	0.034[a]	277	25	0.23	
767_9_3	10 kx	58.8	11.5x8.54	0.034[a]	305	25	-1.15	
767_9_4	10 kx	58.8	11.51x8.50	0.034[a]	361	25	-1.60	
767_9_5	10 kx	58.8	11.55x8.35	0.034[a]	288	25	0.29	
767_9_6	5 kx	29.4	23.1x16.8	0.068[a]	1085	6.25	-0.20	0.158
767_9_7	5 kx	29.4	23.06x16.9	0.068[a]	870	6.25	1.74	
767_9_8	5 kx	29.4	22.99x16.84	0.068[a]	890	6.25	-1.51	
767_9_9	2 kx	11.8	57.29x42.29	0.22[b]	1467	1	-2.44	0.054
767_9_10	2 kx	11.8	57.29x42.03	0.22[b]	1438	1	1.55	
767_9_11	2 kx	11.8	57.37x41.95	0.22[b]	1763	1	0.86	

a. minimum equivalent diameter particle counted having an area of at least 3.1 x 1/scale on a side.
b. minimum equivalent diameter particle counted having an area of at least 5.1 x 1/scale on a side.

7.0 Carbon / Aluminum Test: S768

The final carbon / metal combination investigated in SIRENS was Lexan carbon and aluminum. Interest in aluminum results from the metal's thermophysical properties being close in value to those of beryllium, another material in the current ITER design. Both materials are of relatively low densities (1850 kg/m^3 for Be and 2700 kg/m^3 for Al) and melt temperatures (1560 K for Be and 934 K for Al) when compared to other metals considered for ITER. Because of difficulty in working with beryllium, aluminum has been used to simulate the thermal response of the low density, low melting point material when exposed to high heat flux. A single Lexan carbon and aluminum test (S768) was performed in SIRENS with sample material placed in the source section in the segmented configuration. Table 7.1 gives the test summary.

Table 7.1. Carbon / Aluminum test results summary.

	C / Al Test (S768)			
Energy (J)	7.068			
Fluence (MJ/m^2)	6.44			
Duration (μs)	70			
Lexan sleeve #1 Δm (mg)	8.82			
Aluminum sleeve #1 Δm (mg)	169.09			
Lexan sleeve # 2 Δm (mg)	11.99			
Aluminum sleeve #2 Δm (mg)	204.27			
Lexan sleeve #3 Δm (mg)	11.02			
Aluminum sleeve #3 Δm (mg)	212.40			
Scaled Aluminum Δm (mg/kJ/cm)	27.62			
Scaled Lexan Δm (mg/kJ/cm)	1.50			
Cathode Δm (mg)	56.0			
	Δm (mg)	$d_{50\%}$ (μm)	GSD	R^2
Button 1	0.69	0.281	3.0803	0.995
Button 2	0.79	0.216	3.1913	0.976
Button 3	0.59	0.154	2.421	0.977
Button 4	0.50	*	*	*
Button 5	0.57	0.126	2.890	0.942
Button 7	1.02	*	*	*
Button 9	-1.89	0.153	3.176	0.970
Button 17	-0.75	*	*	*

Note: Asterisk (*) denotes analysis not performed.

The Lexan carbon / aluminum test was performed with a discharge energy of 7.068 kJ. Measured voltage and current traces are given in Figure 7.1, followed by discharge power and energy in Figure 7.2. Electrical energy obtained from integrated power is slightly greater than the value obtained from capacitor bank loss (7.178 kJ versus 7.068 kJ). This 1.6% difference is within experimental error. Both current and voltage traces are typical of tests with this configuration.

Table 7.2 contains the mass measurement data for source section and button component material. Total mass loss from the aluminum sleeves was found to be 27.62 mg/kJ/cm; a test previously performed in SIRENS with only aluminum in the source section gave a mass loss of 20.0 mg/kJ/cm [3]. Erosion from the Lexan sleeves in this test was measured to be 1.5 mg/kJ/cm, also somewhat greater than the 0.6 mg/kJ/cm measured in S760 and S761 with only Lexan in the source section. An important item must be noted regarding the expected response of Be to a similar thermal loading. Sublimation enthalpy of Be (36 MJ/kg) is larger than the corresponding value for Al (11.9 MJ/kg), meaning that less Be would be vaporized from the surface. The contribution of melting to material erosion, however, remains an important issue for further investigation. Button mass measurements included in Table 7.2 indicate significant particle mass deposition on the button surfaces, with greatest deposition on buttons close to the source exit. End plate buttons were again chipped and broken from debris and high velocity particulate, accounting for the measured mass loss.

Representative SEM micrographs from button 2 of S768 are shown in Figure 7.3. A large population of small particles is observed in the 3 kx images, and many large particles are observed in the 1 kx image. Particle shapes are somewhat irregular and display hazy boundaries. This could be the result of liquid material impacting and solidifying as it cools on the button surface, with concurrent deposition of smaller particles. EDXA mapping shown in Figure 7.4 indicates that carbon and aluminum are possibly mixed together in these particles. Although the carbon map contains very few counts from the EDXA detector, they do appear to concentrate on regions where Al resides. Particle size distributions from buttons 1, 2, 3, 5, and 9 are given as Figure 7.5-9. Most of these distributions do not follow the log-normal approximation, given the poor fit and large GSD values. This likely results from the hazy particle boundaries and irregular, extended shapes.

Figure 7.1. Voltage and current traces for Lexan carbon / aluminum test S768.

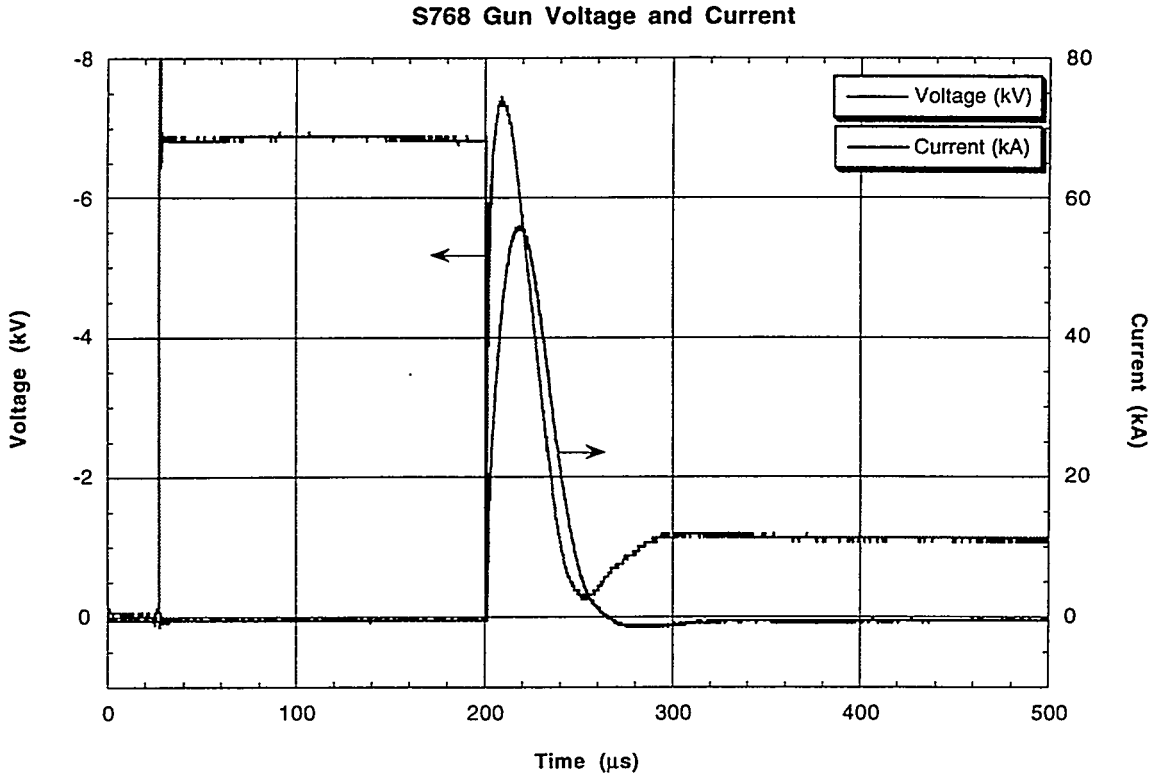

Figure 7.2. Power and energy traces for Lexan carbon / aluminum test S768.

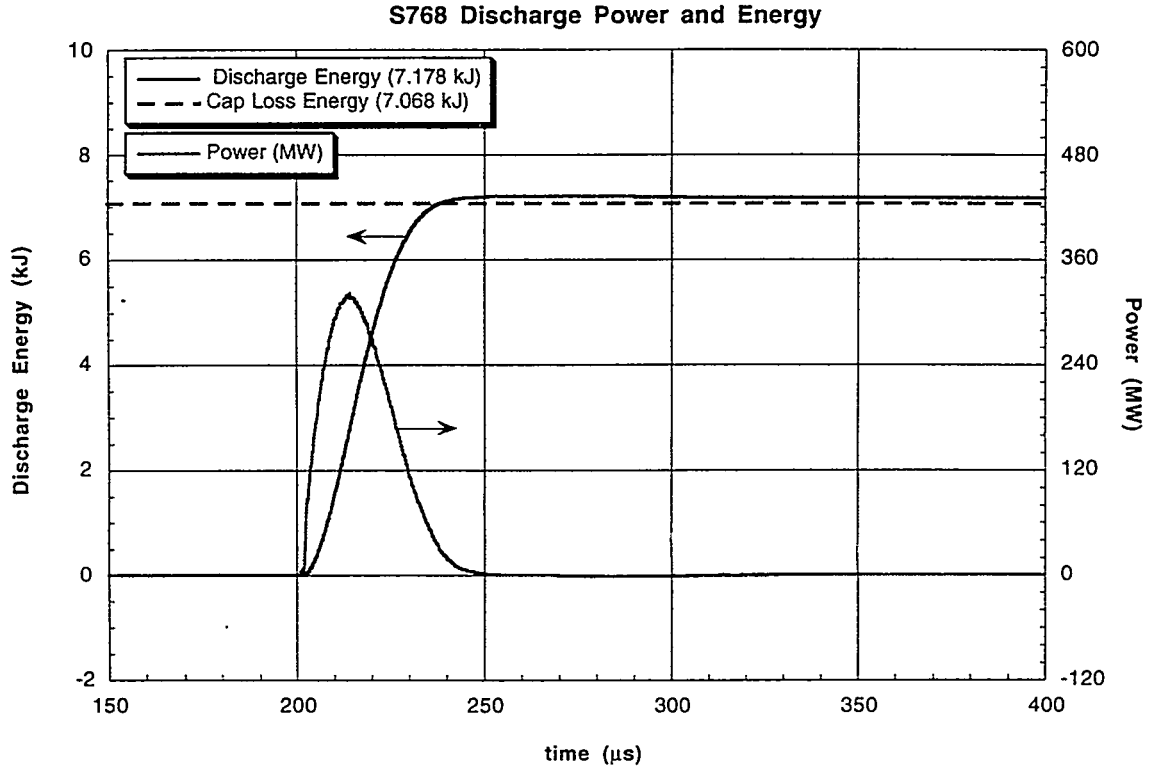

Table 7.2. Lexan carbon / aluminum test mass measurements.

S768: Carbon / Aluminum Segmented Configuration

Source Section Components:			
component	pre-test wt. (g)	post-test wt. (g)	Δ wt. (mg)
cathode	10.43571	10.37970	56.00
long maycor	2.92739	-destroyed-	-
Lexan sleeve #1	0.31891	0.31009	8.82
aluminum sleeve #1	0.62125	0.45216	169.09
Lexan sleeve #2	0.32850	0.31651	11.99
aluminum sleeve #2	0.68511	0.48084	204.27
Lexan sleeve #3	0.30213	0.29111	11.02
aluminum sleeve #3	0.67653	0.46413	212.40
short maycor	1.02266	-destroyed-	-

Substrate Components:			
wall button	pre-test wt. (g)	post-test wt. (g)	Δ wt. (mg)
1	1.29043	1.29113	0.69
2	1.30244	1.30323	0.79
3	1.19476	1.19535	0.59
4	1.17109	1.17159	0.50
5	1.24126	1.24183	0.57
7	1.31376	1.31478	1.02
9	1.34776	1.34587	-1.89
17	1.07173	1.07098	-0.75

Notes: (1) All weight measurements are taken 3+ times and averaged.
(2) Δm uncertainty is ± 0.05 mg.

Figure 7.3. Representative SEM micrographs from button 2 of S768.

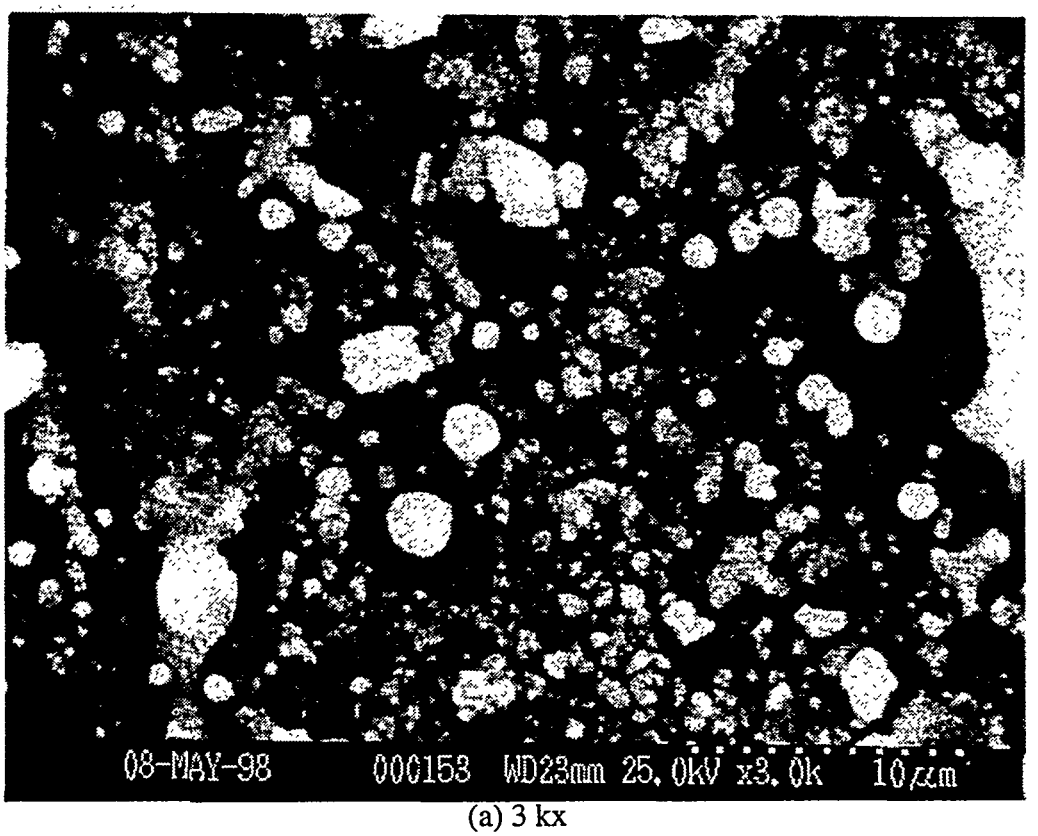

(a) 3 kx

Figure 7.3.cont.

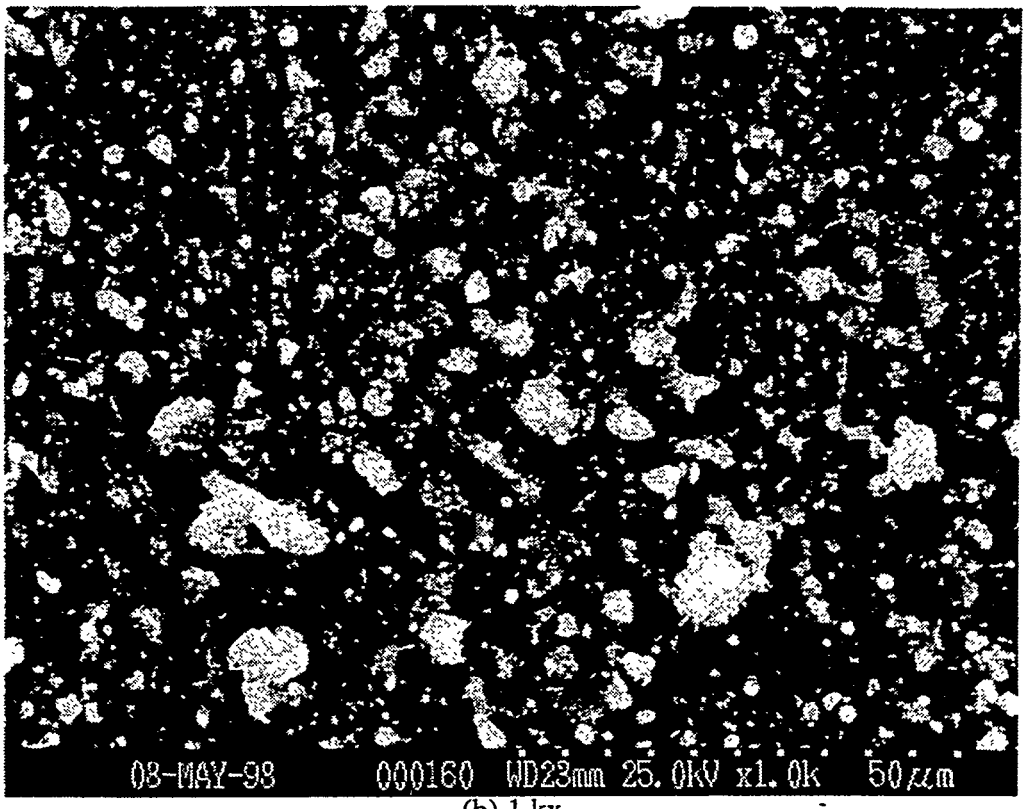

(b) 1 kx

Figure 7.4. EDXA mapping results of a button 2 region containing Al particles.

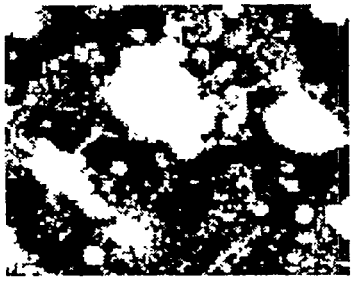

(a) secondary electron map @ 10 kx

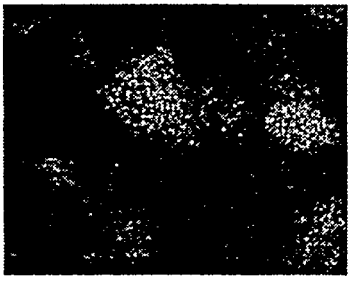

(b) Al Kα map

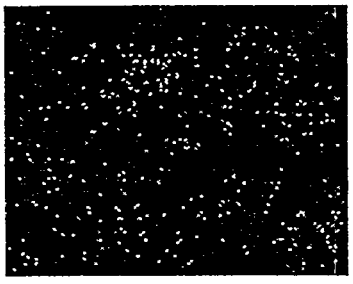

(c) C Kα map

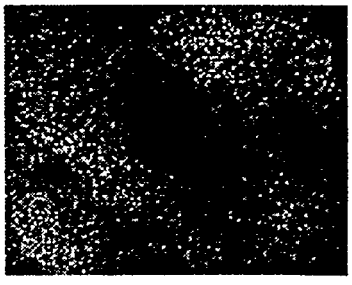

(d) Si Kα map

Figure 7.5. Carbon / Aluminum test (S768) button 1 particle size distribution.

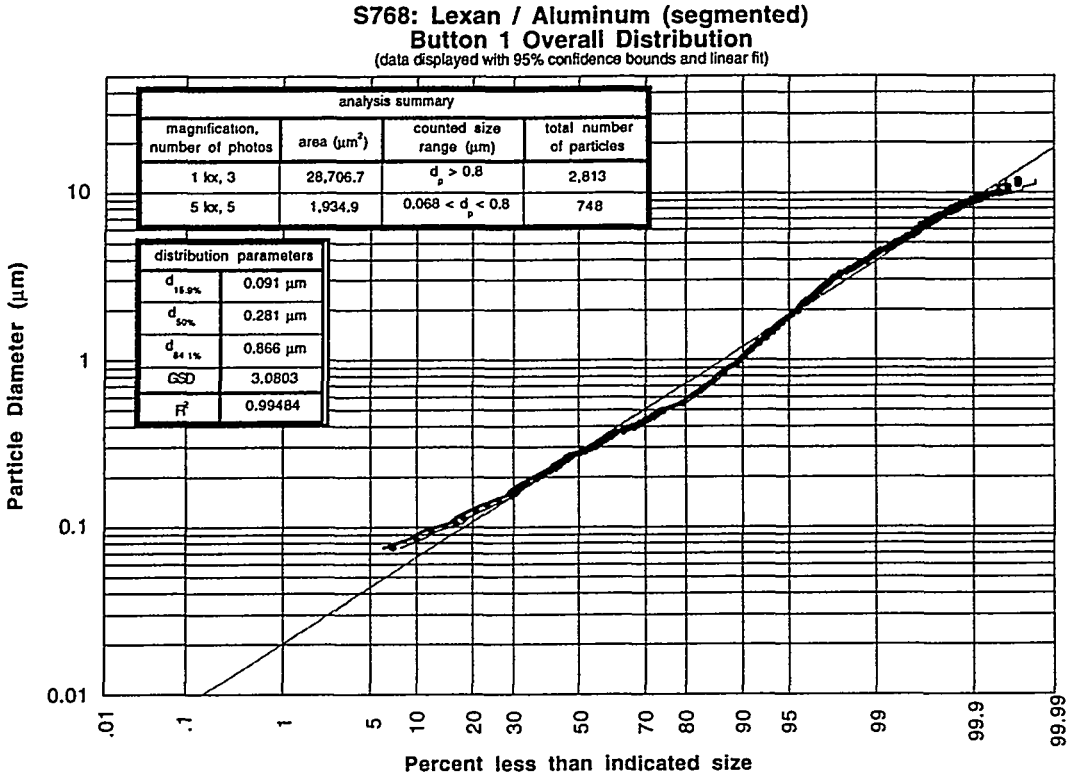

Data Summary Table:

photo	mag	scale (pixel/μm)	size (μm²)	min. d_{eq} (μm)	# of particles	scale factor	KW Test z-value	Overall p-value
768_1_1	5 kx	29.4	23.06x16.77	0.068[a]	211	25	-1.25	0.509
768_1_2	5 kx	29.4	22.96x17.01	0.068[a]	119	25	1.59	
768_1_3	5 kx	29.4	22.96x16.70	0.068[a]	114	25	-0.14	
768_1_4	5 kx	29.4	22.89x16.97	0.068[a]	143	25	0.18	
768_1_5	5 kx	29.4	22.96x16.8	0.068[a]	161	25	-0.09	
768_1_6	1 kx	5.88	115.3x83.33	0.44[b]	1048	1	-0.69	0.081
768_1_7	1 kx	5.88	114.6x83.33	0.44[b]	857	1	2.19	
768_1_8	1 kx	5.88	115.3x82.82	0.44[b]	908	1	-1.44	

a. minimum equivalent diameter particle counted having an area of at least 3.1 x 1/scale on a side.
b. minimum equivalent diameter particle counted having an area of at least 5.1 x 1/scale on a side.

Figure 7.6. Carbon / Aluminum test (S768) button 2 particle size distribution.

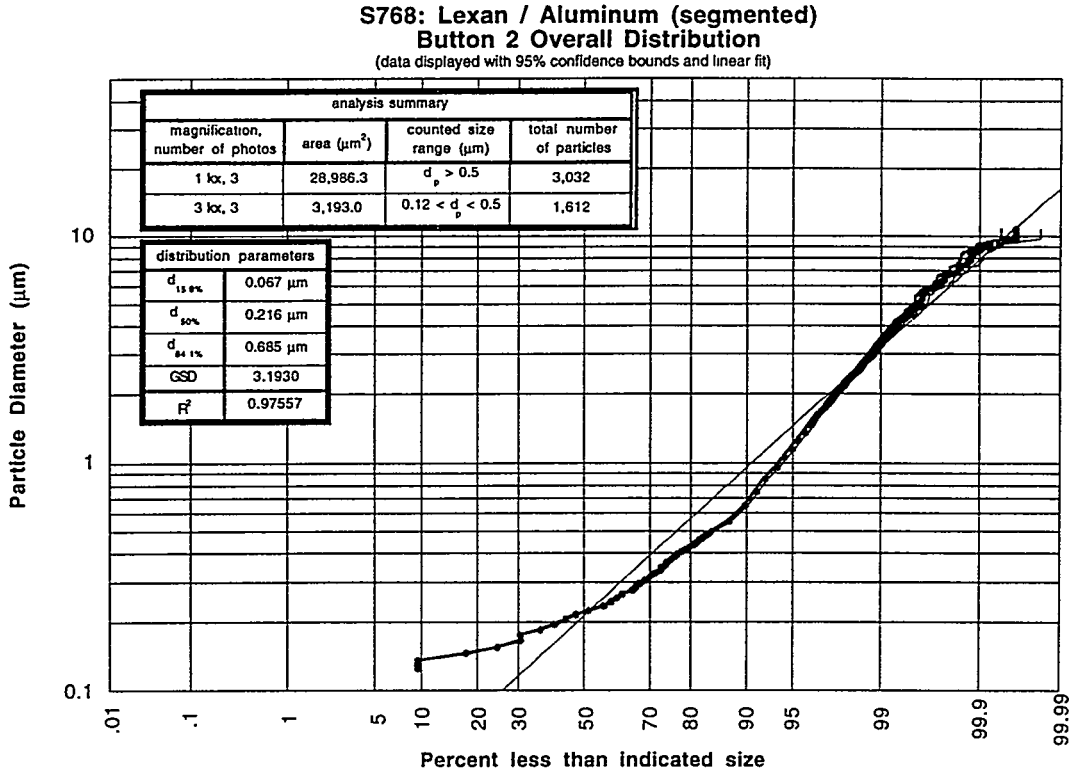

Data Summary Table:

photo	mag	scale (pixel/µm)	size (µm²)	min. d_{eq} (µm)[a]	# of particles	scale factor	KW Test z-value	Overall p-value
768_2_1	3 kx	17.6	38.3x28.07	0.12	584	9	0.52	0.200
768_2_2	3 kx	17.6	38.52x27.5	0.12	644	-	-failed-	
768_2_3	3 kx	17.6	38.47x27.61	0.12	463	9	-1.76	
768_2_4	3 kx	17.6	38.24x27.61	0.12	565	9	1.14	
768_2_5	1 kx	5.88	115.3x84.18	0.34	1165	-	-failed-	0.857
768_2_6	1 kx	5.88	115.0x83.16	0.34	843	1	0.55	
768_2_7	1 kx	5.88	115.7x83.16	0.34	942	1	-0.28	
768_2_8	1 kx	5.88	115.5x84.86	0.34	1247	1	-0.24	

a. minimum equivalent diameter particle counted having an area of at least 3.1 x 1/scale on a side.

Figure 7.7. Carbon / Aluminum test (S768) button 3 particle size distribution.

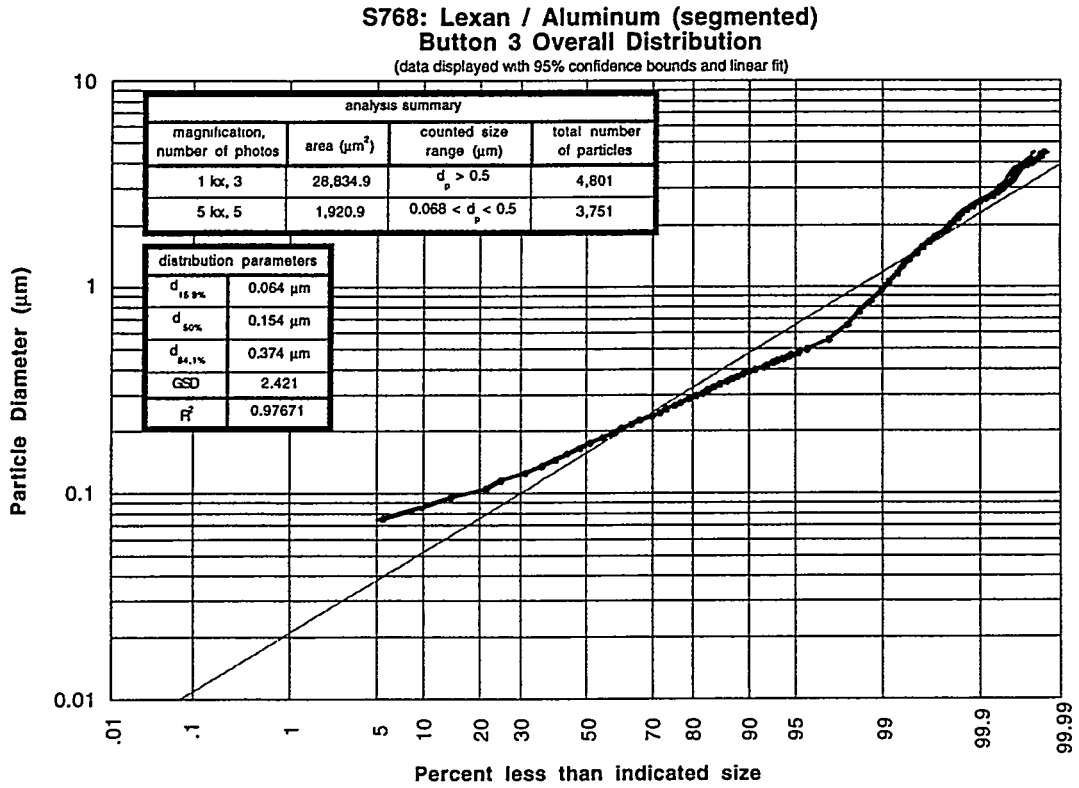

Data Summary Table:

photo	mag	scale (pixel/μm)	size (μm²)	min. d_{eq} (μm)[a]	# of particles	scale factor	KW Test z-value	Overall p-value
768_3_1	5 kx	29.4	22.86x17.01	0.068	650	25	-1.56	0.126
768_3_2	5 kx	29.4	23.10x16.67	0.068	679	25	-0.17	
768_3_3	5 kx	29.4	22.96x16.6	0.068	702	25	1.78	
768_3_4	5 kx	29.4	22.96x16.53	0.068	940	25	1.21	
768_3_5	5 kx	29.4	22.86x16.9	0.068	780	25	-1.38	
768_3_6	1 kx	5.88	113.8x83.67	0.34	1991	1	-0.70	0.196
768_3_7	1 kx	5.88	115.0x84.18	0.34	1579	1	-0.93	
768_3_8	1 kx	5.88	115.1x83.33	0.34	1231	1	1.79	

a. minimum equivalent diameter particle counted having an area of at least 3.1 x 1/scale on a side.

Figure 7.8. Carbon / Aluminum test (S768) button 5 particle size distribution.

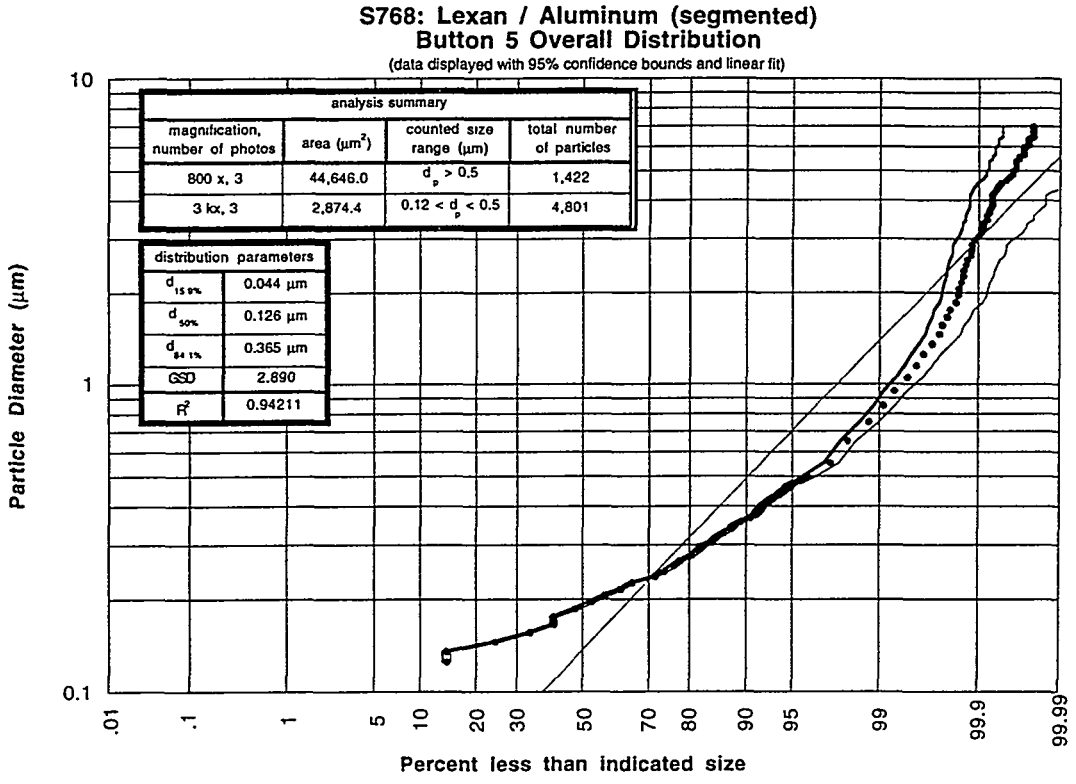

Data Summary Table:

photo	mag	scale (pixel/μm)	size (μm²)	min. d_{eq} (μm)[b]	# of particles	scale factor	KW Test z-value	Overall p-value
768_5_1	3 kx	17.6	38.58x26.65	0.12	1196	14.1	3.02	0.05
768_5_2	3 kx	17.6	38.18x27.84	0.12	405	14.1	-0.94	
768_5_3	3 kx	17.6	38.64x27.39	0.12	383	14.1	-2.78	
768_5_4[a]	800 x	4.72	142.8x103.8	0.42	471	1	-3.48	0.000
768_5_5[a]	800 x	4.72	143.0x103.8	0.42	404	1	3.97	
768_5_6[a]	800 x	4.72	142.8x103.8	0.42	547	1	-0.32	

a. All images obtained at 800x failed the Kruskal-Wallis test (i.e. $p < 0.05$) but were used in generation of the overall size distribution.
b. minimum equivalent diameter particle counted having an area of at least 3.1 x 1/scale on a side.

Figure 7.9. Carbon / Aluminum test (S768) button 9 particle size distribution.

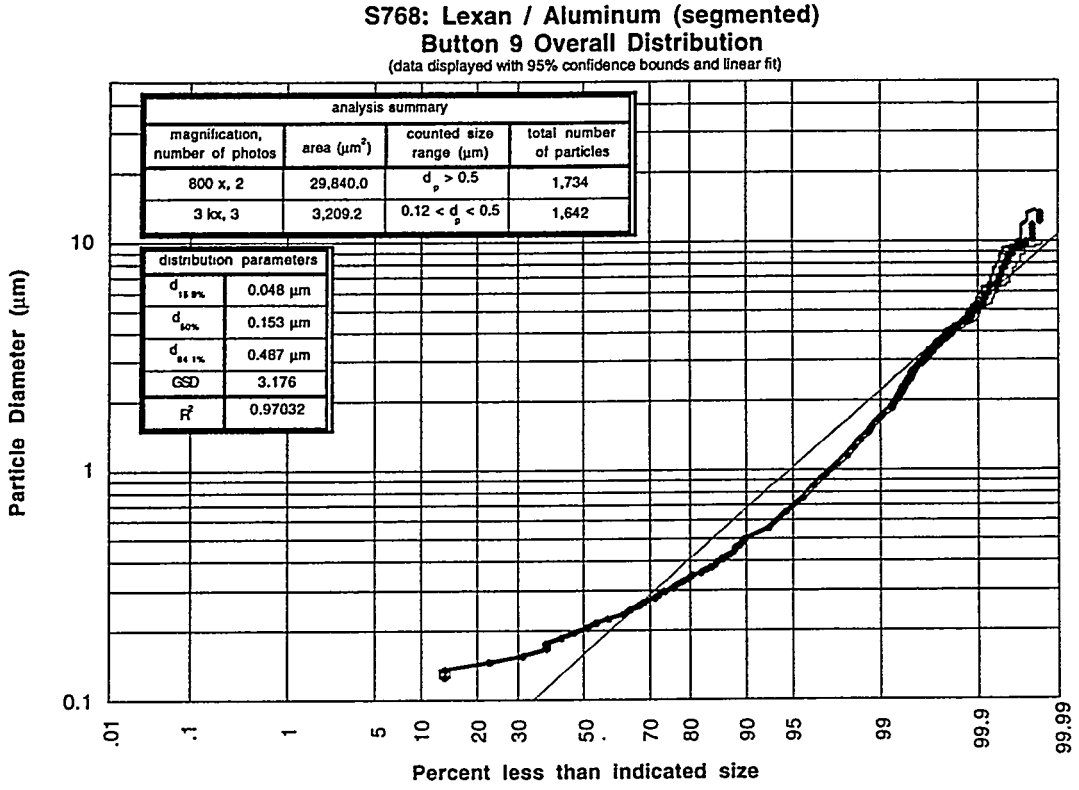

Data Summary Table:

photo	mag	scale (pixel/μm)	size (μm²)	min. d_{eq} (μm)[a]	# of particles	scale factor	KW Test z-value	Overall p-value
768_9_1	3 kx	17.6	38.35x27.61	0.12	370	14.1	-0.81	0.477
768_9_2	3 kx	17.6	38.3x28.12	0.12	527	14.1	1.14	
768_9_3	3 kx	17.6	38.47x27.9	0.12	745	14.1	-0.39	
768_9_4	800 x	4.72	143.0x105.1	0.42	837	1	1.20	0.228
768_9_5	800 x	4.72	143.2x104.0	0.42	1454	-	-failed-	
768_9_6	800 x	4.72	142.4x104.0	0.42	897	1	-1.20	

a. minimum equivalent diameter particle counted having an area of at least 3.1 x 1/scale on a side.

8.0 Conclusion

Carbon-based materials, specifically graphite, are attractive for use as plasma facing components in ITER since the advantages provided by carbon's thermophysical properties are suitable to the harsh conditions present in a fusion reactor. Extending the use of carbon to ITER, however, adds a level of risk in accident scenarios because hazards are associated with the production carbon particulate (i,e. dust) generated from vaporization of exposed surface material. Characterization of such particulate is important for safety analysis. This report presents data relevant to disruption-induced mobilization of carbon and carbon / metal mixtures of materials. Tests were performed with the SIRENS high heat flux facility on Lexan polycarbonate, UTR-22 and ATJ grade graphite, Lexan / copper mixture (two configurations), Lexan / SS316 (two configurations), Lexan / tungsten mixture, and Lexan / aluminum mixture. Particulate produced from each test was collected and analyzed to determine the underlying particle size distribution. Table 8.1 gives a summary of the results obtained from each test.

Several important results were obtained from this experimental campaign. Carbon particles from Lexan and graphite tests were consistently produced in the sub-micron range (~0.1 μm) and displayed shapes that were neither spherical nor large, flat flakes. Tests with graphite carbon produced two distinct particle size groups: one group centered about 0.1 μm and another centered about 10 μm. The larger particles were found only near the end plate of the collection chamber and are possibly the result of severe internal heating and subsequent mechanical failure of the graphite sleeve. Larger particles were also produced in the carbon / metal tests, although their contribution to the overall count population was small. This tended to give CMD's slightly greater than CMD's from the pure carbon tests but much less than CMD's for pure metal tests [3]. Particle shapes were not too different from that found in the carbon tests, although many more spherical particles were observed. Another interesting observation from carbon / metal tests is increased sample sleeve mass loss for both carbon sleeves and metal sleeves when compared to tests with a single material. A reasonable explanation for this synergistic effect has not yet been discovered. Finally, EDXA analysis of particulate collected from the carbon / metal tests indicates constituency to be both carbon and metal species.

In addition to answering questions raised by the results of these experiments, future work in the investigation of disruption-induced particulate mobilization include:

- improved characterization of energy transfer from the electrical discharge to the sample materials in the SIRENS source section
- determination the contribution of a melt layer on a metal sample to particle production
- investigation of particle formation mechanisms responsible for the particulate size distributions observed in these tests
- determination of the significance of these mechanisms to particle production in ITER

Table 8.1. Summary test data and particle size distribution parameters.

	Lexan Test 1 (S760)			Lexan Test 2 (S761)		
Energy (J)	6050			6423		
Lexan Δm (mg/kJ/cm)	0.597			0.676		
	$d_{50\%}$ (μm)	GSD	R^2	$d_{50\%}$ (μm)	GSD	R^2
Button 1	0.069	2.144	0.992	0.073	2.230	0.997
Button 2	*	*	*	*	*	*
Button 3	*	*	*	0.079	2.056	0.997
Button 5	0.166	2.480	0.989	*	*	*
Button 7	*	*	*	*	*	*
Button 9	0.097	2.584	0.994	0.081	1.96	0.987
Button 17	*	*	*	*	*	*

	UTR-22 Graphite Test (S763)			ATJ Graphite Test (s764)		
Energy (J)	7195			7162		
Carbon Δm (mg/kJ/cm)	-destroyed-			-destroyed-		
	$d_{50\%}$ (μm)	GSD	R^2	$d_{50\%}$ (μm)	GSD	R^2
Button 1	0.102	2.330	0.993	0.115	2.130	0.996
Button 2	*	*	*	*	*	*
Button 3	0.114	2.630	0.990	0.086	2.521	0.982
Button 5	*	*	*	0.075	2.970	0.996
Button 7	*	*	*	0.318	2.762	0.980
Button 9	0.096	3.568	0.966	0.544	3.464	0.969
Button 17	*	*	*	*	*	*

	Lexan / Copper Test, Short (S765)			Lexan / Copper Test, segmented (S769)		
Energy (J)	6822			7143		
Copper Δm (mg/kJ/cm)	48.26			23.78		
Lexan Δm (mg/kJ/cm)	1.64			1.75		
	$d_{50\%}$ (μm)	GSD	R^2	$d_{50\%}$ (μm)	GSD	R^2
Button 1	0.123	2.313	0.997	0.356	2.451	0.995
Button 2	*	*	*	0.203	2.173	0.987
Button 3	0.119	2.232	0.995	0.246	2.190	0.993
Button 5	*	*	*	*	*	*
Button 7	*	*	*	*	*	*
Button 9	0.200	2.468	0.989	*	*	*
Button 17	*	*	*	0.353	2.954	0.992

Table 8.1.cont.

	Lexan / SS316 Test, Short (S766)			Lexan / SS316 Test, Segmented (S770)		
Energy (J)	7127			7055		
SS316 Δm (mg/kJ/cm)	25.65			24.36		
Lexan Δm (mg/kJ/cm)	0.975			1.40		
	$d_{50\%}$ (μm)	GSD	R^2	$d_{50\%}$ (μm)	GSD	R^2
Button 1	0.116	2.003	0.996	0.135	2.742	0.993
Button 2	0.116	2.133	0.998	*	*	*
Button 3	0.099	2.141	0.994	0.094	2.445	0.972
Button 5	0.113	1.998	0.997	*	*	*
Button 7	*	*	*	*	*	*
Button 9	0.123	2.533	0.989	0.278	2.465	0.996
Button 17	*	*	*	*	*	*

	Lexan / Tungsten Test (S767)			Lexan / Aluminum Test (S768)		
Energy (J)	7302			7068		
Metal Δm (mg/kJ/cm)	16.85			27.62		
Lexan Δm (mg/kJ/cm)	0.82			1.50		
	$d_{50\%}$ (μm)	GSD	R^2	$d_{50\%}$ (μm)	GSD	R^2
Button 1	0.097	2.028	0.992	0.281	3.080	0.995
Button 2	0.109	2.309	0.984	0.216	3.191	0.976
Button 3	*	*	*	0.154	2.421	0.977
Button 5	0.139	1.927	0.986	0.126	2.890	0.942
Button 7	*	*	*	*	*	*
Button 9	0.121	2.493	0.985	0.153	3.176	0.970
Button 17	*	*	*	*	*	*

Acknowledgments and Disclaimer

Sincere appreciation goes out to the Fusion Safety Program at the INEEL, specifically Kathryn A. McCarthy, David A. Petti, Galen R. Smolik, and William J. Carmack. This work is supported by US DOE, Director of Energy Research, Office of Fusion Energy, under grant C87-101407 task 007 and UCSD ITER 10112833.

This report is an account of work assigned to the U.S. Home Team under Task Agreement No. S81TT08 within the Agreement among the European Atomic Energy Community, the Government of Japan, the Government of the Russian Federation, and the Government of the United States of America on Cooperation in the Engineering Design Activities for the International Thermonuclear Experimental Reactor ("ITER EDA Agreement") under the auspices of the International Atomic Agency (IAEA). The report has not been reviewed by the ITER Publications Office.

References

[1] K. A. McCarthy, D. A. Petti, W. J. Carmack, and G. R. Smolik, "The Safety Implications of Tokamak Dust Size and Surface Area" presented at the Fourth International Symposium on Fusion Nuclear Technology, Tokyo, Japan, April 7-11, 1997, accepted for publication in *Fusion Engineering and Design.*

[2] Sharpe, J.P., M. Bourham, "Scoping of SIRENS for Wall Vaporization Studies," EDF No.: ITER/US/97/TE/SA-14, June, 1997.

[3] Sharpe, J.P., M. Bourham, "Characterization of Disruption-Induced Particulate from ITER-Relevant Materials," EDF No.: ITER/US/97/TE/SA-21, November, 1997.

[4] Carmack, W.J., et al., "DIII-D Dust Particulate Characterization," EDF No.: ITER/US/97/TE/SA-8, March 1997.

[5] R. Little, A. Costley, G. Federici, F. Heckendorn, S. J. Piet, "Minutes of the 1997 Dust Coordination Meeting," S 81 MI 16 07-06-18 R 0.2, July 2, 1997.

[6] Carmack, W.J., et al., "Analysis and Characterization of TFTR Tokamak Dust," EDF No.: ITER/US/98/TE/SA-8, April 30 1998.

Appendix: Associated paper presented at 1998 ANS Fusion Topical Meeting:

Sharpe, et al., "Generation and Characterization of Carbon Particulate in Disruption Simulations," presented at the ANS Thirteenth Topical Meeting on the Technology of Fusion Energy, Nashville, TN, June 7-11, 1998, to be published in *Fusion Technology.*

Presented at the Thirteenth Topical Meeting on the Technology of Fusion Energy
June 7-11, 1998, Nashville, TN

GENERATION AND CHARACTERIZATION OF CARBON PARTICULATE IN DISRUPTION SIMULATIONS*

J.P. Sharpe, M. Bourham, J.G. Gilligan
Department of Nuclear Engineering
North Carolina State University
P.O. Box 7909
Raleigh, NC 27695-7909
(919) 515-2301

ABSTRACT

The SIRENS high heat flux facility at NCSU has been used to generate particulate representative of material mobilized during a hard disruption in a fusion reactor. The electrothermal (ET) plasma source in SIRENS has been found to be suitable for disruption simulation. Particulate generation occurs in both the fusion reactor and the ET source as material mobilized from the plasma-surface interface expands into a large volume. The response of carbon-based material and carbon/metal mixtures to disruption simulation in SIRENS has been studied and the resulting particle size data are presented in this paper. Specific materials investigated include Lexan polycarbonate, graphite grades UTR-22 and ATJ, and combinations of Lexan with each copper, stainless steel 316, tungsten, and aluminum.

I. INTRODUCTION

Plasma-facing material in future tokamak reactors will be subject to intense heat loading during hard disruptions, causing severe erosion of exposed surfaces and shortening of component lifetime. The International Thermonuclear Experimental Reactor (ITER), for example, has the potential for disruption heat loads up to 100 MJ/m^2 upon the divertor area over a 10 ms time period. Candidate materials potentially in contact with plasma during disruptions must have favorable thermophysical properties to withstand extreme heat loading. With acceptable heat capacity, thermal conductivity, sublimation enthalpy, and low atomic number, carbon graphite is often used for plasma-facing surfaces in present tokamaks.

Carbon particulate (dust) generated from vaporization during a disruption is a concern because of tritium retention within the dust. If a release pathway is present, the tritiated dust will contribute to the radiological source term of the accident scenario. Another concern with the presence of carbon dust is the effects of chemical reactivity- specifically hydrogen production in a steam ingress accident. In order to quantify each of these concerns in a defensible safety analysis, physical properties of the generated carbon particulate must be well known[1]. Experimental investigation is required in a device that is capable of simulating heat loads on the order of those expected in hard disruptions.

One technique for disruption simulation and subsequent particle formation involves the use of an electrothermal (ET) plasma source. The ET facility SIRENS at North Carolina State University has been modified to study disruption-induced aerosol mobilization for ITER relevant materials[2]. Electrothermal plasma sources have been used to simulate disruptions because magnitudes and physical mechanisms of heat transfer in the ET source are similar to those in a tokamak disruption. Changes to the SIRENS facility have allowed experiments in which material is mobilized within the narrow ET source and expanded into a large chamber. This expansion generates particulate in a fashion similar to that from hard disruptions expected in ITER.

A series of experiments have been performed with SIRENS to simulate the erosion and mobilization effects of carbon-based materials exposed to hard disruption conditions. Specifically, size distributions have been produced for particulate generated by exposing carbon and carbon/metal surfaces to heat fluxes on the order of 6 MJ/m^2 for 80 μs. This paper presents particle size distributions obtained from testing polycarbonate (Lexan) and graphitic carbon (grades UTR-22 and ATJ), as well as Lexan-carbon and metal combinations with each copper,

* Work supported by the US Department of Energy, Office of Energy Research, under grant DE-FG02-96ER54363.

stainless steel 316 (SS316), tungsten, and aluminum (for beryllium simulation). A general discussion of the experimental procedure is first given, followed by separate discussions on each material or combination tested, and concluded with a summary of overall observations.

II. EXPERIMENTAL PROCEDURE

The experimental configuration used to investigate disruption-induced mobilization of carbon-based materials follows that described in [2]. Optimal configuration for particulate generation requires placement of the sample material within the SIRENS plasma source section. To this end, sample material was fabricated into a cylindrical sleeve of 0.397 cm ID, 0.714 cm OD, and a length specified by application, and placed into a Lexan inner insulator of 0.714 cm ID and 11.8 cm length. These components are placed in a Lexan outer insulator and then into a SS304 anode housing, which is bolted to a large vacuum chamber and connected to a pulse power delivery system. This entire assembly is referred to as the SIRENS source section. High heat flux exposure to the inner surface of the sample material is achieved by drawing an intense electrical arc between the point cathode and annular anode, separated by a length of 8.8 cm. Similar to the expected response of an exposed surface in an ITER disruption, radiant energy deposited on the sample surface mobilizes material by ablation, vaporization, and possibly melting; this mobilized mass flows from the open end of the source section into a large glass expansion cell (cylindrical chamber of 17.8 cm ID, 76.2 cm length). Cooling of the vapor during expansion allows particle formation and growth. This particulate is transported to the wall of the expansion cell and is intercepted at discrete locations by circular collection substrates (buttons). Following the test, buttons are removed, weighed for relative mass gain, and observed under high magnification of a scanning electron microscope (SEM). Photographic images of a button's surface are obtained and the particles are sized and counted from these images, generating the particulate size frequencies for that button[2]. These measured frequencies are then fitted to the log-normal distribution. The reported values are the fitted size distribution parameters: count median diameter (CMD), geometric standard deviation (GSD), and linear correlation coefficient (R^2).

Successful generation of carbon particulate required utilizing various configurations in the placement, or "stacking order", of test material within the inner insulator. Tests with Lexan-only sleeves were performed with the entire exposed length (8.8 cm) consisting of Lexan. For graphite, a series of tests was performed with different configurations to find a stacking order that generates a sufficient amount of particulate. Difficulties encountered in the graphite tests will be discussed in Section III. These difficulties influenced the selection of Lexan for carbon/metal mixture tests. Using Lexan as the carbon-based material in these tests is justifiable given that sufficient heat flux is available to completely dissociate the polycarbonate into its elemental constituents. Atomic and molecular hydrogen, oxygen (H, H_2, O and O_2), and potentially molecular methane (CH_4) are non-condensables that have little impact on particle formation of the dominant condensable species, i.e. carbon. Water vapor is unlikely to form into an appreciable amount because of the stoichiometic balance of H and O. Two primary configurations were used in the carbon/metal mixture tests: a "short" configuration test to characterize the particles formed when the condensing species is predominately carbon, and a "segmented" configuration test to characterize particles formed from roughly equivalent surface areas of carbon and metal exposed to a high heat flux. The short configuration consists of a 1 cm length of metal surrounded by two Lexan sleeves 3 cm and 3.5 cm in length. The segmented configuration is made of three sets of Lexan/metal pairs with each component 1.0 cm in length, giving a total exposed length of 6.0 cm. Figure 1 depicts both configurations.

Relative position of collection buttons on the expansion chamber inside wall are given in Table 1. Buttons were constructed from 0.5 in. (1.27 cm) diameter glass slides 0.1 mm thick mounted onto an equivalent diameter washer (for structural support). Note the non-conductive nature of the glass required a 200 nm layer of sputtered gold coating of the button surface for analysis in the SEM. This coating process was shown not to affect particle size analysis.

Figure 1. Carbon/metal test sleeve configurations.

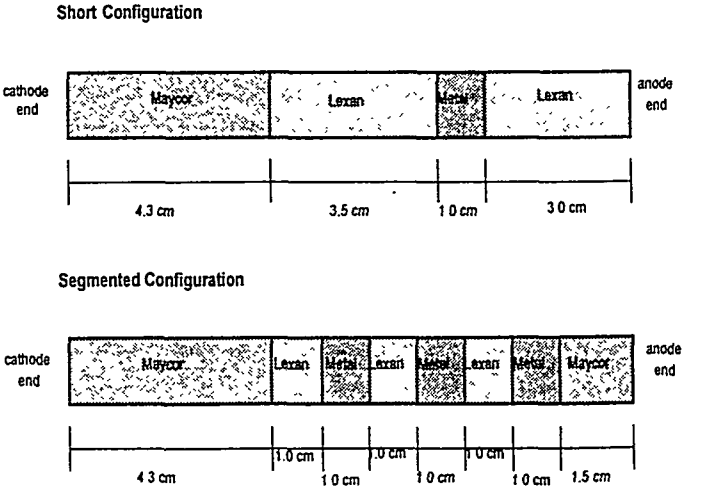

Table 1. Collection Button Locations

Button number	Axial distance from source (cm)	Azimuth angle (deg.)*
1	12.7	0
2	12.7	180
3	31.75	45
4	31.75	225
5	50.8	90
7	69.9	135
	End-plate at 73.66 cm radius (cm)	angle (deg.)**
9	3.0	0
17	4.5	224

* chamber top aligned to 0°
** end-plate 90° aligned to chamber 0°

III. CARBON RESULTS

Two different types of carbon-based material have been used in SIRENS to produce particulate: Lexan polycarbonate and graphitic carbon. Lexan is often employed as the ablative surface in ET devices. It is known to produce significant quantities of soot composed of carbon particulate. This soot is generated from Lexan by mechanisms similar to those that generate dust from graphite exposed to disruption heat loads. Therefore particulate produced from Lexan is of interest for the purpose of comparison with that produced by graphite, and because Lexan is a convenient substitute when graphite cannot be used, as with the carbon/metal tests.

A. Lexan Polycarbonate

Two independent tests were performed in SIRENS using Lexan as the carbon-based material. Table 2 displays total discharge energy, sample mass loss Δm, and particle size distribution parameters for each test. Sample mass loss has been scaled to total discharge energy and total exposed length of material (e.g. for S760, 31.77 mg / 6.050 kJ / 8.8 cm = 0.597 mg/kJ/cm). Button mass increase from deposited carbon soot was negligible.

Particle size distribution analysis followed the methodology developed by Carmack, et. al [3]. Analysis for particle size distribution was performed on buttons 1, 3, and 9 for S760 and buttons 1, 5, and 9 for S761. These buttons sufficiently represent different locations for collection available in the expansion chamber. Although the mass of deposited material was negligible, button surfaces displayed a large number of particles when viewed in the SEM. Figure 2 shows the resulting particle size distribution found for button 1 of S760. An important result is that generally for the Lexan tests the data are reasonably well represented by a log-normal distribution, as reflected in the values of R^2.

B. Graphite Carbon

Particulate production from graphitized carbon was investigated with two different grades: UTR-22 and ATJ. Generating sufficient quantities of particulate required electrical discharges of ~7 kJ, and because graphite is electrically conductive, source section configuration was slightly modified from that used for the Lexan tests. Following a series of exploratory tests, the most useful configuration placed short graphite sleeves near the exit of the source section.

Table 3 gives a summary of important parameters from the graphite tests. Mass loss from the graphite sleeves was unobtainable because they were destroyed during the discharge. This likely resulted from a current path developing within the conductive graphite at some point during the discharge. Resistive energy dissipation within the sample caused intense internal heating and vaporization, resulting in mechanical failure of the material. In fact, particulate collected near the end of the expansion chamber (buttons 7 and 9) for the ATJ graphite test appeared to consist of two general particle groups: very fine particles (~0.1 μm) possibly associated with vaporized material and very large particles (~10+ μm) resulting from the fragmentation of solid graphite grains. A similar observation was made by a Russian group in their plasma disruption simulator tests[4]. Figure 3 displays the particle size distribution for button 9 of S764 (with ATJ graphite). There is an apparent shift in the center of the distribution when compared to particulate collected much closer to the exit of the source section. A log-probability plot (part b of the figure) also shows the overall shape is not well represented by a log-normal distribution.

Size distributions for particulate collected close to the source exit of the ATJ test and particulate collected from the UTR-22 test reasonably compare to results of the Lexan tests. Average CMD for the Lexan tests was 0.094 ± 0.033 μm and the graphite tests (excluding buttons 7 and 9 of the ATJ test) gave 0.098 ± 0.014 μm as the average CMD. An SEM micrograph from ATJ test button 3 is shown in Figure 4, indicating the general size and shape of particles collected from the graphite tests. Although a few particles from the larger group are present, the population is dominated by the number of particles in the smaller group. Larger particles are represented in the resulting size distributions by increased values of GSD. This accounts for the greater GSD values from the graphite tests compared those from the Lexan tests.

Table 2. Lexan Carbon Test Summary

	Lexan Test 1 (S760)			Lexan Test 2 (S760)		
Energy Δm	6050 J 0.597 mg/kJ/cm			6423 J 0.676 mg/kJ/cm		
Button	CMD (μm)	GSD	R^2	CMD (μm)	GSD	R^2
1	0.069	2.14	0.992	0.073	2.23	0.997
3	-	-	-	0.079	2.06	0.997
5	0.166	2.48	0.989	-	-	-
9	0.097	2.58	0.994	0.081	1.96	0.987
	Test 1 Average CMD: 0.111±0.041 μm			Test 2 Average CMD: 0.077± 0.034 μm		
Overall Lexan CMD: 0.094±0.033 μm						

Table 3. Graphite Carbon Test Summary

	UTR-22 Test (S763)			ATJ Test (S764)		
Energy Δm	7195 J -sample destroyed-			7162 J -sample destroyed-		
Button	CMD (μm)	GSD	R^2	CMD (μm)	GSD	R^2
1	0.102	2.33	0.993	0.115	2.13	0.996
3	0.114	2.63	0.990	0.086	2.52	0.982
5	-	-	-	0.075	2.97	0.996
7	-	-	-	0.318	2.76	0.969
9	0.096	3.57	0.966	0.544	3.464	0.969
	UTR-22 Average CMD: 0.104±0.008 μm			ATJ Average CMD: 0.228± 0.181 μm		
Overall Graphite CMD*: 0.098±0.014 μm						

* Excludes data from ATJ Test buttons 7 and 9.

Figure 2. Particle size distribution for S760 Button 1.

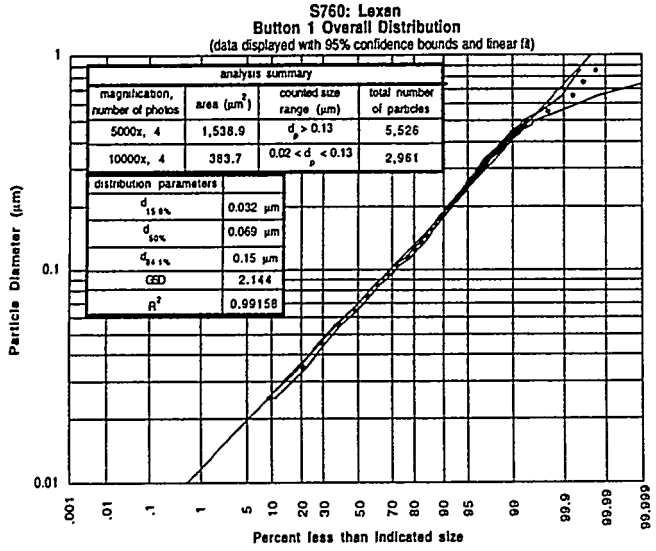

Figure 3. Particle size distribution for S764 Button 9.

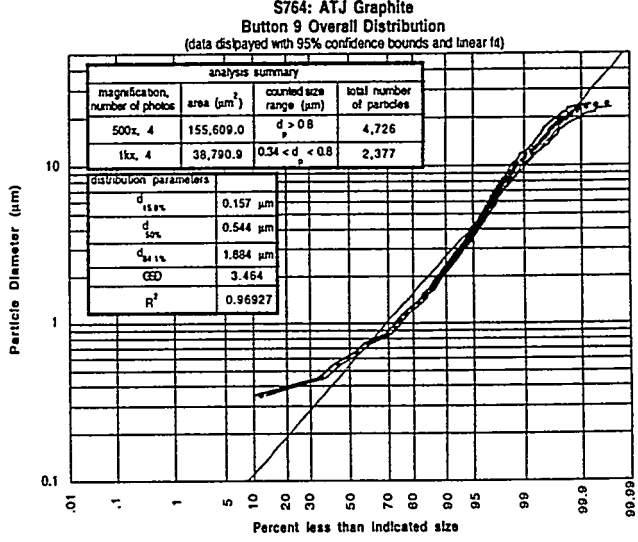

Figure 4. SEM micrograph of carbon particles from the ATJ graphite test (S764, button 3).

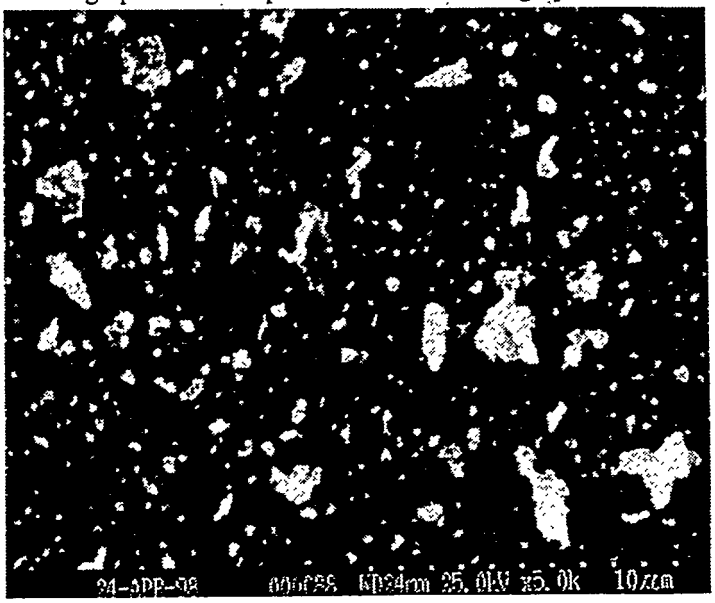

IV. CARBON / COPPER MIXTURE RESULTS

Particle formation in the presence of two or more condensing species is of interest because several different materials are present in the interior of a fusion reactor's vacuum vessel which may be exposed to heat loading and vaporization during disruptions. To investigate this situation, several tests have been performed in SIRENS with multiple materials placed in the source section and exposed to the high intensity arc. The first of these tests involved a mixture of Lexan and copper. Lexan was chosen as the carbon-based material because of its convenience of use in the source section and the resulting carbon particles from the Lexan tests were of similar size and shape as the particles generated in the graphite tests.

Two different source section configurations, short and segmented, were tested with the Lexan-carbon/copper mixture. Table 4 gives a summary of both tests. Sample Δm of the Lexan for each test was greater than that found in tests with only Lexan in the source section (1.64 and 1.75 mg/kJ/cm versus 0.6 mg/kJ/cm). Total copper mass loss from the short configuration test (S765) was much greater than that from the segmented test. A reasonable explanation for this has yet to be discovered, and more tests should be performed. Size distributions generated for particulate collected from the short configuration test have an average CMD (0.147 μm) slightly larger than that of the carbon-only tests (0.096 μm), indicating a small impact from the copper on overall particle size. Increasing the amount of copper in the source section, however, does have a noticeable effect on the resulting size distributions, as found in the results from the segmented configuration test. Here the CMD's are roughly a factor of 3 larger than for the short configuration and carbon-only tests (average CMD of 0.29 μm vs. 0.096 μm).

Table 4. C / Cu Test Summary

	Short Config. (S765)			Segmented Config. (S769)		
Energy	6822 J			7143 J		
C Δm	1.64 mg/kJ/cm			1.75 mg/kJ/cm		
Cu Δm	48.26 mg/kJ/cm			23.78 mg/kJ/cm		
Button	CMD (μm)	GSD	R^2	CMD (μm)	GSD	R^2
1	0.123	2.31	0.997	0.356	2.45	0.995
2	-	-	-	0.203	2.17	0.987
3	0.119	2.23	0.995	0.246	2.19	0.993
9	0.200	2.47	0.989	-	-	-
17	-	-	-	0.353	2.95	0.992
	Short Average CMD: 0.147±0.037 μm			Segmented Average CMD: 0.290± 0.067 μm		

V. CARBON / SS316 MIXTURE RESULTS

The intended use of stainless steel type 316 (SS316) for many internal components of the ITER vacuum vessel makes this material important in an investigation of disruption-induced mobilization and safety analysis. Testing in SIRENS of Lexan carbon and SS316 has been done in both the short and segmented source section configurations. Table 5 shows test energy, sample mass loss, and size distribution parameters for the two tests. As with the carbon/copper tests, sample Δm of the Lexan carbon was greater than the mass loss found from tests with Lexan-only sleeves. Unlike the carbon/copper tests, however, the metal (SS316) mass loss for both short and segmented configurations match. Size distributions generated from collected particulate of the short configuration test (S766) are close to those found in the Lexan and graphite carbon tests. Particulate collected from the segmented configuration test have CMD values close to the carbon-only tests, but the GSD values are higher because of the contribution of large particles associated with the SS316 metal. The mechanism leading to the formation of these large particles has not yet been uncovered.

Table 5. Lexan-C / SS316 Test Summary

	Short Config. (S766)			Segmented Config. (S770)		
Energy	7127 J			7055 J		
C Δm	0.975 mg/kJ/cm			1.40 mg/kJ/cm		
S316 Δm	25.65 mg/kJ/cm			24.36 mg/kJ/cm		
Button	CMD (μm)	GSD	R^2	CMD (μm)	GSD	R^2
1	0.116	2.00	0.996	0.135	2.74	0.993
2	0.116	2.13	0.998	-	-	-
3	0.099	2.14	0.994	0.094	2.45	0.972
5	0.113	1.20	0.997	-	-	-
9	0.123	2.53	0.989	0.278	2.50	0.996
	Short Average CMD: 0.113±0.008 μm			Segmented Average CMD: 0.169± 0.079 μm		

VI. CARBON / TUNGSTEN MIXTURE RESULTS

Another material of interest in disruption-induced mobilization studies is tungsten. A single test, S767, has been performed in SIRENS with Lexan carbon and tungsten sleeves placed in the source section. The configuration used for this test was different from the short and segmented configurations of the other carbon/metal tests because only one sample sleeve length of tungsten was available (3.0 cm). The tested configuration consisted of sample sleeves in the lengths (ordered from cathode to anode ends): 4.3 cm Maycor insulator, 3.0 cm Lexan, 3.0 cm tungsten, and 1.5 cm length Maycor. Table 6 contains a summary of test

Table 6. Lexan-C / W and Lexan-C / Al Test Summaries

	C/W Test (S767)			C/Al Test (S768)		
Energy	7302 J			7068 J		
C Δm	0.82 mg/kJ/cm			1.50 mg/kJ/cm		
metal Δm	16.85 mg/kJ/cm			27.62 mg/kJ/cm		
Button	CMD (μm)	GSD	R^2	CMD (μm)	GSD	R^2
1	0.097	2.03	0.992	0.281	3.08	0.995
2	0.109	2.31	0.984	0.216	3.19	0.976
3	-	-	-	0.154	2.42	0.977
5	0.139	1.93	0.986	0.126	2.89	0.942
9	0.121	2.49	0.985	0.153	3.176	0.970
	C/W Average CMD: 0.117±0.015 μm			C/Al Average CMD: 0.186± 0.056 μm		

results. Lexan sample mass loss (0.82 mg/kJ/cm) was less than values from the other carbon/metal tests, but agrees well with the mass loss from Lexan-only tests. Sample Δm of the tungsten sleeve was also lower than that found in other carbon/metal tests. Size distribution parameters of collected particulate match reasonably well with particulate from Lexan and graphite tests, possibly indicating that tungsten has an insignificant effect on particle formation.

VII. CARBON / ALUMINUM MIXTURE RESULTS

The final carbon/metal combination investigated in SIRENS was Lexan carbon and aluminum. Interest in aluminum results from the metal's thermophysical properties being close in value to those of beryllium, another material used in the current ITER design. Because of difficulty in working with beryllium, aluminum has been used to simulate the thermal response of the low density, low melting point material when exposed to high heat flux. A single Lexan carbon and aluminum test (S768) was performed in SIRENS with sample material placed in the segmented source section configuration. Table 6 contains resulting mass loss and particle size data. Lexan carbon sample Δm matches Lexan mass loss from the other carbon/metal tests and aluminum sample Δm is slightly higher. Size distribution parameters reflect the contribution large particles to the overall population. CMD and GSD values are greater than those from Lexan and graphite carbon, similar to the carbon/copper and carbon/SS316 segmented configuration tests. An investigation to discover the mechanisms responsible for this result is presently underway.

VIII. CONCLUSION

Disruption simulation tests have been performed with the SIRENS high heat flux facility on Lexan carbon, grades UTR-22 and ATJ graphitic carbon, and carbon/metal mixtures with Lexan carbon and each copper, SS316, tungsten, and aluminum. Particulate produced from each test was collected and analyzed to determine the underlying particle size distribution. Lexan and graphite carbon tests generated particles with comparable size distributions. Short configuration tests with Lexan carbon and metals generated particulate with CMD's slightly greater than those of carbon-only tests, although GSD's of the mixture tests were greater due to contribution of large particles. Segmented configuration tests generally displayed greater difference from the carbon-only tests, again reflecting the role of larger particles in the overall distribution.

ACKNOWLEDGMENTS

Sincere appreciation goes out to the Fusion Safety Program at the INEEL, specifically Kathryn A. McCarthy, David A. Petti, Galen R. Smolik, and William J. Carmack. Thanks also to K. Verghese and Doug Peplow for useful discussion. This work is supported by US DOE, Office of Fusion Energy, under grant DE-FG02-96ER54363.

DISCLAIMER

REFERENCES

[1] K. A. McCarthy, D. A. Petti, W. J. Carmack, and G. R. Smolik, "The Safety Implications of Tokamak Dust Size and Surface Area" presented at the Fourth International Symposium on Fusion Nuclear Technology, Tokyo, Japan, April 7-11, 1997, accepted for publication in *Fusion Engineering and Design.*

[2] Sharpe, J.P, et al., "Experimental Investigation Into Aerosol Mobilization Resulting from Fusion Reactor Disruptions," *Fusion Technology*, vol. 30, pp.1424-1428, November 1996.

[3] Carmack, W.J., et al., "DIII-D Dust Particulate Characterization," ITER EDF No. ITER/US/97/TE/SA-8, March 1997.

[4] R. Little, A. Costley, G. Federici, F. Heckendorn, S. J. Piet, "Minutes of the 1997 Dust Coordination Meeting," S 81 MI 16 07-06-18 R 0.2, July 2, 1997.